Idaho National Engineering and Environmental Laboratory

INEEL/EXT-02-00589
Volume 2
Revision 2.2
October 2003

SCDAP/RELAP5-3D© CODE MANUAL

VOLUME 2: MODELING OF REACTOR CORE AND VESSEL BEHAVIOR DURING SEVERE ACCIDENTS

SCDAP/RELAP5-3D© Code Development Team

BECHTEL BWXT IDAHO, LLC

INEEL/EXT-02-00589
Volume 2
Revision 2.2

SCDAP/RELAP5-3D© CODE MANUAL VOLUME 2: MODELING OF REACTOR CORE AND VESSEL BEHAVIOR DURING SEVERE ACCIDENTS

SCDAP/RELAP5-3D© Code Development Team

October 2003

Idaho National Engineering and Environmental Laboratory
BECHTEL BWXT IDAHO, LLC
Idaho Falls, Idaho 83415

Prepared Under DOE Contract No. DE-AC07-99ID13737

ABSTRACT

The SCDAP/RELAP5-3D© code has been developed for best-estimate transient simulation of light water reactor coolant systems during a severe accident. The code models the coupled behavior of the reactor coolant system and reactor core during severe accidents as well as large and small break loss-of-coolant accidents, operational transients such as anticipated transient without SCRAM, loss of offsite power, loss of feedwater, and loss of flow. The coolant system behavior is calculated using a two-phase model allowing for unequal temperatures and velocities of the two phases of the fluid, and the flow of fluid through porous debris and around blockages caused by reactor core damage. The reactor core behavior is calculated using models for the ballooning and oxidation of fuel rods, the meltdown of fuel rods and control rods, fission product release, and debris formation. The code also calculates the heatup and structural damage of the lower head of the reactor vessel resulting from the slumping of reactor core material. A generic modeling approach is used that permits as much of a particular system to be modeled as necessary. Control system and secondary system components are included to permit modeling of plant controls, turbines, condensers, and secondary feedwater conditioning systems.

This volume contains detailed descriptions of the severe accident models and correlations. It provides the user with the underlying assumptions and simplifications used to generate and implement the basic equations into the code, so an intelligent assessment of the applicability and accuracy of the resulting calculation can be made.

CONTENTS

ABSTRACT 1-iii

EXECUTIVE SUMMARY 1-xvii

ACRONYMS 1-xix

1. INTRODUCTION 1-1
   - 1.1 General Code Capabilities 1-1
   - 1.2 Relationship to Other Software 1-2
   - 1.3 Quality Assurance 1-3
   - 1.4 Organization of the SCDAP/RELAP5-3D$^{©}$ Manuals 1-3
   - 1.5 Organization of Volume 2 1-3
   - 1.6 References 1-4

2. HEAT CONDUCTION MODEL FOR CORE COMPONENTS 2-1
   - 2.1 Two-Dimensional Heat Conduction Governing Equation 2-1
   - 2.2 Finite Difference 2-1
   - 2.3 The Alternating Direction Method 2-3
   - 2.4 Matrix Methods 2-4
   - 2.5 OECR Algorithm 2-6
   - 2.6 Volume Averaging 2-6
   - 2.7 Temperature Jump Due to Contact with Slumped Material 2-7
   - 2.8 Reference 2-8

3. MATERIAL OXIDATION MODEL 3-1
   - 3.1 Integral Diffusion Model 3-1
     - 3.1.1 Introduction 3-1
     - 3.1.2 Oxygen Diffusion 3-2
     - 3.1.3 Hydrogen Uptake in Cladding 3-12
     - 3.1.4 Cladding Embrittlement and Hydrogen Release 3-18
   - 3.2 Approximations to Modeling of Oxidation During Meltdown and Reflood 3-24
     - 3.2.1 Affect on Oxidation of Melting of Cladding and Dissolution of UO_2. 3-24
     - 3.2.2 Affect of slumping of cladding on oxidation 3-26
     - 3.2.3 Affect of reflood on oxidation 3-30
     - 3.2.4 Affect of cladding rupture on oxidation 3-31
   - 3.3 Parabolic Kinetics Model for Oxidation of Control Rods 3-32
   - 3.4 References 3-35

4. FUEL ROD MODELS 4-1
   - 4.1 Electrical Heat Generation Model for Fuel Rod Component 4-1

4.2 Fission Product Release Models 4-2
4.2.1 Release Model for Intact Fuel 4-2
4.2.2 Release During UO2 Liquefaction and Fragmentation 4-8
4.2.3 Enthalpy of Released Gases 4-8
4.3 Decay Heat Reduction Due to Fission Product Release 4-11
4.3.1 Fission Product Decay Heat Methodology 4-11
4.3.2 Fission Product Decay Heat Model Results 4-12
4.4 Fuel State Models 4-14
4.5 Fuel Rod Cladding Deformation Model 4-15
4.6 Fuel Rod Internal Gas Pressure Model 4-20
4.7 Liquefaction and Slumping of Fuel Rod Cladding 4-21
4.7.1 Relocation of Melted Cladding in Circumferential Direction 4-22
4.7.2 Amount of Fuel Dissolved by Melted Metallic Portion of Cladding 4-25
4.7.3 Structural Failure of Oxide Layer Retaining Melted Metallic Cladding 4-26
4.7.4 Distance of Slumping of Melted Cladding 4-28
4.8 Liquefaction of Fuel Rod Cladding at Location of Inconel Grid Spacer 4-34
4.8.1 Impact of Grid Spacers on Damage Progression 4-35
4.8.2 Liquefaction of Cladding at Location of Grid Spacers 4-36
4.9 References 4-49
5. MODELS FOR CONTROL RODS, CONTROL BLADES, SHROUDS AND REFLECTORS 5-1
5.1 Ag-In-Cd Control Rod Models 5-1
5.1.1 Control Rod Material Interaction 5-1
5.2 BWR B4C Control Blade and Channel Box Component Model 5-3
5.2.1 Nodal Geometry 5-3
5.2.2 Energy/Conduction Equation 5-5
5.2.3 Melting and Material Interaction Models 5-6
5.2.4 Relocation/Solidification Models 5-7
5.2.5 Oxidation Models 5-7
5.2.6 Stainless Steel 5-8
5.2.9 Radiation Models 5-9
5.2.10 Hydrodynamic Models 5-9
5.3 Simplified B_4C Control Rod Model 5-10
5.3.1 Model Description 5-11
5.3.2 Oxidation 5-12
5.3.3 Temperature Response 5-14
5.3.4 Melting and Relocation 5-17
5.3.5 Slumping 5-18
5.4 Shroud/Reflector Model 5-19
5.4.1 Model Description 5-19
5.4.2 Oxidation 5-19

5.4.3 Melting and Relocation 5-20

5.5 References 5-20

6. RADIATION HEAT TRANSFER MODEL 6-1

6.1 Radiation Model Governing Equations 6-1
6.1.1 View Factors 6-7
6.1.2 Mean Path Length 6-13
6.1.3 Absorptivities and Emissivities 6-13

6.2 References 6-17

7. UPPER PLENUM STRUCTURES AND LOWER CORE PLATE 7-1

7.1 Upper Plenum Structures and Lower Core Plate 7-1

7.1.1 Nodal Geometry 7-1
7.1.2 Energy/Conduction Equation with Melting 7-2
7.1.3 Relocation and Solidification Logic 7-4
7.1.4 Oxidation of Stainless Steel 7-6
7.1.5 Hydrodynamic Interface 7-7

7.2 Lower Core Plate 7-8

7.2.1 Debris Interaction With Core Plate 7-8
7.2.2 Heat Transfer 7-8
7.2.3 Debris Interaction During Core Plate Penetration 7-11

7.3 References 7-13

8. HEATUP OF LOWER HEAD BY SLUMPED REACTOR CORE MATERIAL 8-1

8.1 Two-Dimensional Heat Conduction Model 8-1

8.2 Variable Element Porosity 8-2

8.3 Thermal Conductivity Model 8-3

8.4 Phase Change Model 8-4

8.5 Heat Transfer at Surfaces of Finite-Element Mesh 8-5

8.5.1 Hydrodynamic Boundary Condition 8-5
8.5.2 Ex-Vessel Heat Transfer 8-5

8.6 Heat Transfer in Finite Elements with Liquid-Solid Interface 8-8

8.7 Heat Transfer at Interface of Debris Region and Structure 8-17

8.8 Heat Transfer for Stratified Molten Pool 8-19

8.8.1 Correlations for Natural Convection Heat Transfer 8-19
8.8.2 Temperature of Oxidic and Metallic Pools and Heat Flux to Lower Head ... 8-22

8.9 Movement of Melted Core Plate Material Through Porous Debris 8-29

8.9.1 Models for Movement of Material in Porous Debris 8-30
8.9.2 Effects of Material Movement on Debris Bed Heat Transfer 8-34
8.9.3 Boundary Conditions 8-36
8.9.4 Numerical Solution 8-37

8.10 References 8-44

9. HEAT TRANSFER AND FLOW LOSSES IN POROUS DEBRIS 9-1

9.1 Convective and Radiative Heat Transfer in Porous Debris 9-2

9.1.1 Single Phase Vapor Regime 9-3
9.1.2 Single Phase Liquid Regime 9-7
9.1.3 Heat Transfer for Two-Phase Flow 9-9
9.1.4 Interphase Heat Transfer 9-16

9.2 Flow Losses in Porous Debris 9-16

9.3 Implementation of Heat Transfer Models 9-19

9.4 Implementation of Flow Loss Models 9-21

9.5 References 9-23

10. MODELS FOR BEHAVIOR OF SEVERELY DAMAGED REACTOR CORES 10-1

10.1 Configuration Changes Caused by Damage to Reactor Core 10-1

10.2 Heatup of Location with Relocated Material 10-6

10.3 Formation and Characteristics of Porous Debris 10-6

10.4 Heatup of Porous Debris in Core Region 10-10

10.5 Molten Pool Formation, Spreading and Heatup 10-11

10.5.1 Heat Flux on Inner Surface of Crust 10-12
10.5.2 Stability of Crust Surrounding Molten Pool 10-14
10.5.3 Rate of Spreading of Molten Pool 10-20
10.5.4 Temperature of Molten Pool 10-26

10.6 Interaction of Molten Pool with Structures at Periphery of Core 10-28

10.6.1 Melt Progression in Structure Contacted by Molten Pool 10-28
10.6.2 Slumping of Molten Pool to Lower Head 10-36

10.7 Molten Pool Slumping 10-37

10.8 Fuel-Coolant Interaction During Molten Pool Slumping 10-38

10.8.1 Break-up 10-39
10.8.2 Heat Transfer 10-42
10.8.3 Motion and Settling of Dispersed Drops 10-46

10.9 References 10-48

11. MODELS FOR SMOOTHING TRANSITIONS IN CONFIGURATION OF FUEL RODS 11-1

11.1 Configuration Change Due to Metallic Meltdown 11-1

11.2 Configuration Change Due to Ceramic Meltdown 11-5

11.3 Reference 11-6

12. CREEP RUPTURE OF STRUCTURAL COMPONENTS 12-1

12.1 Description of Models for Creep Rupture 12-1

12.2 References 12-3

13. ANALYSIS OF HIGH TEMPERATURE GAS REACTORS 13-1

13.1 Introduction 13-1

13.2 Transient Temperature Distribution in Reactor Core 13-3

13.3 Flow Losses in HTGR Core 13-13

13.3.1 Flow Losses in Core Region of PB-HTGR 13-13
13.3.2 Flow Losses in Core Region of BT-HTGR 13-15

13.4 Convective Heat Transfer in HTGR 13-15

13.4.1 Convective Heat transfer in Core Region of PB-HTGR 13-16
13.4.2 Convective Heat Transfer in Core Region of BT-HTGR and at Surfaces of Structures between Core and Containment 13-18
13.4.3 Heat Transferred to Gas 13-20

13.5 Oxidation of Graphite in Contact with Air 13-21

13.6 Oxidation of Graphite in Contact with Water Vapor 13-32

13.7 Transport of Decay Heat to Ultimate Heat Sink 13-34

13.8 Ingress of Air after Break in Coolant System 13-42

13.8.1 Potential Limitations of Minority Specie Diffusion Modeling 13-44
13.8.2 Diffusion of Working Fluid 13-44
13.8.3 Limitation on Time Step Due To Diffusion 13-45

13.9 References 13-45

FIGURES

2-1. Definition of mesh for two-dimensional heat conduction. 2-2
2-2. Schematic of jump in temperature caused by contact with slumped material. 2-8
3-1. Schematic of oxygen distribution in fuel rod cladding and surrounding coolant......... 3-2
3-2. Simplified Zr-O phase diagram with homogenized oxide and metal phases. 3-3
3-3. Schematic of hydrogen uptake in cladding. 3-14
3-4. Rate of hydrogen uptake as function of temperature as measured by Steinbruck, et al. 3-16
3-5. The Zirconium-Hydrogen phase diagram. 3-19
3-6. Crack formation in preoxidized Zircaloy during rapid cooldown from 1200 C by steam. 3-20
3-7. Crack formation in preoxidized Zircaloy during rapid cooldown from 1400 C by steam. 3-20
3-8. Temperature history and corresponding hydrogen release. 3-22
3-9. Vertical cross-section of segment of fuel rod with slumped cladding on outside surface of intact cladding. 3-26
4-1. Comparison of calculated hydrogen enthalpy using Equation (4-26) and data from Keenan$^{4-11}$ and Reynolds.4-12.. 4-10
4-2. Decay heat contributions of selected elements (based on total decay heat of all released fission products). 4-14
4-3. Melting and solidification geometry.. 4-15
4-4. Configuration change caused by relocation in circumferential direction of melted cladding. 4-22
4-5. Example of configuration of liquefied metallic layer from PIE results of OECD LOFT FP-2 experiment. 4-23
4-6. Example of asymmetric configuration of liquefied metallic layer from 0.96 m elevation of OECD LOFT FP-2 Test bundle (L1 Area 1). 4-23
4-7. Example of asymmetric shape of liquefied cladding and dissolved fuel from PBF SFD 1-1 experiment.. 4-24
4-8. Schematic of dissolution of fuel by melted cladding. 4-26
4-9. Example from OECD LOFT FP-2 experiment of fully oxidized cladding surrounded by slumped cladding. 4-29
4-10. Schematic of structural support given oxide layer by slumped material adhering to its external surface. 4-29
4-11. Post-test view of fuel bundle of FzK CORA-13 Test. 4-30
4-12. Schematic of slumping of melted cladding after failure of oxide layer retaining it... 4-31
4-13. Distance of slumping of melted cladding. 4-32
4-14. Configuration of grid spacer. 4-35
4-15. Configuration for which parabolic kinetics equation applies. 4-38
4-16. Growth of reaction zone in grid spacer... 4-39
4-17. Growth of reaction zone in fuel rod cladding.. 4-40
4-18. Variable area of contact between grid spacer and fuel rod cladding. 4-46
4-19. Definitions of equivalent thickness of reaction zone. 4-47
4-20. Adjustment in thickness of equivalent reaction zone to account for new contact during time step. 4-49
5-1. Chemical reaction between control rod cladding and guide tube................................ 5-2

5-2. Binary alloy phase diagram of the system Fe-Zr. 5-3
5-3. A typical BWR control blade and fuel assembly. 5-4
5-5. Arrangement of fuel assemblies and control blade in typical BWR core. 5-5
5-4. BWR control blade and channel box component with five temperature nodes and equivalent slab geometry (radial cross-sectional view). 5-5
5-6. Nomenclature used for solution of energy/conduction equations in radial direction. 5-6
5-7. Interface information exchanged between SCDAP and the BWR blade/box model. 5-10
5-8. Nodalization for fuel assemblies and control rods. 5-12
5-9. B4C oxidation rate coefficient as a function of temperature. 5-13
5-10. One-dimensional, two region nodalization for temperature response calculation. 5-15
5-11. Incompressible, viscous film flow over cylindrical geometry. 5-18
5-12. Slumping process for unsupported control rod segment. 5-19
6-1. Radiation exchange between surfaces and between surfaces and gas. 6-2
6-2. Radiation exchange between a rod surface and its surroundings. 6-3
6-3. Geometry for determining view factors between rods. 6-9
7-1. UPS model terminology for example configuration with 4 axial levels. 7-2
7-2. Nomenclature for solution of 1-D heat conduction equation at each axial level. 7-3
7-3. UPS model relocation logic. 7-5
7-4. Representation of molten pool failure and material relocating to core plate 7-9
7-5. Blockage of core plate penetrations by metallic material 7-11
7-6. Blockage of core plate penetration by ceramic material. 7-12
8-1. Predicted heat flux from ex-vessel heat transfer correlations as a function of position and temperature. 8-7
8-2. Identification of elements for which effective thermal conductivity is calculated 8-8
8-3. . Temperature distribution in finite element with liquid-solid interface. 8-9
8-4. Transient temperature distribution through layer of solidified material 8-11
8-5. COUPLE model finite element with solidified layer at angle. 8-14
8-6. . Ratio of local Nusselt number to mean Nusselt number as a function of the angle from core centerline. 8-17
8-7. Schematic defining the location of a typical phase change element. 8-17
8-8. Schematic drawing of oxidic and metallic pools in the lower head. 8-19
8-9. Correlations for heat flux as function of angular position. 8-23
8-10. Schematic of system analyzed to calculate temperatures of oxidic and metallic parts of stratified molten pool. 8-23
8-11. Schematic of system analyzed for calculating thickness of oxidic crust between oxidic and metallic parts of stratified molten pool. 8-28
8-12. Schematic of system represented by COUPLE model (particle size of debris greatly exaggerated). 8-30
13. Schematic of material movement occurring when core plate melts and lower head supports ceramic porous debris. 8-37
8-14. Coordinate system for numerical solution. 8-38
9-1. Relative permeabilities of the liquid and vapor phases. 9-19
10-1. Damage thresholds for changing local configuration of core from intact rods to rubble debris. 10-2

10-2. Damage threshold for changing local configuration of core from intact rods to cohesive debris. 10-3
10-3. Damage threshold for changing local configuration of core from intact rods or rubble debris to molten pool. 10-4
10-4. Damage threshold for changing local configuration of core from intact rods or rubble debris to molten pool. 10-5
10-5. The potential for spreading of the molten pool. 10-12
10-6. Physical process being represented by spreading model. 10-13
10-7. Framework for model calculating stresses in crust surrounding molten pool. 10-15
10-8. Framework for calculation of thickness of crust surrounding molten pool and temperature distribution in crust.l 10-17
10-9. Sequences in process being represented by spreading model. 10-21
10-10. Conditions assumed by model for calculating distance of penetration of molten material into porous debris. 10-23
10-11. Heat transfer from pool of molten debris. 10-27
10-12. Example of molten pool interacting with structure at periphery of core. 10-29
10-13. Cross-section of stainless steel reflector and its relation to reactor core. 10-29
10-14. Material regions and temperature distribution at surface of structure contacted by molten pool. 10-30
10-15. Growth of regions of solidified molten pool material and liquefied structural material at interface with molten pool. 10-31
10-16. Drainage of molten pool due to melting of structure with embedded flow channel. 10-33
10-17. Growth of regions of liquefied structural material and solidified molten pool material at surface of embedded flow channel. 10-35
10-18. Material in molten pool may slump to lower head by two different flow paths through structure at periphery of core. 10-37
10-19. A schematic view of the molten material slumping into the lower plenum. 10-39
10-20. Schematic picture of molten fuel jet and water mixing model.[10-24] 10-40
11-1. Configuration of array of fuel rods during various stages of damage progression. 11-1
11-2. Modeling of cladding meltdown with and without transition smoothing models. 11-2
11-3. Stages of blockage caused by cladding meltdown. 11-4
11-4. Changes in fuel rod configuration caused by fuel melting. 11-6
13-1. Schematic of media in PB-HTGR through which heat is transported in event of conduction cooldown accident. 13-2
13-2. Example of configuration of fuel blocks in BT-HTGR. 13-7
13-3. Schematic of calculation of effective thermal conductivity of homogenized fuel block. 13-8
13-4. Schematic of oxidation in graphite for two ranges of temperature. 13-22
13-5. Schematic of heat transfer from reactor core to earth surrounding reactor. 13-35
13-6. Schematic of modeling for passive cooling to atmosphere, containment, and earth.13-36
13-7. Horizontal cross section of upcomer and downcomer for annular shape of path for upward flow of air. 13-37
13-8. Horizontal cross section of upcomer and downcomer for series of individual flow paths for upward flow of air. 13-38
13-9. Radiation heat transfer for case of individual upcomers arranged in series around reactor vessel. 13-40
13-10. Definition of diffusion labels. 13-43

TABLES

3-1. Definition of symbols in Figure 3-1. 3-2
3-2. Period of hydrogen uptake (parameter teq)as a function of temperature. 3-17
3-3. Conditions for example calculation of rate of heat generation due to hydrogen uptake. 3-18
3-4. Model for determining whether cladding is embrittled. 3-21
4-1. Definition of variables in Equation (4-10). 4-4
4-2. Constants KO and Q in release rate coefficients taken from NUREG/CR-4173. 4-7
4-3. Thermodynamic properties of gap gases 4-9
4-4. Thermodynamic properties of other than hydrogen. 4-10
4-5. Fractional decay heat contributions for selected fission product elements (based on total decay heat from all released fission products). 4-13
4-6. Estimated gamma decay power fractions for released fission products (based on total decay heat from all released fission products). 4-14
4-7. Value of coefficients in equation for growth of reaction zone. 4-39
4-8. Value for coefficient in equation to calculate delay time due to oxide layer. 4-39
6-1. Water vapor absorption. 6-16
7-1. Range for variables used to estimate pool heat transfer parameters, 7-10
8-1. Nucleate boiling correlation constants. 8-6
8-2. Selected Nu vs. Ra Correlations 8-21
9-1. Regimes of convective heat transfer and corresponding ranges in values of volume fraction of liquid and debris temperature. 9-2
9-2. Definition of symbols in Table 9-1 9-2
10-1. Correlations used to calculate friction factor. 10-48
12-1. Equations for calculating the time to creep rupture 12-2
13-2. Tabular correlation for thermal conductivity of fuel compacts. 13-8
13-3. Tabular correlation for thermal conductivity of graphite in fuel blocks. 13-9
13-5. Tabular correlation for volumetric heat capacity of fuel compacts in BT-HTGR. 13-11
13-4. Tabular correlation for volumetric heat capacity of graphite in fuel blocks in BT-HTGR. 13-11
13-6. Correlations for coefficients in kinetics equation for oxidation of graphite in contact with water. 13-33

EXECUTIVE SUMMARY

The specific features of SCDAP/RELAP5-3D$^{©}$ are described in this five volume set of manuals covering the theory, use, and assessment of the code for severe accident applications.

The SCDAP/RELAP5-3D$^{©}$ computer code is designed to calculate for severe accident situations the overall reactor coolant system (RCS) thermal-hydraulic response, core damage progression, and reactor vessel heatup and damage. The SCDAP/RELAP5-3D$^{©}$ code evolved from the RELAP5 and SCDAP/RELAP5 codes developed at the Idaho National Engineering & Environmental Laboratory (INEEL) under sponsorship by the U.S. Nuclear Regulatory Commission (US NRC). Development of the RELAP5 code series began at the INEEL in 1975, while SCDAP development was initiated in the early 1970's with an active linkage to RELAP5 in 1979. The SCDAP/RELAP5-3D$^{©}$ code maintained all of the capabilities and validation history of the predecessor codes, plus the added capabilities sponsored by the DOE.

The RELAP5 code is based on a two-fluid model allowing for unequal temperatures and velocities of the fluids and the flow of fluid through porous debris and around blockages caused by reactor core damage. The models in SCDAP calculate the progression of damage to the reactor core. These models calculate the heatup, oxidation and meltdown of fuel rods and control rods, the ballooning and rupture of fuel rod cladding, the release of fission products from fuel rods, and the disintegration of fuel rods into porous debris and molten material. The SCDAP models also calculate the heatup and structural damage of the reactor vessel lower head resulting from the slumping to the lower head of reactor core material with internal heat generation. SCDAP/RELAP5-3D$^{©}$ can be used in analyses of fission product transport and deposition behavior and containment phenomena by linking it to the detailed fission product code, VICTORIA[1] or CONTAIN[2], respectively.

The SCDAP/RELAP5-3D$^{©}$ code includes many generic component models from which general systems can be simulated. The component models include fuel rods, control rods, pumps, valves, pipes, reactor vessel, electrical fuel rod simulators, jet pumps, turbines, separators, accumulators, and control system components. In addition, special process models are included for effects such as form loss, flow at an abrupt area change, branching, choked flow, boron tracking, and noncondensable gas transport. The code also includes a model for reactor kinetics.

This volume, Volume 2, describes models which are resident only to the SCDAP portion of the code and contains detailed descriptions of the models for calculating damage progression to the reactor core and the lower head of the reactor vessel. It provides the user with the underlying assumptions and simplifications used to generate and implement the basic equations into the code, so that an intelligent assessment of the applicability and accuracy of the resulting calculation can be made.

---

[1] N. E. Bixler, "VICTORIA2.0: A Mechanistic model for Radionuclide Behavior in a Nuclear Reactor Coolant System Under Severe Accident Conditions," NUREG/CR-6131, SAND93-2301, December 1998.

[2] K. D. Bergeron et al., *User's Manual for CONTAIN 1.0, A Computer Code for Severe Nuclear Reactor Accident Containment Analysis*, NUREG/CR-4085, SAND84-1204, May 1985

ACRONYMS

ADI	Alternating Direction Implicit
ANS	American Nuclear Society
ANSI	American National Standards Institute
BWR	Boiling Water Reactor
DOE	U. S. Department of Energy
RCS	Reactor Coolant System
IEEE	Institute of Electrical and Electronic Engineers
INEEL	Idaho National Engineering and Environmental Laboratory
IPR	Independent Peer Review
LOFT	Loss-of-Fluid Test
LWR	Light Water Reactor
NPA	Nuclear Plant Analyzer
NRC	U. S. Nuclear Regulatory Commission
OECR	Odd Even Cyclic Reduction
ORNL	Oak Ridge National Laboratory
PBF	Power Burst Facility
PWR	Pressurized Water Reactor
QA	Quality Assurance
QPP	Quality Program Plan
SNL	Sandia National Laboratory
TMI	Three Mile Island
VFP	Volatile Fission Product

1. INTRODUCTION

The SCDAP/RELAP5-3D© computer code is designed to calculate for severe accident situations the overall reactor coolant system (RCS) thermal-hydraulic response, reactor core and vessel damage progression, and, in combination with VICTORIA,[1-1] fission product release and transport during severe accidents.

1.1 General Code Capabilities

The SCDAP/RELAP5-3D© code contains RELAP5 and SCDAP models. The RELAP5 models calculate the overall RCS thermal-hydraulics, control system interactions, reactor kinetics, and transport of noncondensable gases. A model is also included in RELAP5 to calculate flow losses in porous debris. Although previous versions of the code have included the analysis of fission product transport and deposition behavior using models derived from TRAP-MELT, this capability has been replaced through a data link to the detailed fission product code, VICTORIA. The SCDAP models calculate the heatup and damage progression in the core structures and the lower head of the reactor vessel. The calculations of damage progression include calculations of the meltdown of fuel rods and structures, the fragmentation of embrittled fuel rods, convective and radiative heat transfer in porous debris, the formation of a molten pool of core material, and the slumping of molten material to the lower head.

SCDAP/RELAP5-3D© is capable of modeling a wide range of system configurations from single pipes to different experimental facilities to full-scale reactor systems. The configurations can be modeled using an arbitrary number of fluid control volumes and connecting junctions, heat structures, core components, and system components. Flow areas, volumes, and flow resistances can vary with time through either user-control or models that describe the changes in geometry associated with damage in the core. System structures can be modeled with RELAP5 heat structures, SCDAP core components, or SCDAP debris models. The RELAP5 heat structures are one-dimensional models with slab, cylindrical, or spherical geometries. The SCDAP core components include representative light water reactor (LWR) fuel rods, silver-indium-cadmium (Ag-In-Cd) and B_4C control rods and/or blades, electrically heated fuel rod simulators, and general structures. A two-dimensional, finite element heat conduction model based on the COUPLE[1-2] code may be used to calculate the heatup of the lower head of the reactor vessel and the slumped material supported by the lower head. This model takes into account the decay heat and internal energy of newly fallen or formed debris and then calculates the transport by conduction of this heat in the radial and axial directions to the wall structures and water surrounding the debris. The most important use of this model is to calculate the heatup of the vessel lower head and the timing of its failure in response to contact with material that has slumped from the core region. Other system components available to the user include pumps, valves, electric heaters, jet pumps, turbines, separators, and accumulators. Models to describe selected processes, such as reactor kinetics, control system response, and tracking noncondensable gases, can be invoked through user control.

The SCDAP/RELAP5-3D© code evolved from the RELAP5 and SCDAP/RELAP5 codes developed at the Idaho National Engineering & Environmental Laboratory (INEEL) under sponsorship by the U.S.

Nuclear Regulatory Commission (US NRC). Development of the RELAP5 code series began at the INEEL in 1975, while SCDAP development was initiated in the early 1970's with an active linkage to RELAP5 in 1979. Following the accident at Chernobyl, the U.S. Department of Energy (DOE) began a re-assessment of the safety of its test and production reactors, and chose RELAP5 and SCDAP/RELAP5 as the analytical tools for system safety analysis because of their wide spread acceptance and ease of application to such widely varying systems. Systematic safety analyses were performed for the N reactor at Hanford, the K and L reactors at Savannah River, the Advanced Test Reactor (ATR) at INEEL, the High Flux Isotope Reactor (HFIR) and Advanced Neutron Source (ANS) at Oak Ridge, and the High Flux Beam Reactor at Brookhaven. DOE also chose RELAP5 for the independent safety analysis of the New Production Reactor (NPR) before that program was cancelled.

The application of SCDAP/RELAP5 and RELAP5 to these widely varying reactor designs demanded new modeling capabilities, including non-light water reactor (LWR) materials and geometry. These widely varying demands were met by maintaining a single source with options that could be selected or deselected at compilation. In this fashion both NRC and DOE users could receive maximum benefit from the others development efforts. After the transmittal of SCDAP/RELAP5 MOD3.3 to the NRC, it became clear, however, that the efficiencies realized by the maintenance of a single source code for use by both NRC and DOE were being overcome by the extra effort required to accommodate sometimes conflicting goals and requirements. The codes were therefore “split” into two versions, SCDAP/RELAP5 MOD3.3 for the NRC and SCDAP/RELAP5-3D© for DOE. The SCDAP/RELAP5-3D© code maintained all of the capabilities and validation history of the predecessor codes, plus the added capabilities sponsored by the DOE.

SCDAP/RELAP5-3D© is the latest INEEL-developed code for analyzing transients and accidents in water-cooled nuclear power plants and related systems. The most prominent attribute that distinguishes this code from its predecessors is the fully integrated, multi-dimensional thermal-hydraulic and kinetic modeling capability. Although multi-dimensional capabilities in the RELAP models have been assessed, it should be noted that few of these assessment calculations have used SCDAP models.

1.2 Relationship to Other Software

SCDAP/RELAP5-3D© and RELAP5-3D© were developed in parallel and share a common configuration. Both codes share a common source deck. Separate codes are formed only prior to compilation, so changes made to the source deck are automatically reflected in both codes.

The development and application of the code is also related to several other software packages. Theoretical work associated with the development of PARAGRASS-VFP[1-3] has resulted in model improvements for fission product release. A data link to the VICTORIA code allows for the detailed treatment of phenomena such as fission product and aerosol transport, deposition, and resuspension. A link with PATRAN[1-4] and ABAQUS[1-5] provides the user with the means to calculate the details of lower head failure. Animated plant response displays are possible through links to the Nuclear Plant Analyzer (NPA)[1-6] display software, which gives the user an efficient way of analyzing the large amount of data generated. Detailed plant simulations from accident initiation through release of fission products to the atmosphere are available through links to the CONTAIN[1-7] containment response and CRAC2[1-8] or MACCS[1-9] atmospheric dispersion consequence codes.

1.3 Quality Assurance

SCDAP/RELAP5-3D© is maintained under a strict code configuration system that provides a historical record of the changes made to the code. Changes are made using an update processor that allows separate identification of improvements made to each successive version of the code. Modifications and improvements to the coding are reviewed and checked as part of a formal quality program for software. In addition, the theory and implementation of code improvements are validated through assessment calculations that compare the code-predicted results to idealized test cases or experimental results.

1.4 Organization of the SCDAP/RELAP5-3D© Manuals

The specific features of SCDAP/RELAP5-3D© are described in a five-volume set of manuals covering the theory (Volume 2), user's guidelines and input manual (Volume 3), material properties (Volume 4), and assessment (Volume 5). Although Volume 1 describes (a) the overall code architecture, (b) interfaces between the RELAP5 and SCDAP models, and (c) any system models unique to SCDAP/RELAP5-3D©, the code user is referred to the companion set of six volumes which describe the RELAP5-3D© system thermal-hydraulics and associated models.

Volume 1 presents a description of SCDAP/RELAP5-3D©-specific thermal-hydraulic models (relative to RELAP5-3D©), and interfaces between the thermal-hydraulic models and damage progression models. Volume 2 contains detailed descriptions of the severe accident models and correlations. It provides the user with the underlying assumptions and simplifications used to generate and implement the basic equations into the code, so an intelligent assessment of the applicability and accuracy of the resulting calculation can be made. Volume 3 provides the user's guide and code input for the severe accident modeling. User guidelines are produced specifically for the severe accident code. The user should also refer to the RELAP5-3D© Code Manual Volume V: User Guidelines for a complete set of guidelines. Volume 4 describes the material property library, MATPRO. It contains descriptions of the material property subroutines available for severe accident analysis. Volume 5 documents code assessments. It summarizes the improvements made to various versions of the code and the effect of these improvements on code calculations. A presentation is made of the comparisons of code calculations of a wide range of severe fuel damage experiments with the measured results of these experiments. Also presented are code calculations of the TMI-2 accident and calculations of severe accidents in typical PWRs and BWRs.

1.5 Organization of Volume 2

Volume 2 describes models resident only to the SCDAP portion of the code. Sections 2 and 3 describe the heat conduction and material oxidation models used by the fuel rod and other core component models. Section 4 describes models specific to the fuel rod component, such as cladding ballooning and meltdown. Section 5 describes the other core component models, which include the Ag-In-Cd control rod model, the detailed BWR B_4C control blade and channel box model, the simplified B_4C control rod model, and the flow shroud model. Section 6 describes the calculation of heat transfer by radiation from and to the surfaces of the rods and enclosure structure in fuel assemblies. Section 7 describes the models for heatup and meltdown of upper plenum structures and the lower core plate. Section 8 describes the model for heatup of the reactor vessel lower head and supported debris. The models for heat transfer and flow losses at locations with porous debris are described in Section 9. The models for the formation and heatup of porous and molten debris regions in the reactor core are described in Section 10. This section also describes the model for calculating the timing of the slumping of molten material in the core region to the lower head and the model for calculating the behavior of jets of molten core material penetrating into a pool of water in the lower head. Section 11 discusses the models for smoothing transitions in the configuration of the reactor core. Section 12 describes the creep rupture models.

1.6 References

1-1. N. E. Bixler, *VICTORIA2.0: A Mechanistic Model for Radionuclide Behavior in a Nuclear Reactor Coolant System Under Severe Accident Conditions,* NUREG/CR-6131, SAND93-2301, December 1998.

1-2. E. C. Lemmon, *COUPLE/FLUID: A Two-Dimensional Finite Element Thermal Conduction and Advection Code,* EGG-ISD-SCD-80-1, February 1980.

1-3. J. Rest and S. A. Zawadzki, "FASTGRASS-VFP/PARAGRASS-VFP Version 50531, Users Guide," *Argonne National Laboratory Quarterly Report, January-March 1983,* Volume I, NUREG/CR-3689, ANL-83-85, Volume I, June 1983.

1-4. *PATRAN Plus User's Manual,* Release 2.4, PDA Engineering, Costa Mesa, CA, 1987.

1-5. *ABAQUS User's Manual,* Version 4.6, Hibbitt, Karlsson & Sorensen, Inc., Providence, RI, 1987.

1-6. D. M. Snider, K. L. Wagner, and W. Grush, *Nuclear Plant Analyzer (NPA) Reference Manual Mod1,* EGG-EAST-9096, April 1990.

1-7. K. D. Bergeron et al., *User's Manual for CONTAIN 1.0, A Computer Code for Severe Nuclear Reactor Accident Containment Analysis,* NUREG/CR-4085, SAND84-1204, May 1985.

1-8. L. T. Ritchie et al., *CRAC2 Model Description,* NUREG/CR-2552, SAND82-0342, March 1984.

1-9. D. I. Chanin et al., *MELCOR Accident Consequence Code System (MACCS Version 1.5),* NUREG/CR-4691, SAND86-1562, July 1988, DRAFT.

2. HEAT CONDUCTION MODEL FOR CORE COMPONENTS

This section describes the heat conduction model and methods used to calculate the temperature response for the fuel rod, Ag-In-Cd control rod, B_4C control rod, and shroud components.

2.1 Two-Dimensional Heat Conduction Governing Equation

In the two-dimensional cylindrical coordinate system, the integral form of the heat conduction equation for an isotropic solid continuum is:

$$\int_V \rho c_p \frac{\partial T}{\partial t} dV = \int_V \frac{1}{r}\frac{\partial}{\partial r}\left(rk\frac{\partial T}{\partial r}\right) dV + \int_V \frac{\partial}{\partial z}\left(k\frac{\partial T}{\partial z}\right) dV + \int_V Q_v dV + \int_S Q_s dS \tag{2-1}$$

where

Q_v = volumetric heat source (nuclear, oxidation, W/m^3)

Q_s = surface heat flux (convective, radiative, W/m^2)

T = temperature at location (r, z) at time t where r and z are the radial and axial coordinates respectively (K)

ρc_p = volumetric heat capacitance ($J/m^3 \bullet K$)

k = thermal conductivity ($W/m \bullet K$).

By applying the divergence theorem to the right-hand side of the integral form of the heat conduction equation, the following heat conduction governing equation is obtained:

$$\int_V \rho c_p(T, r, z)\frac{\partial}{\partial t}T(r, z, t) dV = \int_S k(T, r, z)\nabla T(r, z, t) ds + \int_V Q_v(r, z, t) dV + \int_S Q_S(r, z, t) dS \quad . \tag{2-2}$$

2.2 Finite Difference

Heat conduction is calculated using the finite difference and finite volume methods described in Reference 2-1. However, instead of differencing the partial differential equation directly, the integral form of the partial differential equation, Equation (2-2), is differenced. Unlike the finite volume method where the mesh point is placed at half a mesh spacing from the boundary or the interface between two material layers, the mesh points are placed at the boundary or at the interface between two different material layers. While this approach has the advantage of maximizing the accuracy of discretization at the boundary when, for example, a convective boundary condition is imposed, it also means that a control volume surrounding a typical mesh point will, in general, overlap mesh cells that lie in different material layers. Because of this, it is necessary to examine the mesh cells adjacent to a given mesh point (i,j) in some detail.

Consider the four mesh cells surrounding the mesh point (i,j) as shown in Figure 2-1. It is assumed that each of these mesh cells contains only one kind of material so that the thermal conductivity or heat capacitance is essentially constant over each mesh cell. A control volume surrounding the mesh point (i,j) will have $\left(i+\frac{1}{2}, j+\frac{1}{2}\right)$, $\left(i+\frac{1}{2}, j-\frac{1}{2}\right)$, $\left(i-\frac{1}{2}, j+\frac{1}{2}\right)$, and $\left(i-\frac{1}{2}, j-\frac{1}{2}\right)$ as its vertices and will overlap all four mesh cells.

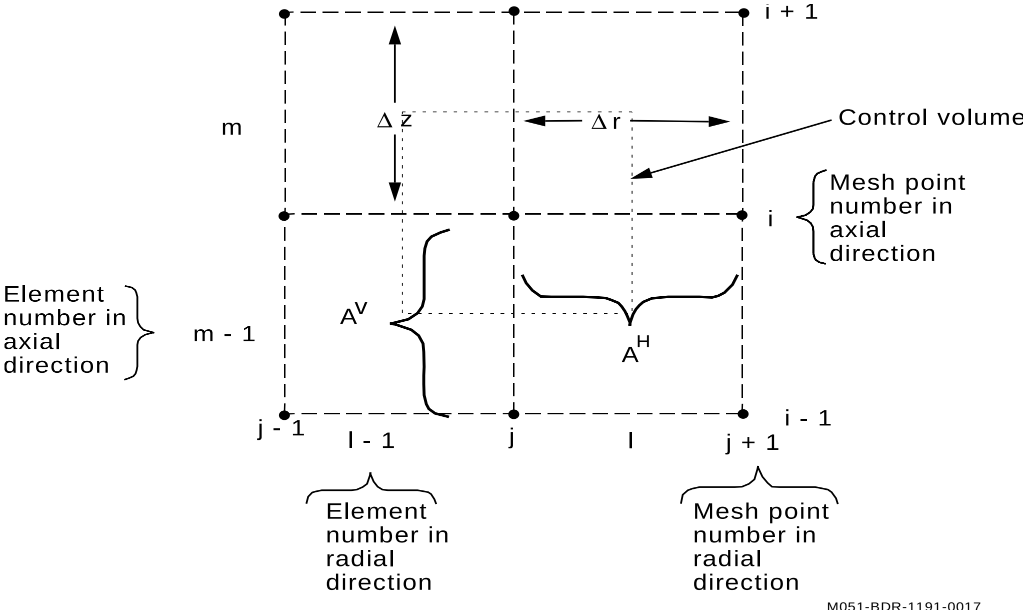
i + 1
m
Δ z
Δ r
Control volume
Mesh point number in axial direction
i
Element number in axial direction
m - 1
A^V
A^H
j - 1
l - 1
j
l
j + 1
i - 1
Element number in radial direction
Mesh point number in radial direction
M051-BDR-1191-0017

Figure 2-1. Definition of mesh for two-dimensional heat conduction.

For an element surrounding the interior point (i,j), the volume integrals of the volumetric heat capacitance and volumetric heat source can be written as

$$G_{ij} = \left(\int_v \rho c_p(T, r, z)dv\right)_{i,j} \tag{2-3}$$

$$= \frac{1}{4}(\rho c_{pl-1,m-1} v_{l-1,m-1} + \rho c_{pl-1,m} v_{l-1,m}) + \frac{1}{4}(\rho c_{pl,m-1} v_{l,m-1} + \rho c_{pl,m} v_{l,m}) \ .$$

$$Q_{ij} = \left(\int_v Q_v(T, r, z)dv\right)_{i,j} \tag{2-4}$$

$$= \frac{1}{4}(Q_{l-1,m-1} v_{l-1,m-1} + Q_{l-1,m} v_{l-1,m} + Q_{l,m-1} v_{l,m-1} + Q_{l,m} v_{l,m}) \ .$$

Here the subscripts l and m denote the mesh cell with element numbers l and m in the radial and axial direction, respectively (see Figure 2-1). By replacing the time derivative and spatial derivatives in Equation (2-2) by backward differencing and central differencing, respectively, the following is obtained:

$$\frac{G_{i,j}(T^{n+1}_{i,j} - T^n_{i,j})}{\Delta t} = A^L_{i,j}(T^n_{i-1,j} - T_{i,j}) + A^R_{i,j}(T^n_{i+1,j} - T_{i,j}) \tag{2-5}$$

$$+ A^T_{i,j}(T^{n+1}_{i,j+1} - T^{n+1}_{i,j}) + A^B_{i,j}(T^{n+1}_{i,j-1} - T^{n+1}_{i,j}) + Q_{i,j} + Q_s\delta_{i-I}\delta_{j-J}$$

where

$$A^{L}_{i,j} = \frac{k_{l-1,m-1}A^{V}_{l-1,m-1}}{2\Delta r_{l-1,m-1}} + \frac{k_{l-1,m}A^{V}_{l-1,m}}{2\Delta r_{l-1,m}} \tag{2-6}$$

$$A^{R}_{i,j} = \frac{k_{l,m-1}A^{V}_{l,m-1}}{2\Delta r_{l,m-1}} + \frac{k_{l,m}A^{V}_{l,m}}{2\Delta r_{l,m}} \tag{2-7}$$

$$A^{T}_{i,j} = (k_{l-1,m}A^{H}_{l-1,m} + k_{l,m}A^{H}_{l,m})/(2\Delta z_{m}) \tag{2-8}$$

$$A^{B}_{i,j} = (k_{l-1,m-1}A^{H}_{l-1,m-1} + k_{l,m-11}A^{H}_{l,m-1})/(2\Delta z_{m-1}) \tag{2-9}$$

$$\delta_{i-I} = 1, i = I(0, i \neq I) \tag{2-10}$$

$$\delta_{j-J} = 1, j = J(0, j \neq J) \tag{2-11}$$

I, J = the total number of mesh points in the axial and radial directions, respectively,

A^{V} = surface area weighting factor in the vertical direction for the given mesh cell,

A^{H} = surface area weighting factor in the horizontal direction for the given mesh cell.

The thermal properties and heat source terms are treated implicitly. This is accomplished by first solving the i multiplied by j difference equations using the alternating direction implicit (ADI) numerical scheme described in Section 2.3. The updated temperature at the current time level n + 1 is then used to recompute the thermal properties and the heat source term. The difference equations are then solved again to give a new updated temperature. This iterative process is terminated when the maximum of the absolute value of the differences between the two successive updated temperatures at all the mesh points is within a 10 K tolerance. The heat sink term is treated explicitly.

2.3 The Alternating Direction Method

If the system of difference equations are solved exactly, the solution method is fully implicit. Since this method involves the solution of a block tridiagonal system of equations, it is more cost effective to use the alternating direction method in SCDAP/RELAP5-3D©. This involves solving the system of equations using only one sweep of the alternating direction method. Because the method can be viewed as a fractional step method for solving Equation (2-1), it has the same order of accuracy as the fully implicit method and it is also unconditionally stable. Specifically, the method can be presented as follows. Form the following equation at each mesh point along each column j (j = 1, ... J):

$$2\frac{G_{i,j}\left(T^{n+\frac{1}{2}}_{i,j} - T^{n}_{i,j}\right)}{\Delta t} = A^{L}_{i,j}(T^{n}_{i-1,j} - T^{n}_{i,j}) + A^{R}_{i,j}(T^{n}_{i+1,j} - T^{n}_{i,j}) \tag{2-12}$$

$$+ A^{T}_{i,j}\left(T^{n+\frac{1}{2}}_{i,j+1} - T^{n+\frac{1}{2}}_{i,j}\right) + A^{B}_{i,j}\left(T^{n+\frac{1}{2}}_{i,j-1} - T^{n+\frac{1}{2}}_{i,j}\right) + Q_{i,j} + Q_{s}\delta_{j-J} \quad . \tag{2-13}$$

This gives rise to the following tridiagonal system of equations

$$A\overline{T}^{n+\frac{1}{2}} = B(\overline{T}^n) \tag{2-14}$$

which is solved for

$$T_{i,j}^{n+\frac{1}{2}}, i = 1 \text{ to } I \tag{2-15}$$

for each column j. This is followed by another fractional time step that completes the time-step advancement by performing a row inversion for each row as follows. Form the following equation at each mesh point along each row i (i = 1,....,I):

$$2\frac{G_{i,j}\left(T_{i,j}^{n+1} - T_{i,j}^{n+\frac{1}{2}}\right)}{\Delta t} = A_{i,j}^{L}(T_{i-1,j}^{n+1} - T_{i,j}^{n+1}) + A_{i,j}^{R}(T_{i+1,j}^{n+1} - T_{i,j}^{n+1}) \tag{2-16}$$

$$+ A_{i,j}^{T}\left(T_{i,j+1}^{n+\frac{1}{2}} - T_{i,j}^{n+\frac{1}{2}}\right) + A_{i,j}^{B}\left(T_{i,j-1}^{n+\frac{1}{2}} - T_{i,j}^{n+\frac{1}{2}}\right) + Q_{i,j} + Q_s\delta_{i-I} \quad . \tag{2-17}$$

Then solving the following tridiagonal system of equations

$$A'\overline{T}^{n+1} = B'\left(\overline{T}^{n+\frac{1}{2}}\right) \tag{2-18}$$

for the updated temperatures $T_{i,j}^{n+1}$ at the time level n + 1 for each row i.

2.4 Matrix Methods

The tridiagonal system of Equations (2-14) or (2-18) can be solved by either by Gaussian elimination methods or odd even reduction methods.

The Gaussian elimination method used in the two-dimensional heat conduction solver of the code is known as the UL factorization method, which is a variant of the more familiar LU factorization method.

The matrix A in the matrix Equation (2-14) or (2-18) is factored into the product of an upper-triangular matrix (U) and a lower-triangular matrix (L) as follows:

$$A = \begin{bmatrix} b_1 & c_1 & 0 & 0 \\ a_2 & b_2 & c_2 & 0 \\ 0 & a_{n-1} & b_{n-1} & c_{n-1} \\ 0 & 0 & a_n & b_n \end{bmatrix} = \begin{bmatrix} G_1 & c_1 & 0 & 0 \\ 0 & G_2 & c_2 & 0 \\ 0 & 0 & G_{n-1} & c_{n-1} \\ 0 & 0 & 0 & G_n \end{bmatrix} \begin{bmatrix} 1 & 0 & 0 & 0 \\ E_2 & 1 & 0 & 0 \\ 0 & E_{n-1} & 1 & 0 \\ 0 & 0 & E_n & 1 \end{bmatrix} = UL \quad . \tag{2-19}$$

It is easily verified that

$G_n = b_n$,

$E_n = a_n/G_n$,

$G_j = b_j - c_jE_{j+1}$, $j = 1,....,n - 1$,

$E_j = a_j/G_j$.

On the other hand, if $Uy = r$, where r is the right hand side of the matrix equation $Ax = r$, the result is

$y_n = r_n/G_n$,

$y_j = (r_j - c_jy_{j+1})/G_j$, $j = 1,....., n - 1$.

The solution of $Ax = r$ can therefore proceed as follows.

1. Factor A into UL,
2. Solve $Uy = r$,
3. Solve $Lx = y$ for the solution x.

If only the matrix equation $Ax = r$ is solved for one right-hand side vector r for a given matrix A, then Steps 1 and 2 can be combined to give the following algorithm.

1. Solve for y in Step 2 above directly by setting

$a_n = a_n/b_n$,

$r_n = r_n/b_n$,

$a_j = a_j/(b_j - a_{j+1}c_j)$, $j = 1,...., n - 1$,

$r_j = (r_j - c_jr_{j+1})/(b_j - a_{j+1}c_j)$, $j = 1,...., n - 1$.

The updated a_j and r_j are the E_j and y_j described in steps 1 and 2 above.

2. Back solve for x by solving $Lx = y$ as follows:

$x_1 = r_1$,

$x_j = r_j - a_jx_{j-1}$, $j = 1,...., n - 1$.

In the code, the above procedure is vectorized by carrying out steps 1 and 2 in the above algorithm simultaneously for all the columns (rows) during the column (rows) inversion step in the ADI schemes. This procedure is most efficient during the column (row) inversion step when there are many rows (columns) and only a few columns (rows). In general, the odd even cyclic reduction (OECR) algorithm is more competitive on vector computers.

2.5 OECR Algorithm

Solving the tridiagonal system of equations Ax = r with the j - 1, j, j + 1 rows displayed, the following applies:

$a_{j-1}x_{j-2} + b_{j-1}x_{j-1} + c_{j-1}x_j = r_{j-1}$,

$a_jx_{j-1} + b_jx_j + c_jx_{j+1} = r_j$,

$a_{j+1}x_j + b_{j+1}x_{j+1} + c_{j+1}x_{j+2} = r_{j+1}$.

If the j - 1 and j + 1 rows are multiplied with $-a_j/b_{j-1}$ and $-c_j/b_{j+1}$, respectively, and added to the j row, the references to the j - 1 and j + 1 variables in the j row are eliminated. In general, if the odd numbered rows are multiplied by suitable scalars and added to the even numbered rows, then the references to the odd numbered variables in the even numbered rows disappear. This permits a large system of equations to be eventually reduced to a system that consists of only one or two equations. The operation count, however, is 17N vs. 8N for Gaussian elimination methods, where N is the order of the matrix so that the method is not competitive on serial machines. On vector computers, the method is known to be several times faster than Gaussian elimination methods for large N, with break even occurring at N = 100. When used with the ADI scheme, the secret of success is to form long vectors of length IJ where I is the number of axial levels and J is the number of radial nodes. The OECR algorithm is then used to reduce the matrix problem on all the mesh points to a system of either I times one or two equations or J times one or two equations depending on whether the ADI sweep is in the axial or radial direction. Note that the variables at each row (column) during the ADI row (column) inversion are not coupled with that at adjacent rows (columns,) so that the I (or J) times 1 or 2 equations can be solved simultaneously at all the I rows or J columns. Hence, the vector length for all the vectors during the OECR algorithm never falls below I or J and the method is therefore significantly more efficient than the usual OECR algorithm when the vector length eventually becomes 1 or 2. This procedure is most easily implemented when the column (row) length is equal to 2^n or 3 multiplied by 2^n when column (row) inversion is performed in the ADI scheme. In the code, odd even reduction is used when the above mentioned criteria are satisfied. Otherwise, the vectorized Gaussian elimination method is used.

2.6 Volume Averaging

Effective material properties and effective volumetric heat generation are applied over a control volume. The following volumetric averaging is applied.

$$(\rho c_p)_{eff} = \frac{\int_V \rho c_p dV}{\int_V dV} \tag{2-20}$$

$$\left(\frac{1}{k}\right)^n_{eff} = \frac{\int_V \frac{1}{k} dV}{\int_V dV} \tag{2-21}$$

$$Q_{veff} = \frac{\int_V Q_v dV}{\int_V dV} \quad . \tag{2-22}$$

2.7 Temperature Jump Due to Contact with Slumped Material

A jump in temperature occurs at a location where hot material from above has slumped into the location and froze. This jump in temperature is calculated assuming the slumped material and the in situ fuel and cladding instantaneously attain thermal equilibrium and a common temperature. The internal energy of the slumping material and the internal energy of the in situ fuel and cladding just before contact are added together and then distributed through their combined masses. A schematic of the combination in internal energies in shown in Figure 2-2. The temperature of the combined configuration just after the instant of contact is calculated by the equation

$$T_J = (c_{PF}M_FT_F + c_{PC}M_CT_C + c_{PS}M_ST_S)/(c_{PF}M_F + c_{PC}M_C + c_{PS}M_S) \tag{2-23}$$

where

T_J = temperature of combined configuration of slumped material and in situ fuel and cladding at instant of contact (K),

T_F = temperature of fuel at location just before contact with slumped material (K),

T_C = temperature of cladding at location just before contact with slumped material (K),

T_S = temperature of slumped material at beginning of slumping (K),

C_{PF} = heat capacity of fuel $(J/kg \cdot K)$,

c_{PC} = heat capacity of cladding $(J/kg \cdot K)$

c_{PS} = heat capacity of slumped material $(J/kg \cdot K)$,

M_F = mass of fuel at location (kg),

M_C = mass of cladding at location (kg),

M_S = mass of slumped material (kg).

In general, contact with slumped material causes the temperature at a location to jump just a few degrees. While the temperature of the slumped material may be a few hundred degrees hotter than the location at which it freezes, the slumped material usually has a much smaller mass than the in situ material it contacts. As a result, the equilibrium temperature of the combined configuration is usually only a few degrees hotter than the temperature of the in situ material before contact. At the location where the slumped material froze and at the end of the time step in which slumped material froze at the location, the temperature of each radial node is set to the value of T_J. After this time, the temperature is calculated by

Equation 2-18 and with the heat capacity at the location increased to account for the heat capacity of the slumped material.

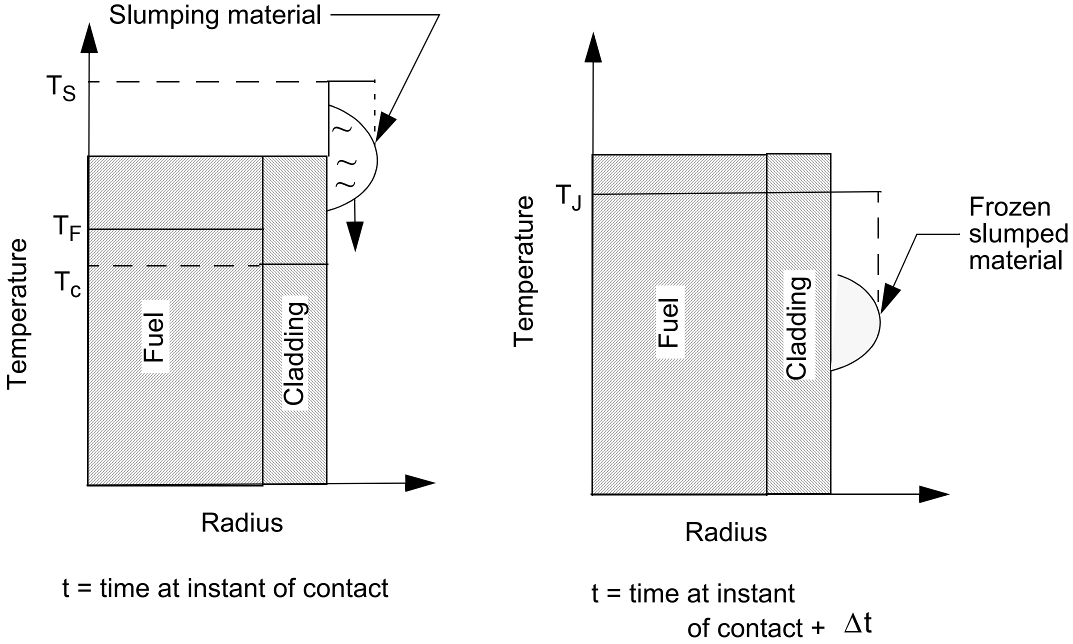
Slumping material
T_S
T_F
T_c
Temperature
Fuel
Cladding
Radius
t = time at instant of contact
T_J
Frozen slumped material
Temperature
Fuel
Cladding
Radius
t = time at instant of contact + Δt

Figure 2-2. Schematic of jump in temperature caused by contact with slumped material.

2.8 Reference

2-1. C. D. Fletcher, *Computational Techniques for Fluid Dynamics, Volume 1,* Springer-Verlag, 1988, pp. 107-121.

3. MATERIAL OXIDATION MODEL

The oxidation of the metallic parts of the reactor core results in heat generation, hydrogen production, and an acceleration in the progression of damage to the reactor core. Two basic types of models are used to calculate this important process; these models are; (1) the integral diffusion model, and (2) the parabolic kinetics model. The integral diffusion model is used to calculate the oxidation of the cladding of fuel rods. This model applies diffusion coefficients and phase diagrams for the oxidic and metallic parts of the cladding to calculate the transient rate of uptake of oxygen and hydrogen in the cladding. The model is applicable to the situations of rapid changes in cladding temperature and steam starvation. The parabolic kinetics model is used to calculate the oxidation of control rods, shrouds with a Zr layer, and fuel rod cladding that has slumped. While this model does not account for some details in the oxidation process taken into account by the integral diffusion model, nevertheless it is more applicable for material whose configuration is uncertain and changing with time, such as slumped fuel rod cladding. The integral diffusion model is described in Section 3.1. The approximations made to the oxidation of fuel rod cladding during the complexities caused by fuel rod meltdown and reflood are described in Section 3.2. The parabolic kinetics model used for calculating the oxidation of control rods is described in Section 3.3.

3.1 Integral Diffusion Model

3.1.1 Introduction

The integral diffusion model[3-4] is used to calculate the oxidation of fuel rod cladding that has not slumped. This model applies Fick's law of diffusion and the phase diagram of the oxidic and metallic parts of the cladding and to calculate the rate of uptake of oxygen in the cladding. The phase diagram determines the stoichiometry (oxygen to metal ratio) at the boundaries of the regions through which the oxygen diffuses, in particular the oxidic and metallic parts of the cladding. Fick's law applies the boundary conditions defined by the phase diagram and calculates the diffusion of oxygen through the oxidic and metallic parts of the cladding. The model can be applied to locations with steam starvation, where the oxidic part of the cladding may be dissolved into its metallic substrate. The model is also applicable to situations with rapidly changing temperature.

The integral diffusion method is applicable to a severe accident code such as SCDAP/RELAP5-3D$^{©}$ wherein oxidation must be calculated at many locations in the reactor core. In this technique, a linear oxygen concentration is assumed in the radial direction through the oxidic part of the cladding and the shape of the oxygen concentration profile in the radial direction is assumed for the metallic substrate. This technique converts the partial differential equations for diffusion into ordinary differential equations in time. The result is a model for oxidation that is a compromise between the computationally simple yet physically oversimplified parabolic kinetics model and the highly descriptive but analytically complex full diffusion theory treatment.

This section is organized into three other parts. In Section 3.1.2, the uptake of oxygen using the integral diffusion method is described. This section also describes the modeling for the possibility of complete dissolution of the oxidic part of the cladding into its metallic substrate. In Section 3.1.3, a model is described for the uptake of hydrogen and the associated heat generation that may occur after the dissolution of the oxidic part of the cladding. In Section 3.1.4, models are described for evaluating the degree of embrittlement of the cladding due to hydrogen uptake.

3.1.2 Oxygen Diffusion

The calculation of the oxidation of fuel rod cladding involves the calculation of the diffusion of oxygen through three regions. These three regions are; (1) boundary layer at the external surface of the cladding, (2) oxide layer, and (3) metallic substrate. A schematic of the oxygen distribution in these three regions is shown in Figure 3-1. The figure shows oxygen concentration as a function of radial position. In the bulk gas, the oxygen concentration is expressed as the mole fraction of H_2O in the bulk gas. In the cladding, the oxygen concentration is expressed as the ratio of oxygen to Zr atoms. The symbols in Figure 3-1 are defined in Table 3-1.

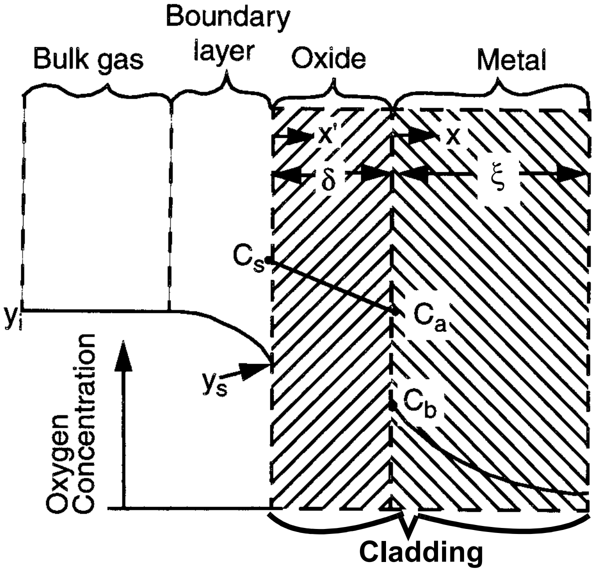

Figure 3-1. Schematic of oxygen distribution in fuel rod cladding and surrounding coolant.

Table 3-1. Definition of symbols in Figure 3-1.

Symbol	Units	Definition
y_i	-	*mole fraction of* H_2O *in bulk gas at axial node i*
y_s	-	*mole fraction of* H_2O *in gas at outer surface of oxide layer*
C_s	-	*O/Zr ratio at external surface of oxide layer*
C_a	-	*O/Zr ratio at inner surface of oxide layer;* $1.97 \leq C_a \leq 1.985$ *for temperature less than 1773 K,* $C_a = 1.72$ *for temperature greater than 1773 K.*
C_b	-	*O/Zr ratio at outer surface of metallic layer (terminal solubility)*
δ	*m*	*thickness of oxide layer*
ξ	*m*	*thickness of metallic layer*
x'	*m*	*spatial coordinate for oxide layer*

Table 3-1. Definition of symbols in Figure 3-1. (Continued)

Symbol	Units	Definition
x	*m*	*spatial coordinate for metallic layer*

The overall oxygen transport is calculated by coupling the equations that calculate the diffusion of oxygen through the three layers shown in Figure 3-1. The integral diffusion method of solution as derived by Olander[3-4] is used. The distance steam penetrates into the fuel-cladding gap from the point of cladding rupture is assumed to be negligible. Theoretical analyses and experimental results have shown the distance of penetration to be small when compared to the overall length of fuel rods.[3-5,3-20,3-21] Thus, the cladding inner surface boundary condition for the diffusion equation is defined simply to be a gradient of zero in oxygen concentration.

Oxygen transport is governed to a significant extent by the phase diagram for the Zr - O system. Figure 3-2 shows the simplified phase diagram[3-4] employed. The symbols in this figure are the same as those defined in Table 3-1. In a steam-rich environment, C_s equals 2.00 and the outer surface is stoichiometric oxide ZrO_2. In a steam-starved environment, y_s may be small enough that C_s is less than 2.00. When C_s is reduced in value to the O / Zr ratio of the lower phase boundary of zirconia ($C_s = C_a$ as shown in Figure 3-2), the oxide layer gradually dissolves into the metallic layer and eventually may completely disappear. When this occurs, hydrogen begins to diffuse into the metallic layer.

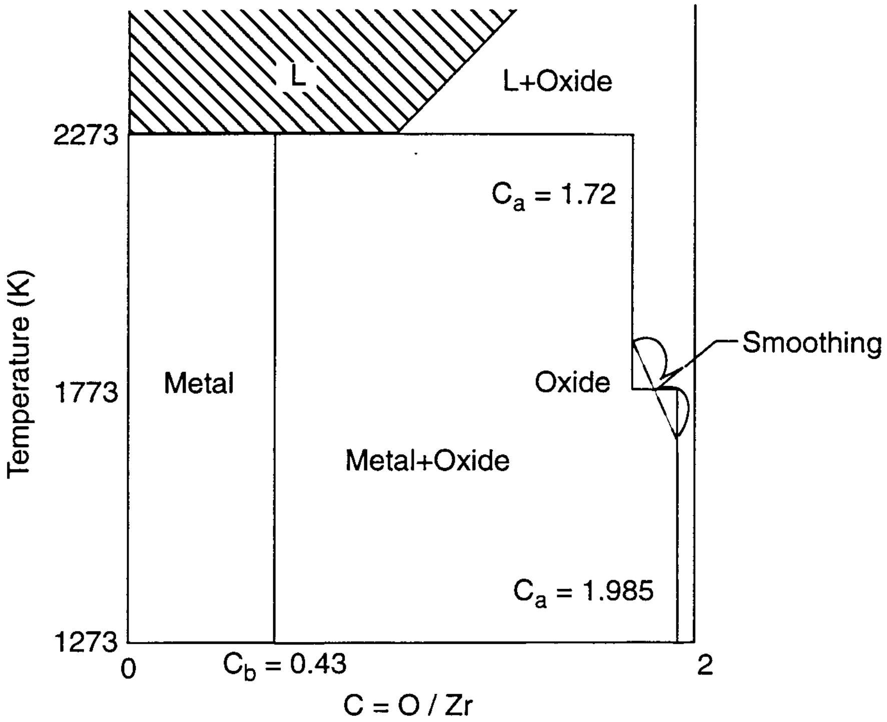

Figure 3-2. Simplified Zr-O phase diagram with homogenized oxide and metal phases.

The equations for calculating the oxygen diffusion through the three layers shown in Figure 3-1 are described next.

The flux of water vapor through the gas boundary layer is calculated by the equation

$$\dot{w} = k_g C_g (y_i - y_s) \tag{3-1}$$

where

$\dot{w}$ = mass flux of oxygen through the gas boundary layer $(\mathrm{kg-moles/m^2 \cdot s})$,

k_g = mass transfer coefficient (m/s),

C_g = molar density of the bulk gas $(p_{tot}/RT)(\mathrm{kg-mole/m^3})$,

p_{tot} = total pressure of the bulk gas (Pa),

R = universal gas constant $(\mathrm{Pa \cdot m^3/kg{-}mole \cdot K})$,

T = temperature of bulk gas (K),

y_i = mole fraction of H_2O in the bulk gas at location of axial node i,

y_s = mole fraction of H_2O in the gas at the cladding outer surface.

The mass transfer coefficient k_g is calculated using the analogy between heat and mass transfer. According to this analogy,

$$k_g = \frac{NuD_g}{d_h} \tag{3-2}$$

where

Nu = Nusselt number of the bulk gas $\left(\frac{hd_h}{k_v}\right)$,

d_h = hydraulic diameter $(s^2 - \pi r_o^2)/(2\pi r_o)$, (m),

h = convective heat transfer coefficient $(\mathrm{W/m^2 \cdot K})$,

D_g = binary diffusivity in $H_2O + H_2$ mixture (m^2/s),

k_v = thermal conductivity of the bulk gas $(\mathrm{W/m \cdot K})$,

s = pitch of the fuel rods (m),

r_o = outer radius of rods (m).

The heat and mass transfer analogy is valid provided that the Prandtl number is approximately equal to the Schmidt number for the gas mixture.[3-19] For the wide range in coolant pressures and temperatures that are possible during a severe accident, wide variations in Prandtl number and Schmidt number occur. For some range of conditions, these two numbers may vary significantly from each other and result in a loss of accuracy in the mass transfer calculation. However, the oxidation of fuel rods is generally not limited by the rate of mass transfer through the boundary layer, and the Prandtl and Schmidt numbers are not expected to have a large variance for extended periods of time over a large region of the reactor core. Therefore, the heat and mass transfer analogy is still an appropriate analysis tool to apply.

The variable D_g will be calculated by the model for mass diffusivity currently in SCDAP/RELAP5-3D©. This model is applicable to gas mixtures composed of several species. An alternative model for a mixture of H_2O and H_2 is presented in MATPRO (See Volume 4, Section 16).

The diffusion of oxygen through the gas boundary layer and then through the oxide layer can be regarded as two steps in series. Thus, diffusion through the two layers is equal and expressed by the equation

$$\dot{w} = \rho_{ox} D_{ox} (C_s - C_a) / \delta \tag{3-3}$$

where

ρ_{ox} = molar density of ZrO_2 (kg-mole/m^3) (47 kg-mole/m^3),

D_{ox} = diffusion coefficient of oxygen in the oxide layer (m^2/s).

The correlation to be used for D_{ox} is given in MATPRO (See Volume 4, Section 16). The linear profile for oxygen concentration and the steady state modeling of mass transfer implied by Equation (3-3) have been shown to incur errors of less than 1% in the calculated oxygen uptake.$^{3-4}$ The small error in calculation is due to the driving force (C_s - C_a) being a small fraction of C_a.

The value of C_s in Equation (3-3) is very close to 2.0 as long as the gas at the cladding surface contains at least a small fraction of water vapor$^{3-4}$. Thus, for usual applications, Equation (3-1) and Equation (3-3) can be combined to give

$$y_s = y_i - \frac{D_{ox} \rho_{ox} (2 - C_a)}{k_g C_g \delta} . \tag{3-4}$$

The value of C_s is a function of temperature and the partial pressures of steam and hydrogen in the gas adjacent to the cladding surface. This function is described in MATPRO (See Volume 4, Section16). A study applying this functional relation for C_s will be performed to determine how sensitive calculated results are to the value of C_s.

When y_s as calculated by Equation (3-4) is negative, the oxygen uptake is limited to the flux through the gas boundary layer as given by Equation (3-1) with y_s equal to 0.0. Thus for this condition, C_s is calculated using

$$C_s = C_a + \frac{k_g C_g y_i \delta}{\rho_{ox} D_{ox}} . \tag{3-5}$$

The overall mass balance for zirconium is calculated by the equation

$$\xi_o = \xi_1 + G\delta_o = \xi + G\delta \qquad (3\text{-}6)$$

where

ξ_o = as-fabricated thickness of cladding (m),
ξ_1 = thickness of metallic layer at time 0.0 (m),
δ_o = thickness of oxide layer at time 0.0 (m),
ξ = thickness of metallic layer at time t (m),
δ = thickness of oxide layer at time t (m),
G^{-1} = Pilling-Bedworth ratio of ZrO_2 (G=0.67).

Oxygen transport in the metallic layer is governed by Fick's law, with a convective term that accounts for the moving oxide-metal interface. Fick's law is expressed by the equation

$$\frac{\partial c}{\partial t} = D_m \frac{\partial^2 c}{\partial x^2} + G\frac{d\delta}{dt}\frac{\partial c}{\partial x} \qquad (3\text{-}7)$$

where

c = O/Zr ratio in the metallic layer at time t and at radial coordinate x,
x = distance from moving interface, as shown in Figure 3-1 (m),
t = time (s),
D_m = diffusion coefficient of oxygen in α - Zr (m^2/s).

The initial and boundary conditions for the above equation are

$$c(x, o) = c_o \qquad (3\text{-}8)$$

where

c_o = oxygen concentration in as-fabricated Zircaloy

$$c(o, t) = C_b \qquad (3\text{-}9)$$

$$\frac{\partial c(\xi, t)}{\partial x} = 0.0 \qquad (3\text{-}10)$$

The boundary condition applied in Equation (3-10) is based on the assumption that the rate of oxygen entering the cladding at the inner surface is negligible. If the fuel and cladding are not forced into contact and the location is more than a few centimeters from the point of cladding rupture, this assumption is justified.[3-5] The boundary condition is appropriate for cladding that has ballooned but not melted.

The analysis of a melted metallic layer in contact with an oxide layer (ZrO_2) on one side and fuel (UO_2) on the other side is an extension in modeling that goes beyond the scope of this model development effort. A framework for this extended model is established by the model described in this document. In order to accomplish this extension, the boundary condition represented by Equation (3-10) needs to define the oxygen flux at the dissolution front in the fuel. Boundary conditions at moving positions would be required at both sides of the melted Zr layer. Mass diffusion in the fuel would need to be calculated, and an account made of the effect of dissolved UO_2 on diffusion in the metallic layer. While this extension requires considerable modeling effort, it has the virtue of accounting for the effect of UO_2 dissolution on ZrO_2 dissolution.

The correlation to be used for D_m in Equation (3-7) is given in MATPRO.

The integral diffusion method is applied by integrating Equation (3-7) with respect to x over the thickness of the metallic layer. The integration is performed over the domain ($0 < x < \xi$). The result of this integration is

$$\frac{d}{dt}(\xi\bar{c}) = D_m\left[\left(\frac{\partial c}{\partial x}\right)_\xi - \left(\frac{\partial c}{\partial x}\right)_0\right] + G\frac{d\delta}{dt}\left[c(\xi, t) - C_b\right] \tag{3-11}$$

where

$\bar{c}$ = average O/Zr ratio in the metallic layer.

The variable $\bar{c}$ is calculated by the equation

$$\bar{c} = \frac{1}{\xi}\int_0^\xi c(x, t)dx\,. \tag{3-12}$$

Equation (3-11) is converted to an ordinary differential equation by choosing an approximate distribution c(x,t) that automatically satisfies the boundary conditions as expressed by Equation (3-9) and Equation (3-10) and contains a single time-dependent parameter whose value at t = 0 satisfies the initial conditions expressed by Equation (3-8). Such an approximate distribution is given by the function

$$c = C_b\frac{\exp((-\phi/E) + \exp\{-(1-\phi)/E\})}{1 + \exp(-1/E)} \tag{3-13}$$

$$\phi = \frac{x}{2\xi} \quad 0 \le \phi \le \frac{1}{2}\,.$$

The substitution of Equation (3-13) into Equation (3-11) results in the equation for calculating the rate of change of the average O/Zr ratio in the metallic layer. The result of this substitution is;

$$\frac{d}{dt}\left(\frac{\bar{c}}{c_b}\right) = \frac{D_m}{(2E\xi)^2}\left(\frac{\bar{c}}{c_b}\right) - \frac{G}{\xi}\left[1 - \frac{2\exp\left(-\frac{1}{2E}\right)}{1 + \exp\left(-\frac{1}{E}\right)}\right] \tag{3-14}$$

The variable E is a function of time. It is evaluated by the relationship between E and the average O/Zr ratio in the metallic layer. This relationship is obtained by substituting Equation (3-13) into Equation (3-12). The result of this substitution is

$$\frac{\bar{c}}{C_b} = 2E\frac{1-\exp(-1/E)}{1+\exp(-1/E)}. \tag{3-15}$$

The rate of movement of the inside surface of the oxide layer is equal to the difference between the oxygen flux on the outside surface of the metallic layer and the oxygen flux on the inside surface of the oxide layer. This relation is expressed by the equation

$$\rho_{ox}(C_a - C_b)\frac{d\delta}{dt} = \rho_M D_M\left(\frac{\partial c}{\partial x}\right)_o - \rho_{ox} D_{ox}\left(\frac{\partial c'}{\partial x'}\right)_\delta \tag{3-16}$$

where

$\left(\frac{\partial c}{\partial x}\right)_o$ = O/Zr gradient in the metallic layer at its interface with the oxide layer,

$\left(\frac{\partial c'}{\partial x'}\right)_\delta$ = O/Zr gradient in the oxide phase at its interface with the metallic layer,

ρ_m = molar density of Zr in the metallic layer (kg-mole/m^3).

The value of ρ_m is given by the equation

$$\rho_m = \rho_{ox}/G = \rho_{ox}/0.67. \tag{3-17}$$

The oxygen concentration distribution in the oxide layer is assumed to be linear. Thus the variable $(\partial c'/\partial x')_\delta$ in Equation (3-16) is given by the equation

$$\left(\frac{\partial c'}{\partial x'}\right)_\delta = (C_a - C_s)/\delta. \tag{3-18}$$

Substituting Equation (3-18) into Equation (3-16), replacing ρ_m with its equivalent of ρ_{oX}/G, and evaluating the oxygen concentration gradient at x = 0 in Equation (3-16) using Equation (3-13) yields the equation

$$G(C_a - C_b)\frac{d\delta}{dt} = -\frac{D_m C_b}{4E^2\xi}\left(\frac{\bar{c}}{C_b}\right) + \frac{GD_{ox}}{\delta}(C_s - C_a). \tag{3-19}$$

Equation (3-19), Equation (3-6), Equation (3-11), and Equation (3-15) are a coupled set of equations used to solve for the unknown variables δ, ξ, $\bar{c}$, and E, respectively.

The calculated value of δ is used to determine whether the Zr-H reaction begins in the cladding. If δ is greater than zero, then the oxide layer insulates the metallic layer from the hydrogen in the bulk gas. If δ is equal to zero, then hydrogen diffuses into the metallic layer.

The integral method is used to calculate oxygen transport in the two other possible cladding states, namely the state where no oxide layer is present and the state where no metallic layer is present. The description of the solution for these states covers the other possible states of the cladding.

In the event that the oxide layer has dissolved completely into the metallic layer and is no longer present, the oxygen transport in the metallic layer is then governed by the equation

$$\frac{\partial c}{\partial t} = D_m \frac{\partial^2 c}{\partial x^2} . \tag{3-20}$$

The boundary condition for Equation (3-20) at the outer surface of the metallic layer is the oxygen flux through the gas phase boundary. This boundary condition is expressed by the equation

$$k_g[C_g y_i - c(o,t)] = -D_M \rho_M \left(\frac{\partial c}{\partial x}\right)_0 . \tag{3-21}$$

The absence of the oxide layer is assumed to imply a steam-starved interface. Thus, c(o,t) = 0.0.

At the inner surface of the metallic layer, the zero flux condition applies; i.e.,

$$\left(\frac{\partial c}{\partial x}\right)_{\xi_o} = 0. \tag{3-22}$$

The initial condition for Equation (3-20) is the oxygen distribution in the metallic layer at the time the oxide layer just disappeared. The integral method will also be applied to solve for Equation (3-20). The approximate oxygen distribution as defined by Equation (3-13) is used to solve Equation (3-20). The terminal oxygen solubility at the outer surface of the metallic layer (variable C_b in Equation (3-13)) is replaced by the undetermined function c(0,t):

$$c = c(0,t)\frac{\exp(-\phi/E) + \exp\{-(1-\phi)/E\}}{1 + \exp(-1/E)} \tag{3-23}$$

where

$$\phi = \frac{x}{2\xi_o} \quad 0 \le \phi \le \frac{1}{2} .$$

The average oxygen concentration in the metallic phase is thus given by the equation

$$\frac{\bar{c}}{c(0,t)} = 2E\frac{1-\exp(-1/E)}{1+\exp(-1/E)}. \tag{3-24}$$

Substituting the approximate oxygen distribution as given by Equation (3-24) into Equation (3-21) and using Equation (3-24) to eliminate the surface concentration defines the parameter E according to

$$E = \left\{\frac{D_M\rho_M C_b}{4\xi_o k_g C_g y_i}\left(\frac{\bar{c}}{C_b}\right)\right\}^{1/2}. \tag{3-25}$$

The concentration of oxygen at the external surface of the metallic layer can be determined by solving Equation (3-24) for c(0,t). The result is

$$\frac{c(0,t)}{C_b} = \frac{(\bar{c}/C_b)}{2E}\frac{1+\exp(-1/E)}{1-\exp(-1/E)}. \tag{3-26}$$

Finally, the integration of Equation (3-20) with respect to x over the domain ($0 < x < \xi_0$) results in the equation

$$\frac{d}{dt}\left(\frac{\bar{c}}{C_b}\right) = \frac{k_g C_g y_i}{\rho_M \xi_o C_b}. \tag{3-27}$$

Equation (3-25) and Equation (3-27) are a set of two coupled equations used to solve for the two variables E and $\bar{c}$, respectively. Equation (3-26) is also applied at each time step to determine whether the surface concentration c(o,t) has returned to the terminal solubility C_b. If the value of the right hand side of Equation (3-26) is greater than unity, then c(o,t) has exceeded the surface solubility and the oxide layer forms again.

The case of an oxide layer propagating to the inner surface of the cladding is presented next. The time at which the oxide layer propagates to the inner surface is designated by the symbol t_{sw}. The average O/Zr ratio in the oxide layer and the oxygen concentration gradient through the oxide layer are given by the equations

$$\bar{c}' = \frac{1}{2}(C_s + C_a), \tag{3-28}$$

$$\frac{dc'}{dx'} = -\frac{C_s - C_a}{\xi_o/G}. \tag{3-29}$$

For $t > t_{sw}$, the oxygen concentration distribution through the oxide layer is no longer linear. The gradient for the oxygen concentration distribution at the inner surface of the cladding is given by the equation

$$\left(\frac{}{\partial x'}\right)_{\xi_o / G} = 0 . \tag{3-30}$$

To track the approach of the oxide layer to complete conversion to stoichiometric ZrO_2, the oxygen concentration distribution through the oxide layer is assumed to be approximated by the following function:

$$c' = C_s - a\left(\eta + \frac{1}{2}\eta^2 - \frac{2}{3}\eta^3\right) \tag{3-31}$$

where

$$\eta = \frac{x'}{\xi_o / G}$$

The polynomial function in Equation (3-31) has only one minimum for positive values of η, and that occurs at $\eta = 1$, thereby satisfying Equation (3-30)[3-4].

In Equation (3-31), the variable “a” is a function of time that is to be determined. Equation (3-18) has only one minimum for positive values of η, and that occurs at $\eta = 1$, which results in the boundary condition for the inner surface of the cladding being satisfied as expressed by Equation (3-30).

The average oxygen concentration in the oxide layer (approximated by Equation (3-31)) is given by the equation

$$\bar{c}' = \int_0^1 c' d\eta = C_s - \frac{1}{2}a . \tag{3-32}$$

The gradient in the oxygen concentration at the outer surface of the oxide layer is given by the equation

$$\left(\frac{dc'}{d\eta}\right)_0 = -a . \tag{3-33}$$

Equation (3-33) satisfies Equation (3-29) when the function a(t) at time t_{sw} has the following value;

$$a(t_{sw}) = C_s - C_a . \tag{3-34}$$

Oxygen diffusion in the oxide layer is governed by Fick’s law as expressed by the equation

$$\frac{\partial c'}{\partial t} = D_{ox}\frac{\partial^2 c'}{\partial x'^2} . \tag{3-35}$$

Equation (3-35) can be integrated with respect to x’ over the cladding thickness of $(0 < x' < (\xi_0 / G))$. The oxygen concentration gradients at the inner and outside surfaces of the oxide layer are calculated from Equation (3-30) and Equation (3-33), respectively. The result is an ordinary differential equation for the variable a(t) expressed as follows

$$\frac{da}{dt} = \frac{2D_{ox}}{(\xi_o/G)}a \quad t \geq t_{sw}. \tag{3-36}$$

The initial condition for Equation (3-36) is given by Equation (3-34). Since the variable D_{ox} varies with temperature and thus in severe accident conditions varies with time, Equation (3-36) cannot be directly integrated and instead must be solved numerically.

The oxygen uptake rate is determined from the solution of Equation (3-36) in conjunction with

$$\dot{w} = -\rho_{ox}D_{ox}\left(\frac{\partial c'}{\partial x'}\right)_0 = -\frac{\rho_{ox}D_{ox}}{\xi_o/G}\left(\frac{dc'}{d\eta'}\right)_0 = \frac{\rho_{ox}D_{ox}}{\xi_o/G}a \tag{3-37}$$

where

$\dot{w}$ = oxygen uptake rate (kg - moles/m^2 · s).

The heat generation caused by oxygen uptake is calculated by the equation

$$q_{ox} = f_c H_r (A_{zr}/A_{ox}) 2\pi r_o \dot{w} \tag{3-38}$$

where

q_{ox} = rate of heat generation caused by oxygen uptake (W/m),

f_c = fraction of circumference of cladding with metallic substrate (1.0 before cladding melting and f_{cm} after cladding melting),

f_{cm} = fraction of circumference of cladding with melted metallic substrate (defined by cladding meltdown model),

A_{zr}, A_{ox} = molecular weights if Zr and oxygen, respectively (91.22 and 32.0),

r_o = radius of outer surface of cladding (m).

A complete set of equations have now been expressed for calculating oxygen diffusion through the cladding for the three possible phase states of the cladding.

3.1.3 Hydrogen Uptake in Cladding

The disappearance of the cladding oxide layer in a region of the reactor core with hydrogen-rich fluid results in the diffusion of hydrogen into the cladding. The uptake of hydrogen results in heat generation and embrittlement of the cladding. The calculation of the time that the oxide layer may disappear has been presented in Section 3.1.2. This section presents a set of equations that can be solved to calculate the uptake of hydrogen in the cladding. Equations are also presented for calculating the effect of hydrogen uptake on fuel rod heatup cladding structural integrity.

A simplified approach for calculating the rate of hydrogen uptake is used. This approach capitalizes on the numerical results of detailed calculations. A schematic for the hydrogen uptake in the cladding model is shown in Figure 3-3. A detailed model for hydrogen uptake involves the coupling of several phenomena; (1) diffusion of hydrogen from the fluid adjoining the external surface of the cladding through the cladding into the fuel-cladding gap, (2) ternary diffusion of a mixture of Xe, He, and H_2 in the axial direction through the fuel-cladding gap and then through the breach in the cladding caused by cladding rupture, (3) release from fuel of Xe, and (4) diffusion of He from the upper fuel rod plenum into the fuel-cladding gap[3-5]. Calculations have shown that hydrogen uptake occurs rapidly until the equilibrium solubility of the cladding is attained. In a calculation with conditions typical of a severe accident, hydrogen uptake to equilibrium solubility occurred in about 50 s[3-5]. This period of time is small when compared to the period of time for evolution of the important damage progression events occurring during a severe accident. The rate of hydrogen permeation into the cladding was calculated to be much greater than the rate of hydrogen diffusion of hydrogen from the breach site. Also, the amount of hydrogen that can be absorbed by the fuel-cladding gap is small compared to the amount of hydrogen that can be absorbed by the cladding. In view of the short time period for hydrogen uptake and the small amount of hydrogen absorption and diffusion in the fuel-cladding gap, the modeling of the axial diffusion of hydrogen through the fuel-cladding gap and then its diffusion out of the breach site is not justified. Therefore, a simplified approach to calculating hydrogen uptake will be taken. If assessment indicates that this simplified approach is not justified, then an integral diffusion method similar to that used for oxygen uptake can be implemented.

The equilibrium solubility of hydrogen in the Zircaloy is assumed to be governed by Sievert's law.[3-6] According to Sievert's law for Zr-H interaction, the equilibrium solubility is given by the equation

$$C_H = A_{SH} \exp\left(-\frac{\Delta H_H}{RT}\right)(p_{H_2})^{0.5} \tag{3-39}$$

where

C_H = H/Zr ratio of the metal in equilibrium with the gas containing H_2 at a pressure of (p_{H_2}),

A_{SH} = Sievert's law constant,

ΔH_H = enthalpy of solution (kcal/mol),

R = universal gas constant (1.987 cal/mole · K),

T = temperature of cladding (K),

(p_{H_2}) = partial pressure of hydrogen (atm).

Sievert's law constant is given by the equation[3-6]

$$A_{SH} = e^{\Delta S/R} \tag{3-40}$$

where

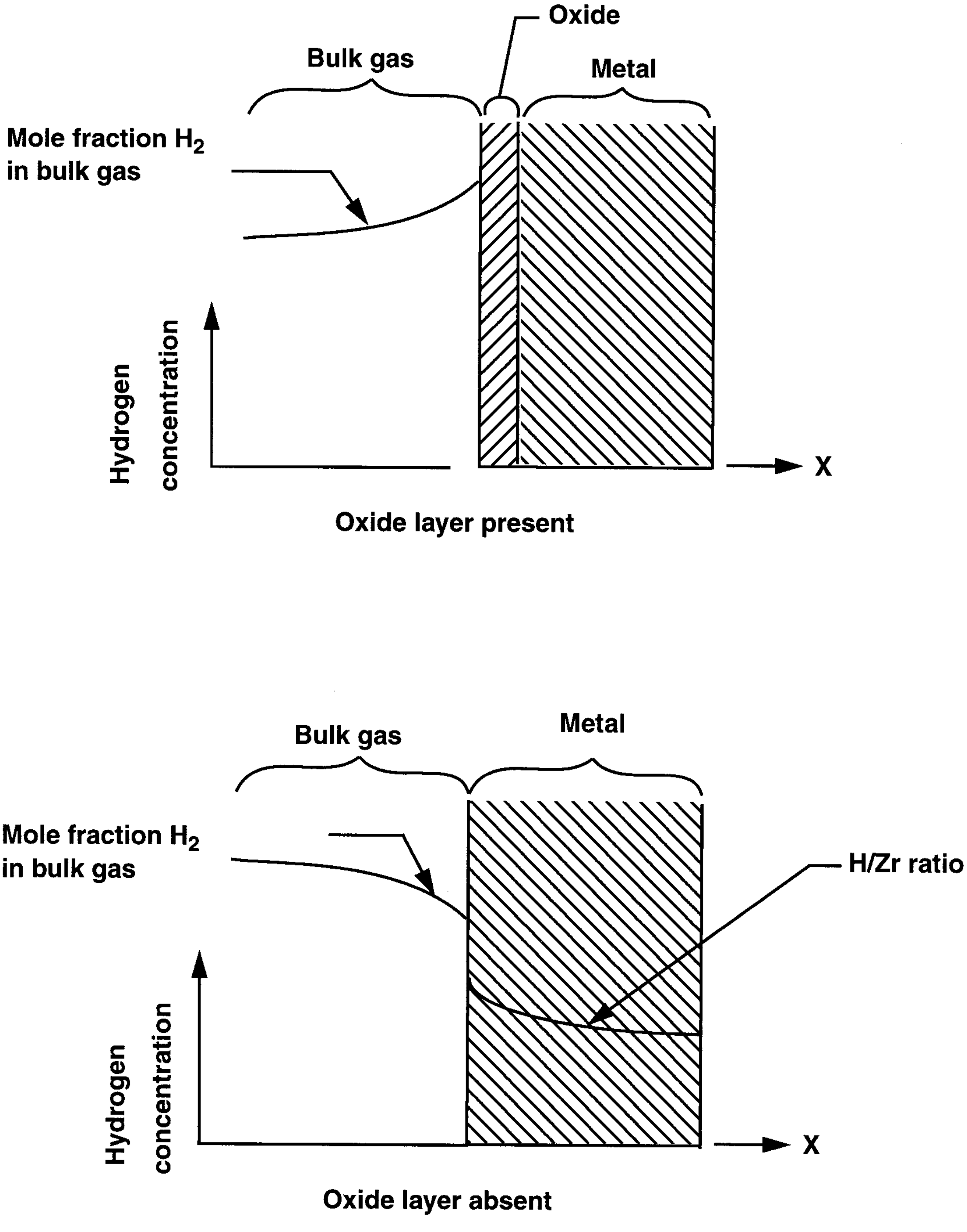
Oxide
Bulk gas
Metal
Mole fraction H_2 in bulk gas
Hydrogen concentration
X
Oxide layer present
Bulk gas
Metal
Mole fraction H_2 in bulk gas
H/Zr ratio
Hydrogen concentration
X
Oxide layer absent

Figure 3-3. Schematic of hydrogen uptake in cladding.

ΔS = entropy of solution of hydrogen in zirconium (cal/mol · K).

According to experimental results obtained by Moalem and Olander[3-6], the entropies and enthalpies of solution of hydrogen in zirconium vary somewhat with the oxygen content and the phase (α or β) of the zirconium. Representative values for severe accident analysis are:

$$\Delta S = -12.5\,\mathrm{cal/mol \cdot K} \tag{3-41}$$

and

$$\Delta H_H = -13.1\ \mathrm{Kcal/mol}. \tag{3-42}$$

Since the enthalpy of solution (ΔH_H) is negative, the Zr-H_2 reaction is exothermic and thus causes an increase in the heatup of the cladding.

Substituting the values ΔS and ΔH_H given by Equation (3-41) and Equation (3-42) into Equation (3-40) and Equation (3-39) results in the following equation for C_H:

$$C_H = 1.85 x 10^{-3} \exp(6593/T)(p_{H_2})^{0.5}\ . \tag{3-43}$$

For cladding at a temperature of 2000 K and a hydrogen pressure of 0.1 MPa (1 atm), the value of C_H as calculated by Equation (3-43) is 0.05. For cladding at a temperature of 2000 K and a hydrogen pressure of 3 MPa (30 atm), the value of C_H is 0.27. For cladding at a temperature of 1273 K and a hydrogen pressure of 0.1 MPa (1 atm), the value of C_H is 0.33.

The rate of hydrogen uptake after disappearance of the oxide layer is based on Olander's numerical results[3-5] and not upon mechanistic modeling. According to Olander's numerical results, the hydrogen uptake in severe accident conditions attains an equilibrium level in ~ 50 s. This calculated rate of hydrogen uptake is consistent with the rate of hydrogen uptake measured by Steinbruck, et al.[3-7] The hydrogen uptake is assumed to follow a parabolic kinetics rule. Thus, the rate of hydrogen uptake is assumed to be given by the equation

$$\frac{dw_h}{dt} = \frac{K_h(T)}{w_h} \tag{3-44}$$

where

w_h = uptake of hydrogen (ratio of hydrogen concentration in cladding to hydrogen concentration at equilibrium level),

$K_h(T)$ = parabolic kinetics constant for uptake of hydrogen, which is a function of temperature (1/s), t = time (s).

The initial condition for Equation (3-44) is

$$w_h(t_{dis}) = 0.0 \ . \tag{3-45}$$

For analysis of hydrogen uptake during isothermal conditions, the value of K(T) does not change with time. Thus, Equation (3-44) can be integrated to give

$$w_h = [2K_h(t - t_{dis})]^{0.5} \tag{3-46}$$

where

t_{dis} = time at which the oxide layer on the external cladding surface disappeared (s).

At the hydrogen equilibrium concentration, C_H, the value of w_h is one.

The time to attain an equilibrium hydrogen concentration is assumed to be t_{eq} . Substituting these values into Equation (3-46) and solving for K_h, the result is:

$$K_h(T) = \frac{1}{2t_{eq}} \ . \tag{3-47}$$

The value t_{eq} is a function of temperature. The approximate dependence of t_{eq} on temperature has been investigated by Steinbruck, et al.[3-7] Figure 3-4 is a plot of the rate of hydrogen uptake as a function of

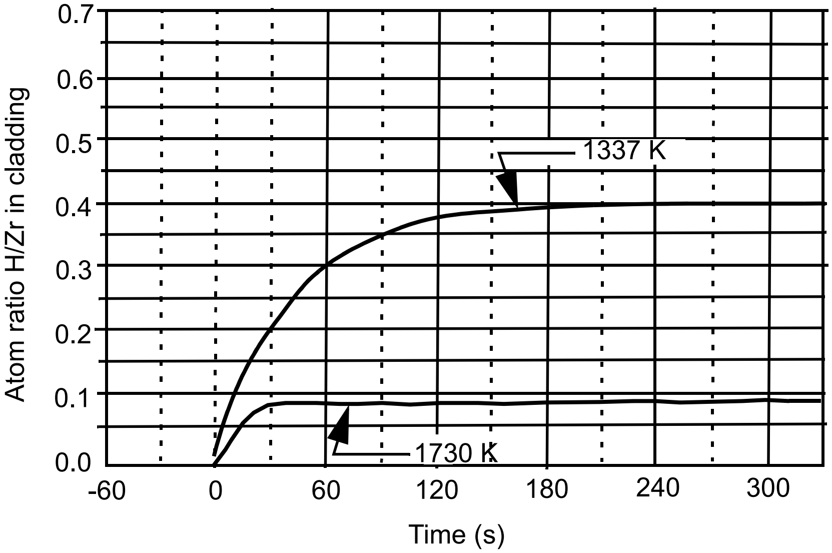

Figure 3-4. Rate of hydrogen uptake as function of temperature as measured by Steinbruck, et al.

temperature as measured by Steinbruck, et al. The approximate value of t_{eq} as indicated by the experimental results is shown in Table 3-2. For cladding at a temperature of 1730 K, the value of t_{eq} is 30 s. For cladding at a temperature of 1435 K, the value of t_{eq} is 120 s. For temperatures between the temperature values shown in Table 3-2, the value of t_{eq} will be found by linear interpolation.

Table 3-2: Period of hydrogen uptake (parameter t_{eq})as a function of temperature.

Cladding temperature (K)	t_{eq} (s)
<1240	*300*
1240	*300*
1340	*200*
1435	*120*
1540	*60*
1640	*40*
1730	*30*
>1730	*30*

The uptake of hydrogen is an exothermic reaction that accelerates the heatup of the fuel rod. The heatup due to hydrogen uptake is calculated by the equation:

$$\dot{Q}_H = -2\pi r_o \xi_o \rho_M \Delta H_{HSI}(C_{H2} - C_{H1}) / \Delta t \tag{3-48}$$

where

$\dot{Q}_H$ = rate of heat generation at an axial node due to uptake of hydrogen (W/m),

r_o = radius of external surface of cladding (m),

Δz = height of axial node (m),

ρ_M = molar density of Zr in zircaloy $(\mathrm{kg \cdot mole/m^3})$,

ξ_o = as-fabricated thickness of cladding (m),

ΔH_{HSI} = enthalpy of solution in SI units $(\mathrm{J/(kg) \cdot mole})$,

C_{H2} = H/Zr ratio in cladding at end of time step,

C_{H1} = H/Zr ratio in cladding at start of time step,

Δt = time step (s).

The enthalpy of solution, ΔH_H, has a value of -13.1 kcal/mol[3] for Zircaloy with a O/Zr ratio of 0.2. Converting the units of the enthalpy of solution to SI units, the result is

$$\Delta H_{HSI} = -3.129 \times 10^6 \tag{3-49}$$

where

ΔH_{HSI} = enthalpy of solution $(J/kg \cdot mole)$.

The enthalpy of solution varies slightly with variations in the O/Zr ratio of the cladding, but may vary significantly with (H/Zr) ratio.[3-19] Since the enthalpy of solution as a function of (H/Zr) ratio is not available at this time, ΔH_{HSI} is assumed not to be a function of (H/Zr) ratio.[3-29]

The rate of heat generation due to hydrogen uptake is calculated to not be as significant as implied by Olander.[3-5] Given the typical severe accident conditions as defined in Table 3-3, Equation (3-42) and Equation (3-46) calculate the average rate of heat generation due to hydrogen uptake through the period of hydrogen uptake to be 36 W/m. This rate of heatup is small when compared to the heat generation rate due to oxidation under these same conditions, which is calculated to be about 400 W/m.

Table 3-3: Conditions for example calculation of rate of heat generation due to hydrogen uptake.

Variable	Units	Value
P_{H2}	*MPa*	*3.0*
T	*K*	*2000*
r_0	*m*	4.8×10^{-3}
ξ_0	*m*	0.6×10^{-3}
ρ_m	*kg-mol/m*^{3}	*70.5*
ΔH_{HSI}	*J/kg-mol*	-3.129×10^6
$C_{H2} - C_{H1}$	*H/Zr ratio*	*0.27*
Δt	*s*	*50.*

After the hydrogen concentration has reached the solubility limit (equilibrium level), further heatup of the cladding results in a reduction in solubility and thus a release of hydrogen. The desorption of hydrogen is endothermic and results in the cladding functioning as a heat sink.

3.1.4 Cladding Embrittlement and Hydrogen Release

Hydrogen may be stored in the cladding due to hydrogen uptake during a period of steam-starved oxidation[3-8,3-9] and then be released during a quenching period when the cladding may crack due to thermal stresses in cladding embrittled by a combination of oxygen and hydrogen uptake.[3-9,3-10] The embrittlement of the cladding decreases its ductility to the point that the stresses induced by a temperature gradient during quenching may result in cracking of the cladding. The model is also applied to determine the time and location where the cladding may crack to the extent that hydrogen absorbed in the metallic phase of the cladding is released and oxygen from the coolant may contact the inner surface of the cladding.

A model accounting for the effect of hydrogen uptake on structural integrity is presented. This model is based on the results of experiments that involved the reflood of hot fuel rods. Neither a theoretical model nor a broadly-based empirical model appropriate for SCDAP/RELAP5-3D© were found in the literature. The phase diagram for the Zr-H system shown in Figure 3-5 provides an indication of the ranges of temperature and hydrogen concentration where cladding may be embrittled. The key feature of this diagram, relative to embrittlement, is the eutectoid reaction at about 550° C (823 K) which upon cooldown produces a brittle hydride phase in equilibrium with zirconium. The Appendix K[3-11] embrittlement criteria defines cladding to be embrittled when it is more than 17% oxidized. This criteria is considered to have enough conservatism that the additional embrittlement due to hydrogen uptake does not need to be taken into account.[3-10] Its conservatism does not make it appropriate for SCDAP/RELAP5-3D©. The Chung and Kassner embrittlement model[3-12] defines cladding to be embrittled when the thickness of the beta phase of the cladding is less than 0.1 mm and the concentration of hydrogen in the metal phase is less than 20 at.% (2200 ppm). Recent experimental results indicate that this model may not account fully for the effect of hydrogen concentration on embrittlement and that it may not be applicable for rapid cooling in a steam environment such as may occur above a quench front.[3-9] So an extension of existing models for embrittlement to account for hydrogen uptake was developed. First, experimental results are compiled that present a picture of the effect of the thickness of the cladding oxide layer and hydrogen concentration on cladding integrity during reflood. Then, an extension is made to the Chung and Kassner model to account for these experimental results.

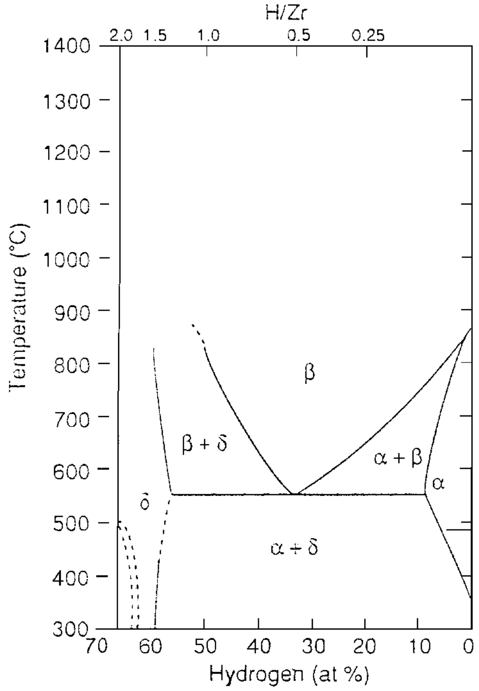

Figure 3-5. The Zirconium-Hydrogen phase diagram.

Experimental results applicable for evaluating the structural integrity of fuel rods during quenching are available from several sources. Results from the QUENCH program at the Forschungszentrum in Karlsruhe, Germany for fuel rods quenched from maximum temperatures of 1473 K and 1673 K are shown in Figure 3-6 and Figure 3-7, respectively.[3-9] The crack density data shown in these figures apply to the rapid cooling in steam (~50 K/s) of fuel rods that were heated in a steam environment to temperatures in the range of 1473 K to 1673 K. As shown in these figures, oxide layer thicknesses less than 0.15 mm did not result in cracking of the cladding. Oxide layer thicknesses in the range 0.15 mm to 0.225 mm resulted in axial cracks that penetrated through the wall of the cladding. Oxide layer thicknesses greater than 0.225 mm resulted in both axial and circumferential cracks in the cladding. In general, axial and circumferential cracks did not occur unless the oxide layer before quenching was greater than 0.2 mm. This threshold thickness increases somewhat with increasing temperature prior to quenching. As shown in Figure 3-6, the threshold thickness was 0.2 mm for a cladding temperature of 1473 K prior to quenching and was 0.225

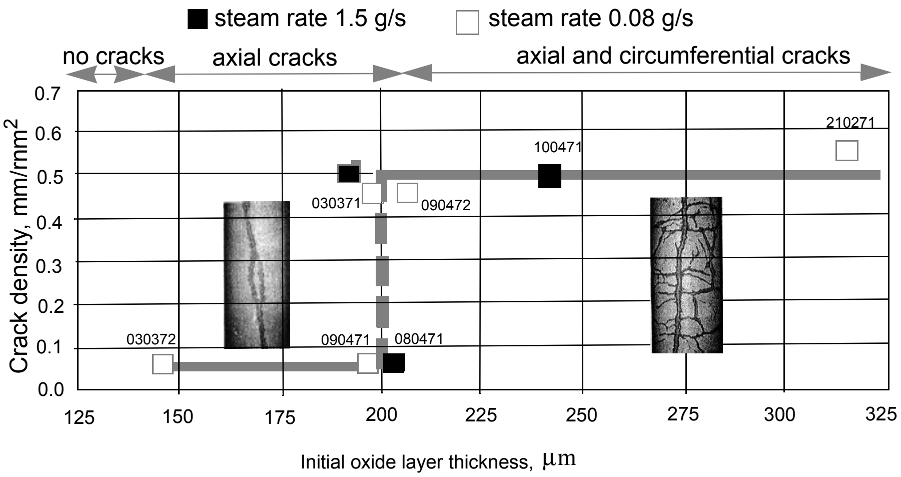

Figure 3-6. Crack formation in preoxidized Zircaloy during rapid cooldown from 1200° C by steam.

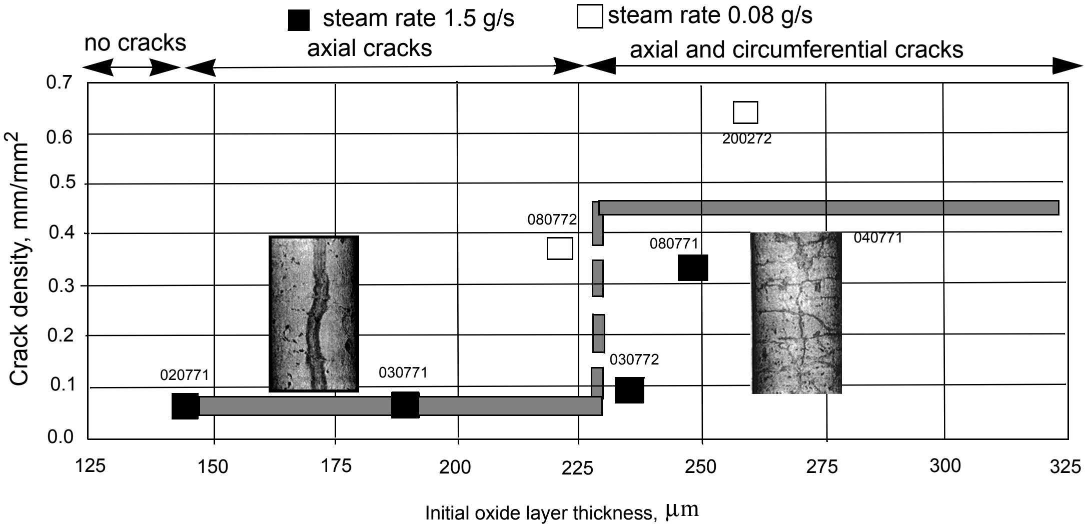

Figure 3-7. Crack formation in preoxidized Zircaloy during rapid cooldown from 1400° C by steam.

mm for a cladding temperature of 1673 K (Figure 3-7). Experiments performed at Argonne National Laboratory on the quenching of hot and partially oxidized fuel rods indicated that cracking of the cladding did not occur provided the thickness of the beta phase of the cladding was greater than 0.1 mm and the hydrogen concentration was less than 20 at.%.**3-12** These experiments quenched the fuel rods with water and involved cooling rates the order of 100 K/s. Experiments performed in the Power Burst Facility at the Idaho National Engineering and Environmental Laboratory on the quenching of hot and partially oxidized fuel rods indicated that cracking of the cladding may occur during quenching when the hydrogen concentration in the cladding exceeds 10 at.%.**3-13** These experiments also quenched the fuel rods with water and involved cooling rates the order of 100 K/s. Experiments performed at the Japan Atomic Energy Research Institute in Japan on the quenching of cladding under reflood conditions for large break Loss of Coolant Accidents indicate that hydrogen concentrations in excess of 20 at.% may contribute to the embrittlement of the cladding.**3-10**

The experimental results were used as a basis for extending the Chung and Kassner embrittlement model to account for hydrogen concentration and thickness of oxide layer. The extended embrittlement model is defined in Table 3-4. Blank column entries in a row indicate that embrittlement for that row is not a function of those column entries. As shown in Table 3-4, cladding with an oxide layer greater than 0.2 mm in thickness is defined to be embrittled independent of the values for beta phase thickness and hydrogen concentration. Cladding with a hydrogen concentration greater than 10 at.% is defined to be embrittled independent of the value of beta phase thickness or oxide layer thickness.

Table 3-4: Model for determining whether cladding is embrittled.

Beta phase thickness	Oxide layer thickness	Hydrogen concentration	Embrittled?
(mm)	(mm)	at.%	yes/no
>0.1	*<0.2*	*<10*	*no*
<0.1	-	-	*yes*
-	*>0.2*	-	*yes*
-	-	*>10*	*yes*

Embrittled cladding is assumed to crack when it is cooled to the temperature of 820 K at a rate greater than 50 K/s. This threshold value for the rate of cooling is based upon experiments that showed cracking of the cladding during quenching.[3-12] The temperature of 820 K is based upon the Zr-H phase diagram and experimental results. As shown previously in Figure 3-5, a phase change occurs in the Zr-H system for a broad range of hydrogen concentrations at a temperature of about 820 K. As shown in Figure 3-8 for an experiment performed for the QUENCH program at FZK, a significant release in absorbed hydrogen was observed to occur as cladding cooled to a temperature of less than 800 K (527° C).**3-9**

Ideally, a calculation would be performed of the stresses and strains in the metallic and oxidic cladding layers due to the large radial temperature gradients which occur during the quenching of hot fuel rods. The calculated stresses and strains would be compared with a model that defined the stresses and

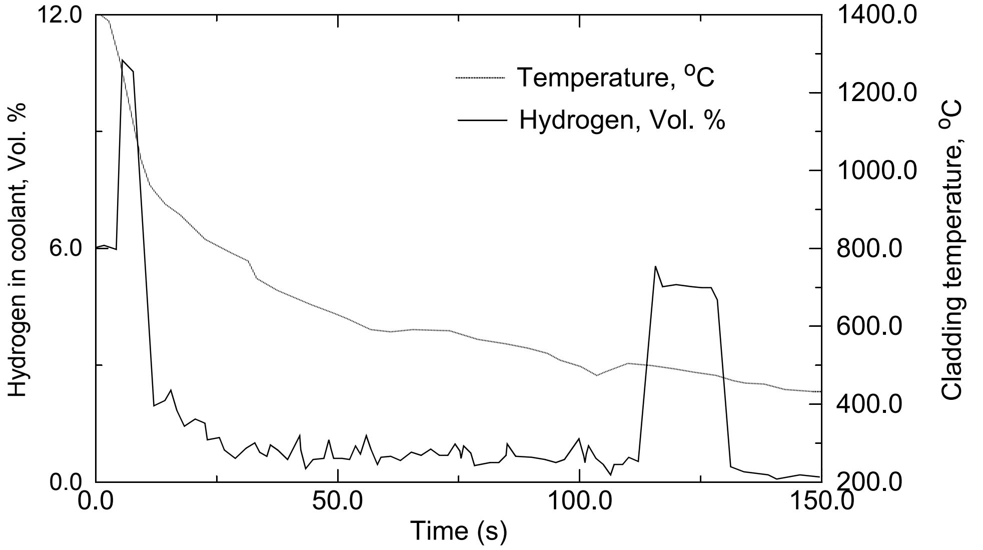

Figure 3-8. Temperature history and corresponding hydrogen release.

strains for cracking of the cladding as a function of temperature and concentrations of hydrogen and oxygen. The application of these models would account for the reduction in ductility of the cladding that occurs in certain phases of the Zr-O and Zr-H phase diagrams. The models to calculate these stresses and strains in the cladding require structural material properties as a function of concentrations of hydrogen and oxygen that are not available for high temperatures. Thus a determination of the times and localities where the cladding cracks can only be based upon experimental results.

As shown in Figure 3-8, the cracking of the cladding during quenching results in release of the hydrogen absorbed in the metallic phase of the cladding. This release of hydrogen is modeled by applying the same simplified approach used in modeling hydrogen uptake after complete dissolution of the oxide layer. This simplified approach was presented in Section 3.2.3 and is justified by experimental results that show hydrogen is quickly released following a change in boundary conditions that allows the release of hydrogen.[3-6] After cracking of the oxide layer occurs, the oxide layer is assumed to apply no resistance to the diffusion of hydrogen from the metallic layer to the bulk coolant. The rate of hydrogen release is based on experimental results shown in Figure 3-8. This figure shows that hydrogen was released at about a constant rate during a 20 s period after the cladding cooled to a temperature less than 800 K. There is no obvious physical reason for hydrogen to be released at a constant rate, but the only available experimental results indicate that this is the case.

Thus, the reduction in fractional hydrogen concentration in the cladding as a function of time is calculated by the equation

$$C_H = C_{HS}\left(1-\left[\frac{(t-t_{crk})}{t_{req}}\right]\right) \tag{3-50}$$

where

C_H = fractional hydrogen concentration at time t (H/Zr ratio),

C_{HS} = fractional hydrogen concentration just before start of cracking of cladding (H/Zr ratio),

t = time (s),

t_{crk} = time at which cladding cracked (s),

t_{req} = experimentally measured release time (s).

Based upon the experimental results shown in Figure 3-8, the variable t_{req} is assigned a value of 20 s.

The release of hydrogen to the bulk coolant during a time step is given by the equation

$$w_{hrci} = 2\pi r_o \Delta z \xi (C_{H1} - C_{H2}) \rho_m \tag{3-51}$$

where

w_{hrci} = kg-mol of H_2 released to bulk coolant due to cracking of cladding at axial node i,

r_o = outer node of cladding at axial node i (m),

Δz = height of axial node i (m),

ξ = thickness of metallic phase of cladding at axial node i (m),

C_{H1} = fractional hydrogen concentration at start of time step (H/Zr ratio),

C_{H2} = fractional hydrogen concentration at end of time step (H/Zr ratio),

ρ_m = molar density of Zr in Zircaloy (70.5 kg-mol/m^3).

Hydrogen release is also caused by the oxidation of cladding.[3-6] This mechanism for release occurs because the hydrogen solubility in ZrO_2 is very small. In this sense, hydrogen behaves similar to the fission product tellurium, which is strongly bound by Zr but not by ZrO_2.[3-6] With respect to tellurium, oxidation "squeezes" the tellurium into the ever diminishing metallic part of the cladding and then a puff of tellurium release occurs as the last small part of the metallic layer is oxidized. Since the concentration of tellurium in the cladding is estimated to be much less than the concentration of hydrogen, oxidation of the cladding is not considered to squeeze hydrogen into the ever diminishing metallic layer. Instead, an immediate release of the hydrogen in the portion of the cladding oxidized during a time step is assumed.

The oxidation driven release of hydrogen is calculated by the equation

$$w_{hroi} = 2\pi r_o \Delta z (\xi_1 - \xi_2) C_H \rho_m \tag{3-52}$$

where

w_{hroi} = kg-mol of hydrogen released to bulk coolant at axial node i,

r_o = outer radius of cladding at axial node i (m),

Δz = height of axial node i (m),

ξ_1 = thickness of metallic layer of cladding at axial node i at start of time step (m),

ξ_2 = thickness of metallic layer of cladding at axial node i at end of time step (m),

C_H = fractional hydrogen concentration at start of time step at axial node i (H/Zr ratio),

ρ_m = molar density of Zr in Zircaloy (70.5 kg-mol/m^3).

3.2 Approximations to Modeling of Oxidation During Meltdown and Reflood

The meltdown and reflood of fuel rods causes complex changes in the configuration of the cladding of the fuel rods. As a result, the modeling of the details of oxidation during meltdown and reflood becomes complex. The melting of the metallic part of the cladding causes two changes in the configuration of the cladding. First, at the onset of melting, the configuration of the cross section of the metallic part changes from an annular configuration to that of a segment of an annulus. The onset of melting of the metallic part also causes the cladding to contact the fuel and dissolve part of it, which changes the diffusivity and stoichiometry of the metallic part of the cladding. If heatup continues after the metallic part of the cladding has melted, the cladding oxide layer retaining the melted metallic part may lose its capability to retain the melted material. If this is the case, the metallic part slumps in the configuration of drops adhering to the outer surface of the oxide layer and then freezes after slumping into a lower and cooler region of the fuel rod. The reflood of hot fuel rods causes extensive cracking of the cladding oxide layer. Mechanistic modeling of these details in changes in configuration and their impact on oxidation cannot be implemented in a practical manner into a systems analysis code such as SCDAP/RELAP5-3D©. So approximations are required to the modeling of oxidation under the conditions of meltdown and reflood. This section describes these approximations. The results of integral fuel rod tests involving fuel rod meltdown and reflood were the basis for developing these approximations.

3.2.1 Affect on Oxidation of Melting of Cladding and Dissolution of UO_2.

The melting of the metallic part of the cladding may reduce the surface area through which oxygen uptake occurs, and may reduces the rate of oxygen uptake per unit length of fuel rod and reduces the linear heat generation due to oxidation. As described further in the section on the liquefaction of fuel rods (Section 4.7), the surface area for oxidation of ballooned fuel rod cladding is reduced because some of the liquefied metallic part of the cladding relocates in the circumferential direction and concentrates in the segment of the circumference with the largest fuel-cladding gap before melting.

The rate of heat generation after cladding melting is calculated by the equation

$$q_{oxm} = f_{cm} H_R (A_{zr} / A_{ox}) 2\pi r_o \dot{w} \tag{3-53}$$

where

q_{oxm} = rate of heat generation due to oxidation after cladding melting (W/m),

f_{cm} = fraction of circumference of cladding with metallic substrate,

A_{zr}, A_{ox} = molecular weights of Zr and oxygen, respectively (91.22 and 32),

r_o = radius of outer surface of cladding (m),

$\dot{w}$ = oxygen uptake rate $(\mathrm{kg} \cdot \mathrm{moles} / \mathrm{m}^2 \cdot \mathrm{s})$.

As described in the section on fuel rod liquefaction (Section 4.7), the variable f_{cm} has a value of 0.5 for ballooned fuel rods and a value of 1.0 for fuel rods that have not ballooned. Excluding affects such as a change in temperature, fuel rod melting of ballooned fuel rods causes a factor of two reduction in the linear heat generation rate due to oxidation. Since the average thickness of the metallic part of the cladding increased following its melting and concentration into a fraction of the circumference of the fuel rod, the oxidation may continue over a longer period of time before terminating due to complete oxidation of the metallic material. These changes in oxidation do not occur for a fuel rod that has not ballooned. In this case, a void does not exist at any point along the circumference into which melted metallic cladding from other points on the circumference could flow.

After melting of the cladding, the rate of oxidation is also affected by the change in stoichiometry of the metallic part of the cladding. The melting of the cladding results in a dissolution of some of the UO_2 in contact with the cladding, which in turn increases the ratio of oxygen to zirconium atoms in the metallic part of the cladding, and which in turn reduces the potential for oxidation. The ratio of oxygen atoms contributed by the dissolution of UO_2 to atoms of Zr in the melted mixture is calculated by the equation

$$N_d = 2(w_u/A_u)/(w_z/A_z) \tag{3-54}$$

where

N_d = ratio of oxygen atoms controlled by the dissolution of UO_2 to atoms of Zr in melted moisture of Zr and UO_2,

w_u = mass of UO_2 in melted mixture of Zr and UO_2 (kg),

A_u = molecular weight of UO_2 (270.07),

w_z = mass of Zr in melted mixture of Zr and UO_2 (kg),

A_z = atomic weight of Zr (91.22).

The reduction in the rate of oxidation caused by UO_2 dissolution is represented through a reduction in the diffusivity of the oxide layer. This reduction is proportional to the ratio of oxygen to zirconium atoms in the mixture of melted Zr and UO_2. The diffusivity is reduced according to the equation

$$D_{oxm} = (1 - f_{om} N_d/(1+N_d))D_{ox} \tag{3-55}$$

where

D_{oxm}	=	adjusted value of diffusion coefficient of oxygen in the oxide layer to represent decrease in oxygen uptake caused by UO_2 dissolved in the metallic part of the cladding (m^2/s),
D_{ox}	=	actual value of diffusion coefficient of oxygen in oxide layer (m^2/s),
f_{om}	=	parameter that scales the reduction in oxygen uptake proportional to the value of N_d.

The value of the parameter f_{om} was determined from analyses of severe fuel damage experiments. Based on these analyses, f_{om} was assigned a value of 1.0.

3.2.2 Affect of slumping of cladding on oxidation

The slumping of melted metallic cladding causes significant changes in the oxidation of fuel rods. The configuration of a fuel rod at a location with slumped cladding is shown in Figure 3-9. First, a significant reduction occurs in the surface area to volume ratio of the slumped material due to it changing from the configuration of a segment of a cylinder to that of a series of drops. Second, the presence of drops of slumped cladding partially blocks the oxidation of the intact cladding onto which the drops adhere. A modification is required to the integral diffusion method to account for the affect of the presence of drops on the oxidation of the intact cladding. Since the drops may change location with time and do not have a stationary configuration, the integral diffusion method is not applicable to the oxidation of the drops. In this case, a method other than the integral diffusion method is required to model the oxidation process.

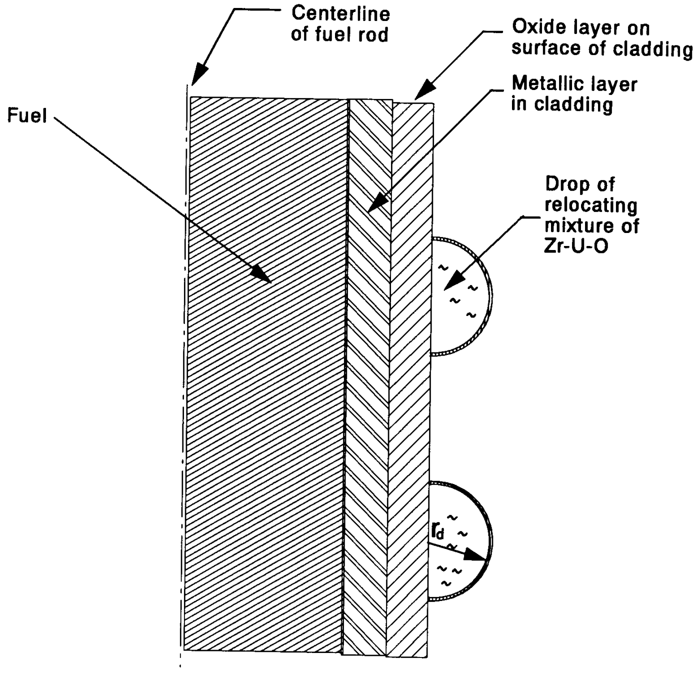
Centerline of fuel rod
Oxide layer on surface of cladding
Metallic layer in cladding
Fuel
Drop of relocating mixture of Zr-U-O
r_d
M259-BDR-0694-002

Figure 3-9. Vertical cross-section of segment of fuel rod with slumped cladding on outside surface of intact cladding.

For the calculation of the oxidation of intact cladding with some drops of slumped cladding adhering to its outer surface, a modification is made to the integral diffusion method to account for the presence of the drops of slumped cladding. The integral diffusion method calculates the average uptake of oxygen in a segment of a cylinder onto which many drops of slumped cladding may adhere. The modification involves calculating an effective surface area for the cylindrical segment that reduces the overall rate of oxygen uptake proportional to the fraction of surface area covered with drops. Then, the effective surface area of the cylindrical segment instead of the actual surface area is applied in calculating the overall rate of oxygen uptake for the cylindrical segment. The basis for calculating the effective surface area is the reduction in oxidation indicated by severe fuel damage experiments. The effective surface area is calculated by the equation

$$A_e = f_c (A - A_c) \tag{3-56}$$

where

A_e = effective area for oxidation of a cylindrical segment of intact cladding (m^2),

A = total surface area of intact cladding, including area underlying drops of relocated cladding (m^2),

f_c = fraction of maximum possible area of cladding covered with drops (assuming drops do not overlap each other) that is effective in blocking oxidation of cladding.

A_c = area of intact cladding covered with drops of slumped cladding, (m^2).

The value of the parameter f_c was determined from analyses of severe fuel damage experiments. Based on these analyses, f_c was assigned a value of 0.5. This value corresponds with the drops of relocated material partially blocking the oxidation of the intact cladding on which it adheres. If the fraction of coolant space at a location is less than 90% filled with slumped material, the minimum value of A_e is constrained to be 33% of the value of A. Otherwise, the value of A_e is constrained to be 10% of the value of A. If reflooding is occurring at a location, A_e is equal to A.

Since the drops of slumped cladding may change location with time and do not have a stationary configuration, the integral diffusion method is not applicable to the oxidation of the drops. Instead, the oxidation of the drops is calculated using the more simplistic but adaptable parabolic kinetics model. The oxidation of the drops of slumped cladding are represented as a diffusion-controlled process with a parabolic rate law under isothermal conditions. As shown in Figure 3-9 and further described in the section on the liquefaction of fuel rods (Section 4.7), the drops are assumed to be in the shape of hemispheres with a radius of r_d.

The oxidation process is represented by the equation

$$\frac{dw}{dt} = \frac{k_{eff}}{2w} \tag{3-57}$$

where

w = oxygen weight gain per unit surface area of drop of slumped cladding ($kg\ O_2/m^2$)

t = time (s)

k_{eff} = effective parabolic constant for oxygen weight gain [$(kg/m^2)^2/s$].

The integration of the above equation with respect to time yields the equation

$$w_1 = (k_{eff}\Delta t + w_0^2)^{0.5} \tag{3-58}$$

where

w_1 = weight gain at end of time step (kg/m^2)

w_0 = weight gain at start of time step (kg/m^2)

Δt = size of time step (s).

The effective parabolic rate constant is determined by interpolation of experimental data. The parabolic rate constants for drops composed of 100% Zr is well-defined by experimental results. For mixtures of Zr and UO_2, however, experimentally determined rate constants are limited. This limitation of experimental results makes it necessary to calculate the rate constants for a mixture of Zr and UO_2 based on an assumption relating the rate constants for the mixture to those for 100% Zr and 100% UO_2. The assumption is that the rate constant changes in a nonlinear manner with the change in mass fraction of UO_2 in the mixture. The rate constant is thus calculated by the equation

$$k_{eff} = (1-f)^3 \cdot k_{zr} + fk_{UO_2} \tag{3-59}$$

where

f = mass fraction of UO_2 in mixture

k_{zr} = parabolic rate constant for oxidation of Zr [$(kg/m^2)^2/s$]

k_{UO_2} = parabolic rate constant for oxidation of UO_2 [$(kg/m^2)^2/s$]

Heat is produced by the oxidation of a mixture of Zr and dissolved UO_2. The heat is produced by the conversion of Zr to ZrO_2 and UO_2 to U_3O_8.

The rate of heat generation is calculated by the equation

$$Q = \left((1-f) \cdot H_{Zr} \cdot \frac{A_{wZr}}{A_{wO2}} + f \cdot H_{UO_2} \cdot \frac{A_{wU}}{A_{wO_2}}\right) \cdot \left(\frac{w_1 - w_0}{\Delta t}\right) \tag{3-60}$$

where

Q = heat generation due to oxidation of drop (W/m^2),

H_{zr} = heat of reaction for Zr (6.45x10^6 J/kg of Zr converted to ZrO$_2$),

A_{wZr} = atomic weight of Zr (91.22),

A_{wO_2} = atomic weight of O$_2$ (32),

H_{UO_2} = heat of reaction of UO$_2$ as obtained from MATPRO (1.84 x 10^5 J/kg of (UO$_2$)$_3$ converted to U$_3$O$_8$),

A_{wU} = atomic weight of (UO$_2$)$_3$ (810).

The total linear heat generation due to oxidation for a cylindrical segment of a fuel rod is the sum of the heat generation due to oxidation of the intact cladding and that due to the oxidation of drops adhering to the intact cladding. Thus, the total linear heat generated due to oxidation is calculated by the equation

$$q_{tox} = q_{ox} + 2N_dQ\pi r_d^2 \tag{3-61}$$

where

q_{tox} = total heat generation due to oxidation for a cylindrical segment where slumped cladding adheres to intact cladding (W/m),

q_{ox} = heat generation due to oxidation of intact cladding (W/m),

N_d = number of drops of slumped cladding per unit length adhering to surface of intact cladding in cylindrical segment (drops/m),

r_d = radius of drops (m).

If some of the drops of slumped cladding overlap other drops, the average rate of oxidation of the drops is reduced. This overlapping is represented by calculating an effective parabolic rate constant which reduces the average rate of oxidation of the drops inversely proportional to the extent of overlapping. The effective parabolic rate constant is calculated by the equation

$$k_{effo} = f_{ov}\, k_{eff} \tag{3-62}$$

$$f_{ov} = f_{bmin} + [(f_{lm} - f_l)/f_{lm}]^2(1 - f_{bmin}) \qquad f_l \le f_{lm} \tag{3-63}$$

$$f_{ov} = f_{bmin} \qquad f_l > f_{lm} \tag{3-64}$$

where

k_{effo} = effective parabolic rate constant to account for some drops of slumped cladding overlapping other drops [(kg/m^2)^2/s],

k_{eff} = parabolic rate constant as calculated above and not accounting for presence of overlapping drops [(kg/m^2)^2/s],

f_l = fraction of flow space at location filled with relocated material (unitless),

f_{ov} = effective fraction of surface area of drops,

f_{bmin} = minimum value of factor on effective fraction of surface area of drops (unitless),

f_{lm} = fraction of flow space filled with slumped material necessary for reducing f_{ov} to minimum value of f_{bmin} (unitless).

The parameter f_{lm} in the above set of equations is defined to have a value of 0.55. The parameter f_{bmin} in the above set of equations is defined to have a value of 0.004.

If reflood is occurring at the location and $f_l < 0.9$, then f_{ov} has a value of 1.0. If reflood is occurring at the location and $f_l \geq 0.9$, then f_{ov} has a value of 0.1.

3.2.3 Affect of reflood on oxidation

The reflood of a hot fuel assembly may cause an acceleration in the oxidation of the fuel assembly.[3-24, 3-27] Experimental results have shown that the acceleration in oxidation is due to cracks that occur in oxide layers during reflood. [3-9, 3-28, 3-30]The cracking is apparently due to thermal stresses induced in the oxide layer by reflood.[3-25] These cracks have such a complex configuration that it is not practical to implement mechanistic models of the cracks and their affect on oxidation into a systems analysis code such as SCDAP/RELAP5-3D©. This section describes the empirical models implemented to approximate the affect of reflood on fuel rod oxidation. Reflood is defined to be occurring at any location where drops of liquid water are present (local volume fraction of liquid > 0.0).

The affect of reflood on the oxidation of intact cladding is represented though a multiplication factor applied to the diffusivity of the oxide layer. If reflood is occurring, the diffusivity of the oxide layer on the intact cladding is calculated by the equation

$$D_{ox} = D_{oxR} \tag{3-65}$$

where

D_{ox} = diffusion coefficient of oxygen in the oxide layer which accounts for cracks after occurrence of reflood at a location (m^2/s),

D_{oxR} = diffusion coefficient for a cracked oxide layer determined from analyses of integral severe fuel damage experiments with reflood.

Based on analyses of integral fuel experiments with reflood, the value of D_{oxR} in the above equation was determined to be 2 x 10^{-6} m^2/s. The studies have also shown that the cracks do not occur unless the thickness of the oxide layer is greater than a threshold value.[3-10] Based on the analyses of severe fuel damage tests with reflood, the value of D_{ox} is equal to that of uncracked oxide for oxide layers with a thickness less than 120 microns.

Drops adhering to the surface of intact cladding are assumed to crack during reflood conditions and to not block the diffusion of steam to the underlying intact cladding. Thus, the parameter f_c, in Equation

(3-56), which defines the effective surface area of drops in blocking the oxidation of intact cladding, has a value of 0.0 for reflood conditions.

The affect of reflood on the oxidation of drops of slumped cladding is represented though cyclic shattering of the oxide layer on the surface of the drops. If reflood is occurring, the oxygen uptake is calculated by the equation

$$w_1 = w_{ls} + w_{ss1} \tag{3-66}$$

where

w_1 = cumulative weight gain of oxygen at end of time step in drop (kg O_2/m^2),

w_{ls} = cumulative weight gain at time of last shattering of oxide layer on outside surface of drop (kg O_2/m^2),

w_{ss1} = weight gain since last shattering of oxide layer at end of time step (kg O_2/m^2).

The oxide layer on the surface of the slumped drops of cladding is assumed to shatter frequently during reflood conditions. The weight gain of oxygen in the drops since the last shattering of the oxide layer is calculated by the equation set

$$w_{ss1} = (k_{eff}\Delta t + w_{sso}^2)^{0.5} \tag{3-67}$$

where

w_{ss1} = weight gain at end of time step since last shattering of oxide layer (kg O_2/m^2),

w_{ss0} = weight gain at start of time step since last shattering of oxide layer (kg O_2/m^2),

t_{ls} = time since last shattering of oxide layer (s),

t_{ps} = time between shattering during reflood conditions (s),

Δt = size of time step (s).

The time between shattering of the oxide layer on the drops of slumped cladding, t_{ps}, was estimated from analyses of integral severe fuel damage tests with reflood. Based on these analyses, the oxide layer is defined to shatter after a weight gain of 0.017 kg O/m^2 during reflood conditions.

3.2.4 Affect of cladding rupture on oxidation

The rupture of fuel rod cladding may result in oxidation of the inside surface of the fuel rod cladding. Theoretical results for the case of large cladding hoop strains[3-5] and experimental results[3-20, 3-10] both indicate that for pin hole size ruptures only a few cm in length of cladding has oxidation of the inside surface. If cladding rupture results in a breach in the form of a long wide-open slit instead of a hole, the length of cladding contacted by steam may equal the length of the slit. Since severe fuel damage tests generally proceed in damage progression significantly beyond the time of cladding rupture, the results of these tests do not indicate the form and length of breach resulting from cladding rupture. Also, no theoretical models are available for calculating the form and length of rupture. Due to this lack of information, a slit over the length of cladding with a hoop strain greater than 0.012 is assumed to exist in cladding that balloons and ruptures under severe accident conditions. The oxidation of the inside surface is assumed to occur along the length of the cladding with a slit.

3.3 Parabolic Kinetics Model for Oxidation of Control Rods

Material oxidation is assumed to behave following the parabolic rate equation

$$\frac{d\delta}{dt} = \frac{A}{\delta}e^{\left(\frac{-B}{T}\right)} \tag{3-68}$$

where

δ = weight gain or layer thickness (kg/m^2 or m)

T = temperature (K)

t = time (s)

A,B = parabolic rate constants taken from MATPRO.

For a constant temperature, this equation can be integrated over the time interval, Δt, to give

$$\delta^2 - \delta_o^2 = 2Ae^{\left(\frac{-B}{T}\right)}\Delta t \tag{3-69}$$

where δ_o is the value at the beginning of the time interval. For zircaloy, three separate parabolic equations are solved for oxygen weight gain and the growth of the α and ZrO_2 layers. For all other materials, only the oxygen weight gain is computed.

The oxidation heat generation rate, Q_{ox}, is computed from the weight gain,

$$Q_{ox} = \frac{M}{M_{(O_2)}}h_r S\frac{dw}{dt} \tag{3-70}$$

where

$M_{(O_2)}$ = molecular weight of oxygen

M = molecular weight of the material

h_r = heat of reaction in J/kg of material reacted

S = original surface area (m^2)

w = oxygen weight gain per unit surface area (kg/m^2).

The original surface area is based on the area prior to any oxidation and does include the effect of deformation.

The hydrogen production rate, $\dot{H}_2$, and steam removal rate, $H_2\dot{O}$, are also computed from the oxygen weight gain and are given by

$$\dot{H}_2 = \frac{1}{8}S\frac{dw}{dt} , \tag{3-71}$$

$$H_2\dot{O} = \frac{9}{8}S\frac{dw}{dt} \quad . \tag{3-72}$$

The oxidation process is subjected to three limits: (1) available material, (2) available steam, (3) diffusion of water vapor. First the oxidation is terminated when the material is fully oxidized. In the case of zircaloy, oxidation is terminated when all the zircaloy is converted to ZrO_2 and for stainless steel, when the iron is converted to FeO_2. The resulting limits on oxygen uptake can then be expressed as

$$w \le \frac{M_{o_2}}{M}\rho\frac{V}{S} , \tag{3-73}$$

where M_{o_2} is the molecular weight of oxygen, M is the molecular weight of material, and ρ and V are the density and volume of the material, respectively. Second, the oxidation rate is limited by the availability of steam.

That is,

$$\frac{dw}{dt} \le \frac{8}{9}\frac{\dot{m}}{S} \tag{3-74}$$

where $\dot{m}$ is the mass flow rate of the steam available to the oxidizing surface. Finally, oxidation is limited by the diffusion of water vapor. The water vapor molar mass flow rate $N_{(H_2O)}$ is driven by the partial pressure of the water vapor, which can be written as

$$\frac{N_{(H_2O)}}{A} = B_{(H_2O)}P_{(H_2O)} \tag{3-75}$$

where

$N_{(H_2O)}$ = molar mass flow rate (kg-mole/s),

A = surface area (m^2),

$B_{(H_2O)}$ = mass transfer coefficient (kg-mole/s • m^2 • Pa),

$P_{(H_2O)}$ = partial pressure of water vapor (Pa).

Using a mass/heat transfer analogy assuming Colburn j factors for heat and mass transfer are equal,[3-1] then

$$\frac{Nu}{RePr^{0.33}} = \frac{Sh}{ReSc^{0.33}} \tag{3-76}$$

where

Nu = Nusselt number, $\frac{hL}{k_{(H_2O)}}$,

$k_{(H_2O)}$ = thermal conductivity of water vapor ($W/m \bullet K$),

h = convective heat transfer coefficient ($W/m^2 \bullet K$),

L = characteristic length (m),

Sh = Sherwood number $\frac{B_{(H_2O)}RTL}{D_v}$,

D_v = mass diffusivity (m^2/s),

R = gas constant ($Pa \bullet m^3/kg\text{-}mole \bullet K$),

T = temperature (K),

Pr = Prandtl number $\frac{C_{p(H_2O)}\mu_{(H_2O)}}{k_{(H_2O)}}$,

$C_{p(H_2O)}$ = specific heat ($J/kg \bullet K$),

$\mu_{(H_2O)}$ = viscosity of water vapor ($kg/s \bullet m$),

Sc = Schmidt number, $\frac{\mu_{(H_2O)}}{\rho_{(H_2O)}D_v}$,

$\rho_{(H_2O)}$ = density of water vapor (kg/m^3).

Using the mass/heat transfer analogy, the rate of oxygen uptake for an oxidizing surface becomes limited by

$$\frac{dw}{dt} \le \frac{m_{O_2}}{2m_{H_2O}}\frac{N_{H_2O}}{A} = \frac{8}{9}\left(\frac{hD_v}{k_{(H_2O)}}\right)\left(\frac{P_{(H_2O)}}{RT}\right)\left(\frac{k_{(H_2O)}}{\rho_{(H_2O)}C_{p(H_2O)}D_v}\right)^{(1/3)} \tag{3-77}$$

where the mass diffusivity is calculated by[3-2]

$$D_v = (1-X)\frac{\mu_{(H_2O)}RT}{PM_{(H_2O)}} + \sum_{i=1}^{n} X_i\frac{\mu_i RT}{PM_i} \tag{3-78}$$

where

$M_{(H_2O)}$ = molecular weight of the water vapor,

M_i = molecular weight of the gas specie i,

$\mu_{(H_2O)}$ = molecular viscosity of the water vapor ($kg/m \bullet s$),

μ_i = molecular viscosity of the gas specie i ($kg/m \bullet s$), P = total pressure (Pa),

X_i = i-th noncondensable gas quality,

X = total noncondensable quality, $\sum_{i=1}^{n} X_i$,

n = number of noncondensable gas species.

3.4 References

3-1. T. K. Sherwood, R. L. Pigford, and C. R. Wilke, *Mass Transfer,* New York: McGraw-Hill, 1975.

3-2. R. B. Bird, W. E. Stewart, and Lightfoot, *Transport Phenomena,* New York: Wiley, 1960.

3-3. E. W. Coryell et al., *Design Report: SCDAP/RELAP5 Reflood Oxidation Model,* EGG-RAAM-10307, October 1992.

3-4. D. R. Olander, “Materials chemistry and transport modeling for severe accident analyses in light-water reactors, I: External cladding oxidation,” Nuclear Engineering and Design 148 (1994), pages 253-271.

3-5. D. R. Olander, “Materials chemistry and transport modeling for severe accident analyses in light-water reactors II: Gap processes and heat release,” Nuclear Engineering and Design 148 (1994), pages 273-292.

3-6. M. Moalem and D. R. Olander, “Oxidation of Zircaloy by Steam,” Journal of Nuclear Materials 182 (1991), pages 170-194.

3-7. M. Steinbruck et al., “Investigations of H_2 absorption of Zircaloy-4 at high temperatures,” Third International QUENCH Workshop, Karlsruhe, Germany, December 2 - 4, 1997.

3-8. H. Chung and G. Thomas, “Zircaloy-Oxidation and Hydrogen-Generation Rates in Degraded-Core Accident Situations,” CONF-821026-13, International Workshop on the Impact of Hydrogen on Water Reactor Safety, Albuquerque, NM, Oct. 3, 1982.

3-9. P. Hofmann et al., “Experiments on the Quench Behavior of LWR Fuel Rod Segments,” Third International QUENCH Workshop, Karlsruhe, Germany, December 2 - 4, 1997.

3-10. T. Furuta, H. Uetsuka, and S. Kawasaki, “Estimation of Conservatism of Present Embrittlement Criteria for Zircaloy Fuel Cladding Under LOCA,” Zirconium in the Nuclear Industry, Sixth International Symposium, ASTM STP 824, D. G. Franklin and R. B. Adamson, Eds., American Society for Testing and Materials, 1984, pages 734-746.

3-11. Appendix K, “ECCS Evaluation Models,” 10 CFR Part 50.46.

3-12. H. M. Chung and T. F. Kassner, “Embrittlement Criteria for Zircaloy Fuel Cladding Applicable to Accident Situations in Light-Water Reactors: Summary Report,” NUREG/CR-1344, ANL-79-48, January 1980.

3-13. S. L. Seiffert, “Effect of Hydrogen on the Oxygen Embrittlement of Beta-Quenched Zircaloy-4 Fuel Cladding,” Zirconium in the Nuclear Industry: Fifth Conference, ASTM STP 754, D. G. Franklin, Ed., American Society for Testing and Materials, 1982, pages 302-328.

3-15. D. A. Petti et al., “Power Burst Facility (PBF) Severe Fuel Damage Test 1-4 Test Results Report,” NUREG/CR-5163, EGG-2542, April, 1989.

3-16. S. Hagen et al., “CORA Experiments in the Materials Behavior of LWR Fuel Rod Bundles at High Temperatures,” Proceedings of the 19th Water Reactor Safety Meeting, NUREG/CP-0119, April 1992.

3-17. Alan D. Knipe et al., “PBF Severe Fuel Damage Scoping Test, Test Results Report,” NUREG/CR-4683, EGG-2413, August 1986.

3-19. R. Viskanta, R. R. Hobbins and H. Esmaili, “Peer Review of the Modeling of Hydrogen Uptake in Fuel Rod Cladding During Severe Accidents, “ERI/NRC 98-204, USNRC Contract No. 04-92-045, October, 1998.

3-20. I. Catton, J. O. Cermak, Y. S. Kuo, and A. R. Wazzan, “An Evaluation of Several Aspects of the Hypothetical Loss-of-Coolant Accident for Light Water Reactors,” University of California at Los Angelos, Rep. UCLA-ENG-7450, 1974.

3-21. L. J. Siefken, “Models for the Configuration and Integrity of Partially Oxidized Fuel Rod Cladding at High Temperatures,” INEEL/EXT-98-00661Rev1, January 1999.

3-22. Z. R. Martinson, D.A. Petti, and B. A. Cook, “Vol. 1: PBF Severe Fuel Damage Test 1-1 Test Results Report,” NUREG/CR-4684, EGG-2463, Volume 1, October 1986.

3-23. D. D. Lanning et al., “Data Report: Full-Length High-Temperature Experiment 5”, PNL-6540, April 1988.r the Nuclear Industry, Sixth International Symposium, ASTM STP 824, 1984, page 734.

3-24. S. Modro and M. Carboneau, “The LP-FP-2 Severe Fuel Damage Scenario and Discussion of the Relative Influence of the Transient and Reflood Phases in Affecting the Final Condition of the Bundle,” *OECD LOFT Final Meeting, Madrid, Spain, May 9-11, 1990.*

3-25. K. Minato et. al., *Zircaloy Oxidation and Cladding Deformation in PWR-Specific CORA Experiments,* KfK 4827, July 1991.

3-26. L. J. Siefken, “Calculation of Hydrogen and Oxygen Uptake in Fuel Rod Cladding During Severe Accidents Using the Integral Diffusion Method -Final Design Report,” INEEL/EXT-99-00571, May 1999.

3-27. S. Hagen et al., “Results of SFD Experiment CORA-13 (OECD International Standard Problem 31),” KfK 5054, Kernforschungszentrum Karlsruhe, February 1993.

3-28. P. Hofmann et al, “Quench Behavior of Zircaloy Fuel Rod Cladding Tubes: Small Scale Experiments and Modelling of the Quench Phenomena,” FZKA 6208, MArch 1999.

3-29. T. Furuta, H. Uetsuka, and S. Kawasaki, “Estimation of conservatism of present embrittlement criteria for Zircaloy fuel cladding under LOCA,” Zirconium for the Nuclear Industry, Sixth International Symp., ASTM Spec. Tech Publ. 824 (1984) 734.(4-42)

3-30. S. M. Jensen, D. W. Akers, and B. A. Pregger, “Postirradiation Examination Data and Analyses for OECD LOFT Fission Product Experiment LP-FP-2,” Volume 1, OECD LOFT-T-3810, December 1989.

4. FUEL ROD MODELS

4.1 Electrical Heat Generation Model for Fuel Rod Component

This model is used to represent electrically heated fuel rods with a central tungsten heater rod. The total power input is specified by user input, while the axial- and temperature-dependent power release is calculated by the model.

The electrical heat generation model computes the axial- and temperature-dependent power release in the heated area of the tungsten heater rod and also includes the effects of the molybdenum and the copper electrodes at the top and bottom of the tungsten heater rod. The model first computes the resistance of copper, molybdenum and tungsten. The model currently has the dimensions of the tungsten rod and molybdenum and copper electrodes at the top and bottom of the tungsten heater rod built into the resistance equations. The specific dimensions are based upon the CORA[4-1] heater rod elements. The resistances are calculated by the equations:

$$R_{Mo} = 2.25 \times 10^{-2} + 5.36 \times 10^{-5}\ T_{Mo} + 1.38 \times 10^{-7}\ T_{Mo}^2 - 2.22 \times 10^{-11}\ T_{Mo}^3\ (\Omega \bullet \text{mm}^2/\text{m}), \tag{4-1}$$

$$R_{Cu} = -7.89 \times 10^{-3} + 9.90 \times 10^{-5}\ T_{Cu} - 5.49 \times 10^{-8}\ T_{Cu}^2 + 3.16 \times 10^{-11}\ T_{Cu}^3\ (\Omega \bullet \text{mm}^2/\text{m}), \tag{4-2}$$

$$R_W(I) = [-0.0261 + 2.63 \times 10^{-4} T(I) + 2.20 \times 10^{-8} T(I)] DZ(I) (3.5368 \times 10^{-2})\ (\Omega),\ I = 1, 2, \ldots NAZ, \tag{4-3}$$

where

NAZ = number of axial levels,

$DZ(I)$ = height of i-th axial node (m),

$T(I)$ = fuel rod centerline temperature at node I (K),

T_{Mo} = $0.5[T(NAZ) + 350]$ (K),

T_{Cu} = $0.5(T_{Mo} + 350)$ (K),

T = fuel center temperature at the 1st axial level (K).

The total resistance is then given by

$$R_t = \sum_{I=1}^{NAZ} R_w(I) + 0.0086(R_{Mo} + R_{Cu}) + 0.0005(\Omega)\quad . \tag{4-4}$$

The power per unit length in each axial node is then

$$UNUC(I) = \frac{R_w(I)}{R_t} \frac{P_t}{D_z(I)} \tag{4-5}$$

where P_t is the total input rod power (W).

4.2 Fission Product Release Models

The models described in this section calculate the rate of fission product release from intact fuel rods and rods that have experienced fuel liquefaction or fragmentation. The models also calculate the enthalpy of the released fission products. This description has been divided into three subsections. The first subsection describes the fission product release models for rods with intact fuel but failed or damaged cladding. The other subsections describe the fission product release during the liquefaction or fragmentation of UO_2 and the enthalpy of released fission products.

4.2.1 Release Model for Intact Fuel

SCDAP/RELAP5-3D© models the release of fission products from the fuel to the gap using a combination of a theoretical model developed by Rest et al.,[4-2] to treat the release of xenon, krypton, cesium, iodine, and tellurium from solid fuel, and empirical models to treat other fission products.[1]

The theoretical model is a simplified version of the FASTGRASS code that has been used for predicting the behavior of fission gas in UO_2-based fuels during steady-state and transient conditions.[4-2,4-3,4-4,4-5] Fission products released from the fuel are assumed to reach the fuel surface by successively migrating from the grains to grain faces and then to the grain edges, where the fission products are released through a network of interconnected tunnels of fission gas induced and fabricated porosity. This model treats the production of gas from fissioning nuclei, bubble nucleation and resolution, bubble migration, bubble coalescence, gas bubble and channel formation on grain faces, interlinked porosity on grain edges, grain boundary microcracking, and grain growth and grain boundary sweeping.

The specific models used for xenon, krypton, cesium, iodine, and tellurium are described by Rest.[4-2,4-3,4-4] For completeness, an example of the equations used to describe the diffusion of gases to grain boundaries is described below. The concentration of atoms, C_g, within the spherical grain satisfies the equation

$$\frac{\partial C_g}{\partial t} = \frac{1}{r^2}\frac{\partial}{\partial r}\left[D_g r \frac{\partial C_g}{\partial r}\right] + K_g \tag{4-6}$$

where

D_g = atom diffusion coefficient

K_g = the rate of generation of atoms.

In general, Equation (4-6) is solved with the boundary conditions

$$C_g = 0 \text{ at } t = 0 \text{ for } 0 \le r \le \frac{d_g}{2} \tag{4-7}$$

---

[1] The theoretical model is based upon PARAGRASS Version 50531, with the cesium iodide chemistry model deactivated because of an error in that version of PARAGRASS that resulted in an error in the iodine release.

$$C_g = 0 \text{ at } r = \frac{d_g}{2} \text{ for } t_o \le t \le t_o + h \tag{4-8}$$

$$\frac{\partial C_g}{\partial r} = 0 \text{ at } r = 0 \text{ for } t_o \le t \le t_o + h \tag{4-9}$$

where

d_g = grain diameter

h = time interval between times t_o and $t_o + h$.

The diffusive flow of the fission gas bubbles to the grain boundaries is also governed by Equation (4-6). For this case, it is assumed that gas bubbles are not being nucleated and are essentially noninteracting.

The coupling of the diffusive flow problem to other processes affecting fission gas behavior (e.g., gas atom resolution, gas atom trapping by gas bubbles) is accomplished by solving equations of the form

$$\frac{dY_i}{dt} = -a_i Y_i^2 - b_i Y_i + C_i \tag{4-10}$$

where

Y_i = density of intragranular gas atoms (bubbles)

$a_i Y_i^2$ = rate at which gas atoms (bubbles) are lost owing to gas bubble nucleation (coalescence)

$b_i Y_i$ = rate at which gas atom (bubbles) are lost owing to diffusive flow and diffusion into gas bubbles (gas atom resolution)

C_i = rate at which gas atoms are gained owing to gas atom resolution and fission of uranium nuclei (i.e., the rate gas bubbles are gained owing to bubble nucleation and diffusion of gas atoms into bubbles).

A more detailed description of the above variables is also given in Table 4-1.

Equation (4-6) is discretized in time using backward Euler approximation to give the following equation:

$$\frac{1}{r^2}\frac{\partial}{\partial r}\left[D_g r^2 \frac{\partial C_g}{\partial r}\right] - \frac{C_g}{h} + \frac{C_g(t-h)}{h} + K_g = 0 \quad . \tag{4-11}$$

By applying a variational principle and setting the first variation to zero,

$$\int_0^{\left(\frac{1}{2}D_g\right)} 4\pi\left[0.5 D_g\left(\frac{\partial C_g}{\partial r}\right)^2 + \frac{C_g 2}{2h} - \frac{C_g(t-h)}{h} + K_g C_g\right] r^2 dr = 0 \quad . \tag{4-12}$$

Table 4-1. Definition of variables in Equation (4-10).

Y_i	$a_iY_i^2$	b_iY_i	C_i
Density of intragranual gas atoms and VFPs	Rate at which gas atoms are lost owing to gas bubble nucleation	Rate at which atoms and VFPs are lost owing to diffusive flow to the grain boundaries, grain boundary sweeping, diffusion into gas bubbles, and chemical reactions	Rate at which atoms and VFPs are gained owing to an atom resolution, a fission of uranium nuclei, and chemical reaction
Density of intragranular gas bubbles	Rate at which gas bubbles are lost owing to bubble coalescence	Rate at which gas bubbles are lost owing to diffusive flow to the grain boundaries, grain boundary sweeping, and gas atom resolution	Rate at which gas bubbles are gained owing to bubble nucleation and diffusion of gas atoms into bubbles
Density of grain-face gas bubbles and VFPs	Rate at which gas bubbles are lost owing to bubble coalescence	Rate at which gas bubbles and VFPs are lost owing to diffusion to grain edges, formation of grain channels, microcracking, and chemical reactions	Rate at which gas bubbles and VFPs are gained owing to intragranular migration to grain faces, and chemical reactions.
Density of grain-edge gas bubbles and VFPs	Rate at which gas bubbles are lost owing to bubble coalescence	Rate at which gas bubbles and VFPs are lost owing to long-range grain-edge bubble interconnection, microcracking, and chemical reactions	Rate at which gas bubbles and VFPs are gained owing to migration of grain-face fission products to grain edges and chemical reactions

The spherical grain is then split into two concentric regions of approximately equal volume. In each region, the gas concentration is represented by a quadratic function. In the Central Region I, the concentration function is constrained to have $\frac{\partial}{\partial r(C_g)} = 0$ at r = 0. In the Outer Region II, the concentration function is constrained to have a value of $C_g = 0$ at $r = \frac{d_g}{2}$. The two functions are also constrained to be continuous at the common boundary of the two regions. This leaves three free parameters, C_1, C_2, and C_3. These are chosen to be gas-atom concentrations at positions corresponding to the midpoint radius of Region 1, the boundary between the regions, and the midpoint radius of Region II, respectively.

Hence, for Region I,

$$C_g = C_1\frac{(0.64 - a^2)}{0.48} + C_2\left[a^2 - \frac{0.167}{0.48}\right] \tag{4-13}$$

and for Region II,

$$C_g = 5C_2(10a^2 - 19a+9) + 10C_3(18a - 10a^2 -8) \tag{4-14}$$

where a is equal to $\frac{2r}{d_g}$. Equations (4-13) and (4-14) are substituted for C_g in Equation (4-12) and an extremum is found by differentiating with respect to C_1, C_2, and C_3 in turn. A set of three linear equations is thus obtained. The solution of this set of equations expressed C_i in terms of D_g, d_g, and q_j. The q_j's, j = 1,2,...13, are integrals which, when directly evaluated, are $q_1 = 4.552$,..., $q_{13} = 0.1083$.

The flux of gas atoms to the boundary (in units of atoms/cm^3•s) is given by

$$J = -6\left(\frac{D_g}{d_g}\right)\frac{\partial C_g}{\partial r}\bigg|_{r = d_g/2} \quad . \tag{4-15}$$

This term J is one of the terms in the expression for the rate at which gas atoms are lost, given by the term b_iY_i in Equation (4-10). It was determined by Wood and Mathews[4-6] that the best expression for the average concentration within the grains, C_g(av), is given by

$$C_g(av) = 0.2876C_1 + 0.2176C_2 + 0.4216C_3 \quad . \tag{4-16}$$

At the end of an iteration, the concentrations C_1, C_2, and C_3 in Equation (4-15) are scaled by imposing the condition that the average concentration equals that calculated by use of Equation (4-10), i.e.,

$$C_g(av) = Y_i \quad . \tag{4-17}$$

The modified C_1, C_2, and C_3 then become the initial values of these concentrations [i.e., C_1(t-h), C_2(t-h), C_3 (t-h)] to be used for the next iteration. The diffusion of gas bubbles is treated analogously to that for fission gas atoms, but with $K_g = 0$ in Equation (4-11).

The elemental fission yields of the fission gases are xenon (0.2635), krypton (0.0465), cesium (0.1507), iodine (0.011), and tellurium (0.02519). These quantities are in units of atoms per fission event. Multiplication by fission rate per unit volume gives the fission gas generation rate in units of atoms/s/m^3. Because very little fission gas is released during steady-state calculations, the calculation of initial inventories is dominated by the fission gas generation rate.

Two options for grain growth are included:

1. An empirical law is used to calculate grain growth; grain boundary sweeping of fission products is proportional to the volume swept by the growing grains.
2. A theoretical grain growth model is fully coupled to the grain boundary sweeping model.

The fission product tellurium is included with iodine, cesium, and cesium iodide. The effects of the oxidation state of the cladding on tellurium release are included (i.e., cladding not completely oxidized and cladding oxidized more than 90%). When the cladding is not more than 90% oxidized, only 1/40 of the tellurium release is allowed to come out. Otherwise, all of the tellurium release comes out of the fuel rod.

Theoretical models to calculate the instantaneous rate of change of the bubble radius have been included. Previous versions of PARAGRASS handled the nonequilibrium growth of gas bubbles by modifying the bubble coalescence rates by an appropriate factor. Equilibrium values of the bubble radius were used in the calculation of various material properties, e.g., the calculation of bubble diffusivities.

The model for the behavior of gas bubbles on grain surfaces has been improved. In a previous version, the effect of external stress on intragranular bubble growth was inadvertently decoupled.

After burst of fuel rods, it is assumed that cesium and iodine will combine to form cesium iodide, with any leftover cesium reacting with water on release from the gap to form cesium hydroxide or any leftover iodine being release as I_2. This assumption is based on fission product chemical states.[4-7]

The interaction of cesium with water releases one-half mole of hydrogen gas per mole of cesium hydroxide. This is accounted for in the model by adding the additional hydrogen release to the total release of noncondensable gases. This reaction also releases energy that is accounted for in the enthalpy of the released gap gases.

Release of less volatile fission products is based on the CORSOR-M model in NUREG/CR-4173.[4-8] It assumes a first-order release rate from each node for each species such that

$$\mathrm{FP} = \mathrm{FFP} \cdot \left(1 - e^{[(-\mathrm{FRC})(\mathrm{DTIME})]}\right) \tag{4-18}$$

where

FFP = mass of the species present at the node at the start of the time step,

FRC = fractional release rate coefficient.

The value of FRC is given by an Arrhenius type equation of the form:

$$\mathrm{FRC} = \mathrm{KO(I)} \bullet e^{\left(\frac{-\mathrm{Q(I)}}{1.987\times10^{-3}\mathrm{T}}\right)} \tag{4-19}$$

where

KO(I) and Q(I)= species-dependent constants, T = nodal absolute temperature,

1.9873×10^{-3} = value of the gas constant multiplied by a unit conversion factor.

The values of the constants KO and Q are given in Table 4-2.

Table 4-2: Constants KO and Q in release rate coefficients taken from NUREG/CR-4173.

Species	KO (min^{-1})	Q (kcal/mol)
UO_2	1.46 E7	143.1
Zr	2.67 E8	188.2
Sn (clad)	5.95 E3	70.8
Fe	2.94 E4	87.0
Ru	1.62 E6	152.8
Zr (clad)	8.55 E4	139.5
Ba	2.95 E5	100.2
Sr	4.40 E5	117.0
Te	2.00 E5	63.8
Ag	7.90 E3	61.4
Cs*	2.00 E5	63.8
I*	2.00 E5	63.8

The control rod release is calculated in the code based on the following method, described also in NUREG/CR-4173.[4-8]

At 1,673 K and only for aerosol release calculations, the control rods are assumed to fail; 5% of the inventory of silver and 50% of the cadmium are released from the nodes reaching this temperature.

From 1,673 to 2,573 K, the cumulative fraction of the inventory released is calculated according to:

$$\text{Silver: FREL} = 0.0005(T - 1673) + 0.05, \tag{4-20}$$

$$\text{Cadmium: FREL} = 0.00033(T - 1673) + 0.50. \tag{4-21}$$

From 2,573 to 3,073 K, the cumulative fractions of the inventory released are calculated according to:

$$\text{Silver: FREL} = 0.001(T - 2573) + 0.5, \tag{4-22}$$

Cadmium: FREL = 0.0004(T - 2573) + 0.8 (4-23)

which results in complete release at 3,073 K.

The cumulative fraction of the inventory released is then scaled by 0.1 for silver and 0.7 for cadmium to take into account the relocation of silver and cadmium.

4.2.2 Release During UO_2 Liquefaction and Fragmentation

The effect of UO_2 liquefaction is modeled by allowing xenon, krypton, cesium, and iodine to be instantaneously released to the gap from any fuel that is liquefied as predicted by the LIQSOL model. During the fragmentation of the UO_2, the fission products accumulated upon grain boundaries, as predicted by the theoretical model, are released instantaneously. Subsequent release within a rubble bed is controlled only by the intragrain processes. The release of other less volatile species is not affected by liquefaction or fragmentation.

4.2.3 Enthalpy of Released Gases

The noncondensable gases released from the gap are hydrogen, helium, krypton, and xenon. Iodine is also assumed to be noncondensable in this model, even though it is slightly soluble in water at high temperatures. The specific heat of the noble gases (helium, xenon, krypton) is nearly constant with temperature. Therefore, the enthalpy of a particular species can be calculated as a function of specific heat and temperature.

The specific heat of hydrogen is a function of temperature, so the enthalpy must be determined by

$$h = h'_o + \int_{T_o}^{T} c_p(T)dT \tag{4-24}$$

where

h = enthalpy of gas (J/kg),

c_p = specific heat of gas (J/kg • K),

T = temperature of gas (K),

h'_o = enthalpy at reference temperature T_o (J/kg),

T_o = reference temperature (K).

The specific heat of hydrogen is expressed as a function of temperature[4-9] as

$$c_p = (a + bT + cT^2 + dT^3 + eT^4)R \quad . \tag{4-25}$$

Inserting Equation (4-25) into Equation (4-24) and integrating yields

$$h = h'_0 + Ra(T - T_0) + \frac{b}{2}(T^2 - T_0^2) + \frac{c}{3}(T^3 - T_0^3) + \frac{d}{4}(T^4 - T_0^4) + \frac{e}{5}(T^5 - T_0^5)\,, \tag{4-26}$$

Reference 4-10 supplies the constants a through e in Equation (4-25) for the temperature range of 300 to 5,000 K, with a reference temperature of 300 K. However, the SCDAP/RELAP5-3D© hydrodynamic model requires that the enthalpy be based on a reference temperature of 0 K. In order to account for this shift in reference temperature, the constant h'_o was adjusted so that the enthalpy calculated with Equation (4-26) coincided with hydrogen enthalpy tables based on a reference temperature of 0 K. The constants in Equation (4-27) (a - e, R,h) are given in Table 4-3. The thermodynamic properties of other gap gases are also given in Table 4-4. Figure 4-1 shows a comparison between enthalpy calculated with Equation (4-27) and low pressure data from Keenan[4-11] and 20 MPa data from Reynolds.[4-12] Note that the calculated enthalpy using Equation (4-27) and the data form Keenan are nearly identical.

Table 4-3. Thermodynamic properties of gap gases

Species	**Heat of formation (J/kg)**	**Heat of solution (J/kg)**	**Heat of fusion (J/kg)**	**Heat of vaporization (J/kg)**	**c_p (J/kg • K)**
CsI[1]		-1.33×10^5	9.18×10^4	5.82×10^5	240.0
CsOH[2]	3.18×10^6	--	--	--	540.0
He[3]	--	--	--	--	5,233.5
Kr[4]	--	--	--	--	248.5
Xe[5]	--	--	--	--	158.5
I_2[6]	--	--	--	--	147.5

---

1. Reference 4-13
2. Reference 4-13
3. Reference 4-14
4. Reference 4-14
5. Reference 4-14
6. Reference 4-14

Table 4-4. Thermodynamic properties of other than hydrogen.

Hydrogen[1] $c_p = (a + bT + cT^2 + dT^3 + eT^4) R$ **(J/kg • K)**						
h_o	**a**	**b**	**c**	**d**	**e**	**Temperature Range (K)**
0.122×10^6	3.05745	2.67652×10^{-3}	-5.80992×10^{-6}	5.52104×10^{-9}	-1.81227×10^{-12}	$300 < T \leq 1{,}000$
0.576×10^5	3,10019	5.11195×10^{-4}	5.26442×10^{-8}	-3.491×10^{-11}	3.69452×10^{-15}	$T > 1{,}000$

---

[1] Reference 4-10

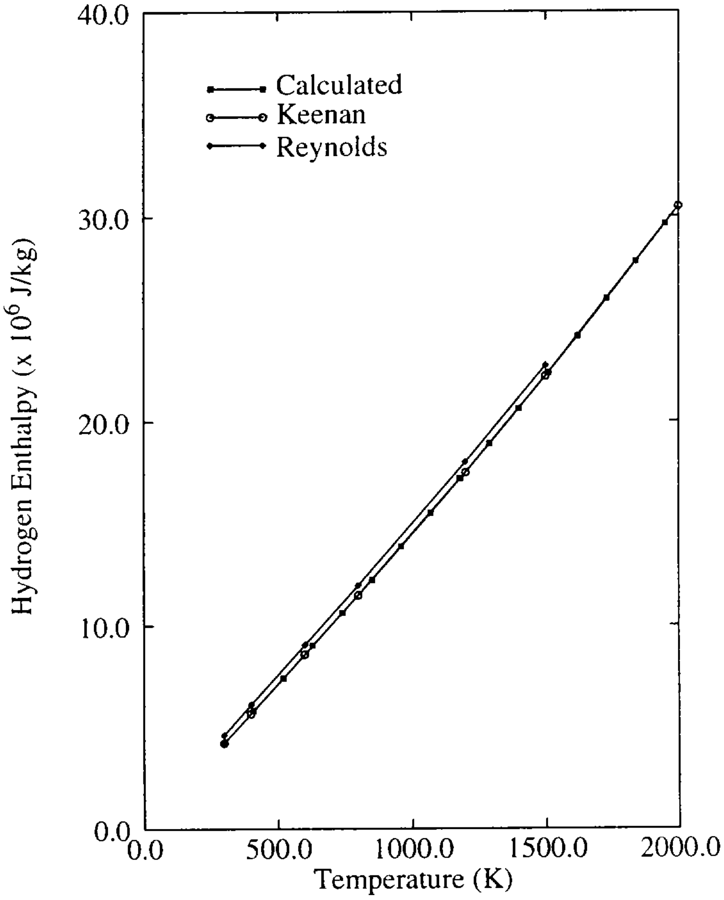

Figure 4-1. Comparison of calculated hydrogen enthalpy using Equation (4-26) and data from Keenan[4-11] and Reynolds.[4-12]

The enthalpy of iodine is assumed to be

$$h(I_2) = c_P T + h_v + h_m \tag{4-27}$$

where

h_v = heat of vaporization (J/kg)

h_m = heat of fusion (J/kg).

To determine the enthalpy of a mixture of noncondensable gases, the enthalpies of the individual species are combined in the following manner: The enthalpy of cesium hydroxide is assumed to be the heat of formation in water, since the reaction occurs when the cesium is released and is a large energy source compared with the energy carried into the reaction by the cesium compound or water. All of the energy from this reaction is assumed to be imparted to cesium hydroxide rather than hydrogen gas.

The enthalpy of cesium iodide is assumed to be

$$h(CsI) = c_P T + h_v + h_s + h_m \tag{4-28}$$

where

h_v = heat of vaporization (J/kg)

h_s = heat of solution (J/kg)

h_m = heat of fusion (J/kg).

The heat of formation is not included because the reaction is thought to occur within the fuel matrix.

4.3 Decay Heat Reduction Due to Fission Product Release

The reduction in fission product decay heat resulting from loss of volatile elements can be accounted for using the model described in Reference 4-7. Fission product decay heat for the intact fuel is calculated from the power history using ANS-5.1. After a major disruptive event, the decay heat reduction is determined from a set of pre-calculated tabular values describing the time-dependent fractional changes in decay heat following fuel disruption. The existing SCDAP tables correspond to several possible irradiation history volatile element release scenarios. This method provides a mechanism for treating decay heat reduction in the disrupted fuel region but provides no information on the distribution of decay power among the released materials.

4.3.1 Fission Product Decay Heat Methodology

This section summarizes the methodology and results of calculations performed to obtain decay heat distributions for the released fission products. Based on model reviews, it was agreed to limit the analysis to one of the irradiation history volatile release scenarios in Reference 4-7 and to isolate contributions from tellurium, iodine, and cesium. Decay heat contributions from the remaining fission products are lumped into a single composite group.

The generic pressurized water reactor (PWR) rapid fuel heatup scenario described in Reference 4-7 was selected for this analysis. Fission product inventories were calculated using ORIGEN2,[4-15] assuming full power operation at the end of an equilibrium cycle. Fuel failure was assumed to occur at 2 minutes after shutdown. Fission product releases were calculated using ORIGEN2 and the time-dependent release rate constants listed in Table 4-5 of Reference 4-7. These best estimate release rate constants are not necessarily the current best estimate values but were used for this analysis to maintain compatibility with the existing SCDAP volatile element release scenarios.

4.3.2 Fission Product Decay Heat Model Results

The time-dependent decay heat contributions from selected elements are shown in Table 4-5 and in Figure 4-2. The decay heat fraction is defined as the ratio of the decay heat from all isotopes of that element to the decay heat of all released fission products. The decay heat contribution from all released fission products other than tellurium, iodine, and cesium is about 76% at 130 seconds and drops to about 23% at 15.6 hours. Table 4-6 lists estimated decay heat gamma fractions for the three elements as a function of time following shutdown.

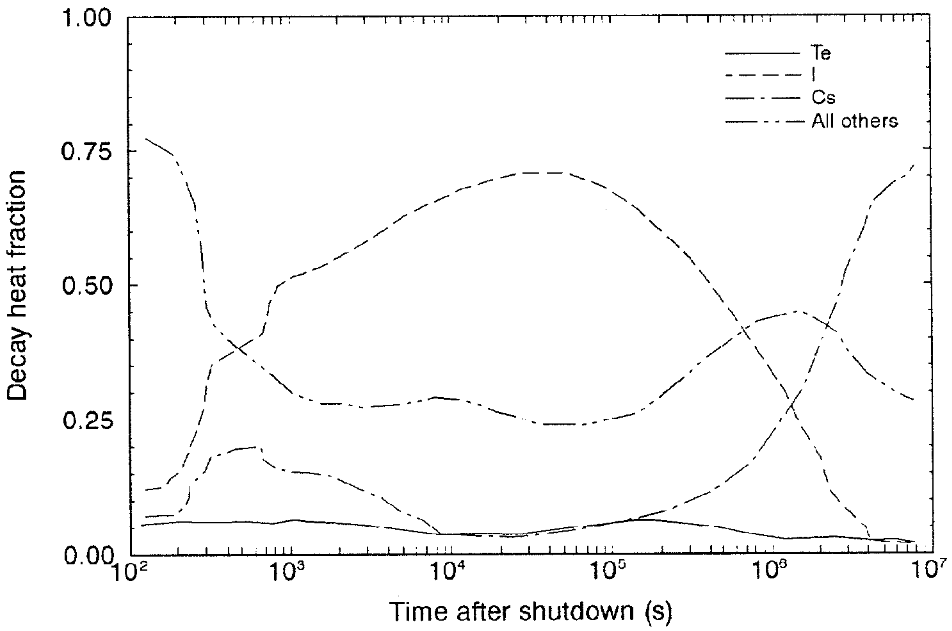

Table 4-5. Fractional decay heat contributions for selected fission product elements (based on total decay heat from all released fission products).

Time after shutdown (s)	Tellurium	Iodine	Cesium
130	0.0485	0.1179	0.0739
150	0.0504	0.1214	0.0756
170	0.0522	0.1248	0.0774
180	0.0531	0.1265	0.0783
200	0.0530	0.1437	0.0891
220	0.0530	0.1594	0.0986
240	0.0529	0.1737	0.1070
260	0.0515	0.2149	0.1286
280	0.0506	0.2440	0.1431
300	0.0502	0.2659	0.1536
320	0.0505	0.3094	0.1732
340	0.0511	0.3313	0.1822
360	0.0518	0.3452	0.1874
480	0.0524	0.3727	0.1948
540	0.0526	0.3839	0.1971
600	0.0528	0.3939	0.1986
660	0.0530	0.4030	0.1995
720	0.0532	0.4113	0.2000
750	0.0518	0.4421	0.1773
780	0.0534	0.4538	0.1710
840	0.0505	0.4729	0.1584
1,020	0.0519	0.4970	0.1516
1,080	0.0534	0.5000	0.1521
1.7783×10^3	0.0498	0.5321	0.1429
3.1623×10^3	0.0436	0.5726	0.1177
5.6234×10^3	0.0359	0.6162	0.0738
1.0000×10^4	0.0288	0.6521	0.0322
1.7783×10^4	0.0267	0.6755	0.0197
3.1623×10^4	0.0311	0.6965	0.0248
5.6234×10^4	0.0381	0.6988	0.0340
1.0000×10^5	0.0448	0.6731	0.0468
1.7783×10^5	0.0484	0.6287	0.0640
3.1623×10^5	0.0448	0.5564	0.0858
5.6234×10^5	0.00354	0.4702	0.1177
1.000×10^6	0.0251	0.3707	0.1772
1.7783×10^6	0.0197	0.2403	0.2944
3.1623×10^6	0.0214	0.0960	0.4814
5.6234×10^6	0.0190	0.0118	0.6532
1.0000×10^7	0.0099	0.0002	0.7123

Figure 4-2. Decay heat contributions of selected elements (based on total decay heat of all released fission products).

Table 4-6. Estimated gamma decay power fractions for released fission products (based on total decay heat from all released fission products).

Time after shutdown(s)	Tellurium	Iodine	Cesium
170	0.6594	0.7832	0.5082
320	0.6616	0.7924	0.5715
540	0.6638	0.7948	0.6025
1080	0.6657	0.7945	0.6379
1.7783×10^3	0.6718	0.7929	0.6723
3.1623×10^3	0.6791	0.7895	0.6983
5.6234×10^3	0.6830	0.7833	0.7169
1.0000×10^4	0.6763	0.7729	0.7642
1.7783×10^4	0.6653	0.7591	0.8506
3.1623×10^4	0.6721	0.7452	0.8663
5.6234×10^4	0.6821	0.7335	0.8673
1.0000×10^5	0.6809	0.7291	0.8670
1.7783×10^5	0.6662	0.7367	0.8659
3.1623×10^5	0.6363	0.7499	0.8639
5.6234×10^5	0.5796	0.7486	0.8606
1.0000×10^6	0.4579	0.7269	0.8554
1.7783×10^6	0.2437	0.6970	0.8477
3.1623×10^6	0.1400	0.6787	0.8386
5.6234×10^6	0.1302	0.6759	0.8314
1.0000×10^7	0.1219	0.6757	0.8267

4.4 Fuel State Models

The fuel rod state modeling includes models for locating the radial position of fuel rod materials and changes in axial power peaking due to fuel axial relocation. Because material with a different peaking factor may be moved to a new axial node location, axial peaking factors are calculated as a function of elevation. Figure 4-3 presents the geometry considered, which accounts for the relocation of material due to liquefaction, flow, and solidification.

The peaking factor in relocated material is found using the following equation:

$${}_cF_{i+1}(z) = \begin{cases} 0 & \text{for } z > z_2 \\ \dfrac{A_a(z)}{A_t(z)}\displaystyle\int_{z_3}^{z_4}\dfrac{F_i(z)A_r(z)}{V_a(z)}dz + \dfrac{{}_cF_i(z)A_c(z)}{A_t(z)} & \text{for } z_1 < z < z_2 \end{cases} \tag{4-29}$$

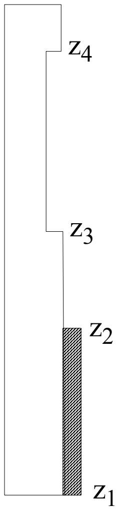

Figure 4-3. Melting and solidification geometry.

where

$_cF_{i+1}(z)$ = nuclear heating axial peaking factor for the crust at time i + 1,

$_cF_i(z)$ = nuclear heating axial peaking factor for the crust at time i,

$F_i(z)$ = nuclear heating average axial peaking factor for z_3 to z_4,

$A_r(z)$ = local area of removed material (m^2),

$A_t(z)$ = total area of crust in the region at the end of time step (m^2),

$A_c(z)$ = crust area at the beginning of the time step (m^2),

$A_a(z)$ = area added to the crust at elevation z during the time step (m^2),

z = axial elevations (m),

V_a = total volume of crust added during the time step (m^3).

4.5 Fuel Rod Cladding Deformation Model

The ballooning of fuel rod cladding and the time and location of rupture of the cladding can have a significant impact on the progression of damage in a reactor core during a severe accident. Several phenomena that may occur during a severe accident are influenced by cladding ballooning and rupture. The most important of these phenomena are cladding oxidation and heatup. If cladding is calculated to balloon and rupture, the heatup due to oxidation may be a factor of 2.6 times larger than that before ballooning and rupture. The factor of 2.6 is the result of the cladding diameter increasing up to a factor of 1.3 due to ballooning and the inside surface area of the cladding being exposed to steam after rupture of the cladding, which doubles the surface area of the cladding that is oxidizing. Other phenomena influenced by cladding ballooning include fission product release from fuels to the coolant and the distribution of flow throughout the reactor core.

The SCDAP/RELAP5-3D© code uses a mechanistic model to calculate the elastic-plastic deformation that can occur in fuel rods during a severe accident. Anisotropic plastic deformation is calculated using the theory of Hill[4-16] and the Prandtl-Reuss equations.[4-17] The model does not take into account circumferential variations in cladding temperature. This model is called the sausage deformation model.

The sausage deformation model is based on the following assumptions:

- Cladding deformation is axisymmetric.
- Cladding deforms like a membrane. There are no bending strains in the cladding.
- Isotropic hardening is assumed in calculating the cladding yield stress.
- Once the outer diameter of the cladding is equal to the fuel rod pitch, no additional cladding deformation takes place.
- Cladding oxidation does not affect the cladding mechanical properties.
- Any constraint imposed by the spacer grids on cladding deformation is ignored.
- For case of external pressure in fuel rod less than internal pressure, once the inner diameter of the cladding is equal to the fuel pellet diameter, no additional cladding deformation takes place.

The sausage deformation model described here is similar to the model available in FRACAS-I,[4-18] except for the following two modifications:

1. Plasticity calculations are based on true strains. FRACAS-I uses engineering strains.
2. Anisotropic properties of cladding are taken into account in the calculation of effective stress and incremental plastic strains. FRACAS-I assumes that plastic deformation of cladding is isotropic.

In this model, the cladding strains are calculated at each component node of a fuel rod group. As cladding experiences elastic-plastic strains, an iterative scheme is required to ensure the convergence of cladding strains. It may be necessary to use a small component time step (the time step used to analyze intact fuel rods) to ensure convergence. Theory used to calculate these strains is described next.

Sausage cladding deformation is a stress driven process. First, the stresses in the cladding are calculated by satisfying the equilibrium conditions at each component node at the beginning of an iteration. The resulting expressions for the stresses are as follows:

$$\sigma_h = \frac{p_g r_i - p_c r_o}{r_o - r_i} \tag{4-30}$$

$$\sigma_a = \frac{p_g r_i^2 - p_c r_o^2}{r_o^2 - r_i^2} \tag{4-31}$$

$$\sigma_r = -0.5(p_c + p_g) \tag{4-32}$$

where

σ_h = hoop stress (Pa),

σ_a = axial stress (Pa),

σ_r = radial stress (Pa),

p_g = gas pressure (Pa),

p_c = coolant pressure (Pa),

r_i = inside radius (m),

r_o = outside radius (m).

Note that the inner and outer radii are current radii in Equation (4-30) through Equation (4-32), so the calculated stresses are true stresses. The effective stress,[4-19] σ_e, is given by

$$\sigma_e = [ACS(\sigma_h - \sigma_a)^2 + AAS(\sigma_a - \sigma_r)^2 + ARS(\sigma_r - \sigma_h)^2]^{0.5} \tag{4-33}$$

where ACS, AAS, and ARS are strength coefficients of anisotropy for calculating effective stress.

These coefficients are calculated with the aid of the MATPRO subroutine CANISO. At the beginning of a time step, the plastic increments during the time step are not known; so during the first iteration, they are assumed to be equal to zero in the calculations of the strength coefficients used in Equation (4-33).

If the effective stress, σ_e, is greater than the corresponding true effective yield stress (calculated using the MATPRO subroutine CSTRES), then the increments in the plastic strains are calculated using the Prandtl-Reuss equations and Hill’s theory for anisotropic plastic deformation.

The effective true strain in the cladding is calculated using the MATPRO subroutine CSTRNI that takes into account the effect of strain rate and cladding temperature. Since plastic deformation is an irreversible process, d_{ep}, the increment in the true effective strain, is zero or positive. The increment in the plastic strain components is calculated as follows:

$$d\varepsilon_{h,\,p} = d_{ep}[A_1(\sigma_h - \sigma_a) + A_2(\sigma_h - \sigma_r)]/\sigma_e\,, \tag{4-34}$$

$$d\varepsilon_{a,\,p} = d_{ep}[A_3(\sigma_a - \sigma_r) + A_1(\sigma_a - \sigma_h)]/\sigma_e\,, \tag{4-35}$$

and

$$d\varepsilon_{r,\,p} = d_{ep}[A_2(\sigma_r - \sigma_h) + A_3(\sigma_r - \sigma_a)]/\sigma_e\,, \tag{4-36}$$

where

$d\varepsilon_{h,p}$ = increment in plastic hoop strain,

$d\varepsilon_{a,p}$ = increment in plastic axial strain,

$d\varepsilon_{r,p}$ = increment in plastic radial strain,

and A_1, A_2, and A_3 are coefficients of anisotropy for calculating plastic strain increments.

The total true hoop strain is

$$\varepsilon_h = \varepsilon_{h,\,e} + \varepsilon_{h,\,t} + \varepsilon_{h,\,p_o} + d\varepsilon_{h,\,p} \tag{4-37}$$

where

ε_h = total hoop strain at the end of the time step

$\varepsilon_{h,e}$ = hoop strain due to elastic deformation $\left[\frac{\sigma_h - \nu(\sigma_a + \sigma_r)}{E}\right]$

$\varepsilon_{h,t}$ = hoop strain due to thermal deformation $(\alpha\Delta T)_h$

$\varepsilon_{h,\,p_o}$ = hoop strain due to plastic deformation at the beginning of the time step

ν = Poisson's ratio

E = elastic modulus (Pa).

Equation (4-37) may be written as

$$\varepsilon_h = [\sigma_h - \nu(\sigma_a + \sigma_r)]/E + (\alpha\Delta T)_h + \varepsilon_{h,\,p_o} + d\varepsilon_{h,\,p}\quad . \tag{4-38}$$

Similarly,

$$\varepsilon_a = [\sigma_a - \nu(\sigma_r + \sigma_h)]/E + (\alpha\Delta T)_a + \varepsilon_{a,\,p_o} + d\varepsilon_{a,\,p} \tag{4-39}$$

and

$$\varepsilon_r = [\sigma_r - \nu(\sigma_a + \sigma_h)]/E + (\alpha\Delta T)_r + \varepsilon_{r,\,p_o} + d\varepsilon_{r,\,p} \quad . \tag{4-40}$$

The hoop strain, ε_h, is used to calculate cladding radii at the end of the iteration as follows:

$$R_{m1} = R_m(1 + \varepsilon_h) \tag{4-41}$$

where

R_m = original cladding mean radius (m),

R_{m1} = cladding mean radius at the end of the iteration (m).

The cladding wall thickness is calculated assuming that the cladding cross-sectional area remains constant:

$$T_{wall} = \frac{A_c}{2\pi(R_{m1})} \tag{4-42}$$

where

T_{wall} = cladding wall thickness at the end of the iteration (m),

A_c = cladding cross-section area (m^2).

So, the cladding radii at the end of the iteration are

$$r_o = R_{m1} + \frac{T_{wall}}{2}, \tag{4-43}$$

$$r_i = R_{ml} - \frac{T_{wall}}{2} \quad . \tag{4-44}$$

The cladding radii in Equations (4-43) and (4-44) are used to calculate the void volume at the end of the iteration.

During the next iteration, the void volumes are used to update the fuel rod gas pressure model (see Section 4.6). The cladding radii from the last iteration [Equations (4-43) and (4-44)] are used to calculate stresses using Equations (4-30) through (4-32). The plastic strain increments from the last iteration using Equations (4-33) through (4-36) are used to calculate anisotropic strength coefficients (calculated using the MATPRO routine CANISO), which are used to calculate the effective stress in Equation (4-33). Then Equations (4-34) through (4-44) are solved. The iteration process continues until the calculated hoop stresses converge for each component node. The converged hoop stresses at each component node are compared with the corresponding failure stresses calculated using the MATPRO routine CMLIMT to determine whether or not the cladding has ruptured. Then the analysis will proceed to the next component time step. Once a fuel rod cladding has ruptured, the cladding deformation calculations for the corresponding fuel rod bundle are no longer performed during the remaining portion of the analysis.

The flow area reduction for each representative fuel rod component is then computed by subtracting the change in the cross-sectional area of the fuel rod from the original flow area. No allowance is made for flow internal to the cladding that could result from cladding failure. The total change in flow area for each thermal-hydraulic volume is then computed from the sum of the changes in flow area for all of the fuel rods. Deformation of other core components, such as control rods or structures, is neglected.

4.6 Fuel Rod Internal Gas Pressure Model

The fuel rod internal gas pressure is computed from the perfect gas law. This includes different volumes of gas at different temperatures as given by

$$P = \frac{N_m R}{\sum_i \frac{V_i}{T_i}} \tag{4-45}$$

where

P = internal gas pressure (Pa),

N_m = moles of gas in fuel rod void volumes (g-mole),

R = universal gas constant (N • m/g-mole • K),

V_i = i-th volume (m^3),

T_i = temperature of gas in i-th volume (K).

The different volumes considered are:

- Plenum volume.
- Fuel void volumes at each axial elevation that are the sum of crack, dish, gap (except contributions due to cladding ballooning), porosity, and roughness volumes.
- Additional gap volumes due to cladding ballooning at each axial elevation.

Thus, the gas pressure model becomes

$$P = \frac{N_m R}{\frac{V_p}{T_p} + \sum_{i=1}^{M} \frac{V_{void,i} + V_{gap,i}}{T_{f,i}}} \tag{4-46}$$

where

V_p = plenum volume (m^3),

T_p = gas temperature in plenum (K), which is assumed to be coolant temperature at the top of the rod plus 6 K,

M = number of axial nodes,

$V_{void,i}$ = fuel void volume in i-th axial node (m^3),

$V_{gap,i}$ = additional gap volume due to cladding ballooning in i-th axial node (m^3),

$T_{f,i}$ = average fuel temperature in i-th axial node (K).

Correlations were developed to account for the effects of fuel burnup and temperature on fuel void volumes for commercial PWR and BWR fuel rods.

4.7 Liquefaction and Slumping of Fuel Rod Cladding

The melting of the metallic part of fuel rod cladding causes significant changes to the oxidation characteristics of the cladding and to the configuration and location of the cladding. The changes caused by melting may include; (1) reduction in fraction of circumference of fuel rod through which oxygen uptake occurs due to movement of metallic part of cladding into the portion of circumference with largest fuel-cladding gap before melting, (2) change in rate of oxidation due to dissolution of UO_2 by the melted metallic part of the cladding, (3) slumping due to loss of restraint from the oxidic part of the cladding, and (4) partial blockage to oxidation of in situ metallic cladding due to drops of slumped material adhering to the surface of the cladding. This section describes the models for calculating the changes in cladding configuration brought on by cladding melting. Section 4.7.1 describes the model for calculating the fraction of the circumference of the cladding in contact with a metallic substrate after the metallic portion has melted. A summary is also provided of the experimental results on which the model is based. Section 4.7.2 describes the model for calculating the amount of fuel dissolved by the melted metallic portion of the cladding. The results of this model affect the rate of oxidation of the melted cladding and the configuration and location of the melted cladding after losing restraint from the surrounding oxidic portion of the cladding. Section 4.7.3 describes the model for evaluating the integrity of the oxidic portion of the cladding retaining melted metallic cladding. This section also describes the affect on the integrity of the oxidic portion of slumped material adhering to its outer surface. Section 4.7.4 describes the model for calculating the configuration and slumping distance of melted cladding for which the surrounding oxidic portion of the cladding has lost its capability to retain it. The results of this model have a significant impact on the calculated oxidation of both the slumped cladding and the in situ cladding to which the slumped cladding adheres. This section also describes the model for calculating the reslumping of cladding which has previously slumped and partially solidified.

In general, empirical models based on the PIE results of severe fuel damage tests are employed to calculate the configuration changes the fuel rod cladding undergoes due to melting. Mechanistic models are not warranted due to large uncertainties in fuel rod geometry and in material properties. Three contributors to the uncertainty in geometry are (1) eccentrically positioned fuel pellets, which result in the fuel rod geometry varying in three dimensions, (2) fuel rod bowing, and (3) fuel pellet cracking. The major contributor to uncertainties in material properties are the structural properties of oxide layers retaining melted Zr. As a result, empirical models for each step of the meltdown process were developed so as to replicate the meltdown observed in severe fuel damage tests.

4.7.1 Relocation of Melted Cladding in Circumferential Direction

Experimental results indicate that after melting the metallic part of the cladding concentrates in the segment of the circumference of the cladding with the largest fuel-cladding gap before the onset of melting. A schematic of the configuration change caused by melting is shown in Figure 4-4. This configuration change reduces the surface area for oxygen uptake and thus results in the reduction of rate of heat heatup, other factors influencing the oxidation rate staying the same. The schematic of the configuration change is based on Post-Irradiation Examinations (PIE) of fuel rods subjected to severe accident conditions. Figure 4-5, Figure 4-6 and Figure 4-7 are examples of observed configurations of the melted metallic portion of cladding. The first two examples are taken from the PIE results for the OECD LOFT FP-2 test,[4-25] and the third example is from the PBF SFD 1-1 test.[4-20] Similar changes in configuration of melted metallic portions of the cladding were observed in other severe fuel damage tests, such as the PBF SFD 1-4 test.[4-21] In general, the PIE results indicate an asymmetric configuration of metallic cladding that melted during the heatup phase of the tests. This asymmetric configuration is the result of the melted cladding at a location concentrating in the portion of the circumference of the cladding with the largest fuel-cladding gap before the onset of cladding melting at that location. After relocation in the circumferential direction, in general about 50% of the circumference of the cladding has a metallic substrate. In a cross section view, the metallic portion of the cladding is configured as a segment of an annulus; in other words, in the shape of a quarter moon.

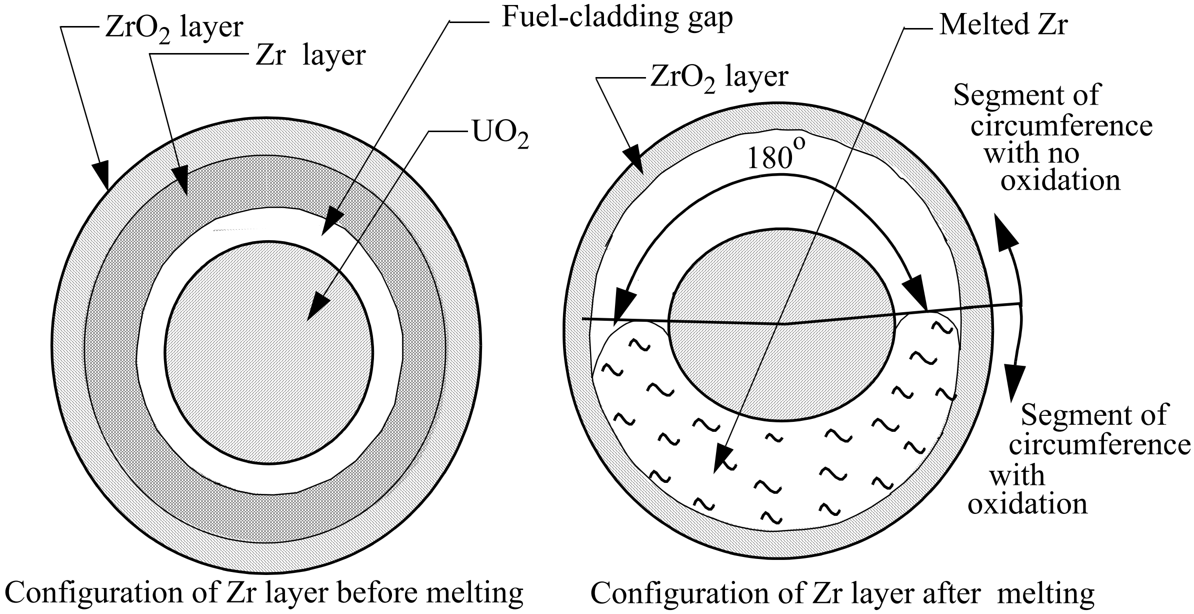
ZrO$_2$ layer
Zr layer
Fuel-cladding gap
UO$_2$
Melted Zr
ZrO$_2$ layer
180°
Segment of circumference with no oxidation
Segment of circumference with oxidation
Configuration of Zr layer before melting
Configuration of Zr layer after melting

Figure 4-4. Configuration change caused by relocation in circumferential direction of melted cladding.

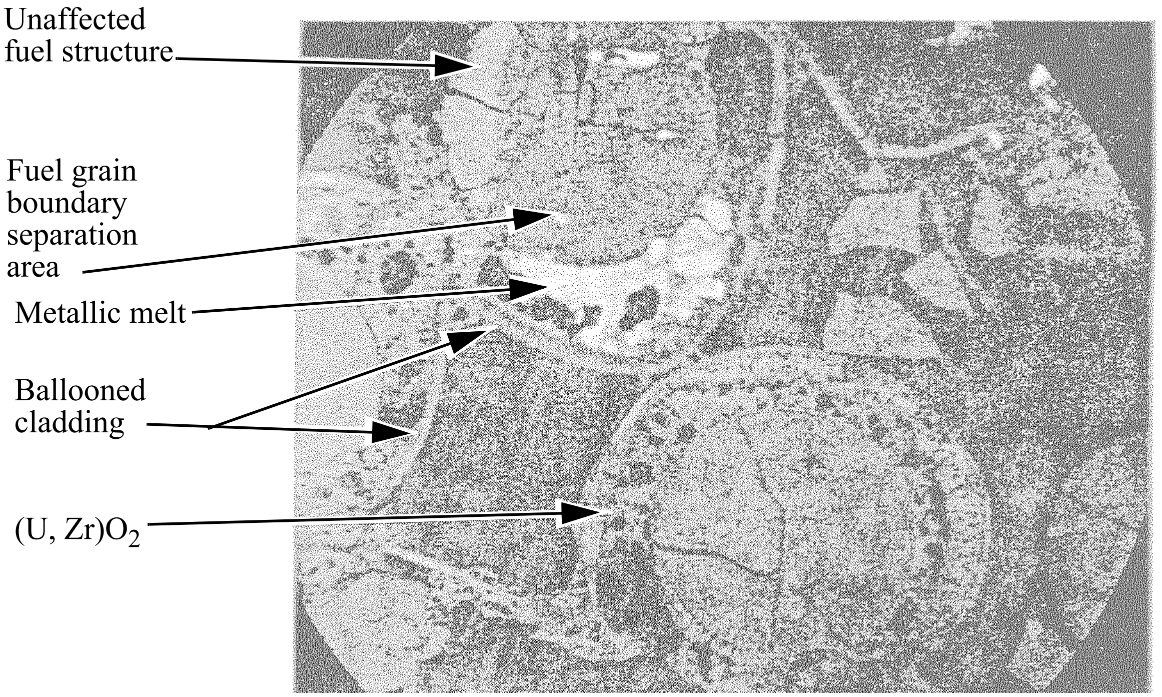
Unaffected fuel structure
Fuel grain boundary separation area
Metallic melt
Ballooned cladding
(U, Zr)O2

Figure 4-5. Example of configuration of liquefied metallic layer from PIE results of OECD LOFT FP-2 experiment.

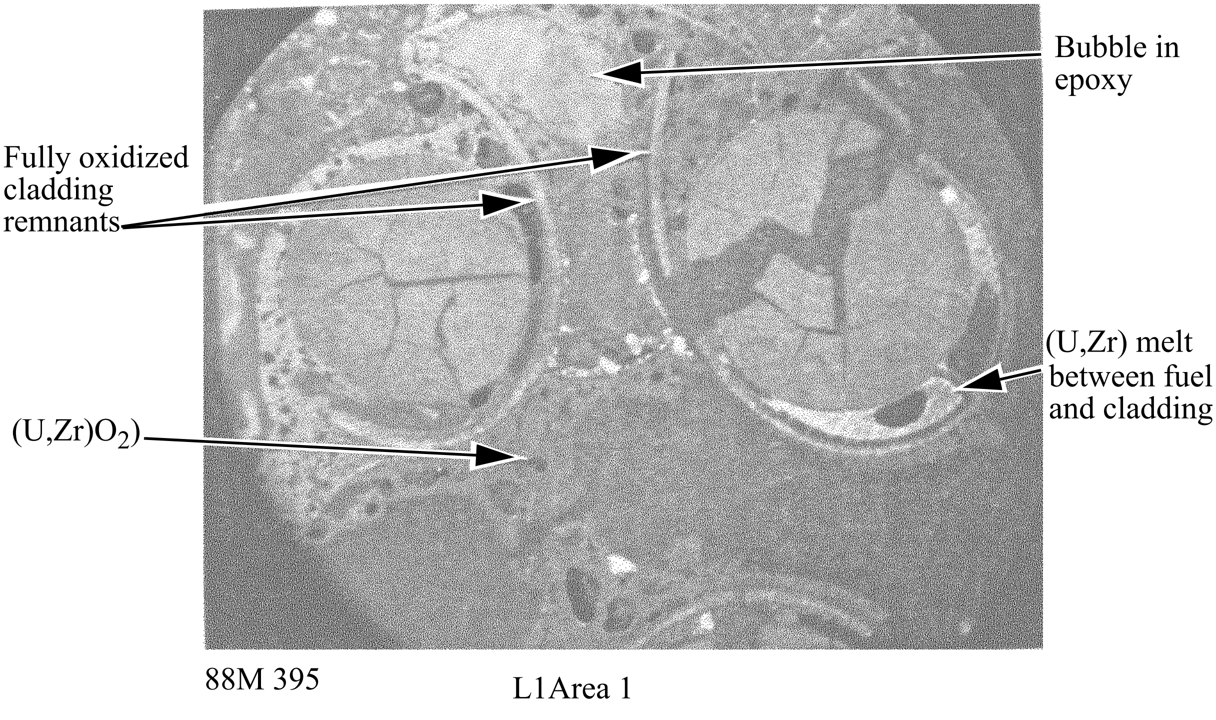
Bubble in epoxy
Fully oxidized cladding remnants
(U,Zr) melt between fuel and cladding
(U,Zr)O2)
88M 395
L1Area 1

Figure 4-6. Example of asymmetric configuration of liquefied metallic layer from 0.96 m elevation of OECD LOFT FP-2 Test bundle (L1 Area 1).

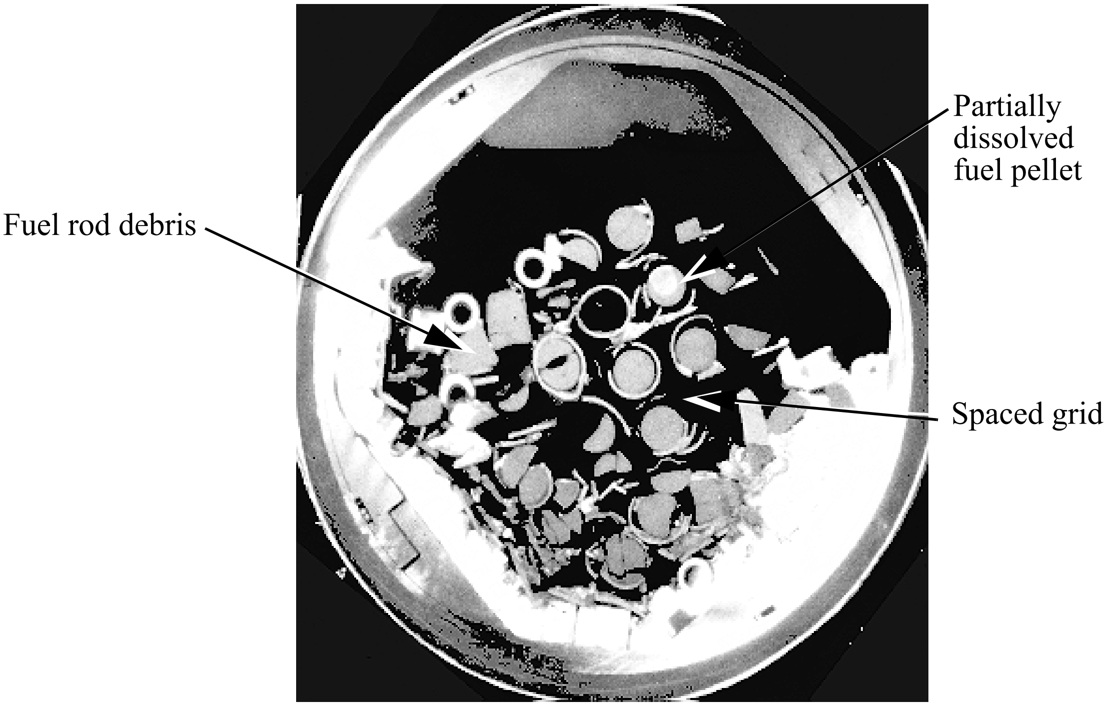

Figure 4-7. Example of asymmetric shape of liquefied cladding and dissolved fuel from PBF SFD 1-1 experiment.

The model for the configuration change of the metallic portion of the cladding at the onset of its melting at any location is expressed by the equation

$$f_{cm} = 1 \quad (T_{MH} < T_{melt} \text{ or } \varepsilon_h < 0.01) \tag{4-47}$$

$$f_{cm} = 0.5 \quad (T_{MH} > T_{melt} \text{ and } \varepsilon_h \geq 0.01)$$

where

f_{cm} = fraction of circumference of cladding with a metallic substrate,

T_{MH} = maximum temperature of cladding during period of severe accident conditions (K),

T_{melt} = melting temperature of metallic portion of cladding (K),

ε = hoop strain of midplane of cladding (unitless).

As indicated by the above set of equations, the melted metallic portion of the cladding is assumed to be constrained from movement in the circumferential direction for hoop strains less than 0.01. In this case, the fuel-cladding gap is small at all locations along the circumference of the cladding.

4.7.2 Amount of Fuel Dissolved by Melted Metallic Portion of Cladding

The metallic portion of the cladding dissolves some of the fuel in contact with it. The rate of dissolution increases with temperature and becomes significant after cladding melting has occurred. The calculation of the amount of dissolved fuel is important for two reasons. First, the subsequent rate of oxidation of the cladding is a function of the amount of fuel dissolved. Second, in the event melted cladding is no longer supported by an oxide layer and thus slumps, the blockage at the location where the slumped cladding froze is proportional to the amount of fuel dissolution.

According to experimental results obtained by Hofmann et al.[4-49]. the fuel dissolution initially occurs rapidly. This rapid period of dissolution is defined to be the incubation period., During this period, the weight percent of UO_2 in the mixture of Zr-U-O increases from zero to 35.8%. After this period, the rate of dissolution follows a parabolic kinetics law expressed by the equation

$$P_2 = 35.8 + \sqrt{(P_1 - 35.8)^2 + 1.0196 \times 10^{15} e\left(-\frac{677200}{RT}\right)\Delta t} \tag{4-48}$$

$$W_u = P_2 \frac{W_Z}{(100. - P_2)} \tag{4-49}$$

$$r_{m2} = \sqrt{r_p^2 - \frac{W_u}{(\rho f_{cm} \pi)}} \tag{4-50}$$

where

P_2 = weight percent of UO_2 at end of time step in mixture of U-Zr-O resulting from fuel dissolution by liquefied zirconium,

P_1 = weight percent of UO_2 at start of time step,

R = universal constant (8.314 J/kg-mole · K),

Δt = time step (s),

W_u = mass of UO_2 dissolved per unit length (kg),

W_z = mass of zirconium liquefied per unit length (kg),

r_{m2} = outer radius of undissolved fuel at end of time step (m),

r_p = outer radius of fuel prior to fuel dissolution (m),

ρ = density of fuel (kg/m^3).

A schematic of the fuel dissolution process for a case in which melted cladding relocated in the circumferential direction is shown in Figure 4-8.

The calculated amount of fuel dissolution is limited to the amount at which equilibrium occurs as determined by the solidus line in the ternary phase diagram for a mixture of Zr-U-O. The calculation of this limit to the fuel dissolution is explained in Volume 4, Section 11. In order to be consistent with the extent

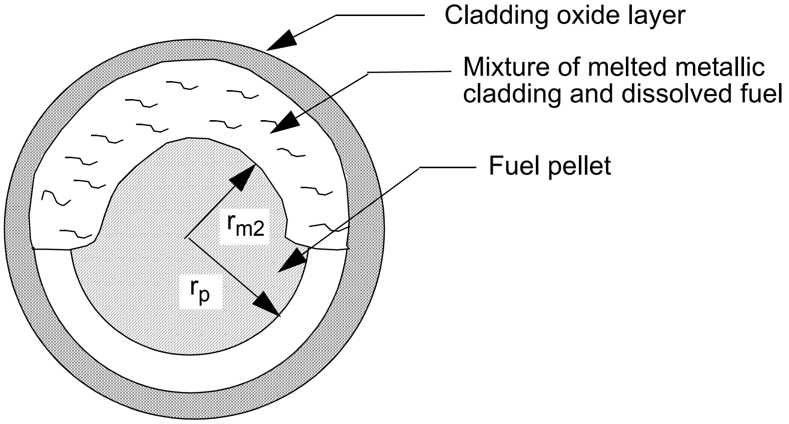

Figure 4-8. Schematic of dissolution of fuel by melted cladding.

of fuel dissolution observed in severe fuel damage tests, the variable r_{m2} in the above equation is further constrained to have a minimum value of $0.90r_p$

4.7.3 Structural Failure of Oxide Layer Retaining Melted Metallic Cladding

An oxide layer may lose its capability to retain melted cladding due to dissolution or to excessive stress. During the change in phase of the metallic layer from solid to liquid, a portion of the oxide layer in contact with the metallic layer is dissolved.[4-32] If this dissolution exceeds a threshold value, a breach occurs in the layer and melted cladding slumps through the breach. Stresses are generated in the oxide layer by a temperature gradient across the oxide layer. When the stress exceeds the failure stress, the oxide layer at that point is regarded as no longer capable of retaining the melted metallic part of the cladding.

Failure of the oxide layer occurs due to dissolution during the melting process when the following conditions are satisfied;

$$I_f = 1 \qquad [m_{fzo} < \ f_{ds} \text{ and } (f_{ox} + f_b f_l) < fs] \tag{4-51}$$

$$I_f = 1 \qquad [\delta_2 > f_{th} d_{ox2}] \tag{4-52}$$

where

I_f = index indicating failure of oxide layer; 0 = no, 1 = yes, if the conditions defined above are not satisfied, $I_f = 0$,

m_{fzo} = ratio of mass of oxide layer at location to total mass of oxide layer and metallic layer at location (unitless),

f_{ds} = threshold value for the mass ratio (unitless),

f_{ox} = fraction oxidation of fuel rod cladding at location (unitless),

f_b = coefficient (unitless),

f_l = fraction of coolant space at location filled with slumped material (unitless),

f_s = necessary value for support factors to prevent failure (unitless),

Based on the analyses of severe fuel damage tests, f_{ds} is the above expression was assigned a value of 0.0885, f_b a value of 0.55, f_s a value of 0.45, and f_{th} a value of 0.5.

The model for stress induced failure of the oxide layer compares the stresses in the oxide layer with the failure stress of the oxide layer. Since there is an order of magnitude uncertainty in the failure stress of the oxide layer and also large uncertainties in other structural properties, an empirically determined constant is needed with this model. A modification of the model developed by Boldyrev, et al.[4-39] is used to calculate the stresses in the oxide layer. According to this model, the maximum circumferential stress in an oxide layer is calculated by the equation

$$\sigma = c_1 \alpha |\Delta T| E \frac{d_{ox2}^2}{(d_{ox2} - c_2 \delta_2)^2} \tag{4-53}$$

where

σ = maximum circumferential stress in oxide layer (Pa),

α = coefficient of thermal expansion of oxide layer (1/K),

ΔT = difference in temperature between inside and outside surfaces of oxide layer (K),

E = modulus of elasticity of oxide layer (Pa),

d_{ox2} = thickness of oxide layer not accounting for fuel dissolution (m),

δ_2 = depth of dissolution of oxide layer (m),

f_{th} = coefficient (unitless).

c_1, c_2 = empirically determined constants, theoretical values; $c_1 = 0.5$, $c_2 = 3.5$ (unitless).

The (δ_2) term in the above equation is calculated by cumulating the values of $(d\delta/dt)\Delta t$ from Equation (3-19) for negative values of $(d\delta_2/dt)$ (dissolution of the oxide layer into the metallic substrate is occurring).

The oxide layer is considered to lose its structural integrity and release retained liquefied material when the following condition holds

$$\sigma > S_u \tag{4-54}$$

where

S_u = ultimate strength of oxide layer as determined by MATPRO[4-36] (Pa).

For an oxide temperature greater than 1869 K, MATPRO assigns S_u a constant value of $1.x10^6$ Pa, with an expected standard error of ± 0.7 times the predicted value. There is an equally large amount of uncertainty in the value of E, the modulus of elasticity of the oxide layer. Since a large amount of uncertainty exists in the values of S_u and E, the variables c and c_2 in the equation for stress were set to values that result in calculated timing for oxide failure being in agreement with the measured results. Values of c_1 equal to 0.50 and c_2 equal to 3.5 achieve this result.

The variable ΔT in Equation (4-52) is not directly calculated by SCDAP; the code calculates the temperatures of the inside and outside surfaces of the cladding but not specifically the inside and outside temperatures of the oxide layer of the cladding. The inside and outside temperatures of the oxide layer are assumed to be same as the inside and outside temperatures of the cladding. Since the thermal conductivity of the ZrO_2 part of the cladding is much less than that of the Zr part, this assumption is appropriate for all oxide layers except a ZrO_2 layer that is thin relative to the Zr layer.

The outer oxide layer at a location with double-sided oxidation is assumed to fail at the instant the metallic layer sandwiched between the inner and outer oxide layers begins to melt. This failure is caused by the volume expansion of the metallic layer as it changes from the solid to the liquid phase. In this case, no void is present to absorb the volume expansion. So the volume expansion forces out the oxide layers to the point a breach occurs in the oxide layers.

A high concentration of slumped material may provide structural support to the oxide layer and prevent its failure. An example of the situation where this structural support may occur is shown in Figure 4-9, which is a post-test photograph of the cross section of the test fuel assembly the OECD LOFT FP-2 test.[4-50] A schematic of this possible structural support is shown in Figure 4-10. To account for the structural support caused by a high concentration of relocated material, the model for stress in the oxide layer is extended as follows;

$$\sigma = 0 \quad (f_{ox} + 0.55 f_{lmax} > 0.45) \tag{4-55}$$

4.7.4 Distance of Slumping of Melted Cladding

The failure of the oxide layer retaining melted cladding causes the melted cladding at the location of the oxide failure to slump and freeze in a lower and cooler position in the fuel assembly. A mechanistic analysis of the motion of the slumping material requires material properties which are not available.[4-44] Experimental results show that the slumped material is generally configured as drops. Figure 4-11 shows a typical configuration of cladding material that has slumped in severe accident conditions. This example is taken from a post-test examination of the fuel bundle in the FzK CORA-13 test.[4-23] A schematic of the slumping cladding material is shown in Figure 4-12. The advancing and receding contact angles of the slumping material as a function of velocity are examples of required material properties for a mechanistic analysis but which are not available. These contact angles are represented in Figure 4-12 by the symbols θ_A and θ_R. Also, a mechanistic model requires the ratio of the surface area wetted by a moving drop to the surface area wetted when the drop is not moving, but a correlation is not available for this ratio. As a result, an empirical model based on the results of severe fuel damage tests is employed. This model

where

f_{ox} = fraction of cladding oxidized (unitless),

f_{lmax} = maximum value in history of fraction of coolant space at location filled with slumped material (unitless).

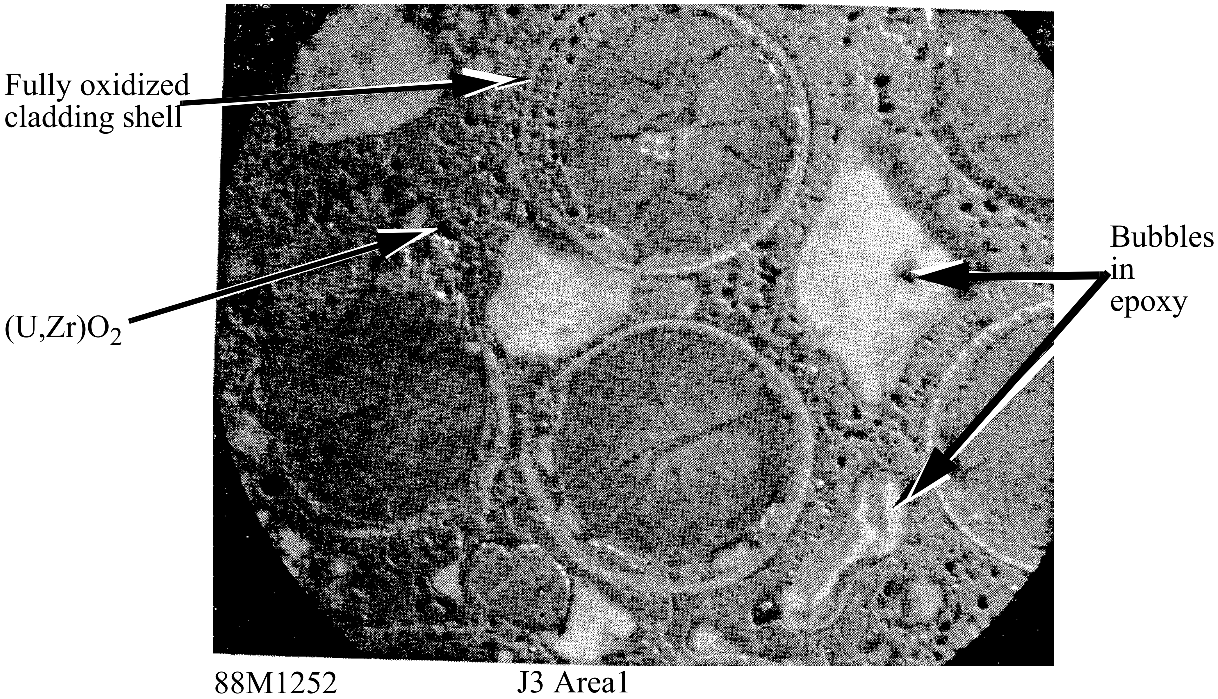
Fully oxidized cladding shell
(U,Zr)O2
Bubbles in epoxy
88M1252
J3 Area1

Figure 4-9. Example from OECD LOFT FP-2 experiment of fully oxidized cladding surrounded by slumped cladding.

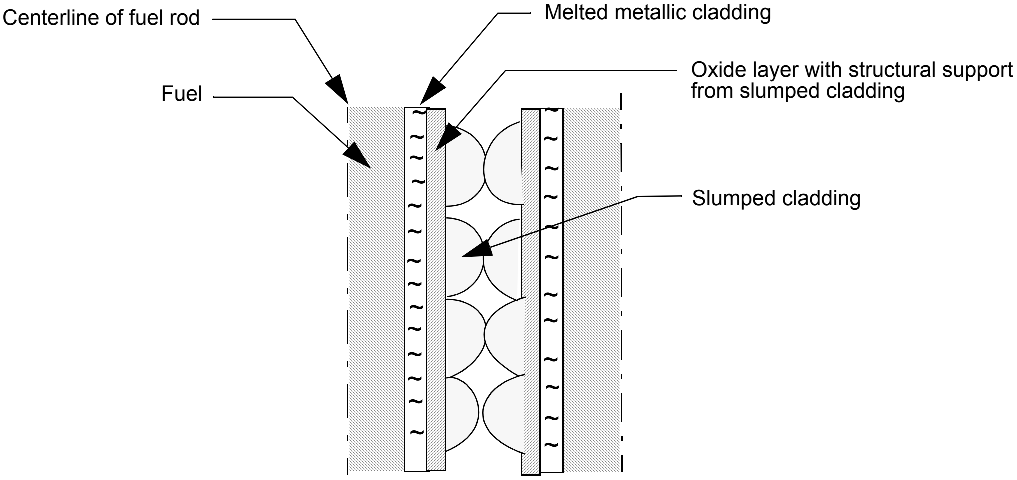
Centerline of fuel rod
Melted metallic cladding
Oxide layer with structural support from slumped cladding
Fuel
Slumped cladding

Figure 4-10. Schematic of structural support given oxide layer by slumped material adhering to its external surface.

calculates the distance of slumping of the melted cladding based on the temperature of the fuel rod

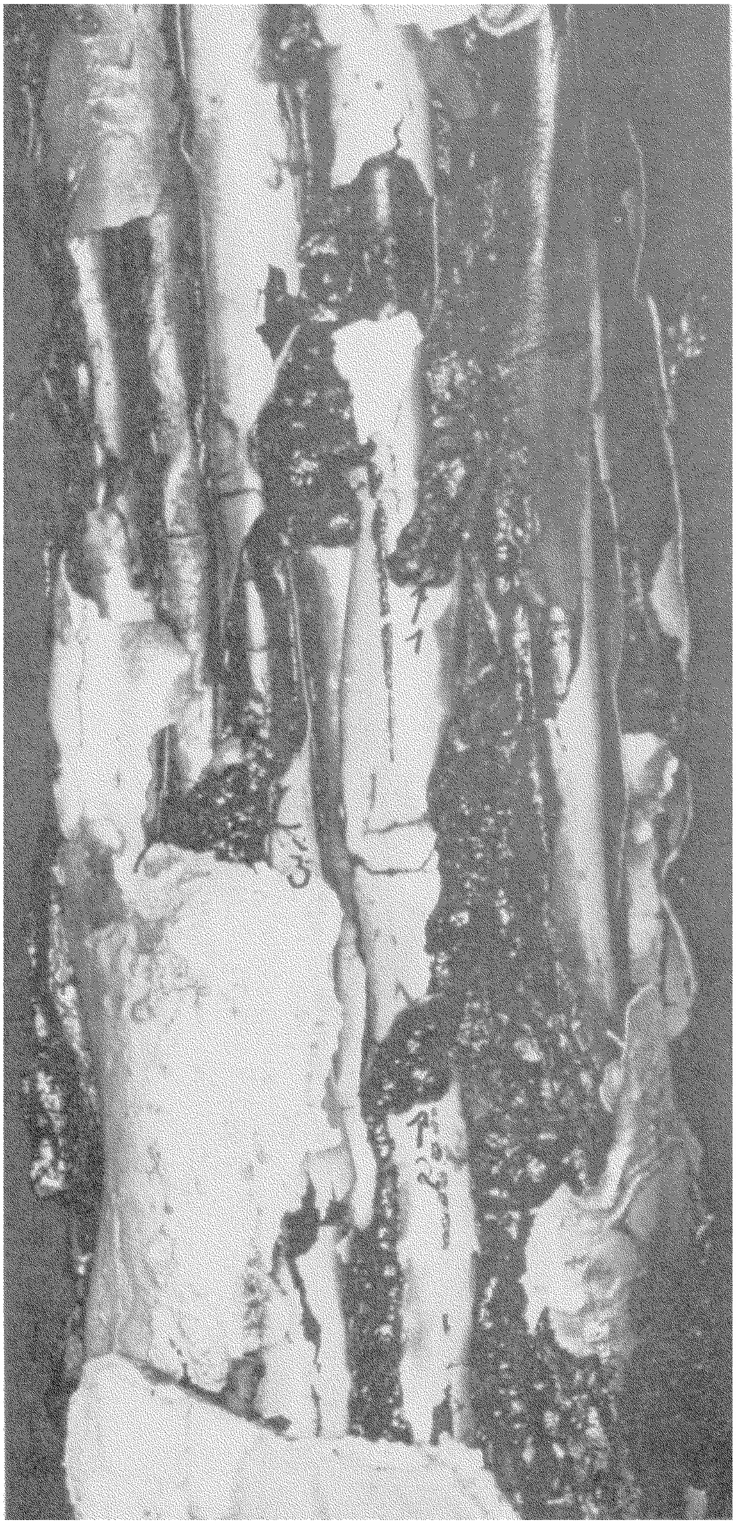

Figure 4-11. Post-test view of fuel bundle of FzK CORA-13 Test.

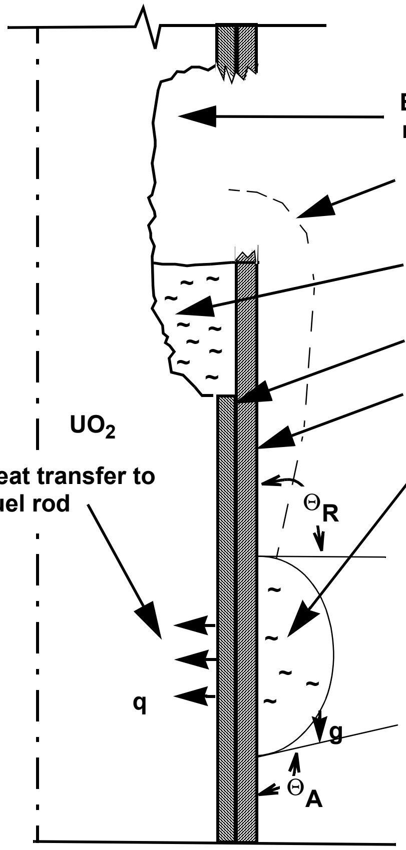
Breach releasing mixture of Zr-U-O
Path of released material
Molten mixture of Zr-U-O
Zr
ZrO_2
UO_2
Mixture of Zr-U-O slumping due to gravity
Heat transfer to fuel rod
Θ_R
q
g
Θ_A

Figure 4-12. Schematic of slumping of melted cladding after failure of oxide layer retaining it.

cladding below the point from which the slumping originates. A schematic of the slumping model is shown in Figure 4-13. The drops are assumed to be hemispherical in shape and to have a radius of 3.5 mm. All of the slumping material is assumed to be on the outside surface of the fuel rod. The distance of slumping of the drops is calculated by the equation set;

$$T_s(z_F) = T_m - T_F \tag{4-56}$$

$$d_s = z_s - z_F$$

where

$T_s(z_F)$ = temperature of surface of cladding at elevation of z_F (K),

T_m = liquidus temperature of slumping material (K),

T_F = temperature differential between liquidus temperature of slumping material and surface temperature that causes slumping material to partially freeze and stop slumping (K),

d_s = distance of slumping (m),

z_s = elevation of origin of slumping material (m),

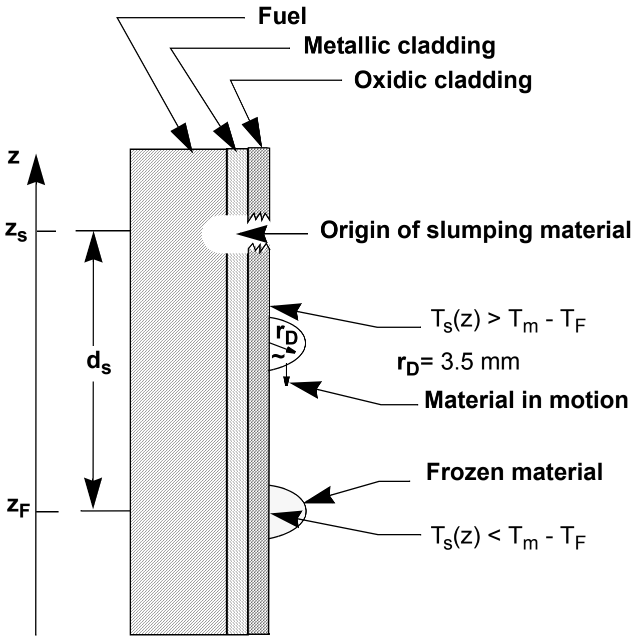

Figure 4-13. Distance of slumping of melted cladding.

z_F = elevation at which slumping stopped (m).

The parameter T_F in the above equation has the value of 50 K. This value is based on the analyses of severe fuel damage experiments. Since a steep axial temperature gradient generally exists in the neighborhood of release of melted cladding, the slumped cladding is calculated in general to slump down just one axial node before freezing and stopping.

The drops are assumed to originate one by one from the location where an oxide layer has lost its capability to retain melted material. Each drop is assumed to originate 1.0 s after the origination of the previous drop. Generally, the volume of liquefied cladding material at a location 0.1 m in height corresponds with the volume of twenty drops. So for such a location, the origination of drops is spread over 20 s.

Heat transfer between the slumped cladding and its substrate causes the slumped cladding to completely freeze and the substrate to increase in temperature. Since the mass of the substrate material is significantly larger than the mass of the slumping material, the temperature of the substrate material generally increases only a few degrees K. The heat transfer between the slumped cladding and its substrate are described in Section 2.7. After the instant when slumped material stopped and a jump in temperature occurred at the location where it stopped, the subsequent temperature history at that location is calculated by the heat conduction model for intact fuel and cladding. The heat capacity and oxidation characteristics at that location are adjusted to account for the presence of the slumped material.

After temporarily freezing, the slumped cladding may again reheat and liquefy. If the slumped cladding has not oxidized to the degree required for its oxide layer to support it, the slumped cladding will slump again when its temperature exceeds the liquidus temperature of the metallic part of the relocated material. If the slumped cladding has oxidized to the extent required for the oxide layer to support the liquefied metallic part of the slumped cladding, then it does not slump again until the oxide layer is so weakened by a temperature increase that the oxide layer cannot support the slumped cladding. Another slumping of previously slumped material is assumed to occur when the following situation is satisfied;

$$I_s = 1 \quad \{[T_D > T_m \quad \text{and} \quad F_{OD} < F_{OC}] \quad \text{or} \quad [T_D > T_w]\} \tag{4-57}$$

where

I_s = indicator of re-slumping of previous slumped material;

0 = no re-slumping, 1 = re-slumping, if the condition defined above is not satisfied, $I_s = 0$,

T_D = temperature of the slumped material (K),

T_m = liquidus temperature of the slumped material (K),

T_w = temperature threshold for oxide layer of slumped material losing capability to support the slumped material (K),

F_{OD} = fraction of slumped material that is oxidized,

F_{OC} = threshold in fraction of oxidation of slumped material resulting in oxide layer of slumped material having capability to support the slumped material.

The value of F_{OC} is a function of the fraction at the coolant space filled with slumped material; it is calculated by the equation

$$F_{OC} = f_{xt} \qquad f_l < f_{r1}\,, \tag{4-58}$$

$$F_{OC} = b_1 f_{xt} \qquad f_l \geq f_{r2}\,,$$

$$F_{OC} = \{[(b_1 - 1.)/(f_{r2} - f_{r1})]f_l + 1. - f_{r1}(b_1 - 1.)/(f_{r2} - f_{r1})\}f_{xt}\ .$$

In the above inequalities, f_l is the fraction of coolant space filled with slumped material, f_{r1} and f_{r2} define the range of f_l for which a linear interpolation is performed, and b_1 and f_{x2} are coefficients (unitless).

The parameter T_w in the above equation has the value of 2800 K and the parameter f_{xt} has the value of 0.045. The value f_{r1} and f_{r2} are 0.3 and 0.55, respectively. The value of b_1 is 0.4.These values are based on the analyses of severe fuel damage experiments.

Re-slumped material is assumed to stop at the first axial node that has a temperature less than the temperature of the axial node from which the material re-slumps. Generally, re-slumped material is calculated to slump down only one axial node per occurrence of re-slumping.

The re-slumped material is assumed to instantly come into thermal equilibrium with the axial node where it stops. A jump in temperature thus occurs at the axial node where the re-slumped material stopped.

The calculation of this jump in temperature is described in Section 2.7. Subsequently, the temperature of the re-slumped material is calculated by the heat conduction model for intact fuel and cladding taking into account the presence of the re-slumped material.

The characteristics of the collection of drops that may refreeze in an axial node are averaged so that one “averaged” drop represents all of the drops that have solidified in the node. The characteristics of the “average” drop are updated each time a new drop freezes in the node. The updated characteristics are computed by the equations;

$$n_k = n_{ko} + 1 \tag{4-59}$$

$$W_{uk} = (n_{ko}\, W_{uko} + W_{udk})/n_k$$

$$W_{zk} = (n_{ko}\, W_{zko} + W_{zdk})/n_k$$

$$W_{gk} = (n_{ko}\, W_{gko} + W_{gdk})/n_k$$

where

n_k = number of frozen drops in axial node k at end of time step

n_{ko} = same as n_k but for start of time step,

W_{uk} = mass of UO_2 in “average” frozen drop at axial node k at end of time step (kg),

W_{uko} = same as W_{uk} but for start of time step (kg),

W_{udk} = mass of UO_2 in drop that solidified in axial node k during time step (kg),

W_{zk} = same as for W_{uk} but for zircaloy (kg),

W_{zko} = same as W_{zk} but for start of time step (kg),

W_{zdk} = same as W_{udk} but for zircaloy (kg),

W_{gk} = weight gain of oxygen in “average” frozen drop at axial node k at end of time step (kg O_2 per m^2),

W_{gko} = same as W_{gk} but for start of time step (kg O_2 per m2),

W_{gdk} = weight gain of oxygen in drop that solidified in axial node k during time step (kg O_2 per m^2).

4.8 Liquefaction of Fuel Rod Cladding at Location of Inconel Grid Spacer

Grid spacers can have a significant impact on damage progression in a reactor core during a severe accident. The configuration of grid spacers varies from reactor to reactor. One design of a grid spacer is shown in Figure 4-14. The grid spacers are made of either zircaloy or Inconel. The impact of grid spacers on damage progression has been revealed by out-of pile experiments in Germany[4-51,4-52,4-53] and Japan,[4-54] in-pile experiments at the PBF facility in Idaho,[4-48] and by examinations of the damaged TMI-2 core.[4-55] The experiments in Germany and Japan have revealed the existence of chemical interactions between Inconel and zircaloy that occur at temperatures as low as 1,273 K, more than 200 K lower than the melting temperature of Inconel. Thus in a reactor core with Inconel grid spacers, the meltdown of the core may begin at a grid spacer location. Also, the PBF experiments and the examination of the TMI-2 core have revealed that grid spacers trap slumping liquefied material. If the grid spacer location at which the material is trapped is sufficiently cool, the material will solidify resulting in a blockage to coolant flow. These various ways in which Inconel grid spacers influence damage progression have made it necessary to incorporate models to predict the interaction of grid spacers with fuel rods.

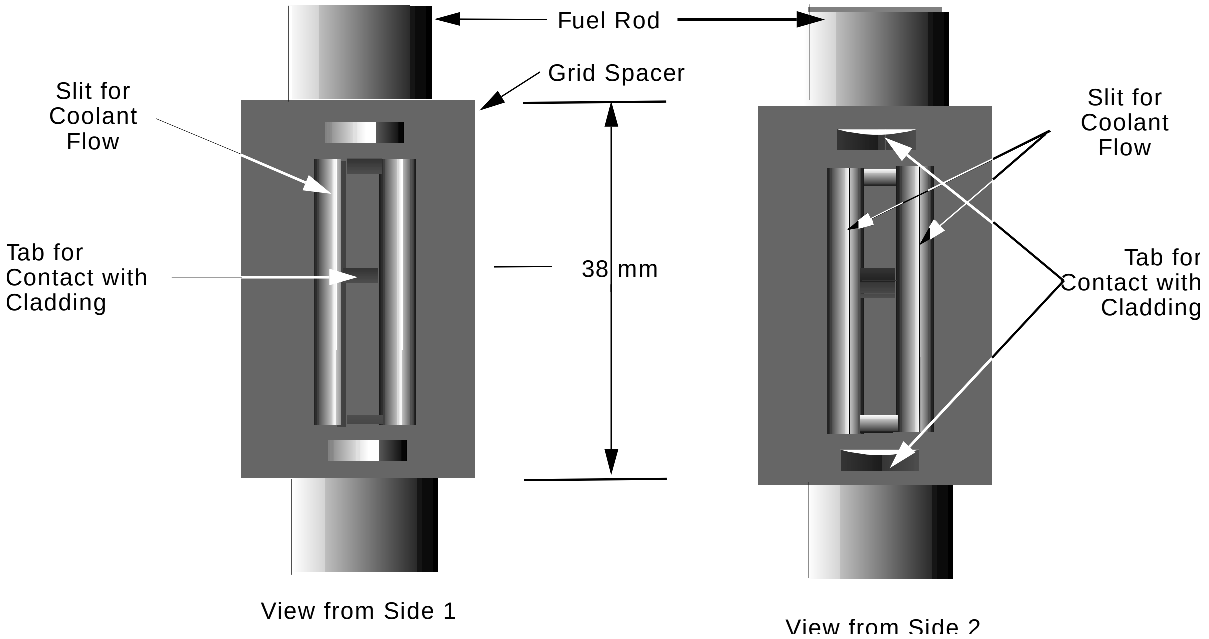

Figure 4-14. Configuration of grid spacer.

4.8.1 Impact of Grid Spacers on Damage Progression

Inconel grid spacers can influence the course of damage in a reactor core by: (a) reacting with fuel rod cladding so that it is weakened and can no longer contain the gases inside the cladding, (b) reacting with fuel rod cladding so that a significant amount of cladding is liquefied and slumps. The two ways Inconel grid spacers influence damage progression are discussed next.

The extent of fuel rod ballooning in a reactor core can be a function of the timing and extent of the chemical reaction between Inconel grid spacers and the fuel rod cladding. For certain severe accident scenarios, the coolant pressure remains high until some time after the chemical reaction between the grid spacers and fuel rod cladding begins. Fuel rod ballooning does not occur due to the large back pressure the coolant applies to the fuel rods. If the pump seals fail and leakage occurs, the coolant pressure will decrease to the point that cladding ballooning may occur. The chemical reaction between Inconel and zircaloy may result in the weakening and failure of the cladding and thus the release of fuel rod gases prior to significant depressurization of the coolant. In this case, cladding ballooning does not occur.

Subsequent damage progression can be a strong function of whether the fuel rods have ballooned. If the fuel rods have not ballooned, the reactor core may continue to heat up at a moderate pace and the cladding may completely oxidize without experiencing any meltdown. But if the fuel rods have ballooned, the heatup may proceed at a rapid pace and the cladding may experience a significant amount of meltdown of metallic cladding and dissolved fuel.[4-56] Differences in the rate of heatup are due to differences in surface areas of the cladding for the two cases described above. In the case of the ballooned cladding, this surface area can be almost 2.6 times larger than when ballooning does not occur. As a result, the heat generated by oxidation of ballooned cladding is a factor of 2.6 times greater. The factor of 2.6 is the result of the cladding diameter increasing by up to a factor of 1.3 due to ballooning and the inside surface area of the cladding being exposed to steam after rupture, which doubles the surface area of the cladding that is oxidizing.[4-48] If the cladding does not begin to balloon until the outside surface of the cladding begins to rapidly oxidize and form an oxide skin that resists ballooning, then the diameter increase of the cladding may be less than 5 to 10%.[4-56]

The results of the CORA experiments, discussed in a reference paper,[4-47] show that even zircaloy grids with small Inconel tabs may cause a chemical reaction that liquefies a small part of the fuel rod cladding causing a pin hole failure in the cladding.[4-58] In this case, the amount of material that liquefies is small, but the formation of the pin hole would result in the release fission products.

Cladding liquefied by chemical reaction with grid spacers will slump in response to gravity and relocate to a lower region of the reactor core. This slumping of liquefied material influences damage progression in several ways. First, the slumping of the cladding and the grid spacer material with which it has reacted results in the transfer of internal energy from a hotter part of the core to a cooler part. This transfer of energy accelerates the heatup of the lower part of the core and brings this part of the core closer to the conditions for rapid oxidation. Second, the slumping material may be trapped at the location of the next grid spacer below it, solidify, and form a blockage to flow. Third, the extent of oxidation in the upper part of the core is reduced due to cladding slumping away from this region.

4.8.2 Liquefaction of Cladding at Location of Grid Spacers

This section presents models for calculating as a function of time the extent of liquefaction of fuel rod cladding and grid spacers due to chemical reaction between zircaloy and Inconel. The time at which this reaction begins is a function of the thickness of the oxide layer on the cladding. The rate of the reaction is a function of temperature.

The models are based on separate-effect experiments performed by Hofmann and his colleagues.[4-51] In these experiments, short rods composed of Inconel 718 (54 wt% Ni, 18 wt% Cr, 18 wt% Fe, 2.9 wt% Mo) were pressed into Zircaloy-4 capsules with an inner hole equal to the diameter of the Inconel rods. The oxide thickness on the inside surface of the Zr capsule was an experiment parameter. Experiments were performed on capsules with oxide layer thicknesses varying from 10 to 100 microns. The capsules were placed in a tube furnace with flowing argon and heated to varying levels of temperature (1,273 to 1,673 K) for varying periods of time. The capsules were then removed from the furnace and a measurement was made of the thickness of the reaction zone between the Inconel rod and the Zr capsule it interfaced. To measure the size of the reaction zones, the capsules were mechanically cut and metallographically prepared for examination using an optical microscope.

Correlations of the rate of reaction as a function of temperature and oxide thickness were obtained by linear regression using the least squares method. Correlations as a function of oxide thickness and temperature were obtained for the delay in the initiation of the reaction caused by the oxide layer. The isothermal growth rates of the reaction zones were found to obey parabolic rate laws, indicating a diffusion-controlled process. The Zr in the zircaloy diffuses into the Inconel and the Ni in the Inconel diffuses into the zircaloy. For temperatures above 1,525 K, small amounts of Inconel were able to dissolve and liquefy large quantities of cladding.

Coefficients for the parabolic kinetics equation were derived from the experimental results to analytically describe the transient growth of the reaction zone on both sides of the interface between the Inconel and zircaloy. The configuration for which the parabolic kinetics equation applies is the one-dimensional slab shown in Figure 4-15. The equation used to determine the rate of growth of the reaction zone on each side of the interface is:

$$d_2 = \left[d_1^2 + Ae^{\left[\frac{-B}{RT}\right]}\Delta t\right]^{0.5} \tag{4-60}$$

where

d_2 = position of boundary of reaction zone at end of time step (m)

d_1 = position at start of time step (m)

A,B = coefficients that vary with oxide thickness, temperature and whether the growth is being calculated in the Zr or Inconel field. These coefficients are defined in Table 4-7

R = universal gas constant [8.314 Pa.m^3/(g-mole • K)]

T = temperature of the reacting material (K)

Δt = time step (s).

An oxide (ZrO_2) layer between the metallic zircaloy and the Inconel was found to delay the start of the chemical reaction between the zircaloy and Inconel. The time to dissolve this layer and initiate the growth of the reaction zone into the metallic zircaloy is calculated by the equation

$$t_d = c_1 e^{\left[\frac{-c_2}{RT}\right]} \tag{4-61}$$

where

t_d = period of time for dissolution of the oxide layer (s)

T = temperature of cladding and grid spacer (K)

c_1, c_2 = coefficients defined in Table 4-8 and that are a function of oxide thickness.

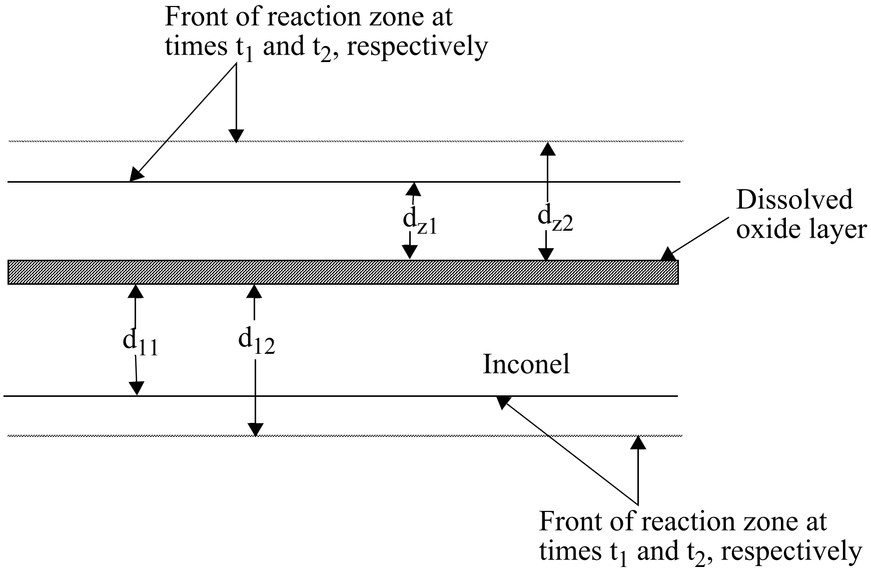
Front of reaction zone at times t_1 and t_2, respectively
d_{z1}
d_{z2}
Dissolved oxide layer
d_{11}
d_{12}
Inconel
Front of reaction zone at times t_1 and t_2, respectively

Figure 4-15. Configuration for which parabolic kinetics equation applies.

A method is next presented for applying Equation (4-60) to fuel rod cladding that interfaces with an Inconel grid spacer. Because the geometry of the two reacting materials in a fuel rod bundle is significantly different from the idealized geometry for which Equation (4-60) applies, two assumptions are required that simplify the calculation of the propagation of the reaction zone.

The first assumption is that the growth of the reaction zones in the grid spacer and cladding follows the paths shown in Figure 4-16 and Figure 4-17. The reaction zone is assumed to first grow in a direction perpendicular to the surface of contact between the cladding and grid spacer. The cross-sectional area of the reaction zone is assumed to stay equal to the area of contact until the reaction zone has propagated to the midplane of the grid spacer panel (line of symmetry between two adjacent fuel rods). After propagating through the thickness of the grid spacer panel, the reaction zone spreads as a circle with an increasing radius through the grid spacer panel. The propagation through the cladding is assumed to follow a similar path as shown in Figure 4-17. The reaction zone first propagates outward from the surface of contact in a perpendicular direction until the entire thickness of the cladding has reacted at the location of contact. Then the reaction zone grows at an equal rate in the circumferential and axial directions. After the reaction zone has spread around the entire circumference, the reaction zone then grows only in the axial direction. Due to the cladding contacting the grid spacer at four symmetrically located points, the propagation of the reaction zone in the circumferential direction is complete when the angle in Figure 4-17 equals $\pi/4$.

Table 4-7: Value of coefficients in equation for growth of reaction zone.

	Inconel	**Inconel**	**Zircaloy**	**Zircaloy**
Oxide thickness (microns)	A (m^2/s)	B (N • m/g-mole)	A (m^2/s)	B (N • m/g-mole)
0	16.6127	-288100	4.6364	-252312
20	1.377×10^{9}	-504679	4.4792	-255162
45	3.489×10^{15}	-69392	4.321×10^{5}	-407522
100	0.8941	-253057	9.512×10^{-4}	-172165

Table 4-8: Value for coefficient in equation to calculate delay time due to oxide layer.

Oxide thickness (microns)	**Coefficient C_1 (s)**	**Coefficient C_2 (N • m/g-mole)**
10	2.661×10^{-8}	2.68438×10^{5}
20	7.700×10^{-17}	5.24339×10^{5}
45	6.762×10^{-15}	4.75227×10^{5}
100	1.875×10^{-9}	3.29218×10^{5}

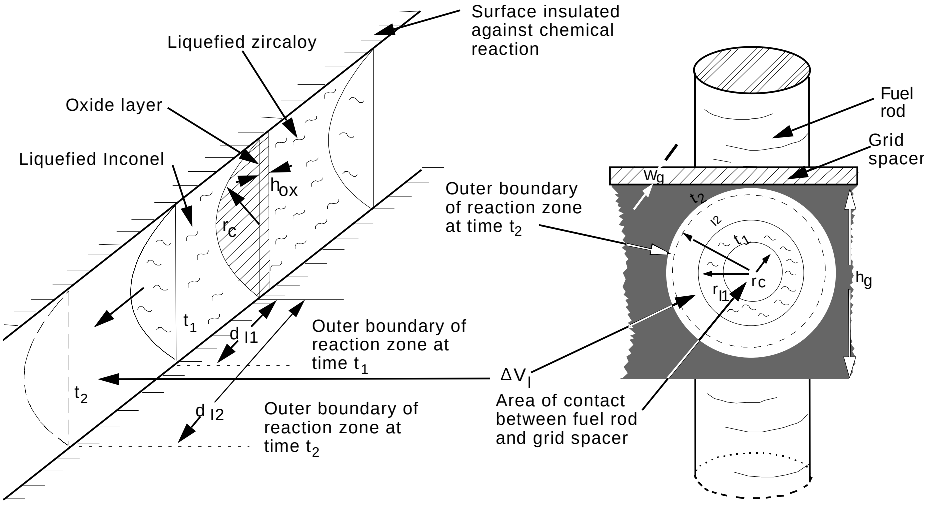
Surface insulated against chemical reaction
Liquefied zircaloy
Oxide layer
Liquefied Inconel
h_{ox}
r_c
t_1
d_{l1}
Outer boundary of reaction zone at time t_1
t_2
d_{l2}
Outer boundary of reaction zone at time t_2
Fuel rod
Grid spacer
w_g
Outer boundary of reaction zone at time t_2
t_2
l_2
t_1
r_c
r_{l1}
h_g
ΔV_l
Area of contact between fuel rod and grid spacer

Growth of reaction zone in one-dimensional system

Growth of reaction in grid spacer in contact with fuel rod cladding

Figure 4-16. Growth of reaction zone in grid spacer.

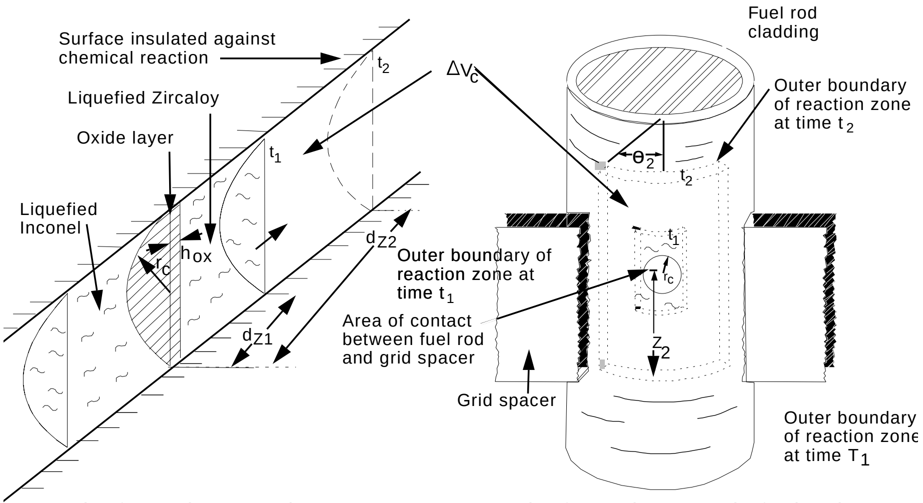
Surface insulated against chemical reaction
Liquefied Zircaloy
Oxide layer
Liquefied Inconel
t_2
t_1
r_c
h_{ox}
d_{Z2}
d_{Z1}
ΔV_c
Fuel rod cladding
Outer boundary of reaction zone at time t_2
θ_2
t_2
t_1
r_c
Z_2
Outer boundary of reaction zone at time t_1
Area of contact between fuel rod and grid spacer
Grid spacer
Outer boundary of reaction zone at time T_1

Growth of reaction zone in one-dimensional system

Growth of reaction zone in fuel rod cladding in contact with grid spacer

Figure 4-17. Growth of reaction zone in fuel rod cladding.

The second assumption applied to the model for growth of the reaction zone is that the rate of growth of the reaction zone is a function of the volume of the reaction zone but not the configuration of the reaction zone, provided the area of contact between the Inconel and zircaloy is the same for each configuration. Figure 4-16 and Figure 4-17 illustrate that determination of the growth of the reaction zones in the grid spacer panels and fuel rod cladding is based on the growth of the reaction zones in an equivalent one-dimensional system. The two geometrical systems are considered to be equivalent since they both have the same area of contact between the zircaloy and Inconel parts of the system. The application of this assumption allows propagation of the reaction zone through the fuel rod cladding and a grid spacer to be determined in a straight forward manner. The growth of the reaction zone in the one-dimensional system, for which Equation (4-60) applies, can be used to determine the growth of the reaction zone in the grid spacer and fuel rod cladding. The growth during one time step in the one-dimensional system is mapped into the actual in-core geometry to determine the growth of the reaction zone in the fuel rod cladding and grid spacer.

The equations for determining the growth of the reaction zone in the cladding and grid spacer can now be derived. The variables to be calculated are shown in Figure 4-16 and Figure 4-17. First the growth of the reaction zone during a time step is calculated for the Inconel and zircaloy parts of a one-dimensional system. These growths are calculated by the equations

$$d_{i2} = \left[d_{i1}^2 + A_i e^{\left[\frac{-B_i}{RT}\right]}\Delta t\right]^{0.5} \tag{4-62}$$

$$d_{z2} = \left[d_{z1}^2 + A_z e^{\left[\frac{-B_z}{RT}\right]}\Delta t\right]^{0.5} \tag{4-63}$$

where

d_{i2} = position of leading edge of reaction zone in Inconel at end of time step (m),

d_{i1} = same as di_2 but for start of time step,

A_i, B_i = coefficients for Inconel that are defined in Table 4-7,

d_{z2} = position of leading edge of reaction zone in zircaloy at end of time step (m),

d_{z1} = same as d_{z2} but for start of time step (m),

T = current temperature of reacting cladding and grid spacer (K),

A_z, B_z = coefficients for zircaloy that are defined in Table 4-7.

The volume increases of the reaction zones in the Inconel and zircaloy during a time step are calculated by the equations

$$\Delta v_i = 0.5\pi(d_{i2} - d_{i1})r_c^2 \tag{4-64}$$

$$\Delta v_z = 0.5\pi(d_{z2} - d_{z1})r_c^2 \tag{4-65}$$

where

Δv_i = increase in volume of reaction zone in Inconel during time step (m^3),

Δv_z = increase in volume of reaction zone in zircaloy during time step (m^3),

r_c = radius of circle with same area as area of contact between grid spacer and fuel rod cladding (m).

The radius of the area of contact is a parameter that can be determined from experimental results. The initial value of this parameter is a function of the area of the grid spacer tab in contact with the fuel rod cladding. This area of contact may increase with time as liquefaction progresses. For the first part of this analysis the area is assumed to remain constant. A method for calculating the rate of melt progression considering a transient area of contact is presented later.

The coefficient of 0.5 in Equations (4-64) and (4-65) stems from the fact that due to symmetry only the growth of the reaction zone on one side of the line of symmetry needs to be considered.

The assumption used for grid spacer reaction zone propagation, shown in Figure 4-16, is next applied. This assumption is represented by the equation

$$\Delta v_g = \Delta v_i \tag{4-66}$$

where

Δv_g = increase in volume of the reaction zone in the grid spacer panel (m^3).

By applying Equation (4-66), the outer boundaries of the reaction zone in the grid spacer panel are then determined from the following equations:

$$w_{i2} = d_{f2} \text{ for } (w_{i2} < 0.5 w_g), \tag{4-67}$$

$$r_{i2} = \left[r_{i1}^2 + \left(\frac{\pi}{4}\right)\frac{\Delta v_i}{w_g}\right]^{0.5} \tag{4-68}$$

where

w_{i2} = distance of propagation of reaction zone at time t_2 into grid spacer panel in direction normal to area of contact (m),

r_{i2} = outer radius of reaction zone in grid spacer panel at time t_2 (m),

r_{i1} = same as r_{i2} but for time t_1 (m),

w_g = thickness of grid spacer panel (m).

Equation (4-67) applies until the reaction zone has propagated into the grid spacer panel a distance equal to half the thickness of the panel ($0.5w_g$). After this time Equation (4-68) applies. Due to symmetry, the equations consider the reaction zone to be confined to half of the grid spacer panel.

The growth of the reaction zone in the fuel rod cladding is calculated in a manner similar to that used to calculate the growth in the grid spacer panel. The increase in volume of the reaction zone in the fuel rod cladding is calculated by the equation

$$\Delta v_c = \Delta v_z \tag{4-69}$$

where

Δv_c = increase in volume during a time step of reaction zone in fuel rod cladding (m^3).

Until the reaction zone has penetrated the thickness of the fuel rod cladding, the outer boundary of the reaction zone is calculated by the equation

$$w_{z2} = d_{z2} \text{ for } w_{z2} < h_c \tag{4-70}$$

where

w_{z2} = distance that reaction zone has penetrated into the cladding at time t_2 (m),

h_c = thickness of metallic part of cladding (m).

After the reaction zone has penetrated the thickness of the cladding, the reaction zone then spreads in the circumferential and axial directions. As stated earlier, the assumption is made that the reaction zone spreads at an equal rate in the axial and circumferential directions. Referring to Figure 4-17, the outer boundaries of the reaction zone are defined by the variables Θ and z, where Θ is the measure of spread of the reaction zone in the circumferential direction (radians), and the variable z is the measure of the spread of the reaction zone in the axial direction (m). The change in volume of the reaction zone during a time step is then calculated by the equation

$$\Delta v_c = A_c(\Theta_1 + \Delta\Theta)\,(z_1 + \Delta z) - 0.5 A_c \Theta_1 z_1 \tag{4-71}$$

where

A_c = cross-sectional area of one radian of metallic part of cladding (m^2),

Θ_1 = angle defining outer boundary of propagation of reaction zone in circumferential direction at start of time step (radians),

$\Delta\Theta$ = change during time step of angle defining propagation of reaction zone in circumferential direction (radians),

z_1 = height of reaction zone at start of time step (m) where reaction zone changes height during time step (m),

Δz = change in height of reaction zone during time step (m).

The variable A_c is calculated by the equation

$$A_c = r_o^2 - (r_o - h_c)^2 \tag{4-72}$$

where

r_o = outer radius of metallic part of cladding (m).

Because the assumption has been made that the reaction zone is growing at equal rates in the circumferential and axial directions, the variable $\Delta\Theta$ is related to the variable Δz by the equation

$$\Delta\Theta = \frac{\Delta z}{r_o} \quad . \tag{4-73}$$

The value of Δz is then determined by substituting Equation (4-73) into Equation (4-71) and solving for Δz. The result is

$$\Delta z = 0.5[(-b + \sqrt{b^2 - 4ac})] \quad . \tag{4-74}$$

The variables b and c in Equation (4-72) are calculated by the equations

$$b = r_o\left[0.5\Theta_1 + \frac{z_1}{r_o}\right] \tag{4-75}$$

$$c = -r_o\frac{\Delta v_z}{A_c} \quad . \tag{4-76}$$

The outer boundaries of the reaction zone at the end of the time step are then determined by the equations

$$\Theta_2 = \Theta_1 + \Delta\Theta \tag{4-77}$$

$$z_2 = z_1 + \Delta z \quad . \tag{4-78}$$

The spread of the reaction zone in the circumferential direction is complete when

$$\Theta_2 = \frac{\pi}{4} \quad . \tag{4-79}$$

After the spread of the reaction zone in the circumferential direction is complete, the reaction zone grows only in the axial direction. The rate of growth is calculated by the equation

$$z_2 = z_1 + \frac{8}{\pi}\frac{\Delta v_z}{A_c} \quad . \tag{4-80}$$

The reaction between the grid spacer and cladding continues until the liquefied material slumps. The liquefied material is considered to slump when the reaction zone in the grid spacer has spread to the bottom of the grid spacer panel. This condition occurs when

$$r_{i2} = 0.5h_g \tag{4-81}$$

where

h_g = height of grid spacer panel (m).

The liquefied material will slump downward into a cooler part of the reactor core and solidify.

The time between the onset of the chemical reaction and the slumping of material liquefied by the chemical reaction can be determined from Equations (4-61), (4-62), (4-64) and (4-81) for isothermal conditions. Equation (4-61) is used to calculate the time to dissolve the oxide shell and Equations (4-62), (4-64), and (4-81) are used to calculate the time to liquefy the grid spacer to the point where it slumps.

Equation (4-81) defines the mass of grid spacer that must be liquefied before slumping occurs and Equations (4-61) and (4-64) define the time to liquefy this mass. This process is expressed by the equation

$$0.5\frac{w_g}{2}\pi(0.5h_g)^2 = 0.5\pi r_c^2\left[A_i e^{\left(\frac{-B_i}{RT}\right)}(t_s - t_d)\right]^2 \tag{4-82}$$

where

t_s = time after the beginning of the chemical reaction at which the liquefied grid spacer material slumps (s),

t_d = time for dissolution of the oxide shell (s) [calculated by Equation (4-61)].

In Equation (4-82), the left side of the equation defines the mass of grid spacer that must be liquefied before slumping occurs and the right side defines the mass of grid spacer liquefied as a function of time. The result of solving Equation (4-82) for the slumping time t_s is

$$t_s = 0.03125\frac{w_g^2 h_g^4}{r_c^4}\left(\frac{1}{A_i e^{\left(\frac{-B_i}{RT}\right)}}\right) \quad . \tag{4-83}$$

Equation (4-83) shows that the slumping time is a strong function of the height of the grid spacer and the area of contact between the grid spacer and cladding.

In view of the importance of area of contact on the rate of liquefaction it is useful to develop a transient model for the area of contact. A simple transient model is one where the area of contact is regarded as fixed until the reaction zone has completely penetrated the thickness of the grid spacer panel at the location of the grid spacer tabs. Thereafter, the area of contact increases are proportional to the increase in the size of the reaction zone in the grid spacer. The model is illustrated in Figure 4-18.

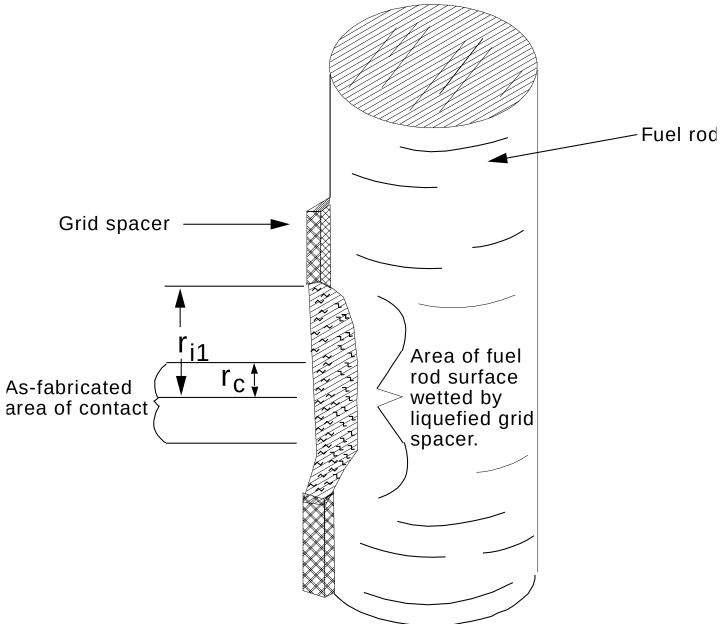

Figure 4-18. Variable area of contact between grid spacer and fuel rod cladding.

This modeling assumption is consistent with the concept of liquefied grid spacer material wetting the fuel rod surface it faces. The model is expressed by the equations

$$r_c = r_{tab} \qquad \text{for} \qquad d_{i2} < 0.5w_{g,} \tag{4-84}$$

$$r_c = r_{i1} \qquad \text{for} \qquad d_{i1} > 0.5w_{g;} \tag{4-85}$$

where

r_c = radius of circle with same area as the area of contact between grid spacer and fuel rod cladding (m),

r_{tab} = area of circle with same area as the area of tab on grid spacer (m),

d_{i2}, r_{i1} = variables defined for Equations (4-62) and (4-68), respectively.

The propagation of the reaction zone varies with location on the interface between the grid spacer and cladding. At the location of the grid spacer tab, propagation is relatively slow because the reaction zone is already thick. The reaction zone propagates rapidly at its leading edge because at that location the reaction zone is thin. Figure 4-19 shows the variation in the thickness of the reaction zone in a grid spacer with respect to the location of the liquefaction of the leading edge. For simplicity, it is useful to have a single variable for Inconel and a single variable for zircaloy to measure the extent of propagation of the reaction in the grid spacer and cladding zones. In the case of a fixed area of contact, these variables were d_{i2} and d_{z2} of Equations (4-62) and (4-63), respectively. In the case of a variable area of contact, a measure of the extent of growth of the reaction zone in the Inconel is provided by the variable d_{ia}, which is defined in Figure 4-19. The variable d_{ia} is the thickness of a uniform reaction zone that results in the same growth as a reaction zone of variable thickness but with the same volume as the uniform reaction zone. This variable is calculated by the equation

$$A_{w2}(d_{ia2} - d_{ia1}) = A_{w1}(d_{i2} - d_{i1}) + (A_{w2} - A_{w1})d_n \tag{4-86}$$

where

A_{w2} = area of contact between Inconel and zircaloy at end of time step (m^2),

A_{w1} = area of contact at start of time step (m^2),

d_{ia2} = value of equivalent depth of reaction zone in Inconel at end of time step (m),

d_{ia1} = same as d_{ia2}, but for start of time step (m),

d_n = depth of propagation of reaction zone at leading edge of reaction zone (m).

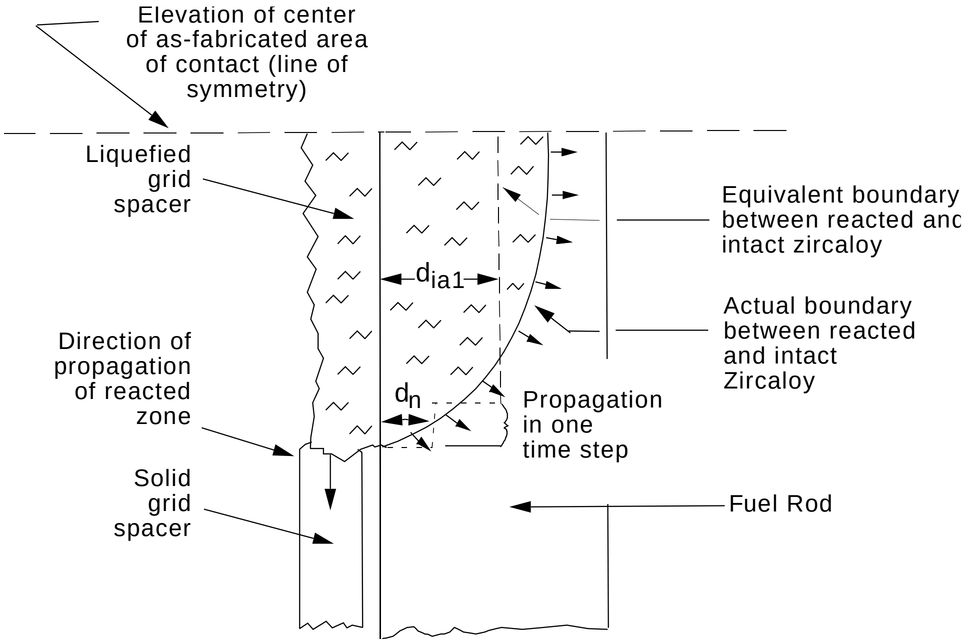
Elevation of center of as-fabricated area of contact (line of symmetry)
Liquefied grid spacer
Equivalent boundary between reacted and intact zircaloy
d_{ia1}
Actual boundary between reacted and intact Zircaloy
Direction of propagation of reacted zone
d_n
Propagation in one time step
Solid grid spacer
Fuel Rod

Figure 4-19. Definitions of equivalent thickness of reaction zone.

The change in location of each of the three fronts as shown in Figure 4-20 are given by the three equations

$$d_{i2} = \sqrt{d^2_{i1} + R_i}, \tag{4-87}$$

$$d_{ia2} = \sqrt{d^2_{ia1} + R_i}, \tag{4-88}$$

$$d_n = \sqrt{R_i}\,; \tag{4-89}$$

where

$$R_i = A_i e^{\left[\frac{-B_i}{RT}\right]} \Delta t\,. \tag{4-90}$$

After substituting Equations (4-87), (4-88), and (4-89) into Equation (4-86) and solving for d_{ia1}, the result is

$$d_{ia1} = 0.5\left[\frac{R_i}{D_i} - D_i\right]; \tag{4-91}$$

where

$$D_i = \frac{A_{w1}}{A_{w2}}\left[\sqrt{d^2_{i1} + R_i} - d_{i1}\right] + \frac{\sqrt{R_i}(A_{w2} - A_{w1})}{A_{w2}}\quad . \tag{4-92}$$

The calculation of the equivalent depth of the reaction zone in the zircaloy is parallel to that for the equivalent depth in Inconel. The result is

$$d_{za1} = 0.5\left[\frac{R_z}{D_z} - D_z\right] \tag{4-93}$$

where

$$D_z = \frac{A_{w1}}{A_{w2}}\left[\sqrt{d^2_{z1} + R_z} - d_{z1}\right] + \frac{\sqrt{R_z}(A_{w2} - A_{w1})}{A_{w2}} \tag{4-94}$$

$$R_z = A_z e^{\left[\frac{-B_z}{RT}\right]} \Delta t\quad . \tag{4-95}$$

The calculation of the melt progression in the grid spacer and fuel rod cladding proceeds basically as described for the case of a constant area between the grid spacer and cladding. The following differences are noted. In Equations (4-62) through (4-65) d_{ia1} and d_{za1} are substituted for d_{i1} and d_{z1}, respectively. In equations (4-64), (4-65), (4-75), and (4-76) the variable r_c as calculated in Equation (4-85) is applied. The new positions of the melt fronts in the Inconel and zircaloy for the one-dimensional system are

$$d_{i2} = d_{i1} + d'_{i2} - d_{ia1}\,, \tag{4-96}$$

$$d_{z2} = d_{z1} + d'_{z2} - d_{za1}\,; \tag{4-97}$$

where

d'_{i2} = location of melt front in Inconel (m),

d'_{z2} = location of melt front in zircaloy (m).

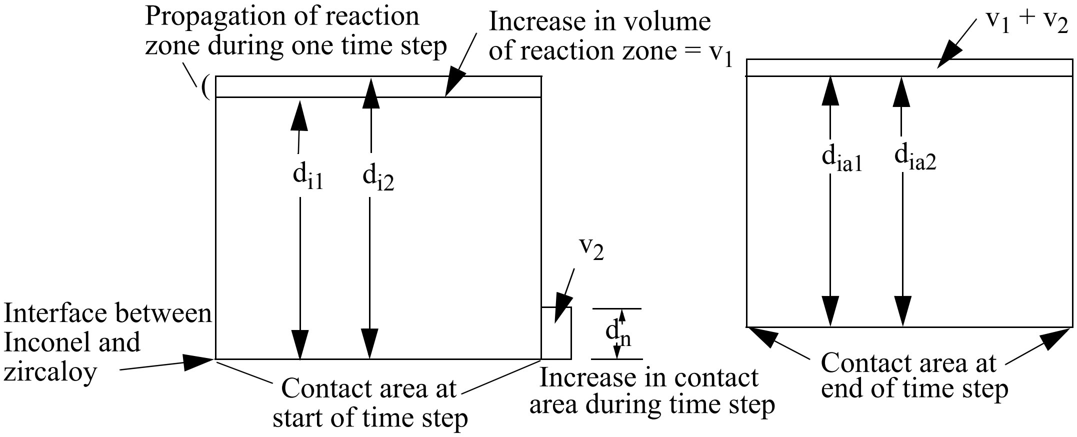
Propagation of reaction zone during one time step
Increase in volume of reaction zone = v_1
$v_1 + v_2$
d_{i1}
d_{i2}
d_{ia1}
d_{ia2}
v_2
d_n
Interface between Inconel and zircaloy
Contact area at start of time step
Increase in contact area during time step
Contact area at end of time step

Figure 4-20. Adjustment in thickness of equivalent reaction zone to account for new contact during time step.

The temperature distribution in a reactor core can be affected in several ways by the relocation of fuel rod cladding that reacted with an Inconel grid spacer. First, the transfer of thermal energy from a location higher in the core to a location lower in the core can accelerate oxidation in the lower part of the core and thus accelerate heatup. Second, relocated cladding can block the flow of coolant, thus causing an increase in heatup of the portion of the reactor core above the blockage location. Third, slumping of the reacted cladding removes metallic material that is oxidizing at a relatively rapid rate and transfers the material to a core location where it may oxidize at a slower rate due to a cooler temperature and more compact geometry.

4.9 References

4-1. S. Hagen et al., “Out-of-Pile Experiments on Severe Fuel Damage Behavior of LWR Fuel Elements (CORA Program),” IAEA-SM-296/26**,** *International Symposium on Severe Accidents in Nuclear Power Plants, Sorrento, Italy, March 21-25, 1988.*

4-2. J. Rest, *Proceedings of the International Meeting on Thermal Nuclear Reactor Safety, Chicago, IL, August 29-September 2, 1982,* NUREG/CP-0027, February 1983, pp. 111-121.

4-3. J. Rest, “Evaluation of Volatile and Gaseous Fission Product Behavior in Water Reactor Fuel Under Normal and Severe Core Accident Conditions,” *Nuclear Technology, 61,* 1983, pp. 33-48.

4-4. J. Rest, “An Improved Model for Fission Product Behavior in Nuclear Fuel Under Normal and Accident Conditions,” *Journal of Nuclear Materials, 120,* 1984, pp. 195-212.

4-5. J. Rest, “The Prediction of Transient Fission-Gas Release and Fuel Microcracking under Severe Core-Accident Conditions,” *Nuclear Technology, 56,* 1981, pp. 553.

4-6. M. H. Wood and J. R. Mathews, “On the Use of Grain Boundary Loss Terms in Fission Gas Release and Swelling Models,” *Journal of Nuclear Materials, 89,* 1980, pp. 53-61.

4-7. B. G. Schnitzler, *Fission Product Decay Heat Modeling for Disrupted Fuel Regions (GDECAY),* EGG-PHYS-5698, December 1981.

4-8. M. R. Kuhlman et al., *CORSOR User's Manual,* NUREG/CR-4173, BMI-2122, March 1985.

4-9. U. S. Nuclear Regulatory Commission, *Technical Bases for Estimating Fission Product Behavior During LWR Accidents,* NUREG-0772, June 1981.

4-10. M. J. Zucrow and J. D. Hoffman, *Gas Dynamics, Volume I,* New York: John Wiley and Sons, 1976.

4-11. J. H. Keenan et al., *Gas Tables,* 2nd Edition, New York: John Wiley and Sons, 1980.

4-12. W. C. Reynolds, *Thermodynamic Properties in S1,* Department of Mechanical Engineering, Stanford University, 1979.

4-13. McGraw-Hill*, Lange's Handbook of Chemistry,* New York: McGraw-Hill Book Co., 1973.

4-14. Y. S. Tailoukian and C. Y. Ho, *Properties of Nonmetallic Fluid Elements, Volume 2,* New York: McGraw-Hill Book Co., 1981.

4-15. A. G. Croff, *ORIGEN-2-A Revised and Updated Version of the Oak Ridge Isotope and Depletion Code,* ORNL-5621, July 1980.

4-16. R. Hill, *The Mathematical Theory of Plasticity,* Oxford: Clarendon Press, 1950, pp. 317-325.

4-17. A. Mendelson, *Plasticity: Theory and Application,* New York: MacMillan, 1968, pp. 100-104.

4-18. M. P. Bohn, *FRACAS: A Subcode for the Analysis of Fuel Pellet Cladding Mechanical Interaction,* TREE-NUREG-1028, April 1977, pp. 29-33.

4-19. D. L. Hagrman, *Zircaloy Cladding Shape at Failure (BALON2),* EGG-CDAP-5397, July 1981.

4-20. Z. R. Martinson, D.A. Petti, and B. A. Cook, "Vol. 1: PBF Severe Fuel Damage Test 1-1 Test Results Report," NUREG/CR-4684, EGG-2463, Volume 1, October 1986.

4-21. D. A. Petti et al, "Power Burst Facility (PBF) Severe Fuel Damage Test 1-4 Test Results Report," NUREG/CR-5163, EGG-2542 R3, April, 1989.

4-22. S. Hagen et al, "Results of SFD Experiment CORA-13 (OECD International Standard Problem 31)," KfK 5054, Kernforschungszentrum Karlsruhe, February 1993.

4-23. B. Adroguer, S. Bourdon, and R. Gonzalez, "Analysis of Fuel-Cladding Interaction in PHEBUS SFD Tests Using ICARE2 Code," IAEA Technical Committee Meeting "Behaviour of Core Materials and Fission Product Release in Accident Conditions in Light Water Reactors," CEN Cadarache, March 16-19, 1992.

4-24. S. M. Jensen, D. W. Akers, and B. A. Pregger, "Postirradiation Examination Data and Analyses for OECD LOFT Fission Product Experiment LP-FP-2," Volume 1, OECD LOFT-T-3810, December 1989.

4-25. D. R. Olander, "Materials chemistry and transport modeling for severe accident analyses in light-water reactors; II: Gap processes and heat release," Nuclear Engineering and Design 148 (1994), pages 273-292.

4-26. A. M. Voltchek and A. V. Nikolaeva, "Hydrogen Interaction with Zircaloy Cladding at High Temperatures," NSI-SARR-32-96, Russian Academy of Sciences, Nuclear Safety Institute, July 1996.

4-27. I. Catton, J. O. Cermak, Y. S. Kuo, and A. R. Wazzan, "An evaluation of several aspects of the hypothetical loss-of-coolant accident for light water reactors," University of California at Los Angeles, Rep. UCLA-ENG-7450, 1974.

4-28. B. Adroguer, S. Bourdon, and R. Gonzalez, “Analysis of Fuel-Cladding Interaction in PHEBUS SFD Tests Using ICARE2 Code,” IPSN, CEA, IAEA Technical Committee Meeting, CEN Cadarache, March 16-19, 1992.

4-29. Akihide Hidaka et al., “Influence of thermal properties of zirconia shroud on analysis of PHEBUS FPT0 bundle degradation test with ICARE2 code,” Nuclear Engineering and Design 168 (1997), 361-371.

4-30. Fumiya Tanabe and Ken Muramatsu, “Thermal-hydraulics in Uncovered Core of Light Water Reactor in Severe Core Damage Accident,” Journal of Nuclear Science and Technology, 23[9], 779-793.

4-31. M. S. Veshchunov and A. V. Palagin, “Investigation of downward relocation of molten materials” Journal of Nuclear Materials 252 (1998) 110-120.

4-32. Aida N. Wilhelm and Eduardo A. Garcia, “Simulation of the Dissolution Kinetics of ZrO_2 by Molten Zircaloy-4 between 2000 and 2400 C,” Journal of Nuclear Materials 171 (1990) JNM01007.

4-33. M. S. Veshchunov and A. V. Berdyshev, “Simultaneous dissolution of UO_2 and ZrO_2 by molten Zr in an oxidizing atmosphere,” Journal of Nuclear Materials 252 (1998) 98-109.

4-34. P. Hofmann et. al., “Mechanishes and chemishes Verhalten von Zircaloy-4 Hullrohren and UO_2-Brennstoff bei hohen Temperaturen,” KfK 4100, Kernforschungszentrum Karlsruhe (1987).

4-35. D. R. Olander, “Materials chemistry and transport modeling for severe accident analyses in light-water reactors - I: External cladding oxidation,” Nuclear Engineering and Design, 148 (1994) 253-271

4-36. The SCDAP/RELAP5 Development Team, “SCDAP/RELAP5/MOD3.2 Code Manual, Volume 4 (Rev. 1); MATPRO - A Library of Materials Properties for Light-Water-Reactor Accident Analysis,” NUREG/CR-6150, INEL-96/0422, Revision 1, October 1997.

4-37. L. J. Siefken, “Preliminary Design Report for Modeling of Hydrogen Uptake in Fuel Rod Cladding during Severe Accidents,” INEEL/EXT-98-00664 (August 1998).

4-38. R. Viskanta, R.R. Hobbins, and H. Esmaili, “Peer Review of the Modeling of Hydrogen Uptake in Fuel Rod Cladding during Severe Accidents,” ER/NRC 98-204 (October 1998).

4-39. A. Boldyrev at al., “Fuel Cladding Deformation Behavior Module (CROX),” NSI-SARR-05-94, Russian Academy of Sciences, Nuclear Safety Institute, 1994.

4-40. T. Furuta, H. Uetsuka, and S. Kawasaki, “Estimation of conservatism of present embrittlement criteria for Zircaloy fuel cladding under LOCA,” Zirconium for the Nuclear Industry, Sixth Int. Symp., ASTM Spec. Tech Publ. 824 (1984) 734.

4-41. E. D. Hindle and C. A. Mann, “An experimental study of the deformation of Zircaloy PWR fuel rod cladding under mainly convective cooling,” Zirconium in the Nuclear Industry, Fifth Int. Symp., ASTM Spec. Tech. Publ. 754 (1982) 284.

4-42. P. Hofmann et al., “Experiments on the Quench Behavior of LWR Fuel Rod Segments,” Third International QUENCH Workshop, Karlsruhe, Germany, December 2 - 4, 1997.

4-43. J. M. Broughton et. al., “PBF LOCA Test Series Report, Tests LOC-3 and LOC-5 Fuel Behavior Report,” NUREG/CR-2073, EGG-2094 (June 1981).

4-44. E. B. Dussan V. and Robert Tas-ping Chow, “On the Ability of Drops or Bubbles to Stick to Non-Horizontal Surfaces of Solids,” *Journal of Fluid Mechanics, 137,* pp 1-29, 1983.

4-45. S. Hagen, L. Sepold, P. Hofmann, and G. Schanz, *Out-of-Pile Experiments on LWR Severe Fuel Damage Behavior, Tests CORA-C and CORA-2,* KfK 4404, September 1988.

4-46. S. Hagen et al., *Results of SFD Experiment CORA-13 (OECD International Standard Problem 31),* KfK 5054, February 1993.

4-47. S. M. Jensen, D. W. Akers, and B. A. Pregger, *Postirradiation Examination Data and Analysis for OECD LOFT Fission Product Experiment LP-FP-2, Volumes 1 and 2,* OECD LOFT-T-3810, December 1989.

4-48. D. A. Petti et al, *PBF Severe Fuel Damage Test 1-4 Test Results Report,* NUREG/CR-5163, EGG-2542, EG&G Idaho, Inc., December 1986.

4-49. P. Hofmann and H. Ostereka, "Dissolution of Solid UO_2 by Molten Zircaloy and the Modeling," Paper IAEA-SM-296/1, *International Symposium on Severe Accidents in Nuclear Power Plants, Sorrento, Italy, March 21-25, 1988.*

4-50. T. R. Goodman, "Application of Integral Methods to Transient Nonlinear Heat Transfer," *Advances in Heat Transfer, 1,* 1964, pp 51-120.

4-51. E. A. Garcia, P. Hofmann, and A. Denis, *Analysis and Modeling of the Chemical Interaction Between Inconel Grid Spacers and Zircaloy Cladding of LWR Fuel Rods; Formation of Liquid Phases Due to Chemical Interaction and its Modeling,* KfK 4921, Kernforschungszentrum Karlsruhe, Germany, July 1992.

4-52. S. Hagen, P. Hofmann, G. Schranz, and L. Sepold, *Interactions in Zircaloy/UO_2 Fuel Rod Bundles with Inconel Spacers at Temperatures above 1,200 °C,* KfK 4378, Kernforschungszentrum Karlsruhe, Germany, September 1990.

4-53. P. Hofmann, E. A. Garcia, and A. Denis, "Low-Temperature Liquefaction of LWR Core Components," *Severe Accident Research Program Partners Review Meeting, Brookhaven National Laboratory, Upton, NY, April 30 - May 4, 1990.*

4-54. F. Nagase et al., *Interaction Between Zircaloy Tube and Inconel Spacer Grid at High Temperature,* JAERI-M 90-165, Japan Atomic Energy Research Institute, August, 1990.

4-55. E. L. Tolman et al., *TMI-2 Accident Scenario Update,* EGG-TMI-7489, December 1986.

4-56. C. L. Hunt, *Effect of Steam Oxidation on the Strain of Fuel Sheathing at High Temperatures,* AECL-5559, August 1976.

4-57. J. K. Hohorst, C. M. Allison, T. J. Haste, R. P. Hiles, and S. Hagen, "Assessment of SCDAP/RELAP5 Using Data from the CORA Melt Progression Experiments," *Severe Accident Modeling Topical Meeting on Nuclear Reactor Thermal Hydraulics (NURETH-5), September 21-24, 1992, Salt Lake City, UT.*

4-58. Wolfgang Hering, "CORA Experiments," *CORA International Workshop, Karlsruhe, Germany, September, 1990.*

4-59. L. J. Siefken, "Models for the Configuration and Integrity of Partially Oxidized Fuel Rod Cladding at High Temperatures," INEEL/EXT-98-00661, Rev. 1, January 1999.

5. MODELS FOR CONTROL RODS, CONTROL BLADES, SHROUDS AND REFLECTORS

5.1 Ag-In-Cd Control Rod Models

Control rod temperatures are computed using the heat conduction model described in Section 2.1. User-specified nuclear heating, chemical heating due to oxidation of the zircaloy guide tube, and convective and radiative heat transfer from the coolant and adjacent fuel rods are considered.

In order to model nonstandard control rod configurations, the ability to specify material by indices has been added. In order to maintain backward compatibility, the default material configuration remains as:

- Control rod absorber material (Ag/In/Cd in PWR's),
- Stainless steel,
- Zircaloy.

5.1.1 Control Rod Material Interaction

A parabolic kinetics model is applied to represent the chemical reaction that takes place between the stainless steel cladding of a pressurized water reactor (PWR) control rod and the Zr guide tube adjacent to it. This chemical reaction causes the cladding and guide tube to liquefy at temperatures below their respective stand-alone melting temperatures. The model calculates the growth of a zone of liquefied material due to the chemical reaction between the iron in the stainless steel cladding of the absorber material and the zirconium in the control rod guide tube. The situation in which the model is applied is shown in Figure 5-1. The stainless steel cladding of the absorber material is assumed to be in contact with the guide tube that surrounds it. The chemical reaction that takes place between the stainless steel and the zirconium is a strong function of temperature. Since the temperature of the control rod varies in the axial direction, the radial extent of the reaction zone also varies in the axial direction. The objective of the model is to calculate, as a function of time, the inner and outer radii of the reaction zone. If the outer radius of the reaction zone reaches the outer radius of the guide tube, then a breach is formed; and liquefied material will slump through the breach.

The outer radius of the reaction zone will be calculated as a function of time by the equation[5-1]

$$r_{soN2} = \left[r_{soN1}^{2} + A\exp\left(-\frac{B}{RT}\right)\Delta t \right]^{0.5} \tag{5-1}$$

where

r_{soN2} = outer radius of reaction zone at end of time step for axial node N (m),

r_{soN1} = outer radius of reaction zone at start of time step (m),

A,B = coefficients that are defined as 1.02 x 10^{-9} m^2/s and 481.8 (unitless) respectively,

R = universal gas constant (8.314 Pa•m^3/(g-mole•K),

T = temperature of reacting materials (K),

Δt = time step size (s).

The equation for calculating the inner radius of the reaction zone, variable r_{sin} of Figure 5-1, is the same as that used to calculate the outer radius, except that the coefficients A and B are defined as 1.19 x 10^{-6} m ^{2}/s and 435.6 (unitless), respectively.

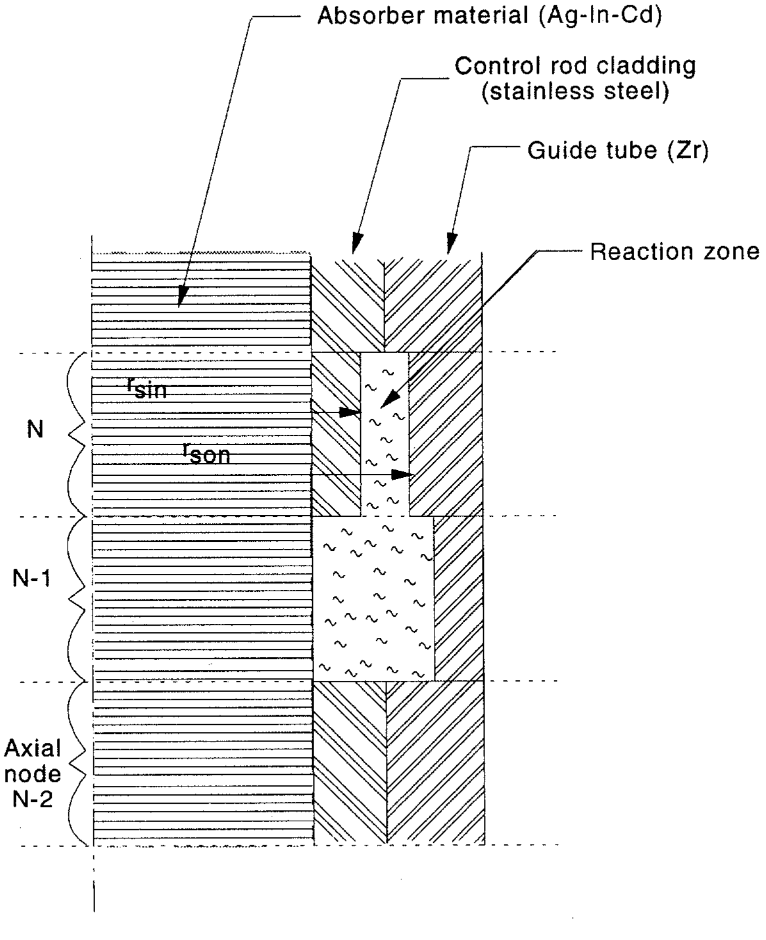
Absorber material (Ag-In-Cd)
Control rod cladding (stainless steel)
Guide tube (Zr)
Reaction zone
r_{sin}
r_{son}
N
N-1
Axial node N-2

Figure 5-1. Chemical reaction between control rod cladding and guide tube.

The binary alloy phase diagram of the Fe-Zr system is used to limit the rate of growth of the reaction zone to that which keeps the material in the reaction zone liquefied. The phase diagram of the Fe-Zr system is shown in Figure 5-2. The symbol L in the top part of the diagram designates the phase that is liquid. The curve below L defines the boundary between a liquefied and solidified mixture as a function of the temperature of the mixture and the fraction of Fe in the mixture. The curve indicates that a liquefied reaction zone begins when the temperature of the control rod cladding and guide tube exceeds 1,201 K. If the Fe content in the reacted zone stays at 24%, then the reaction zone continues to grow at the rate predicted by the kinetics equations. If, on the other hand, the fraction of Fe in the reaction zone increased to 40%, then growth of the reaction zone in the control rod cladding could not continue until the temperature increased to 1,740 K or until enough Zr had liquefied to reduce the fraction of Fe in the mixture to 24%.

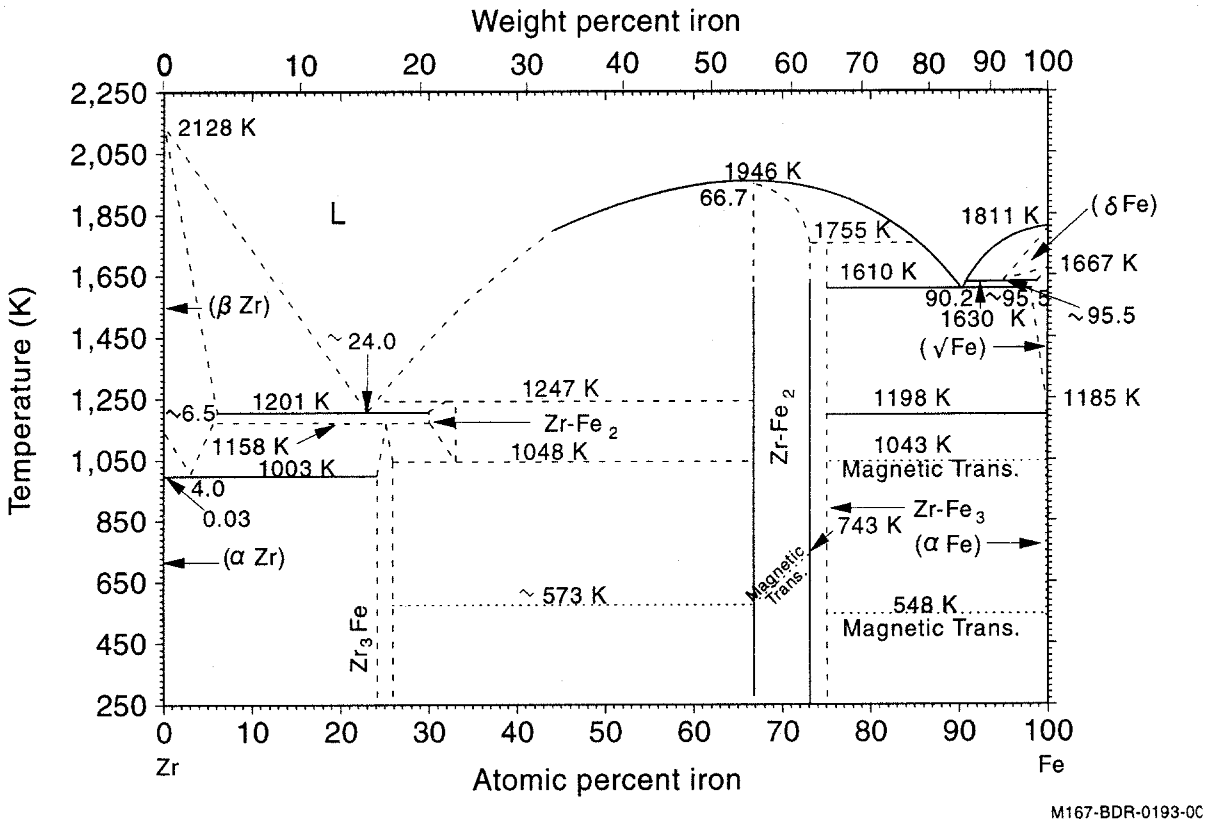

Figure 5-2. Binary alloy phase diagram of the system Fe-Zr.

5.2 BWR B_4C Control Blade and Channel Box Component Model

The BWR blade/box component model was developed at Oak Ridge National Laboratory (ORNL).[5-2] The model is designed to meet two general design requirements. First, the component must be able to represent all BWR geometries of interest, including full-size BWR cores and experimental facilities. Figure 5-3 shows the basic geometry considered. Second, the component must contain sufficient detail to account for all important phenomena, yet use computer resources efficiently. This section provides brief descriptions of the models used to represent the control blade and channel box.

5.2.1 Nodal Geometry

The BWR blade/box component is based on the nodal configuration shown in Figure 5-4. At each axial location, three radial temperature nodes are used for the control blade and two temperature nodes for the channel box. The actual control blade configuration of small rodlets inside a stainless steel-blade sheath is converted into an equivalent slab geometry. The solid structures of the component interact with two RELAP5 hydrodynamic volumes: one for the interstitial region and the other for the fuel bundle region. The gap between the blade sheath and rodlets is modeled. This gap communicates with the interstitial coolant volume through a series of holes in the blade sheath (refer to Figure 5-3). The gap results in two additional surfaces for stainless steel oxidation and also imposes an additional thermal resistance between the blade sheath and rodlets.

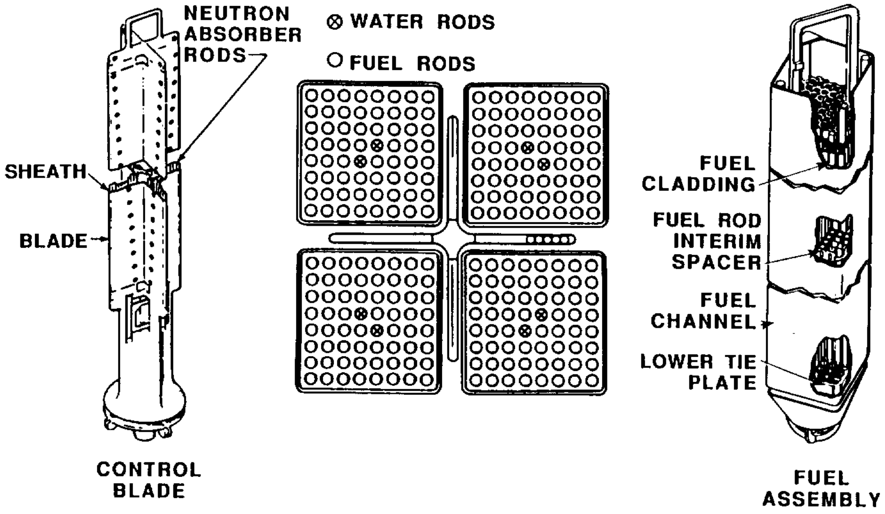

Figure 5-3. A typical BWR control blade and fuel assembly.

The thermal calculations for the BWR blade/box component take advantage of symmetry. The three control blade temperature nodes actually represent only half of a control blade; the other half is identical. The dashed line surrounding the component in Figure 5-4 represents an adiabatic surface. This adiabatic surface is shown as a triangular-shaped symmetrical region on the sketch of a typical BWR core in Figure 5-5. Figure 5-5 also highlights the need for modeling the channel box with two segments. One segment is adjacent to the control blade and the other is adjacent to another channel box. While the case of 8x8 fuel assemblies is shown in Figure 5-5, the modeling is also applicable to fuel assemblies of other sizes, such as 9x9 and 10x10.

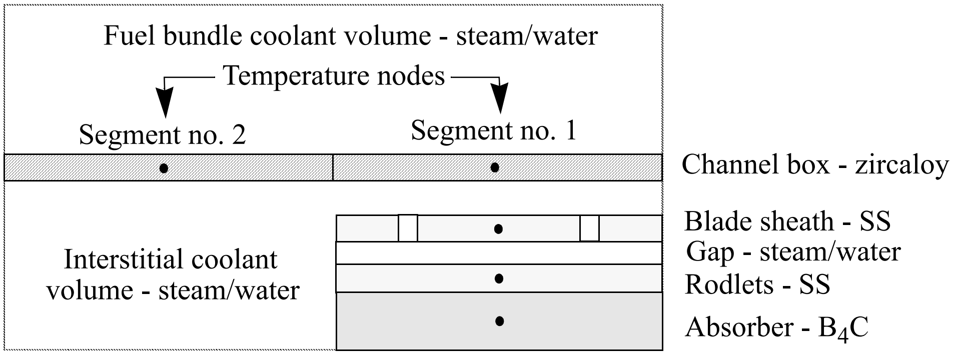
Fuel bundle coolant volume - steam/water
Temperature nodes
Segment no. 2
Segment no. 1
Channel box - zircaloy
Interstitial coolant volume - steam/water
Blade sheath - SS
Gap - steam/water
Rodlets - SS
Absorber - B_4C

Figure 5-4. BWR control blade and channel box component with five temperature nodes and equivalent slab geometry (radial cross-sectional view).

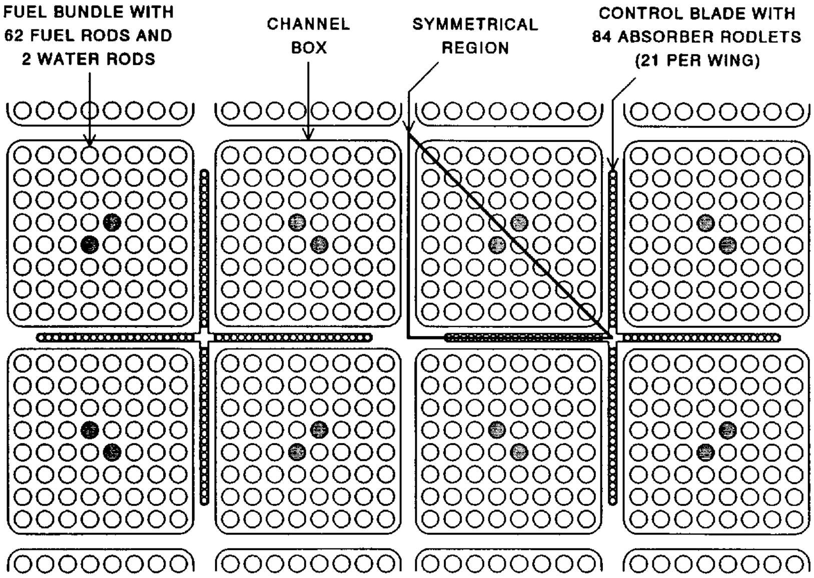
FUEL BUNDLE WITH 62 FUEL RODS AND 2 WATER RODS
CHANNEL BOX
SYMMETRICAL REGION
CONTROL BLADE WITH 84 ABSORBER RODLETS (21 PER WING)

Figure 5-5. Arrangement of fuel assemblies and control blade in typical BWR core.

5.2.2 Energy/Conduction Equation

A finite difference formulation is used to model the thermal responses of the control blade and channel box structures. Using the nomenclature in Figure 5-6, the energy/conduction equation (radial direction) for a channel box node is:

$$AX(TBOX_{new} - TBOX) = AO(TBKO - TBOX_{new}) + AI(TBKI - TBOX_{new}) + QBOX. \tag{5-2}$$

All quantities in this equation are evaluated at the previous time step except for the new channel box temperature, $TBOX_{new}$. The equation is solved implicitly for $TBOX_{new}$.

For the control blade, similar equations are derived for each of the three radial nodes. The three equations are solved implicitly for the new temperatures TCB 1_{new}, $TCB2_{new}$, and $TCB3_{new}$.

As a control blade melts and relocates, some nodes become blocked and others disappear. The BWR blade/box model includes logic to use different energy/conduction equations that depend upon the local situation, including recognition of these blocked/missing nodes. For example, at an axial elevation where there is a blockage in the interstitial volume between the control blade and channel box, there is a radial conduction path through five nodes. The temperatures of these five nodes are solved implicitly.

Axial conduction is included in the BWR blade/box model, but is calculated differently than radial conduction. Axial conduction heat transfer rates are calculated explicitly using previous time step information. These axial conduction rates are then added to the net energy transfer rates (QBOX, QCB1, QCB2, or QCB3) in the energy/conduction equations.

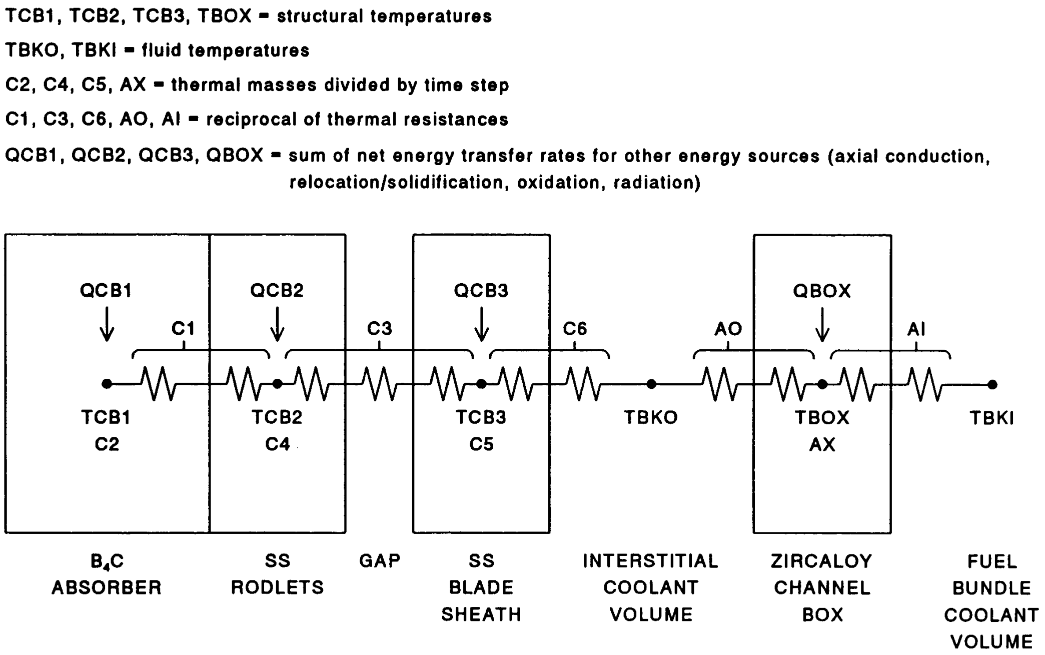
TCB1, TCB2, TCB3, TBOX = structural temperatures
TBKO, TBKI = fluid temperatures
C2, C4, C5, AX = thermal masses divided by time step
C1, C3, C6, AO, AI = reciprocal of thermal resistances
QCB1, QCB2, QCB3, QBOX = sum of net energy transfer rates for other energy sources (axial conduction, relocation/solidification, oxidation, radiation)
QCB1
C1
QCB2
C3
QCB3
C6
AO
QBOX
AI
TCB1
C2
TCB2
C4
TCB3
C5
TBKO
TBOX
AX
TBKI
B4C ABSORBER
SS RODLETS
GAP
SS BLADE SHEATH
INTERSTITIAL COOLANT VOLUME
ZIRCALOY CHANNEL BOX
FUEL BUNDLE COOLANT VOLUME

Figure 5-6. Nomenclature used for solution of energy/conduction equations in radial direction.

5.2.3 Melting and Material Interaction Models

An approximate solution method is used to solve the melting terms in the energy equations. At the end of each time step, the new temperatures calculated from the energy/conduction equations (see Section 5.2.2) are compared with their associated melting temperatures. If a nodal temperature is greater than its melting temperature and the node also contains solid material, then the nodal temperature is adjusted downward to equal its melting temperature and the associated sensible heat is used to melt an appropriate amount of the solid material. This temperature adjustment is not made if the node does not contain any solid material (i.e., if it contains only liquid material).

An approximate method is used to simulate the liquefaction of B_4C/stainless steel and stainless steel/zircaloy eutectics. Material compositions are tracked in each solid node. When B_4C and stainless steel, or stainless steel and zircaloy, are present in a node, these material pairs are allowed to react, using Hofmann's reaction kinetics.[5-3,5-4] After a eutectic interaction has occurred in a node, a failure (liquefaction) temperature is used in the melting calculations rather than the melting temperature of the pure material. The code does not contain correlations for these failure (liquefaction) temperatures; they must be specified by the code user. Based on ORNL analyses of the DF-4 and CORA experiments, the recommended failure (liquefaction) temperature for stainless steel that has reacted with B_4C is 1,505 K. The recommended failure (liquefaction) temperature for zircaloy that has reacted with stainless steel is 1,523 K.

5.2.4 Relocation/Solidification Models

The relocation of molten material is assumed to be controlled by solidification rates. The effects of liquid viscosity and momentum are assumed to be negligible. As molten material relocates downward over an underlying solid structure, it will solidify and transfer heat to the underlying solid. In the BWR blade/box model, molten material is allowed to relocate downward until it either solidifies or moves past the bottom of the defined core. Solidification heat transfer rates at each axial node are calculated explicitly using previous time step information. These solidification rates are then added to the net energy transfer rates (QBOX, QCB1, QCB2, or QCB3) in the energy/conduction equations (see Section 5.2.2).

The code does not contain correlations for heat transfer between molten material and the underlying solid. The code user must specify heat transfer coefficients for molten stainless steel and for molten zircaloy. Based on ORNL analyses of the DF-4 and CORA experiments, the recommended heat transfer coefficients for both stainless steel and zircaloy are 3,400 $W/(m^2 \bullet K)$.

The relocation logic in the BWR blade/box model allows for horizontal movement of molten material when a blockage inhibits downward movement. For example, if there is a blockage in the interstitial volume between the control blade and channel box, and the adjoining channel box node has failed, then molten control blade material is allowed to relocate through the original location of the channel box wall and into the fuel-bundle region. If the adjoining channel box node has not failed, and the region beyond the tip of the control blade remains open, then molten material is allowed to relocate laterally from segment No. 1 to segment No. 2. If both horizontal directions are blocked, then molten material is allowed to pool up on top of the interstitial blockage.

5.2.5 Oxidation Models

The oxidation of stainless steel, zircaloy, and B_4C is included in the BWR blade/box model. Oxidation heat generation rates at each axial node are calculated explicitly using previous time step information. These oxidation rates are then added to the net energy transfer rates (QBOX, QCB1, QCB2, or QCB3) in the energy/conduction equations (see Section 5.2.2). Hydrogen production rates are also calculated at each axial node. The oxidation correlations provided in the model are described below.

5.2.6 Stainless Steel

Stainless steel at high temperatures (close to its melting point) reacts vigorously with steam to yield metal oxides and large quantities of hydrogen. The reaction is similar to that of Zr/H_2O, but the stainless steel reaction energy is considerably less than that of Zr/H_2O per unit mass of metal reacted. In addition to iron (Fe), the oxidation of Cr and Ni is considered because these elements make up ~18% and ~8%, respectively, of stainless steel. Note that the oxidation of Cr is the major contributor to the total reaction energy.

Baker's criteria[5-5] is used for determining steam rich, hydrogen excess, or steam lean conditions. The oxidation correlations used for these three conditions are described below. For a situation where the reaction rate is controlled by gaseous diffusion, the Baker/Just approach[5-6] is used.

For steam rich conditions, White's kinetic correlation[5-7] is used. The essential chemical reactions for these conditions are:

$$2Cr + 3H_2O \longrightarrow Cr_2O_3 + 3H_2, \tag{5-3}$$

$$3Fe + 4H_2O \longrightarrow Fe_3O_4 + 4H_2, \tag{5-4}$$

$$Ni + H_2O \longrightarrow NiO + H_2, \tag{5-5}$$

$$3FeO + H_2O \longrightarrow Fe_3O_4 + H_2\ . \tag{5-6}$$

For hydrogen excess conditions, Baker's correlation[5-5] is used. Ni does not react under these conditions. The oxidation of steel will form a "spinal" compound:

$$2Cr + Fe + 4H_2O \longrightarrow FeO{*}Cr_2O_3 + 4H_2\ . \tag{5-7}$$

For steam lean conditions, a mean of the above steam rich and hydrogen excess correlations is used. Ni does not react under these conditions. The essential chemical reactions are:

$$2Cr + 3H_2O \longrightarrow Cr_2O_3 + 3H_2, \tag{5-8}$$

$$Fe + H_2O \longrightarrow FeO + H_2\ . \tag{5-9}$$

5.2.7 Zircaloy. The following parameters are calculated: (a) ZrO_2 layer growth, (b) alpha-Zr- oxygen saturated layer growth, and (c) total zircaloy weight gain. No reaction is considered for temperatures

< 923 K. For temperatures > 923 K, three temperature regions are considered:

- 923 - 1,173 K, oxide layer approximately obeys cubic kinetics,
- ²1,323 - 1,853 K, oxide layer follows parabolic kinetics,
- > 1,853 K, reaction accelerates because of changes in oxide microstructure.

The region between 1,173 - 1,323 K is approximated by logarithmic interpolation between the low and middle regions. The Springfields[5-8] oxidation correlation is used at low temperatures (923 - 1,173 K); the Cathcart and Pawel[5-9] oxidation correlation is used at medium temperatures (1,323 - 1,853 K). At high temperatures (> 1,853 K), the Urbanic/Heidrick oxidation correlation[5-10] is used.

5.2.8 Boron Carbide. B_4C oxidation/reduction predictions are obtained from the advanced $B_4C/H_2/H_2O$ chemistry package, which performs a chemical equilibrium calculation using a free energy minimization solution method. The package was developed by E. C. Beahm of ORNL's Chemical Technology Division. It is based on the SOLGASMIX code.[5-11] Beahm's package was modified so that it could be interfaced with the BWR blade/box model. The equilibrium calculation includes the following chemical species: H_2, $H_3B_3O_6$, O_2, H_2O, HBO_2, B_4C (l), CO, BH_3, B_2O_3 (l,s), CH_4, B_2H_6, B, CO_2, BOH, C, B_2O_3 (g), O, Ar.

5.2.9 Radiation Models

Radiation calculations on the fuel-bundle side of the channel box are performed externally by the SCDAP radiation model. The two segments of the channel box are treated independently within the SCDAP radiation model. Radiation calculations on the interstitial side of the channel box are performed internally by the BWR blade/box model. Radiation is modeled in the radial direction between the control blade and the two channel box segments.

When the local fluid void fraction is greater than a threshold value (0.5), radiation heat transfer rates at each axial node are calculated explicitly using previous time step information. These radiation rates are then added to the net energy transfer rates (QBOX, QCB1, QCB2, or QCB3) in the energy/conduction equations (see Section 5.2.2).

5.2.10 Hydrodynamic Models

All hydrodynamic parameters used in the BWR blade/box model are obtained from the RELAP5 database. These hydrodynamic parameters are shown in Figure 5-7 along with the other interface information that is exchanged with SCDAP. The steam, hydrogen, and inert (primarily argon) mass flow rates, along with the fluid pressures, are used in the oxidation models to calculate the partial pressures of steam and hydrogen. The fluid temperatures, convective heat transfer coefficients, and time step are used in the energy/conduction equations (see Section 5.2.2). The fluid void fractions are used in the radiation models to determine when radiation heat transfer should be included. The radiation heat transfer rates on the fuel-bundle side of the channel box (both segments) are obtained from the SCDAP radiation model.

The parameters returned from the BWR blade/box model to SCDAP are shown in the lower half of Figure 5-7. The average wall temperatures, which are used as boundary conditions by RELAP5, are calculated as weighted averages relative to the surface areas of the nodes exposed to each coolant volume. Blocked/missing nodes will sometimes reduce the number of nodes exposed to a coolant volume. For example, at an axial elevation where there is a blockage in the interstitial volume between the control blade and channel box, segment No. 2 of the channel box will be the only node exposed to the interstitial volume. This situation is properly accounted for in the average wall temperature calculations. The blockage will also reduce the flow area of the coolant volume, and this information is returned to RELAP5.

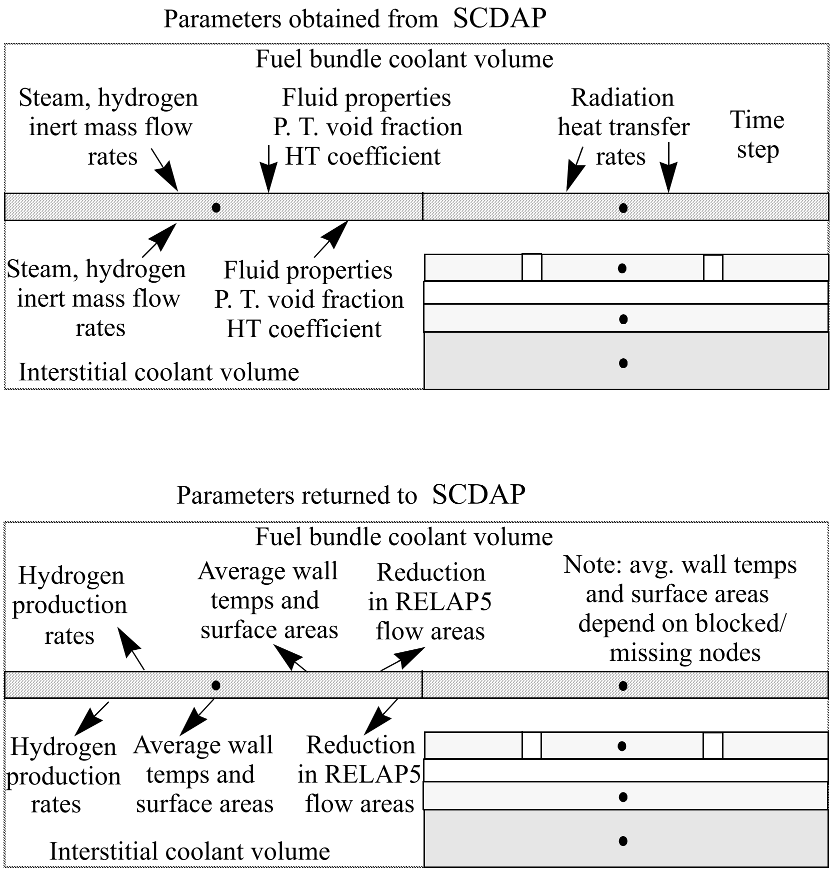
Parameters obtained from SCDAP
Fuel bundle coolant volume
Steam, hydrogen inert mass flow rates
Fluid properties P. T. void fraction HT coefficient
Radiation heat transfer rates
Time step
Steam, hydrogen inert mass flow rates
Fluid properties P. T. void fraction HT coefficient
Interstitial coolant volume
Parameters returned to SCDAP
Fuel bundle coolant volume
Hydrogen production rates
Average wall temps and surface areas
Reduction in RELAP5 flow areas
Note: avg. wall temps and surface areas depend on blocked/ missing nodes
Hydrogen production rates
Average wall temps and surface areas
Reduction in RELAP5 flow areas
Interstitial coolant volume

Figure 5-7. Interface information exchanged between SCDAP and the BWR blade/box model.

5.3 Simplified B_4C Control Rod Model

This section describes the simplified B_4C control rod model. This model is designed to represent PWR control rods that use B_4C as the absorber material. The model can also represent in a simplified manner the control blade in BWR reactors.

The existence of significant amounts of control rod material in a BWR core might have an important influence on the overall behavior of core degradation and fission product transport during a severe accident event. The stainless steel cladding/sheath and the boron carbide (B_4C) control rod absorber can be oxidized in the high temperature steam environment. The exothermic oxidation can raise the core temperature, thus increasing the core heatup rate. The combustible gases, such as H_2, CO, and CH_4, generated through control rod oxidation might pose an additional threat to the containment integrity. The borates, produced in the B_4C oxidation, can react to produce cesium borates and alter the distribution of iodine between cesium iodide, hydrogen iodide, and elemental iodine. In order to address these possible impacts, a BWR control rod model has been developed. The model describes the oxidation of the stainless steel cladding/sheath, the B_4C absorber, the heatup, the melting, and the relocation of the B_4C control rods during a BWR severe accident event.

5.3.1 Model Description

This section describes the typical BWR fuel assemblies and control rod module and the possible geometrical modeling of the actual configuration. It also presents the theory for the oxidation kinetics of the stainless steel cladding/sheath and the B_4C absorber. Models for describing the control rod temperature response, control rod melting and relocation, and the slumping of unsupported control rod segments are also provided.

A typical BWR control rod consists of a sheathed cruciform array of stainless steel tubes filled with B_4C powder. Each control rod is surrounded by four fuel assemblies. The absorber tube sheath and the tube cladding are made of Type 304 stainless steel. The B_4C powder in the absorber tubes is compacted to about 70% of the theoretical density. The B_4C is longitudinally separated into individual compartments by stainless steel balls held in place by a slight crimp in the tube. The control rods are cooled (heated during accident conditions) by the core bypass flow. The tube sheaths are perforated to allow the coolant to circulate freely about the absorber tubes.

Due to the complexity of the actual configuration, a cylindrical rod geometry is assumed in this model. For each B_4C control rod, the equivalent stainless steel cladding outer radius and thickness are used to represent both tube cladding outer radius, thickness, and the associated portion of the stainless steel sheath for this tube. There are several types of nodalizations that can be used to model the geometry of fuel assemblies and the control rod module, as shown in Figure 5-8. As shown in Figure 5-8a, the control rod module together with the four surrounding fuel assemblies are considered as a single channel. The enclosure of the channel is modeled by an equivalent shroud component. The four fuel assemblies can be modeled by one to four individual fuel components. The control rod module is modeled by a BWR control rod component. Figure 5-8b shows a different type of nodalization. Each of the four fuel assemblies is modeled by a fuel component and an enclosure shroud component which forms an individual channel. The control rod module is modeled by a control rod component and its bypass core flow to form an additional channel. The third type of nodalization is shown in Figure 5-8c. The four fuel assemblies are modeled by a representative channel with a fuel component and a surrounding shroud component. The control rod module is modeled by a core bypass channel with a control rod component.

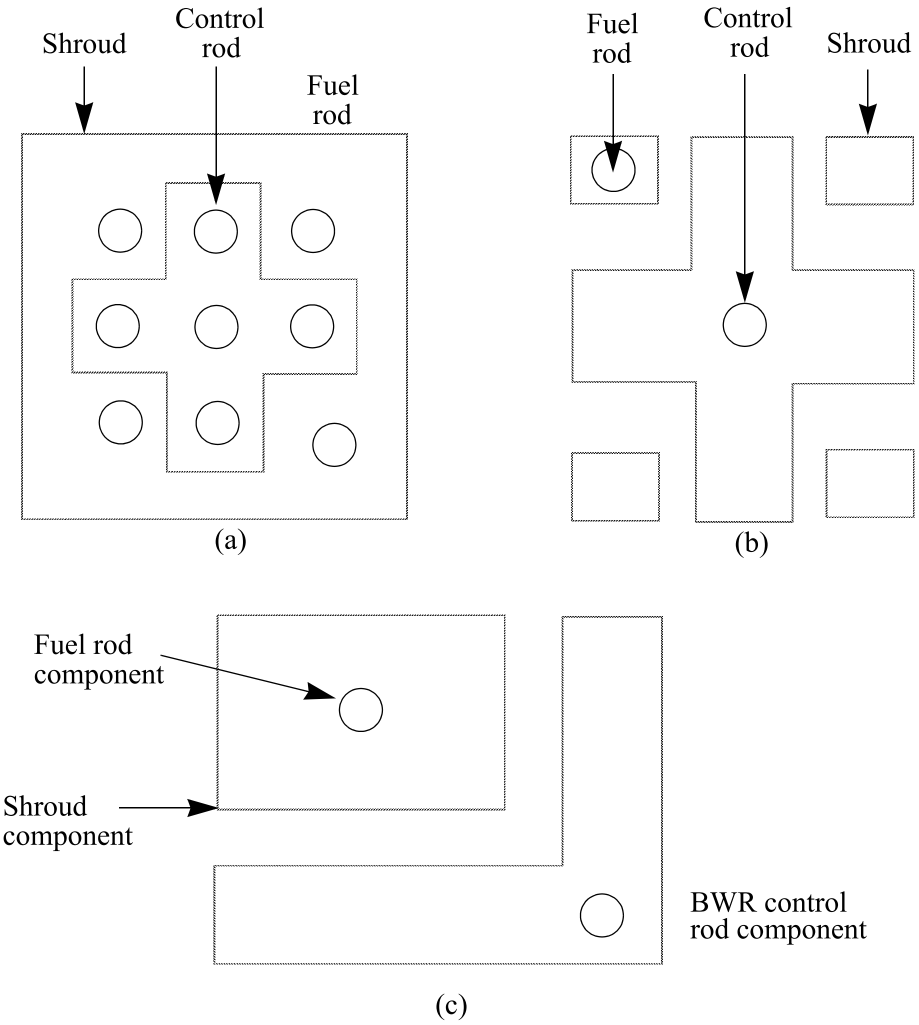
Shroud
Control rod
Fuel rod
(a)
Fuel rod
Control rod
Shroud
(b)
Fuel rod component
Shroud component
BWR control rod component
(c)

Figure 5-8. Nodalization for fuel assemblies and control rods.

5.3.2 Oxidation

The stainless steel oxidation considers the following chemical reaction:

$$Fe + H_2O \longrightarrow FeO + H_2 \quad . \tag{5-10}$$

The stainless steel weight gain and the FeO layer growth are defined by Equation (3-68). Hydrogen production and heat generation are handled by the oxidation model described in Section 3.

For the oxidation of B_4C absorber, the current model considers the following chemical reaction:

$$B_4C + 7\ H_2O \longrightarrow 2\ B_2O_3 + 7\ H_2 + CO \quad . \tag{5-11}$$

Due to the lack of experimental data, an exponential oxidation model is used and is described by the following equations:

$$\frac{dM_{BC}}{dt} = -R(T)M_{BC} \tag{5-12}$$

$$R(T) = CT + D \tag{5-13}$$

where

M_{BC} = mass of B_4C at time t (kg)

R(T) = reaction rate coefficient, assumed to be a linear function of the B_4C temperature (T).

The reaction rate coefficient is further assumed to be zero when the B_4C temperature is < 1,700 K (stainless steel cladding melting point) and 1.0 at 2,700 K (B_4C melting point). Thus, the linear fitting constants, C and D, are 1.0 E-3 and -1.7, respectively. The reaction rate coefficient R(T) as a function of B_4C temperature is shown in Figure 5-9. If the B_4C temperature is assumed to be constant during a time step, t, the above equation can be integrated to obtain

$$M_{BC} = M_{BC,O}e^{[-R(T)\Delta t]} \tag{5-14}$$

where $M_{BC,O}$ is the mass of B_4C at the beginning of the current time step. Once the mass of oxidized B_4C during the current time step is known, the oxidation heat generation can be obtained from the reaction heat.

Both the stainless steel and B_4C oxidation consider the unoxidized mass limitation and the steam supply limitation during each time step advancement.

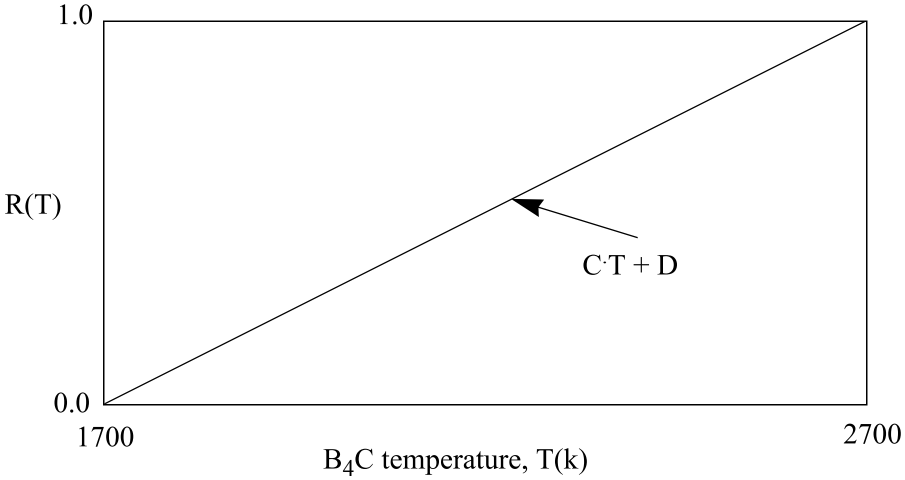

Figure 5-9. B_4C oxidation rate coefficient as a function of temperature.

5.3.3 Temperature Response

A one-dimensional, two region energy balance equation is used to predict the absorber and cladding temperature responses. The schematic nodalization for the temperature response calculation is shown in Figure 5-10. The differential equations that govern the region temperature response can be written as:

$$M_1 C_1 \frac{dT_1}{dt} = Q_{cond} + Q_{ox,\,1} \tag{5-15}$$

$$M_2 C_2 \frac{dT_2}{dt} = -Q_{cond} + Q_{conv} + Q_{rad} + Q_{ox,\,2} \tag{5-16}$$

where

M_1, M_2 = mass of absorber and cladding, respectively (kg),

C_1, C_2 = specific heat of absorber and cladding, respectively ($J/kg \cdot K$),

t = time (s),

Q_{cond} = conduction heat transfer rate at the interface between the absorber and the cladding regions (W),

Q_{conv} = convective heat transfer rate at the control rod surface (W),

Q_{rad} = radiation heat transfer rate at the control rod surface (W),

$Q_{ox,1}$ = B_4C oxidation heat generation rate (W),

$Q_{ox,2}$ = stainless steel oxidation heat generation rate (W).

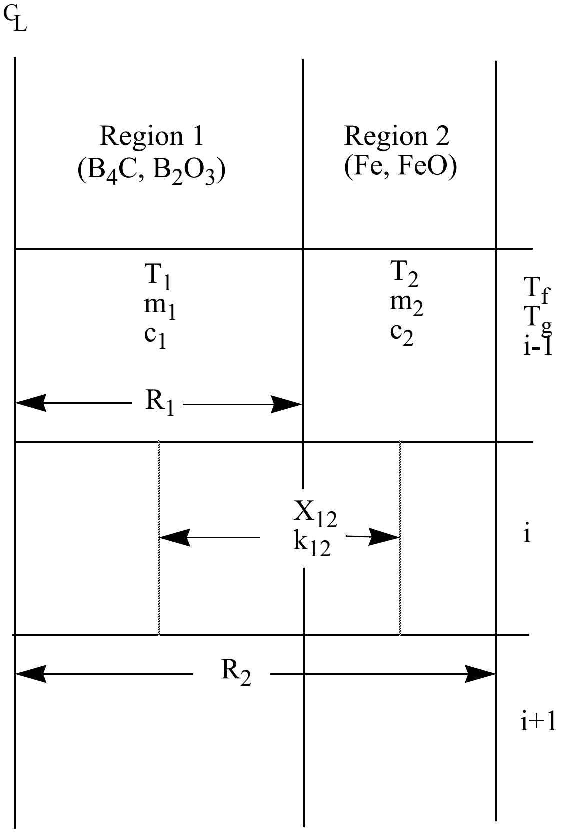

Figure 5-10. One-dimensional, two region nodalization for temperature response calculation.

The convective and conductive heat transfer rates can further be expressed as

$$Q_{conv} = A_2[(h_f\,(T_f - T_2) + h_g\,(T_g - T_2)] \tag{5-17}$$

$$Q_{cond} = k_{12}A_1\left(\frac{T_2 - T_1}{X_{12}}\right) \tag{5-18}$$

where

A_1, A_2 = surface areas of absorber and cladding, respectively

h_f, h_g = convective heat transfer coefficients between rod surface and liquid phase coolant, and between rod surface and vapor phase coolant, respectively

T_f, T_g = temperatures for the liquid phase and vapor phase coolant

k_{12} = effective conductivity across the absorber and the cladding regions

X_{12} = effective conduction distance.

The convective heat transfer rate between the control rod surface and the surrounding coolant is calculated using the RELAP5 heat transfer package. The calculation of radiation heat transfer rate depends on the geometric model. For the first type of model, as shown in Figure 5-8a, the radiation heat transfer rate is calculated as in the original SCDAP radiation model. For the other types of geometrical models, as shown in Figure 5-8b and Figure 5-8c, radiation heat exchange between two parallel planes (fuel canister wall and control rod sheath) is assumed. The radiation heat transfer rate on one of the control rod surfaces can be expressed as:

$$Q_{rad} = \frac{\frac{\sigma A}{n}(T_s^4 - T_2^4)}{\frac{1}{\varepsilon_s} + \frac{1}{\varepsilon_2} - 1} \tag{5-19}$$

where

$\varepsilon_s, \varepsilon_2$ = surface emissivities for fuel assembly canister wall and control rod sheath

A = surface area for fuel assembly canister wall or control rod sheath which are facing each other

T = temperature at the outer surface of the fuel assembly canister wall

n = number of control rod tubes within a control rod module

σ = Stefan-Boltzmann constant.

During a time step, Δt, Equations (5-15) and (5-16) can be expressed in difference forms

$$M_1C_1(T_1^{(n)} - T_1^{(o)}) = \frac{k_{12}A_1\Delta t(T_2^{(n)} - T_1^{(n)})}{X_{12}} + Q_{ox,\,1}^{(n)}\Delta t \tag{5-20}$$

$$\begin{aligned} M_2C_2(T_2^{(n)} - T_2^{(o)}) &= \frac{-k_{12}A_1\Delta t(T_2^{(n)} - T_1^{(n)})}{X_{12}} \\ &+ A_2\Delta t[h_f^{(n)}(T_f^{(n)} - T_2^{(n)}) + h^{(n)}(T_g^{(n)} - T_2^{(n)}) + Q_{rad}^{(n)}\Delta t + Q_{ox,\,2}^{(n)}\Delta t] \quad . \end{aligned} \tag{5-21}$$

The end timestep temperatures, $T_1^{(n)}$ and $T_2^{(n)}$, can be solved in terms of the beginning timestep temperatures, $T_1^{(o)}$ and $T_2^{(o)}$, explicitly.

When the control rod cladding is melted away, the B_4C absorber is then exposed to the coolant. The temperature response of the B_4C region is predicted according to a lumped parameter calculation. The difference equation during the timestep, t, is

$$M_1C_1(T_1^{(n)} - T_1^{(o)}) = A_1\Delta t[h_f^{(n)}(T_f^{(n)} - T_1^{(n)}) + h_g^{(n)}(T_g^{(n)} - T_1^{(n)}) + Q_{rad}^{(n)}\Delta t + Q_{ox,\,1}^{(n)}\Delta t] \quad . \tag{5-22}$$

The end timestep temperature, $T_1^{(n)}$, can then be obtained.

5.3.4 Melting and Relocation

Following the conduction solution, should melting occur during the current time step, the amount of material melted is calculated. Since the melting of the materials is not implicitly calculated in the conduction solution, the actual temperature is recalculated through balancing the material internal energy and the heat of fusion.

The downward movement of the molten material is calculated based on the well developed, model for incompressible viscous film flow over a cylindrical geometry. Considering a cylindrical geometry, as shown in Figure 5-11, the force balance for the liquid film can be expressed as:

$$\frac{d}{dr}(\gamma\xi_{\gamma z}) = \gamma\rho g \tag{5-23}$$

where

$$\xi_{\gamma z} = -\mu\frac{dV_z}{d\gamma} \quad . \tag{5-24}$$

The boundary conditions are

$$\xi_{yz} = 0 \text{ for } \gamma = R_2 \tag{5-25}$$

$$V_z = 0 \text{ for } \gamma = R_1 \tag{5-26}$$

where

γ = the radial coordinate

ρ = the liquid film density

g = gravitational acceleration

μ = the liquid film viscosity

ξ_{yz} = viscous shear force

R_1, R_2 = outer radii for the solid and liquid layers

$V_z(\gamma)$ = downward liquid film velocity.

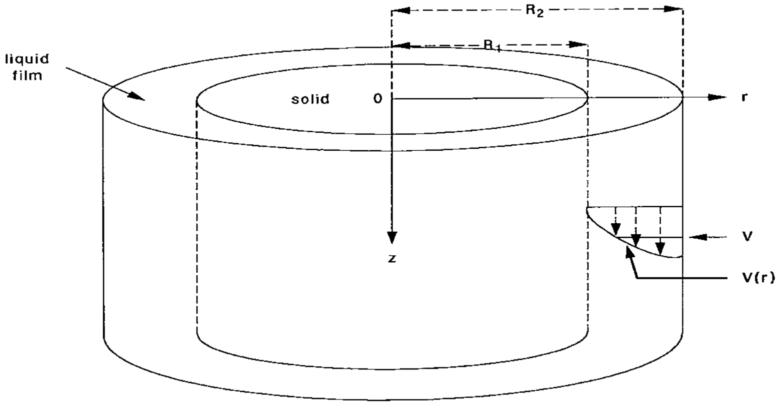

Figure 5-11. Incompressible, viscous film flow over cylindrical geometry.

From the above equations, the liquid film velocity profile can be obtained as

$$V_z(\gamma) = \frac{\rho g}{4\mu}(R_1^2 - \gamma^2) + \frac{\rho g R_2^2}{2\mu}\ln\left(\frac{\gamma}{R_1}\right) \quad . \tag{5-27}$$

After integrating the velocity profile across the liquid film, the average film velocity, V, is

$$V = \frac{R_1^4}{R_2^2 - R_1^2} + \frac{\rho g}{\mu} + \frac{4x^2 - 1 - 3x^4}{8} + \frac{x^4}{2}\ln(x) \tag{5-28}$$

where $x = \frac{R_2}{R_1}$. Thus, during a time step Δt, the liquid film will travel a distance of $V\Delta t$.

During a time step, the actual computation process starts from the top elevation of the control rod. If melting and relocation occur at the top elevation, the molten material moves to the next lower elevation. The internal energy associated with the relocated molten material is assumed to instantly exchange with the internal energy of the material at this lower elevation. Should the liquefied material at this new elevation still appear, the downward moving calculation for the liquefied material is continued. The process is repeated until the lowest elevation is reached. The amount of molten material dripped below the bottom of the control rod is also tracked for each time step.

5.3.5 Slumping

If the material, which is located anywhere in the middle section of a control rod, has depleted during a time step, then the unsupported control rod segment, located above the empty section, is assumed to fill the empty section and leave an empty region at the top. This slumping process is shown in Figure 5-12. All of the hydraulic volume connections, the changes of the coolant flow area, and the coolant hydraulic diameter are also updated.

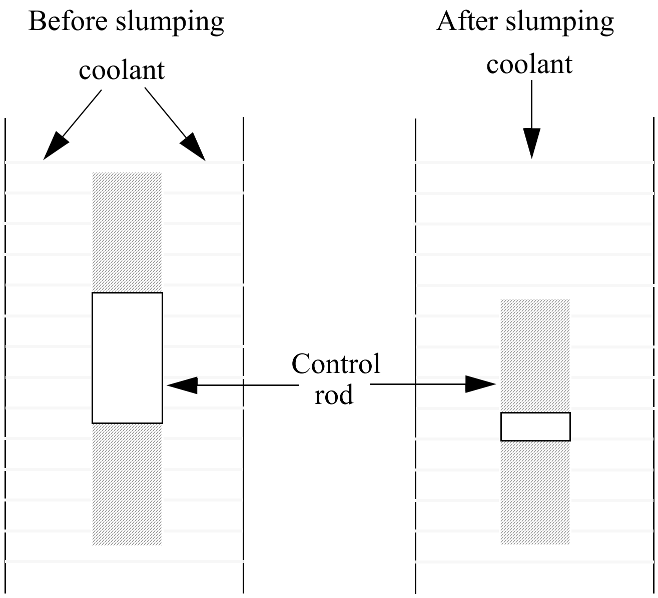

Figure 5-12. Slumping process for unsupported control rod segment.

5.4 Shroud/Reflector Model

Structures in the core other than fuel and control rods are modeled with the shroud/reflector component. This component represents cylindrical structures with a wall thickness much smaller than the radius of the cylinder.

5.4.1 Model Description

This component models a cylindrical shaped structure within the reactor core. The temperature distribution in the structure is calculated using the basic heat conduction equation described in Section 2.1. An internal heat generation term can be specified by the user. The structures can be defined by multiple layers of materials, with the oxidation and relocation of exterior layers due to melting considered.

The shroud/reflector component requires two to three sets of boundary conditions, depending on the configuration specified by the user. In the minimum configuration, the user must specify a hydrodynamic volume on the internal (reactor) side of the component, as well as on the external side. Additionally, the user may specify a hydrodynamic volume representing flow channels embedded within the structure.

5.4.2 Oxidation

Oxidation is modeled using the parabolic rate equations described in Section 3.3. Because of the generalization of this component, oxidation is limited to three types of materials. These types of materials are zircaloy based materials (material indices 1 through 3 in Appendix A of Volume III), iron based materials (material indices 18 and 19) and user-specified materials (indices 10 through 12 and 50 through 59). Zircaloy layers are oxidized using the same kinetics as described for fuel rods.

The stainless steel oxidation considers the following chemical reaction, which assumes steam lean as opposed to steam rich conditions:

$$Fe + H_2O \longrightarrow FeO + H_2 \ . \tag{5-29}$$

The stainless steel weight gain and the FeO layer growth are defined by Equation (3-68). Hydrogen production and heat generation are handled by the oxidation model described in Section 3.

5.4.3 Melting and Relocation

In the situation where the component reaches melting and relocation conditions, and the primary material is zircaloy, the molten zircaloy relocates downward to a region where the structural surface temperature is 200 K less than the solidus temperature of zircaloy. In the situation where the primary material is stainless steel, the material melts and relocates as described in Section 9.6.

Structures with exterior layers or composed entirely of non-zircaloy/non-iron materials can also be modeled; however, oxidation rate equations must be user-specified and no material relocation or loss of geometry can be considered. Both melting and nonmelting models can be used for the structures outside the core as well. The same material limitations apply.

5.5 References

5-1. W. Hering and P. Hofmann, *Material Interactions During Severe LWR Accidents (Draft),* KfK-5125, February 1994.

5-2. F. P. Griffin and K. A. Smith, *BWR Control Blade/Channel Box Interaction and Melt Relocation Models for SCDAP,* ORNL/NRC/LTR-92/12/R1, December 31, 1992.

5-3. P. Hofmann, E. A. Garcia, and A. Denis, "Low-Temperature Liquefaction of LWR Core Components," *Severe Accident Research Program Partners Review Meeting, Brookhaven National Laboratory, Upton, NY, April 30 - May 4, 1990.*

5-4. P. Hofmann, M. Markiewicz, and J. Spino, "Reasons for the Low-Temperature Failure of BWR Absorber Elements," *Severe Accident Research Program Partners Review Meeting, Idaho Falls, ID, April 10-14, 1989.*

5-5. L. Baker, Jr., *An Assessment of Existing Data on Zirconium Oxidation Under Hypothetical Accident Conditions in Light Water Reactors,* ANL/LWR/SAF 83-3, 1983.

5-6. L. Baker and L. C. Just, *Studies of Metal-Water Reactions at High Temperatures, III. Experimental and Theoretical Studies of the Zirconium-Water Reaction,* ANL-6548, May 1962.

5-7. J. F. White et al., *Seventh Annual Report-AEC Fuels and Materials Development Program,* GEMP-1004, March 1968.

5-8. T. J. Haste et al., *Zircaloy Oxidation Kinetics in the Temperature Range 700-1300 ^oC,* IAEA-TC-657/4.7, September 1988.

5-9. J. V. Cathcart et al., *Zirconium Metal-Water Oxidation Kinetics, IV - Reaction Rate Studies,* ORNL/NUREG-17, 1977.

5-10. V. F. Urbanic and T. R. Heidrick, “High-Temperature Oxidation of Zircaloy-2 and Zircaloy-4 in Steam,” *Journal of Nuclear Materials, 75,* 1978, pp. 251-61.

5-11. Gunnar Eriksson, “Thermodynamic Studies of High-temperature Equilibriums, SOLGASMIX, a Computer Program for Calculation of Equilibrium Compositions in Multiphase Systems,” *Chemical Scripta, Volume 8, Number 3,* 1975, pp. 100-103.

6. RADIATION HEAT TRANSFER MODEL

This section describes the radiation heat transfer model used for a LWR core. The radiation model analyzes the radiation exchange between the various components in the core, including the coolant. The model calculates the radiation heat flux absorbed by the coolant and the radiant heat exchange between the surfaces of any vessel component (fuel rod, control rod, or shroud). The radiant heat exchange is a thermal boundary condition used in severe accident analysis of fuel rods, control rods, and flow shrouds.

6.1 Radiation Model Governing Equations

A mechanistic radiative heat transfer formulation, which accounts for each surface, the vapor, and each droplet, is complex. To develop such a detailed model for SCDAP/RELAP5-3D© would not be cost effective. Instead, simplified models are used without unduly sacrificing the accuracy of the results.

The radiation model presented here is similar to those developed earlier[6-1,6-2,6-3,6-4,6-5,6-6,6-7,6-8] for nuclear reactor applications. The solution method used is the net radiation method for an enclosure. Each component (fuel rod, control rod, or shroud) surface forms one side of an enclosure with n sides, and the enclosure is filled with coolant (see Figure 6-1). The radiation heat transfer equation for each surface describes radiation exchange with all the surfaces (including itself if it radiates to itself) and absorption and emittance by the enclosed coolant. The n equations are solved simultaneously by a matrix inversion method to obtain the radiosity (the sum of emitted and reflected radiation energy rates) of each surface. The difference between the radiosity and incident energy from the surroundings gives the net heat flux to or from a surface. The algebraic sum of net heat flux corresponding to each surface gives the total radiation heat absorbed by the coolant.

To derive the governing equation of radiation heat exchange for a surface, the following assumptions were made:

- All surfaces are gray, that is, the absorption is independent of wavelength
- All surfaces are diffuse for emission and the isotropic portion of the reflected radiant energy.
- Each surface has a uniform temperature and emits radiation uniformly.
- Of the reflected radiation from a surface i, a fraction $(1 - \mu_i)$ is reflected isotropically (diffuse uniformly in all the directions); and the rest, μ_i, is reflected back toward the origin of the incident radiation.
- The coolant absorbs and emits radiation.

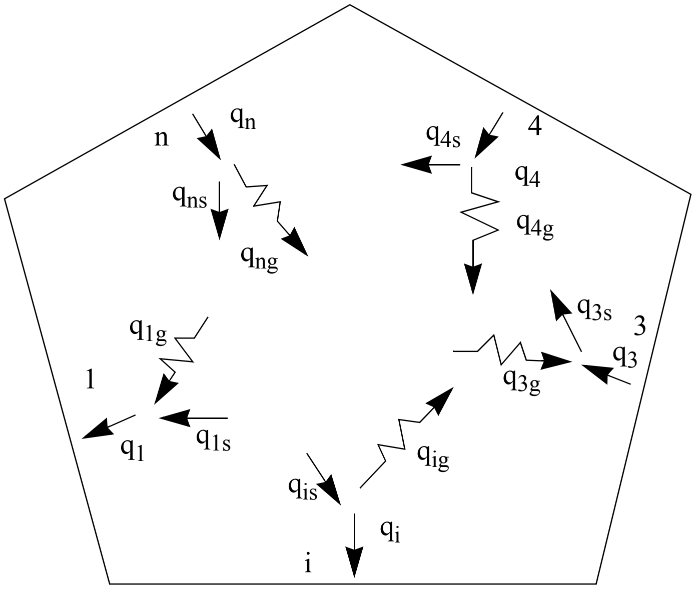

Figure 6-1. Radiation exchange between surfaces and between surfaces and gas.

- The coolant is assumed to be steam only with no entrained droplets.

Figure 6-2 shows the radiation exchange mechanism for any surface i. I_i is the rate of radiant flux incoming from the surroundings (other surfaces, gas, and possibly surface i). A portion, a_i, of I_i is absorbed by the surface i, and the remaining (1 - a_i) is reflected to the surroundings. The surface i also emits radiation. Thus, the outgoing radiation energy flux rate (radiosity), E_i, from a surface i is composed of emitted and reflected radiation. This gives

$$E_i = \varepsilon_i \sigma T_i^4 + \rho_i I_i = \varepsilon_i \sigma T_i^4 + (1 - \varepsilon_i) I_i \tag{6-1}$$

where

E_i = rate of radiant energy outgoing (radiosity) from a unit area of surface i (W/m^2)

ε_i = the emissivity of surface i (equal to a_i for a gray diffuse surface)

σ = Stefan-Boltzmann constant (5.668×10^{-8} W/m^2 • K^4)

T_i = the temperature of surface i (K)

ρ_i = the reflectivity of surface i equals $(1 - a_i) = (1 - \varepsilon_i)$

I_i = the rate of radiant energy incident upon a unit area of surface i (W/m^2).

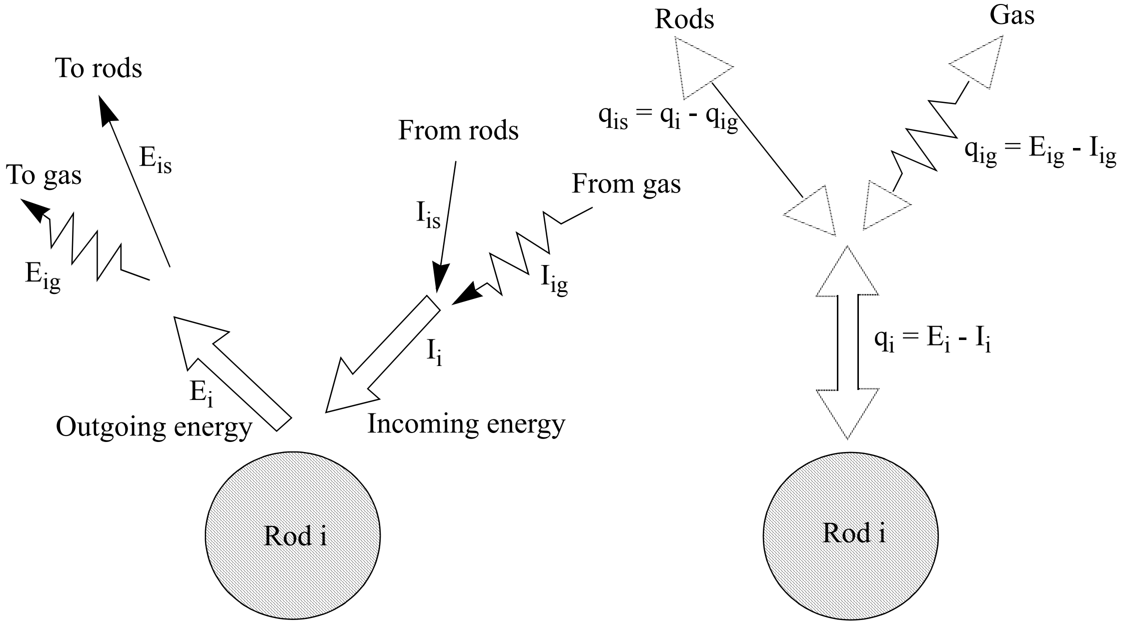

Figure 6-2. Radiation exchange between a rod surface and its surroundings.

Here a relation, $\rho_i = (1 - a_i) = (1 - \varepsilon_i)$, has been used for an opaque gray surface. The incoming flux, I_i, is the sum of the portions of the energy leaving all the surfaces of the enclosure that arrives at the ith surface. The reflected radiation from a surface will mainly leave the surface in a direction that forms an equal but opposite angle with the surface normal to the direction of the incident radiation, whereas the emitted radiation leaves in all the directions. Therefore, for large or curved surfaces, generally the radiation is reflected backward toward the origin of the incident radiation. Hence, it is assumed[6-6,6-7] that a fraction, μ, of the incident reflection is reflected backward and the remaining radiation $(1 - \mu)$ is reflected uniformly in all the directions.

The isotropic part of the outgoing radiation (radiosity), E_i^A, from a surface i is given by

$$E_i = \varepsilon_i \sigma T_i^4 + (1 - \mu_i)(1 - \varepsilon_i) I_i \qquad (6\text{-}2)$$

and the anisotropic part, which is reflected back to the j-th surface, E_{ij}^A, is given by

$$E_{ij}^A = \mu_i(1-\varepsilon_i)I_i \tag{6-3}$$

or

$$\sum_{i=1}^{n} I_{ij} = \frac{1}{\mu_i(1-\varepsilon_i)}\sum_{i=1}^{n} E_{ij}^A \quad . \tag{6-4}$$

The total incoming radiation onto surface i is the sum of incoming radiation from all the directions, I_{ij}, including itself:

$$I_i = \sum_{i=1}^{n} I_{ij} \quad . \tag{6-5}$$

Combining Equations (6-2), (6-4), and (6-5), the following equation is obtained:

$$E_i = \varepsilon_i \sigma T_i^4 + \frac{(1-\mu_i)}{\mu_i}\sum_{i=1}^{n} E_{ij}^A \quad . \tag{6-6}$$

The incident radiation from the j-th surface reaching the i-th surface consists of the following parts:

- Isotropic part of the radiosity of the j-th surface multiplied by the view factor from surface j to surface i.
- The anisotropic part of the radiation emitted in the direction of i-th surface; the total radiosity, sum of (1) and (2), is reduced by the transmissivity of the coolant.
- Radiation emitted by the coolant itself.

Therefore,

$$A_i I_{ij} = (E_j^I A_j F_{ji} + E_{ji}^A A_j)\tau_{ji} + \varepsilon_{gji}\sigma T_g^4 A_j F_{ji} \tag{6-7}$$

where

A_i = the area of surface i (m^2)

F_{ji} = the view factor of surface j to surface i

τ_{ji} = the transmissivity of coolant from surface j to surface i $= e^{(-K_{gji}L_{ji})}$

ε_{gji} = $(1 - \tau_{ji})$.

Here L_{ji} is the mean path (beam) length between surfaces i and j. K_{gji} is the absorption coefficient (absorptivity per unit length) for the vapor medium and has the units of m^{-1}. Because liquid droplets are assumed to be absent in the path between i and j, the absorption coefficient for liquid K_{lji} is taken as zero. Therefore, τ_{ji} and ε_{gji} are equal to $e^{-K_{gji}L_{ji}}$ and $(1 - \tau_{ji})$, respectively. In the radiation equations, the gas temperature is indexed to the SCDAP/RELAP5-3D© vapor temperature in the hydrodynamic volume in which the SCDAP component exists.

From the view factor reciprocity relation,

$$A_iF_{ij} = A_jF_{ji} \quad . \tag{6-8}$$

Equation (6-7) is simplified to

$$I_{ij} = \left[E_j^I F_{ij} + E_{ji}^A \frac{A_j}{A_i}\right]\tau_{ji} + \varepsilon_{gji} T_g^4 \sigma F_{ij} \quad . \tag{6-9}$$

Substituting the expression for I_{ji} in Equation (6-4)

$$E_{ij}^A = \mu_i(1-\varepsilon_i)\left[\left(E_j^I F_{ij} + E_{ji}^A \frac{A_j}{A_i}\right)\tau_{ji} + \varepsilon_{gji} T_g^4 \sigma F_{ij}\right] \quad . \tag{6-10}$$

By interchanging the i and j in Equation (6-10), an expression for E_{ji}^A is obtained

$$E_{ji}^A = \mu_j(1-\varepsilon_j)\left[\left(E_i^I F_{ji} + E_{ij}^A \frac{A_i}{A_j}\right)\tau_{ij} + \varepsilon_{gij} T_g^4 \sigma F_{ji}\right] \quad . \tag{6-11}$$

Eliminating E_{ji}^A from Equations (6-10) and (6-11), the expression for E_{ij}^A is obtained

$$E_{ij}^A = \frac{\mu_i(1-\varepsilon_i)F_{ij}\{[E_j^I + \mu_j(1-\varepsilon_j)E_i^I\tau_{ij}]\tau_{ij} + \sigma\varepsilon_{gij}T_g^4[1+\mu_j(1-\varepsilon_j)\tau_{ji}]\}}{[1-\mu_i(1-\varepsilon_i)\mu_j(1-\varepsilon_j)\tau_{ij}\tau_{ji}]} \quad . \tag{6-12}$$

Combining Equations (6-6) and (6-7), a relation for E_i^I is obtained

$$E_i^I = \frac{\varepsilon_i\sigma T_i + (1-\mu_i)(1-\varepsilon_i)\sum_{j=1} F\{[E_j + \mu_j(1-\varepsilon_j)\tau_{ij}E_i]\tau_{ji} + \sigma\varepsilon_{gji}T_g^4[1+\mu_j(1-\varepsilon_j)\tau_{ij}]\}}{[1-\mu_i(1-\varepsilon_i)\mu_j(1-\varepsilon_j)\tau_{ij}\tau_{ji}]} \quad . \tag{6-13}$$

Equation (6-11) is written in the following form:

$$\sum_{j=1}^{n}\left\{\left[1-\sum_{k=1}^{n}\frac{(1-\mu_i)(1-\varepsilon_i)\mu_k(1-\varepsilon_k)\tau_{ki}\tau_{ik}F_{ik}}{1-\mu_i(1-\varepsilon_i)\mu_k(1-\varepsilon_k)\tau_{ki}\tau_{ik}}\right]\delta_{ij}-\frac{(1-\mu_i)(1-\varepsilon_i)\tau_{ji}F_{ij}}{1-\mu_i(1-\varepsilon_i)\mu_j(1-\varepsilon_j)\tau_{ji}\tau_{ij}}\right\}E_j^I$$

$$= \varepsilon_i\sigma T_i^4+\sigma(1-\mu_i)(1-\varepsilon_i)\sum^{n}\frac{\varepsilon_{gji}T_g^4[1+\mu_j(1-\varepsilon_j)\tau_{ij}]F_{ij}}{1-\mu_i(1-\varepsilon_i)(1-\varepsilon_j)\tau_{ji}\tau_{ij}} \qquad (6\text{-}14)$$

where δ_{ij} is the Kronecker delta function and is defined as

$$\delta_{ij} = \begin{cases} 1 \ \text{when} \ (i = j) \\ 0 \ \text{when} \ (i \neq j) \end{cases} \quad . \qquad (6\text{-}15)$$

Equation (6-14) is solved for E_j^I by using a matrix inversion method.

As mentioned earlier, in the absence of liquid droplets, ε_{lji} is zero and ε_{gji} is equal to $(1 - \tau_{ji})$. If the radiation exchange is assumed to be isotropic (i.e., $\mu_i = 0$ and $\mu_j = 0$), Equation (6-14) becomes

$$\sum_{i=1}^{n}[\delta_{ij}-(1-\varepsilon_i)\tau_{ji}F_{ij}]E_j = \varepsilon_i\sigma T_i^4+\sigma(1-\varepsilon_i)\sum_{i=1}^{n}\varepsilon_{gji}T_g^4F_{ij} \quad . \qquad (6\text{-}16)$$

The surface heat flux q_i is the difference between the outgoing and incident radiation and can be written as

$$q_i = E_i - I_i \quad . \qquad (6\text{-}17)$$

Substituting for E_i from Equation (6-1)

$$q_i = [e\ \sigma T_i^4+(1-\varepsilon_i)I_i]-I_i \quad . \qquad (6\text{-}18)$$

Substituting for I_i from Equation (6-2)

$$q_i = \varepsilon_i\left[\sigma T_i^4-\frac{(E_i^I-\varepsilon_i\sigma T_i^4)}{(1-\mu)(1-\varepsilon_i)}\right] = \frac{\varepsilon_i}{(1-\mu)(1-\varepsilon_i)}\{\sigma T_i^4[1-\mu(1-\varepsilon_i)]-E_i^I\} \quad . \qquad (6\text{-}19)$$

The net heat flux, q_i, to or from any surface i consists of two parts, as shown in Figure 6-2. One part is the net heat flux exchange with other surfaces, q_{is}; and the other part is the net flux exchange with the coolant gas, q_{ig}. It implies that whatever net surface to surface heat flux, q_{is}, is released by the hotter rods gets absorbed by the cooler rods. Therefore,

$$Q_r = \sum_{i=1}^{n} A_i q_{is} = 0 \quad . \tag{6-20}$$

This leads to the relation

$$Q_t = \sum_{i=1}^{n} A_i q_i = \sum_{i=1}^{n} A_i (q_{ig} q_{is}) = \sum_{i=1}^{n} A_i q_{ig} + \sum_{i=1}^{n} A_i q_{is} \quad . \tag{6-21}$$

Substituting for $\sum_{i=1}^{n} A_i q_{is}$ from Equation (6-20)

$$Q_t = \sum_{i=1}^{n} A_i q_{ig} = Q_g \quad . \tag{6-22}$$

This means that the algebraic sum of net heat flux exchange with the surroundings for all the surfaces, Q_t, equals the total heat absorbed by the coolant gas, Q_g.

The total energy absorbed by the coolant, Q_t, can be found by the following relation:

$$Q_t = \sum_{i=1}^{n} A_i q_i = \sum_{i=1}^{n} \frac{A_i \varepsilon_i}{(1-\mu_i)(1-\varepsilon_i)} \sigma T_i^4 [1 - \mu_i (1 - \varepsilon_i)] - E_i^I \quad . \tag{6-23}$$

The energy absorbed by the gas, Q_g, is also given by the following relation:

$$Q_g = \sum_{i=1}^{n} A_i \sum_{i=1}^{n} [a_{gij} (E_i^I F_{ij} + E_{ij}^A) - \varepsilon_{gij} \sigma T_g^4 F_{ij}] \quad . \tag{6-24}$$

The first term on the right hand side of Equation (6-24) is the amount of radiation absorbed by the vapor along the path i to j. The second term is the amount of radiation emitted by the vapor phase.

6.1.1 View Factors

The following expressions for the view factors have been derived using the crossed string method. This method is described in several textbooks.[6-9,6-10] Cox,[6-11] Mandell,[6-12] and Evans[6-13] have used this method to derive view factors between rods for nuclear reactor applications. With reference to Figure 6-3, the view factor of Rod 1 with respect to Rod 2 (closest to Rod 1), F_{12}, is given by the following:

$$F_{12} = 0.5 + \frac{R_2 - R_1}{2\pi R_1}\cos^{-1}\left[\frac{R_2 - R_1}{P_{12}}\right] - \frac{R_1 + R_2}{2\pi R_1}\sin^{-1}\left\{\frac{[P_{12}^2 - (R_1 + R_2)^2]^{1/2}}{P_2}\right\} + \frac{1}{2\pi R_1}\{[P_{12}^2 - (R_1 + R_2)^2]^{1/2} - [P_{12}^2 - (R_1 - R_2)^2]^{1/2}\} \tag{6-25}$$

where

R_1, R_2... = the radii of Rods 1, 2, ... respectively (m)

P_{12}, P_{23}... = the pitches between Rods 1 and 2, Rods 2 and 3, ...respectively (m).

For $R_1 = R_2 = R$ and $P_{12} = P$, Equation (6-25) reduces to the following:

$$F_{12} = 0.5 - \frac{1}{\pi}\sin^{-1}\left[\frac{(P^2 - 4R^2)^{1/2}}{P}\right] + \frac{1}{2\pi R}[(P^2 - 4R^2)^{1/2} - P] \quad . \tag{6-26}$$

For diagonally located rods, the view factor F_{13} (refer to Figure 6-3) is given by the following relation, which can be derived using the crossed string method:

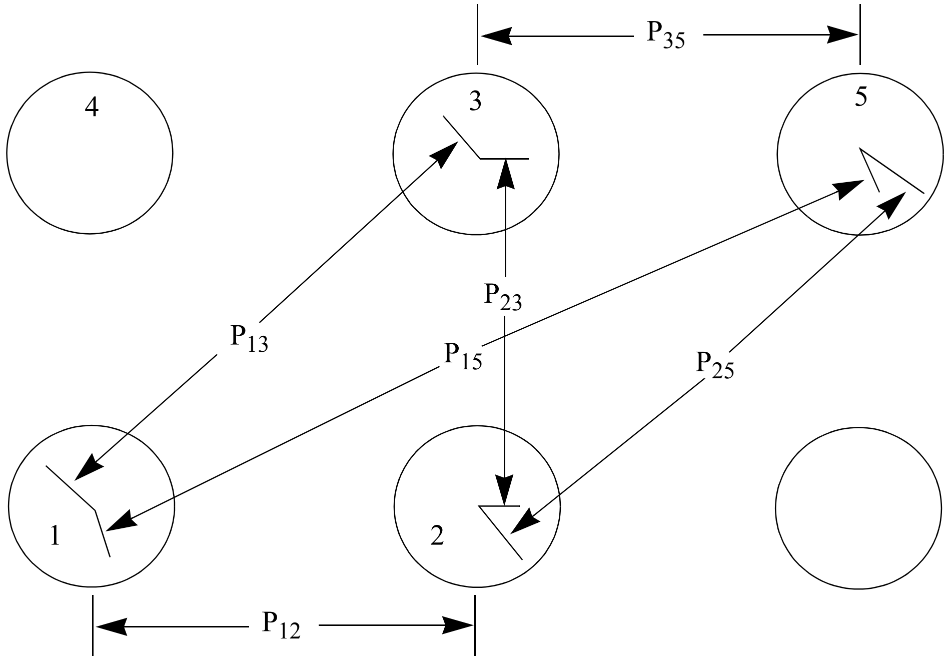
P35
4
3
5
P13
P23
P15
P25
1
2
P12

Figure 6-3. Geometry for determining view factors between rods.

$$
\begin{aligned}
F_{13} = \Bigg\{ \quad & 2\sqrt{P_{13}^2-(R_1+R_3)^2}-\sqrt{P_{12}^2-(R_1+R_2)^2}-\sqrt{P_{23}^2-(R_2+R_3)^2} \\
& -\sqrt{P_{34}^2-(R_3+R_4)^2}-\sqrt{P_{14}^2-(R_1+R_4)^2} \\
& + R_2\left[-\frac{\pi}{2}+\sin^{-1}\left(\frac{\sqrt{P_{12}^2-(R_1+R_2)^2}}{P_{12}}\right)+\sin^{-1}\left(\frac{\sqrt{P_{23}^2-(R_2+R_3)^2}}{P_{23}}\right)\right] \\
& + R_4\left[-\frac{\pi}{2}+\sin^{-1}\left(\frac{\sqrt{P_{34}^2-(R_3+R_4)^2}}{P_{34}}\right)+\sin^{-1}\left(\frac{\sqrt{P_{14}^2-(R_1+R_4)^2}}{P_{14}}\right)\right] \\
& + R_1\left[\frac{\pi}{2}+\sin^{-1}\left(\frac{\sqrt{P_{12}^2-(R_1+R_2)^2}}{P_{12}}\right)+\sin^{-1}\left(\frac{\sqrt{P_{14}^2-(R_1+R_4)^2}}{P_{14}}\right)\right] \\
& + R_3\left[\frac{\pi}{2}+\sin^{-1}\left(\frac{\sqrt{P_{23}^2-(R_2+R_3)^2}}{P_{23}}\right)+\sin^{-1}\left(\frac{\sqrt{P_{34}^2-(R_3+R_4)^2}}{P_{34}}\right)\right] \\
& -2(R_1+R_3)\sin^{-1}\left(\frac{\sqrt{P_{13}^2-(R_1+R_3)^2}}{P_{13}}\right) \Bigg\}\frac{1}{4\pi R_1} \quad .
\end{aligned}
\tag{6-27}
$$

For $R_1 = R_2 = R_3 = R_4 = R$, $P_{12} = P_{23} = P_{34} = P_{41} = P$, and $P_{13} = P_{24} = \sqrt{2}P$, (6-27) simplifies to the following form:

$$
\begin{aligned}
F_{13} = \frac{1}{2\pi R}\Bigg\{ \quad & \sqrt{2P^2-R^2}-2\sqrt{P^2-R^2}+R\left[-\frac{\pi}{2}+2\ \sin^{-1}\left(\frac{\sqrt{P^2-R^2}}{P}\right)\right]+ \\
& +R\left[\frac{\pi}{2}+2\ \sin^{-1}\left(\frac{\sqrt{P^2-R^2}}{P}\right)\right]-2R\ \sin^{-1}\left(\frac{\sqrt{2P^2-R^2}}{\sqrt{2}P}\right)\Bigg\} \quad .
\end{aligned}
\tag{6-28}
$$

Derivation of view factors of a third nearest rod (Figure 6-3), F_{15}, is similar to that for the diagonal rod:

$$\begin{aligned} F_{15} = \Bigg\{ & 2\sqrt{P_{15}^2 - (R_1 + R_5)^2} - \sqrt{P_{12}^2 - (R_1 + R_2)^2} - \sqrt{P_{25}^2 - (R_2 + R_5)^2} \\ & - \sqrt{P_{35}^2 - (R_3 + R_5)^2} - \sqrt{P_{13}^2 - (R_1 + R_3)^2} \\ & + R_1\left[\frac{\pi}{4} + \sin^{-1}\left(\frac{\sqrt{P_{12}^2 - (R_1 + R_2)^2}}{P_{12}}\right) + \sin^{-1}\left(\frac{\sqrt{P_{13}^2 - (R_1 + R_3)^2}}{P_{13}}\right) - 2\sin^{-1}\left(\frac{\sqrt{P_{15}^2 - (R_1 + R_5)^2}}{P_{15}}\right)\right] \\ & + R_3\left[-\frac{\pi}{4} + \sin^{-1}\left(\frac{\sqrt{P_{25}^2 - (R_2 + R_5)^2}}{P_{25}}\right) + \sin^{-1}\left(\frac{\sqrt{P_{35}^2 - (R_3 + R_5)^2}}{P_{35}}\right) - 2\sin^{-1}\left(\frac{\sqrt{P_{15}^2 - (R_1 + R_5)^2}}{P_{15}}\right)\right] \\ & - R_2\left[\frac{\pi}{4} - \sin^{-1}\left(\frac{\sqrt{P_{12}^2 - (R_1 + R_2)^2}}{P_{12}}\right) + \sin^{-1}\left(\frac{R_2 + R_5}{P_{25}}\right)\right] \\ & - R_3\left[\frac{\pi}{4} - \sin^{-1}\left(\frac{\sqrt{P_{35}^2 - (R_3 + R_5)^2}}{P_{35}}\right) + \sin^{-1}\left(\frac{R_1 + R_3}{P_{13}}\right)\right] \Bigg\}\left(\frac{1}{4\pi R_1}\right) . \end{aligned} \tag{6-29}$$

For $R_1 = R_2 = R_3 = R_5 = R$, the relation for view factor F_{15} simplifies to the following:

$$\begin{aligned} F_{15} = {} & \frac{1}{4\pi R}[2\sqrt{P_{15}^2 - 4R^2} - \sqrt{P_{12}^2 - 4R^2} - \sqrt{P_{25}^2 - 4R^2} - \sqrt{P_{35}^2 - 4R^2} - \sqrt{P_{13}^2 - 4R^2}] \\ & + \frac{1}{4\pi}\left[2\sin^{-1}\left(\frac{\sqrt{P_{12}^2 - 4R^2}}{P_{12}}\right) + 2\sin^{-1}\left(\frac{\sqrt{P_{35}^2 - 4R^2}}{P_{35}}\right) + \sin^{-1}\left(\frac{\sqrt{P_{15}^2 - 4R^2}}{P_{15}}\right) + \sin^{-1}\left(\frac{\sqrt{P_{25}^2 - 4R^2}}{P}\right)\right] \\ & - \frac{1}{\pi R}\left[\sin^{-1}\left(\frac{\sqrt{P_{15}^2 - 4R^2}}{P_{15}}\right) - \sin^{-1}\left(\frac{2R}{P_{25}}\right) - \sin^{-1}\left(\frac{2R}{P_{13}}\right)\right] . \end{aligned} \tag{6-30}$$

For the rods placed in a square geometry, this expression is further simplified to the following. In this case,

$$P_{12} = P_{35} = P, P_{25} = P_{13} = \sqrt{2}P \text{ and } P_{15} = \sqrt{5}P \quad .$$

$$\begin{aligned} F_{15} = {} & \frac{1}{4\pi R}2\sqrt{5P^2 - 4R^2} - 2\sqrt{2P^2 - 4R^2} - 2\sqrt{P^2 - 4R^2} + 4\sin^{-1}\frac{\sqrt{P^2 - 4R^2}}{P} + -2\sin^{-1}\frac{\sqrt{5P^2 - 4R^2}}{\sqrt{5}P} \\ & + \sin^{-1}\frac{\sqrt{2P - R4^2}}{\sqrt{2}P} \quad + \frac{1}{2\pi}\sin^{-1}\left(\frac{\sqrt{P^2 - 4R^2}}{P}\right) - 2\sin^{-1}\left(\frac{\sqrt{5P^2 - 4R^2}}{5P}\right) - 2\sin^{-1}\frac{\sqrt{2R}}{P} \quad . \end{aligned} \tag{6-31}$$

All the view factors described above are for cylindrical rods of infinite length. According to Juul,[6-14] for a typical reactor core $\frac{P}{R} \approx 3.0$ the application of infinite length view factors to a case of finite length does not cause any significant error (~5%). Therefore, it is reasonable to use Equations (6-25) through (6-31) to calculate view factors for rods of finite length.

To evaluate view factors between all the rods in a bundle, the following methodology and assumptions are used.

For any surface in an enclosure, the summation rule,

$$\sum_{i = 1}^{n} F_{ij} = 1 \tag{6-32}$$

must be satisfied. This rule implies that for an enclosure, all the radiant energy leaving any surface must reach other surfaces (including itself). In the present model, no rod sees another rod beyond two rows or columns. This assumption implies that a portion of energy leaving a rod that would have reached some rods lying beyond two rows or columns has to be accounted for elsewhere. Therefore, the residual view factor of a component group is distributed to other component groups in proportion to the original view factors. To calculate the view factor, F_{ij}, from one component group i to another component group j, the following relation is used:

$$F_{IJ} = \frac{1}{N_I} \sum_{i = 1}^{N_I} \sum_{i = 1}^{N_J} F_{ij} \tag{6-33}$$

where

N_I = the number of rods in component group I

N_J = the number of rods in component group J.

All the rods in one component group have the same radius. The view factor evaluation also must satisfy the reciprocity rule, $A_I F_{IJ} = A_J F_{JI}$. This rule implies that the ratio of the view factors of two surfaces with each other is equal to the inverse of the ratio of their respective areas. Therefore, the view factors F_{IJ} for I > J have been obtained by the reciprocity rule. For I < J, the view factors are obtained from first principles and by using Equation (6-33). For I + J, the summation rule is used to obtain the view factor of a component group to itself.

If a shroud is present around a bundle of M x N size, only the outermost rows and columns of rods (i = 1 or M, or j = 1 or N) are considered to exchange radiant energy with the shroud. In such a case, the residual view factor for these peripheral rods is accounted for in the view factor to the shroud. Thus, for these rods, $R_{ii} = 0$; but the component group I to which the rod i belongs can still see itself, that is, F_{II} can be nonzero. If a rod is missing in the peripheral location of the bundle, the rod next to it in the inner row and column ($1 < i < M$ or $1 < i < M$) is allowed to exchange energy with the shroud just as a peripheral rod. The view factors of the shroud also have to satisfy the summation and reciprocity rules.

6.1.2 Mean Path Length

According to Siegel and Howell[6-9], mean path length is defined as a fictitious length (i.e., the radius of a gas hemisphere) such that the radiation heat flux to the center of its base is equal to the average radiation flux exchange by the gas and two surface areas containing the actual volume of gas.

For any two areas A_i and A_j located at a distance of S (shortest distance along the path of radiation), let β_i and β_j be the angles between the shortest distance line and the normals on the two surfaces, respectively. Then the mean path length, L_{ij}, can be evaluated by

$$L_{ij} = \frac{1}{a_{gij}} \ln \frac{1}{A_i F_{ij}} \int_{A_i}\int_{A_j} e^{(-a_{gij} S)} \frac{\cos\beta_i \cos\beta_j}{\pi S^2} dA_i dA_j \quad . \tag{6-34}$$

This equation is difficult to evaluate for a reactor vessel with complicated rod geometry. Therefore, as is done for other radiation models,[6-1, 6-4] the mean path length is taken to be equal to, or a function of, the distance between the two geometries for which the radiation solution is being sought. The path length between any two rods is obtained by the following equation:

$$L_{ij} = P_{ij} - \frac{\pi}{2}(R_i + R_j) \quad . \tag{6-35}$$

To calculate the average path length between two component groups, the path length between any two rods (subcomponents) is weighted by the corresponding view factor. If N_I and N_J are the number of rods (subcomponents) in component groups I and J, respectively, then the average path length between any two component groups and J is given by (optically this approximation)

$$L_{ij} = \frac{\sum_{i=1}^{N_I}\sum_{j=1}^{N_J} F_{ij} L_{ij}}{\sum_{i=1}^{N_I}\sum_{j=1}^{N_J} F_{ij}} \quad . \tag{6-36}$$

6.1.3 Absorptivities and Emissivities

The absorptivities and emissivities of the surfaces are obtained from MATPRO.

When the cladding surface temperature has not exceeded 1,500 K, the surface emissivity (which equals absorptivity) is modeled by Equation (6-37). For oxide layer thicknesses of 3.88 x 10^6 m or greater,

$$\varepsilon_1 = 0.808642 - 50.0\ d \tag{6-37}$$

where

ε_1 = hemispherical emissivity (unitless)

d = oxide layer thickness (m).

When the maximum cladding temperature has exceeded 1,500 K, emissivity is taken to be the larger of 0.325 and

$$\varepsilon_2 = \varepsilon_1 \exp\left[\frac{1500 - T}{300}\right] \tag{6-38}$$

where

ε_1 = value for emissivity obtained from Equation (6-37)

T = maximum cladding temperature (K).

Zirconium oxide thickness would be expected to vary from zero to about 900 µm. A value of 300 µm is taken that results in an average value of ε_1 of 0.7936. The shroud surface is assumed to have the same radiation properties as the fuel rods.

Vapor absorptivities and emissivities are calculated in the same manner as is done in the TRAC-BD1 code.[6-1] For vapor, the absorption coefficient K_{gij} is evaluated after determining emissivity and absorptivity

$$K_{gij} = \frac{\ln(1 - a_{gij})}{L_{ij}} \quad . \tag{6-39}$$

The emissivity and absorptivity of the gaseous medium are obtained in a manner similar to that used in TRAC-BD1.[6-1] That method is reproduced here for the sake of completeness.

The emissivity of an absorbing gaseous medium for monochromatic radiation of wave length λ is given by the following equation:

$$\varepsilon_\lambda = 1 - e^{(-K_\lambda p L_{ij})} \tag{6-40}$$

where

p = pressure (Pa)

K_λ = spectral absorption coefficient (Pa x μm)$^{-1}$.

The total hemispherical emittance is defined as the ratio of the emissive power e of a given surface to that of a black surface e_b at the same temperature.

$$e_g = \frac{e}{e_b} = \frac{\int_o^\infty \varepsilon_\lambda e_{b\lambda}(T)d\lambda}{\int_o^\infty e_{b\lambda}(T)d\lambda} = \frac{\int_o^\infty \varepsilon_\lambda e_{b\lambda}(T)d\lambda}{\sigma T^4} \quad . \tag{6-41}$$

The Planck function, $e_{b\lambda}$is given by

$$e_{b\lambda} = \frac{\frac{2\pi hC^2}{\lambda^3}}{e^{\left(\frac{hC}{\lambda kT}\right)} - 1} \tag{6-42}$$

where

h = Planck's constant, (6.625 x 10^{-34} J•s)

k = Boltzmann's constant (1.38 x 10^{-23} J/K)

C = the speed of light in the medium, speed of light in vacuum/refractive index of the medium (2.998 x 10^8 m/s)/refractive index of the medium.

The absorptivity, a_λ, of the medium is obtained by evaluating an equation similar to that for emissivity at the temperature of the surface emitting the radiation incident on the absorbing medium.

$$a_\lambda = \frac{\int_o^\infty a\ e_{b\lambda}(T_s)d\lambda}{\sigma T_s^4} \tag{6-43}$$

where $a_\lambda = \varepsilon_\lambda$ by Kirchhoff's law in thermodynamic equilibrium.

The absorption spectrum of water vapor is considered to consist of six major absorption bands, as reported by Hottel and Sarofim.[6-15] Table 6-1 shows the wave length and absorption coefficients, $K_{\lambda o}$, of these bands at 300 K. At other temperatures, absorption coefficients can be obtained by

$$K_{\lambda} = K_{\lambda o}\left(\frac{300}{T}\right) \quad . \tag{6-44}$$

The values of K_{λ} used in the present model are assumed to be constant within each wave length band and zero elsewhere. Therefore, integral relations for emissivity and absorptivity can be approximated as the sums over the wavelength bands given in Table 6-1.

Table 6-1. Water vapor absorption.

Wavelength at band center (μm)	**Minimum wavelength (μm)**	**Maximum wavelength (μm)**	**Absorption coefficient $K_{\lambda o}$ (Pa x μ)$^{-1}$**
1.1	1.1017	1.1809	0.523
1.38	1.3243	1.4405	13.42
1.87	1.7693	1.9829	16.38
2.87	2.495	2.942	204.19
6.3	5.2854	7.7942	283.64
20.0	12.43	51.1509	94.65

$$\varepsilon_g = \frac{1}{\sigma T^4}\sum_{i=1}^{6} \varepsilon_{\lambda i} e_{\lambda i}\ (T)\Delta\lambda_i \tag{6-45}$$

$$a_g = \frac{1}{\sigma T_s^4}\sum_{i=1}^{6} \varepsilon_{\lambda i} e_{\lambda i}(T_{s)})\Delta\lambda_i \tag{6-46}$$

where

i = wavelength band index

$e_{\lambda i}$ = average value of the Planck black body function evaluated at the wavelength at band center

T = temperature of the gaseous medium

6.2 References

6-1. J. W. Spore et al., *TRAC-BD1: An Advanced Best Estimate Computer Program for Boiling Water Reactor Loss of Coolant Accident Analysis*, NUREG/CR-2178, EGG-2109, October 1981.

6-2. J. W. Spore, M. M. Giles, and R. W. Shumway, “A Best Estimate Radiation Heat Transfer Model Developed for TRAC-BD1,” ASME Paper No. 80-HT-68, *20th Joint ASME/AIChE National Heat Transfer Conference, Milwaukee, WI, August 1981.*

6-3. C. J. Shaffer, “Importance of Thermal Radiation to Steam in Rod Bundles,” *Topical Meeting on Water Reactor Safety, Salt Lake City, UT, March 26-28, 1973, pp. 371-379.*

6-4. D. A. Mandell, *A Radiative Heat Transfer Model for the TRAC Code*, NUREG/CR-0994, LA-7965-MS, November 1979.

6-5. J. G. M. Anderson et al., *NORCOOL I, A Model for the Analysis of a BWR Under LOCA Conditions*, NORHAV-D-47, August 1977.

6-6. J. G. M. Anderson and H. Abel-Larsen, *CORECOOL Model Description of the Programme*, RISO-M-2138, November 1978.

6-7. J. G. M. Anderson and C. L. Tien, “*Radiation Heat Transfer in a BWR Fuel Bundle Under LOCA Conditions*,” Fluid Flow and Heat Transfer Over Rod or Tube Bundles, S. C. Yao and P. A. Pfund (eds.), ASME, New York, NY, 1979, pp. 197-207.

6-8. K. H. Sun, J. M. Gonzales-Santalo, and C. L. Tien, “Calculations of Combined Radiation and Convection Heat Transfer in Rod Bundle Under Emergency Cooling Conditions,” *Journal of Heat Transfer, 98,* 1976, pp. 414-420.

6-9. R. Siegel and J. R. Howell, *Thermal Radiation Heat Transfer*, New York: McGraw-Hill Book Company, 1972.

6-10. E. M. Sparrow and R. D. Cess, *Radiation Heat Transfer*, Belmont: Brooks/Cole Publishing Company, 1966.

6-11. R. L. Cox, *Radiative Heat Transfer in Arrays of Parallel Cylinders*, ORNL-5239, June 1977.

6-12. D. A. Mandell, “Geometric View Factors for Radiative Transfer Within Boiling Water Reactor Fuel Bundles,” *Nuclear Technology, 52,* 1981, pp. 383-392.

6-13. D. R. Evans, *The MOXY Digital Computer Program for Boiling Water Reactor Core Thermal Analysis*, RE-A-77-081, September 1981.

6-14. N. H. Juul, “View Factors in Radiation Between Two Parallel Oriented Cylinders of Finite Lengths,” *Journal of Heat Transfer, 104,* 1982, pp. 384-388.

6-15. H. C. Hottel and A. F. Sarofim, *Radiative Transfer*, New York: McGraw-Hill Book Company, 1967.

7. UPPER PLENUM STRUCTURES AND LOWER CORE PLATE

SCDAP/RELAP5-3D$^{©}$ calculates the oxidation and meltdown of structures above and below the reactor core which may influence the overall behavior of the reactor coolant system. These structures include the core plate and upper plenum structure.

7.1 Upper Plenum Structures and Lower Core Plate

The upper plenum structure (UPS) model for SCDAP/RELAP5-3D$^{©}$ has been developed to represent the severe accident response of structures located in the upper plenums of PWRs or BWRs. It includes generalized features that allow a single model to represent a range of geometric configurations. Unlike the RELAP5 heat structure model, the UPS model includes calculations for oxidation, melting, and downward relocation. This chapter provides a brief description of the model used to represent the upper plenum structures.

7.1.1 Nodal Geometry

The UPS model is based on the general configuration shown in Figure 7-1. The user divides an upper plenum structure into axial levels (the example in Figure 7-1 shows four axial levels). At each axial level, the structure can be defined as having either a vertical orientation (with left and right surfaces) or a horizontal orientation (with bottom and top surfaces). The temperature gradient through the structure is represented at each axial level by one or more conduction nodes defined by the user. Conduction and other heat transfer processes are modeled in a direction perpendicular to the structure orientation. Conduction heat transfer between axial levels is not considered.

The UPS model is based on a slab geometry with rectangular coordinates, but can be applied to a cylindrical structure such as a tube if the wall thickness is small relative to the radius of curvature. The physical dimensions specified by the user at each axial level are the structure surface area and the thicknesses of the conduction nodes. An upper plenum structure interacts with RELAP5 hydraulic volumes at both the left and right (or bottom and top) surfaces of the structure. This interaction includes convective heat transfer and oxidation.

All major structures in PWR and BWR upper plenums are made of stainless steel. The UPS model is therefore solved based upon the premise that there is a single material (stainless steel) with a unique melting temperature (i.e., there are no material interactions). Because the upper plenum structures have no internal heat sources, all heating and melting occurs at the outer surfaces. As a structure melts, molten material should not become superheated to any significant extent because either; (1) the molten material will quickly relocate to a lower elevation or below the bottom of the structure, or (2) more of the underlying solid structure will melt (this applies even when molten material accumulates on top of a horizontal surface.

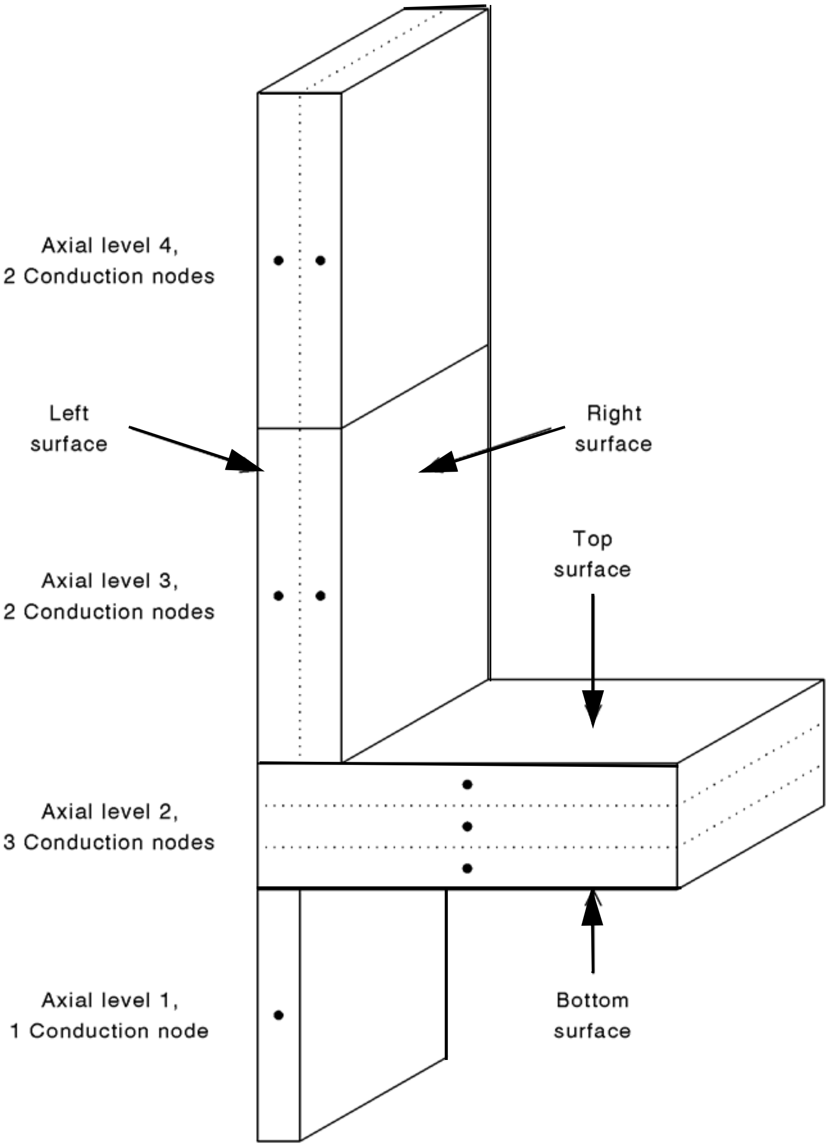
Axial level 4,
2 Conduction nodes
Left
surface
Right
surface
Top
surface
Axial level 3,
2 Conduction nodes
Axial level 2,
3 Conduction nodes
Axial level 1,
1 Conduction node
Bottom
surface

Figure 7-1. UPS model terminology for example configuration with 4 axial levels.

7.1.2 Energy/Conduction Equation with Melting

The differential equation for 1-D conduction heat transfer with melting is non-linear and requires a specialized solution method to account for the heat of fusion. A two-step process is applied in the UPS model. First, the conduction equation is solved without consideration of melting using an implicit solution method to ensure numerical stability. Then, if melting occurs during the timestep, the conduction solution is repeated to account for the change of phase. A finite difference formulation in terms of the nodal temperatures is used to model the thermal response of an upper plenum structure. Using the nomenclature defined in the Figure 7-1, the energy/conduction equation for the first node (left side of Figure 7-1) is Equation (7-1).

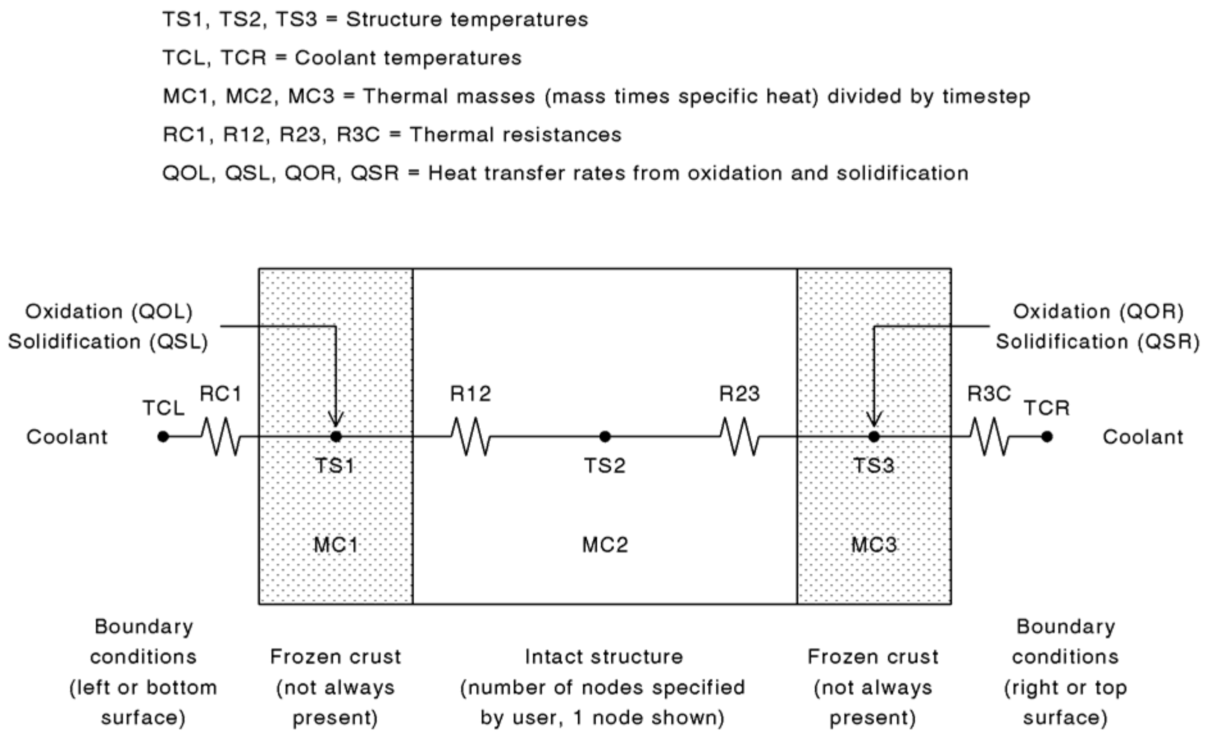
TS1, TS2, TS3 = Structure temperatures
TCL, TCR = Coolant temperatures
MC1, MC2, MC3 = Thermal masses (mass times specific heat) divided by timestep
RC1, R12, R23, R3C = Thermal resistances
QOL, QSL, QOR, QSR = Heat transfer rates from oxidation and solidification
Oxidation (QOL)
Solidification (QSL)
Oxidation (QOR)
Solidification (QSR)
TCL
RC1
R12
R23
R3C
TCR
Coolant
Coolant
TS1
TS2
TS3
MC1
MC2
MC3
Boundary conditions (left or bottom surface)
Frozen crust (not always present)
Intact structure (number of nodes specified by user, 1 node shown)
Frozen crust (not always present)
Boundary conditions (right or top surface)

Figure 7-2. Nomenclature for solution of 1-D heat conduction equation at each axial level.

$$\mathrm{MC1}(\mathrm{TS1}_{\mathrm{new}} - \mathrm{TS1}_{\mathrm{old}}) = \frac{(\mathrm{TCL} - \mathrm{TS1}_{\mathrm{new}})}{\mathrm{RC1}} + \frac{(\mathrm{TS2}_{\mathrm{new}} - \mathrm{TS1}_{\mathrm{new}})}{\mathrm{R12}} + \mathrm{QOL} + \mathrm{QS(L.)} \tag{7-1}$$

When similar finite difference equations are written for the other nodes, they form a linear system of algebraic equations with a tridiagonal arrangement as shown in Equation (7-2).

$$\begin{bmatrix} \mathrm{MC1} + \frac{1}{\mathrm{R12}} + \frac{\mathrm{RC1}}{1} & \frac{-1}{\mathrm{R12}} & 0 \\ \frac{-1}{\mathrm{R12}} & \mathrm{MC2} + \frac{1}{\mathrm{R12}} + \frac{1}{\mathrm{R23}} & \frac{-1}{\mathrm{R23}} \\ 0 & \frac{-1}{\mathrm{R23}} & \mathrm{MC3} + \frac{1}{\mathrm{R23}} + \frac{1}{\mathrm{R3C}} \end{bmatrix} \begin{bmatrix} \mathrm{TS1}_{\mathrm{new}} \\ \mathrm{TS2}_{\mathrm{new}} \\ \mathrm{TS3}_{\mathrm{new}} \end{bmatrix} = \begin{bmatrix} \mathrm{MC1\ TS1}_{\mathrm{old}} + \frac{\mathrm{TCL}}{\mathrm{RC1}} + \mathrm{QOL} + \mathrm{QSL} \\ \mathrm{MC2\ TS2}_{\mathrm{old}} \\ \mathrm{MC3\ TS3}_{\mathrm{old}} + \frac{\mathrm{TCR}}{\mathrm{R3C}} + \mathrm{QOR} + \mathrm{QSR} \end{bmatrix} . \tag{7-2}$$

Material properties (specific heat, etc.) for the matrix elements are obtained from the MATPRO library. The nodal temperatures at a new time ($\mathrm{TS1}_{\mathrm{new}}$, etc.) are calculated simultaneously from the temperatures at the previous time ($\mathrm{TS1}_{\mathrm{old}}$, etc.) using standard matrix methods.

The implicit solution method for the conduction equation involves a single iteration during a time step to account for any melting. The temperatures of the boundary nodes at a new time are compared with the melting temperature of stainless steel. If the new temperature of a boundary node is greater than the melting temperature, then that node is removed from the calculation and treated as a constant-temperature conduction boundary condition for the adjacent node. For example, if the above matrix solution predicts $TS1_{new} > TS1_{melt}$, then the first equation is removed from the matrix and $TS1_{new} = TS1_{melt}$ for the second equation

$$\begin{bmatrix} MC2 + \frac{1}{R12} + \frac{1}{R23} & \frac{-1}{R23} \\ \frac{-1}{R23} & MC3 + \frac{1}{R23} + \frac{1}{R3F} + \frac{1}{R3G} \end{bmatrix} \begin{bmatrix} TS2_{new} \\ TS3_{new} \end{bmatrix} = \begin{bmatrix} MC2\ TS2_{old} + \frac{TS1_{melt}}{R12} \\ MC3\ TS3_{old} + \frac{TFR}{R3F} + \frac{TGR}{R3G} + QOR + QSR \end{bmatrix} . \qquad (7\text{-}3)$$

The implicit solution for the time step is then repeated to determine the new temperatures of the remaining nodes. The conduction/energy equation for the melting boundary node is used to determine the melting heat transfer rate Equation (7-4)

$$QMELT = \frac{(TCL - TS1_{melt})}{RC1} + \frac{(TS2_{new} - TS1_{melt})}{R12} + QOL + QSL - MC1(TS1_{melt} - TS1_{old}) \qquad (7\text{-}4)$$

and, correspondingly, the mass of stainless steel that melts during the time step.

The melting temperature of stainless steel oxides is greater than the melting temperature of the pure metal. In the UPS model, the stainless steel oxides do not melt, but rather are carried away as a solid with the pure metal as it melts. The mass ratio of oxides carried away with molten metal is 0.5.

The implicit matrix solution of the energy/conduction equation described in this section is implemented in the UPS model for a user-defined number of conduction nodes at each axial level. When all of the stainless steel in a node melts and relocates downward, that node is removed from the solution. When all of the nodes at an axial level melt, the structure at that axial level is removed from the solution and no longer interacts through convective heat transfer and oxidation with the adjoining RELAP5 hydraulic volumes. It is assumed that all portions of a structure located above an axial level that is completely melted are supported from the side or above and do not collapse downward.

7.1.3 Relocation and Solidification Logic

While it is recognized that PWR or BWR upper plenum structures should begin melting at the lowest axial level and that the resulting molten material would relocate downward directly into the core region, the design report EGG-RAAM-11500[7-1] recommends a more generalized relocation and solidification formulation. Accordingly, the UPS model allows for possible freezing of molten stainless steel on the surfaces of upper plenum structures and also permits molten stainless steel to run down vertical surfaces and to collect on horizontal surfaces.

The relocation logic depends on the surface orientation at an axial level and can be explained with the aid of Figure 7-3, which shows a sketch of the possible relocation paths. For a vertical orientation, molten material moves downward along both the left and right surfaces (path 1). A momentum equation is not solved for this downward movement; this material is instead assumed to flow at a constant velocity of 0.5 m/s. Molten material that does not solidify at the lowest axial level of a structure relocates below the defined structure (path 2).

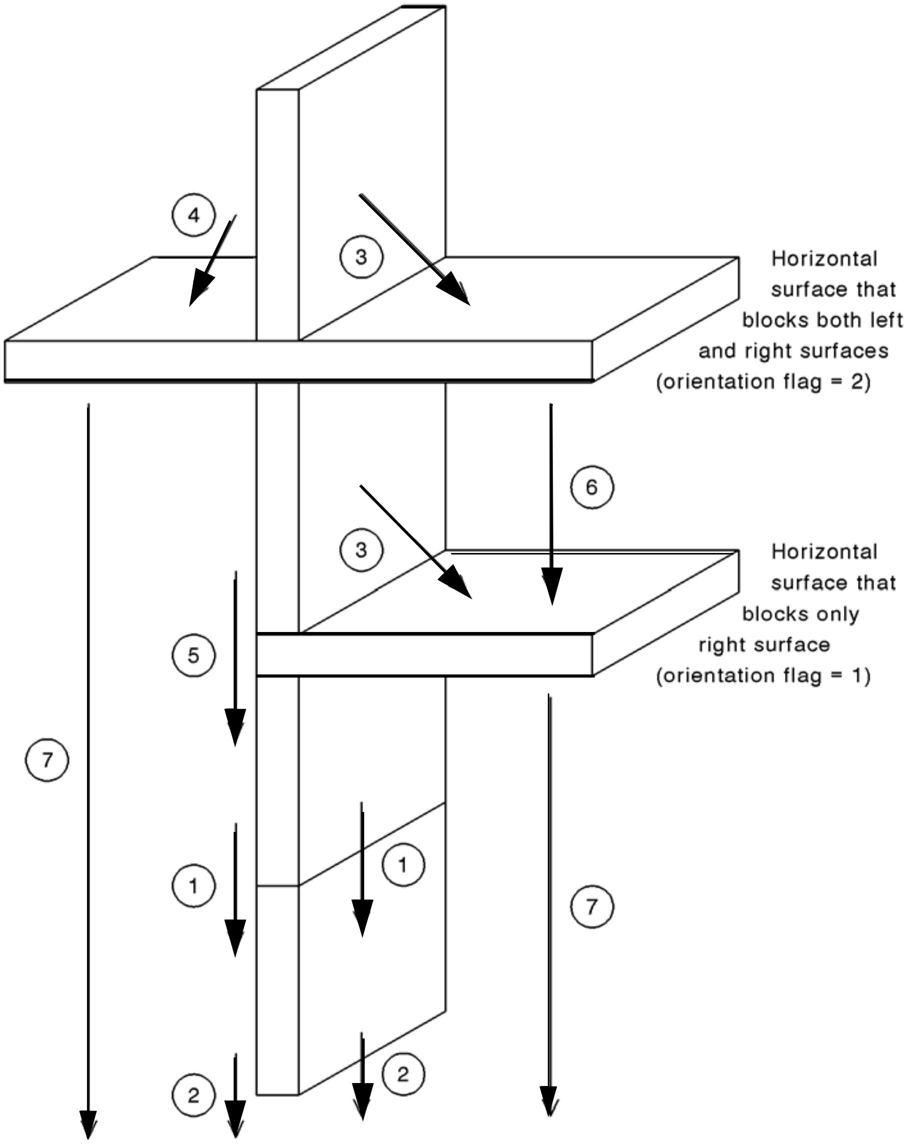
④
③
Horizontal surface that blocks both left and right surfaces (orientation flag = 2)
⑥
③
Horizontal surface that blocks only right surface (orientation flag = 1)
⑤
⑦
①
①
⑦
②
②

Figure 7-3. UPS model relocation logic.

A horizontal surface can block molten material that relocates from an overhead vertical surface. There are two types of horizontal surfaces depending on a user-specified orientation flag (see Figure 7-3). Both types of horizontal surfaces block relocation from a right surface (path 3). One type of horizontal surface also blocks relocation from a left surface (path 4) while the other type does not block relocation from a left surface (path 5). Whenever a horizontal surface blocks relocation, molten material accumulates on its top surface, where it remains until the entire structure at that axial level melts. Molten material from the top or bottom surfaces of a horizontal structure falls freely until it either reaches the next intact horizontal surface (path 6) or relocates below the defined structure (path 7).

The solidification logic allows molten material to transfer heat to and freeze on the left and right surfaces of a vertical structure and the top surface of a horizontal structure. At the beginning of each time step (before the 1-D conduction solution described in Section 7.1.2), solidification heat transfer rates from any molten material to the underlying surfaces (variables QSL and QSR in Figure 7-2) are calculated at each axial level from (1) a heat transfer coefficient, (2) the surface areas of the molten material, and (3) the temperature differences between the molten material and the surface nodes. The heat transfer coefficient used in the UPS model (estimated by assuming pure conduction in the thermal boundary layer) is 17,000 $W/(m^2 \cdot K)$. The surface areas of the molten material may be less than the surface areas of the structure because a layer of molten material is assumed to have a minimum thickness of 0.002 m to account for rivulet flow.

The solidification heat transfer rates are applied as boundary conditions in the energy/conduction equation and are also used to determine the mass of molten material that solidifies during a time step. The solidification calculations include logic to create new crust nodes (refer to Figure 7-2) when the original intact nodes have not begun to melt or have partially melted and then refilled with frozen material.

7.1.4 Oxidation of Stainless Steel

The oxidation logic for the UPS model, which has been adapted from the BWR control blade/channel box component, accounts for oxidation of stainless steel with a chemical composition of 74% Fe, 18% Cr, and 8% Ni. At the beginning of each time step (before the 1-D conduction solution described in Section 7.1.2), oxidation heat generation rates (variables QOL and QOR in Figure 7-2) are calculated at each axial level. These heat generation rates (Cr is an important contributor to these heats of reaction) are applied as boundary conditions in the energy/conduction equation. Steam consumption and hydrogen generation rates are also calculated. The reaction rates are calculated from oxidation kinetics correlations and are limited by the amounts of steam and stainless steel available for reaction.

Three oxidation kinetics correlations are provided for steam-rich, hydrogen-excess, and steam-lean coolant conditions. The applicable correlation is determined using Baker's criteria[7-2] based on the partial pressures of steam and hydrogen present in the coolant. Different combinations of oxide species (FeO, Fe_3O_4, Cr_2O_3, and NiO) are generated for each of these three coolant conditions. The oxidation correlations used for the three coolant conditions are described below.

For steam-rich conditions, White's kinetics correlation[7-3,7-4] is used. The essential chemical reactions for these conditions are:

$$\begin{array}{ccccccccc} 2\,Cr & + & 3\,H_2O & \rightarrow & Cr_2O_3 & + & 3\,H_2 \\ 3\,Fe & + & 4\,H_2O & \rightarrow & Fe_3O_4 & + & 4\,H_2 \\ Ni & + & H_2O & \rightarrow & NiO & + & H_2 \\ 3\,FeO & + & H_2O & \rightarrow & Fe_3O_4 & + & H_2 \end{array}$$

For hydrogen-excess conditions, Baker's correlation[7-2] is used. Ni does not react under these conditions. The oxidation of stainless steel will form a “spinel” compound:

$$2\,Cr + Fe + 4\,H_2O \rightarrow FeO{*}Cr_2O_3 + 4\,H_2$$

For steam-lean conditions, a mean of the above steam-rich and hydrogen-excess correlations is used. Ni does not react under these conditions. The essential chemical reactions are:

$$\begin{array}{ccccccccc} 2\,Cr & + & 3\,H_2O & \rightarrow & Cr_2O_3 & + & 3\,H_2 \\ Fe & + & H_2O & \rightarrow & FeO & + & H_2 \end{array}$$

Whenever an upper plenum structure is at a temperature below the melting temperature of stainless steel, the oxidation rate is generally predicted to be limited by the reaction kinetics. However, when the structure begins to melt and the oxide layer is carried away with the molten stainless steel (refer to the discussion in Section 7.1.2), the oxidation rate is much higher and is limited only by the availability of steam. If sufficient steam is available, the oxidation heat generation will continue to melt the structure without any outside heat sources.

7.1.5 Hydrodynamic Interface

The interface logic controls information exchanges between SCDAP/RELAP5-3D© and the UPS model. The information exchanged is required for the calculation of oxidation and convective heat transfer. The parameters passed to the UPS oxidation calculation at the beginning of each time step are the partial pressures of steam and hydrogen and the mass flow rate of steam available for oxidation. When the user specifies that several UPS surfaces are adjacent to the same hydraulic volume, then the amount of steam available for oxidation at a surface is partitioned using a surface-area-weighted average for the volume. The parameters returned by the oxidation calculation at the end of each time step are the hydrogen generation rate and enthalpy. RELAP5 calculates the steam consumption rate from this hydrogen generation rate.

The parameters passed to the UPS convective heat transfer calculation at the beginning of each time step are the coolant (liquid and vapor) average temperature and average heat transfer coefficient. A SCDAP utility subroutine (HTRC1) is used to calculate the average heat transfer coefficient for several single- and two-phase coolant conditions. The parameters returned by the convective heat transfer calculation to RELAP5 at the end of each time step are the average heat transfer rate from the wall to the coolant (liquid and vapor) and the vapor mass generation rate at the wall.

The convection boundary conditions are treated implicitly in the 1-D conduction solution described in Section 7.1.2. The heat transfer rates from the coolant to the surfaces of an upper plenum structure are calculated simultaneously in the matrix solution from the coolant temperatures (variables TCL and TCR in Figure 7-2) and the surface node temperatures. This implicit treatment helps to minimize numerical instabilities, especially when nodal masses become very small because an upper plenum structure is melting, or when coolant temperatures are changing rapidly.

7.2 Lower Core Plate

The model for the lower core plate includes generalized features that allow a single model to represent a range of geometric configurations. The user divides a core plate structure into a series of horizontal plates at different axial levels, with each plate having a bottom and top surface. The temperature gradient through each plate is represented by one or more conduction nodes. Conduction and other heat transfer processes are modeled in a direction perpendicular to the structure orientation.

The model is based on a slab geometry with rectangular coordinates, with the physical dimensions specified by the user at each axial level. A structure interacts with hydraulic volumes at both the bottom and top surfaces of the structure. The model is solved based upon the premise that each plate consists of a single user-specified material with a unique melting temperature. Because the structures have no internal heat sources, all heating and melting occurs at the outer surfaces. As a structure melts, molten material should not become superheated to any significant extent because either (1) the molten material will quickly relocate to a lower elevation or below the bottom of the structure or (2) more of the underlying solid structure will melt.

7.2.1 Debris Interaction With Core Plate

There are four potential sources for molten or partially molten material which may move below the bottom of the active core. These four sources are:

- melting of core structures,
- in-core molten pool,
- upper plenum structure melting,
- user-defined slumping.

The flow of molten material from the four sources first passes through the core plate. If no core plate has been specified, the sources are combined to form the scalar variables representing each of the tracked species which is then used by the FCI or COUPLE model as appropriate. If a core plate is modeled, then the slumping material impinges upon the appropriate plate, and is represented by the core plate model until the material falls through the core plate as shown in Figure 7-4.

If sufficient detail is specified by the user, a portion of the core plate model may be modeled as being directly below and connected to, each annular ring in the core region. Within an annular ring the debris material will be represented with a uniform height (i.e., self-leveling) across the horizontal surface. Mass transfer to an adjacent annular ring will occur when the debris height reaches a user-defined value.

7.2.2 Heat Transfer

As material is relocated to the upper surface of the core plate, the core plate model has the capability of tracking the formation of a pool of molten material above the plate, and the transfer of heat across a crust of solidified material which may form between molten debris material and the core plate.

For steady state heat transfer, data are usually correlated in terms of the surface-averaged Nusselt number, Nu, a modified Rayleigh number, Ra, and the fluid Prandtl number, Pr, which are defined by

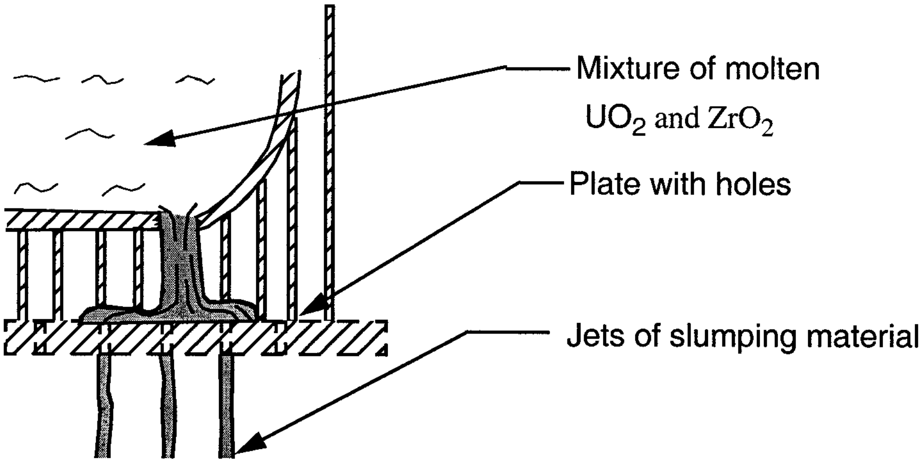
Mixture of molten
UO_2 and ZrO_2
Plate with holes
Jets of slumping material

Figure 7-4. Representation of molten pool failure and material relocating to core plate

$$Nu = \frac{hL}{k} = \frac{q''}{\frac{k}{L}\Delta T} \tag{7-5}$$

$$Ra = \frac{G\beta q'''L^5}{\alpha\nu k} \tag{7-6}$$

(7-7)

$$Pr = \frac{\nu}{\alpha} \tag{7-8}$$

where

k	=	thermal conductivity of the liquid in the molten pool (W/m^2K)
h	=	average heat transfer coefficient (W/m^2-K)
L	=	a characteristic length; in a rectangular geometry, this study has used the pool height (m)
g	=	acceleration due to gravity (m/s^2)
β	=	volumetric coefficient of expansion (1/K)
α	=	thermal diffusivity (m^2/s)
ν	=	kinematic viscosity (m^2/s)
q'''	=	volumetric heat generation rate (W/m^3)
q''	=	heat flux from molten pool.

For transient heat transfer, data may be correlated using the Fourier number, Fo, and the transient Rayleigh number, Ra', which are defined by

$$\mathrm{Fo} = \frac{\alpha t}{L^2} \tag{7-9}$$

$$\mathrm{Ra}' = \frac{\mathrm{Ra}}{\mathrm{Nu}} \tag{7-10}$$

Representative ranges for the dimensionless heat transfer groups defined above were quantified using representative upper and lower input values and using results from a representative SCDAP/RELAP5-3D© calculation[7-4, 7-5, 7-6]. Values estimated from these sources are summarized in Table 7-1. Using the values from this table, the Rayleigh number is estimated to range from 10^{13} to 10^{17}, and the debris Prandtl number is estimated to range from 0.03 to 0.8.

Table 7-1. Range for variables used to estimate pool heat transfer parameters,

Property	Ceramic (UO2 at ~3200 K)	Metallic Material (SS-304 at ~1700 K	80% UO2/20% ZrO2 (by weight) at ~2900 K
ρ, *kg/m3*	*8400*	*7250*	*9300*
cp, J/kg-K	*500*	*560*	*650*
k, W/m-K	*3.8*	*38*	*3.8*
β, K^{-1}	*1.6e-4*	*3.5e-4*	*7.51e-5*
α, m^2/s	*9.0e-7*	*9.4e-6*	*6.2e-7*
ν, m^2/s	*5.4e-7*	*3.2e-7*	*4.8e-7*
Pr	*0.6*	*0.03*	*0.8*

The correlations proposed by Steinberner and Reineke[7-7] are the most applicable for pools that may form during a severe accident[7-5]. These correlations were obtained from facilities at higher Rayleigh numbers (between 8×10^{12} and 4×10^{13}), and they appear to be consistent with much of the data obtained from lower Rayleigh number investigations. Based upon this recommendation, the lower core plate model uses the Steinberner and Reineke correlation for rectangular geometries.

$$\mathrm{Nu}_u = 0.345\mathrm{Ra}^{0.233} \tag{7-11}$$

$$\mathrm{Nu}_d = 1.389\mathrm{Ra}^{0.095} \tag{7-12}$$

7.2.3 Debris Interaction During Core Plate Penetration

The most important calculation of the core plate model is the modeling of material flow through the plate and the potential blockage of the penetrations through the core plate. Without a blockage, relocating material will flow through the core plate region with no delay, and the core plate will have minimal impact upon the analysis. Two approaches were used to model core plate blockage, depending on whether or not the debris is primarily metallic or ceramic.

7.2.3.1 Metallic Blockage

The results of the XR2-1 experiment indicates that, at least for BWR geometries, molten metallic material slumping onto the core plate region solidifies to form localized (non-coherent blockages, and then remelts in response to continued heating of the structures. Modeling the flow of molten metallic material through the core plate penetrations is done by modeling a vertical structure of the same material as the plate, with molten debris flowing past it. Calculations of mass and heat transfer are performed in a manner identical to that used for flow of the metallic material over the core component surface. As material freezes on the wall, the flow area through the penetration is reduced, as shown in Figure 7-5, and if appropriate, plugged.

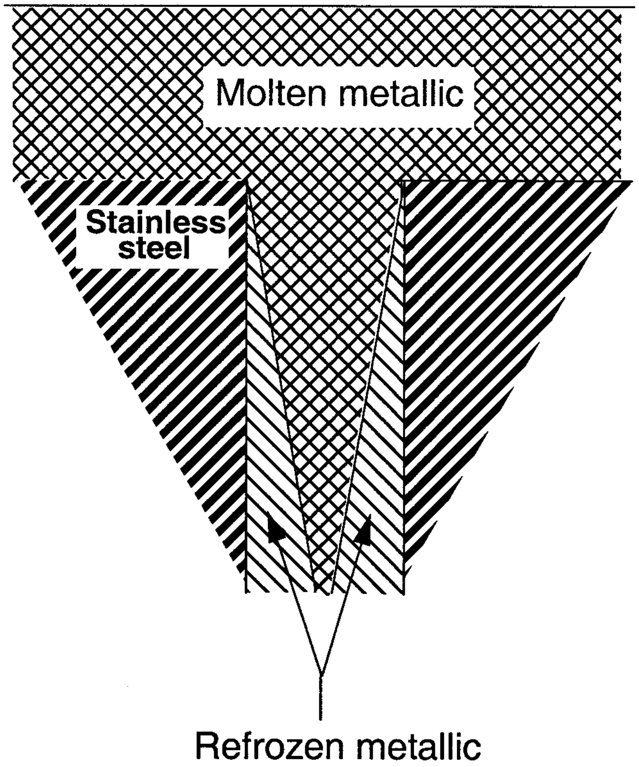

Figure 7-5. Blockage of core plate penetrations by metallic material

7.2.3.2 Ceramic Blockage

The available information about damage progression in the core plate region during the late phase of a severe accident (when the ceramic material forms an in-core porous debris bed and molten pool) is less definitive than that for metallic debris. The XR2-1 experiment did not address the late phase, but recent BWR and PWR accident simulations predict that a large molten ceramic pool will propagate, either downward past the bottom of active fuel or peripherally to the core barrel and then downward into the core plate region. The core plate model must then determine whether this molten ceramic material quickly flows through the core plate penetrations, or whether the penetrations are plugged, thereby forcing the molten ceramic to melt through the core plate.

The results of experiments on UO_2 fuel flow and freezing are not consistent with the typical concept of molten material freezing on the sides of the penetration until sufficient crust growth plugs the penetration, as described in the previous section. A conduction controlled analytical formulation for solidification predicts that molten material penetrates significantly greater distances before plugging occurs than is experimentally observed[7-8]. It has been concluded that UO_2 flowing over steel behaves in a manner that prevents the formation of a stable crust at the wall and, therefore, UO_2 penetration is controlled by turbulent heat transport from the slug of molten ceramic material to the structure. This conclusion leads to the concept of the material flow illustrated in Figure 7-6, which shows the existence of a two-phase ceramic slurry flowing through the core plate penetration with no crust formation along the walls. In such a case, the plugging of the core plate penetrations can not be modeled using the traditional methods described for the metallic plugging.

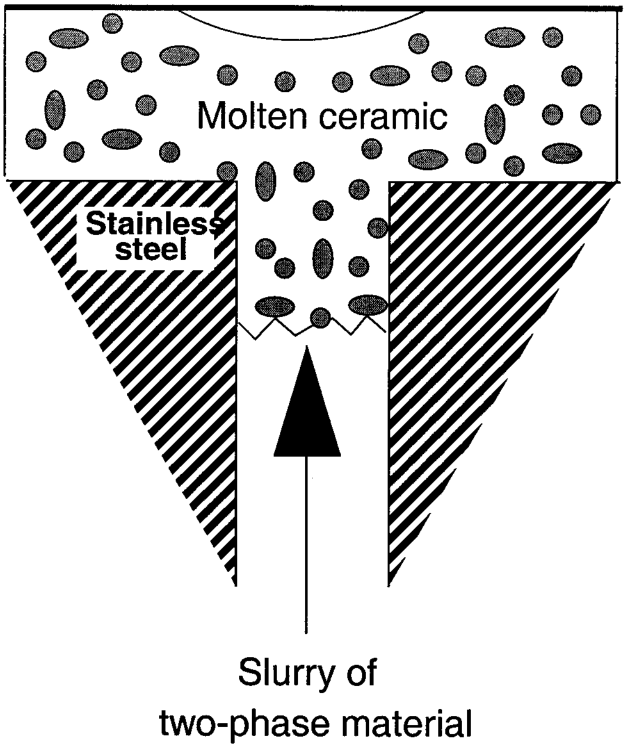

Figure 7-6. Blockage of core plate penetration by ceramic material.

In order to model the plugging of the core plate penetrations by molten ceramic material, a correlation for the penetration of a flowing ceramic through a steel channel[7-9] is used. If the correlation predicts that the slurry will penetrate a distance less than the core plate thickness, then the penetration will be modeled as plugged. This correlation for the core plate penetration distance is:

$$X_P = \frac{1}{2}\frac{D}{f}\left(\frac{\frac{L_f}{c_f} + T_{f,0} - T_{f,mp}}{T_{f,0} - T_{s,mp}}\right)\left(\frac{1}{1 + \frac{T_{f,mp} - T_{s,mp}}{\frac{L_s}{c_s} + T_{s,mp} - T_{s,0}}}\right) \tag{7-13}$$

where

X_p = Penetration distance

D = channel diameter

f = coefficient of friction

L = latent heat of fusion

c = heat capacity

T = Temperature (subscripts f = fuel, s = steel, mp = melting point, 0 = temperature at channel entrance or initial wall temperature.

The method in which the core plate model interacts with either the Fuel-Coolant Interaction (FCI) model or the COUPLE module is straightforward. In the event that no core plate structure has been defined, then slumping mass and energy from each of the four potential sources is summed and then delivered to the FCI model. It should be noted that the material is modeled as arriving at the lower head in a single large jet. If a core plate structure is defined, then the material leaving the lowest plate is delivered to the FCI model, and is represented as arriving as the same number of jets as surviving penetrations.

7.3 References

7-1. C. M. Allison and S. A. Chavez, *Proposed SCDAP/RELAP5/MOD3.1 Model Additions to Treat the Behavior of Upper Plenum and Core Plate Structures During the Later Phases of a Severe Accident (Draft)*, EGG-RAAM-11500, September 1994.

7-2. L. Baker, Jr., *An Assessment of Existing Data on Zirconium Oxidation Under Hypothetical Accident Conditions in Light Water Reactors*, ANL/LWR/SAF 83-3, Argonne National Laboratory, 1983.

7-3. J. F. White, et al., *Seventh Annual Report - AEC Fuels and Materials Development Program*, GEMP-1004, March 1968.

7-4. C. M. Allison, J. L. Rempe, and S. A. Chavez, *Final Design Report on SCDAP/RELAP5 Model Improvements - Debris Bed and Molten Pool Behavior*, INEL-96/0487, December 1996.

7-5. J.L. Rempe and C.M. Allison, “Improved Models for Predicting Heat Transfer from a Molten Pool”, *Thermal Hydraulic Division Proceedings of the 1995 ANS Winter Meeting,* October 1995.

7-6. M.M. Pilch, et al., *The Probability of Containment Failure by Direct Containment Heating in Surry*, Appendix E, NUREG/CR-6109, May 1995.

7-7. U. Steinberner and H.H. Reineke, “Turbulent Buoyancy Convection Heat Transfer with Internal Heat Sources”, Proc. 6th Int. Heat Transfer Conf., Vol. 2, pp305-310, Paper NC-21, toronto, Canada, August 1978.

7-8. D.H. Cho, M. Epstein, R.P. Anderson, D.R. Armstron, “Transient Freezing in a Tube Flow,” in Reactor Development Program Progress Report, ANL-RDP-37, 7.12, Argonne National Laboratory (1975).

7-9. M. Epstein, et al., “Transient Freezing of a Flowing Ceramic Fuel in a Steel Channel*”*, *Nuclear Science and Engineering*: 61, 310-323 (1976).

8. HEATUP OF LOWER HEAD BY SLUMPED REACTOR CORE MATERIAL

A model based upon the COUPLE[8-1] code is used to calculate the heatup of reactor core material that slumps to the lower head of the reactor vessel and is subsequently represented as debris. This model takes into account the decay heat and initial internal energy of slumped debris and then calculates the transport by conduction of this heat in the radial and axial directions to the wall structures and water surrounding the debris. Perhaps the most important use of this model is to calculate the heatup of the vessel wall so that the time at which the vessel may rupture can be determined. Notable capabilities include the modeling of the following phenomena and conditions: (a) spatially varying porosity, (b) thermal conductivity of porous material, (c) a debris bed whose height grows sporadically with time, (d) radiation heat transfer in a porous material, and (e) natural circulation of melted debris. The limitations of this model are: (a) molten material does not flow into an adjacent porous region, (b) oxidation does not occur in the debris bed, and (c) fission product release does not occur in the debris bed.

8.1 Two-Dimensional Heat Conduction Model

COUPLE, a two-dimensional finite element in space and finite difference in time steady state and transient heat conduction code, was implemented in SCDAP/RELAP5-3D© to predict debris behavior in the lower head of a reactor. The code was developed to handle multi-layer planer or axisymmetric solids with temperature dependent anisotropic properties. Due to the two-dimensionality of the code, there is increased coupling between nodes related to the use of the finite element formulation.

To employ the finite element method to solve heat conduction problems, a mesh describing a two dimensional cross section of a structure needs to be generated. The nodes and elements created when a mesh is generated represent, for SCDAP/RELAP5-3D©, a structure such as the lower head of a reactor. [Nodes are defined to lie on element boundaries where adjacent elements are considered to be connected.] Temperatures in each element in a region of interest are approximated using a discretization procedure. The functions used to approximate or interpolate the temperature in an element are defined in terms of temperature, initially unknown, at specified nodes. Once the node temperatures have been determined, the element temperatures are defined using interpolation procedures.

The COUPLE code solves heat transfer problems subject to boundary conditions of the first kind (Dirichlet), second kind (Neuman) and the third kind (combination of the first and second) and/or non-linear boundary conditions such as radiation. A boundary condition of the first kind implies that the temperatures are prescribed along the boundary surface. A boundary condition of the second kind implies that the normal derivatives of the temperatures are prescribed at the boundary surface. To determine the initial temperature distribution, the code solves the following two-dimensional energy equation:

$$(\rho C_v)_e \frac{\partial T}{\partial t} = \frac{\partial}{\partial x}\left(k_e \frac{\partial T}{\partial x}\right) + \frac{\partial}{\partial y}\left(k_e \frac{\partial T}{\partial y}\right) + Q_D(x, y) - Q_c(x, y) \qquad (8\text{-}1)$$

where

$(\rho C_v)_e$ = $\varepsilon (\rho C_v)_1 + (1 - \varepsilon) (\rho C_v)_s$,

ρ = density (kg/m^3),

C_v = constant volume specific heat,

k = thermal conductivity,

$Q_D(x,y)$ = volumetric heat generation rate at location with coordinates of (x,y) (W/m^3),

$Q_c(x,y)$ = heat transferred at location (x,y) by convection and radiation from particles of debris to fluid in interstices of the particles (W/m^3),

T = temperature,

ε = porosity (pore volume/total volume),

e = equivalent,

l = liquid,

s = solid.

When liquid water is present in the interstices of debris, the heat transfer by convection dominates over heat transfer by conduction. In this case, the equivalent conductivity term in the above equation, k_e, is set to zero. The variable $Q_c(x,y)$ is calculated by the model for heat transfer in porous debris, which is described in Section 9.0.

8.2 Variable Element Porosity

The COUPLE code allows each element in the debris bed model to have the porosity resulting from the conditions in that element. The porosity of each element can vary with time. The thermal property of each element is determined by

$$\Phi = \varepsilon \phi_f + (1 - \varepsilon) \phi_s \quad (8\text{-}2)$$

where

Φ = average thermal property value, such as thermal conductivity or specific heat,

ϕ = thermal property,

ε = porosity,

f = fluid,

s = solid.

If the porosity is zero, the element represents a volume containing solid debris material, whereas a porosity value of 1.0 means the element is completely filled with coolant. A value between 0.0 and 1.0 indicates that the volume contains both coolant and debris material.

8.3 Thermal Conductivity Model

The heat transfer in a dry porous bed involves both conduction and radiation. The overall thermal conductivity of the bed can be represented as

$$k_e = k_c + k_r \tag{8-3}$$

where

k_e = total effective conductivity (W/mK),

k_c = effective conductivity (conduction only) (W/mK),

k_r = radiative conductivity (W/mK).

A number of thermal conductivity models have been proposed for modeling a dry porous bed. Reference 8-2 gives a good review and comparison of five such models. The Imura-Takegoshi[8-3] model for thermal conductivity combined with the Vortmeyer[8-4] radiation model yields a good overall result and produces an upper bound on the temperature.

The Imura-Takegoshi model[8-3] in equation form is given as follows:

$$k_c = \left[\Psi + \frac{1 - \Psi}{\phi + \frac{1 - \phi}{\nu}}\right] k_g , \tag{8-4}$$

$$\phi = 0.3\varepsilon^{1.6}\upsilon^{-0.044} , \tag{8-5}$$

$$\upsilon = \frac{k_s}{k_g} , \tag{8-6}$$

$$\Psi = \frac{\varepsilon - \phi}{1 - \phi} \tag{8-7}$$

where

k_g = thermal conductivity of fluid or vapor in pores $W/m \cdot K$,

k_s = thermal conductivity of solid material $W/m \cdot K$,

ε = porosity of debris.

The Vortmeyer model[8-4] is given as

$$k_r = 4\eta\sigma d_p T^3 \tag{8-8}$$

where

η = radiation exchange factor (user-defined value, with default value of 0.8),

σ = Stefan-Boltzmann constant $W/m^2 \cdot K^4$ (5.668 x 10^{-8}),

d_p = particle diameter (m),

T = temperature (K).

The combined Imura-Takegoshi and Vortmeyer model is used in the COUPLE subroutine, CNDUCT.

A lower bound model is available in the literature which combines a conduction model by Wilhite[8-5] with a radiation model by Luikov.[8-6] This lower bound model has not been applied by the COUPLE model.

8.4 Phase Change Model

At the present time, there are two generally accepted ways to numerically approximate a phase change problem. One method uses a moving mesh technique. The moving mesh technique is usually applied to one-dimensional problems. This technique is not easily applied to two-dimensional problems because mesh distortion may result.

The other method uses a fixed mesh and is usually referred to as an enthalpy method. The particular method implemented is described in Reference 8-2. The method uses the material enthalpy to determine an effective density times specific heat (ρC_p) value to use in Equation (8-1). The enthalpy change per unit volume is defined as

$$dH = \rho C_p dT \tag{8-9}$$

thus, (8-10)

$$\rho C_p = \frac{dH}{dT} \tag{8-11}$$

which can be written as

$$\rho C_p = \left(\frac{dH}{dX}\right)\left(\frac{dX}{dT}\right) \tag{8-12}$$

where X is the coordinate boundary of a phase change (m).

For computational purposes, it is easier to calculate $\frac{dH}{dX}$ and $\frac{dX}{dT}$ than it is $\frac{dH}{dT}$ directly. The necessary coding required to use this approach is contained in the subroutine USERP.

8.5 Heat Transfer at Surfaces of Finite-Element Mesh

There are two types of boundary conditions that may be applied at the surface of the COUPLE finite element mesh. The first makes use of a connection to a hydrodynamic volume, thereby allowing heat transfer to and from a surrounding fluid. The ability of the SCDAP/RELAP5-3D© code has been extended to allow a second type of boundary condition from the exterior surface of a hemispherical reactor vessel lower head. This extension makes use of a set of preliminary boiling curves to allow the code user to assess the affects of reactor vessel cavity flooding.

8.5.1 Hydrodynamic Boundary Condition

Convective and radiative heat transfer boundary conditions may be applied at all external surfaces of a finite-element mesh. Convective heat transfer coefficients and radiation sink temperatures are determined at the surfaces of the COUPLE finite element mesh through interfaces with the RELAP5 code.[8-7] The boundary conditions are

$$(-K_{et})\frac{\partial}{\partial n}T(z_b, r_b) = h_c(z_b, r_b)[T(z_b, r_b) - T_c(z_b, r_b)] + q_{rad}(z_b, r_b) \tag{8-13}$$

where

$T(z_b,r_b)$ = temperature of external surface of node on COUPLE finite element mesh with coordinates of z_b, r_b (K),

z_b = elevation of node on external surface of finite element mesh (m),

r_b = radius of node on external surface of finite element mesh (m),

n = coordinate in direction normal to external surface (m),

$h_c(z_b,r_b)$ = RELAP5-calculated convective heat transfer coefficient for node on external surface with coordinates z_b,r_b ($W/m^2 \bullet K$),

$T_c(z_b,r_b)$ = RELAP5 calculated temperature of the fluid at surface coordinates z_b, r_b (K),

$q_{rad}(z_b,r_b)$ = radiation heat flux (W/m^2).

8.5.2 Ex-Vessel Heat Transfer

The NRC sponsored an experimental program to evaluate the heat transfer from the outside of a hemispherical reactor vessel which has been flooded. In order to allow the code user to assess the effects of flooding of the reactor vessel cavity, a set of experimental boiling curves was implemented. The heat transfer data consist of

- A set of correlations describing the heat flux as a function of contact angle and ΔT between the vessel surface and a bulk temperature.
- A correlation for Critical Heat Flux as a function of contact angle.

The set of nucleate boiling curves for heat transfer from the outside of a flooded reactor vessel are of the form: $q'' = a\Delta T + b\Delta T^2 + c\Delta T^3$. Two sets of constants for each of five locations along the hemispherical lower vessel head were determined. One set of constants was for heat transfer to a bulk temperature of 90 ^oC and a second set for heat transfer to a bulk temperature of 100 ^oC (at atmospheric pressure). These constants are defined in Table 8-1.

Table 8-1. Nucleate boiling correlation constants.

l/D[1]	**a**		**b**		**c**	
	90 ^oC	**100 ^oC**	**90 ^oC**	**100 ^oC**	**90 ^oC**	**100 ^oC**
0.00		3840	319	334	-2.83	-4.54
0.20	4016	5530	430	380	-4.13	-5.63
0.35		515	337	1109	2.61	-18.50
0.50			891	960	-9.04	-8.18
0.75			529	134	0.08	13.00

---

[1] l/D is the ratio of the distance from the centerline of the vessel to the radius of the hemispherical head. The angle of contact is $0.5\pi\left(\frac{l}{d}\right)$.

These correlations yield a boiling curve as a function of the temperature difference between vessel surface and a bulk temperature, with a valid range from approximately 4 K to the temperature difference which causes a critical heat flux (CHF). The correlation for CHF as a function of contact angle is

$$q_{chf} = 0.4(1 + 0.021\theta - (0.007\theta)^2)(1 + 0.036\Delta T_{sub}) \qquad (8\text{-}14)$$

where

q_{chf} = the critical heat flux in MW/m^2,

θ = the contact angle,

Δt_{sub} = the degree of subcooling.

This experimental data was applied in the following manner:

Nucleate Boiling:

- For a ΔT (between vessel surface and bulk temperature) between 0 and 4 K, a linear interpolation is applied between a heat flux of zero at zero ΔT to the heat flux predicted by the appropriate correlation at a ΔT of 4 K.

- Between a ΔT of 4 K and the ΔT which corresponds to CHF, the appropriate correlation is used. The ΔT at CHF is determined by iteratively increasing the ΔT until either the predicted critical heat flux is reached or the heat flux predicted by the correlation begins to decrease.

Transition:

- After Critical Heat Flux is reached, the predicted transition heat flux is linearly extrapolated from the CHF to a user-defined heat transfer coefficient to vapor. The slope of this linear extrapolation is 5,400. The user-defined heat transfer coefficient to vapor is defined in Word 2 of Card 50004000 and has a default value of zero.

Vapor Heat Transfer:

- Heat transfer to vapor is modeled when a location on the external surface of the lower head is uncovered. This rate of heat transfer is governed by a user-defined heat transfer coefficient which is defined by Word 2 of Card 50004000 and has a default value of zero. The heat flux is not permitted to decrease below the heat flux predicted with this user-defined value.

An application of the data for saturated conditions is shown graphically in Figure 8-1. for each of the specified contact angles.

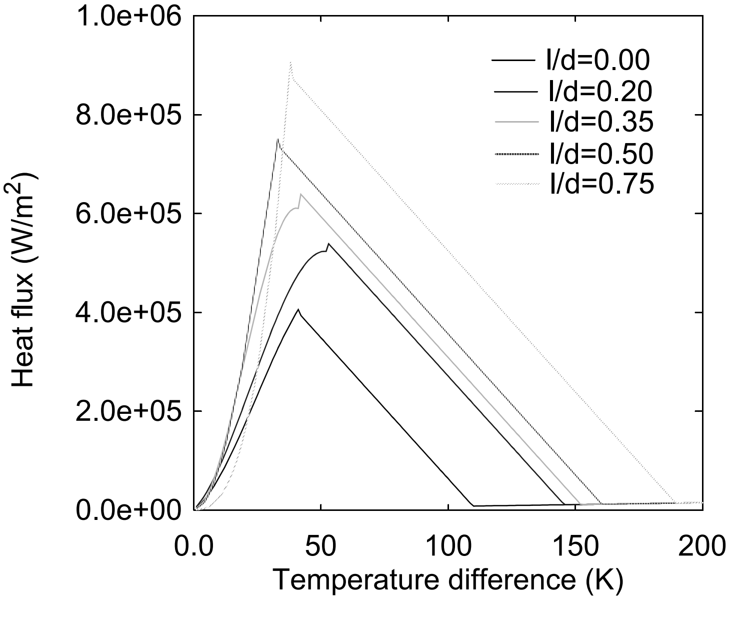

Figure 8-1. Predicted heat flux from ex-vessel heat transfer correlations as a function of position and temperature.

8.6 Heat Transfer in Finite Elements with Liquid-Solid Interface

The COUPLE model calculates an effective thermal conductivity to represent the heat transfer in regions that contain partially or completely molten core material and where the heat transfer is dominated by natural convection instead of by conduction. The effective thermal conductivity is defined to be the thermal conductivity for solid state conduction that results in the same heat transfer as that occurring due to natural convection. The effective thermal conductivity is calculated for elements that are partially or completely molten. Figure 8.2 is a schematic of a COUPLE mesh that shows the finite elements in a COUPLE mesh at which an effective thermal conductivity is calculated. In Figure 8-2 the symbol k_{eff} is the effective thermal conductivity of the element, k_{matpro} is the thermal conductivity of the element as calculated by MATPRO, and k_{nc} is the thermal conductivity of the element that accounts for natural convection. The calculation of effective thermal conductivity accounts for a mesh size that is much larger than the thickness of the layer of solidified material in the element and accounts for a nonlinear temperature distribution through a mesh with a liquid-solid interface.

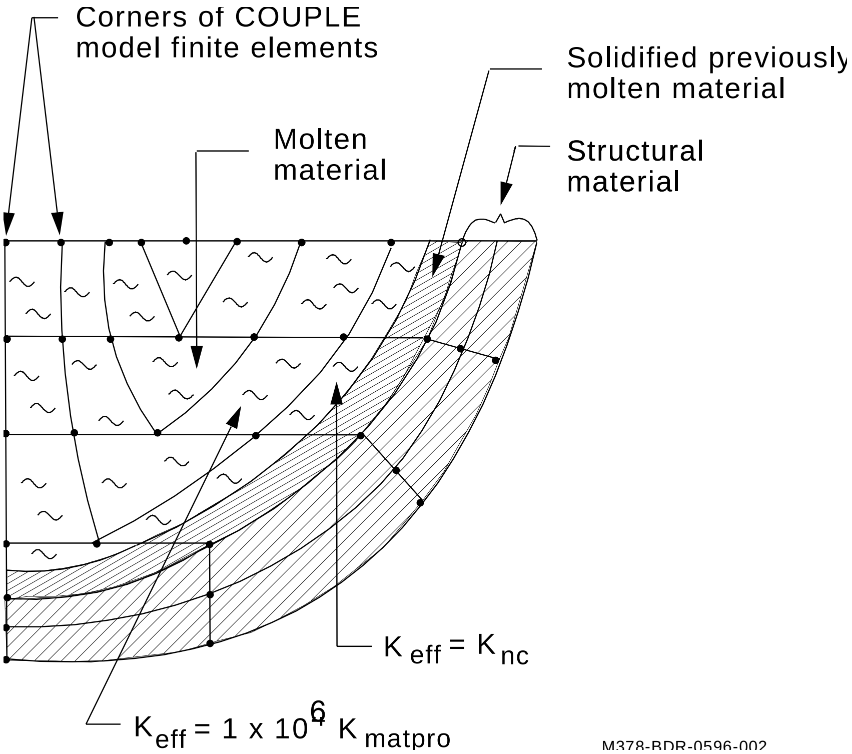
Corners of COUPLE model finite elements
Solidified previously molten material
Molten material
Structural material
$K_{eff} = K_{nc}$
$K_{eff} = 1 \times 10^6 K_{matpro}$
M378-BDR-0596-002

Figure 8-2. Identification of elements for which effective thermal conductivity is calculated.

The effective thermal conductivity of completely molten finite elements is multiplied by a large number to represent mixing of the molten material due to natural convection. The natural convection heat transfer correlations used to calculate heat transfer at the liquid-solid interfaces assume a uniform temperature for the bulk molten material. Therefore the multiplication factor on thermal conductivity for elements with molten material needs to be sufficiently large so all elements containing molten material are at about the same temperature. If a multiplication factor of 1×10^6 is used, the maximum variation in the calculated temperature of molten material is less than 4 K.

A local heat transfer model is applied to calculate the effective thermal conductivity of a COUPLE finite element containing molten material that interfaces with solidified material. The temperature distribution through such an element is not linear as is assumed by the basic COUPLE model. Instead the temperature distribution is as shown in Figure 8-3 Heat is driven by natural convection through the molten material in the left part of the element to the liquid-solid interface and then is transferred by conduction through the solidified layer to the right boundary of the element. The local heat transfer model has the capability of calculating the heat transfer through the interior of the element and the heat flux at the right boundary of the element taking into account the nonlinear temperature distribution through the element. The heat flux calculated at the right boundary of the element by the local model is used to calculate the effective thermal conductivity of the element that results in the same heat flux at the right boundary when the temperature distribution through the element is assumed to be linear. In Figure 8-3, the symbol T_m is the bulk temperature of the molten material, T_L is the liquidus temperature of the molten material, and T_W is the temperature at the right boundary of the finite element, the interface with structural material. The use of a local model for heat transfer allows a mesh size to be used that is large compared to the thickness of the layer of solidified material.

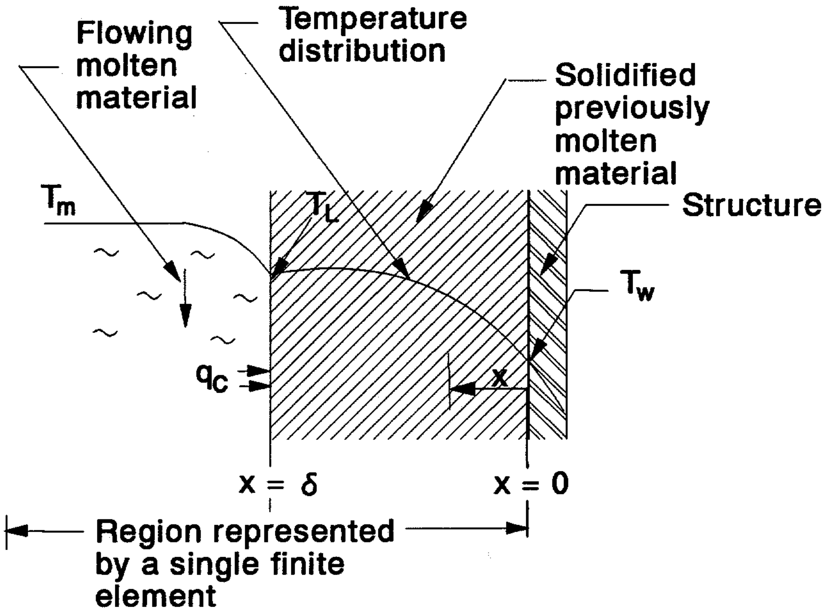

Figure 8-3. Temperature distribution in finite element with liquid-solid interface.

The local model for heat transfer requires the thickness of the layer of solidified material. Using the coordinate system shown in Figure 8-4, the equation for the thickness of the solidified layer was derived as presented in Reference 8-8. First, the transient one-dimensional heat conduction equation for the layer of solidified material is applied. This equation is

$$k\frac{\partial^2 T}{\partial x^2} = \rho c_p \frac{\partial T}{\partial t} - q_v \tag{8-15}$$

where

k = thermal conductivity of solidified material (W/m^{2}K),

T = temperature (K),

x = position coordinate in solidified layer measured from wall (m),

ρ = density of solidified material (kg/m^3),

c_p = specific heat of solidified material (J/kg^{2}K),

t = time from start of solidification (s),

q_v = volumetric heat generation in crust (W/m^3).

The integration of Equation (8-15) from x to δ is

$$k\frac{\partial T}{\partial x}\bigg|_{\delta} - k\frac{\partial T}{\partial x}\bigg|_{x} = \rho c_p \int_x^{\delta} \frac{\partial T}{\partial t}dx - q_v(\delta - x)\ (8\text{-}15) \tag{8-16}$$

where

d = thickness of solidified layer (m).

Next, the boundary condition at x = δ is substituted into Equation (8-16). This boundary condition is

$$k\frac{\partial T}{\partial x}\bigg|_{\delta} = h_m(T_m - T_L) + \rho h_{fus}\frac{d\delta}{dt} \tag{8-17}$$

where

h_m = heat transfer coefficient due to natural convection in molten material (W/m^{22}K),

T_m = temperature of molten material (K),

T_L = liquidus temperature of material (K),

h_{fus} = latent heat of fusion of core material (J/kg).

Substituting Equation (8-17) into Equation (8-16) and rearranging the terms, the result is

$$k\frac{\partial T}{\partial x}\bigg|_{x} = \rho h_{fus}\frac{d\delta}{dt} + h_m(T_m - T_L) - \rho c_p \int_x^{\delta} \frac{\partial T}{\partial t}dx + q_v(\delta - x) \quad . \tag{8-18}$$

The heat flux at x = 0, where the solidified material interfaces with the structural material, is given by

Equation (8-18) as

$$k\frac{\partial T}{\partial x}\bigg|_o = \rho h_{fus}\frac{d\delta}{dt} + h_m(T_m - T_L) - \rho c_p\int_o^\delta \frac{\partial T}{\partial t}dx - q_v\delta \quad . \tag{8-19}$$

Rearranging Equation (8-19), the equation for the transient thickness of the solidified layer is

$$\frac{d\delta}{dt} = -\frac{h_m(T_m - T_L)}{\rho h_{fus}} + \frac{k}{\rho h_{fus}}\frac{\partial T}{\partial x}\bigg|_o + \frac{c_p}{h_{fus}}\int_o^\delta \frac{\partial T}{\partial t}dx - \frac{q_v\delta}{\rho h_{fus}} \quad . \tag{8-20}$$

The heat flux at x = 0 is assumed to be approximated by the equation

$$k\frac{\partial T}{\partial x}\bigg|_o = \frac{k(T_L - T_w)}{\delta} \tag{8-21}$$

where

T_w = temperature at the interface of the solidified material with the structural material. This temperature is assumed to be equal to that calculated at this location by the COUPLE model at the previous time step or iteration (K).

Next, the integral in Equation (8-20) is calculated assuming a linear temperature distribution through the layer of solidified material. The assumption is also made that the COUPLE model is using sufficiently small time steps that the change in thickness of the layer during a time step is small. The changes in temperature distribution in the solidified layer are then as shown in Figure 8-4.

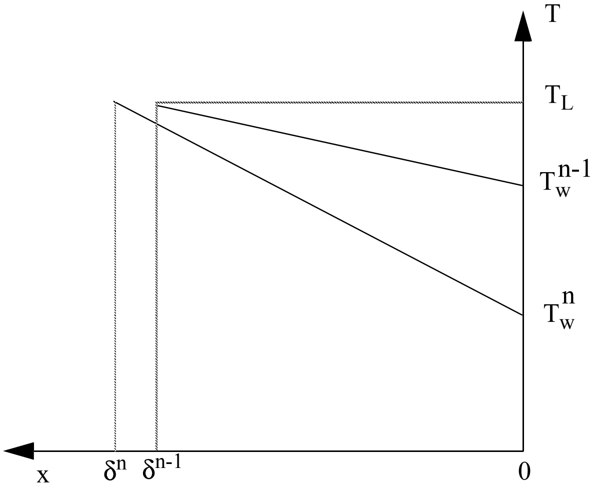

Figure 8-4. Transient temperature distribution through layer of solidified material.

In the figure, T_w^n is the temperature of the right boundary of the finite element at the n-th time step of the COUPLE model. The spatial variation of the rate of change of temperature is given by the equation;

$$\frac{\partial T}{\partial t} = \frac{(T_w^n - T_w^{n-1})}{\Delta t}\frac{(\delta^{n-1} - x)}{\delta^{n-1}} \tag{8-22}$$

where

T_w^n = temperature at interface of solidified material with structural material at n-th COUPLE model time step (K),

Δt = COUPLE model time step (5),

δ^{n-1} = thickness of layer of solidified material at (n-1)th COUPLE model time step (m).

The integral of Equation (8-22) with respect to x is;

$$\int_o^\delta \frac{\partial T}{\partial t}dx = 0.5\frac{(T_w^n - T_w^{n-1})}{\Delta t}\delta^{n-1} \quad . \tag{8-23}$$

Substituting Equations (8-21) and (8-23) into Equation (8-20), the equation for the rate of change of the thickness of the solidified layer becomes

$$\frac{d\delta}{dt} = \frac{k}{\rho h_{fus}}\frac{(T_L - T_w^n)}{\delta} - \frac{h_m(T_m - T_L)}{\rho h_{fus}} + 0.5\frac{c_p}{h_{fus}}\frac{(T_w^n - T_w^{n-1})\delta}{\Delta t} - \frac{q_v\delta}{\rho h_{fus}} \quad . \tag{8-24}$$

Equation (8-24) is solved in two domains. For a small value of δ an analytical solution is obtained. For larger values, Equation (8-24) is solved numerically. A numerical evaluation of the terms in Equation (8-24) indicates that only the first term on the right hand side of Equation (8-24) is significant when the value of δ is less than 1 x 10^{-3}. In this case, Equation (8-24) simplifies to

$$\frac{d\delta}{dt} = \frac{k}{\rho h_{fus}}\frac{(T_L - T_w^n)}{\delta} \quad . \tag{8-25}$$

Equation (8-25) is the parabolic kinetics equation. The solution to this equation is

$$\delta^{n+1} = \left[\delta^n + \frac{2k(T_L - T_w^n)}{\rho h_{fus}}\Delta t\right]^{0.5} \quad . \tag{8-26}$$

For a value of δ greater than or equal to 1 x 10^{-3}, a numerical explicit method is used to solve Equation (8-24). The equation is solved by the equation;

$$\frac{d\delta}{dt} = \frac{k}{\rho h_{fus}}\frac{(T_L - T_w^n)}{\delta^n} - \frac{h_m T_m - T_L}{\rho h_{fus}} + \frac{0.5c_p}{h_{fus}}\frac{(T_w^n - T_w^{n-1})\delta^n}{\Delta t} - \frac{q_v\delta^n}{\rho h_{fus}} \quad . \tag{8-27}$$

Equations (8-26) and (8-27) are next applied to calculate the thickness of the solidified layer at the current time step. The current thickness is calculated by Equation (8-28)

$$\delta^{n+1} = \delta^n + \frac{d\delta}{dt}\Delta t \tag{8-28}$$

where

δ^{n+1} d^{n+1} = thickness of solidified layer at current time step (m).

The effective thermal conductivity is next calculated so the finite element calculated heat flux at its right boundary is equal to the heat flux calculated by Equation (8-19), which is the equation as calculated by the localized heat transfer model for the heat flux at the surface of the wall that supports the solidified layer. These two heat fluxes are equal when the following equation is satisfied:

$$k_{eff}\left(\frac{\partial T}{\partial x}\right)_e = \rho h_{fus}\frac{d\delta}{dt} + h_m(T_m - T_L) - 0.5\rho c_p\frac{(T_w^n - T_w^{n-1})}{\Delta t}\delta^{n-1} + q_v\delta \tag{8-29}$$

where

k_{eff} = effective thermal conductivity of finite element (W/m•K),

$\left(\frac{\partial T}{\partial x}\right)_e$ = temperature gradient through finite element in direction normal to the liquid-solid interface. This variable is calculated by the COUPLE model using previous time step or iteration temperatures (k/m).

The only unknown variable in Equation (8-29) is k_{eff}. Solving for k_{eff}, the result is

$$k_{eff} = \left[\rho h_{fus}\frac{d\delta}{dt} + h_m(T_m - T_L) - 0.5\rho c_p\frac{T_w^n - T_w^{n-1}}{\Delta t}\delta^{n-1} + q_v\delta\right] \Big/ \left(\frac{\partial T}{\partial x}\right)_e \tag{8-30}$$

For a COUPLE model finite element next to the inner surface of a hemispherical lower head, the solidified layer is at an angle. The effective thermal conductivity is calculated taking into account the angle of the solidified layer. An example of a COUPLE model finite element with a solidified layer at an angle is shown in Figure 8-5.

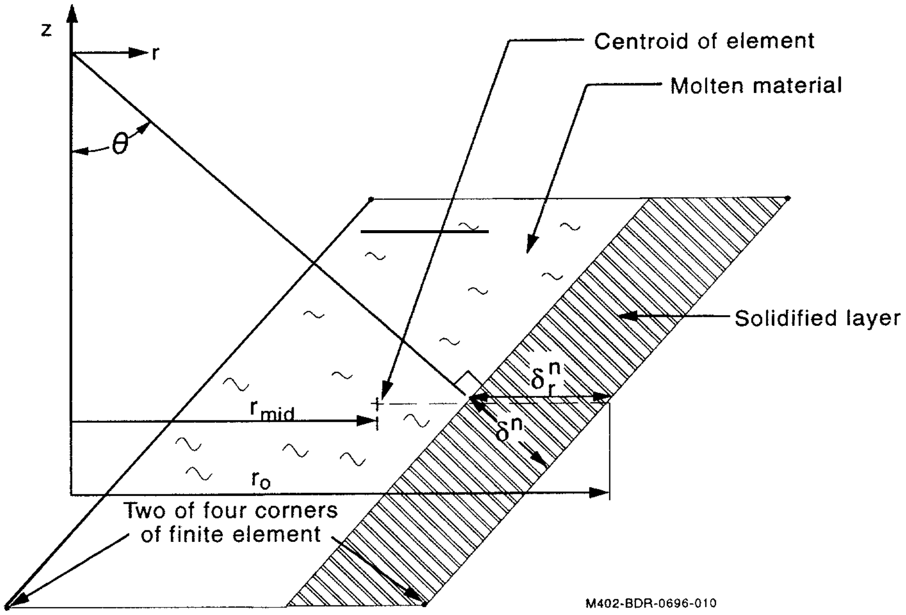
z
r
θ
Centroid of element
Molten material
Solidified layer
δ_r^n
δ^n
r_{mid}
r_o
Two of four corners
of finite element
M402-BDR-0696-010

Figure 8-5. COUPLE model finite element with solidified layer at angle.

For this case, the effective thermal conductivity in the radial direction is calculated by the equation

$$k_{effr} = \frac{r_o}{r_{mid}}\sin(\theta)k_{eff} \tag{8-31}$$

where

k_{effr} = effective thermal conductivity in radial direction (W/m•K),

r_o = radius at mid-height of right boundary of finite element (m),

r_{mid} = radius to centroid of element (m),

k_{eff} = effective thermal conductivity as calculated by Equation (8-30) (W/m•K),

The use of the term (r_o/r_{mid}) in Equation (8-31) results in the COUPLE model calculating the heat flux at the wall (right boundary of the finite element) instead of the centroid of the element.

The effective thermal conductivity in the axial direction is calculated by Equation (8-32)

$$k_{effa} = \cos(\theta)\, k_{eff} \tag{8-32}$$

where

k_{effa} = effective thermal conductivity in axial direction (W/m•K).

The variable h_m in Equation (8-30), namely the heat transfer coefficient for the liquid-solid interface due to natural convection in the molten material, is calculated using correlations developed from experimental data.[8-9,8-10,8-11,8-12] These correlations were developed from the results of experiments that measured the natural convection heat transfer coefficients at the boundary of a pool of fluid with internal heat generation. The correlations calculate heat transfer coefficients at the bottom and top surfaces of the molten pool and at the sides of the molten pool. The heat transfer coefficients can be calculated using either correlations for steady-state natural convection or using correlations for transient natural circulation. The user selects whether steady-state or transient correlations are to be used. The steady-state heat transfer coefficients at the various locations on the boundaries of the molten pool are calculated by the equations[8-12]

$$h_u = 0.345\frac{k}{R}Ra^{0.233}, \tag{8-33}$$

$$h_d = 0.54\frac{k}{R}Ra^{0.18}f(\theta), \tag{8-34}$$

where

h_u = heat transfer coefficient at liquid-solid interface for top upper crust of molten pool (W/m^2•K),

h_d = heat transfer coefficient at liquid-solid interface for crust at bottom or side of molten pool (W/m^2•K),

k = thermal conductivity of the melt in the boundary layer adjacent to the phase change interface (W/m•K),

R = effective radius of the molten region, $\left(\frac{1.5V_{pool}}{\pi}\right)^{0.333}$ (m),

Ra = Rayleigh number associated with the molten pool,

V_{pool} = volume of molten material (m^3),

$f(\theta)$ = factor that varies with angular position.

The Rayleigh number is defined as

$$Ra = \frac{g\beta QR^5}{\alpha\nu k} \tag{8-35}$$

where

g = gravitational constant (9.8 m/s^2),

Q = volumetric heat generation rate (W/m^3),

β = coefficient of volumetric expansion (1/K),

α = thermal diffusivity (m^2/s),

ν = kinematic viscosity of the molten materials (m^2/s).

Experimental results published by Jahn and Reineke[8-10] and others indicate that the local downward heat transfer coefficient is a function of the angular position with respect to the centerline of the molten pool. Results show that the ratio of the local Nusselt number to the mean Nusselt number $\left(\frac{NU_l}{NU_m}\right)$ varies from 0.15 at $\theta = 0.0$ to 1.45 at $\theta = 90.0$. The results are approximated as shown in Figure 8-6, where θ is determined is shown in Figure 8-7. The elements which are determined to be in the process of phase change are identified by the code; and the appropriate upward and downward heat transfer coefficients are applied.

In the calculation of transient natural circulation, the heat transfer coefficients at the liquid-solid interface are calculated by the equations

$$h_u = 0.250\frac{k}{R}Ra'^{0.304}, \tag{8-36}$$

$$h_d = 0.472\frac{k}{R}f(\theta)Ra'^{0.220}, \tag{8-37}$$

$$Ra' = \frac{g\beta R^3 \Delta T}{\alpha\nu}; \tag{8-38}$$

where

h_u = heat transfer coefficient on liquid-solid interface at top surface of molten pool ($W/m^2{\bullet}K$)

h_d = heat transfer coefficient on liquid-solid interface at bottom or side of molten pool ($W/m^2{\bullet}K$),

Ra' = transient Raleigh number,

ΔT = difference between maximum temperature of molten pool and the liquidus temperature of material in molten pool (K).

The difference between the liquidus and solidus temperature of the molten pool, (T_{liq} - T_{sol}), is assumed to be 43 K, which is appropriate for a mixture of UO_2 and ZrO_2.

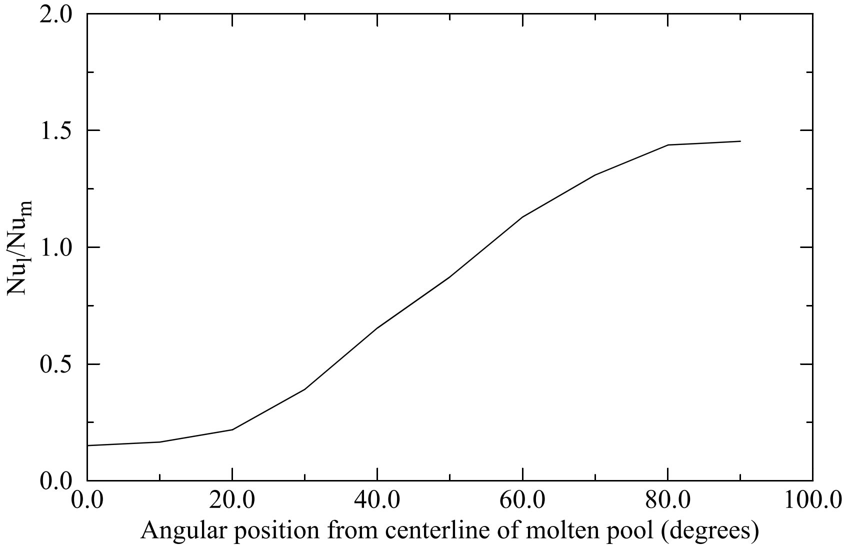

Figure 8-6. Ratio of local Nusselt number to mean Nusselt number as a function of the angle from core centerline.

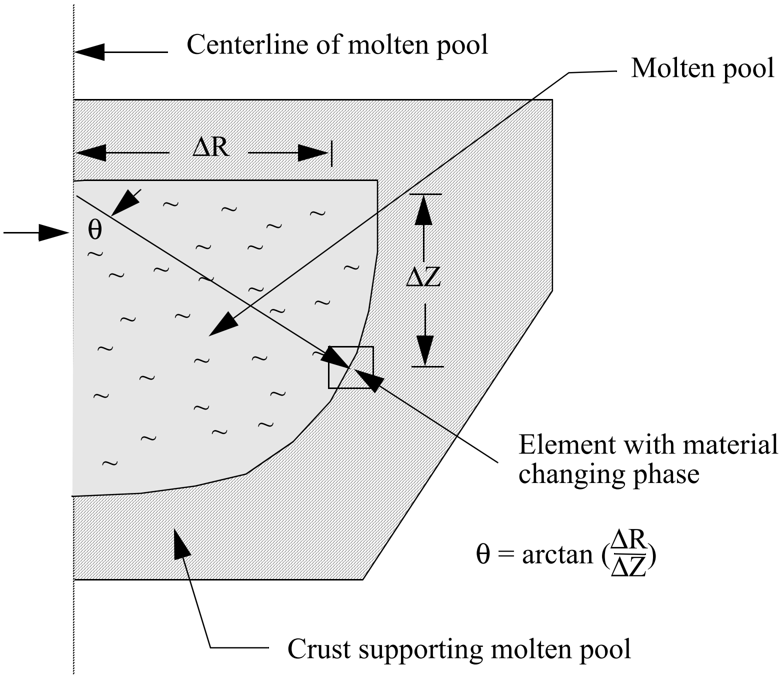
Centerline of molten pool
Molten pool
ΔR
θ
ΔZ
Element with material changing phase
$\theta = \arctan\left(\frac{\Delta R}{\Delta Z}\right)$
Crust supporting molten pool

Figure 8-7. Schematic defining the location of a typical phase change element.

8.7 Heat Transfer at Interface of Debris Region and Structure

The rate of heat transfer from a debris region into a structure in contact with the debris is a strong function of the conditions at the interface between the debris and structure. The modeling of this heat transfer is performed using the null element concept in COUPLE. A null element is an element with zero volume where the nodes overlay the interface between the debris and the structure. Null elements are defined by the code user along possible interfaces between debris and structure. The heat transfer through the null elements is calculated by the equation

$$q_i = h_{gap} (T_d - T_s) \tag{8-39}$$

where

q_i = heat flux across the interface (W/m^2),

h_{gap} = heat transfer coefficient for interface between debris and structure ($W/m^2 \bullet K$). (This variable is defined by the code user in convectsets input of the COUPLE model and the suggested default value is 500 $W/m^2 \bullet K$),

T_d = temperature of debris at the interface (K),

T_s = temperature of structure at the interface (K).

The debris and structure nodes have the same coordinates but different identification numbers. The debris node is part of a finite element modeling the debris and the structure node is part of a finite element modeling the structure in contact with the debris. The heat flux calculated by Equation (8-39) is applied at both the surface of the finite element with debris that faces the structural element and the surface of the structural element that faces the debris element.

The modeling of the gap heat transfer coefficient is divided into three regimes: (1) solidified debris, (2) partially liquefied debris, and (3) completely liquefied debris. For the solidified debris regime, the heat transfer is a function of the surface roughness of the debris and structure and of other parameters. For this regime, the debris model does not attempt to calculate the gap heat transfer coefficient. Instead, the gap heat transfer coefficient is defined from user input. In the liquefied debris regime, the gap heat transfer coefficient is set to a value of 10,000 $W/m^2 \bullet K$, which in effect defines the thermal resistance at the gap to be zero. In the partially liquefied regime, the heat transfer coefficient is calculated by the equation

$$h_{gap} = h_{liq} + (h_{us} - h_{liq})(T_{liq} - T_{DI}) / (T_{liq} - T_{sol}) \tag{8-40}$$

where

h_{liq} = heat transfer coefficient for interface for case of debris at interface being completely liquefied (10,000 $W/m^2 \bullet K$),

h_{us} = user-defined heat transfer coefficient for interface between debris and structure ($W/m^2 \bullet K$),

T_{liq} = liquidus temperature of debris at interface (K),

T_{DI} = temperature of debris at interface with structural material (K),

T_{sol} = solidus temperature of debris at interface (K).

The value of ($T_{liq} - T_{sol}$) is assumed to be 43 K, which is appropriate for a mixture of UO_2 and ZrO_2.

8.8 Heat Transfer for Stratified Molten Pool

In a severe accident scenario, fuel and metal components such as cladding and core plate may melt and slump into the lower head of the reactor vessel. Heat generated in fuel heats up the slumped material and the lower head. In the event that the fuel and metal components become molten, natural convection driven heat transfer from the molten material to the inside surface of the lower head occurs. This section describes a model for calculating the natural convection driven heat transfer for the case of the lighter metallic constituents in the molten material separating from the heavier oxidic components and residing as a metallic pool on top of the oxidic pool. A schematic of such a molten pool is shown in Figure 8-8.

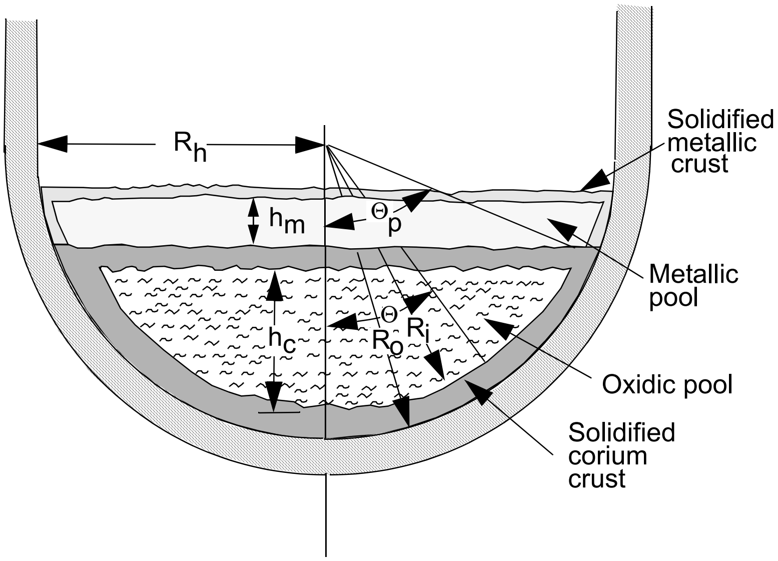

Figure 8-8. Schematic drawing of oxidic and metallic pools in the lower head.

At present no well-accepted criterion or correlation exists for determining whether the materials in the molten pool are mixed together or stratify into oxidic and metallic parts. Therefore, the SCDAP/RELAP5-3D© user selects the behavior to be analyzed. If a well-mixed pool is the selected behavior, then the heat transfer from the molten pool is calculated as described in the last part of Section 8.6. If behavior that causes the molten pool to stratify into oxidic and metallic parts is selected, then the heat transfer from the two parts of the molten pool are calculated as described in this section.

8.8.1 Correlations for Natural Convection Heat Transfer

The temperature gradients in the oxidic and metallic pools generate natural convection currents. Researchers have developed correlations for natural convection in hemispherical and cylindrical pools. Some of the basic phenomena and applicable correlations are reviewed in the following. When a liquid pool is heated, the buoyant and viscous forces act in opposite directions on a fluid volume. The ratio of buoyant and viscous forces times the ratio of convective and conduction heat transfer is the characteristic dimensionless parameter called the Rayleigh number. If the liquid volume is heated by external means, this number is called "external" Rayleigh number and is denoted by Ra. If the heating is caused by internal volumetric heat generation, this number is called “internal” or “modified” Rayleigh number, Ra'. These two dimensionless numbers, Ra and Ra', are defined as

$$Ra = \frac{g\beta\Delta TL^3}{\alpha\nu} \tag{8-41}$$

$$Ra' = \frac{g\beta q_v L^5}{\alpha\nu k} \tag{8-42}$$

where

Ra = external Rayleigh number of molten pool,

Ra' = internal Rayleigh number of molten pool,

g = acceleration due to gravity (m/s^2),

β = coefficient of thermal expansion of molten pool (1/K),

ΔT = temperature difference between bulk molten pool and the boundary (K),

q_v = volumetric heat generation rate in molten pool (W/m^3),

L = characteristic length of molten pool (m),

α = thermal diffusivity of molten pool (m^2/s),

ν = kinematic viscosity of molten pool (m^2/s),

k = thermal conductivity of molten pool (W/m ŽK).

The liquid pool heat transfer is correlated with the Rayleigh number through the Nusselt number. Most of the correlations for the Nusselt number of a pool are expressed in the form,

$$Nu = aRa'^b \tag{8-43}$$

where

Nu = Nusselt number,

a, b = numerical constants.

The heat transfer is related to the Nusselt number through the relation

$$h = kNu/L \tag{8-44}$$

where

h = heat transfer coefficient at the boundary (W/m^2 ŽK).

Various researchers have used different values for the characteristic length. These values are: (1) the maximum radius of the liquid surface at the top of the pool, (2) maximum depth of the liquid pool, (3) an average of the maximum pool radius and the pool depth, and (4) radius of an equivalent hemispherical pool. In a correlation for Nusselt number, where $b \approx 0.2$, the characteristic length term cancels and will not make any significant difference to the value of convective heat transfer coefficient, h. In general, the researchers have used the depth of the pool as the characteristic length in their developed heat transfer correlations.

The two Rayleigh numbers are related by a correlation

$$Ra' = Ra\left(\frac{\dot{q}_v L^2}{k\Delta T}\right) \tag{8-45}$$

where $\frac{\dot{q}_v L^2}{k\Delta T}$ is called Damkohler number.

Heat transfer corrections were selected for the upward and downward directions in the oxidic part of the molten pool and for the upward and sideward directions in the metallic part of the molten pool.[8-32] The selected correlations are listed in Table 8-2. For each of the two parts of the molten pool, namely the oxidic and metallic parts, the table presents the heat transfer correlation to be applied at each segment of their boundaries. The table also shows the range in Rayleigh number for which each selected correlation is valid. The selected correlations have been previously subjected to peer review for application to the analysis of a molten pool in the lower head of a LWR.[8-35]

Table 8-2. Selected Nu vs. Ra Correlations .

	Heat Transfer Direction	Nu versus Ra Correlation	Rayleigh No. Range	Reference
With Internal Heat Generation (Oxidic Pool)	*Up*	$Nu_u = 0.345Ra'^{0.233}$ $Nu_u = 0.9Ra'^{0.2}$	$10^{10} \le Ra' \le 3.0 \cdot 10^{13}$ $10^{14} \le Ra' \le 10^{17}$	*Steinberner*[8-33] *Theofanous*[8-34]
	Down	$Nu_m = 0.048Ra'^{0.27}$ $Nu_m = 0.038Ra'^{0.35}$	$10^{12} \le Ra' \le 3 \cdot 10^{13}$ $3 \cdot 10^{13} \le Ra' \le 7 \cdot 10^{14}$	*Theofanous*[8-34] *Theofanous*[8-35]

Table 8-2. Selected Nu vs. Ra Correlations (Continued).

Without Internal Heat Generation (Metallic Pool)	*Up*	$\mathrm{Nu_u} = 0.051\mathrm{Ra}^{0.333}$	$3 \cdot 10^5 \le \mathrm{Ra} \le 7 \cdot 10^9$	*Globe and Dropkin*[8-36]
	Sideward	$\mathbf{Nu}_{\mathrm{ms}} = \left[\mathbf{0.825} \div \frac{0.387\mathrm{Ra}^{0.1666}}{\{1 + (0.492/\mathrm{Pr})^{0.562}\}^{0.2963}}\right]^2$ $\mathrm{Nu_{ms}} = 0.15\mathrm{Ra}^{0.333}$	$\mathrm{Ra} > 2 \times 10^7$	*Churchill*[8-37] *modified Globe and Dropkin*[8-35]

The heat flux is a function of angular position at the boundary of an oxidic molten pool which faces a hemispherical-shaped lower head. This angular dependence as obtained from the mini-ACOPO experiments is described by the correlation,[8-35]

$$f_d(\theta) = 0.1 + 1.08\left(\frac{\theta}{\theta_p}\right) - 4.5\left(\frac{\theta}{\theta_p}\right)^2 + 8.6\left(\frac{\theta}{\theta_p}\right)^3 \quad , \ 0.1 \le \frac{\theta}{\theta_p} \le 0.6 , \tag{8-46}$$

$$f_d(\theta) = 0.41 + 0.35\left(\frac{\theta}{\theta_p}\right) + \left(\frac{\theta}{\theta_p}\right)^2 \quad , \ 0.6 < \frac{\theta}{\theta_p} \le 1 \tag{8-47}$$

where

$f_d(\theta)$ = multiplier to Nusselt number in oxidic pool that accounts for variation in downward heat flux with respect to angular position,

θ = polar angle on the lower head (see Figure 8-8.) (radians),

θ_p = polar angle of top of oxidic pool (see Figure 8-8.) (radians).

An alternative distribution in heat flux with respect to angular position was obtained from experiments performed at University of California at Los Angeles (UCLA).[8-35, 8-38] This angular dependence of heat flux is shown in Figure 8-9. The code user may select either the mini-ACOPO based correlation or the correlation based on experiments performed at UCLA.

8.8.2 Temperature of Oxidic and Metallic Pools and Heat Flux to Lower Head

This section describes the heat balance performed to calculate the transient temperatures of the oxidic and metallic parts of a molten pool in the lower head of a reactor vessel. The section also describes the calculation of the heat transfer at each point of the inner surface of the lower head. The calculations involve a summation of the heat transfer occurring at each segment of the boundaries of the two parts of the molten pool. The heat transfer at the boundary is calculated using the heat transfer correlations presented in the previous section. The oxidic and metallic pools are each assumed to be well-mixed due to natural convection.[8-39] The system analyzed to calculate the temperatures of the two regions is shown in Figure 8-10. The mathematical nomenclature used to perform the heat balance is also shown in the figure.

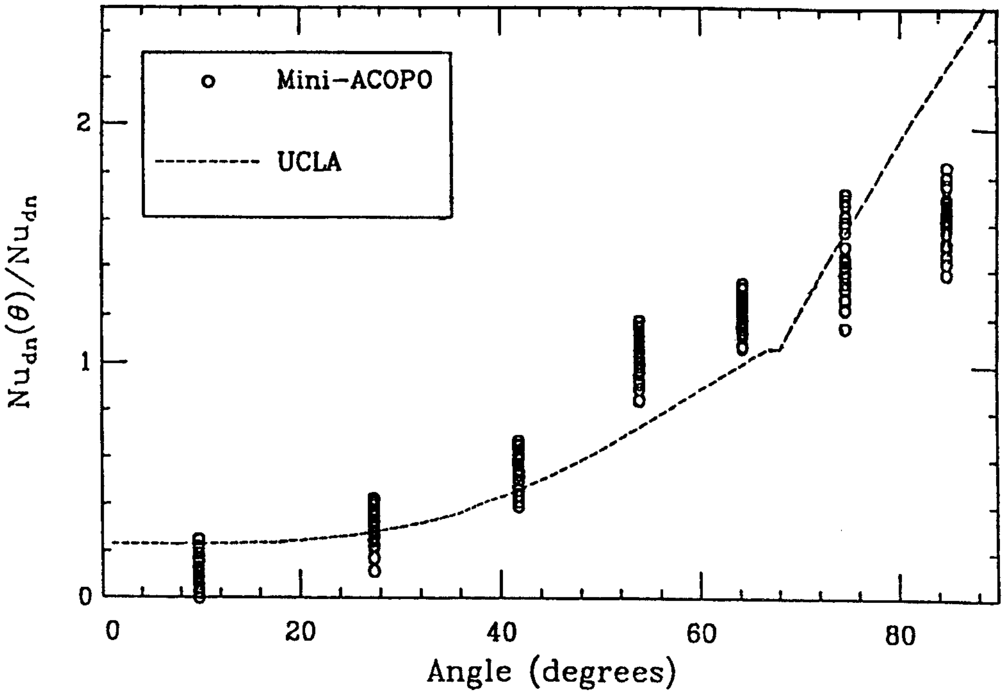

Figure 8-9. Correlations for heat flux as function of angular position.

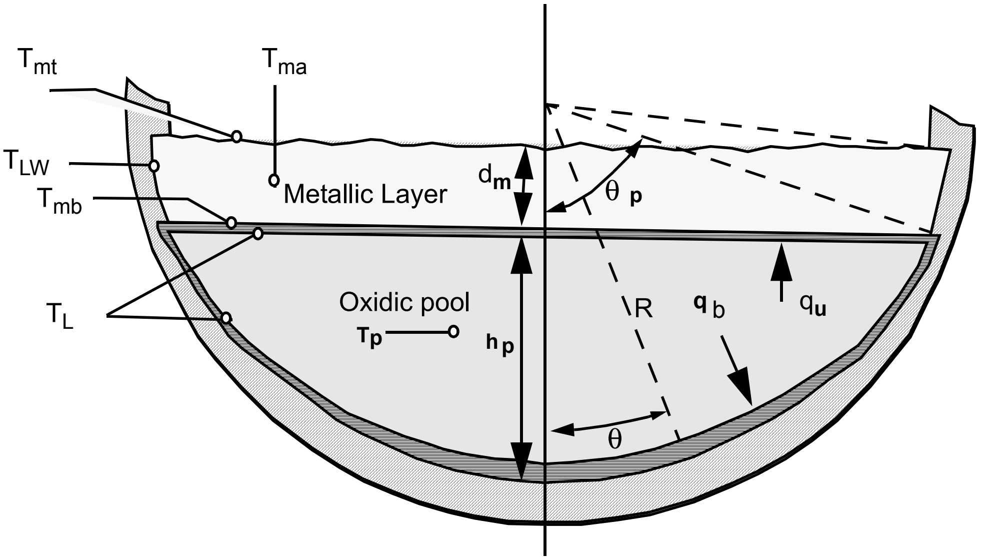

T_{mt}
T_{ma}
T_{LW}
T_{mb}
T_L
Metallic Layer
d_m
θ_p
Oxidic pool
T_p
h_p
R
q_b
q_u
θ

Figure 8-10. Schematic of system analyzed to calculate temperatures of oxidic and metallic parts of stratified molten pool.

The following assumptions are applied in calculating the transient temperatures of the two parts of the molten pool and in calculating the heat flux at each point of the inner surface of the lower head;

1. Oxidic and metallic parts of the molten pool are each well-mixed,
2. Metallic pool contacts only the upper (mostly vertical) inner surface of lower head,
3. Rayleigh numbers are within range of validity identified in Table 8-2.,
4. Length characteristic for heat transfer of oxidic pool is its depth at its centerline,
5. Length characteristic for heat transfer of metallic pool is its depth,
6. No material slumps into molten pool.

Assumption No. 2 limits the valid range of application to lower heads that are almost filled with molten oxidic material. Since a lower head almost filled with molten oxidic material imparts a much larger thermal load to the lower head than a lower head less than 50% filled, this assumption does not limit the validity of the modeling for the case of most interest. Assumption No. 6 is applied because the correlations for heat transfer assume steady state conditions, and frequent slumping of material into the molten pool violates the assumption of steady state conditions. Since the most important period of application of the modeling is the period in which the thermal load to the lower head is maximum, and this period is expected to occur after slumping of core material has terminated, this assumption does not overly restrict the valid range of application of the modeling.

For the oxidic pool, the internal energy change during a time step is equal to the internal heat generation in the oxidic pool minus the heat loss at the boundaries of the pool. The heat balance is expressed by the equation

$$M_p c_p \Delta T_p = \left[V_p Q_p - \int_o^{\theta_p} q_b(\theta) R d\theta - A_i q_u \right] \Delta t \tag{8-48}$$

where

M_p = mass of molten oxidic material (kg),

c_p = heat capacity of molten oxidic material $(J/kg \cdot K)$,

ΔT_p = temperature change of oxidic pool during time step (K),

V_p = volume of oxidic pool (m^3),

Q_p = volumetric heat generation rate of oxidic pool (W/m^3),

θ = angular position of point on hemispherical surface of oxidic pool, (radians),

θ_p = polar angle of top of oxidic pool (see Figure 8-8.) (radians),

R = radius of inner surface lower head (m),

$q_b(\theta)$ = heat flux on bottom boundary of molten pool at angular position of (θ),

$(\mathrm{W/m^2})$,

A_i = area of interface between oxidic and molten pool (m^2),

q_u = heat flux at top surface of molten pool (W/m^2),

Δt = size of time step (s).

The variable $q_b(\theta)$ in the above equation is calculated by the equation

$$q_b(\theta) = f_d(\theta) k_p Nu_{dp}((T_p - T_L)/h_p) \tag{8-49}$$

where

$f_d(\theta)$ = function defining variation with respect to angular position of downward Nusselt number for oxidic pool defined in Equations (8-46) and (8-47) or from Figure 8-9.

k_p = thermal conductivity of molten pool $(\mathrm{W/m \cdot K})$,

Nu_d = Nusselt number in downward direction for oxidic pool,

T_p = volume-averaged temperature of oxidic pool (K),

T_L = liquidus temperature of oxidic pool (K),

h_p = depth of oxidic pool (m).

The heat flux calculated by the above equation is a boundary condition applied at the inner surface of the crust of frozen material at the inner surface of the lower head in order to calculate the transient temperature distribution in the lower head. The details of this calculation are described in Section 7.6.

The variable q_u in Equation (8-48) is calculated by the equation

$$q_u = k_p Nu_u (T_p - T_L)/h_p \tag{8-50}$$

where

Nu_u = Nusselt number in upward direction for oxidic pool (defined in Table 8-2.)

After Equations (8-49) and (8-50) have been substituted into Equation (8-48), then Equation (8-48) is solved for the change in temperature of the oxidic pool during a time step.

The change in temperature of the metallic pool during a time step is calculated by the following equation for heat balance

$$M_s c_{ps} \Delta T_{ma} = [A_i k_m Nu_m (T_{mb} - T_{ma}) / d_m - A_t k_m Nu_m (T_{ma} - T_{mt}) / d_m \qquad (8\text{-}51)$$

$$-A_s k_m Nu_{ms} (T_{ma} - T_{LW}) / d_m] \Delta t$$

where

M_s = mass of material in metallic pool on top of oxidic pool (kg),

c_{ps} = heat capacity of material in metallic pool $J/(kg \cdot K)$,

ΔT_{ma} = change in bulk average temperature of metallic pool during time step (K),

k_m = thermal conductivity of metallic pool $(W/m \cdot K)$,

Nu_m = Nusselt number for heat transfer at bottom and top surfaces of metallic pool,

d_m = depth of metallic pool (m),

T_{ma} = bulk average temperature of metallic pool (K),

T_{mb} = temperature of bottom surface of metallic pool (K),

A_t = area of top surface of metallic pool (m^2),

T_{mt} = temperature of top surface of metallic pool (K),

A_s = area of interface of metallic pool with inner surface of lower head (m^2),

Nu_{ms} = Nusselt number for heat transfer in sideward direction from metallic pool to inner surface of lower head (defined in Table 8-1.),

T_{LW} = liquidus temperature of lower head (K).

The Nusselt number for heat transfer at the bottom and top surfaces of the metallic pool, Nu_m, taken from Reference 8-35, is given by the equation

$$Nu_m = 0.059 Ra^{0.333} \qquad (8\text{-}52)$$

The Nusselt number for heat transfer at the side of the metallic pool, Nu_{ms}, is taken either from the modified Globe and Dropkin correlation, shown in Table 8-2., or from the Churchill and Chu correlation. The Churchhill and Chu correlation is;

$$Nu_{ms} = \left[0.825 + \frac{0.387Ra^{0.166}}{\{1 + (0.492/Pr)^{0.5625}\}^{0.2963}}\right]^2 \tag{8-53}$$

Equation (8-51) requires the temperatures of the metallic pool at its bottom and top surfaces. These temperatures are determined from heat balances performed for the bottom and top surfaces of the metallic pool. Thus, the temperature of the bottom surface of the metallic pool is obtained from the following equation for heat balance;

$$k_m Nu_m[T_{mb} - T_{ma}]/d_m = q_u \tag{8-54}$$

The temperature for the top surface of the metallic pool is obtained from the following equation for heat balance;

$$k_m Nu_m[T_{ma} - T_{mt}]/d_m = \varepsilon\sigma[\,T_{mt}^4 - T_c^4\,] + h_c[T_{mt} - T_c] \tag{8-55}$$

where

ε = emissivity of top surface of metallic layer,

σ = Stefan-Boltzmann constant ($5.668 \times 10^{-8}\ W/m^2 \cdot K^4$),

T_c = temperature of coolant at top surface of metallic layer (K),

h_c = coefficient for convective heat transfer to coolant at top surface of metallic layer $(W/m^2 \cdot K)$.

If the sink temperature for radiative and convective heat transfer is equal to the temperature of the top surface of the metallic pool (adiabatic surface), then from Equation (8-55) the temperature of the top surface is equal to the bulk average temperature of the metallic pool. This equality results in the term in Equation (8-51) for heat transfer from the top surface of the metallic pool being equal to zero, as is appropriate for an adiabatic top surface.

After the bulk average temperatures of the oxidic and metallic parts of the molten pool have been calculated using Equations (8-48) and (8-51), the boundary conditions are then available for calculating the temperature distribution in the lower head. The details of this calculation are described in Reference 1. One of the boundary conditions needed for this calculation is the heat flux on the inner surface of the crust adjacent to the oxidic part of the molten pool; this boundary condition is calculated by Equation (8-49). Another needed boundary condition is the heat flux on the inner surface of the lower head adjacent to the metallic pool. This boundary condition is calculated by the equation

$$q_w = k_m Nu_{ms}(T_{ma} - T_{LW})/d_m \tag{8-56}$$

where

q_w = heat flux at inner surface of lower head adjacent to metallic layer (W/m^2).

If a crust of frozen ceramic material forms between the ceramic molten pool and the metallic pool, then the two molten regions stay separated from each other. But if this crust vanishes, then the ceramic and metallic material may mix. A calculation of the thickness of the crust is useful for estimating whether the two material regions stay separated or may mix. A schematic of the crust and the nomenclature for the calculation of the crust thickness are shown in Figure 8-11. The thickness is calculated from the heat balance equation that equates the heat flux at the bottom surface of the crust with the rate of conduction through the crust. Thus,

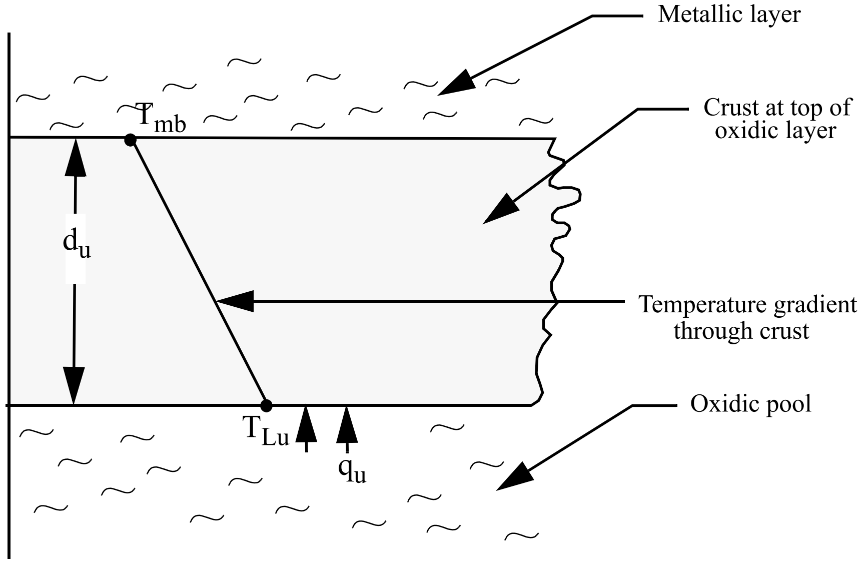
Metallic layer
Crust at top of oxidic layer
T_{mb}
d_u
Temperature gradient through crust
Oxidic pool
T_{Lu}
q_u

Figure 8-11. Schematic of system analyzed for calculating thickness of oxidic crust between oxidic and metallic parts of stratified molten pool.

$$k_{uf}[T_L - T_{mb}]/d_u = q_u \tag{8-57}$$

where

k_{uf} = thermal conductivity of frozen oxidic material $(W/m \cdot K)$,

T_L = liquidus temperature of oxidic pool (K).

The above equation has d_u as its only unknown variable; thus it is used to calculate the thickness of the crust separating the two molten regions. The value of d_u is displayed by SCDAP/RELAP5-3D© to indicate the degree to which the two molten regions can be regarded as separated. In general, the crust thickness is estimated to be less than 0.03 m.[8-35]

If the top surface of the metallic pool is in contact with steam instead of liquid water, then in general a crust of frozen metallic material will not form at the top surface.[8-35]

The calculation of the heat transfer in the metallic pool requires two properties that are not defined in the MATPRO part of SCDAP/RELAP5-3D©. These properties are the coefficient of thermal expansion and the viscosity of liquefied stainless steel. These properties are obtained from Reference 8-35 and are correlated as follows;

$$\beta_s = 1.2 \times 10^{-4} \tag{8-58}$$

where

β_s = coefficient of thermal expansion of liquefied stainless steel (1/K).

$$\mu_s = 2.21 \times 10^{-4} \exp(5776/T) \tag{8-59}$$

where

μ_s = dynamic viscosity of liquefied stainless steel $(\mathrm{kg/m \cdot s})$,

T = temperature of liquefied stainless steel (K).

8.9 Movement of Melted Core Plate Material Through Porous Debris

In the event of a severe accident in a Light Water Reactor (LWR), particles of a ceramic mixture of UO_2 and ZrO_2 may stack in the lower head of the reactor vessel and form a porous debris bed. A schematic of the porous debris bed is shown in Figure 8-12. The slumping of jets of a mixture of molten $(U, Zr)O_2$ into a pool of water in the lower head is an example of a reactor core degradation event that may occur during a severe accident and result in the configuration of material shown in Figure 8-12. If the severe accident is not terminated, then eventually core plate material may melt and slump onto the top of the bed of ceramic particles. The core plate is generally composed of stainless steel and thus melts at a much lower temperature than the particles of $(U, Zr)O_2$ (1700 K versus ~3000 K). The subsequent heatup of the debris bed and lower head is a function of the extent to which the melted core plate permeates into the bed of $(U, Zr)O_2$ particles. This section describes a model for calculating the permeation of the melted core plate material into the porous debris bed and the affect of the permeation on the heatup of the debris bed and lower head supporting the debris bed. A more detailed description of the model and its calculations are given in Reference 8-40 and Reference 8-41.

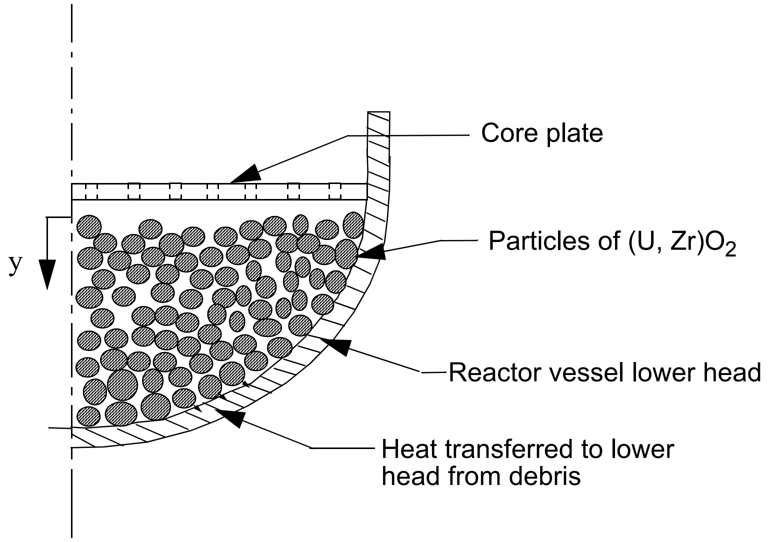
Core plate
Particles of $(U, Zr)O_2$
y
Reactor vessel lower head
Heat transferred to lower head from debris

Figure 8-12. Schematic of system represented by COUPLE model (particle size of debris greatly exaggerated).

This section is organized as follows. Section 8.9.1 describes the model applied to calculate the movement of liquefied core plate material through the interstices in a matrix of porous $(U, Zr)O_2$ debris. Section 8.9.2 describes the effect of liquefied material movement on debris bed heat transfer. Section 8.9.3 describes the boundary conditions for porous debris with liquefied material slumping onto it and liquefied material permeating to the bottom of it. The numerical solutions for the processes being modeled are described in Section 8.9.4.

8.9.1 Models for Movement of Material in Porous Debris

This section describes the model to be applied for calculating the movement liquefied core plate material through the interstices in a matrix of porous material. The system to be analyzed has been previously shown in Figure 8-12. The movement of the liquefied material is driven by several forces, including gravity, capillary force, and pressure gradient. Resistances to movement are caused by viscous forces, turbulence and form losses due to a continuous contraction and expansion of flow areas as the liquefied material flows through the porous debris. The resistances to movement increase with the velocity of the moving material. The balancing of the forces driving the movement of the liquefied material with the forces resisting the movement results in a conservation of momentum equation for the liquefied material.

The following assumptions are applied to simplify the modeling in a manner that maintains an accuracy of solution of the same order of magnitude as the uncertainties of governing material properties and debris behavior.

1. The porous medium is composed only of $(U, Zr)O_2$ particles.

2. The material permeating the porous medium is composed only of stainless steel.

3. Stainless steel does not chemically react with $(U, Zr)O_2$.

4. The (U, Zr)O_2 particles do not melt.

5. The permeating stainless steel is in thermal equilibrium with the (U, Zr)O_2 particles it contacts.

6. Stainless steel does not permeate through any location with a temperature less than the solidus temperature of stainless steel (1671 K).

7. Stainless steel does not permeate through any location with a temperature greater than the melting temperature of (U, Zr)O_2 (~3000 K).

8. Gas does not flow through the porous debris bed.

9. Water is not present at any location with liquefied stainless steel.

10. Capillary forces are negligible.

11. The frictional drag on the liquefied stainless steel is balanced by the force of gravity with the result of quasi-steady flow of the liquefied material through the voids in the debris bed (acceleration of liquefied material and momentum flux are small compared to gravity).

12. The relative passability of the debris bed is equal to its relative permeability.

13. Liquefied stainless steel does not move in the radial direction; this assumption is based on the expectation of debris characteristics and extent of saturation that are almost uniform in the radial direction.

14. The effect of a wall (lower head) on the movement of the liquefied stainless steel is negligible.

In general, the assumptions are consistent with the expected behavior of the core plate and the expected characteristics of lower plenum debris. The omission of the inertial and capillary terms in the momentum equation is based on order of magnitude analyses; the results of these analyses are presented in Reference 8-40. The thermal equilibrium of the permeating core plate material with the debris particles it contacts is also justified by an order of magnitude analysis presented in Reference 8-40. Factors in this justification are the relatively slow motion of the permeating material and the relatively small mass of the permeating stainless steel compared to the mass of the debris particles it contacts.

Taking into account the above assumptions, the conservation of momentum equation for the liquefied material is given by the equation.[8-30, 8-42]

$$\frac{\mu_l j}{k_l k} + \frac{\rho_l j^2}{m_l m} = \rho_l g \tag{8-60}$$

where

μ_l = dynamic viscosity of liquefied material ($kg/m \cdot s$),

j = superficial velocity of liquefied material (m/s),

k = Darcy permeability (m^2),

k_l = relative permeability (unitless),

m = passability of debris bed (m),

m_l = relative passability of debris bed (unitless),

ρ_l = density of liquefied material (kg/m^3),

g = acceleration of gravity ($9.8\ m/s^2$).

The second term of the above equation is the turbulent drag counterpart to the viscous drag represented by the first term.

The Darcy permeability is calculated by the equation

$$k = \frac{\varepsilon^3 D_P^2}{150(1-\varepsilon)^2} \tag{8-61}$$

where

ε = porosity of the debris bed (unitless),

D_P = diameter of particles in debris bed (m).

The passability of the debris bed is calculated by the equation

$$m = \frac{\varepsilon^3 D_P}{1.75(1-\varepsilon)} \tag{8-62}$$

In general the relative passability is less than the relative permeability, but they are assumed to be equal for this analysis.[8-43] Thus,

$$m_l = k_l \tag{8-63}$$

The relative permeability is a function of the effective saturation of the debris bed and the Darcy permeability. The relative permeability is calculated by the equation[8-30]

$$\begin{aligned} k_l &= S_e^3\ ,\ S_e > 0 \\ k_l &= 0,\ S_e \le 0 \end{aligned} \tag{8-64}$$

where

S_e = effective saturation of debris bed (unitless).

The effective saturation is calculated by the equation[8-30]

$$S_e = \frac{S - S_r}{1 - S_r} \tag{8-65}$$

where

S = true saturation of debris bed; volume fraction of liquefied material in pores of debris bed (unitless),

S_r = residual saturation of debris bed (unitless).

The residual saturation, S_r, is a function of the surface tension of the liquid and of the degree of wetting of the solid material by the liquefied material. Reference 8-30 provides an empirical equation for calculating residual saturation that is appropriate for debris resulting from the disintegration of nuclear reactor cores. This equation is

$$S_r = \begin{cases} \dfrac{1}{86.3}\left[\dfrac{\gamma\cos(\theta)}{k\rho_l g}\right]^{0.263} & ;0 \le \theta \le 90^\circ \\ 0 & ;90^\circ < \theta \le 180^\circ \end{cases} \tag{8-66}$$

where

γ = surface tension of the liquid (N/m),

θ = wetting contact angle (degrees).

In the case of liquefied material that does not wet the solid material ($90^o < \theta < 180^o$), the residual saturation is equal to zero. An example of such a system is a debris bed composed of (U, Zr)O_2 and liquefied stainless steel.[8-30] In this case, bulk motion occurs at a relatively low values of bed saturation.

The conservation of mass equation is applied to obtain the relation of the rate of change with time of the local saturation of the debris bed to the local velocity of the liquefied debris. The result is the equation

$$\frac{\partial S}{\partial t} = -\frac{\partial j}{\partial y} \qquad (T_s < T_{sol}) \tag{8-67}$$

where

t = time (s),

y = spatial coordinate that defines elevation (defined in Figure 8-12.)(m).

Equations (8-60) and (8-67) are a set of two equations for solving for the variables j and S. The terms k_l and m_l in Equation (8-60) are a function of S and thus contribute to the nonlinearity of the set of equations. Although the momentum equation in the model described in Reference 8-30 omits the turbulent term in Equation (8-60), Reference 8-40 performed a study indicating that for a saturated debris bed the omission of the turbulent term results in a factor of three overprediction of the velocity of the liquefied material. So the turbulent term is being retained for the present model.

8.9.2 Effects of Material Movement on Debris Bed Heat Transfer

The movement of liquefied core plate material through the interstices in a porous debris bed results in the transport of energy within the debris bed. In addition, the movement of the liquefied material through the debris bed influences the thermal conductivity and heat capacity of the debris bed. As a result, the movement of liquefied material may have a significant influence on the temperature distribution within the debris bed. This section defines the change made to the heat transport equations in the COUPLE model (described in Section 8.1) to account for the effect of material movement on temperature distribution.

The COUPLE model calculates the transport of heat through a porous medium by the equation

$$(\rho c_v)_e \frac{\partial T}{\partial t} = \frac{\partial}{\partial x}\left(k_e \frac{\partial T}{\partial x}\right) + \frac{\partial}{\partial y}\left(k_e \frac{\partial T}{\partial y}\right) + Q_D(x, y) - Q_c(x, y) \tag{8-68}$$

where

$(\rho c_v)_e$ = $(1 - \varepsilon_h)(\rho c_v)_m$,

ρ = density (kg/m^3),

c_v = constant volume specific heat $(J/kg \cdot K)$,

k_e = effective thermal conductivity $(W/m \cdot K)$,

$Q_D(x,y)$ = volumetric heat generation rate at location with coordinates of (x, y) (W/m^3),

$Q_c(x,y)$ = heat transferred at location (x, y) by convection and radiation from particles of debris to fluid in interstices of the particles (W/m^3),

T = temperature of debris (K),

ε_h = heat conduction porosity of debris; $\varepsilon(1 - S)$ (unitless),

S = saturation of debris bed,

x = spatial coordinate in horizontal direction (m),

y = spatial coordinate in vertical direction (m),

m = subscript indicating mixture of stainless steel and $(U, Zr)O_2$.

The above equation calculates heat transport through debris by conduction and radiation. To account for the transport of heat by the movement of liquefied material, the Q terms in the above equation are replaced by the term

$$Q_N = Q_D(x, y) - Q_c(x, y) + Q_T \tag{8-69}$$

where

Q_N = net volumetric heat generation rate (W/m^3),

Q_T = effective heat generation due to movement of liquefied material (W/m^3).

The variable Q_T in the above equation is a function of the rate of flow of the liquefied material and the temperature gradient in the debris bed. Taking into account the instant thermal equilibrium of the liquefied material with the debris it contacts (Assumption Number 5 in Section 8.9.1) this variable is calculated by the equation

$$Q_T = -\rho_l c_p j \frac{\partial T}{\partial y} \tag{8-70}$$

where

j = superficial velocity of liquefied material (m/s),

ρ_l = density of liquefied material (kg/m^3),

c_p = heat capacity of liquefied material $(J/kg \cdot K)$,

$\frac{\partial T}{\partial y}$ = temperature gradient in debris bed in direction of movement of liquefied material (K/m).

The movement of liquefied material through the interstices of a porous debris bed influences the effective thermal conductivity of the debris bed. The effective thermal conductivity is a function of the heat transport porosity of the debris bed, as described in Section 8.3. The heat transport porosity is a function of the saturation of the debris as calculated by the equation

$$\varepsilon_h = \varepsilon(1 - S) \tag{8-71}$$

where

ε_h = heat transport porosity (unitless),

ε = porosity for movement of fluid (unitless),

S = degree of saturation of interstices of debris particles with liquefied or previously liquefied core plate material (unitless).

When the degree of saturation is equal to 1.0, then no pores are present and the conduction of heat is not reduced due to porosity.

8.9.3 Boundary Conditions

This section describes the boundary conditions applied to the model for movement of liquefied core plate material through a ceramic porous debris bed below the core plate. A schematic of the boundary conditions for the model is shown in Figure 8-13.

For the top of the debris bed, the equation for the velocity of the liquefied material, namely Equation (8-60), is replaced by the equation

$$j_T = G/\rho_l \tag{8-72}$$

where

j_T = superficial velocity of liquefied material at top surface of debris bed (m/s),

G = rate of melting of structure above debris bed per unit of cross sectional area (kg/s)/m^2.

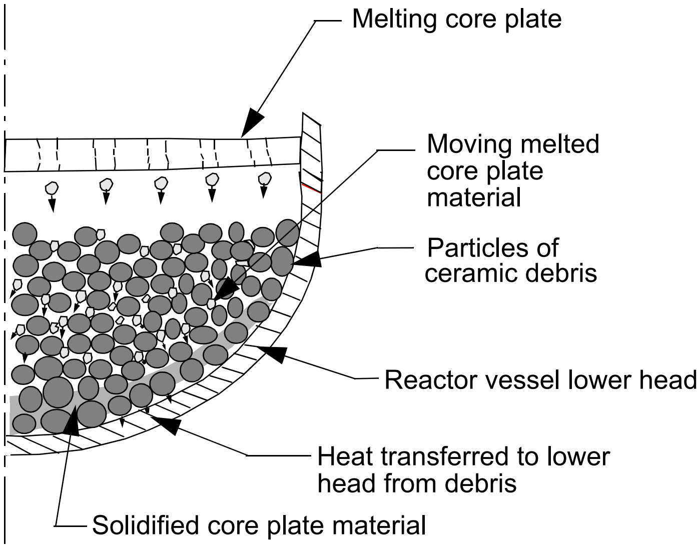
Melting core plate
Moving melted core plate material
Particles of ceramic debris
Reactor vessel lower head
Heat transferred to lower head from debris
Solidified core plate material

Figure 8-13. Schematic of material movement occurring when core plate melts and lower head supports ceramic porous debris.

The variable G is either calculated by the core plate model[8-44] or user-defined; the user selects the option.

The heat transfer at the bottom boundary of the debris bed is increased by the movement of melted core plate material to the bottom boundary. The heat transfer at the bottom boundary is proportional to the gap heat transfer coefficient defined for the interface of the debris and the lower head supporting the debris. This gap heat transfer coefficient is user-defined. For any location on the interface that has been contacted by liquefied material, the user-defined gap heat transfer coefficient is replaced by a gap heat transfer coefficient with a value of $10{,}000\ \mathrm{W/m^2 \cdot K}$, which simulates the heat transfer across a gap filled with material with a relatively large thermal conductivity.

8.9.4 Numerical Solution

An explicit, iterative scheme for numerical solution is used to solve for the distribution in velocity and debris bed saturation. The coordinate system and the nodalization for the numerical solution are shown in Figure 8-14. The debris bed is divided into a stack of control volumes. The control volumes are connected to each other with junctions. The extent of bed saturation is calculated for each control volume and the velocity of the liquefied material is calculated at each junction. The scheme for the numerical solution is based on the concept that the velocity gradient changes at a slower rate than the degree of bed saturation. In the first step for the first iteration, the change in bed saturation for each control volume is calculated using previous time step velocities at the junctions of the control volumes. Next, the end of time step velocity at each junction is calculated using the values for bed saturation calculated in the previous step. Next, the bed saturation in each central volume is calculated using the velocities just calculated for the end of the time step. If at any control volume the difference between the last two values calculated for bed saturation is greater than the tolerance for error in bed saturation, another iteration is performed. Subsequent iterations are performed until convergence is obtained at each control volume.

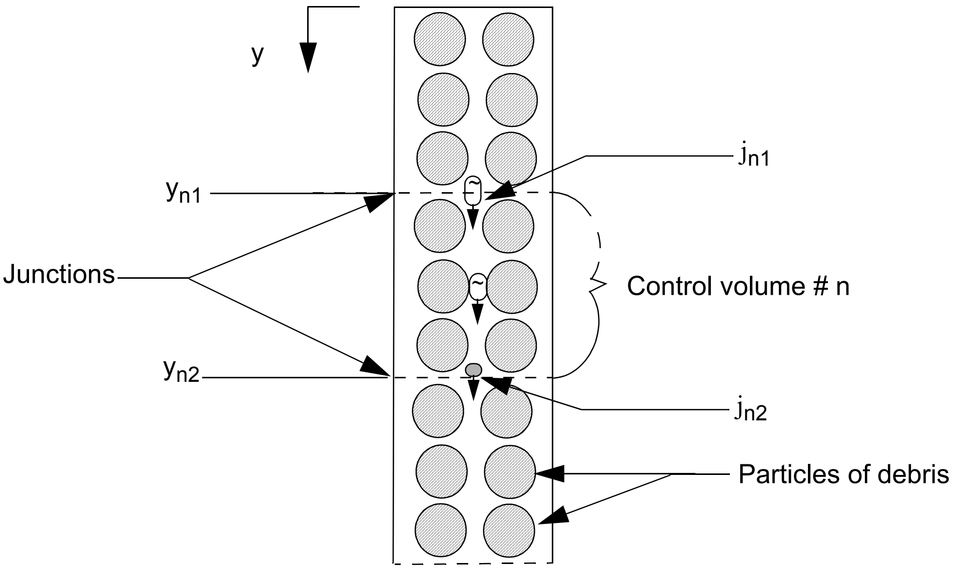

Figure 8-14. Coordinate system for numerical solution.

The equations in the numerical solution scheme are arranged as follows. First, a guess of the end of time step bed saturation is calculated using the equation

$$S_n^{m+1} = S_n^m - \left[\frac{(j_{n2}^m - j_{n1}^m)}{(y_{n2} - y_{n1})}\right]\Delta t \tag{8-73}$$

where

m = time step number,

S_n^{m+1} = bed saturation at control volume n at end of time step,

S_n^m = same as S_n^{m+1}, but for start of time step,

j_{n2}^m = superficial velocity at start of time step of liquefied material at junction at downwind side of control volume n (m/s),

j_{n1}^m = same as j_{n2}^m, but for junction at upwind side of control volume n (m/s),

y_{n2} = elevation of junction at downwind side of control volume n (m),

y_{n1} = elevation of junction at upwind side of control volume n (m),

Δt = time step (s).

In the above equation, the control volumes are assumed to have uniform cross sectional areas.

Two categories of porosity are calculated at each control volume at each time step. One category of porosity, named the mass transport porosity, is used in the equations that calculate the flow of liquefied material. For this category, the volumes of liquid and gas are lumped together to represent the porosity. The other category of porosity, named the heat conduction porosity, is used in the equations that calculate the conduction of heat through the debris bed. For this category, the volumes of solid material and liquefied debris are lumped together.

The heat conduction porosity is related to the mass transport porosity by the equation

$$\varepsilon_h = \varepsilon(1 - S_n^{m+1}) . \tag{8-74}$$

where

ε_h = heat conduction porosity (unitless),

ε = mass transport porosity (unitless),

S_n^{m+1} = saturation of debris bed (unitless).

Next, the Darcy permeability and the passability of the debris bed are updated using the equations

$$k_n = \frac{\varepsilon^3 D_P^2}{150(1-\varepsilon)^2} \tag{8-75}$$

$$m_n = \frac{\varepsilon^3 D_P}{1.75(1-\varepsilon)} \tag{8-76}$$

where

k_n = Darcy permeability of debris bed at control volume n (m^2),

m_n = passability of debris bed at control volume n (m).

Then, the effective saturation of the debris bed at the end of the time step for each control volume is calculated using the equation

$$S_{en}^{m+1} = \frac{S_n^{m+1} - S_r}{1 - S_r} \tag{8-77}$$

where

S_{en}^{m+1} = effective saturation at control volume n at end of time step.

The residual saturation, S_r, is a function of material properties, namely wetting angle, surface tension, Darcy permeability, and liquid density; it is calculated using Equation (8-66).

Next, the relative permeability of the debris bed at the end of the time step for each control volume is calculated using the equation

$$k_{ln}^{m+1} = [S_{en}{}^{m+1}]^3 \tag{8-78}$$

where

k_{ln}^{m+1} = relative permeability at control volume n at end of time step.

The relative passability of the debris bed at the end of the time step for each control volume is calculated using the equation

$$m_{ln}^{m+1} = k_{ln}^{m+1} \tag{8-79}$$

where

m_{ln}^{m+1} = relative passability of debris bed at control volume n at end of time step.

Next, the velocity of the liquefied material at each junction is calculated using Equation (8-60). For numerical solution, terms in this equation are combined as follows

$$A[j_i^{m+1}]^2 + Bj_i^{m+1} + C = 0 \tag{8-80}$$

where

j_i^{m+1} = superficial velocity at junction i at end of time step (m/s),

A = $\dfrac{\rho_l}{m_{li}^{m+1}\ m_i}$

B = $\dfrac{\mu_l}{k_{\ li}^{m+1}\ k_i}$

C = $-\rho_l\ g$

ρ_l = density of liquefied debris (kg/m^3),

μ_l = dynamic viscosity of liquefied material $(\mathrm{kg/m \cdot s})$,

g = acceleration of gravity (9.8 m/s^2),

m_i = passability at junction i (m),

m_{li}^{m+1} = relative passability at junction i at end of time step (unitless),

k_i = permeability at junction i (m^2),

k_{li}^{m+1} = relative permeability at junction i at end of time step (unitless).

The junction numbers are related to the control volume numbers by the equations

$$i_u = n \tag{8-81}$$

$$i_d = n+1 \tag{8-82}$$

where

i_u = upstream junction of control volume n,

i_d = downstream junction of control volume n.

The relative permeability and passability at junction i are defined to be the average of the values of these variables at the two control volumes upwind and downwind of junction i.

Applying the quadratic equation, the superficial velocity of the liquefied material at each node at the end of the time step is calculated using the equation

$$j_i^{m+1} = \frac{-B \pm [B^2 - 4AC]^{0.5}}{2A} \tag{8-83}$$

The above equation has two values. Since the liquefied material can only flow down, only the positive value is applied.

At the top junction in the debris bed, the superficial velocity is calculated by the equation

$$j_1 = G/\rho_l \tag{8-84}$$

where

j_1 = superficial velocity at top junction in debris bed (m/s), G = rate of melting of structure above the debris bed per unit of cross sectional area $(kg/s)/m^2$.

At the bottom junction, the boundary condition corresponding to an impermeable boundary is imposed. Thus,

$$j_{nb} = 0.0 \tag{8-85}$$

where

j_{nb} = superficial velocity at bottommost junction in debris bed (m/s).

Two constraints are applied to the motion of liquefied material. First, if the temperature at a location is less than the melting temperature of stainless steel, then that location is impermeable. Second, if the temperature at any location is greater than the melting temperature of a mixture of UO_2 and ZrO_2, then that location is impermeable. This constraint is based on the assumption that melted (U, Zr)O_2 will flow a small distance, freeze, and form an impermeable crust. These constraints are applied by the equation

$$j_i^{m+1} = 0 \left(\begin{array}{l} T_i < T_{ms} \\ T_i > T_{mu} \end{array} \right. \tag{8-86}$$

where

T_i = temperature at junction i,

T_{ms} = solidus temperature of stainless steel (1671 K),

T_{mu} = solidus temperature of mixture of UO_2 and ZrO_2 (~2830 K).

If a crust of frozen (U, Zr)O_2 existed at a location before the melting of the core plate began, then that location is implicitly represented as impermeable from the assignment of a porosity of zero for that location.

The bed saturation in each control volume at the end of the time step is then calculated using Equation (8-73) with the start of time step superficial velocities in this equation replaced with the end of time superficial velocities calculated by Equation (8-83).

The fractional difference in bed saturation between two successive iterations is calculated by the equation

$$f_n = \frac{\left|S_n^{r+1} - S_n^r\right|}{0.5(S_n^{r+1} + S_n^r)} \tag{8-87}$$

where

f_n = fractional difference in value of S_n^{m+1} between two successive iterations,

r = iteration number,

S_n^r = value of S_n^{m+1} at r-th iteration.

If the value of f_n at any control volume is greater than the tolerance in error for bed saturation, another iteration is performed. The value of the tolerance in error is defined by the user; the results of a sensitivity study indicate that a value of 0.001 is appropriate.

After convergence of the debris bed saturation at each control volume has been obtained, the effect of the movement of liquefied material during the time step on heat transport is calculated. First, Equation (8-70) is used to calculate the term added to the volumetric heat generation rate for each control volume to account for the transport of liquefied material. Then, the heat conduction porosity for each control volume is updated to account for the addition or subtraction of material from each control volume during the time step. Then, the volume fractions of stainless steel and (U, Zr)O_2 at each control volume are updated to account for the addition or subtraction of material from each control volume during the time step. The particle size at each control volume is assumed to not be influenced by the presence of liquefied debris or frozen previously liquefied debris.

The volumetric heat generation at a control volume to account for the thermal effect of the addition by flow of liquefied material to the control volume is calculated by the equation

$$Q_{Tn} = -0.5(j_{n1} + j_{n2})\rho_1 c_p (T_{n2} - T_{n1}) / (y_{n2} - y_{n1}) \tag{8-88}$$

where

Q_{Tn} = heat transported into control volume n due to movement of liquefied material (W/m^3),

c_p = heat capacity of liquefied material flowing into control volume n $(J/kg \cdot K)$,

T_{n2} = temperature at downwind junction of control volume n (K),

T_{n1} = temperature at upwind junction of control volume n (K).

Next, the calculation is made of the volume fractions of stainless steel and (U, Zr)O_2 at each control volume. The volume fraction of stainless steel is calculated by the equation

$$f_{sn} = \varepsilon S_n^{m+1} / ((1-\varepsilon) + \varepsilon S_n^{m+1}) \tag{8-89}$$

where

f_{sn} = volume fraction of stainless steel at control volume n at end of time step.

The volume fraction of (U, Zr)O_2 is calculated by the equation

$$f_{un} = (1-\varepsilon)/(\varepsilon S_n^{m+1} + (1-\varepsilon)) \tag{8-90}$$

where

f_{un} = volume fraction of (U, Zr)O_2.

8.10 References

8-1. E. C. Lemmon, *COUPLE/FLUID: A Two-Dimensional Finite Element Thermal Conduction and Advection Code,* EGG-ISD-SCD-80-1, February 1980.

8-2. J. E. Kelly, J. T. Nitchevek, and M. L. Schway, "Heat Transfer Characteristics of Dry Porous Particular Beds with Internal Heat Generation," *Proceedings of ASME/JSME Thermal Engineering Joint Conference, Honolulu, HI, Volume 4, 1983,* p. 83.

8-3. S. Imura and E. Takegoshi, "Effect of Gas Pressure on the Effective Thermal Conductivity of Pack Beds," *Heat Transfer Japanese Research, 3,* 4, 1974, p. 13.

8-4. D. Vortmeyer, "Radiation in Packed Solids," *6th International Heat Transfer Conference, Toronto, Canada, 1978.*

8-5. G. P. Wilhite, D. Kunii, and J. M. Smith, "Heat Transfer in Beds of Fine Particles (Heat Transfer Perpendicular to Flow)," *AIChE Journal, 8,* 3, 1952, p. 340.

8-6. A. V. Luikov, A. G. Shashkov, L. L. Vasiliev, and Yu E. Fraiman, "Thermal Conductivity of Porous Systems," *International Journal of Heat Mass Transfer, 11,* 1968, p. 117.

8-7. L. J. Siefken et al., *Extension to SCDAPRELAP5/MOD2 Debris Analysis Models for the Severe Accident Analysis of SRS Reactors, Final Design Report,* EGG-EAST-8508, June 1989.

8-8. J. M. Savino and R. Siegel, "An Analytical Solution for Solidification of a Moving Warm Liquid onto an Isothermal Wall," *Int. J. Heat and Mass Transfer, 12,* July 1969, pp. 803-809.

8-9. M. Epstein and H. K. Fauske, *The TMI-2 Core Relocation - Heat Transfer and Mechanisms,* EGG-TMI-7956, July 1987.

8-10. M. Jahn and H. H. Reineke, "Free Convection Heat Transfer with Internal Heat Source, Calculations and Measurements," *Proceedings of the International Meeting on Thermal Nuclear Reactor Safety,* NUREG/CR-0027, 2, February 1983, pp. 996-1010.

8-11. M. Jahn and H. Reineke, "Free Convection Heat Transfer with Internal Heat Sources, Calculations and Measurements," *Proceedings of the 5th International Heat Transfer Conference, Tokyo, Japan, September 1974.*

8-12. C. M. Allison, J. L. Rempe, and S. A. Chavez, “Final Design Report on SCDAP/RELAP5 Model Improvements - Debris Bed and Molten Pool Behavior,” INEL-96/0487, December 1996.

8-13. S. Paik and L. J. Siefken, “Extensions to SCDAP/RELAP5 Code for the Modeling of Thermal-Hydraulic Behavior in Porous Debris Beds - Preliminary Design Report,” EGG-RAAM-10683, March 1993.

8-14. V. K. Dhir, R. Viskanta, and H. Esmaili, “Review of Extensions to SCDAP/RELAP5 Code for the Modeling of Thermal-Hydraulic Behavior in Porous Debris”, U. S. Nuclear Regulatory Commission Contract NRC 04 92-045, Task 3, June 1993.

8-15. V. X. Tung, “Hydrodynamic and Thermal Aspects of Two-Phase Flow Through Porous Media,” Ph. D. Thesis, University of California, Los Angeles, 1988.

8-16. D. K. Edwards, V. E. Denny and A. Mills, Jr., “Transfer Process”, McGraw-Hill Book Comp., New York, New York, 1979.

8-17. The RELAP5 Development Team, “RELAP5/MOD3 Code Manual, Vol. IV: Models and Correlations,” NUREG/CR-5535, INEL-95/0174, August 1995.

8-18. D. J. Gunn, “Transfer of Heat or Mass to Particles in Fixed and Fluidized Beds,” Int. J. Heat and Mass Transfer, Vol. 21, 1978, pp. 467-476.

8-19. W. M. Rohsenow, “A Method for Correlating Heat Transfer Data for Surface Boiling of Liquids,” Trans. ASME, 1952, p. 969.

8-20. J. S. Ded and J. H. Lienhard, “The Peak Pool Boiling Heat Flux from a Sphere,” AIChE Journal, Vol. 18, No. 2, 1972.

8-21. V. K. Dihr and G. P. Purohit, “Subcooled Film-Boiling Heat Transfer from Spheres,” Nuclear Engineering and Design, Vol. 47, 1978, pp.49-66.

8-22. W. Chu, V. K. Dhir, and J. S. Marshall, “Study of Pressure Drop, Void Fraction and Relative Permeabilities of Two-Phase Flow through Porous Media,” AICHE Symposium Series, Vol. 79, No. 225, 1983, pp. 224-235.

8-23. V. X. Tung and V. K Dhir, “A Hydrodynamic Model for Two-Phase Flow Through Porous Media,” Int. J. Multiphase Flow, Vol. 14, No. 1, 1988 pp. 47-65.

8-24. V. X. Tung, V. K. Dhir, and D. Squarer, “Forced Flow Cooling Studies of Volumetrically Heated Porous Layers,” Second International Topical Meeting on Nuclear Reactor Thermal-Hydraulics, Santa Barbara, California, USA, January 11-14, 1983.

8-25. M. Chung and I. Catton, “Post-Dryout Heat Transfer in a Multi-Dimensional Porous Bed,” Nuclear Engineering and Design, 128, 1991, pp. 289-304.

8-26. I. Catton and M. Chung, “Two-Phase Flow in Porous Media with Phase Change: Post-Dryout Heat Transfer and Steam Injection,” Nuclear Engineering and Design, 151, 1994, pp. 185-202.

8-27. N. K. Tutu et al., “Debris Bed Quenching under Bottom Flood Conditions (In-Vessel Degraded Core Cooling Phenomenology),” NUREG/CR-3850, 1984.

8-28. E. A. Harvego and L. J. Siefken, “SCDAP/RELAP5 Modeling of Fluid Heat Transfer and Flow Losses through Porous Debris in a Light Water Reactor,” Eight International Conference on Nuclear Engineering, Baltimore, Maryland USA, April 2-6, 2000.

8-29. R. Byron, Warren E. Stewart, and Edwin N Lightfoot,” Transport Phenomena,” John Wiley and Sons, New York 1960.

8-30. R. C. Schmidt and R. D. Gasser, “Models and Correlations of the Debris Late-Phase Melt Progression Model,” SAND93-3922, 1997.

8-31. L. J. Siefken, E. W. Coryell, S. Paik, and H. Kuo, “SCDAP/RELAP5 Modeling of Heat Transfer and Flow Losses in Lower Head Porous Debris,” INEEL/EXT-98-00820, Rev. 2, July 1999.

8-32. L. J. Siefken and M. S. Sohal,” A Heat Transfer Model for a Stratified Corium-Metal Pool in the Lower Plenum of a Nuclear Reactor,” INEEL/EXT-99-00763, Rev. 1, January 2000.

8-33. U. Steinberner and H. H. Reinke, “Turbulent Buoyancy Convection Heat Transfer with Internal Heat Source,” Sixth International Heat Transfer Conference, Toronto, Canada, August 7-11, 1978, Vol. 2, NC-21, pp. 305-311, Hemisphere Publishing Corp., Washington, DC.

8-34. T. G. Theofanous, M. Maguire, S. Angelini, and T. Salmassi, “The First Results from the ACOPO Experiment,” Proceedings of International Topical Meeting on Probabilistic Safety Assessment (PSA ‘96), Sept. 29-Oct. 3, 1996, pp. 1343-1350.

8-35. T. G. Theofanous, C. Liu, S. Additon, S. Angelini, O. Kymalainen, and T. Salmassi, “In-Vessel Coolability and Retention of a Core Melt,” Report DOE/ID-10460, Vol. 1, Chapter 5, July 1995.

8-36. S. Globe and D. Dropkin, “Natural Convection Heat Transfer in Liquid Confined by Two Horizontal Plates and Heated from Below,” J. Heat Transfer, 81, 1959, pp. 24-28.

8-37. Churchill, S. W. and H. S. Chu, Int. J., Heat Mass Transfer, 18, 1323 (1975).

8-38. F. J. Afsia and V. K. Dhir, “An Experimental Study of Natural Convection in a Volumetrically Heated Spherical Pool Bounded on Top with a Rigid Wall,” in In-Vessel Coolability and Retention of a Core Melt, edited by Theofanous et al., Report DOE/ID-10460, Vol. 1, Appendix C, July 1995.

8-39. K. M. Kelkar, K. M. Khankari, and S. V. Patankar, Computational Modeling of Turbulent Natural Convection in Flows Simulating Reactor Core Melt, Report by Innovative Research, Inc. to Sandia Nation Laboratories, December 1993.

8-40. L. J. Siefken, “SCDAP/RELAP5 Modeling of Movement of Melted Material Through Porous Debris in Lower Head,” INEEL/EXT-98-1178 Rev. 2, October 1999,

8-41. L. J. Siefken and E. A. Harvego, “SCDAP/RELAP5 Modeling of Movement of Melted Material through Porous Debris in Lower Head,” Proceedings of the Eighth International Conference on Nuclear Engineering, April 2-6, 2000, Baltimore, MD USA.

8-42. L. J. Siefken, “SCDAP/RELAP5 Modeling of Movement of Melted Material Through Porous Debris in Lower Head,” INEEL/EXT-98-01178, December 1998.

8-43. Mo Chung and Ivan Catton, “Post-Dryout Heat Transfer in a Multi-Dimensional Porous Bed,” Nuclear Engineering and Design 128 (1991) pages 289-304.

8-44. E. W. Coryell and F. P. Griffin, “SCDAP/RELAP5 Lower Core Plate Model,” INEEL/EXT-99-01029, September, 1999.

9. HEAT TRANSFER AND FLOW LOSSES IN POROUS DEBRIS

The SCDAP/RELAP5-3D$^{©}$ models for heat transfer and flow losses in porous debris are based on different principles than those for the corresponding behavior in fuel assemblies and pipes. During a severe accident in a LWR, porous debris may accrete in the core region and in the lower head. The porous debris in the core region generally results from the reflood of embrittled fuel rods, such as when accumulator water partially floods a reactor core with partially oxidized and embrittled fuel rod cladding. The porous debris in the lower head generally results from molten material in the core region slumping in the configuration of jets, and then penetrating a pool of water in the lower head, where the jets break into a large number of particles and the particles partially quench. Porous debris generally consists of small particles packed closely together. The fluid flowing through the porous debris follows a tortuous path through the interstices of the debris particles. As a result of these differences in configuration between porous debris and structures such as fuel assemblies and pipes, principles different than those for these structures need to be applied to the analysis of porous debris. The different principles applied by SCDAP/RELAP5-3D$^{©}$ include Darcy's Law for flow losses and correlations specific to porous debris for convective heat transfer. These principles are applied to porous debris in the core region and in the lower head of the reactor vessel. The RELAP5 momentum equations for the vapor and liquid phases in debris regions apply the calculated flow losses for debris and the RELAP5 energy equations for the liquid and vapor phases in debris regions apply the calculated heat transfer for debris. The calculated heat transfer is also applied by the two-dimensional heat structure model for debris in the lower head (described in Section 8) and by the simplified heat structure model for debris in the core region (described in Section 10.4).

To simplify the models for heat transfer and flow loss in porous debris calculations, the following assumptions are made.

1. Debris particles are assumed to be spherical, uniform in size, and with regular packing. Since models do not exist to calculate for severe accident situations a distribution in sizes of particles with a non-spherical shape, this assumption is not restrictive.

2. Debris particles are greater than the smallest possible bubble size, which is assumed to be approximately 3.5 mm.

3. Porosity is assumed to range between 0.4 and 0.5. This assumption keeps the debris porosity within the range of application of most of the correlations applied to calculate heat transfer and flow losses.

4. The mesh size for the two-dimensional heat structure model or the simplified debris heat structure model is significantly larger than the size of the debris particles. The satisfaction of this requirement maintains the applicability of the convective heat transfer models for porous debris.

The information in this section is arranged as follows. The correlations and models for convective heat transfer in porous debris are described in Section 9.1. The models for flow losses in porous debris are described in Section 9.2. The interfaces of the models for convective heat transfer in porous debris with the two-dimensional heat structure model and with the simplified debris heat structure model are described in Section 9.3. The interface of the models for flow losses in porous debris with the RELAP5 momentum equations for the liquid and vapor phases is described in Section 9.4.

9.1 Convective and Radiative Heat Transfer in Porous Debris

This section describes the calculation of convective heat transfer in porous debris. Six different regimes of heat transfer are taken into account. For each regime, a correlation obtained from heat transfer experiments on porous debris is applied to calculate the convective heat transfer as a function of the local debris temperature and the local fluid conditions.

Correlations to calculate convective heat transfer have been developed for the full range of conditions that are possible in porous debris during a severe accident. The range of conditions are grouped into regimes distinguished from each other by the volume fraction of the liquid phase of water in the debris and by the temperature of the particles in the debris. The heat transfer regimes range from nucleate boiling in two-phase coolant to natural convection in steam. The various convective heat transfer regimes and the corresponding ranges in values of volume fraction of liquid and debris temperature are identified in Table 9-1. The symbols used in Table 9-1 are defined in Table 9-2. Several temperature thresholds are identified for transition from one heat transfer regime to another. One of these temperature thresholds, T_{sat}, is determined by the water properties package for SCDAP/RELAP5-3D©. Another threshold temperature, T_{TF}, is determined from experimental results. The other temperature thresholds are determined by matching a heat flux from one regime of heat transfer with the heat flux from the interfacing heat transfer regime.

Table 9-1. Regimes of convective heat transfer and corresponding ranges in values of volume fraction of liquid and debris temperature.

Phase state of fluid	Mode of heat transfer	Range of void fraction of vapor	Range of debris temperature (K)
single phase vapor	*forced convection and natural convection*	*1.0*	$T_D > T_{sat}$
single phase liquid	*forced convection and natural convection*	*0.0*	$T_D \leq T_{sat}$
two-phase	*nucleate boiling*	- -	$T_{CN} < T_D < T_{nuc}$
two-phase	*transition boiling*	- -	$T_{nuc} < T_D < T_{TF}$
two-phase	*film boiling*	$\alpha_g \leq \alpha_4$	$T_D > T_{TF}$
two-phase	*transition from film boiling to convection to vapor*	$\alpha_4 \leq \alpha_g < 1.0$	$T_D > T_{TF}$

Table 9-2. Definition of symbols in Table 9-1

Symbol	Units	Definition
α_g	- -	*volume fraction of vapor in fluid*
T_D	*K*	*temperature of debris*
T_{sat}	*K*	*saturation temperature of fluid*

Table 9-2. Definition of symbols in Table 9-1 (Continued)

Symbol	Units	Definition
T_{CN}	K	*temperature of debris at which heat flux using convection correlation equals heat flux using nucleate boiling correlation*
T_{nuc}	K	*temperature of debris at which heat flux using nucleate boiling correlation equals critical heat flux*
T_{TF}	K	*temperature of debris at which transition boiling heat transfer ends and film boiling heat transfer begins*
α_4	- -	*void fraction at which flow regime changes from inverted slug-mist flow to mist flow (~0.925).*

9.1.1 Single Phase Vapor Regime

The heat transfer correlation developed by Tung[9-9] is used to calculate the debris-to-vapor convective heat transfer. In this correlation, the Nusselt number is given by the equation

$$\mathrm{Nu_{conv}} = 0.27\mathrm{Re}^{0.8}\mathrm{Pr}^{0.4} \tag{9-1}$$

where

$\mathrm{Nu_{conv}}$ = Nusselt number for convection,

Re = Reynold's number,

Pr = Prandtl number.

The Nusselt number for convection is given by the equation

$$\mathrm{Nu_{conv}} = (\mathrm{hD_p})/\mathrm{k_g} \tag{9-2}$$

where

h = convective heat transfer coefficient $(\mathrm{W/m^2 \cdot K})$,

$\mathrm{D_p}$ = effective diameter of debris particle (m),

$\mathrm{k_g}$ = thermal conductivity of vapor $(\mathrm{W/m \cdot K})$.

The Reynold's number is given by the equation

$$\mathrm{Re} = \rho_g v_g D_p / \mu_g \tag{9-3}$$

where

ρ_g = density of vapor (kg/m^3),

v_g = velocity of vapor (m/s),

D_p = effective diameter of debris particle (m),

μ_g = viscosity of vapor $(\mathrm{kg/m \cdot s})$.

The Prandtl number is given by the equation

$$\mathrm{Pr} = \mu_g c_g / k_g \tag{9-4}$$

where

μ_g = viscosity of vapor $(\mathrm{kg/m \cdot s})$,

c_g = heat capacity of vapor $(\mathrm{J/kg \cdot K})$,

k_g = thermal conductivity of vapor $(\mathrm{W/m \cdot K})$.

The ranges of parameters for which this correlation is based are

$$0.7 \le \mathrm{Pr} \le 5$$

$$18 \le \mathrm{Re} \le 2400$$

$$0.4 \le \varepsilon \le 0.5 \quad .$$

For the case of low fluid velocity, the Nusselt number for natural convection is calculated. If the Nusselt number for natural convection is greater than forced convection, then the natural convection Nusselt number is applied. The natural convection Nusselt number is taken from Edwards, Denny and Mills[9-10] as

$$\mathrm{Nu_{nat}} = \mathrm{KRa}^{0.25} \tag{9-5}$$

where

$\mathrm{Nu_{nat}}$ = Nusselt number for natural convection,

$$K = \begin{cases} 0.3 & 0 \le \mathrm{Ra} \le 50 \\ 0.4 & 50 \le \mathrm{Ra} \le 200 \\ 0.5 & 200 \le \mathrm{Ra} \le 10^6 \\ 0.6 & 10^6 \le \mathrm{Ra} \le 10^8 \end{cases}$$

Ra = Rayleigh number.

It should be mentioned that equation (9-5) was originally developed for a single sphere. The underlying hypothesis for applying this correlation to the current porous medium environment is well documented in Reference 9-9.

The Rayleigh number is calculated by the equation

$$Ra = Gr \bullet Pr = \frac{\rho_g^2 g D_p^3 \beta \Delta T}{\mu_g^2} Pr \tag{9-6}$$

where

g = acceleration of gravity (m/s^2),

β = volume coefficient of expansion of vapor (1/K),

ΔT = local temperature difference between debris and vapor (T_D - T_g).

The heat transferred to the vapor by convection is calculated by the equation

$$Q_{conv} = A_s \max(Nu_{conv}, Nu_{nat}) \frac{k_g}{D_p}(T_D - T_g) \tag{9-7}$$

where

Q_{conv} = heat transferred to vapor by convection (W/m^3),

A_s = surface area of debris per unit volume (m^2/m^3),

T_D = temperature of debris particles (K),

T_g = temperature of vapor (K).

If the value of Re is less than the range of applicability for Nu_{conv} $(Re < 8)$, then only Nu_{nat} is used in Equation (9-7).

The surface area of debris per unit volume is calculated by applying the assumption that the particles are spherical in shape and uniform in size. The resulting equation is

$$A_s = \frac{6(1 - \varepsilon)}{D_p} \tag{9-8}$$

where

ε = porosity of debris.

The heat transferred to the vapor by radiation is calculated by the equation[9-11]

$$Q_{rad} = A_s F_g \sigma (T_D^4 - T_g^4) \tag{9-9}$$

where

Q_{rad} = heat transferred to vapor by radiation (W/m^3),

F_g = gray-body factor,

σ = Stefan-Boltzmann constant (5.668 x 10^{-8} W/m^{2}K^4).

The gray body factor is calculated by the equation

$$F_g = 1/[R_1(1 + R_3/R_1 + R_3/R_2)] \tag{9-10}$$

where

R_1 = $(1-\varepsilon_g)/\varepsilon_g$,

R_2 = $1/\varepsilon_g$,

R_3 = $1 + (1-\varepsilon_D)/\varepsilon_D$,

ε_g = $1-\exp(-a_g L_m)$,

ε_D = emissivity of debris particles,

a_g = absorption coefficient for vapor,

L_m = mean path length (m).

The absorption coefficient, a_g is calculated by the SCDAP subroutine EMISSV.[9-11]An estimation of the mean path is obtained by assuming it equal to the hydraulic diameter.[9-11] Assuming the particles are spheres of uniform size in a regular packed matrix, the hydraulic diameter is estimated by the equation

$$L_m = \frac{4\varepsilon D_p}{6(1-\varepsilon)}. \tag{9-11}$$

The total heat transfer to the vapor is then

$$Q_{cg} = Q_{conv} + Q_{rad} \tag{9-12}$$

where

Q_{cg} = total heat transfer to vapor (W/m^3).

For the RELAP5 control volume in which this heat transfer occurs, the terms for the RELAP5 energy equation are calculated as follows;

$$q_i = Q_{cg} v_i \tag{9-13}$$

$$qwg_i = q_i \tag{9-14}$$

$$gammaw_i = 0.0 \tag{9-15}$$

where

q_i = rate of energy transfer from location with porous debris to RELAP5 control volume, which is the control volume the location resides in (W),

v_i = volume of i-th location with porous debris (volume of particles and their interstices)(m^3),

qwg_i = rate of energy transfer to vapor in RELAP5 control volume (W),

$gammaw_i$ = rate of vapor generation in RELAP5 control volume due to heat transfer from particles at location (kg/s).

9.1.2 Single Phase Liquid Regime

The heat transfer correlation presented by Gunn[9-12] is used to calculate the volumetric heat transfer coefficient for the covered regime. This correlation is applicable for water that is either subcooled or saturated. The correlation for the Nusselt number is given by the equation

$$Nu = (7 - 10\varepsilon + 5\varepsilon^2)(1 + 0.7Re^{0.3}Pr^{0.333}) + (1.33 - 2.4\varepsilon + 1.2\varepsilon^2)Re^{0.7}Pr^{0.333} \tag{9-16}$$

where

Pr = Prandtl number.

The Prandtl number is calculated by the equation

$$Pr = \mu_f c_f / k_f \tag{9-17}$$

where

μ_f = viscosity of the liquid $(kg/m \cdot s)$,

c_f = heat capacity of the liquid $(J/kg \cdot K)$,

k_f = thermal conductivity of the water $(W/m \cdot K)$.

The Reynold's number is calculated by the equation

$$Re = v_f \rho_f l / \mu_f \tag{9-18}$$

where

v_f = velocity of the liquid (m/s),

ρ_f = density of the liquid (kg/m^3),

l = characteristic length as defined below (m).

The volumetric heat transfer coefficient is calculated by the equation

$$h_v = Nu \frac{k_f}{l^2} . \tag{9-19}$$

The characteristic length is calculated by the equation

$$l = b / a \tag{9-20}$$

where

b = inertial coefficient in Kozeny-Carman equation (1/m^2),

a = viscous coefficient in Kozeny-Carman equation (1/m^2).

The coefficients b and a are calculated by the equations

$$b = 1.75(1 - \varepsilon) / \varepsilon^3 D_p , \tag{9-21}$$

$$a = 150(1 - \varepsilon)^2 / \varepsilon^3 D_p^2$$

where

ε = porosity of debris,

D_p = effective diameter of debris particles (m).

The total heat transfer to the fluid is calculated by the equation

$$Q_{cf} = h_v (T_D - T_f) \tag{9-22}$$

where

Q_{cf} = total heat transfer to the fluid (W/m^3),

T_D = surface temperature of debris (K),

T_f = temperature of liquid (K).

For the RELAP5 control volume in which this heat transfer occurs, the terms for the RELAP5 energy equation are calculated as follows;

$$q_i = v_i Q_{cf} \tag{9-23}$$

$$qwg_i = 0.0 \tag{9-24}$$

$$gammaw_i = 0.0 \tag{9-25}$$

The forced convection and natural convection heat transfer to the liquid phase can also be calculated using Equation (9-1) and Equation (9-6) with liquid phase properties substituted for vapor phase properties.[9-7] The characteristic length scale can be defined in two different ways for these modes of heat transfer, as is shown by Equations (9-2) and (9-3).

9.1.3 Heat Transfer for Two-Phase Flow

The debris-to-fluid heat transfer in the two-phase region is a complex process. The heat transfer modeling is consistent with the flow regime modeling. Since there is an absence of experimental data and theoretical models for local heat transfer coefficients for two-phase conditions, a simplified approach is required.

Four convective heat transfer modes are considered: (1) nucleate boiling; (2) transition boiling; (3) film boiling; and (4) transition from film boiling to convection to vapor. The mode of heat transfer in effect is a function of the debris temperature and the volume fraction of vapor in the fluid. The range of conditions for each heat transfer mode are summarized in Table 9-1. The symbols in Table 9-1 have been defined in Table 9-2. Heat transfer by radiation is also taken into account.

9.1.3.1 Nucleate Boiling

The heat transfer coefficient for nucleate boiling is calculated using a correlation for pool boiling developed by Rohsenow[9-13] and used by Tutu, et al.[9-21] This correlation is

$$h_{snuc} = 4.63x10^6 f(prop)(T_D - T_{sat})^m \tag{9-26}$$

where

h_{snuc} = heat transfer coefficient for nucleate boiling mode of heat transfer ($W/m^2 \cdot K$),

f(prop) = function that is a combination of fluid properties as defined below,

m = exponent that is a function of particle diameter as defined below.

The fluid properties function is

$$f(prop) = \frac{\mu_f c_{pf}^3}{(h_{fg}^2)\left[\frac{\sigma}{g(\rho_f - \rho_g)}\right]^{0.5}\left(\frac{c_{pf}\mu_f}{k_f}\right)^{4.913}} \tag{9-27}$$

where

μ_f = viscosity of liquid water $(kg/m \cdot s)$,

c_{pf} = heat capacity of liquid water $(J/kg \cdot K)$,

h_{fg} = latent heat of vaporization (J/kg),

σ = surface tension (kg/s^2),

g = acceleration of gravity (9.8 m/s^2),

ρ_f = density of saturated liquid (kg/m^3),

ρ_g = density of saturated vapor (kg/m^3),

k_f = thermal conductivity of liquid water ($W/m \cdot K$).

The exponent m is calculated by the equation[9-7]

$$m = 3.3 - 9.0e^{-d} \tag{9-28}$$

where

$$d = \left\{\frac{D_p}{\left[\frac{\sigma}{g(\rho_f - \rho_g)}\right]^{0.5}}\right\}^{0.5}.$$

If d is calculated to be less than 1.41, then d is set to a value of 1.41 $(m \geq 1.1)$.

For the RELAP5 control volume in which this heat transfer occurs, the terms for the RELAP5 energy equation are calculated as follows;

$$q_i = A_s h_{snuc}(T_D - T_{sat})v_i \tag{9-29}$$

$$qwg_i = 0.0 \tag{9-30}$$

$$gammaw_i = q_i/h_{fg} \tag{9-31}$$

where

A_s = surface area of particles per unit volume (m^2/m^3),

h_{fg} = heat of vaporization (J/kg).

The debris temperature at which the transition from the forced convection to single phase liquid to the nucleate boiling mode of heat transfer takes place is equal to T_{CN}. T_{CN} is determined by solving the following equation.

$$h_v(T_{CN} - T_{sat}) = 4.63 \times 10^6 f(prop)(T_{CN} - T_{sat})^{m+1} A_s \tag{9-32}$$

where

h_v = volumetric heat transfer coefficient for forced convection to liquid,

T_{CN} = temperature of debris at which heat flux using forced convection correlation equals heat flux using nucleate boiling correlation (K),

A_s = surface area of particles as defined by Equation (9-8) (m^2/m^3).

The maximum temperature of debris for the nucleate boiling mode of heat transfer is determined by solving the following equation for T_{nuc}.

$$4.63 \times 10^6 f(prop)(T_{nuc} - T_{sat})^m (T_{nuc} - T_{sat}) = q_{CHF} \tag{9-33}$$

where

T_{nuc} = maximum particle temperature for nucleate boiling mode of heat transfer (K),

q_{CHF} = critical heat flux calculated as shown below (W/m^2).

The critical heat flux is calculated by a correlation for spheres developed by Ded and Lienhard:[9-14]

$$q_{CHF} = 0.11 F_d h_{fg} \rho_g [g\sigma((\rho_f - \rho_g)/\rho_g^2)]^{0.25} \tag{9-34}$$

where

F_d = factor correcting for debris particle size as defined below,

h_{fg} = latent heat of vaporization (J/kg),

g = acceleration of gravity (9.8 m/s^2),

ρ_f = density of saturated liquid (kg/m^3),

ρ_g = density of saturated liquid (kg/m^3),

σ = surface tension (kg/s^2).

The factor F_d is calculated by the equation[9-7]

$$F_d = 1 - 3.8e^{-d} \tag{9-35}$$

where

$$d = \left\{ \frac{D_p}{\left[\frac{\sigma}{g\rho_f - \rho_g}\right]^{0.5}} \right\}^{0.5} .$$

If d is calculated to be less than 1.41, then d is set to a value of 1.41.

9.1.3.2 Film Boiling

The correlation developed by Dhir and Purohit[9-15] is used to calculate the surface heat transfer coefficient for the film boiling mode of heat transfer. According to their correlation, the Nusselt number is calculated by the equation

$$Nu = \frac{hD_p}{k_g} = \overline{Nu_0} + \overline{Nu_{nc}}\frac{Pr_g Sc}{Pr_f Sh \mu_f} + \frac{Pr_g}{Sh}\frac{\sigma(T_w^4 - T_{sat}^4)D_p}{h_{fg}\mu_g} \tag{9-36}$$

$$\overline{Nu_0} = 0.8\left[\frac{g\rho_g(\rho_f - \rho_g)h_{fg}D_p^3}{\mu_g k_g \Delta T_w}\right]^{1/4} \tag{9-37}$$

and

$$\overline{Nu_{nc}} = 0.9\left[\frac{g\rho_f^2 - C_{pf}\beta_f \Delta T_{sub} D_p^3}{\mu_f k_f}\right]^{1/4} \tag{9-38}$$

where

Nu = Nusselt number for film boiling mode of heat transfer, hD_p/k_g,

$\overline{Nu_0}$ = Nusselt number based on the saturated film boiling heat transfer coefficient averaged over the particle, $\bar{h}_0 D_p/k_g$,

$\overline{Nu_{nc}}$ = Nusselt number based on the natural convection heat transfer coefficient averaged over the particle, $\bar{h}_{nc} D_p/k_f$,

C_{pf}, C_{pg} = specific heats of liquid and vapor phases $(J/kg \cdot K)$,

D_p = effective diameter of particles (m),

g = acceleration of gravity (9.8 m/s^2),

h = heat transfer coefficient $(W/m^2 \cdot K)$,

$\bar{h}_0$ = saturated pool film boiling heat transfer coefficient $(W/m^2 \cdot K)$,

$\bar{h}_{nc}$ = natural convection heat transfer coefficient averaged over the surface of the sphere $(W/m^2 \cdot K)$,

h_{fg} = latent heat of vaporization (J/kg),

k_g k_f = thermal conductivity of vapor, liquid $(W/m \cdot K)$,

Pr_f, Pr_g, = Prandtl number of liquid and vapor phases ($C_{pf}\,\mu_f/k_f$, $C_{pg}\mu_g/k_g$),

Sc = liquid subcooling parameter, $C_{pf}\Delta T_{sub}/h_{fg}$,

Sh = vapor superheat parameter, $C_{pg}\Delta T_w/h_{fg}$,

T_{sat} = saturation temperature (K),

T_w = particle surface temperature (K),

ΔT_{sub} = difference between the saturation temperature of liquid and the bulk temperature of liquid $(T_{sat} - T_{bulk})$,

ΔT_w = difference between the wall temperature and the saturation temperature of the liquid (T_w - T_{sat}),

β_f = coefficient of thermal expansion of liquid phase (1/K),

ρ_g = density of saturated vapor (kg/m^3),

μ_f = viscosity of liquid phase $(kg/m \cdot s)$,

ρ_f = density of saturated liquid (kg/m^3),

μ_g = viscosity of saturated vapor $(kg/m \cdot s)$,

σ = Stefan-Boltzmann constant (5.669×10^{-8} $W/m^2 \cdot K^4$).

Equation (9-36) includes the energy transfer by conduction and radiation across the film. Generally, the energy transferred by radiation is about 10% of the total energy. The numerical constant in Equation (9-38) would be about 0.5 for natural convection over a sphere with no slip at the surface and about 0.7 with slip.

This correlation was developed using spheres of steel, cooper and silver. Experimental results indicate that for particles with an oxide layer on the surface and a low superheat, the Nusselt number may be 80% higher than for particles with a polished surface.[9-9] At high superheats, the heat transfer coefficients for oxidized and polished particles converge. Although particles in a debris bed in a nuclear reactor are expected to be oxidized, they may also be extremely hot, so a multiplier to account for oxidized surfaces is not applied.

The surface heat transfer coefficient for film boiling is calculated by the equation

$$h_{sfb} = (Nu)\frac{k_g}{D_p} \tag{9-39}$$

where

h_{sfb} = surface heat transfer coefficient for film boiling ($W/m^2 \cdot K$).

For the RELAP5 control volume in which film boiling heat transfer occurs, the terms for the RELAP5 energy equation are calculated as follows;

$$q_i = A_s h_{sfb}(T_d - T_{sat})v_i \tag{9-40}$$

$$qwg_i = 0.0 \tag{9-41}$$

$$gammaw_i = q_i/h_{fg}. \tag{9-42}$$

9.1.3.3 Transition Boiling

In the transition boiling mode of heat transfer, when the debris temperature is between T_{nuc} and T_{TF}, the heat transfer coefficient is calculated by the equation

$$h_{str} = \frac{(T_D - T_{nuc})}{(T_{TF} - T_{nuc})}[h_{sfb} - h_{snuc}] + h_{snuc} \tag{9-43}$$

where

h_{str} = heat transfer coefficient for transition boiling mode of heat transfer ($W/m^2 \cdot K$),

T_{TF} = debris temperature at which transition boiling heat transfer ends and film boiling heat transfer begins.

The variable T_{TF} is calculated by the equation[9-7];

$$T_{TF} = 0.16\frac{\rho_g h_{fg}}{k_g}\left[\frac{g(\rho_f - \rho_g)}{(\rho_f + \rho_g)}\right]^{2/3}\left[\frac{\mu_g}{g(\rho_f + \rho_g)}\right]^{1/3}\left[\frac{\sigma}{g(\rho_f + \rho_g)}\right]^{1/2} + T_{sat}\,. \tag{9-44}$$

For the RELAP5 control volume in which transition boiling heat transfer occurs, the terms for the RELAP5 energy equation are calculated as follows;

$$q_i = A_s h_{str}(T_d - T_{sat})v_i \tag{9-45}$$

$qwg_i = 0.0$

$gammaw_i = q_i/h_{fg}$.

9.1.3.4 Transition from Film Boiling to Convection to Steam

The transition from the film boiling mode of heat transfer to the convection to steam mode of heat transfer is assumed to occur when the void fraction of vapor is between α_4 and 1. The transition from the inverted slug-mist flow regime to the mist flow regime occurs at a void fraction α_4. The value of α_4 is approximately equal to 0.925[9-6]. In this range of void fractions, the heat transfer to the liquid and vapor phases is calculated by the equations

$$Q_{cf} = (1 - W_{fg})A_s h_{sfb}(T_D - T_{sat}) \tag{9-46}$$

$$Q_{cg} = W_{fg}Q_{conv} \tag{9-47}$$

where

Q_{cf} = total heat transfer to liquid phase by convection (W/m^3),

Q_{cg} = total heat transfer to vapor phase by convection (W/m^3),

W_{fg} = weighting function as defined below,

Q_{conv} = heat transfer to vapor as calculated by Equation (9-7) of Section 9.1.1 (W/m^3).

The weighting function is[9-9]

$$W_{fg} = y^2(3 - 2y) \tag{9-48}$$

where

W_{fg} = weighting function for interpolation between film boiling and convection to vapor modes of heat transfer, y = $\frac{\alpha_g - \alpha_4}{1 - \alpha_4}$,

α_g = volume fraction of vapor,

α_4 = void fraction at which flow regime changes from inverted slug-mist flow to mist flow.

For the RELAP5 control volume in which the transition from film boiling to convection heat transfer is occurring, the terms for the RELAP5 energy equation are calculated as follows;

$$q_i = Q_{cf} + Q_{cg} \tag{9-49}$$

$$qwg_i = Q_{cg} \tag{9-50}$$

$$gammaw_i = Q_{cg}/h_{fg}. \tag{9-51}$$

9.1.4 Interphase Heat Transfer

Heat transfer between the liquid and vapor phases of the fluid in porous debris is modeled in an approximate manner. The thermal equilibrium model is used. This model is applied by setting the phasic interfacial heat transfer coefficients to a large value for RELAP5 control volumes that contain porous debris. The suitability of this assumption is assessed by comparing calculated and measured temperatures at the top of an initially hot debris bed that was quenched from the bottom. The temperature history in this region of the debris bed is significantly influenced by the temperature of the steam flowing through the debris bed. If the calculated and measured temperatures in this region of the debris bed are in good agreement, then the simplifying assumption of thermal equilibrium of the liquid and vapor phases is suitable. Assessment results have shown good agreement between calculated and measured temperatures at the top of an initially hot debris bed quenched from the bottom.[9-22]Thus, the assumption of thermal equilibrium of the liquid and vapor phases is generally suitable.

9.2 Flow Losses in Porous Debris

This section describes the modeling of flow losses in porous debris. The flow losses in porous debris are due to friction and area changes (form losses). The flow losses are calculated in terms of drag force (pressure loss gradient) in the liquid and vapor phases as calculated by Darcy's Law[9-23]and extended for two-phase flow.

Several assumptions are applied to derive a model for flow losses with simplified computations and yet an adequate description of the physical processes producing flow losses. These assumptions are; (1) capillary forces are negligible (2) relative passabilities of the liquid and vapor phases are equal to the relative permeabilities of the two phases, respectively, and (3) interfacial drag is not significant. Numerical studies have shown that calculated results are rather insensitive to the assumption regarding the relative passabilities.[9-20]Interfacial drag is considered to not be significant for debris with particles that are not large (diameter < 5 mm).[9-20]

The flow losses for porous debris are calculated as a function of several variables; (1) debris porosity, (2) diameter of particles in debris, (3) viscosities and densities of the liquid and vapor phases of water in the debris, (4) volume fractions of the liquid and vapor phases of water, and (5) velocities of the liquid and vapor phases. The flow losses are expressed in terms of drag forces on the liquid and vapor phases. The drag forces are calculated by the equations[9-9,9-17, 9-19]

$$F_{pg} = \varepsilon\left[\frac{\mu_g j_g}{k\,k_{gr}} + \frac{\rho_g j_g^2}{m\,m_{gr}}\right] \tag{9-52}$$

$$F_{pf} = \varepsilon\left[\frac{\mu_f j_f}{k\,k_{fr}} + \frac{\rho_f j_f^2}{m\,m_{fr}}\right] \tag{9-53}$$

where

F_{pg}, F_{pf} = flow resistances to the vapor and liquid phases, respectively (N/m^3),

ε = porosity of the debris,

μ_g, μ_f = viscosities of the vapor and liquid phases, respectively (kg/m · s),

ρ_g, ρ_f = densities of the vapor and liquid phases, respectively (kg/m^3),

j_g, j_f = superficial velocities of the vapor and liquid phases respectively (m/s),

k = Darcy permeability of the debris (m^2),

k_{gr}, k_{fr} = relative permeabilities for the vapor and liquid phases, respectively (unitless),

m = passability of the debris bed (m),

m_{gr}, m_{fr} = relative passabilities for the vapor and liquid phases, respectively (unitless).

The second term on the right hand side of the above equations represents the turbulent drag counterpart to the viscous drag represented by the first term.

The Darcy permeability is calculated by the equation

$$k = \frac{\varepsilon^3 D_p^2}{150(1-\varepsilon)^2} \tag{9-54}$$

where

D_p = effective diameter of particles in debris (m).

The passability of the debris bed is calculated by the equation

$$m = \frac{\varepsilon^3 D_p}{1.75(1-\varepsilon)} \tag{9-55}$$

The relative permeabilities and passabilities of the debris bed are a function of the effective saturation of the debris bed, which is calculated by the equation

$$S = \frac{S_t - S_r}{1 - S_r} \tag{9-56}$$

where

S = effective saturation of debris bed,

S_t = true saturation of debris bed (volume fraction of liquid water in interstices of debris bed),

S_r = residual saturation.

The residual saturation is calculated by the equation[9-24]

$$S_r = 0.0116\left[\frac{\sigma\cos\theta}{k\rho_f g}\right] \tag{9-57}$$

where

Sr = residual saturation,

σ = surface tension (N/m),

g = acceleration of gravity (9.8 m/s2),

θ = wetting contact angle (radians).

The wetting contact angle is assumed to have a value of 0.785 radians.[9-25]

The relative permeabilities of liquid and vapor phases are calculated by the equations[9-20]

$$k_{rg} = 1.0e^{-4.43S} \tag{9-58}$$

$$k_{rf} = 0.0226e^{3.79S} \quad (9\text{-}59)$$

The relative permeabilities of the two phases as a function of effective saturation are plotted in Figure 9-1. The relative permeability of the vapor phase approaches a value of 1.0 as the effective saturation approaches 0.0. Similarly, the relative permeability of the liquid phase approaches 1.0 as the effective saturation approaches 1.0.

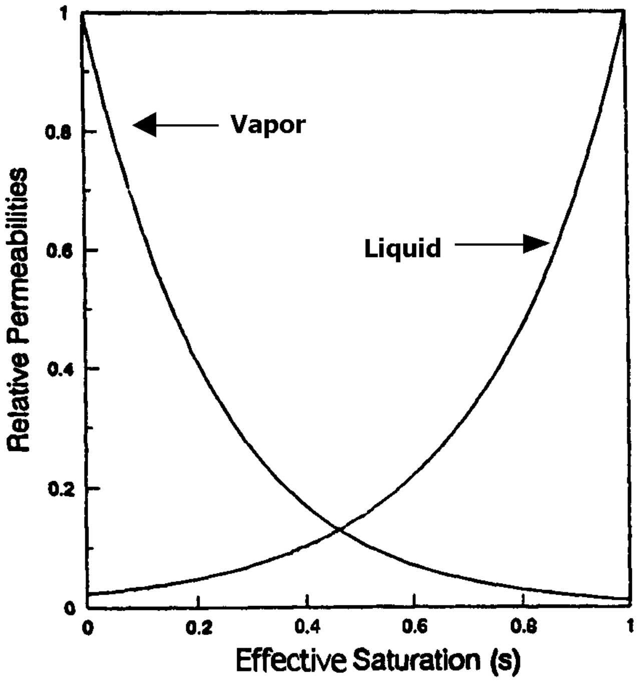

Figure 9-1. Relative permeabilities of the liquid and vapor phases.

The models for relative permeability and relative passability as developed by Tung and Dhir [9-9, 9-17] have also been implemented into SCDAP/RELAP5-3D© and may be used as an alternative to the models for these variables described above. Although the Tung and Dhir models involve considerably more equations than the models described above, calculations have shown the two models produce similar results.

9.3 Implementation of Heat Transfer Models

The calculated convective and radiative heat transfer from debris to fluid is input to the RELAP5 energy equation and to the debris heat structure models. For debris at a temperature greater than the temperature of the fluid in its interstices, the calculated heat transfer is a source term for the RELAP5 energy equation and a corresponding sink term for the debris heat structure models.

A condensed form of the RELAP5 energy equation is

$$\frac{\partial}{\partial t}(\alpha_g\rho_g U_g) + \ldots = Q_{wg} + \Gamma_w h'_g + \ldots \tag{9-60}$$

$$\frac{\partial}{\partial t}(\alpha_f\rho_f U_f) + \ldots = Q_{wf} - \Gamma_w h'_f + \ldots \tag{9-61}$$

where

t = time (s),

α_g, α_f = vapor and liquid volume fractions, respectively,

ρ_g, ρ_f = vapor and liquid densities, respectively (kg/m^3),

U_g, U_f = vapor and liquid specific internal energies, respectively (J/kg),

Q_{wg}, Q_{wf} = rate of heat transfer from structure or particle surfaces to vapor and liquid, respectively (W/m^3),

Γ_w = volumetric vapor generation rate ($kg/m^3 \cdot s$),

h'_g , h'_f = enthalpy associated with interphase mass transfer near surface of structures or particles for vapor and liquid phases, respectively (J/kg).

In the first two equations above, the terms Q_{wg}, Q_{wf}, and Γ_w are defined from variables calculated by the debris heat transfer models described in Section 9.1. Applying the variables calculated in Section 9.1. These three terms are calculated by the equations;

$$Q_{wg} = qwg_i / V + Q'_{wg} \tag{9-62}$$

$$Q_{wf} = (q_i - qwg_i) / V + Q'_{wf} \tag{9-63}$$

$$\Gamma_w = gammaw_i / V + \Gamma_w' \tag{9-64}$$

where

V = volume of the RELAP5 control volume that i-th location with debris resides in (m^3),

Q'_{wg} = rate of heat transfer to vapor in control volume from structures or particles at other locations within the RELAP5 control volume (W),

Q'_{wf} = rate of heat transfer to liquid in control volume from structures or particles at other locations within the RELAP5 control volume (W),

Γ_w' = volumetric rate of vapor generation from structures or particles at other locations within the RELAP5 control volume ($kg/m^3 \cdot s$),

q_i = heat transferred by convection and radiation from i-th location with debris to the RELAP5 control volume it resides in (W),

qwq_i = rate of heat transfer from i-th location with debris to vapor in the RELAP5 control volume it resides in (W),

$gammaw_i$ = rate of vapor generation at i-th location with debris in the RELAP5 control volume it resides in (kg/s).

The transfer of heat to the fluid in the interstices of the porous debris results in a corresponding removal of heat from the debris. The heatup of porous debris in the core region is described in Section 10.4. For this debris, the term in its energy equation representing removal of heat by convection and radiation is calculated by the equation

$$Q_{rmn} = q_i \tag{9-65}$$

where

q_i = heat transferred by convection and radiation from i-th location with porous debris (W),

Q_{rmn} = rate of heat transfer from debris particles to the fluid at the i-th location with debris, which is located at m-th axial node of n-th group of fuel rods (W).

The heatup of porous debris in the lower head of the reactor vessel is described in Section 8. For this debris, the term in its energy equation representing removal of heat by convection and radiation is calculated by the equation

$$Q_c(x,y) = q_i / v_i \tag{9-66}$$

where

$Q_c(x,y)$ = rate of heat transfer from particles to fluid in interstices for location with coordinates (x,y) in lower head of reactor vessel (W/m^3),

q_i = heat transferred by convection and radiation from i-th location (coordinates of (x,y)) with porous debris (W),

v_i = volume of i-th location with porous debris (m^2).

9.4 Implementation of Flow Loss Models

The models for the flow losses of fluid in porous debris were implemented into the RELAP5 field equations for the momentum of the liquid and vapor phases. The flow losses are incorporated in the terms in the field equations for losses due to friction and form. A condensed version of the RELAP5 field equation for the momentum of the vapor phase is

$$\alpha_g\rho_g\frac{\partial v_g}{\partial t} + \frac{1}{2}\alpha_g\rho_g\frac{\partial v_g^2}{\partial_x} = -\alpha_g\frac{\partial P}{\partial x} - (\alpha_g\rho_g)FWG(v_g) + \alpha_g\rho_g H_{lossg}\frac{(\partial v)}{\partial x} + \ldots \tag{9-67}$$

$$\Gamma_g(v_l - v_g) - (\alpha_g\rho_g\alpha_f\rho_f)(v_g - v_f)$$

$$-C\alpha_g\alpha_f\rho_m\left[\frac{\partial(v_g - v_f)}{\partial t} + v_f\frac{\partial v_g}{\partial x} - v_g\frac{\partial v_f}{\partial x}\right]$$

where

α_g = volume fraction of vapor phase in flow space,

ρ_g = density of vapor phase (kg/m^3),

v_g = velocity of vapor phase (m/s),

t = time (s),

x = spatial coordinate (m),

P = pressure of fluid (N/m^2),

FWG = vapor wall drag coefficients (s^{-1}),

H_{lossg} = term representing flow loss due to abrupt area change and other losses (m/s).

In the above equation, the first term on the left hand side of the equation is the acceleration of the vapor, the second term on the left hand side is the momentum flux, the second term on the right hand side is the pressure drop due to wall friction, and the third term on the right hand side is the pressure drop due to form loss.

For a location in the reactor vessel with porous debris, all of the flow losses are represented by the H_{lossg} term in the above equation. The FWG term, which represents losses due to friction, is set to zero. The H_{lossg} term is calculated using the drag forces calculated by the equations shown in Section 9.2 and which include losses due to friction. The H_{lossg} term is calculated by the equation

$$H_{lossg} = 0.5k_{Lg}v_g \tag{9-68}$$

where

k_{Lg} = loss coefficient corresponding with velocity v_g (unitless).

The loss coefficient k_{Lg} is related to the drag force term for vapor by the equation

$$0.5k_{Lg}\alpha_g\rho_g v_g^2 = F_{pg}\Delta x \tag{9-69}$$

where

Δx = distance of fluid flow (m).

Solving the above equation for k_{Lg}, the result is

$$k_{Lg} = \frac{2(\Delta x)F_{pg}}{\varepsilon\alpha_g\rho_g v_g^2} . \tag{9-70}$$

The value of k_{Lg} as calculated above is used in the RELAP5 momentum equation for the vapor phase for locations in the reactor vessel with porous debris.

The flow loss term in the momentum equation for the liquid phase is calculated in a manner parallel to that shown above for the vapor phase.

9.5 References

9-1. M. Jahn and H. H. Reineke, “Free Convection Heat Transfer with Internal Heat Source, Calculations and Measurements,” *Proceedings of the International Meeting on Thermal Nuclear Reactor Safety,* NUREG/CR-0027, 2, February 1983, pp. 996-1010.

9-2. M. Jahn and H. Reineke, “Free Convection Heat Transfer with Internal Heat Sources, Calculations and Measurements,” *Proceedings of the 5th International Heat Transfer Conference, Tokyo, Japan, September 1974.*

9-3. C. M. Allison, J. L. Rempe, and S. A. Chavez, “Final Design Report on SCDAP/RELAP5 Model Improvements - Debris Bed and Molten Pool Behavior,” INEL-96/0487, December 1996.

9-4. The RELAP5 Development Team, *RELAP5/MOD3 Code Manual, Models and Correlations,* NUREG/CR-5535, INEL-95/0174, Vol. IV, August 1985.

9-5. The SCDAP/RELAP5 Development Team, “SCDAP/RELAP5/MOD3.2 Code Manual, Volume II: Damage Progression Model Theory,” NUREG/CR-6150, Vol. 2, Rev. 1 (INEL-96/0422), July 1998.

9-6. S. Paik and L. J. Siefken, “Extensions to SCDAP/RELAP5 Code for the Modeling of Thermal-Hydraulic Behavior in Porous Debris Beds - Preliminary Design Report,” EGG-RAAM-10683, March 1993.

9-7. V. K. Dhir, R. Viskanta, and H. Esmaili, “Review of Extensions to SCDAP/RELAP5 Code for the Modeling of Thermal-Hydraulic Behavior in Porous Debris”, U. S. Nuclear Regulatory Commission Contract NRC 04 92-045, Task 3, June 1993.

9-8. The RELAP5 Development Team, “RELAP5/MOD3 Code Manual, Vol. I: Code Structure, System Models, and Solution Methods,” NUREG/CR-5535, INEL-95/0174, August 1995.

9-9. V. X. Tung, “Hydrodynamic and Thermal Aspects of Two-Phase Flow Through Porous Media,” Ph. D. Thesis, University of California, Los Angeles, 1988.

9-10. D. K. Edwards, V. E. Denny and A. Mills, Jr., “Transfer Process”, McGraw-Hill Book Comp., New York, New York, 1979.

9-11. The RELAP5 Development Team, “RELAP5/MOD3 Code Manual, Vol. IV: Models and Correlations,” NUREG/CR-5535, INEL-95/0174, August 1995.

9-12. D. J. Gunn, “Transfer of Heat or Mass to Particles in Fixed and Fluidized Beds,” Int. J. Heat and Mass Transfer, Vol. 21, 1978, pp. 467-476.

9-13. W. M. Rohsenow, “A Method for Correlating Heat Transfer Data for Surface Boiling of Liquids,” Trans. ASME, 1952, p. 969.

9-14. J. S. Ded and J. H. Lienhard, “The Peak Pool Boiling Heat Flux from a Sphere,” AIChE Journal, Vol. 18, No. 2, 1972.

9-15. V. K. Dihr and G. P. Purohit, “Subcooled Film-Boiling Heat Transfer from Spheres,” Nuclear Engineering and Design, Vol. 47, 1978, pp.49-66.

9-16. W. Chu, V. K. Dhir, and J. S. Marshall, “Study of Pressure Drop, Void Fraction and Relative Permeabilities of Two-Phase Flow through Porous Media,” AICHE Symposium Series, Vol. 79, No. 225, 1983, pp. 224-235.

9-17. V. X. Tung and V. K Dhir, “A Hydrodynamic Model for Two-Phase Flow Through Porous Media,” Int. J. Multiphase Flow, Vol. 14, No. 1, 1988 pp. 47-65.

9-18. V. X. Tung, V. K. Dhir, and D. Squarer, “Forced Flow Cooling Studies of Volumetrically Heated Porous Layers,” Second International Topical Meeting on Nuclear Reactor Thermal-Hydraulics, Santa Barbara, California, USA, January 11-14, 1983.

9-19. M. Chung and I. Catton, “Post-Dryout Heat Transfer in a Multi-Dimensional Porous Bed,” Nuclear Engineering and Design, 128, 1991, pp. 289-304.

9-20. I. Catton and M. Chung, “Two-Phase Flow in Porous Media with Phase Change: Post-Dryout Heat Transfer and Steam Injection,” Nuclear Engineering and Design, 151, 1994, pp. 185-202.

9-21. N. K. Tutu et al., “Debris Bed Quenching under Bottom Flood Conditions (In-Vessel Degraded Core Cooling Phenomenology),” NUREG/CR-3850, 1984.

9-22. E. A. Harvego and L. J. Siefken, “SCDAP/RELAP5 Modeling of Fluid Heat Transfer and Flow Losses through Porous Debris in a Light Water Reactor,” Eight International Conference on Nuclear Engineering, Baltimore, Maryland USA, April 2-6, 2000.

9-23. R. Byron, Warren E. Stewart, and Edwin N. Lightfoot,” Transport Phenomena,” John Wiley and Sons, New York 1960.

9-24. R. C. Schmidt and R. D. Gasser, “Models and correlations of the Debris Late-Phase Melt Progression Model,” SAND93-3922, 1997.

9-25. L. J. Siefken, E. W. Coryell, S. Paik, and H. Kuo, “SCDAP/RELAP5 Modeling of Heat Transfer and Flow Losses in Lower Head Porous Debris,” INEEL/EXT-98-00820, Rev. 2, July 1999.

9-26. The SCDAP/RELAP5 Development Team,” SCDAP/RELAP5/MOD3.3 Code Manual, Volume 5, Development Assessment,” NUREG/CR-6150, Rev. 2, to be published.

9-27. L. J. Siefken and M. S. Sohal,” A Heat Transfer Model for a Stratified Corium-Metal Pool in the Lower Plenum of a Nuclear Reactor,” INEEL/EXT-99-00763, Rev. 1, January 2000.

9-28. U. Steinberner and H. H. Reinke, “Turbulent Buoyancy Convection Heat Transfer with Internal Heat Source,” Sixth International Heat Transfer Conference, Toronto, Canada, August 7-11, 1978, Vol. 2, NC-21, pp. 305-311, Hemisphere Publishing Corp., Washington, DC.

9-29. T. G. Theofanous, M. Maguire, S. Angelini, and T. Salmassi, “The First Results from the ACOPO Experiment,” Proceedings of International Topical Meeting on Probabilistic Safety Assessment (PSA ‘96), Sept. 29-Oct. 3, 1996, pp. 1343-1350.

9-30. T. G. Theofanous, C. Liu, S. Additon, S. Angelini, O. Kymalainen, and T. Salmassi, “In-Vessel Coolability and Retention of a Core Melt,” Report DOE/ID-10460, Vol. 1, Chapter 5, July 1995.

9-31. S. Globe and D. Dropkin, “Natural Convection Heat Transfer in Liquid Confined by Two Horizontal Plates and Heated from Below,” J. Heat Transfer, 81, 1959, pp. 24-28.

9-32. Churchill, S. W. and H. S. Chu, Int. J., Heat Mass Transfer, 18, 1323 (1975).

9-33. F. J. Afsia and V. K. Dhir, “An Experimental Study of Natural Convection in a Volumetrically Heated Spherical Pool Bounded on Top with a Rigid Wall,” in In-Vessel Coolability and Retention of a Core Melt, edited by Theofanous et al., Report DOE/ID-10460, Vol. 1, Appendix C, July 1995.

9-34. K. M. Kelkar, K. M. KJhankari, and S. V. Patankar, Computational Modeling of Turbulent Natural Convection in Flows Simulating Reactor Core Melt, Report by Innovative Research, Inc. to Sandia Nation Laboratories, December 1993.

9-35. The SCDAP/RELAP5 Development Team, “SCDAP/RELAP5/MOD3.2 Code Manual, MATPRO - A Library of Materials Properties for Light-Water-Reactor Accident Analysis,” NUREG/CR-6150, Vol. 4, Rev. 1, INEL-96/0422, July 1998.

9-36. L. J. Siefken, “SCDAP/RELAP5 Modeling of Movement of Melted Material Through Porous Debris in Lower Head,” INEEL/EXT-98-1178 Rev. 2, October 1999,

9-37. L. J. Siefken and E. A. Harvego, “SCDAP/RELAP5 Modeling of Movement of Melted Material through Porous Debris in Lower Head,” Proceedings of the Eighth International Conference on Nuclear Engineering, April 2-6, 2000, Baltimore, MD USA.

9-38. R. C. Schmidt and R. D. Gasser, “Models and Correlations of the DEBRIS Late-Phase Melt Progression Model,” SAND93-3922, September 1997.

9-39. L. J. Siefken, “SCDAP/RELAP5 Modeling of Movement of Melted Material Through Porous Debris in Lower Head,” INEEL/EXT-98-01178, December 1998.

9-40. Mo Chung and Ivan Catton, “Post-Dryout Heat Transfer in a Multi-Dimensional Porous Bed,” Nuclear Engineering and Design 128 (1991) pages 289-304.

9-41. E. W. Coryell and F. P. Griffin, “SCDAP/RELAP5 Lower Core Plate Model,” INEEL/EXT-99-01029, September, 1999.

10. MODELS FOR BEHAVIOR OF SEVERELY DAMAGED REACTOR CORES

Damage mechanisms exist during a severe accident in an LWR that can change a reactor core from an array of distinct cylindrical fuel rods located in the center of the reactor vessel to a deep debris bed located in the bottom of the vessel. The reactor vessel becomes vulnerable to heatup and damage after the core has relocated to the lower head. The TMI-2 accident[10-1,10-2] and severe fuel damage experiments[10-3,10-4,10-5,10-6,10-7,10-8] have shown reactor core damage proceeds through several stages before the core slumps to the lower head. These stages of damage progression include (a) embrittlement of cladding due to oxidation, (b) melting of metallic cladding and dissolution of fuel in contact with liquefied cladding, (c) slumping of liquefied cladding and dissolved fuel due to failure of the oxide shell containing the liquefied mixture, (d) solidification of the slumped mixture at a lower and cooler location in the core and concurrent formation of a nonporous debris region that blocks the flow of coolant, (e) meltdown of the reactor core into a molten pool supported by the frozen previously molten ceramic material, and (f) melt-through or structural failure of the crust of frozen material supporting the molten pool and slumping of the molten pool to the bottom of the reactor vessel. An hour or more of time may elapse before damage has progressed through these six stages. This order of damage progression is established by the differences in melting temperatures of the metallic and ceramic parts of the reactor core and the fact that the lower part of the reactor is the last part of the core to be uncovered by water, and that this part has a lower level of decay heat than the center of the core.

The damage progression can be either abated or intensified by the injection of water into the reactor vessel. On one hand, the injected water may cool the damaged core and stop damage progression. On the other hand, the injected water may shatter embrittled fuel rods so that the fuel rod fragments slump into the configuration of a porous debris bed or the injected water may fuel an oxidation excursion of fuel rod cladding in the parts of the reactor core where the oxidation was steam starved.

Models to predict the progression of reactor core damage have been developed and incorporated into SCDAP/RELAP5-3D©. These models calculate the changes in the configuration of the reactor core as damage progresses. The models also calculate the heatup and progression of melting in the damaged regions of the reactor core. This section describes these models for damage progression.

10.1 Configuration Changes Caused by Damage to Reactor Core

The reactor core can change into three basic configurations as damage progresses during a severe accident. In the first configuration, nonporous debris supported by intact fuel rods extends radially across part of the core. This configuration is the result of the meltdown of the metallic part of the reactor core. The second basic configuration is that of a porous debris bed. The third basic configuration is that of a molten pool supported and contained by nonporous debris supported by intact fuel rods. Before damage has occurred, the configuration of the core is characterized by parameters such as rod spacing and rod diameter. After damage has occurred, the configuration is characterized by parameters such as depth and porosity of debris. If the porosity is large and the debris is covered with water, most of the decay heat in the debris can be removed by convective cooling. But, if the porosity is small and the debris bed is deep, then a large molten pool may develop. At this stage, there is the potential for rapid slumping of a large amount of hot material onto the lower head of the reactor vessel and the possibility of a vigorous thermal attack of the lower head.

The damage thresholds that result in the formation of debris are shown in Figure 10-1 to Figure 10-4. Each of these figures show part of a reactor core that for illustration is simply nodalized with three axial nodes and two rod groups. The bottom part of these figures show variables that describe the state of the core in this region. Each change in the state of the reactor core that causes a local change in configuration of the reactor core is identified with a configuration change number. A total of five configuration changes are identified in these figures.

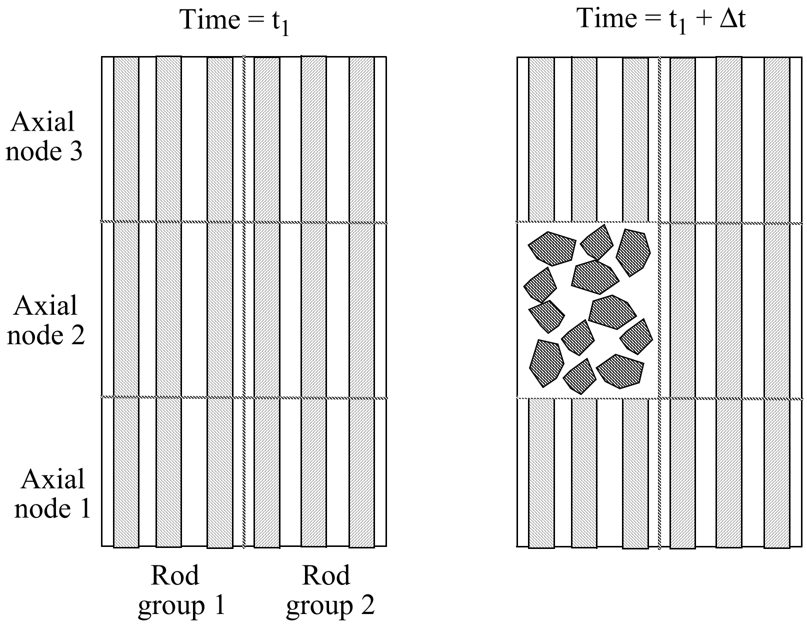

Core state change that results in change in configuration for axial node 2 of Rod Group 1

Configuration Change No.	Time = t_1	Time = $t_1 + \Delta t$
1	$T(2,1) > T_{frag}$ $\Delta r_{\beta}(2,1) < 0.1$ $T_{zrm} < T_{mx} < T_s$	$T(2,1) < T_{frag}$ $\Delta r_{\beta}(2,1) < 0.1$ $T_{zrm} < T_{mx} < T_s$
2	$T(2,1) < T_{Zr\ melt}$ $\Delta r_{ox}(2,1) < 1.E-2$	$T(2,1) > T_{Zr\ melt}$ $\Delta r_{ox}(2,1) < 1.E-2$

Figure 10-1. Damage thresholds for changing local configuration of core from intact rods to rubble debris.

The variables in Figure 10-1 are defined as follows. The variable T(2,1) is the temperature of the material at axial node 2 of Rod Group 1. The variable Δr_{β} (2,1) is the thickness in mm of the beta phase of the zircaloy in the cladding at axial node 2 of Rod Group 1. The variable Δr_{ox} (2,1) is the thickness in mm of the oxide layer of the cladding at axial node 2 of Fuel Rod Group 1. The variable T_{mx} is the maximum

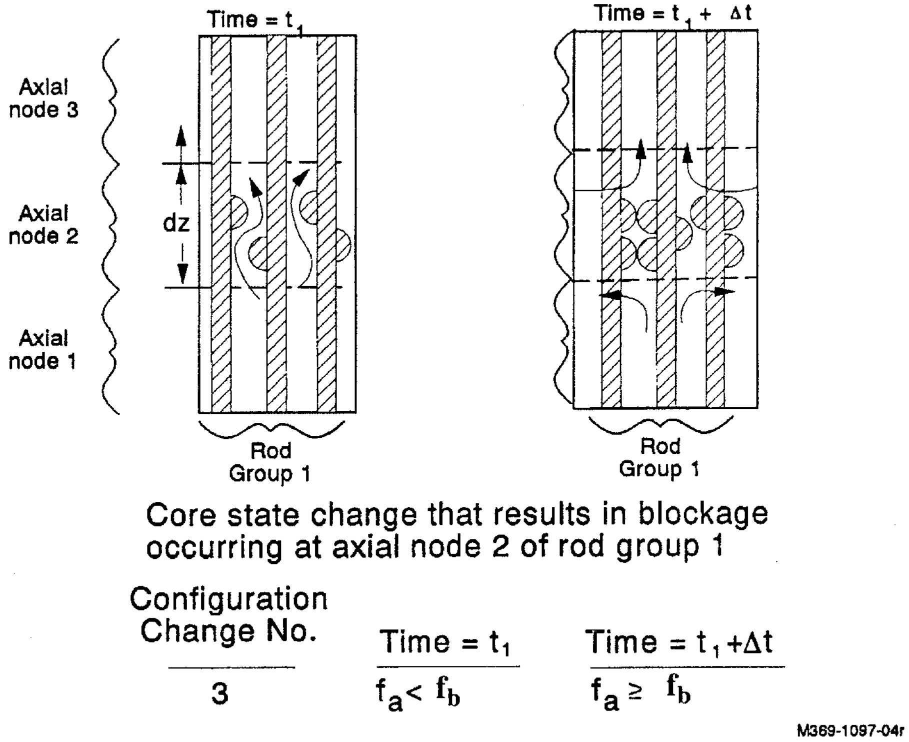
Time = t1
Time = t1 + Δt
Axial node 3
Axial node 2
Axial node 1
dz
Rod Group 1
Rod Group 1
Core state change that results in blockage occurring at axial node 2 of rod group 1
Configuration Change No.
Time = t1
Time = t1 +Δt
3
fa< fb
fa ≥ fb
M369-1097-04r

Figure 10-2. Damage threshold for changing local configuration of core from intact rods to cohesive debris.

temperature of the fuel in the fuel rod during the period in which damage was occurring to the fuel rod (K), the variable T_{mzr} is the melting temperature of the fuel rod cladding (K), the variable T_s is the solidus temperature of the fuel in the fuel rod (K), and the variable Δt is the time step (s).

Figure 10-1 shows damage thresholds that result in intact fuel rods changing into rubble debris. This figure uses the location of the core at axial node 2 of Rod Group 1 as an example. The figure shows two different changes in the state of the reactor core at axial node 2 of Rod Group 1 that result in the rods at this location changing from the configuration of intact rods to that of rubble debris. The first change is the result of the temperature of embrittled fuel rods decreasing to where it is less than the fragmentation temperature, defined to be the saturation temperature plus 100 K. The second change applies to fuel rods that have not significantly oxidized. In this case, if the temperature at this location exceeds the melting temperature of the zircaloy cladding and the fuel rod cladding is only slightly oxidized, the fuel rods disintegrate into rubble debris. If the material at the bottom and top of axial node 2 has changed to rubble debris, then the material at axial node 2 is also considered to change to the configuration of rubble debris.

Figure 10-2 shows the change in state that results in a location of the reactor core having a blockage. In this figure, the variable f_a is the fraction of surface area of the fuel rod cladding covered with drops of relocated material that has slumped from a higher elevation and frozen. The variable f_b is the fraction of surface area that needs to be covered with relocated material in order to cause a blockage to coolant flow in the axial direction at that interval of elevation. On the basis of severe fuel damage experiments, a value

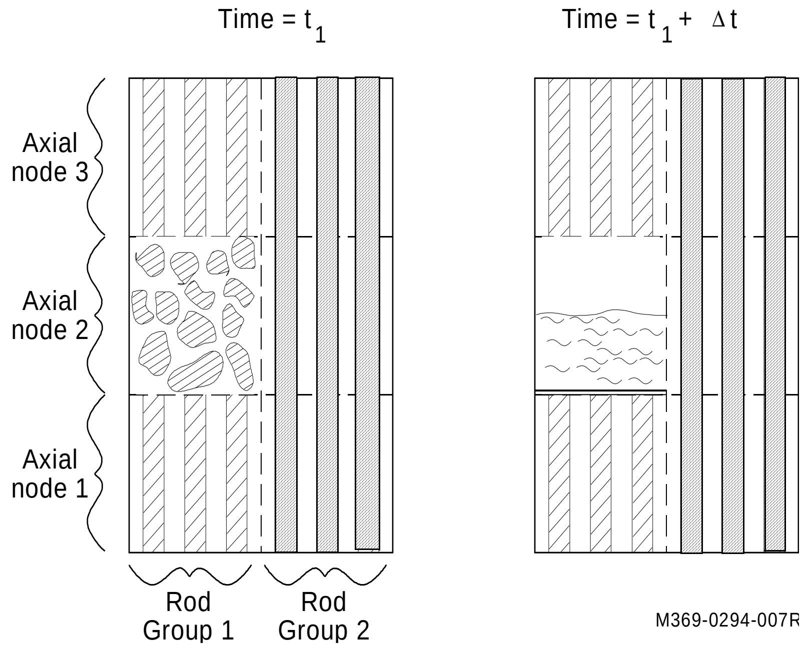

Core state change that results in change in configuration for axial node 2 of Rod Group 1

Configuration Change No.	Time = t_1	Time = $t_1 + \Delta t$
4	$T(2,1) < T_{\text{melt Zr-U-O}}$	$T(2,1) \geq T_{\text{melt Zr-U-O}}$

Axial node — Rod group

Figure 10-3. Damage threshold for changing local configuration of core from intact rods or rubble debris to molten pool.

between 0.2 and 0.5 is recommended for this user defined variable. The default value is 0.2. The drops of relocated material do not block flow in a direction perpendicular to the longitudinal axis of the fuel rods. The material in an axial node with drops of relocated material continues to be represented as intact fuel rods. In Figure 10-2, Δt is the period of time between the arrival of the first drop of relocating material at axial node 2 and satisfying the criterion for imposing a complete blockage at axial node 2.

Figure 10-3 and Figure 10-4 show the changes in state of the reactor core that result in the formation of a molten pool. Figure 10-3 shows molten pool formation due to temperature change. If the temperature at any location in the reactor core exceeds the liquefaction temperature of the mixture of UO_2 and ZrO_2 ($T_{\text{melt Zr-U-O}}$), then that location of the core is regarded as having molten material and is subsequently represented by the molten pool model. The example shown in Figure 10-3 has the location that became molten previously being rubble debris. In Figure 10-3, Δt is the period of time from the occurrence of the state shown for t_1 to the time that the temperature of Rod Group 1 at axial node 2 exceeded the liquidus temperature of the mixture. Figure 10-4 shows the case of a location with rubble debris being supported by a crust on the top of molten material beneath it. If the effective stress of the crust exceeds the ultimate strength of the crust, then the rubble debris is regarded as sinking into the molten pool and becoming part

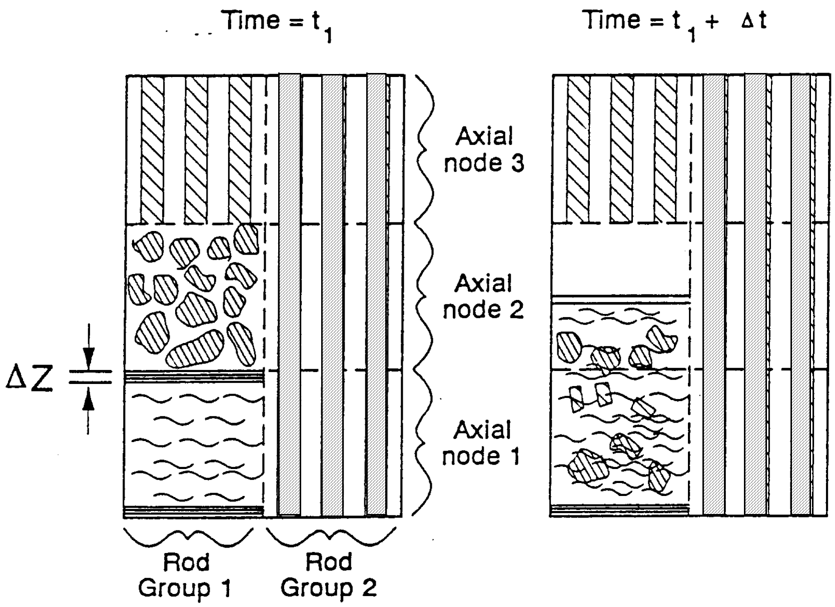

Core state change that results in change in configuration for axial node 2 of Rod Group 1

Configuration Change No.	Time = t_1	Time = t1 + Δt
5	$\sigma_c < \sigma_u$	$\sigma_c \geq \sigma_u$

Figure 10-4. Damage threshold for changing local configuration of core from intact rods or rubble debris to molten pool.

of the molten pool. In this figure, σ_c is the effective stress in the crust (MPa), and σ_u is the ultimate strength at the crust (MPa).

The spreading of a molten pool due to gravity driving the molten material through adjacent porous regions can also result in locations in a reactor core changing from the configuration of intact fuel rods or rubble debris to the configuration of a molten pool. This process for changing the configuration of a reactor core is described in Section 10.5.3.

The changes in configuration of the reactor core due to meltdown, namely Configuration Change Numbers 3 and 4, are calculated as occurring gradually rather than occurring in a single time step. In Configuration Change Number 3, the configuration changes as a function of f_a. For Configuration Change Number 4, the configuration changes as a function of temperature, beginning at the time that the temperature exceeds the solidus temperature of the mixture of UO_2 and ZrO_2. These gradual changes in configuration are described in more detail in Section 11 which describes the transition smoothing models.

10.2 Heatup of Location with Relocated Material

The presence on the outer surface of fuel rods of relocated material is a damage state caused by the meltdown of control rods and the metallic part of fuel rods. The meltdown may begin as soon as a region of the core exceeds the temperature for eutectic melting of stainless steel clad control rods with Ag-In-Cd absorber material. This temperature is about 1,500 K. The meltdown may become widespread when a region of the reactor core exceeds the melting temperature (about 2,200 K) of the fuel rod cladding. The meltdown and subsequent solidification of the relocated material may result in a blockage to coolant flow.

The heatup of a location of the reactor core with relocated material is calculated by the same two-dimensional heat conduction model that calculates the heatup of intact fuel rods. This model is described in Section 2. The material layout and boundary conditions for this model are modified from those for intact fuel rods in order to represent the material that slumped into the space between the fuel rods. The surface area in contact with coolant is reduced to account for the presence of the relocated material. This reduction in surface area is calculated by the transition smoothing models and is described in Section 11. The heat generation at a location with relocated material is increased to account for the heat generation in the material that slumped into the location.

10.3 Formation and Characteristics of Porous Debris

The thermal shocking by reflood water of a reactor core embrittled by oxidation results in the formation of porous debris. This section describes models for the formation and heatup of porous debris in the region of the reactor core.

A study performed by Haggag[10-9,10-10] concluded that the Chung and Kassner model[10-11] accurately predicts the embrittlement and fragmentation of oxidized fuel rods. According to this model, cladding is embrittled when

$$\Delta r_{beta} < 0.1 \tag{10-1}$$

where Δr_{beta} is the thickness of the cladding in the beta phase (mm).

A review[10-12] of experimental results of fuel rods that have been quenched after heatup and oxidation has shown that fuel rod degeneration into particles is a function of several variables, including, (1) temperature of the cladding during quenching, (2) extent of cladding meltdown, and (3) maximum temperature of the fuel during the damage progression period before quenching. The experimental results indicate that embrittled fuel rods locally degenerate into particles during quench when the following local conditions are satisfied;

$$T_{clad} < T_{frag} \tag{10-2}$$

$$f_d < 1. \tag{10-3}$$

$$T_{mzr} < T_{mx} < T_s \tag{10-4}$$

where

T_{clad} = local temperature of cladding (K),

T_{frag} = user-defined temperature for fragmentation during quench (K). Default value is saturation temperature of coolant in debris plus 100 K,

f_d = fraction of surface area of cladding that is covered with drops of relocated material,

T_{mzr} = melting temperature of cladding (K),

T_{mx} = maximum fuel temperature at this location in period from start of accident to present time (K),

T_s = solidus temperature of fuel (K).

The porous debris resulting from the degeneration of fuel rods into particles is characterized by porosity and particle size. Experimental results[10-12] indicate that the porosity and particle size are a function of the maximum temperature of the fuel during the damage progression period before quenching. The experimental results indicate that the functional relation of these characteristics with fuel temperature is approximately:

$$\phi = \phi_c + f_T (\phi_h - \phi_c) \tag{10-5}$$

$$d = d_c + f_T (d_h - d_c) \tag{10-6}$$

where

ϕ = debris porosity,

ϕ_c = porosity of debris from fuel rods that disintegrate with $f_T < 0.0$,

ϕ_h = porosity of debris from fuel rods that disintegrate with $f_T > 0.0$,

f_T = maximum local fuel temperature in period from start of accident to present time,

d = diameter of debris particles (m),

d_c = diameter of fuel particles from fuel rods that disintegrate with $f_T < 0.0$ (m),

d_h = diameter of fuel particles from fuel rods that disintegrate with $f_T > 1.0$ (m).

The governing variable in Equations (10-5) and (10-6) is f_T, a measure of the maximum local fuel temperature in period from start of accident to present time. This variable is calculated by the equation

$$f_T = \left(\frac{T_{mx} - T_{mzr}}{T_s - T_{mzr}}\right) \tag{10-7}$$

where

T_{mx} = maximum local fuel temperature in period from start of accident to present time (K),

T_{mzr} = melting temperature of cladding (K),

T_s = solidus temperature of fuel (K).

Equations (10-5) and (10-6) calculate debris porosity and particle size by interpolating the experimentally measured values of these variables with respect to the maximum historical temperature of the fuel from the start of the accident to the present time. For fuel rods with a value of f_T less than 0.0, experimental results indicate that the debris porosity and particle size are approximately given by the equations

$$\phi_c = \frac{A_f}{p^2} \tag{10-8}$$

$$d_c = \left(\frac{3}{\pi}\right)\left(\frac{p^2}{r_o}\right)\left(1 - \frac{A_f}{p^2}\right) \tag{10-9}$$

where

p = pitch of fuel rods (m^2),

r_o = outer radius of fuel rods (m),

A_f = flow area per rod (m^2).

The variable A_f in Equations (10-8) and (10-9) is calculated by the equation

$$A_f = p^2 - \pi r_o^2 \tag{10-10}$$

For fuel rods with a value of $f_T \geq 1.0$, experimental results indicate that the debris porosity and particle size are approximately given by the equations

$$\phi_h = 0.54 \tag{10-11}$$

$$d_h = 0.1\ d_{pel} \tag{10-12}$$

where

d_{pel} = as-fabricated diameter of fuel pellets.

For $0 < f_T < 1.0$, the value of the debris porosity is obtained by interpolating between ϕ_c and ϕ_h with respect to f_T. Similarly, the value of the diameter of the debris particles is obtained by interpolating between d_c and d_h with respect to f_T.

Equations (10-8) and (10-9) are derived by calculating the debris characteristics that result in the same porosity and hydraulic diameter as intact fuel rods. The porosity of intact fuel rods is calculated by the equation

$$\phi_c = \frac{p^2 - \pi r_o^2}{p^2} \tag{10-13}$$

where

ϕ_c = porosity of debris that represents intact fuel rods.

The hydraulic diameter of a bed or rubble porous debris is

d_{hd} = 4(bed fluid volume)/(surface area of particles),

$$d_{hd} = \frac{4\phi_c d_p}{6(1-\phi_c)} = \frac{\frac{2}{3}A_f d_p}{p\left(1 - \frac{A_f}{p^2}\right)} \quad . \tag{10-14}$$

The hydraulic diameter of an array of intact fuel rods is given by the equation

$$d_{hi} = \frac{4A_f}{2\pi r_o} = \frac{2A_f}{\pi r_o} \quad . \tag{10-15}$$

The particle size that results in a bed of rubble debris having the same hydraulic diameter as an array of intact fuel rods is derived by equating Equation (10-14) to (10-15) and solving the resulting equation for particle diameter. Equating Equation (10-14) and (10-15), the result is

$$\frac{2A_f}{\pi r_o} = \frac{\frac{2}{3}A_f d_p}{p\left(1 - \frac{A_f}{p^2}\right)} \quad . \tag{10-16}$$

Solving the above equation for d_p, the result is

$$d_p = \frac{3}{\pi}\left(\frac{p^2}{r_o}\right)\left(1 - \frac{A_f}{p^2}\right) \quad . \tag{10-17}$$

Flow resistance may increase by a factor of 100 at a location where fuel rods have broken into particles. This increase of flow resistance is in part due to the fact that fluid in a debris region contacts more surface area than fluid in a rod-like region and in part due to the tortuous flow paths in porous debris. If a RELAP5 control volume contains fuel rods that have changed from rod-like configuration to porous debris, then the flow losses for that volume are calculated as described in Section 9.2.

Another mechanism for fragmentation of a reactor core is instigated by the melting of cladding with a very thin oxide layer. The small amount of dissolved oxygen in the oxide layer is not sufficient to wet the fuel. Evidence for this mechanism is the debris formed in the upper part of the fuel bundle in the PBF Severe Fuel Damage Experiment 1-4.[10-13] Little oxidation occurred in this part of the fuel bundle due to steam starvation. Post irradiation examination results for this experiment indicate that the debris in the upper part of the bundle had characteristics similar to the upper debris bed in the damaged TMI-2 core. This mode of debris formation is modeled to occur when

$$T_{clad} > T_m \text{ and } t_{ox} < 1 \times 10^{-2} \qquad (10\text{-}18)$$

where

T_m = the melting temperature of the metallic cladding (approximately 2,200 K),

t_{ox} = the thickness of the cladding oxide (mm).

10.4 Heatup of Porous Debris in Core Region

The heatup of porous debris in the core region is calculated using a lumped mass approach. The debris particles at an axial node of a fuel rod group are considered to constitute one lumped mass. Convective heat transfer between the debris particles and the fluid in the debris bed is considered to be the only mechanism that can remove heat from the debris. The debris heatup is calculated by the equation

$$(M_1C_{p1} + M_2C_{p2} + \ldots)_{ij}\frac{dT_{ij}}{dt} = P_{ij}A_{ij}\Delta z_{ij} - Q_{rij} \qquad (10\text{-}19)$$

where

M_{1ij} = mass of a type of material 1 at axial node i of fuel rod group j (kg),

C_{p1ij} = constant pressure specific heat of material 1 at axial node i of fuel rod group j (J/kg•K),

T_{ij} = average temperature of the debris particles at axial node i of fuel rod group j (K),

P_{ij} = volumetric heat generation rate (W/m^3),

A_{ij} = cross-sectional area (m^2),

Δz_{ij} = height of the i-th axial node (m),

Q_{rij} = rate of heat transfer from the debris particles to the fluid at the i-th axial node of fuel rod group j (W).

The heatup model accounts for decay heat in the debris particles and heat generation due to oxidation of the particles. The model accounts for the heat of fusion of each material in the debris. The model is applied when the debris temperature is less than the fuel and cladding oxide liquefaction temperature. When the debris temperature exceeds the liquefaction temperature, the debris temperature is calculated by the molten pool model described in the following section.

A location that disintegrates into debris may represent a combination of fuel rods and control rods. Any residue of control rods at that location is considered to be well mixed with the fuel rod debris.

The heat removal term Q_{rij} in Equation (10-19) is based upon the heat transfer model specific to porous debris and calculated in subroutine htrc3b. The model to be applied is selected by the code user. The term is calculated by the equation

$$Q_{rij} = q_{sij} A_{sij} \tag{10-20}$$

where

q_{sij} = heat flux on surface of debris particles at the i-th axial node of the j-th fuel rod group as calculated by SCDAP subroutine htrc3b (W/m^2),

A_{sij} = total surface area of debris particles at the i-th axial node of the j-th fuel rod group (m^2).

The subroutine htrc3b calculates the heat flux at the surface of the debris as a function of the local coolant conditions and debris temperature.

10.5 Molten Pool Formation, Spreading and Heatup

The first occurrence of the melting of fuel and cladding oxide (ceramic melting) marks a significant advancement in the severity of an accident. If the melting has been driven by decay heat and not by oxidation, then in the absence of core reflood, melt progression will steadily progress from this time onward. The molten material does not immediately slump from the core region. Instead, the liquefied material permeates into a colder region of the core and freezes. But, as liquefaction continues the possibility increases that the pool may melt the material supporting it and a large quantity of molten material may suddenly slump into the lower head of the reactor vessel. Thus, the unabated melting of fuel can lead to a thermal attack on the reactor vessel and a significant increase in the severity of an accident.

A partially molten reactor core is shown in Figure 10-5. In the case shown in the figure, the reactor core was nodalized into four axial nodes and three flow channels that are oriented in the axial direction. The material in axial nodes 2 and 3 of flow channel 1 has been heated to the point where it is molten (ceramic melting). Gravitational forces provide the potential for the spreading of this molten material. If the region surrounding the molten material is significantly cooler than the freezing temperature of the molten material, then a stable crust of previously molten material is formed. This crust holds the molten material in place. If the region surrounding the molten material is hot, then a stable crust does not form and the force of gravity causes the molten material to spread downward and laterally. In the example shown in Figure 10-5, models are applied to calculate the rate of spreading of molten material from flow channel 1 to flow channel 2 and from axial node 2 to axial node 1. The potential for spreading of the molten material is also a function of the volume of the molten material and its temperature. The larger the volume of molten material and the hotter its temperature, the greater the potential there is for the molten material to melt the crust at its boundary and spread.

The modeling of the heatup and the spreading of the molten material is performed by the molten pool model. Figure 10-6 shows the situation being represented by the model. The molten material in the molten pool is assumed to be mixed together due to turbulent natural convection. The molten pool model calculates the transient temperature and the rate of spreading of the molten pool. The model performs its

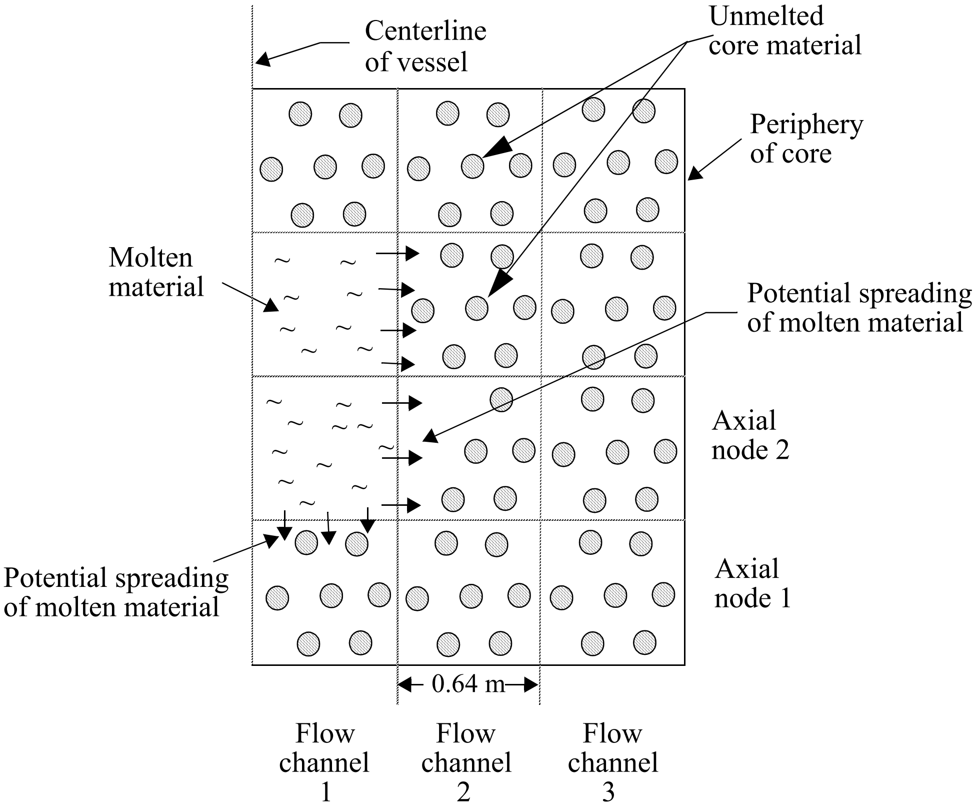
Centerline of vessel
Unmelted core material
Periphery of core
Molten material
Potential spreading of molten material
Axial node 2
Axial node 1
Potential spreading of molten material
0.64 m
Flow channel 1
Flow channel 2
Flow channel 3

Figure 10-5. The potential for spreading of the molten pool.

calculations at each time step of the code in four steps. In the first step, the heat fluxes on the inner surfaces of the crust containing the molten pool are calculated. These heat fluxes vary with location; the heat flux on the upper part of the crust is significantly larger than that on the bottom. In the second step, the thickness, temperature, and structural stability of the crust are determined. If the crust is stable, the molten material stays in place. Otherwise, the molten material spreads. In the third step the rate of spreading of the molten pool at each boundary location is calculated. For boundary locations where the crust is stable, the rate of spreading is equal to zero. Finally, in the fourth step, the temperature of the molten material is calculated based on the difference between the heat generated in the molten pool and the heat transferred from the molten pool at its boundary. The calculations performed in each of these four steps are described below.

10.5.1 Heat Flux on Inner Surface of Crust

The heat fluxes on the inner surface of any portion of the crust in contact with the molten pool are calculated using correlations developed from experimental data. These correlations were developed from the results of experiments that measured the natural convection heat transfer coefficients at the boundary of a pool of fluid with internal heat generation. The correlations calculate the heat flux at the bottom and top surfaces of the molten pool and at the sides of the molten pool. The heat fluxes can be calculated using either correlations for steady-state natural convection or transient natural circulation. The user selects whether steady-state or transient correlations are to be used. For the election of steady-state natural

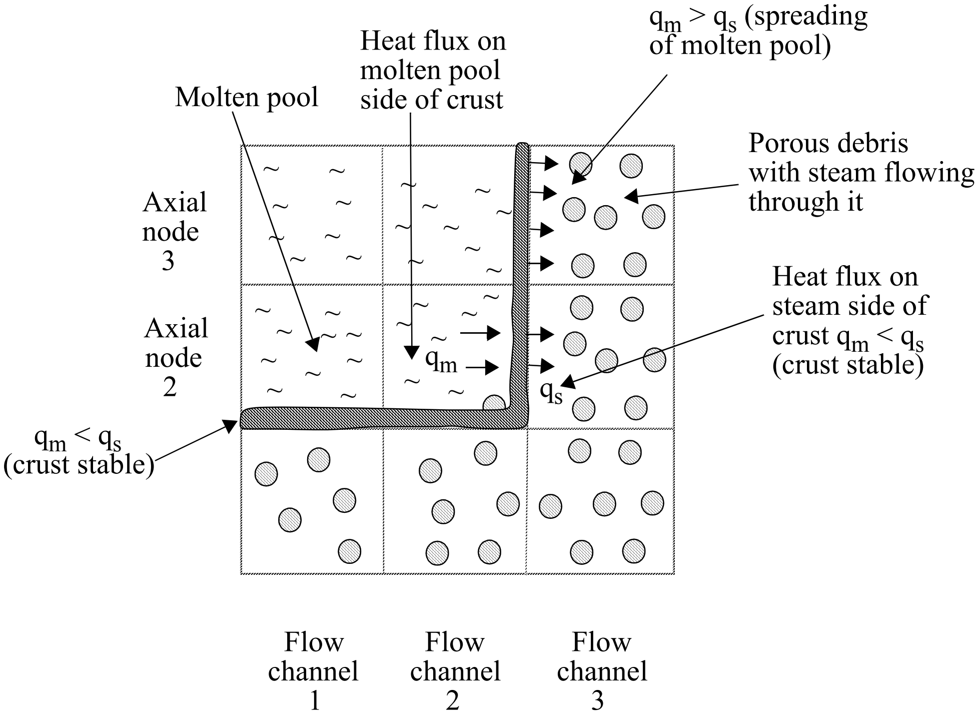
Molten pool
Heat flux on molten pool side of crust
qm > qs (spreading of molten pool)
Porous debris with steam flowing through it
Axial node 3
Axial node 2
qm
qs
Heat flux on steam side of crust qm < qs (crust stable)
qm < qs (crust stable)
Flow channel 1
Flow channel 2
Flow channel 3

Figure 10-6. Physical process being represented by spreading model.

convection, the heat fluxes at the various locations on the boundary of the pool are calculated by the equations

$$q_u = 0.345\mathrm{Ra}^{0.233}\frac{k\Delta T}{R} \tag{10-21}$$

$$q_b = 0.54\mathrm{Ra}^{0.18}\left(\frac{H}{R}\right)^{0.26}\frac{k\Delta T}{R} \tag{10-22}$$

$$q_l = 0.85\mathrm{Ra}^{0.19}\frac{k\Delta T}{R} \tag{10-23}$$

where

q_u = heat flux from molten pool to crust at top of molten pool (W/m^2),

q_b = heat flux from molten pool to crust at bottom of molten pool (W/m^2),

q_l = heat flux from molten pool to crust at side of molten pool (W/m^2),

Ra = Rayleigh number of the liquid in the molten pool, ($g\beta q_d L^5/\alpha\nu k$),

k = thermal conductivity of the liquid in the molten pool (W/m•K),

ΔT = difference in temperature between temperature of molten pool and its melting temperature (K), R = radius of molten pool at its upper surface (m),

H = depth of molten pool (m),

L = characteristic length (m) (assumed equal to depth of molten pool),

g = acceleration due to gravity (m/s^2),

β = volumetric coefficient of expansion (1/K),

α = thermal diffusivity (m^2/s),

ν = kinematic viscosity (m^2/s),

q_d = volumetric heat generation rate (W/m^3).

The radius of the molten pool is assumed equal to the radius of a hemisphere that has the same volume as the volume of molten material. The variable R is thus calculated by the equation

$$R = \left(\frac{1.5V_{pool}}{\pi}\right)^{0.33333} \tag{10-24}$$

where

V_{pool} = volume of molten material (m^3).

Since the molten pool is assumed to be in the configuration of a hemisphere, H = R. Thus, the (H/R) term in the equation for q_b is always equal to 1.

If the transient natural convection correlation is selected, the heat fluxes at the various locations on the boundary of the pool are calculated by the equations[10-14]

$$q_u = 0.250Ra'^{0.304}k\frac{\Delta T}{R}, \tag{10-25}$$

$$q_b = 0.472\left(\frac{H}{R}\right)^{0.317}Ra'^{0.220}k\frac{\Delta T}{R}, \tag{10-26}$$

$$q_l = 0.818Ra'^{0.235}k\frac{\Delta T}{R} \tag{10-27}$$

where

Ra' = transient Raleigh number, $\left(\frac{g\beta L^3\Delta T}{\alpha\nu}\right)$.

10.5.2 Stability of Crust Surrounding Molten Pool

A molten pool may either stay in place or spread radially and downward. If the molten pool is surrounded by steam and debris considerably cooler than the liquidus temperature of the material in the molten pool, then a thick crust will form around the pool and hold it in place. If the coolant surrounding the molten pool is at about the same temperature as the liquidus temperature of the material in the molten pool, then the crust surrounding the molten pool will be thin. If the crust is thin or the stresses in the crust are large relative to its ultimate strength, then the crust may fail removing the constraint on molten pool spreading. This section describes the calculations performed to determine whether the crust at every location remains stable and contains the molten pool or whether the crust may fail at any point and allow the molten pool to spread through that point.

The stability of a crust surrounding a molten pool is a function of several variables, including the thickness of the crust and the differential pressure between the fluid inside the crust and that outside of the crust. A schematic of a crust surrounding the molten pool and a definition of the variables utilized to calculate the crust stability are shown in Figure 10-7. The crust thickness is defined to be the thickness of the load bearing part of the crust, which in turn is defined to be the part of the crust at a temperature less than 2,250 K.[10-14] The temperature threshold of 2,250 K was selected because experimental data indicate the ultimate strength of UO_2 to be extremely small for temperatures greater than 2,250 K. The pressure acting on the inside surface of the crust, P_I, is the system pressure in the reactor core region just prior to the molten pool being enveloped with a crust. The crust at the bottom of the molten pool is assumed to be supported by intact portions of fuel rods and thus not vulnerable to failure from loads applied by pressure or weight. The bottom crust, however, is not capable of containing the molten material it supports unless its thickness is greater than the as-fabricated diameter of the fuel rods in the reactor core. The code user has the option to define a different minimum thickness of the bottom crust in order for it to seal in the molten material it supports.

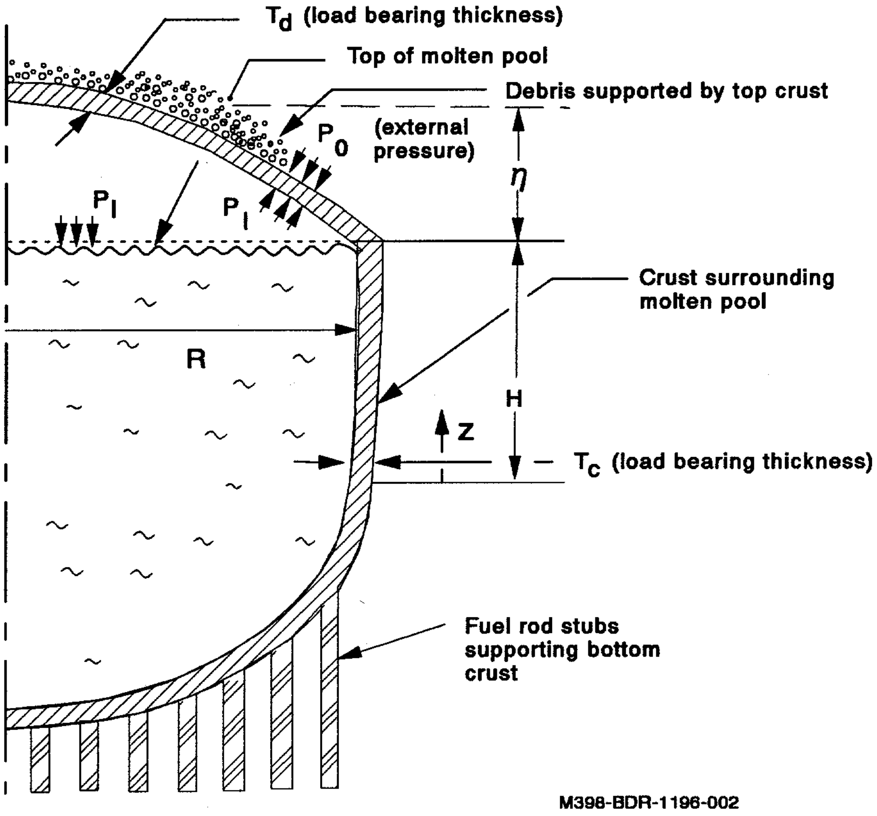
T_d (load bearing thickness)
Top of molten pool
Debris supported by top crust
P_0 (external pressure)
η
P_I
P_I
Crust surrounding molten pool
R
H
z
T_c (load bearing thickness)
Fuel rod stubs supporting bottom crust
M398-BDR-1196-002

Figure 10-7. Framework for model calculating stresses in crust surrounding molten pool.

Analysis of the stresses in the crust surrounding the molten pool has shown that the juncture of the top and side crusts are the only location vulnerable to failure from stresses applied by pressure and weight.[10-14] The stress at this juncture is calculated by the equation

$$\sigma_{\theta d} = \frac{1}{4}\left[\frac{R^2}{t_d \eta} + \frac{\eta}{t_d}\right]\left[P_I - P_o - \frac{W_D}{\pi R^2}\right] \tag{10-28}$$

where

$\sigma_{\theta d}$ = tangential stress in crust above molten pool (Pa),

R = radius of molten pool at top surface (m),

t_d = thickness of crust above molten pool (m),

η = height of crust above molten pool at center relative to that at edge (m),

P_I = gas pressure acting on inside surface of crust (Pa),

P_o = fluid pressure acting on outside surface of crust (Pa),

W_D = weight of material that is supported by crust above molten pool (N).

The stability of the upper crust is determined by comparing its stress with its ultimate strength. The criterion for stability is:

$$F_A \sigma_{\theta d} < S_u (T_D) \tag{10-29}$$

where

$S_u (T_D)$ = ultimate strength of crust at the temperature of T_D (Pa),

T_D = average temperature of crust (K),

F_A = factor that adjusts stress at failure calculated by Equation (10-28), which assumes the crust to have a large amount of ductility, to equal the stress at failure as calculated by the detailed structural analysis code, ABAQUS.[10-15] This factor is equal to 3.2 for η equal to 0.5 m, R equal to 1.5 m, and a pre-CHF mode of heat transfer occurring at the outer surface of the crust.

The ultimate strength of the crust is calculated assuming that the crust is composed only of UO_2. This assumption is required because experimental results regarding the ultimate strength of a mixture of UO_2, ZrO_2, Zr, and stainless steel are not available. The ultimate strength of UO_2 is represented by the following correlation;

$$S_u (T) = 1.\ \mathrm{x}\ 10^6 (0.020876T + 92.233) \qquad T < 1{,}609\ \mathrm{K}, \tag{10-30}$$

$$S_u (T) = 1.\ \mathrm{x}\ 10^6 (-0.19598T + 441.22) \qquad 1{,}609\ \mathrm{K} < T < 2{,}250\ \mathrm{K}, \tag{10-31}$$

$$S_u (T) = 0.0 \qquad T > 2{,}250\ \mathrm{K}\ . \tag{10-32}$$

If a crust does not extend across the top of the molten pool, the pool is not sealed from system pressure. Thus, p_I equal p_o and the pressure differential term is zero in the stress equation for the crust.

The thickness of the crust and the temperature distribution through the crust are calculated using an integral method assuming steady-state heat transfer. The framework for these calculations is shown in Figure 10-8.

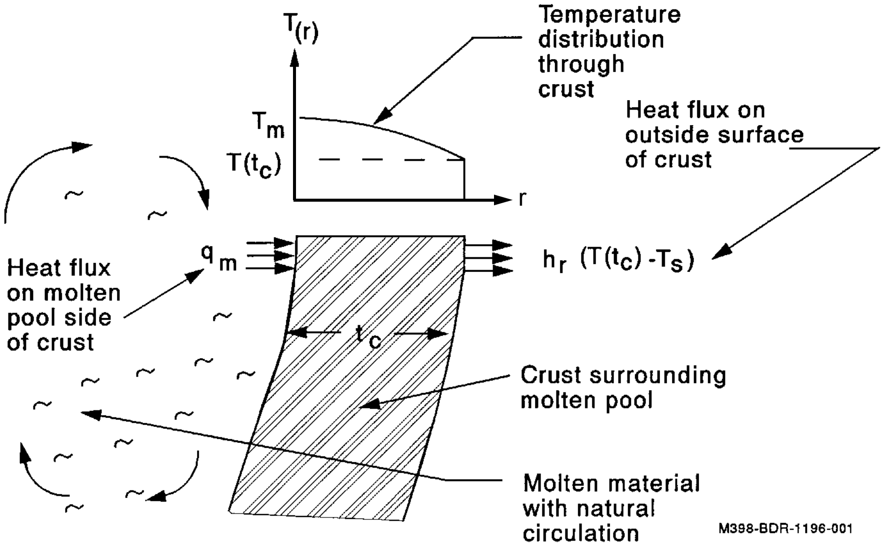
T(r)
Temperature distribution through crust
Heat flux on outside surface of crust
Tm
T(tc)
r
qm
hr (T(tc) -Ts)
Heat flux on molten pool side of crust
tc
Crust surrounding molten pool
Molten material with natural circulation
M398-BDR-1196-001

Figure 10-8. Framework for calculation of thickness of crust surrounding molten pool and temperature distribution in crust.1

The temperature distribution through the crust is assumed to be represented by the equation

$$T(r) = Ar^2 + Br + C \tag{10-33}$$

where

T(r) = temperature of crust at radial coordinate r (K),

A, B, C = coefficients whose values are determined from boundary conditions,

r = radial coordinate (m).

The coefficients A, B, and C and the crust thickness, t_c, are a set of four unknown variables that are solved using the steady-state heat conduction equation and three boundary conditions. The steady-state heat conduction equation is

$$k\left[\frac{\partial T(0)}{\partial r} - \frac{\partial T(t_c)}{\partial r}\right] = t_c q_{dc} \tag{10-34}$$

where

k = thermal conductivity of crust (W/m•k),

q_{dc} = power density in crust (W/m^3).

A boundary condition on the left side of the crust is

$$-k\frac{\partial T(0)}{\partial r} = q_m \tag{10-35}$$

where

q_m = heat flux imposed upon left side of crust by natural convection in molten pool (W/m^2).

Another boundary condition on the left side of the crust is

$$T(0) = T_m \tag{10-36}$$

where

T_m = solidus temperature of crust (K).

The third boundary condition applies the heat flux boundary condition on the right side of the crust. This boundary condition is expressed by the equation

$$h_r\,(T(t_c) - T_s) = q_m + t_c\,q_{dc} \tag{10-37}$$

where

h_r = combined radiative and convective heat transfer coefficient on right surface of crust (W/m^2•K),

T_s = fluid temperature at right side of crust (K).

The variable h_r is calculated by the equation

$$h_r = \sigma\varepsilon[T(t_c)^2 + T_s^2][T(t_c) - T_s] + h_c \tag{10-38}$$

where

σ = Boltzmann-Stefan constant (5.6697x10^{-8} W/m^2•K^4),

ε = emissivity factor (assumed to be 0.7),

h_c = convective heat transfer coefficient on right surface of crust (W/m^3•K).

Values for the four unknown variables are next determined. From the first boundary condition for the left side of the crust,

$$-k\frac{\partial T(0)}{\partial r} = -kB = q_m \quad . \tag{10-39}$$

Thus

$$B = -\frac{q_m}{k} \quad . \tag{10-40}$$

From the second boundary condition for the left side of the crust,

$$T(0) = C = T_m \quad . \tag{10-41}$$

Next, the value of A is obtained by applying the steady-state heat conduction equation and using the parabolic temperature distribution for T(r). The result is

$$k\left[\frac{\partial T(0)}{\partial r} - \frac{\partial T(t_c)}{\partial r}\right] = k\left[-\frac{q_m}{k} - 2At_c + \frac{q_m}{k}\right] = t_c q_{dc} \quad . \tag{10-42}$$

Solving the above equation for A, the result is

$$A = \frac{-q_{dc}}{2k} \quad . \tag{10-43}$$

The boundary condition for the right side of the crust is next used to solve for the last unknown variable, namely, t_c. Putting this equation in terms of the known variables A, B, and C, the result is

$$h_r[T(t_c) - T_s] = h_r\left(\frac{-q_{dc}t_c^2}{2k} - \frac{q_m t_c}{k} + T_m - T_s\right) = q_m + t_c q_{dc} \quad . \tag{10-44}$$

Solving the above equation for t_c, the result is:

$$t_c = \frac{-\left(\frac{q_m}{k} + \frac{q_{dc}}{h_r}\right) + \left[\left(\frac{q_m}{k} + \frac{q_{dc}}{h_r}\right)^2 + \frac{4q_{dc}}{2k}\left(T_m - T_s - \frac{q_m}{h_r}\right)\right]^{0.5}}{\frac{q_{dc}}{k}} \quad . \tag{10-45}$$

Since the variable h_r is a function of the temperature of the right side of the crust and thus the crust thickness, the above equation must be solved by iteration. A value for h_r is first estimated assuming the right side of the crust is at the solidus temperature of the crust material. Then, t_c, A, B, and C are solved and a corrected temperature for the right side of the crust obtained. The iteration continues until the fractional change [(current value minus previous iteration value)/previous iteration value] in crust thickness in two successive iterations is less than 0.01.

The thickness of the load bearing part of the crust is determined by calculating the crust radius where the temperature is equal to the temperature above which the ultimate strength of the crust is zero, namely the temperature of 2,250 K. This radius is given by the equation

$$Ar_b^2 + Br_b + C = 2,250 \tag{10-46}$$

where

r_b = radius at which temperature of crust is equal to 2,250 K (m).

The load bearing thickness is then given by the equation

$$t_{cb} = t_c - r_b \tag{10-47}$$

where t_{cb} = load bearing thickness of crust (m).

10.5.3 Rate of Spreading of Molten Pool

The model for calculating the spreading rate of molten material is based on the concept of a sporadically moving crust enveloping the pool. The crust experiences repeated cycles of melting, flowing, and freezing. After the molten material penetrates some distance into the porous debris, its leading edge is cooled to the point of freezing and the spreading temporarily stops. The spreading resumes when the material between the original position of the crust and its current position has completely melted and is mixed with the other material in the molten pool.

The physical process being represented by the spreading model consists of five steps, as shown in Figure 10-9. The modeling of these five steps defines the movement and the thickness of the boundary layer that envelopes the molten pool. In the first step, a portion of the crust enveloping the molten pool melts through or fails structurally at some point. In the second step, the molten material spreads into the porous debris. Because the porous debris is cooler than the molten material, heat is removed from the spreading molten material and transferred to the porous debris. In the third step, the leading edge of the spreading molten material freezes and temporarily stops the spreading of the molten material. In the fourth step, the region penetrated by the spreading material, namely the region between the previous location of the crust and its current location, is assumed to heat adiabatically. This region, a mixture of solid and liquid material, is assumed to not be mixed with the molten pool until all solid material in the zone has melted. The melting is caused by decay heat in the solid material and in the molten material that penetrated the porous debris. In the fifth step, the molten pool expands to the inner surface of the crust formed by the freezing of the leading edge of the spreading molten material. The material through which the molten material spread is mixed into the molten pool. The modeling of this five step process results in a model that calculates the rate of spreading of molten material as a function of the temperature and size of the molten pool, the flow rate and temperature of the fluid flowing through the porous debris adjacent to the molten pool, and the porosity and particle size of the porous debris adjacent to the molten pool.

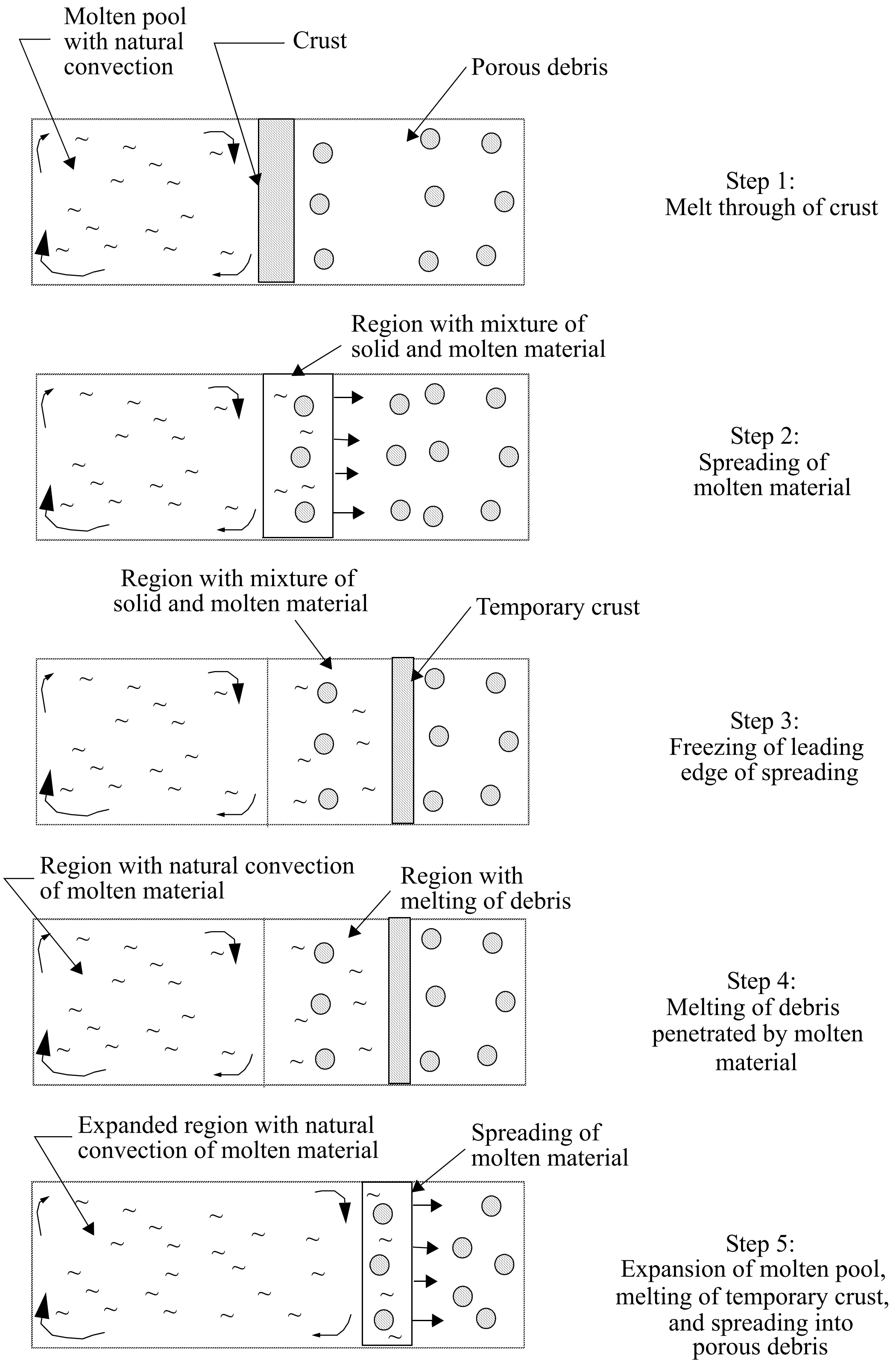
Molten pool
with natural
convection
Crust
Porous debris
Step 1:
Melt through of crust
Region with mixture of
solid and molten material
Step 2:
Spreading of
molten material
Region with mixture of
solid and molten material
Temporary crust
Step 3:
Freezing of leading
edge of spreading
Region with natural convection
of molten material
Region with
melting of debris
Step 4:
Melting of debris
penetrated by molten
material
Expanded region with natural
convection of molten material
Spreading of
molten material
Step 5:
Expansion of molten pool,
melting of temporary crust,
and spreading into
porous debris

Figure 10-9. Sequences in process being represented by spreading model.

The molten pool spreading model uses the following assumptions: (1) the material at the leading edge of the molten pool does not mix with the molten material behind it; (2) the thickness of the leading edge is equal to the diameter of the porous debris particles; (3) the leading edge of the spreading molten material instantly heats the in situ porous debris to its temperature on contact; (4) material at the leading edge is at its solidus temperature. As a result of using these assumptions, the model calculates the leading edge of spreading molten material to be eventually cooled to the point where it is completely frozen.

Figure 10-10 shows in schematic form the heat transfer concept being used. In the top part of the figure, molten material has begun to spread into the porous debris. The molten material is spreading from left to right. The temperature distribution in the porous debris is shown below the schematic representation of the spreading molten material. The temperature of the porous debris is initially less than the solidus temperature of the molten material, represented by the symbol T_S. Thus, the porous debris is a sink for the heat in the leading edge of the spreading molten material. As the leading edge advances, it is continually cooled and eventually becomes completely frozen. This state of the spreading process is shown in the bottom part of Figure 10-10. The advancement is then temporarily stopped until the solid material behind the leading edge is completely melted and mixed with the molten pool. Then, if the crust melts through or is structurally unstable spreading of the molten material continues. The structural stability of the crust is based on the thickness of the crust as calculated in Section 10.5.2.

The model to calculate the rate of spreading of molten material has two parts: (1) the calculation to determine the distance molten material spreads before its leading edge is frozen and (2) the calculation of time to melt the solid porous material through which the leading edge moved and which is left behind. This solid material was heated to its solidus temperature when the leading edge contacted it, but it is not completely melted until its internal energy increases by the value of its heat of fusion. The derivation of the equations to calculate each of these parts of the model are presented next.

The model to calculate the distance the leading edge of the molten material moves before freezing is next derived. The movement is assumed to be stopped when the leading edge becomes completely frozen. The change in internal energy of the leading edge of molten material spreading into porous debris is calculated by the equation

$$du = \frac{(1-\varepsilon)A_w\rho_D c_p[T_S - T_D(x)]dx}{\varepsilon A_w \rho_m \Delta x_c} \qquad (10\text{-}48)$$

where

u = internal energy of leading edge of molten material spreading into porous debris (J/kg),

ε = porosity of debris,

A_w = cross-sectional area of molten material penetrating porous medium (m^2),

$T_D(x)$ = temperature of debris at position x (K),

x = distance leading edge of molten material has penetrated into porous debris (m),

ρ_m = density of molten material (kg/m^3),

ρ_D = density of material constituting the porous debris (kg/m^3),

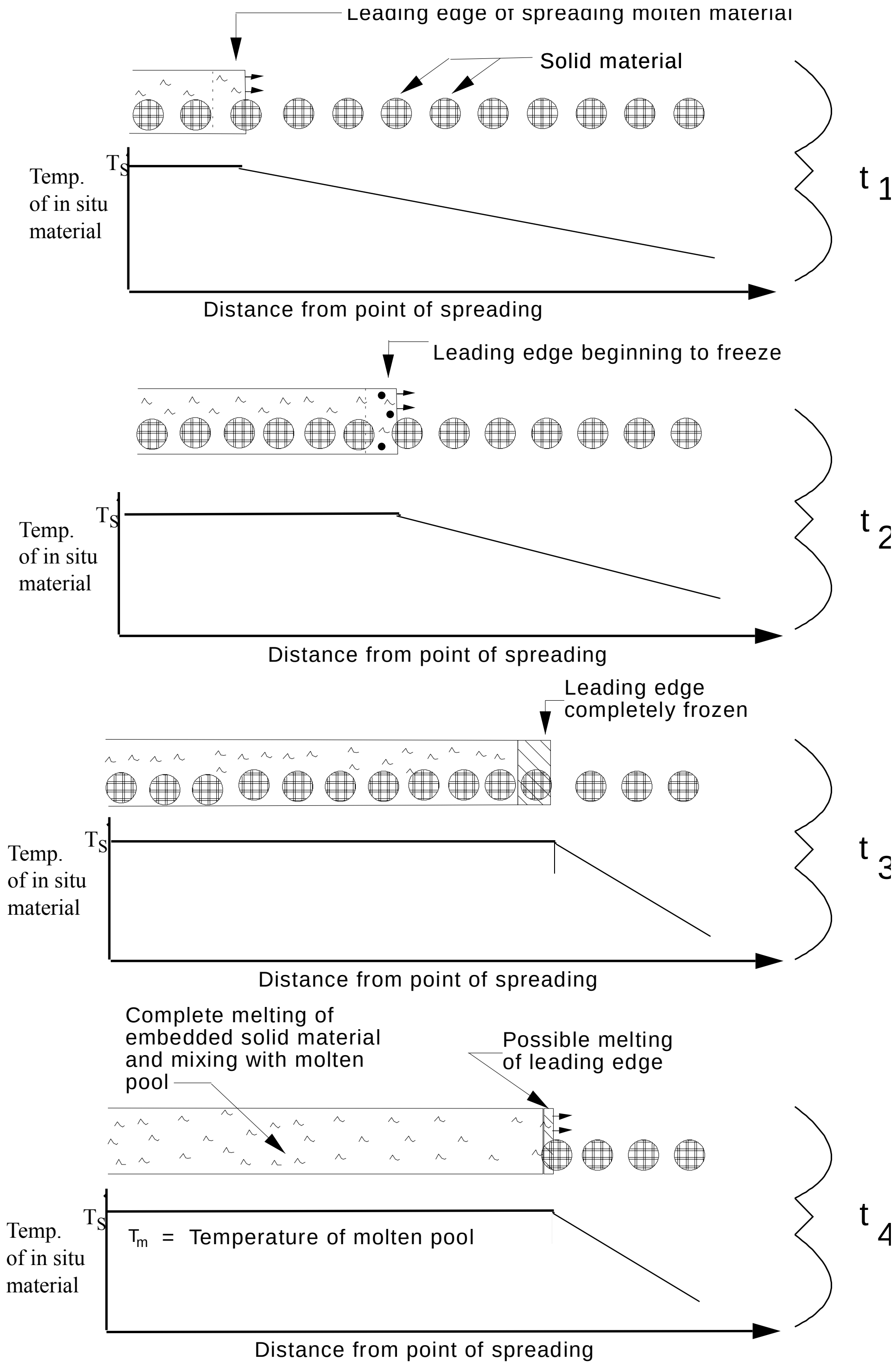
Leading edge of spreading molten material
Solid material
Temp. of in situ material
T_S
t_1
Distance from point of spreading
Leading edge beginning to freeze
Temp. of in situ material
T_S
t_2
Distance from point of spreading
Leading edge completely frozen
Temp. of in situ material
T_S
t_3
Distance from point of spreading
Complete melting of embedded solid material and mixing with molten pool
Possible melting of leading edge
Temp. of in situ material
T_S
T_m = Temperature of molten pool
t_4
Distance from point of spreading

Figure 10-10. Conditions assumed by model for calculating distance of penetration of molten material into porous debris.

c_p = heat capacity of debris (J/kg•K),

T_S = solidus temperature of molten pool and porous debris (K),

Δx_c = length of leading edge (m).

In Equation (10-48), the term $(1 - \varepsilon) A_w\rho_D c_p [T_S - T_D(x)] dx$ represents the energy (J) removed from the leading edge of the spreading molten material after it has spread the distance dx into the porous debris. This energy is transferred to the porous debris and heats the porous debris to the temperature T_S. The mass receiving this energy is represented by the term $(1 - \varepsilon) A_w\rho_D dx$. The mass of the leading edge of the spreading molten material is represented by the term $\varepsilon A_w\rho_m\Delta x_c$.

The variable Δx_c is assumed to be a function of the size of the particles in the porous debris. In particular, Δx_c is assumed to be defined by the equation

$$\Delta x_c = 2r_p \tag{10-49}$$

where

r_p = radius of particles constituting the porous debris (m).

Applying the definition of the leading edge, Equation (10-48) becomes

$$du = \frac{(1-\varepsilon)\rho_D c_p[T_S - T_D(x)]dx}{2\varepsilon\rho_m r_p} \quad . \tag{10-50}$$

The temperature distribution in the porous debris is assumed to decrease with distance from the crust in a linear manner. The distribution is given by the equation

$$T_D(x) = T_S - \frac{\partial T}{\partial x}x \quad . \tag{10-51}$$

Substituting Equation (10-51) into Equation (10-50) results in the equation

$$du = \frac{(1-\varepsilon)\rho_D c_p\left[T_S - \left(T_S - \frac{\partial T}{\partial x}x\right)\right]dx}{2\varepsilon\rho_m r_p} = \frac{(1-\varepsilon)\rho_D c_p\frac{\partial T}{\partial x}x dx}{2\varepsilon\rho_m r_p} \quad . \tag{10-52}$$

Integration of Equation (10-52) results in

$$u = \frac{(1-\varepsilon)\rho_D c_p\frac{\partial T}{\partial x}x^2}{4\varepsilon\rho_m r_p} \quad . \tag{10-53}$$

Spreading is assumed to be stopped when the energy removed from the spreading material equals the heat of fusion of the molten material. The distance of spreading that causes a stoppage due to freezing is given by the equation

$$u = h_f = \frac{(1-\varepsilon)\rho_D c_p \frac{\partial T}{\partial x}\Delta x_p^2}{4\varepsilon\rho_m r_p} \tag{10-54}$$

where

h_f = heat of fusion of molten material (J/kg),

Δx_p = distance that molten material spreads into porous debris (m).

Solving Equation (10-54) for Δx_p, the result is

$$\Delta x_p = \left[\frac{4\varepsilon\rho_m r_p h_f}{(1-\varepsilon)\rho_D c_p \frac{\partial T}{\partial x}}\right]^{0.5} . \tag{10-55}$$

The second part of the spreading model calculates the period of time required to melt the in situ porous debris through which the molten material has spread. The simplifying assumption made is that no heat is conducted or convected out of the in situ porous debris through which the molten material has spread. In other words, the porous debris is heated adiabatically. The porous debris is heated to its solidus temperature by the leading edge of the spreading molten pool. Therefore, melting of the porous debris is not complete until the internal energy of the porous debris has increased by the value of the heat of fusion of debris. The heat to melt the porous debris is supplied by the decay heat in the molten material and porous debris. The heat balance equation is thus

$$[(1-\varepsilon)\, q_D + \varepsilon q_m]\, V\Delta t_m = (1-\varepsilon)\rho_D h_{fD} V \tag{10-56}$$

where

q_D = volumetric heat generation rate in the porous debris (W/m^3),

q_m = volumetric heat generation rate in the molten material (W/m^3),

V = volume of molten material and porous debris (m^3),

h_{fD} = heat of fusion of porous debris (J/kg),

Δt_m = time to melt the in situ porous debris (s).

The left side of Equation (10-56) represents the heat input to the in situ porous debris and the right side represents the energy required to melt the in situ porous debris.

Solving Equation (10-56) for the time to melt the in situ porous debris, the result is

$$\Delta t_m = \frac{(1-\varepsilon)\rho_D h_{fD}}{(1-\varepsilon)q_D + \varepsilon q_m} . \tag{10-57}$$

The rate of spreading of molten material can now be determined by combining Equations (10-55) and (10-57). Equation (10-56) calculates the distance the molten material spreads before it is plugged by the freezing material at its leading edge. Equation (10-57) calculates the time required to melt the in situ porous debris penetrated by the molten material. After the porous debris has melted, natural convection heat transfer in the molten pool can again melt the crust formed by the freezing of the leading edge of the spreading molten material. If the crust is not stable, then spreading of the molten material continues. The rate of spreading of the molten material is calculated by the equation

$$\vec{v} = \frac{\Delta x_p}{\Delta t_m} = \frac{(1-\varepsilon)q_D + \varepsilon q_m}{(1-\varepsilon)\rho_D h_{fD}}\left[\frac{4\varepsilon\rho_m r_p h_f}{(1-\varepsilon)\rho_D c_p \frac{\partial T}{\partial x}}\right]^{0.5} . \tag{10-58}$$

The rate of spreading is a function of the porosity and particle size of the in situ porous debris, the temperature gradient in the porous debris, and the volumetric heat generation rate in the molten material and porous debris. The rate of spreading decreases with decreasing porosity and particle size. The rate of spreading also decreases with an increasing temperature gradient in the porous debris. The rate of spreading increases with an increasing volumetric heat generation rate in the porous debris and molten material.

Equation (10-58) is applied wherever gravity can drive molten material through porous debris. It is applied at the sides and bottom of the molten pool locations where the crust is not structurally stable. It is not applied at locations along the top surface of the molten pool.

10.5.4 Temperature of Molten Pool

Heat is transferred by natural convection from the interior to the exterior of a pool of molten core material. Figure 10-11 shows the overall heat loss from a molten pool.

The change in temperature of the molten pool during a time step is calculated by

$$\Delta T_{pool} = \left\{\left(V_l Q_l - \sum_{i=1}^{N} q_{si} A_{si}\right)\Delta t - \Delta m[c_m(T_o - T_m) + h_{fm}]\right\} / \rho_l c_{pl} V_l \tag{10-59}$$

where

ΔT_{pool} = temperature change of the molten pool during a time step (K),

V_l = volume of the molten pool (m^3),

Q_l = volumetric heat generation in the molten pool (W/m^3),

q_{si} = heat flux from the molten pool into i-th section of crust (W/m^2). For each section of crust, the heat flux is calculated by the equation appropriate for its position in the boundary of the molten pool, as described in Section 10.5.1,

A_{si} = area of i-th section of crust (m^2),

N = total number of sections of crust,

Δt = time step (s),

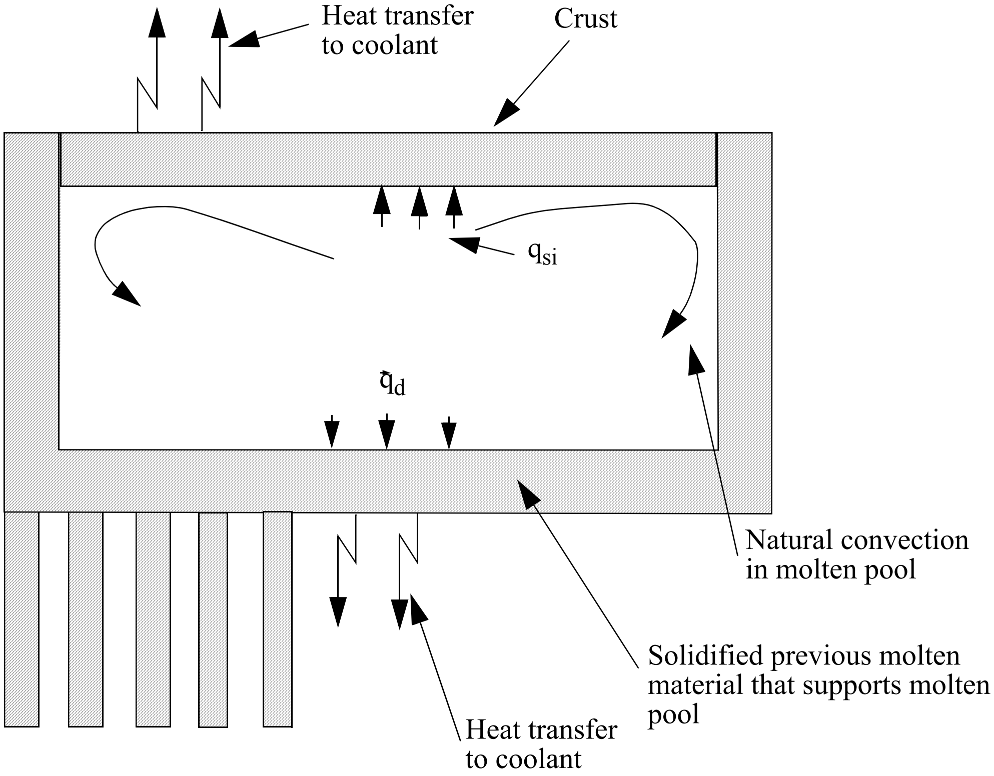
Heat transfer
to coolant
Crust
q_{si}
q_d
Natural convection
in molten pool
Solidified previous molten
material that supports molten
pool
Heat transfer
to coolant

Figure 10-11. Heat transfer from pool of molten debris.

ρ_l = density of the molten pool (kg/m^3),

c_{pl} = heat capacity of the molten pool (J/kg•K),

Δm = mass of material that joined molten pool during time step due to slumping of material into molten pool or due to melting of material at boundary of molten pool (kg),

c_m = heat capacity of material that became part of molten pool during time step (J/kg•K),

h_{fm} = heat of fusion of material that joined molten pool during time step (J/kg). If material already melted at time it joined molten pool, this term is equal to zero,

T_0 = temperature of molten pool at start of time step (K),

T_m = start of time step temperature of material that became part of molten pool during time step (K).

The variable Δm in the above equation is calculated by the model for calculating the rate of spreading of molten material through porous debris, which is described in Section 10.5.3. In the event that the crust above the molten pool fails in a structural sense during the time step and this crust supported rubble debris, Δm is equal to the mass of rubble debris supported by the crust.

10.6 Interaction of Molten Pool with Structures at Periphery of Core

This section describes the models for calculating the interaction of a pool of molten core material with structures at the periphery of the core. These models are applied when fuel rods at the periphery of the core have become molten and the molten material then contacts structures at the periphery of the core. The models calculate the heat transfer from the molten material to the structures and the melt progression that takes place in the structures. If a melt through is calculated of a structure that contains the molten pool, the model then calculates the amount of material that drains out of the molten pool and determines where this material drains to. The models are applicable to two types of structures at the periphery of a core or fuel bundle. These structures are: (1) stainless steel reflector with embedded flow channels, and (2) ZrO_2 shroud at periphery of fuel bundles in severe accident experiments such as the FPT0 test conducted in the PHEBUS-FP facility.[10-16]

An example of the possible interaction of a molten pool in the core region with a structure at the periphery of the core is shown in Figure 10-12. In this example, the structure has an embedded flow channel. A cross-section of the reflector is shown in Figure 10-13. The molten pool has a temperature perhaps 1,000 K higher than the melting temperature of the structure. When the molten pool comes in contact with the structure, the structure may begin to melt at the point of contact and the melting may propagate into the structure. If the melting continues, the structure may melt to the location of an embedded flow channel. Then material from the molten pool will drain into the flow channel. If the structure below the point of melt through is cold, the material draining through the embedded flow channel will solidify and plug the draining of the molten pool. The molten pool interaction model described in this section calculates the distance from the point of melt through to the point where the plugging of the material draining from the molten pool occurs. This distance is noted by the symbol X_p in Figure 10-12. If the structure is hot or the point of melt through is near the bottom of the reactor core, then the material from the molten pool will drain to the lower head of the reactor. If the cross-section of the structure at the periphery of the core is melted completely through, then the molten material will flow down the outside of the structure and drain to the lower head of the reactor.

10.6.1 Melt Progression in Structure Contacted by Molten Pool

The contact of a structure by a molten pool may result in the simultaneous melting of the structure and solidification of material from the molten pool. The four material regions that may exist at a surface in contact with the molten pool are shown in Figure 10-14. The material regions are: (1) molten pool; (2) layer of solidified material from molten pool (identified as crust in Figure 10-14), (3) layer of melted structural material; and (4) unmelted portion of structure. The temperature distribution through the four material regions is also shown in Figure 10-14. The temperature represented in Figure 10-14 by the symbol T_{mp} is equal to the solidification temperature of the molten material at the interface between the molten pool and the crust. The temperature at the interface of the liquefied and solid parts of the structure is equal to the liquefaction temperature of the structure. This temperature is represented in Figure 10-14 by the symbol T_{mss}. The temperature at the interface of the region of solidified molten pool material and liquefied structural material is designated by the symbol T_i.

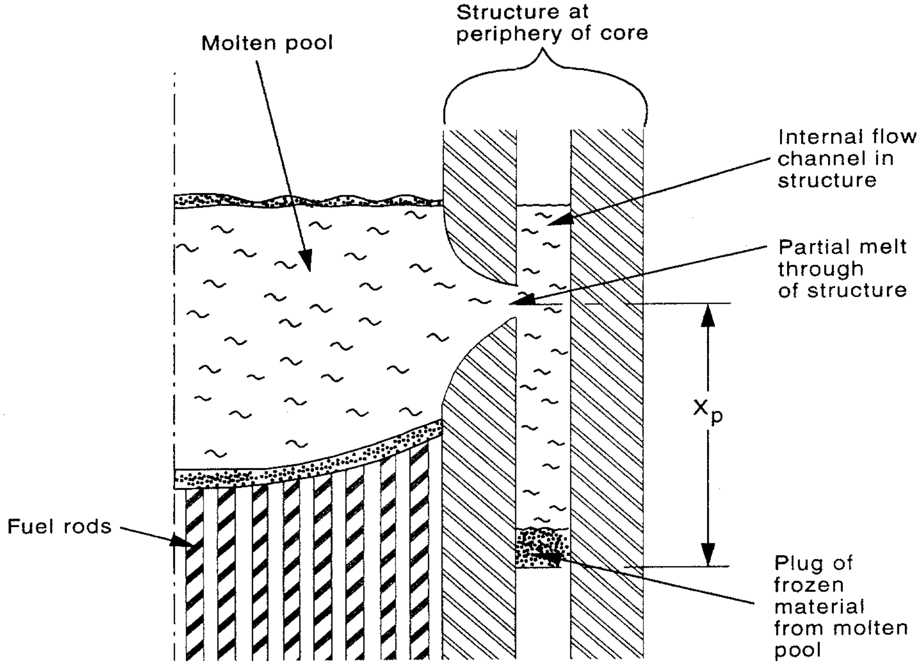
Structure at periphery of core
Molten pool
Internal flow channel in structure
Partial melt through of structure
X_p
Fuel rods
Plug of frozen material from molten pool

Figure 10-12. Example of molten pool interacting with structure at periphery of core.

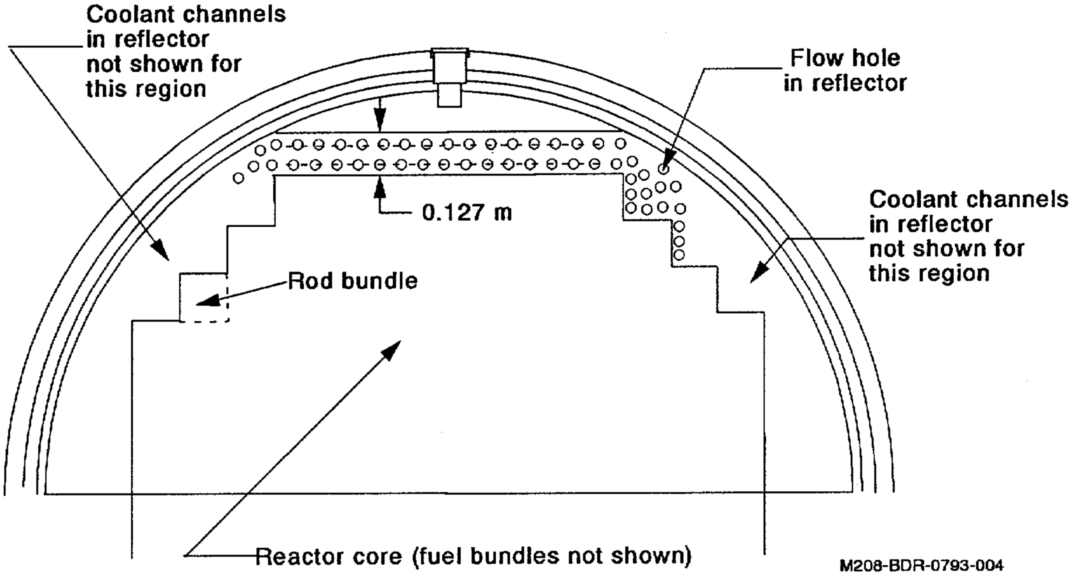
Coolant channels in reflector not shown for this region
Flow hole in reflector
0.127 m
Coolant channels in reflector not shown for this region
Rod bundle
Reactor core (fuel bundles not shown)
M208-BDR-0793-004

Figure 10-13. Cross-section of stainless steel reflector and its relation to reactor core.

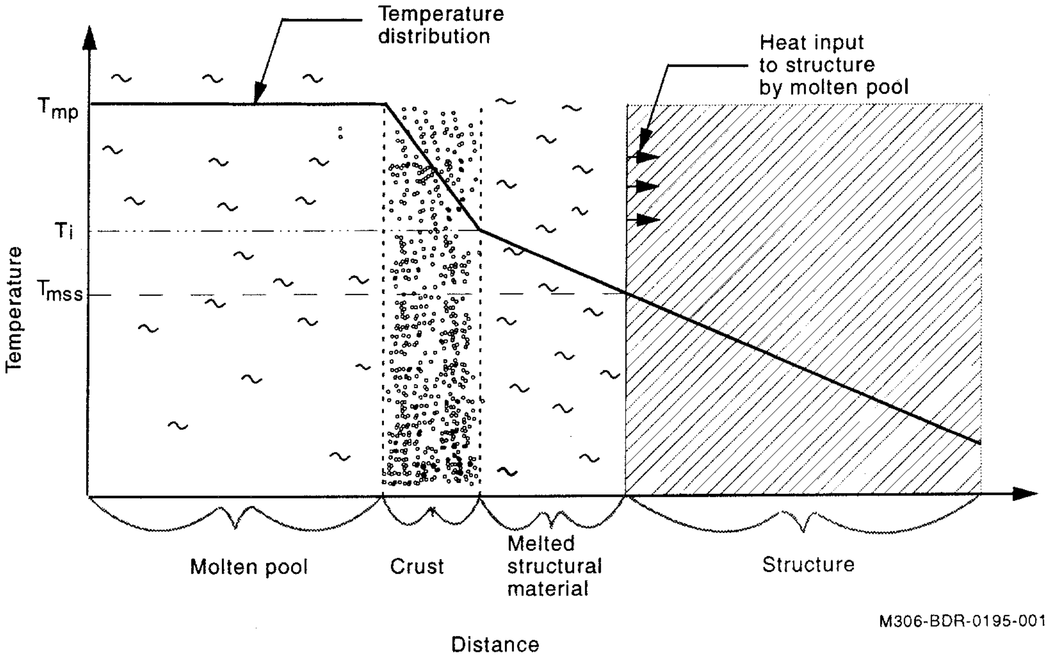
Temperature distribution
Heat input to structure by molten pool
T_{mp}
T_i
T_{mss}
Temperature
Molten pool
Crust
Melted structural material
Structure
M306-BDR-0195-001
Distance

Figure 10-14. Material regions and temperature distribution at surface of structure contacted by molten pool.

The temperature at the interface of the region of solidified molten pool material and liquefied structural material, T_i, is calculated assuming quasi-steady heat transfer and one-dimensional slab geometry. The temperature is calculated by the equation

$$T_i = \frac{k_c T_{mp}/t_c + k_{ss} T_{mss}/t_{ss} + \ddot{q}_c t_c}{(k_{ss}/t_{ss}) + (k_c/t_c)} \tag{10-60}$$

T_i = temperature at interface of solidified molten pool material and liquefied structural material (K),

k_c = thermal conductivity of crust (W/m • K),

T_{mp} = solidification temperature of molten pool material (K),

t_c = thickness of crust of solidified molten pool material (m),

k_{ss} = thermal conductivity of structural material (W/m • K),

T_{mss} = liquefaction temperature of structural material (K),

t_{ss} = thickness of melted layer of structural material (m),

$\dddot{q}_c$ = volumetric heat generation in crust (W/m^3).

The growth in the thickness of the crust is a function of the extent of natural convection in the molten pool and temperature gradient through the crust of solidified material. The growth of the crust thickness and the two heat fluxes that govern growth are shown in schematic form in Figure 10-15.

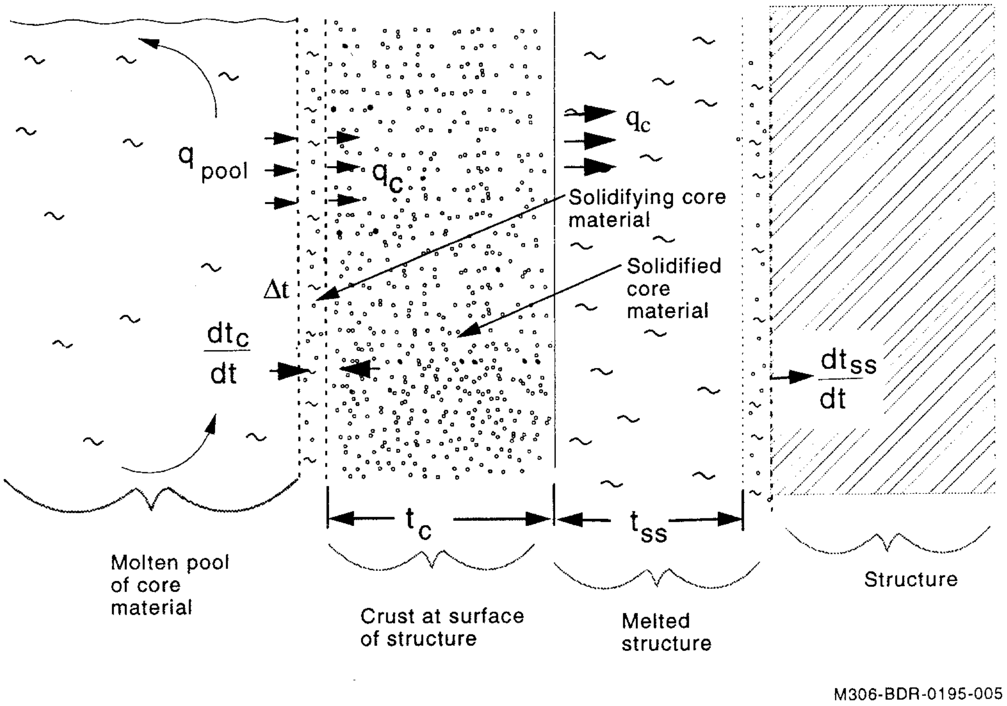
q pool
q c
q c
Solidifying core material
Solidified core material
Δt
dt c / dt
dt ss / dt
t c
t ss
Molten pool of core material
Crust at surface of structure
Melted structure
Structure
M306-BDR-0195-005

Figure 10-15. Growth of regions of solidified molten pool material and liquefied structural material at interface with molten pool.

The growth is calculated by the equation

$$\frac{dt_c}{dt} = -\frac{(q_{pool} - q_c)}{\rho_c h_{fc}} \qquad (10\text{-}61)$$

where

t_c = thickness of region of solidified molten pool material crust (m),

t = time (s),

q_{pool} = heat flux due to natural convection in molten pool (W/m^2),

q_c = heat flux into crust of solidified molten pool material (W/m^2),

h_{fc} = heat of fusion of molten pool material (J/kg),

ρ_c = density of molten pool material (kg/m^3).

The crust of solidified material from the molten pool is unstable due to contact with the molten pool on one side and liquefied structural material on the other side. After the thickness of the region of liquefied structural material has increased to a certain value, the crust may break up. If the user defines the thickness for break up to be zero, then a stable crust never forms and the maximum possible rate of melting of the structure is calculated. If the user defines the thickness for break up to be very large, then the crust never breaks up and the minimum possible rate of melting of the structure is calculated. Thus the user has the capability to determine the bounds of the rate of melting of the structure at the periphery of the core.

The variable q_{pool} in Equation (10-61) is calculated by the molten pool model as described in Section 10.5. If the molten pool is large and has a temperature in excess of 2873 K, then the variable q_{pool} in Equation (10-61) may be larger than the variable q_c, in which case the crust is calculated to decrease in thickness. The variable q_c in Equation is calculated by the equation

$$q_c = \frac{(T_{mp} - T_i)k_c}{t_c} \tag{10-62}$$

where

k_c = thermal conductivity of crust ($W/m \bullet K$).

The growth in thickness of the region of liquefied structural material is a function of the rate of heat transfer into the structure by the molten pool and the rate at which heat is conducted into the interior of the structure. The growth is calculated by the equation

$$\frac{dt_{ss}}{dt} = \frac{\left[\frac{(T_i - T_{mss})k_{ss}}{t_{ss}} - \frac{\partial T}{\partial r}(k_{ss})\right]}{\rho_{ss}h_{fss}} \tag{10-63}$$

where

t_{ss} = thickness of region of liquefied structural material (m),

$\frac{\partial T}{\partial r}$ = temperature gradient in structure at melt front (K/m),

ρ_{ss} = density of structural material (kg/m^3),

h_{fss} = heat of fusion of structural material (J/kg).

A structure with an embedded flow channel in contact with a molten pool may melt to the extent that a path is formed for a partial drainage of the molten pool. An example of structural melting that may cause a partial draining of the molten pool is shown in Figure 10-16. In this example, the upper part of the structure has melted through to the location of an embedded flow channel. After melt through to the location of the embedded flow channel, the material in the molten pool drains down the embedded flow channel. If the point of melt through is near the bottom of the structure, the molten pool drains until the elevation of its upper surface is the same as the elevation of the point of melt through. If the point of melt through is not near the bottom of the structure, the molten pool material draining into the embedded flow channel will freeze and plug the drainage. The molten pool material freezes because its solidification temperature is much higher than the liquefaction temperature of the structure. The distance between the point of melt through and the location at which a plug of frozen molten pool material forms is designated by the symbol X_p in Figure 10-16.

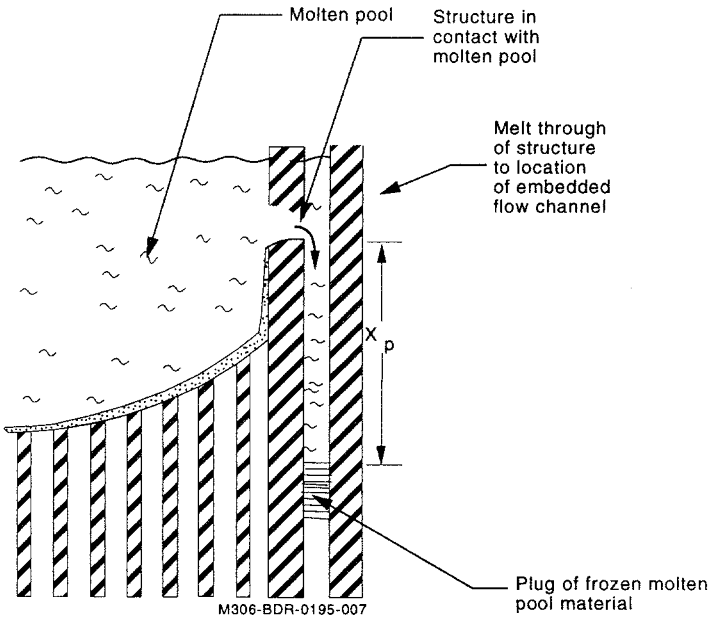
Molten pool
Structure in contact with molten pool
Melt through of structure to location of embedded flow channel
X_p
Plug of frozen molten pool material
M306-BDR-0195-007

Figure 10-16. Drainage of molten pool due to melting of structure with embedded flow channel.

This distance is calculated using an equation derived by Epstein et al.[10-17] The equation is

$$X_p = \frac{1}{2}\frac{D}{f}\left[\frac{(L_f)/C_f + T_{fo} - T_{f,\,tmp}}{T_{fo} - T_{s,\,mp}}\right] \times \left[\frac{1}{1 + \dfrac{(T_{f,\,mp} - T_{s,\,mp})}{(L_s/C_s + T_{s,\,mp} - T_{so})}}\right] \tag{10-64}$$

where

X_p = distance from point of melt through to plug of frozen material from molten pool (m),

D = diameter of embedded channel (m),

f = friction factor [~ 0.005],

L_f = heat of fusion of molten pool material (J/kg),

C_f = heat capacity of molten pool material (J/kg • K),

T_{fo} = initial temperature of molten pool material that penetrates embedded channel, (K)

$T_{f,mp}$ = melting temperature of molten pool material (K),

$T_{s,mp}$ = melting temperature of structure (K),

L_s = heat of fusion of structure (J/kg),

C_s = heat capacity of structure (J/kg • K),

T_{so} = initial temperature of structure that is contacted by flowing molten material (K).

As an example of the distance from the point of melt through to the location of the plug, the following case at the time of melt through to the embedded flow channels is defined; (1) structure is composed of stainless steel; (2) temperature of structure is 1,000 K, (3) molten pool material is at a temperature of 3,100 K, and (4) diameter of the embedded flow channel is 10 mm. According to Equation (10-64), the distance from point of melt through to the plug is calculated to be 0.25 m.

A structure that has material from the molten pool drain into its embedded flow channel may experience heatup and melt progression due to the internal energy in the molten pool material and due to decay heat in this material. The melt progression that may occur in the neighborhood of the flow channel is shown in Figure 10-17. The transfer of heat from the hot molten pool material to the structure causes a region of liquefied structural material to develop and increase in size. The heat transfer to the structure causes the molten pool material to solidify. The increases in thicknesses of the regions of liquefied structural material and solidified molten pool material are calculated by equations similar to those used to calculate the solidification and liquefaction that takes place at the interface between the structure and the molten pool. The temperature at the interface of the region of solidified molten pool material and liquefied structural material is first calculated on the basis of quasi-steady heat transfer. The temperature on the right side of the region of solidified molten pool material is equal to the solidification temperature of the molten pool material. The temperature on the left side of the liquefied structural material is equal to the liquefaction temperature of the structural material. The interface temperature is calculated by the equation

$$T_{ie} = \frac{k_c T_{mp}/t_{ce} + k_{ss} T_{mss}/t_{se} + \ddot{q}_c t_{ce}}{(k_{ss}/t_{se}) + (k_c/t_{ce})} \tag{10-65}$$

where

T_{ie} = temperature at interface of solidified molten pool material and liquefied structural material interface (K),

k_c = thermal conductivity of solidified molten pool material (W/m • K),

T_{mp} = solidification temperature of molten pool material (K),

t_{ce} = thickness of region of solidified molten pool material in embedded flow channel

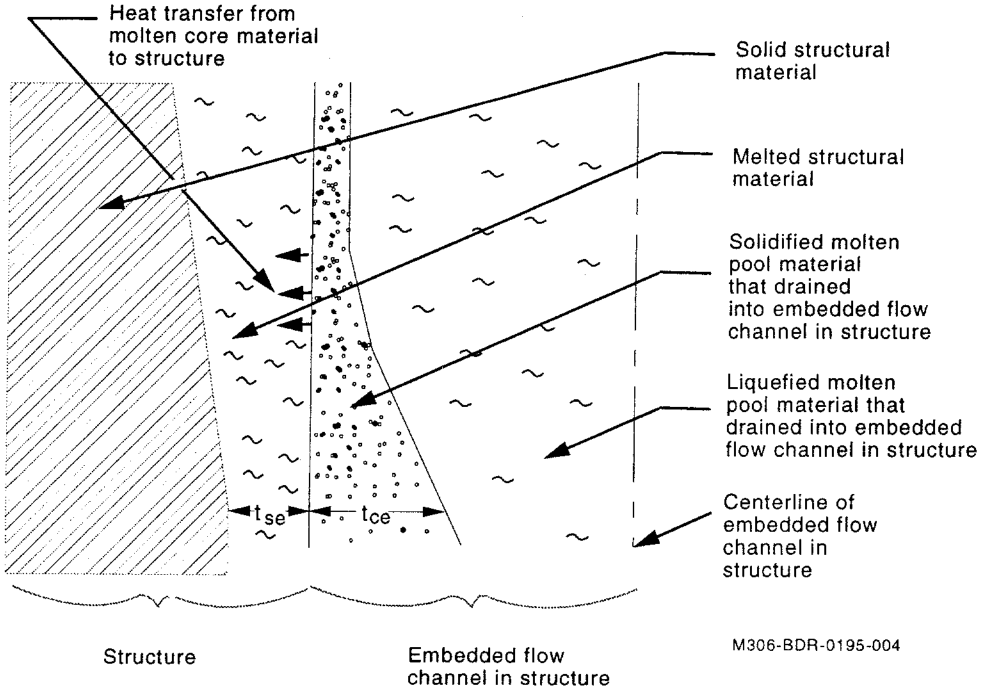
Heat transfer from molten core material to structure
Solid structural material
Melted structural material
Solidified molten pool material that drained into embedded flow channel in structure
Liquefied molten pool material that drained into embedded flow channel in structure
Centerline of embedded flow channel in structure
t_{se}
t_{ce}
Structure
Embedded flow channel in structure
M306-BDR-0195-004

Figure 10-17. Growth of regions of liquefied structural material and solidified molten pool material at surface of embedded flow channel.

(m),

k_{ss} = thermal conductivity of structural material (W/m • K),

T_{mss} = liquefaction temperature of structural material (K),

t_{se} = thickness of region of liquefied structural material (m),

$\dddot{q}_c$ = volumetric heat generation in solidified molten pool material (W/m^3).

The rate of increase in thickness of the region of liquefied structural material is calculated using the equation

$$\frac{dt_{se}}{dt} = \frac{\left[\frac{(T_{ie} - T_{mss})k_{ss}}{t_{ss}} - \frac{k_{ss}\partial T_{se}}{\partial r}\right]}{\rho_{ss}h_{fss}} \tag{10-66}$$

where

$\frac{dt_{se}}{dt}$ = rate of increase in thickness of region of liquefied structural material (m/s),

$\frac{\partial T_{se}}{\partial r}$ = temperature gradient in structure at left edge of region of liquefied structural, material (K/m),

ρ_{ss} = density of structural material (kg/m^3),

h_{fss} = heat of fusion of structural material (J/kg).

Heat is transferred through the column of hot liquefied molten pool material to the structure by conduction. The heat flux at the interface of the solidified and liquefied regions of structural material is calculated on the basis of quasi-steady heat transfer using the equation

$$q_{ie} = \frac{r_{em}^2 \dddot{q}_c}{2 r_{em}} \tag{10-67}$$

where

q_{ie} = heat flux at interface of column of liquefied structural material and region of solidified molten pool material (W/m^2),

r_{em} = radius of embedded flow channel (m),

$\dddot{q}_c$ = volumetric heat generation in molten pool material (W/m^3).

The rate of increase in thickness of the solidified molten pool material is calculated by the equation

$$\frac{dt_{ce}}{dt} = \frac{\left[\frac{(T_{mp} - T_{ie})k_c}{t_{ce}} - q_{ie}\right]}{\rho_c h_{fc}} \tag{10-68}$$

where

$\frac{dt_{ce}}{dt}$ = rate of increase in thickness of region of solidified material from molten pool (m/s),

ρ_c = density of molten pool material (kg/m^3),

h_{fc} = heat of fusion of molten pool material (J/kg).

Equations (10-65) through (10-68) are applied at each axial node in the structure at which its embedded flow channel contains molten pool material.

If the molten pool material liquefies a significant portion of the structure, then there is the possibility that the molten pool material will slump farther down the embedded flow channel even though it is solidified. A preliminary criterion for this slumping is applied. If the thickness of the region of liquefied structural material around the embedded flow channel is greater than 10 mm, then the molten pool material is assumed to slump down in the embedded flow channel to the next node below the axial node at which it first plugged.

10.6.2 Slumping of Molten Pool to Lower Head

Two possible flow paths to the lower head of the reactor vessel for molten pool material may be formed by melting of the structure at the periphery of the core. These two flow paths are shown in Figure 10-18. The first flow path is that which results by melting through the entire thickness of the structure. If a complete melt through occurs, the molten pool will drain through the path formed by melting and slump down the outside surface of the structure to the lower head. The second flow path results when molten pool material melts the structure through to an embedded flow channel and then a plug of solidified molten pool material does not form. In this case, the molten pool will drain through the path formed by melting of the structure and then slump through the embedded flow channel to the lower head. In both cases, the molten pool model calculates the pool drains until the elevation of its upper surface has decreased to the elevation of the point of structural melt through.

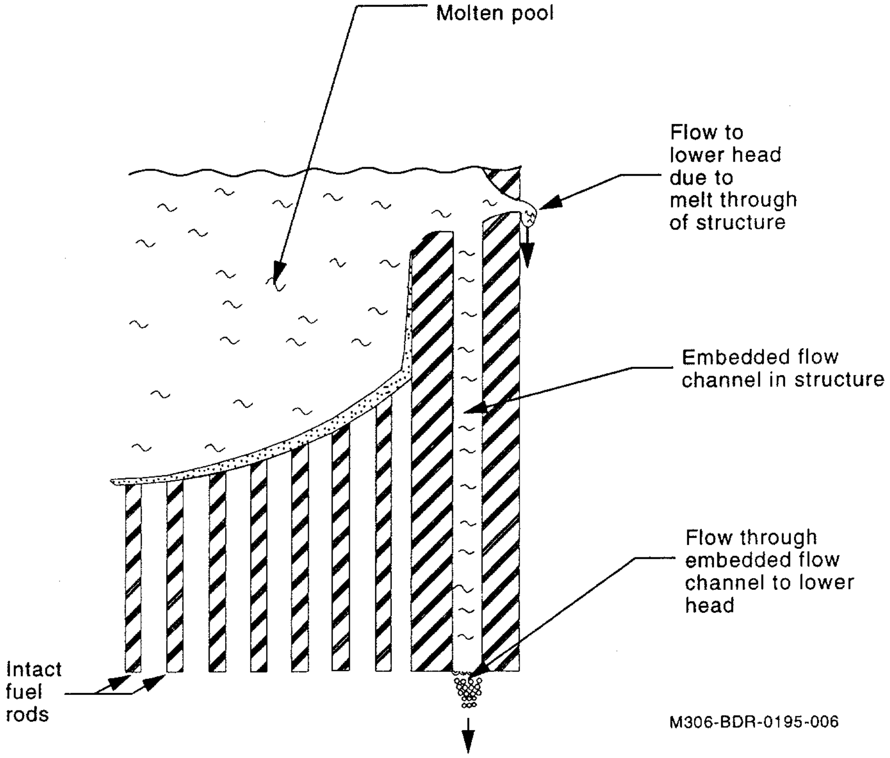
Molten pool
Flow to lower head due to melt through of structure
Embedded flow channel in structure
Flow through embedded flow channel to lower head
Intact fuel rods
M306-BDR-0195-006

Figure 10-18. Material in molten pool may slump to lower head by two different flow paths through structure at periphery of core.

10.7 Molten Pool Slumping

This section describes the models that determine when material from a molten pool in the core region slumps from this region to the lower head of the reactor vessel. Three events are considered to trigger this slumping. The first event is the melting or structural failure of the vertically oriented crust at the periphery of the core that was containing the molten pool and keeping it from slumping into the core bypass region. The second event is the structural failure of the crust at the top of the molten pool that supported core material above the molten pool. This event is considered to cause slumping of the molten pool to the lower head only when the molten pool had already spread to the periphery of the core. The third event is the propagation of the molten pool to the bottom of the core. In order to have the capability to perform a sensitivity study on the timing of core slumping, an option is provided for the code user to prescribe the molten pool to slump to the lower head at the instant the molten pool has spread to the periphery of the core. Unless a structure at the periphery of the core such as a reflector is being modeled, any event that triggers slumping of the molten pool is assumed to result in slumping of the entire molten pool.

The calculated time of slumping of a molten pool to the lower head should be regarded as having a large degree of uncertainty. Even for a well-defined manufactured structure, the time of failure may be difficult to predict. For a structure that evolves during a severe accident and has uncertainties in configuration, composition, load, and temperature, the prediction of the time of failure is an order of magnitude more difficult. This large uncertainty in the calculation of crust failure requires the severe accident analyst to examine the effect of the failure criteria upon the calculated course of a severe accident. To perform the sensitivity study suggested above, the code user may define the failure criteria to be used for a SCDAP/RELAP5-3D© calculation in Word 1 of Card 40001100. If a value of 1 is defined for Word 1 on Card 40001100, then material in the molten pool is calculated to slump as soon as any part of the molten pool contacts the periphery of the reactor core. If Word 1 on this card is assigned a value of zero, then material in the molten pool does not slump until the molten pool has contacted the periphery of the reactor core and a structural failure of the crust supporting the molten pool occurs.

The degree of interaction of the slumping material with the water through which it falls is either defined by the code user or calculated using a fuel-coolant interaction model. If the user defines that no interaction takes place, then the slumping core material is considered to fall as an intact stream and no transfer of internal energy from the slumping material to water occurs. The slumping material accumulating in the lower head is considered to have no porosity. If the user defines a complete interaction between slumping material and the water through which it falls, then the slumping material is considered to break up into small particles and transfer all of its internal energy instantly to the water. The slumping material that accumulates in the lower head is considered to have a porosity of 0.5 and a particle size of 10 mm. The transfer of internal energy from the slumping material to water may cause a large amount of vapor generation and significantly increase the pressure in the reactor vessel. If the user defines the fuel-coolant interaction model to be used, then the porosity and particle size of the settled slumped material is a function of the calculated extent of breakup of the slumped material.

A sensitivity study of the behavior of slumping material is considered the best approach due to large uncertainties in the size and configuration of the breach through which the molten material drains. Also, an analysis of the breakup of slumping material is complicated by structures in the reactor vessel, such as core former plates, baffle plates, fuel rods, and spacer grids. As a result, it is necessary to enable a severe accident analyst to perform a sensitivity study of the behavior of slumping material. The code user is provided the capability to define the history of slumping molten material to the lower head and the characteristics of the debris in the lower head.

10.8 Fuel-Coolant Interaction During Molten Pool Slumping

A stream of molten material slumping from the core region to the lower head of the reactor vessel may break-up into many small drops as it penetrates into a pool of water in the lower head. The fuel-coolant interaction model in SCDAP/RELAP5-3D© calculates the extent of break-up. A schematic of molten material slumping from the reactor core into the lower plenum is shown in Figure 10-19. The molten material is composed of molten fuel, cladding and molten structure. The molten material flowing through the openings in the lower core structure is configured as a jet and interacts with the coolant in the lower plenum. The fuel-coolant interaction model analyzes the slumping molten fuel, and calculates molten fuel breakup, heat transfer to water and steam, relocation of the molten droplets, and the size of the partially solidified particles that settle to the bottom of the lower plenum. This section is divided into three parts. Section 10.8.1 describes the model for calculating the breakup of a jet of molten material penetrating

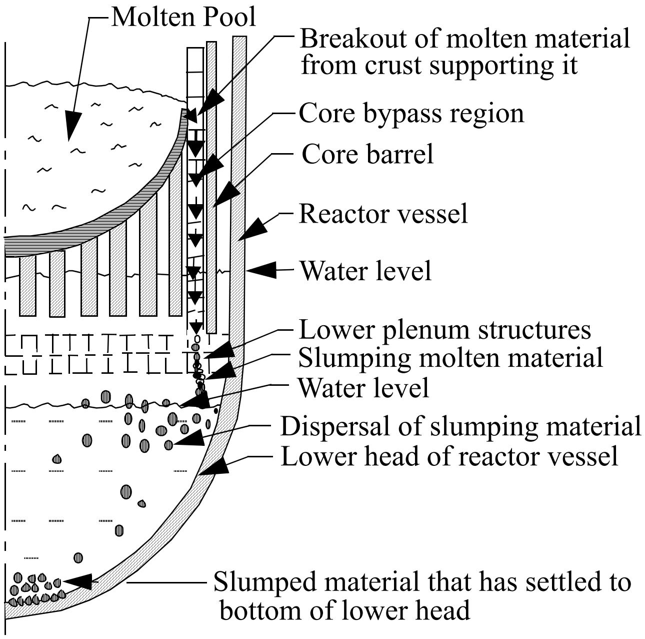
Molten Pool
Breakout of molten material from crust supporting it
Core bypass region
Core barrel
Reactor vessel
Water level
Lower plenum structures
Slumping molten material
Water level
Dispersal of slumping material
Lower head of reactor vessel
Slumped material that has settled to bottom of lower head

Figure 10-19. A schematic view of the molten material slumping into the lower plenum.

into a pool of water. Section 10.8.2 describes the model for calculating heat transfer between the dispersed drops of molten material and surrounding fluid. Section 10.8.3 describes the model for calculating the motion and settling of the dispersed drops.

10.8.1 Break-up

The implemented Fuel-Coolant Interaction (FCI) model is based upon the Chu and Corradini[10-33,10-32] liquid jet break-up model, shown in Figure 10-20, and incorporated in the TEXAS-V code. The two major break-up mechanisms modeled are; (1) Kelvin-Helmholtz (K-H) instability causing jet surface erosion, and (2) Rayleigh-Taylor (R-T) instability causing further fragmentation of discrete droplets already broken off from the jet. The model user is required to specify the diameter, temperature, and velocity of the liquid jet. In implementing the FCI model into SCDAP/RELAP5-3D©, the assumption was made that the leading edge of the jet is stationary. This assumption results in the calculation of no breakup due to boundary layer stripping. A schematic of the fuel-coolant interaction process is shown in Figure 10-20. In this figure, “k” is an index indicating a location in the stream of slumping material. Material located at “k+1” is just upstream of material located at “k”.

The effect of K-H instability is dominant along the body of the jet, where K-H waves develop because of the relative velocity between the fuel jet and the surrounding fluid. According to Corradini et al.,[10-27]the melt erosion rate, M_{KH}, is proportional to the increase in volume flux of the waves growing on the jet surface. The volume flux is approximately equal to the product of growth speed of the wave amplitude, $n\lambda$, and the cross-sectional area of a wave, $C_0\lambda^2$. As the K-H waves on the jet surface grow in size, droplets of molten material break away. Corradini et al.,[10-27] have given the mass erosion rate by K-H instability of one wavelet as

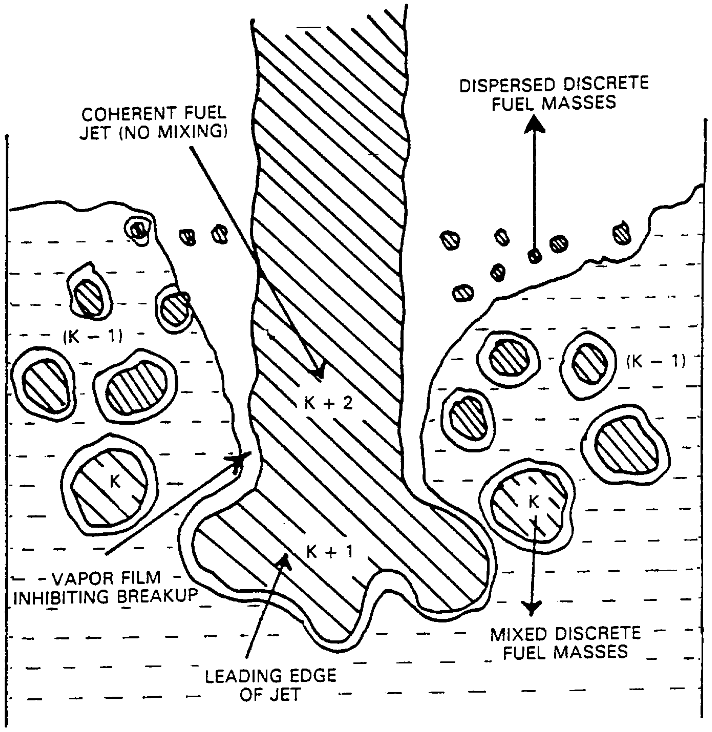
COHERENT FUEL JET (NO MIXING)
DISPERSED DISCRETE FUEL MASSES
(K − 1)
(K − 1)
K + 2
K
K
K + 1
VAPOR FILM INHIBITING BREAKUP
MIXED DISCRETE FUEL MASSES
LEADING EDGE OF JET

Figure 10-20. Schematic picture of molten fuel jet and water mixing model.[10-24]

$$\frac{dM_{KH}}{dt} = \lambda^2(n\lambda)\rho_p \tag{10-69}$$

where

$\frac{dM_{KH}}{dt}$ = mass transfer rate due to K-H instability (kg/s),

$n\lambda$ = the growth speed of the disturbance wave with amplitude λ,

n = the time constant for disturbance waves.

The total erosion rate for a jet surface area can be obtained by

$$\frac{dM_{KH}}{dt} = C_0A(n\lambda)_{max}\rho_p \tag{10-70}$$

where

C_0 = relates the cross-sectional area of the wavelet base (λ^2) to the effective jet surface area (A) and is taken to be 0.01,

$(n\lambda)_{max}$ = the wavelength having the maximum growth rate.

Terms n_{max} and λ_{max} are determined using the analysis given by Epstein and Fauske.[10-24] The largest wavelength of a disturbance, λ_{max}, is related to the minimum wave number, k_{min}, as $\lambda_{max} = 2\pi/k_{min}$. Two bounding conditions are used based on the condition of the continuous fluid surrounding the fuel jet. If the continuous fluid is mostly water (void fraction < 0.2), the condition of "thin film" is used. If the continuous fluid is a mixture of liquid and vapor (void fraction > 0.2), the condition of "thick film" is applied.

For a thin film case,

$$n_{max}^2 = 0.14814\rho_p \frac{\rho_p^{\ 2}\rho_l^3 U_{rel}^{\ 6}}{(\rho_p + \rho_l)^4(\sigma_p + \sigma_l)^2} \tag{10-71}$$

where

k_{min} = $2\rho_p\rho_l(U_l - U_p)^2 / 3(\rho_p + \rho_l)(\sigma_p + \sigma_l)$.

For a thick film case,

$$n_{max}^2 = \frac{0.14814\rho_p^{\ 3}\rho_s^{\ 3}U_{rel}^{\ 6}}{(\rho_p + \rho_s)^4\sigma_p^{\ 2}} \tag{10-72}$$

where

k_{min} = $2\rho_p\rho_s(U_s - U_p)^2 / 3(\rho_p + \rho_s)\sigma_p$,

ρ_l, ρ_s = densities of liquid (water) and gas (steam), respectively (kg/m^3),

σ_l = the surface tension of liquid (water) (N/m).

Initially, the eroded mass forms droplets with diameter equal to λ_{max} and can further breakup according to the R-T instability criteria shown in Equation (10-80).

Chu[10-32]developed the theoretical model for R-T instability. The model used in SCDAP/RELAP5-3D© was simplified as a linear correlation of the theoretical model. Thus, for droplets broken off from the jet, the diameter of the droplet at a new time step (n+1), is calculated as follows

$$D_p^{n+1} = D_p^n(1 - C_1\Delta t_b We^{0.25}) \tag{10-73}$$

where

D_p^{n+1}, D_p^n = fuel particle diameters at time n+1 and n, respectively;

C_1 = a constant determined empirically as

$$C_1 = 0.1093 - 0.0785\left(\frac{\rho_l}{\rho_p}\right)^{0.5}$$

Δt_b = a non-dimensional time step, defined as

$$\Delta t_b = U_{rel}\frac{(t^{n+1} - t^n)}{D_p^n}\left(\frac{\rho_l}{\rho_p}\right)^{0.5} \quad . \tag{10-74}$$

We and D_p^n are calculated at the current time.

A droplet is calculated to split during a time step when the following criterion is satisfied

$$D_P^{n+1} \le 2f_b r_p \tag{10-75}$$

$$f_b = \left(\frac{1}{N_p}\right)^{0.333}$$

where

r_p = radius of droplet before splitting (m),

f_b = factor whose value depends upon the number of droplets that a given droplets splits into,

N_p = 2,

f_b = 0.7937 for $N_p = 2$.

10.8.2 Heat Transfer

A rapid rate of heat transfer to the surrounding fluid may occur from drops of molten material dispersed by breakup of a jet of slumping molten material. This heat transfer may boil off a significant amount of water and change the conditions of the coolant where jet breakup is occurring. This section describes the models for calculating heat transfer from the drops to the coolant.

During breakup of fuel particles (prior to settling at the lower plenum bottom), the heat transfer between the fuel particles and a structure such as the lower head is neglected.

To calculate the heat transfer between the fragmented fuel droplets and the surrounding fluid, the droplets are modeled as mobile SCDAP heat structures. A mobile heat structure is defined for each unique collection of drops created by FCI. The motion of the droplets (and therefore the heat structures) is calculated using a Lagrangian framework.

The heat transfer between the droplets and the surrounding fluid is modeled by the correlations used by Chu[10-32] from the TEXAS code. The liquid droplets are surrounded by a blanket of vapor film which is surrounded by continuous liquid. In this case, the fuel droplet transfers heat mainly by convective film boiling and radiation to the surrounding liquid. The heat transfer rate from the fuel droplet to the surroundings can be defined as:

$$\dot{Q}_p = \dot{Q}_{film} + \dot{Q}_{rad} \tag{10-76}$$

where

$\dot{Q}_p$ = heat transfer from the fuel droplet to the surroundings (W),

$\dot{Q}_{film}$ = the convective (forced/free) film boiling heat transfer rate from the fuel particle to the vapor-liquid interface (between the vapor film and the continuous liquid) at the saturation temperature, $= \pi D_p^2 h_{film}(T_p - T_{sat})$ (W),

h_{film} = the convective film boiling heat transfer coefficient (to be defined)($W/m^2 \cdot K$),

$\dot{Q}_{rad}$ = the radiative heat transfer rate from the fuel droplet to the saturated vapor-liquid interface (of the vapor film) at saturation temperature, $= \pi D_p^2 h_{rad}(T_p - T_{sat})$,

h_{rad} = the radiative heat transfer coefficient (to be defined)($W/m^2 \cdot K$),

T_{sat} = saturation temperature of water (K).

The convective film boiling heat transfer coefficient, h_{film}, around a sphere is taken from the correlations developed by Dhir and Purohit.[10-34]

$$h_{film} = \text{Max}\ (h_{free}, h_{forced}) \tag{10-77}$$

where

h_{free} = natural convection film boiling heat transfer coefficient, $= h_{sat} + h_{nc}\dfrac{\Delta T_{sub}}{\Delta T_p}$ ($W/m^2 \cdot K$),

h_{forced} = forced convection film boiling heat transfer coefficient $= h_{sat} + 0.8Re^{0.5}\left[1 + \dfrac{\Delta T_{sub}}{\Delta T_p}\left(\dfrac{k_f}{k_g}\right)\right]\dfrac{k_g}{D_p}$ ($W/m^2 \cdot K$),

h_{sat} = free convection film boiling heat transfer coefficient for saturated liquid boiling averaged over a sphere, which is actually a modification[10-37] of the correlation given by Bromley et al.,[10-37] for horizontal cylinders (by changing the numerical multiplier from 0.62 to 0.8 and disregarding the radiation heat transfer) $= 0.8\left[g\rho_g k_g^3 h_{fg}\dfrac{(\rho_f - \rho_g)}{D_p \Delta T_p \mu_g}\right]^{0.25}$ ($W/m^2 \cdot K$),

h_{nc} = natural convection heat transfer coefficient averaged over a sphere (fuel drop) $= 0.9\left[g\rho_f^2 k_f^3 C_{pf}\beta\dfrac{\Delta T_{sub}}{(D_p \mu_f)}\right]^{0.25}$ ($W/m^2 \cdot K$),

h_{fg} = latent heat of evaporation (J/kg),

ΔT_{sub} = liquid subcooling = $(T_{sat} - T_f)$ (K),

ΔT_p = superheat of the fuel drop $(T_p - T_{sat})$ (K),

ρ_f = density of liquid phase of water (kg/m^3),

ρ_g = density of vapor phase of water (kg/m^3),

k_g = thermal conductivity of the vapor ($W/m^2 \cdot K$),

k_f = thermal conductivity of liquid ($W/m^2 \cdot K$), Re = Reynolds number based on the relative velocity between the fuel drop and surrounding liquid and fuel drop diameter as the characteristic length, $(\rho_f D_p U_{rel}/\mu_f)$,

μ_f = dynamic viscosity of the liquid $\left(\frac{kg}{m \cdot s}\right)$,

β = volumetric coefficient of the thermal expansion of liquid (1/K),

D_p = diameter of fuel drop (m),

U_{rel} = velocity of drop relative to its surrounding fluid (m/s).

h_{rad} is defined as radiation heat transfer between two concentric gray surfaces as follows:

$$h_{rad} = \sigma F_{pi} \frac{\left(T_p^4 - T_{sat}^4\right)}{\Delta T_{sat}} \tag{10-78}$$

where

σ = Stefan Boltzmann constant, 5.668 x 10^{-8} W/($m^2 \cdot K^4$),

F_{pi} = emissivity factor between the fuel drop and the vapor-liquid interface.

The emissivity factor in the above equation is calculated by the equation

$$F_{pi} = 1/[1. + (1-\varepsilon_p)/\varepsilon_p + (1-\varepsilon_f)/\varepsilon_f] \tag{10-79}$$

where

$\varepsilon_p, \varepsilon_f$ = emissivities of the fuel particle and liquid, respectively.

The temperature of the dispersed drops of material are calculated by two methods. The first method is used when the material is at a temperature that is greater than its solidus temperature. In this temperature regime, the heat transfer and changes in internal energy of the material are rapid. A simple method is used that ensures an energy balance is maintained as the change from liquid phase to solid phase occurs in the material. The second method is used when the dispersed droplets of material are at a temperature less than their solidus temperature. This method solves the equation for the transient temperature of a small particle with a uniform temperature.

In the first method, used for $T_P^n > T_S$ the temperature of drops of material are calculated by the equations,

$$h_{tot} = h_{film} + h_{rad}, \tag{10-80}$$

$$\Delta t = t^{n+1} - t^n, \tag{10-81}$$

$$\begin{aligned} u_p(t^{n+1}) &= u_p(t) - \left[h_{tot}(T_P^n - T_{sat}\right)4\pi r_p^2 / 1.333\pi r_p^3\rho_p + q_d(t^{n+1} - t^n)/\rho_p\Big](t^{n+1} - t^n) \\ &= u_p(t^n) - \left[h_{tot}(T_P^n - T_{sat}\right)4\pi r_p^2 + 1.333 q_d \pi r_p^3\Big]\Delta t / \left(1.333\pi r_p^3\rho_p\right), \\ T_P^{n+1} &= f\left(u_p(t^{n+1})\right). \end{aligned} \tag{10-82}$$

where

h_{tot} = total heat transfer coefficient ($W/m^2 \cdot K$),

$u_p(t^{n+1})$ = internal energy of particle at time t^{n+1}(J/kg),

Δt = time step (m),

t^n = time at end of n-th time step (s),

h_{film} = convective film boiling heat transfer coefficient ($W/m^2 \cdot K$),

h_{rad} = radiation heat transfer coefficient ($W/m^2 \cdot K$),

T_P^n = temperature of fuel drop at n-th time step (K),

T_{sat} = saturation temperature of water (K),

r_p = radius of drop (m),

ρ_p = density of drop (kg/m^3),

f(u) = temperature of material as function of its internal energy (K),

T_s = solidus temperature of material (K),

q_d = internal heat generation rate in drop (W/m^3).

The function f(u) is evaluated by the SCDAP subroutine named mixdlt.

In the second method, used for $T_P^n < T_s$, the temperature of the droplets of material are calculated by solving the heat balance equation;

$$1.333\pi r_p^3\, \rho_p c_p \frac{dT_p}{dt} = 1.333\pi r_p^3\, q_d - 4\pi r_p^2\, h_{tot}(T_p - T_{sat}). \tag{10-83}$$

To facilitate integration of the above differential equation, the terms are arranged to be

$$\left(\frac{dT_p}{dt}\right) + \frac{3h_{tot}T_p}{\rho_p c_p r_p} = \frac{q_d}{\rho_p c_p} + \frac{3h_{tot}T_{sat}}{\rho_p c_p r_p}. \tag{10-84}$$

The initial condition to the above equation is

$$T_p = T_p^n \text{ at } t = t_n . \tag{10-85}$$

The solution to the above equation is

$$T_p^{n+1} = A + \left\{T_p^n - A\right\}e^{-B\Delta t} \tag{10-86}$$

$$A = \frac{\dfrac{q_d}{\rho_p c_p} + \dfrac{3h_{tot}T_{sat}}{\rho_p c_p r_p}}{\dfrac{3h_{tot}}{\rho_p c_p r_p}} , \tag{10-87}$$

$$B = \frac{3h_{tot}}{\rho_p c_p r_p} . \tag{10-88}$$

10.8.3 Motion and Settling of Dispersed Drops

The momentum change of the dispersed drops is calculated taking into account the acceleration of gravity and the drag exerted on the drops due to contact with fluid. The rate of change of velocity of a drop is calculated by the equation

$$\frac{dV_p}{dT} = g - \frac{f_d}{1.333\pi r_p^3 \rho_p} \tag{10-89}$$

where

V_p = velocity of drop (m/s),

g = acceleration of gravity (m/s^2),

f_d = drag force (N).

The drag force is the sum of the drag force due to contact with the liquid phase of water and the drag force due to contact with the vapor phase of water. The drag force due to contact with the liquid phase of water is calculated by the equation

$$f_{df} = 0.5\pi\alpha_f r_p^2 \rho_L (V_L - V_p)^2 f_{cf} \tag{10-90}$$

where

f_{df} = drag force due to contact with liquid phase of water (N),

α_f = volume fraction of liquid phase of water at location of drop,

V_p = velocity of drop (m/s),

V_L = velocity of liquid phase of water (m/s),

f_{cf} = friction factor for contact with liquid phase.

The drag force due to contact with the vapor phase of water is calculated by the equation

$$f_{dg} = 0.5\pi(a - \alpha_f)r_p^2\rho_g(V_g - V_p)^2 f_{cg}$$

where

f_{dg} = drag force due to contact with vapor phase of water (N),

V_g = velocity of vapor phase of water(m/s),

f_{cg} = friction factor for contact with vapor phase.

The total drag force is calculated by the equation

$$f_d = f_{df} + f_{dg}\,. \tag{10-91}$$

The friction factors in the equations for drag force are calculated as a function of the Reynolds numbers for the liquid and vapor phases. The Reynolds number for the liquid phase is calculated by the equation

$$Re_f = 2r_p(V_L - V_p)(\rho_L/\mu_L) \tag{10-92}$$

where

Re_f = Reynolds number for liquid phase,

μ_L = dynamic viscosity of liquid phase $(kg/m \cdot s)$.

The Reynolds number for the vapor phase is calculated by the equation

$$Re_g = 2r_p(V_g - V_p)\rho_g/\mu_g$$

where

Re_g = Reynolds number for vapor phase,

μ_g = dynamic velocity for vapor phase $(kg/m \cdot s)$.

The correlation used to calculate the friction factor is a function of the Reynolds number.[10-36] The correlations used for a range of Reynolds numbers are shown is Table 10-1. In this table, f_c is the friction factor for either the liquid or vapor phases, depending upon whether the Reynolds number is for the liquid or vapor phases.

The momentum change of the drops due to contact with the liquid and vapor phases of water is assumed to be small compared to the momentum of the water. Thus, the momentum change of the water due to contact with the drops is not calculated.

Table 10-1. Correlations used to calculate friction factor.

Correlation	Range of Reynolds number
$f_c = 24/Re$	Re ≤ 1
$f_c = (24/Re)[1 + 0.102Re^{0.955}]$	1 < Re ≤ 2
$f_c = (24/Re)[1 + 0.115Re^{0.802}]$	2 < Re < 21
$f_c = (24/Re)[1 + 0.189Re^{0.632}]$	2 < Re < 200
$f_c = 0.28 + 6/Re^{0.5} + 21/Re$	200 < Re < 4000

The change in elevation of a drop is calculated by the equation

$$z_p^{n+1} = z^n - 0.5\left(V_p^n + V_p^{n+1}\right)\Delta t \tag{10-93}$$

where

z_p^{n+1} = elevation of drop at time t^{n+1} (m),

V_p^{n+1} = velocity of drop at time t^{n+1} (m/s),

Δt = time step (s).

When the elevation of a drop has decreased to where it is equal to the elevation of the surface of a structure underneath the drop, then the drop has settled and its velocity is set equal to zero.

10.9 References

10-1. E. L. Tolman et al., *TMI-2 Accident Scenario Update,* EGG-TMI-7489, December 1986.

10-2. M. L. Russell, “TMI-2 Core Geometry,” *Proceedings of the TMI-2 Topical Meeting, Washington, D.C., November 1988.*

10-3. S. Hagen et al., “Out-of-Pile Experiments on Severe Fuel Damage Behavior of LWR Fuel Elements (CORA Program),” IAEA-SM-296/26**,** *International Symposium on Severe Accidents in Nuclear Power Plants, Sorrento, Italy, March 21-25, 1988.*

10-4. D. A. Petti et al, *PBF Severe Fuel Damage Test 1-4 Test Results Report,* NUREG/CR-5163, EGG-2542, December, 1986.

10-5. Z. R. Martinson et al., *PBF Severe Fuel Damage Test 1-1 Test Results Report,* NUREG/CR-4684, EGG-2463, October 1986.

10-6. A. B. Wahba and E. F. Hicken, "Ten Years of Experimenting in the Loss of Fluid Test (LOFT) Facility," *Atomkernenergie-kerntechnik, 49,*No. 1/2, 1986, pp. 68-73.

10-7. R. O. Gauntt et al., *The DF-4 BWR Control Blade/Channel Box Fuel Damage Experiment,* NUREG/CR-4671, SAND86-1443 (draft), March 1988.

10-8. D. O. Lanning and N. J. Lombardo, *Data Report for Full Length High Temperature Experiments,* PNL-6540, April 1988.

10-9. F. M. Haggag, *Zircaloy Cladding Embrittlement Criteria: Comparison of In-Pile and Out-of-Pile Results,* NUREG/CR-2757, July 1982.

10-10. F. M. Haggag, *Fuel Bundle Damage Propagation Models for SCDAP,* EGG-NSMD-5738, June 1983.

10-11. H. M. Chung and T. F. Kassner, *Embrittlement Criteria for Zircaloy Fuel Cladding Applicable to Accident Situations in Light Water Reactors,* NUREG/CR-1344, ANL-79-48, January 1980.

10-12. R. L. Orr, O. D. Sherby, and J. E. Dorn "Correlation of Rupture Data for Metals at Elevated Temperatures," *Transactions of the ASME, 46,* 1954, p. 113.

10-13. R. R. Hobbins et al., "PBF Severe Fuel Damage Test 1-4 Melt Progression Scenario," *Severe Accident Research Program Partner's Review Meeting, Sandia National Laboratory, Albuquerque, NM, April 25-30, 1988.*

10-14. C. M. Allison, J. L. Rempe, and S. A. Chavez, "Final Design Report on SCDAP/RELAP5 Model Improvements - Debris Bed and Molten Pool Behavior," INEL-96/0487, December 1996.

10-15. *ABAQUS User's Manual,* Version 4.6, Providence, RI: Hibbit, Karlsson and Sorensen, Inc., 1987.

10-16. S. Bourdon et al., "FPT0 Pre-test Calculations: SCDAP/RELAP5 Sensitivity Studies and COUPLE Calculations," *Note Technique SEMAR 93/55, IPSN-DRS/SEMAR/LPA/93-332, Institut De Protection et de Surete Nucleaire,* CADARACHE, 1993.Michael Epstein et al., "Transient Freezing of a Flowing Ceramic Fuel in a Steel Channel," *Nuclear Science and Engineering, 61,* 1976, pp. 310-323.

10-17. Michael Epstein et al., "Transient Freezing of a Flowing Ceramic Fuel in a Steel Channel," *Nuclear Science and Engineering, 61,* 1976, pp. 310-323.

10-18. P. Hofmann and H. Ostereka, "Dissolution of Solid UO_2 by Molten Zircaloy and the Modeling," Paper IAEA-SM-296/1, *International Symposium on Severe Accidents in Nuclear Power Plants, Sorrento, Italy, March 21-25, 1988.*

10-19. T. Heames et al., *VICTORIA: A Mechanistic Model of Radionuclide Behavior in the Reactor Coolant System Under Sever Accident Conditions*, NUREG/CR-5545, SAND90-0756, Rev. 1, December 1992.M. L. Corradini, B. J. Kim, and M. D. Oh, "Vapor Explosions in Light Water Reactors: A Review of Theory and Modeling," *Progress in Nuclear Energy, 22,* 1, 1988, pp. 1-117.

10-20. M. L. Corradini, "Vapor Explosions: A Review of Experiments for Accident Analysis," *Nuclear Safety, 32,* 3, 1991, pp. 337-362.

10-21. T. Ginsburg, "Liquid Jet Breakup Characterization with Application to Melt-Water Mixing," *Proceedings of the International ANS/ENS Topical Meeting on Thermal reactor Safety, San Diego, California, February 2-6, 1986, pp. 11.4-1-11.4-18.*

10-22. M. Burger, S. H. Cho, E. V. Berg, and A. Schatz, "Breakup of Melt Jets as Pre-Condition for Premixing: Modeling and Experimental Verification," *Nuclear Engineering and Design,* 155, 1995, pp. 215-251.

10-23. T. G. Theofanous and M. Saito, "An Assessment of Class-9 (Core-Melt) Accidents for PWR Dry-Containment Systems," *Nuclear Engineering and Design, 66,* 1982, p. 307.

10-24. M. Epstein and H. K. Fauske, "Steam Film Instability and the Mixing of Core-Melt Jets and Water," *ANS Thermal Hydraulic Division Proceedings, ASME/AIChE National Heat Transfer Conference, Denver, CO, August 1985.*

10-25. S. Chandrasekhar, *Hydrodynamic and Hydromagnetic Stability,* Oxford: Clarendon Press, 1961, Chapters 10 and 11.

10-26. C. C. Chu, J. J. Sienicki, B. W. Spencer, W. Frid, and G. Lwenhielm, "Ex-Vessel Melt-Coolant Interaction in Deep Water Pool: Studies and Accident Management for Swedish BWRs," *Nuclear Engineering and Design, 155,* 1995, pp. 155-213.

10-27. M. L. Corradini, M. El-Beshbeeshy, S. Nilsuwankowsit, and J. Tang, "Fuel Fragmentation Model Advances Using TEXAS-V," To be published.

10-28. D. Magallon and H. Hohmann, "High Pressure Corium Melt Quenching Tests in FARO," Nuclear Engineering and Design, 155, 1995, pp. 253-270.

10-29. H. Hohmann, D. Magallon, H. Schins, and A. Yerkess, "FCI Experiments in the Aluminum Oxide/Water System," *Nuclear Engineering and Design, 155,* 1995, pp. 391-403.

10-30. D. Magallon and H. Hohmann, "Experimental Investigation of 150-kg scale Corium Melt Jet Quenching in Water," *Proceedings of the 7th International Meeting on Nuclear Reactor Thermal-Hydraulics (NURETH-7), Saratoga Springs, NY, September 10-15, 1995,* NUREG/CP-0142, pp. 1688-1711.

10-31. I. Huhtiniemi, H. Hohmann, and D. Magallon, "FCI Experiments in the Corium/Water System," *Proceedings of the 7th International Meeting on Nuclear Reactor Thermal-Hydraulics (NURETH-7), Saratoga Springs, NY, September 10-15, 1995,* NUREG/CP-0142, pp. 1712-1727.

10-32. C. C. Chu, "One Dimensional Transient Fluid Model for Fuel-Coolant Interaction Analysis," Ph. D. Thesis, University of Wisconsin, Madison, WI, 1986.

10-33. C. C. Chu and M. L. Corradini, "One-Dimensional Transient Fluid Model for Fuel/Coolant Interaction Analysis," *Nuclear Engineering and Design, 101,* 1989, pp. 48-71.

10-34. V. K. Dhir and G. P. Purohit, "Subcooled Film-Boiling Heat Transfer from Spheres," *Nuclear Engineering and Design, 47,* 1978, pp. 49-66.

10-35. L. R. Bromley, N. R. LeRoy, and J. A. Robbers, "Heat Transfer in Forced Convection Film Boiling," *Industrial and Engineering Chemistry, 45,* 1953, pp. 2,639 - 2,646.

10-36. K. V. Beard and H. R. Pruppacher, "Determination of the Terminal Velocity and Drag of Small Water Drops by Means of a Wind Tunnel," *J. Atmos. Sci.*, 26, 1066 (1969).

10-37. L. J. Siefken and M. S. Sohal, "Design Report on Model Development for Molten Fuel-Coolant Interaction During Melt Slumping," INEEL/EXT-92-00084, Rev. 1, March 1998.

11. MODELS FOR SMOOTHING TRANSITIONS IN CONFIGURATION OF FUEL RODS

This section describes models that are used to smooth the transition in configuration of fuel rods subjected to severe accident conditions. As a severe accident continues in time, damage increases and the fuel rod configuration may change from the configuration of an array of vertically oriented cylinders to a molten pool. Several intermediate configurations may also occur. One intermediate configuration is an array of fuel rods with drops of relocated material over a relatively small span of elevation. This configuration occurs in fuel rods that experience melting and slumping of the cladding. Another intermediate configuration is that a bed of porous debris. This configuration occurs when embrittled fuel rods are quenched. The configuration of an array of fuel rods during the various stages of damage progression that occur during a severe accident are shown in Figure 11-1. Results from fuel rod experiments using severe accident conditions indicate that a change from one of these configurations to another occurs gradually over a period of time. The purpose of transition smoothing models in SCDAP/RELAP5-3D© is to calculate these gradual changes in configuration and the effect of these changes on oxidation and thermal-hydraulic parameters.

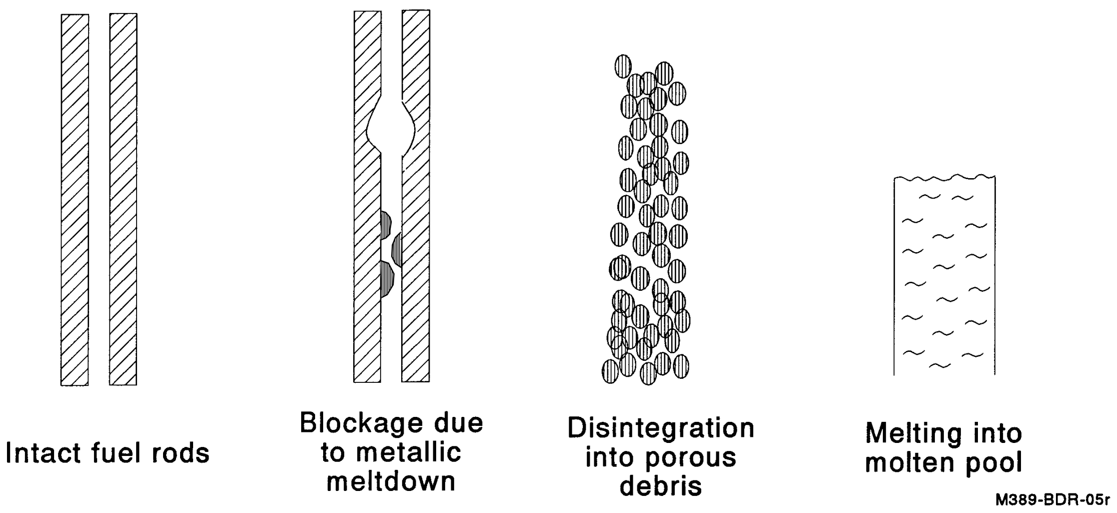
Intact fuel rods
Blockage due to metallic meltdown
Disintegration into porous debris
Melting into molten pool
M389-BDR-05r

Figure 11-1. Configuration of array of fuel rods during various stages of damage progression.

The transition smoothing models are applied to two damage progression scenarios: (1) configuration change due to meltdown of the fuel rod cladding, and (2) configuration change due to melting of the fuel. The transition smoothing models in these two areas are described in Section 11.1 and Section 11.2, respectively.

11.1 Configuration Change Due to Metallic Meltdown

Transition smoothing models are applied to calculate and account for the gradual change in configuration that occurs as liquefied cladding with dissolved fuel breaks out of the cladding oxide shell containing it slumps downward and freezes in a lower and cooler region. The meltdown modeled with and without the transition smoothing models is shown in Figure 11-2. Without the transition smoothing models, all the liquefied cladding at an axial node is calculated to slump together and freeze together. This modeling results in a more abrupt change in configuration than observed in experiments such as the CORA-13 test.[11-1] With the transition smoothing model, a drop by drop slumping of the cladding is calculated which is more representative of the meltdown observed in experiments. The drops of the frozen cladding cause a blockage that increases in size as more and more drops freeze in the same neighborhood. The transition smoothing models also increase the flow resistance and decrease the flow area as more and more drops freeze in the neighborhood.

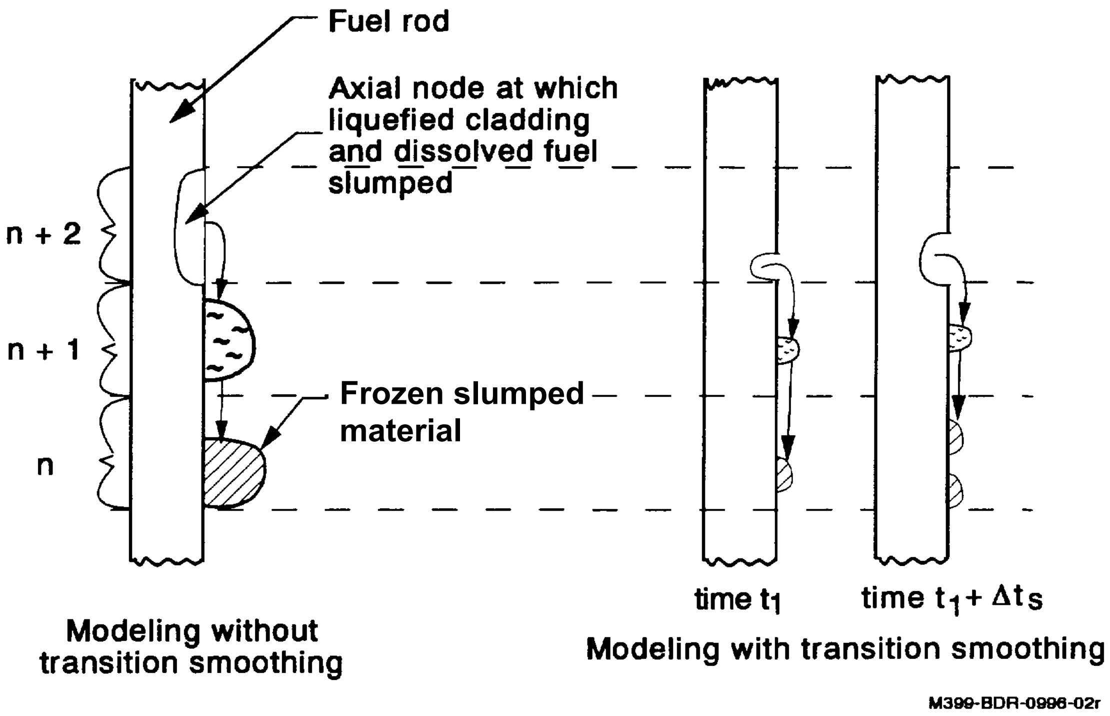
Fuel rod
Axial node at which liquefied cladding and dissolved fuel slumped
n + 2
n + 1
n
Frozen slumped material
time t1
time t1 + Δts
Modeling without transition smoothing
Modeling with transition smoothing
M399-BDR-0996-02r

Figure 11-2. Modeling of cladding meltdown with and without transition smoothing models.

An empirical equation is used to calculate the period of time between the slumping of each drop of cladding from an axial node. The equation is

$$\Delta t_s = 1.0 \tag{11-1}$$

where

Δt_s = time between slumping of drops (s)

Using the above equation, the slumping of an axial node is typically spread over approximately 20 s. About twenty drops result from the complete slumping of an axial node.

The collection of frozen drops at an axial node have common values determined by mass weighted averaging. The variables describing the collection of frozen drops are: (1) number of frozen drops, (2) weight gain of frozen drops (kg O_2/m^2), (3) mass of UO_2 in drops (kg), and (4) mass of Zr in drops (kg). These variables are updated whenever another drop freezes in the axial node. The updated values are calculated by the equations

$$n_{d2} = n_{d1} + 1 \tag{11-2}$$

$$W_{d2} = \frac{n_{d1} W_{d1} + W_{dnew}}{n_{d2}} \tag{11-3}$$

$$W_{f2} = \frac{n_{d1} W_{f1} + W_{fnew}}{n_{d2}} \tag{11-4}$$

$$W_{z2} = \frac{n_{d1} W_{z1} + W_{znew}}{n_{d2}} \tag{11-5}$$

where

n_{d1}, n_{d2} = number of collective frozen drops at axial node at start and end of time step, respectively, for time step in which a drop solidifies in node,

W_{d1}, W_{d2} = weight gain of collective frozen drops at start and end of time step, respectively (kg O^2/ m^2),

W_{dnew} = weight gain of drop that froze in axial node during time step (kg O^2/m^2),

W_{f1}, W_{f2} = mass of UO_2 in collective frozen drops at start and end of time step, respectively (kg),

W_{fnew} = mass of UO_2 in drop that froze in axial node during time step (kg),

W_{znew} = mass of Zr in drop that froze in axial node during time step (kg),

W_{z1}, W_{z2} = mass of Zr in collective frozen drops at start and end of time step, respectively (kg).

A collection of frozen drops may cause a significant blockage to coolant flow. Three stages of blockage are shown in Figure 11-3. The loss coefficients and flow area applied by the RELAP5 code for a location with frozen drops are adjusted to account for the blockage caused by the frozen drops. The loss coefficients are calculated by the equation

$$K_l = K_{lo} + (K_{lb} - K_{lo}) f_l^y \tag{11-6}$$

where

f_l = measure of extent of blockage,

K_l = loss coefficient at axial node with blockage,

K_{lo} = loss coefficient before blockage,

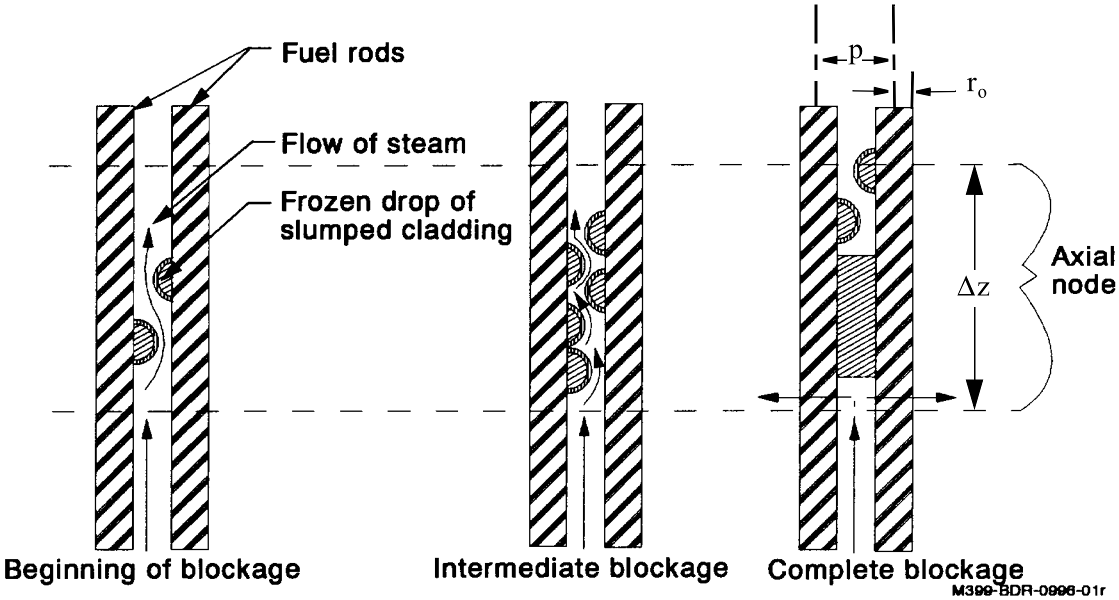
Fuel rods
Flow of steam
Frozen drop of slumped cladding
p
r_o
Δz
Axial node
Beginning of blockage
Intermediate blockage
Complete blockage
M399-BDR-0996-01r

Figure 11-3. Stages of blockage caused by cladding meltdown.

K_{lb} = loss coefficient just before complete blockage (estimated value of 500),

y = exponent with estimated value of 3.

The extent of blockage is measured by the variable f_l. This variable is calculated by the equation

$$f_l = v_d/(p^2 - \pi r_o^2)\Delta z \tag{11-7}$$

where

v_d = volume of drops of relocated material in an axial node (m^3),

p = pitch of fuel rods (m),

r_o = outer radius of fuel rods at an axial node (m),

Δz = height of an axial node (m).

The forward and reverse loss coefficients at both ends of a RELAP5 control volume are adjusted to account for a blockage in that control volume.

The change in flow area caused by the presence of relocated material is calculated by the equation

$$A = A_o(1 - 0.9\, f_l) \qquad (f_l > C_u) \tag{11-8}$$

$A = 0 \qquad (f_l > C_u)$

where

A_o = $p^2 - \pi r_o^2 \quad (m^2)$,

A = flow area accounting for blockage (m^2),

C_u = coefficient estimated to have value of 0.95.

When $f_l > C_u$, the flow area is zero and complete blockage occurs with respect to axial flow.

The change in surface area for convective cooling caused by the presence of relocated material is also calculated as a function of the amount of relocated material. The surface area is calculated by the equation.

$$A_s = 2\pi r_o \Delta z(1 - f_l^{0.5}) \tag{11-9}$$

where

A_s = surface area of fuel rod in contact with coolant (m^2).

11.2 Configuration Change Due to Ceramic Meltdown

The onset of melting of the fuel pellets in an array of fuel rods marks the beginning of a large change in the configuration of the array of rods. As heatup continues and more and more fuel melts, the fuel rods will gradually change in configuration from an array of vertical cylinders to a molten pool. Figure 11-4 shows the progression of configuration changes of an array of fuel rods from the onset of fuel melting to the formation of a molten pool. In the intermediate stage of melting, the fuel rods are severely distorted and their configuration approaches that of debris.

The blockage due to configuration changes caused by melting of the fuel pellets are represented by an increase in the loss coefficients and a decrease in the flow area for a RELAP5 control volume where fuel melting is occurring. The loss coefficients are calculated by the equation

$$K_l = K_{lo} + (K_{lb} - K_{lo})f_m^x \tag{11-10}$$

where

f_m = measure of extent of ceramic melting,

x = exponent with estimated value of 0.5.

The governing variable in the above equation is f_m, which is a measure of the extent of melting of the fuel. The melting takes place over a temperature range due to the eutectic reaction between the fuel and the

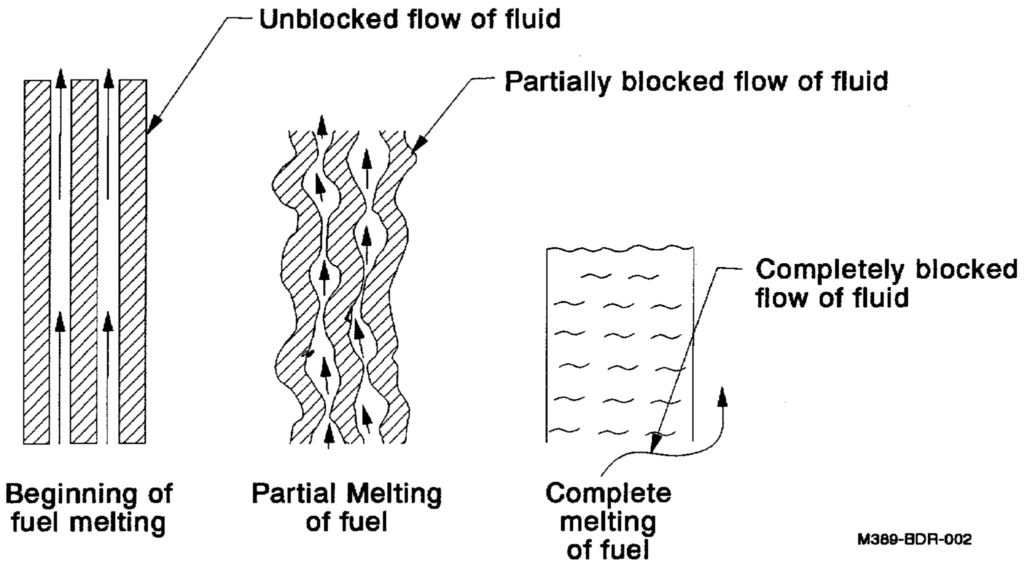
Unblocked flow of fluid
Partially blocked flow of fluid
Completely blocked flow of fluid
Beginning of fuel melting
Partial Melting of fuel
Complete melting of fuel
M389-BDR-002

Figure 11-4. Changes in fuel rod configuration caused by fuel melting.

cladding. Thus, the extent of fuel melting can be represented by the average temperature of the fuel relative to the solidus and liquidus temperatures of this eutectic reaction. This variable is calculated by the equation

$$f_m = \left(\frac{T_f - T_s}{T_L - T_s}\right) \tag{11-11}$$

where

T_f = average temperature of fuel pellet (K),

T_s = solidus temperature of fuel (K),

T_L = liquidus temperature of fuel (K).

The change in flow area with respect to the extent of fuel melting is calculated by the equation

$$A = A_o(1 - c_l f_m^z) \qquad (0 < f_m < 1.) \tag{11-12}$$

$$= 0.0 \qquad (f_m \geq 1.)$$

where

c_l = coefficient with estimated value of 0.5,

z = exponent with estimated of 0.5.

11.3 Reference

11-1. S. Hagen et al., *Results of SFD Experiment CORA-13 (OECD International Standard Problem 31),* KfK 5054, February 1993.

12. CREEP RUPTURE OF STRUCTURAL COMPONENTS

12.1 Description of Models for Creep Rupture

A model based on creep rupture theory is used to calculate the damage and nearness to rupture of structural components selected by the code user. Two different theories are applied: (1) Larson-Miller,[12-1] and (2) Manson-Haferd.[12-2] The particular theory to be applied is dependent on the material composition and stress. The materials that can be modeled for creep rupture are (a) A-508 Class 2 carbon steel, (b) 316 stainless steel, and (c) Inconel 600. For 316 stainless steel and Inconel 600 materials, the Larson-Miller theory is used. For A-508 Class 2 carbon steel, the Manson-Haferd theory is applied for the lower range of stress and the Larson-Miller theory for the higher range of stress.

Criteria for choosing the theory best suited for a particular material and temperature range are presented by Goldhoff.[12-3] His criteria determine the applicable theory by examining the results of creep rupture tests performed on specimens at a constant stress and temperature. After tests have been performed with a range of stresses and temperatures, the data are plotted to produce a family of curves of the log of rupture versus temperature and the log of rupture time versus reciprocal temperature. The Larson-Miller theory[12-1] gives the best prediction when the family of curves on a plot of log of rupture time versus reciprocal of test temperature meet at a point with a value of 1/T = 0, where T = temperature in degrees R. The Dorn[12-4] theory is used when the family of curves are parallel. The Manson-Haferd theory[12-2] is used when the family of curves on a plot of rupture time versus temperature meet at a point.

A parameter that measures creep damage is calculated at each time step for each structure being monitored for creep rupture. The creep damage is evaluated by the equation

$$D_c(t + \Delta t) = D_c(t) + \frac{\Delta t}{t_r(t)} \tag{12-1}$$

where

$D_c(t)$ = creep damage at time t,

Δt = time step at current problem time (s),

$t_r(t)$ = time required for the structure to fail by creep rupture at the current state of temperature and stress (s),

t = problem time (s).

If the value of D_c is zero, the structure has not experienced any creep damage. If the value is one, the structure has failed due to creep damage.

The equation for calculating t_r is dependent on the material composition and stress. The equations for three materials considered by SCDAP/RELAP5-3D© are shown in Table 12-1. The Manson-Haferd theory is applied to A-508 carbon steel for effective stresses less than 14 ksi (96.6 MPa). The Larson-Miller theory is applied to this material for effective stresses greater than 14 ksi (96.6 MPa) and to 316 stainless steel and Inconel 600 at all levels of stress. The temperature term in the equations shown in Table 12-1 is the average temperature through the thickness of the wall. For the lower head of a reactor vessel, the stress term in the equations in Table 12-1 is calculated by the equation

$$\sigma = (P_i r_i^2 - P_o r_o^2)/(r_o - r_i)(r_o - r_i) + 0.5(P_i - P_o) \tag{13}$$

where

σ = stress in creep rupture equations (converted from Pa to ksi),

P_i = internal pressure on structure (Pa),

P_o = external pressure on structure (Pa),

r_i = inner radius of structure (m),

r_o = outer radius of structure (m).

For cylindrical shaped structures, the stress term in Table 12-1 is calculated by the equation

$$\sigma = (P_i r_i - P_o r_o)/(r_o - r_i) \quad . \tag{14}$$

Tests were performed at the INEEL to obtain creep rupture data on A-508 Class 2 carbon steel.[12-5] Data were obtained in the temperature range of 900 to 1,025 K and in the stress range of 56 to 141 MPa. The creep rupture data for 316 stainless steel were obtained from Reference 12-3. Data were available in the temperature range of 700 to 1,089 K. The creep rupture data for Inconel 600 were obtained from Reference 12-3 and were available in the temperature range of 811 to 1,366 K.

Table 12-1. Equations for calculating the time to creep rupture.

Material	Range of stress	Equation for creep rupture time[1]
Carbon steel A-508	$0.0 < \sigma < 14.0$	$t_r = 10^{\left[\frac{T - 1503.69}{P} + 3.499\right]}$ $P = 158.233 \log(\sigma) - 255.346$
	$14.0 \geq \sigma$	$t_r = 10^{\left[\frac{P}{T} - 20\right]}$ $P = 9603.0 \log(\sigma) + 46454.0$

Table 12-1. Equations for calculating the time to creep rupture. (Continued)

Material	Range of stress	Equation for creep rupture time[1]
316 stainless steel	$0.0 < \sigma < 52.0$	$t_r = 10^{\left[\frac{P}{T} - 20\right]}$ $P = -13320.0 \log(\sigma) + 54870.0$
	$52.0 \geq \sigma$	$t_r = 10^{\left[\frac{P}{T} - 20\right]}$ $P = -64000.0 \log(\sigma) + 142000.0$
Inconel 600	$0.0 < \sigma$	$t_r = 10^{\left[\frac{P}{T} - 15\right]}$ $P = -11333.0 \log(\sigma) + 43333.0$

---

[1] t_r = time to rupture (h), T = average temperature of structure (R), σ = stress in structure (ksi).

12.2 References

12-1. F. R. Larson and J. Miller, “A Time Temperature Relationship for Rupture and Creep Stress,” *Transactions of the ASME,* July 1952, pp. 765-775.

12-2. S. S. Manson and A. M. Haferd, “A Linear Time Temperature Relation for Extrapolation of Creep and Stress Rupture Data,” *NACA TN, 2890,* March 1953.

12-3. R. M. Goldhoff, “A Comparison of Parameter Methods for Extrapolating High Temperature Data,” *ASME Journal of Basic Engineering,* 1959, pp. 629-643.

12-4. R. L. Orr, O. D. Sherby, and J. E. Dorn “Correlation of Rupture Data for Metals at Elevated Temperatures,” *Transactions of the ASME, 46,* 1954, p. 113.

12-5. B. L. Harris, V. N. Shah, and G. E. Korth, *Creep Rupture Failure of Three Components of the Reactor Primary Coolant System During the TMLB’ Accident,* EGG-EA-7431, November 1986.

13. ANALYSIS OF HIGH TEMPERATURE GAS REACTORS

13.1 Introduction

Leading reactor designs for the future production of nuclear energy and process heat for hydrogen production are the Pebble-Bed High Temperature Gas Reactor (PB-HTGR)[13-6,13-7,13-8] and the Block-Type High Temperature Gas Reactor (BT-HTGR).[13-7,13-8,13-9,13-10] These reactors can have a direct Brayton thermodynamic cycle for very efficient conversion of nuclear power into electricity and exhibit relatively benign behavior under various accident conditions. The PB-HTGRs and BT-HTGRs use helium as the primary coolant and graphite as the material for moderating neutrons. The PB-HTGR reactor core is configured as a deep bed of spherical pebbles the size of billiard balls (diameter of approximately 60 mm). Each pebble has an exterior layer of graphite surrounding an inner graphite matrix with about 15,000 embedded small fuel particles (diameter of about 0.5 mm). The BT-HTGR reactor core is configured as blocks of graphite containing fuel compacts (fuel rods) and coolant channels. The fuel compacts are composed of graphite with fuel particles. For both the PB-HTGR and BT-HTGR, the fuel particles have a ceramic coating that retains fission products even during temperature escalations caused by a reactor accident. The capability of the ceramic coating to retain fission products may be sufficient to preclude the requirement for a sealed containment and to preclude development of guidelines for the evacuation of the public in the event of a reactor accident.[13-11] The fuel in these reactors can sustain a high level of burnup and thus promotes a reduction in radioactive waste. Also, the helium coolant does not become radioactive with irradiation and thus contributes further to a reduction in radioactive waste. After burnup, the fuel particles can be placed without processing in a wet or dry repository and remain resistant to corrosion for hundreds of thousands of years.[13-12,13-13] The great difficulty in breaking down the coatings on spent fuel particles promotes proliferation resistance.[13-13] The reactors can be built as small as 100 MWe and thus can be built with a relatively small capital investment. The high thermal efficiency of the reactors also reduces cost and waste.

This report describes models implemented into SCDAP/RELAP5-3D© for equipping the code to calculate the transient behavior of PB-HTGRs and BT-HTGRs. The USNRC sponsored a predecessor of the SCDAP/RELAP5-3D© code for best-estimate, detailed calculations of the transient behavior of Generation II and III reactors,[13-14] and models for phenomena unique to other reactor types are straightforwardly integrated into its proven capabilities for calculating the transient behavior of complex nuclear reactor systems.[13-15,13-16,13-17,13-18,13-19] In particular, the code's capability to model all aspects of the behavior of a broad range of fluids and to calculate the changes in the reactivity of the reactor core due to changes in reactor conditions are applicable to any type of reactor design. Any number of fluid volumes, fuel structures, pipe structures, vessel structures, and turbines can be connected together so as to represent any reactor system or experimental facility. While the code has the proven capability to calculate the transient behavior of Generation II and III light water reactors (LWRs), the code requires new models to address the unique fuel materials and configurations in PB-HTGRs and BT-HTGRs.

In the event of an accident in a PB-HTGR or BT-HTGR, major safety objectives include (1) maintaining the reactor core at a temperature below the temperature at which the fission product retention capability of coated fuel particles begins to degrade, and (2) ensuring the integrity of the outer protective graphite layer of the fuel pebbles for PB-HTGRs and ensuring the integrity of the graphite blocks for BT-HTGRs. If the integrity of the fuel pebbles in the PB-HTGR and the graphite blocks in the BT-HTGR is not degraded by oxidation (graphite burn off), then the coatings of the fuel particles in the fuel pebbles and fuel compacts cannot oxidize and lose the capability to retain fission products. An accident in which these safety objectives are especially challenged is one that results in a depressurized reactor coolant system with no forced coolant flow.[13-6,13-9,13-20,13-21,13-22,13-23] Such an accident has been termed a conduction cooldown accident because the conduction mode of heat transfer plays an important role in transporting the reactor decay heat to its ultimate heat sink such as the earth surrounding the reactor building. A schematic of the media through which heat transport occurs for a PB-HTGR is shown in Figure 13-1. Although not shown in this figure, heat is also transported through media above and below the reactor core. A break in the coolant system is one event that may result in a conduction cooldown accident. After the occurrence of such an accident, the ingress of air and resulting oxidation and heatup of the reactor core may have a strong influence on the transient behavior of the reactor. In such a situation, the calculation of the maximum temperature of the reactor fuel and the extent of burn-off of graphite provide fundamental measures of the safety of the reactor.

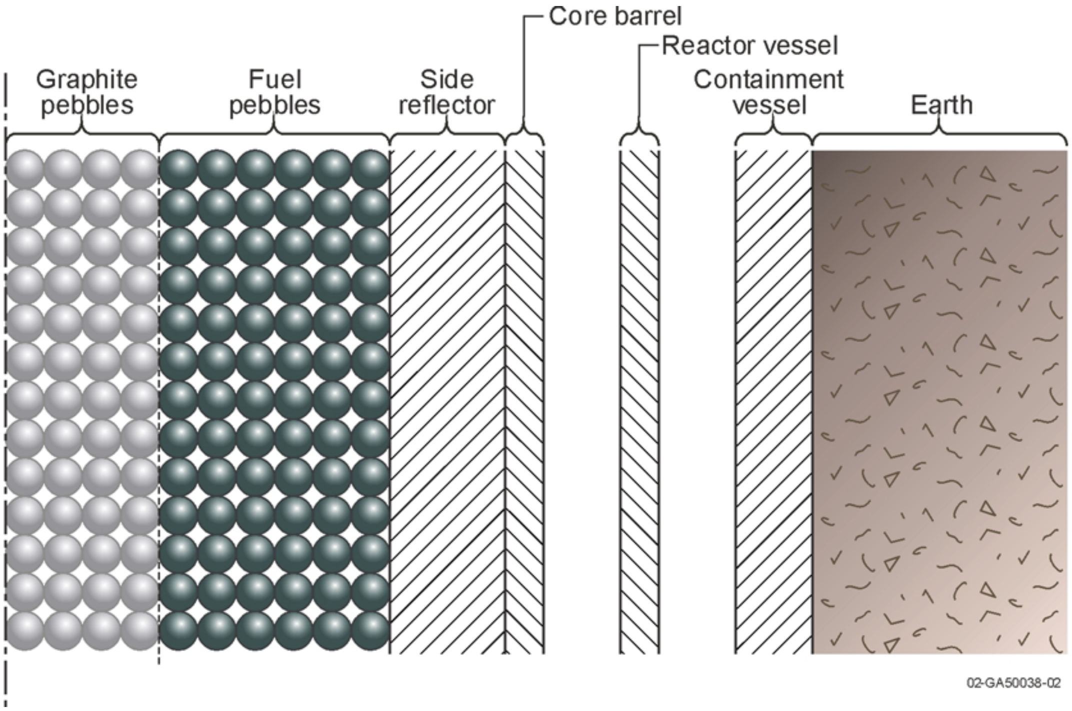

Figure 13-1. Schematic of media in PB-HTGR through which heat is transported in event of conduction cooldown accident.

Six phenomena have been identified that are unique to PB-HTGR and BT-HTGR transient analysis and that play an important role in determining the maximum reactor core temperature and the extent of graphite oxidation. These unique phenomena are (1) transport of decay heat by conduction and radiation through a porous or heterogeneous medium from the interior to the exterior of the reactor core, (2) convective heat transfer in the porous medium of a PB-HTGR, (3) flow losses in a porous medium of PB-HTGRs, (4) transport of heat by a combination of radiation, natural convection and conduction from exterior surface of the reactor core to an ultimate heat sink such as the earth surrounding the reactor building, (5) oxidation of graphite in the reactor core, and (6) molecular diffusion of air into the reactor core from a break in the reactor coolant system. Models for these phenomena will be developed and implemented into the SCDAP/RELAP5-3D© code.

This report is organized as follows. Section 13.2 describes the model for calculating the transport of decay heat from the interior to the exterior of the reactor code by conduction and radiation through a porous or heterogeneous medium. This model is used to calculate the long-term transient two-dimensional (radial and axial) temperature distribution in the reactor core for the case of no significant flow of gas through the reactor core. Section 13.3 describes the model for calculating flow losses in the reactor core of PB-HTGRs. Section 13.4 describes the models for calculating the convective heat transfer in the reactor cores of PB-HTGRs and BT-HTGRs. Models for calculating the heat and gases produced by the oxidation of graphite in contact with air are described in Section 13.5. The oxidation of graphite due to the ingress of water is described in Section 13.6. The modeling of the transport of heat from the reactor core to the ultimate heat sink such as the earth surrounding the reactor containment is described in Section 13.7. Section 13.8 describes the model for calculating the ingress of air into the reactor by molecular diffusion from the location of a break in the coolant system. This model plays an important role in calculating the time at which vigorous natural circulation may begin and dramatically increase the ingress of air into the reactor core. The modeling of the ingress of air also involves the extension of the fluid behavior modeling in SCDAP/RELAP5-3D© to represent gases composed of mixtures of oxygen, carbon dioxide, and carbon monoxide. The references are presented in Section 13.9.

13.2 Transient Temperature Distribution in Reactor Core

In the event of a large break in the primary system of a PB-HTGR or BT-HTGR, the long-term temperature distribution in the reactor core is the result of the transport of decay heat by conduction and radiation through the porous or heterogeneous medium of the reactor core to its exterior surface. The temperature distribution through the reactor core is calculated solving the two-dimensional (radial-axial) heat conduction equation using effective thermal conductivities to represent heat transfer by conduction and radiation in a porous or heterogeneous medium. The heterogeneous solid part of the reactor core and its gaseous parts are homogenized as a continuum with heat transfer characteristics representative of the actual heterogeneous configuration of the reactor core. Using the two-dimensional cylindrical coordinate system, the equation solved for the transient temperature distribution of the reactor core is the integral form of the heat conduction equation for an anisotropic continuum. This equation is:[13-24]

$$\int_v \rho c_p \frac{\partial T}{\partial t} dv = \int_v \frac{\partial}{r\partial r}\left(r k_r \frac{\partial T}{\partial r}\right) dv + \int_v \frac{\partial}{\partial z}\left(k_z \frac{\partial T}{\partial z}\right) dv + \int_v Q_v dv + \int_s Q_s ds \tag{13-1}$$

where

Q_v = net volumetric heat generation (nuclear and oxidation heat generation and heat removal by convective cooling, W/m^3),

Q_s = heat flux at the boundaries of the continuum (convective, radiative, W/m^2),

T = temperature at location (r, z) at time t where r and z are the radial and axial coordinates, respectively (K),

ρc_p = volumetric heat capacitance (J/m^3-K),

k_r, k_z = effective thermal conductivity in the radial and axial directions, respectively (W/m-K).

Equation (13-1) is solved using the finite difference and finite volume methods.[13-24,13-25]

The effective thermal conductivity is calculated as a function of the temperature, composition, and configuration of the various elements in the reactor core. The calculated effective thermal conductivity accounts for several modes of heat transfer, including heat conduction through the solid parts of the core, heat conduction through gases in the interstices in a PB-HTGR core and through gases in the coolant channels and gaps in a BT-HTGR core, radiation heat transfer across interstices in a PB-HTGR core and across coolant channels and gaps in a BT-HTGR core, and heat conduction through points of contact of the pebbles in a PB-HTGR core. The effective thermal conductivity for the core of the PB-HTGR is calculated by the No correlation[13-26] or the Tanaka and Chisaka correlation for a discontinuous solid system.[13-27] The effective thermal conductivity for the core of the BT-HTGR is calculated by the Tanaka and Chisaka correlation for a continuous solid system. The No correlation is an empirically based correlation applicable only to a PB-HTGR core. The Tanaka and Chisaka correlations have application to a wide range of heterogeneous media.

The No correlation for effective thermal conductivity[13-26] combines the conduction and radiation contributions to heat transfer into one simple empirical correlation. This correlation is applicable only for a bed of fuel pebbles similar to that from which data was obtained for establishing the correlation. This correlation is

$$k_r = k_z = 1.1536\text{e-}4(T - 273.16)^{1.6632} \tag{13-2}$$

where

$k_r = k_z$ = effective overall thermal conductivity in radial and axial directions (W/m-K),

T = temperature (K).

The Tanaka and Chisaka correlation for the case of a medium in the configuration of a continuous system of solid material is expressed by the equation

$$k = \left[A + (1 - A)\frac{\log[1 + 2B(k_{por}/k_s - 1)]}{2B(1 - k_s/k_{por})}\right]k_s + k_{rad} \tag{13-3}$$

where

k = overall effective thermal conductivity of a heterogeneous medium (W/m-K),

A = 2(1 - ε)/(2 + ε),

B = (1 - ε)/3,

ε = porosity of the medium,

k_s = thermal conductivity of the solid material in the porous medium (W/m-K),

k_{por} = thermal conductivity of the material or gas in the pores of the porous medium (W/m-K),

k_{rad} = contribution of radiation heat transfer to effective thermal conductivity (W/m-K).

In the above equation, the "A" term represents the parallel void ratio and the "B" term represents the series void ratio. For the case of the material in the pores of the medium being composed only of gas, the thermal conductivity of the pores is calculated by subroutine gascns in the Material Properties Package (MATPRO) in SCDAP/RELAP5-3D©.[13-28] The porosity of the reactor core of a PB-HTGR is calculated by the empirical equation[13-26]

$$\varepsilon = 0.375 + 0.78 / (D_{bed} / D_p)^2 \tag{13-4}$$

where

D_{bed} = diameter of pebble bed (m),

D_p = diameter of pebbles (m).

The above equation is appropriate for spherical pebbles that are randomly packed.

The lower bound on effective thermal conductivity is calculated by representing the elements in the medium as not being in significant contact with each other and thus forming a discontinuous system of solid material. The Tanaka and Chisaka correlation for this configuration is expressed by the equation

$$k = \left[A_2 + (1 - A_2)\frac{\log[1 + 2B_2(k_s / k_{por} - 1)]}{2B_2(1 - k_{por} / k_s)}\right]k_{por} + k_{rad} \tag{13-5}$$

where

A_2 = $2\varepsilon/(3 - \varepsilon)$,

B_2 = $\varepsilon/3$.

In applying the above equation to a PB-HTGR, the thermal conductivities in the radial and axial direction are $k_r = k_z = k$.

The thermal conductivity of the solid material in the fuel region of a PB-HTGR is equal to the thermal conductivity of the fuel pebbles. A correlation for the thermal conductivity of the fuel pebbles is[13-29]

$$k_s = 127.68\left[\left(\frac{0.06829 - 0.3906\text{e-}4(T - 273.16)}{n_{fs} + 1.931\text{e-}4(T - 273.16)}\right) + 1.228\text{e-}4(T - 273.16) + 0.042\right] \tag{13-6}$$

where

n_{fs} = fast neutron irradiation dose $[(\text{fast neutrons/m}^2)/1\text{x}10^{21})]$.

For the PB-HTGR, the radiation contribution term is applied in the overall effective thermal conductivity for the Tanaka and Chisaka correlation. This radiation term is calculated by the equation

$$k_{rad} = 4e_m\varepsilon\sigma D_p T^3 \tag{13-7}$$

where

e_m = emissivity of surface of the pebbles,

σ = Stefan-Boltzmann constant (5.66840-8 W/m^2-K^4),

D_p = diameter of pebbles (m),

T = temperature of pebbles (K).

The code user may select either the No correlation or the Tanaka and Chisaka correlation for a discontinuous solid system as the correlations to be applied for calculating the effective thermal conductivity of a PB-HTGR core.

For a PB-HTGR with fuel pebbles with a diameter of 50 mm in a packed bed with a porosity of 0.388 and a temperature of 1200 K, the effective thermal conductivities as calculated by the continuous solid system and the discontinuous solid system versions of the Tanaka and Chisaka correlation are 19.1 W/m-K and 9.9 W/m-K, respectively. The conductivities of the fuel pebbles and the gas in the interstices of the fuel pebbles were 42.8 W/m-K and 0.4009 W/m-K, respectively. The radiation contribution term in these correlations had a value of 6.08 W/m-K. This value of the radiation contribution is based on an emissivity of 0.8 for the surface of the fuel pebbles. For the same conditions, the No model calculates a thermal conductivity of 11.7 W/m-K. The thermal conductivities as calculated by the No correlation and the Tanaka and Chisaka correlation for a discontinuous solid system are in fairly close agreement (11.7 W/m-K versus 9.9 W/m-K).

The thermal conductivity of the reflector material outside the fueled region of a PB-HTGR is calculated by the equation[13-29]

$$k_{rfl} = 115.\left[1. - 1.084\left(\frac{T-273.16}{1000.}\right) + 0.743\left(\frac{T-273.16}{1000.}\right)^2 - 0.213\left(\frac{T-273.16}{1000.}\right)^3\right] \tag{13-8}$$

where

k_{rfl} = thermal conductivity of reflector (W/m-K).

The thermal conductivity of the carbon bricks insulating the reactor vessel is calculated by the correlation

$$k_{brk} = 5 + 3e\text{-}3(T - 273.16) \tag{13-9}$$

where

k_{brk} = thermal conductivity of the carbon bricks (W/m-K).

For the effective thermal conductivity in the radial direction of BT-HTGRs, the Tanaka and Chisaka correlation for a continuous solid system is always applied. The Tanaka and Chisaka correlation is extended to account for the heterogeneous composition of the fuel and reflector blocks and to account for gaps between the blocks.

The overall effective thermal conductivity in the radial direction of fuel blocks in a BT-HTGR is calculated by applying in two stages the Tanaka and Chisaka correlation for continuous solid systems, and then applying a term to account for radial gaps between the blocks. Figure 13-2 shows an example of the configuration of fuel blocks. A schematic of this method of calculating the overall thermal conductivity of a homogenized fuel block is shown in Figure 13-3. In the first stage, the effective thermal conductivity of the part of the fuel blocks with graphite block material and fuel compacts is calculated. In this stage, the fuel compacts are the discontinuous part of the medium and the graphite block material is the continuous part of the medium. The thermal conductivity of the discontinuous part of the medium is the thermal conductivity of the fuel compacts and the thermal conductivity of the continuous part of the medium is the thermal conductivity of the graphite block material. The thermal conductivities of the fuel compacts and graphite block material (H-451 graphite) are calculated using the tabular correlations shown in Tables 13-2 and 13-3, respectively.[13-30] The thermal conductivities at temperatures in between the temperature entries in the tables are found by interpolation. In the second stage, the effective thermal conductivity of the fuel block exclusive of the radial gaps between the fuel blocks is calculated. In this stage, the coolant channels are the porous part of the system and the homogenized block material and fuel compacts are the solid part of the system. The thermal conductivity of the gases in the coolant channel is calculated using a revised version of the gascns subroutine of the MATPRO database in SCDAP/RELAP5-3D©.[13-28,13-31] The thermal conductivity of the solid part of the system for the second stage of calculations is calculated using the effective thermal conductivity calculated in the first stage of the calculations.

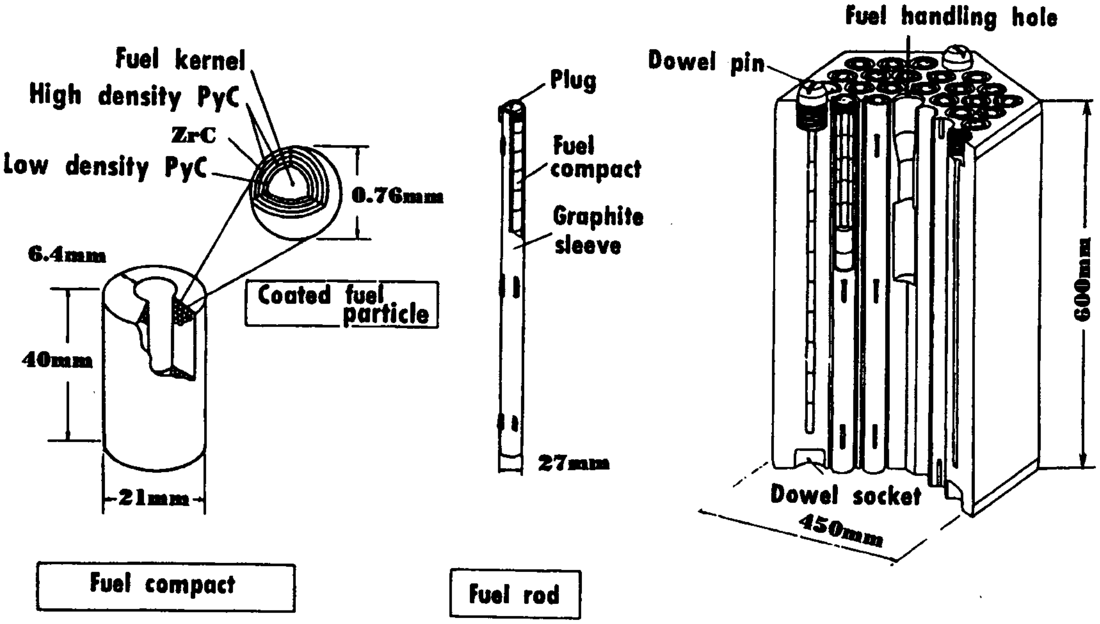

Figure 13-2. Example of configuration of fuel blocks in BT-HTGR.

The presence of radial gaps between fuel blocks in a BT-HTGR is taken into account by applying an equation for effective thermal conductivity of a medium with radial gaps in it.[13-32]

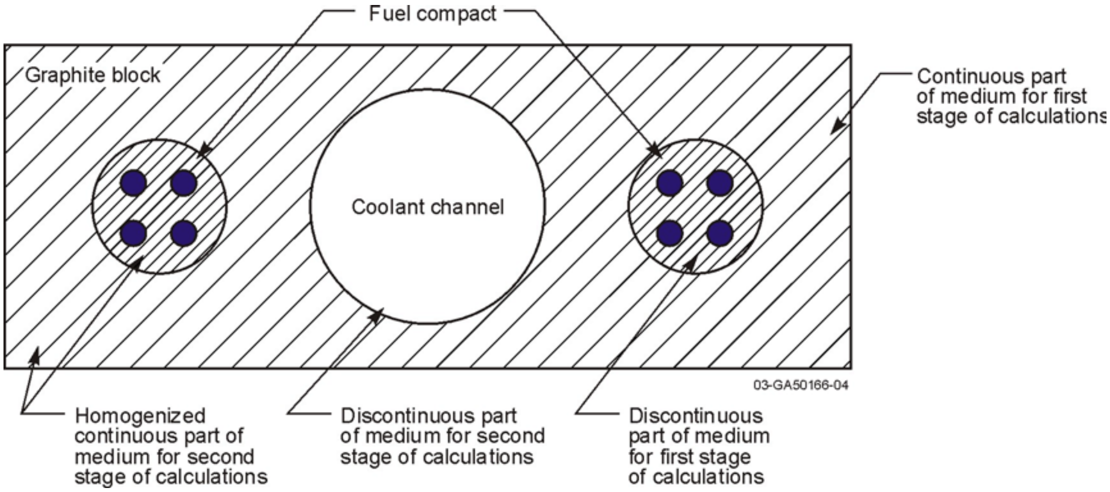
Fuel compact
Graphite block
Continuous part of medium for first stage of calculations
Coolant channel
03-GA50166-04
Homogenized continuous part of medium for second stage of calculations
Discontinuous part of medium for second stage of calculations
Discontinuous part of medium for first stage of calculations

Figure 13-3. Schematic of calculation of effective thermal conductivity of homogenized fuel block.

Table 13-2. Tabular correlation for thermal conductivity of fuel compacts.

Temperature (K)	Thermal conductivity (W/m-K)
255.38	4.84
394.27	5.34
533.16	5.84
672.05	6.34
810.94	6.83
949.83	7.33
1088.7	7.83
1227.6	8.36
1366.5	8.82
1505.4	9.32
1644.3	9.82
1783.2	10.3
1922.0	10.8
2060.9	11.3
2199.9	11.8

Table 13-3. Tabular correlation for thermal conductivity of graphite in fuel blocks.

Temperature (K)	Thermal conductivity (W/m-K)
255.38	29.0
338.56	29.0
533.16	29.0
672.05	29.0
810.94	29.0
949.83	30.0
1088.7	32.3
1227.6	34.6
1366.5	36.9
1505.4	39.2
1644.3	41.5
1783.2	41.5
1922.0	41.5

$$k_r = \frac{1}{\left(\frac{1}{h_{gap}\Delta r_{gap}}\right) + \frac{1}{k_{sg2}}} \tag{13-10}$$

where

k_r = overall effective thermal conductivity in radial direction of fuel blocks (W/m-K),

h_{gap} = conductance of radial gaps between blocks (W/m^2-K),

Δr_{gap} = width of fuel of blocks (m),

k_{sg2} = effective thermal conductivity from second stage of calculations for effective thermal conductivity in radial direction of blocks (W/m-K).

The conductance of the radial gap between fuel and reflector blocks is calculated using the equation

$$h_{gap} = k_{gas}/t_{gap} \tag{13-11}$$

where

k_{gas} = thermal conductivity of the gas in the gap (W/m-K),

t_{gap} = thickness of the gap in the radial direction (m).

The effective thermal conductivity in the axial direction of BT-HTGRs is calculated assuming no discontinuities in the axial direction. The effective thermal conductivity is calculated using the tabular correlation for graphite thermal conductivity described in Table 13-3. A multiplier is applied to account for the reduction in area due to the presence of coolant channels and fuel compacts. The thermal conductivity in the axial direction in the BT-HTGR is calculated by the equation

$$k_z = (1 - f_c)(1 - f_{cm})k_B \tag{13-12}$$

where

k_z = effective thermal conductivity of fuel block in axial direction and with multiplier to account for reduction in area for heat conduction due to presence of coolant channels and fuel compacts (W/m-K),

f_c = fraction of area of coolant channel in horizontal plane with respect to entire area of fuel block in horizontal plane,

f_{cm} = fraction of area of fuel compacts in horizontal plane with respect to area exclusive of area of coolant channels of fuel block in horizontal plane,

k_B = thermal conductivity of graphite in fuel block (calculated by tabular correlation in Table 13-3) (W/m-K).

The effective thermal conductivity in the radial direction of reflector blocks is calculated using the tabular correlation for graphite thermal conductivity described in Table 13-3 and assuming no heterogeneity.[13-30]

The volumetric heat capacitance of the fuel pebbles and reflector material in a PB-HTGR [ρc_p term in Equation (13-1)] is calculated by the equation[13-29]

$$\rho c_p = 1.75e6(1 - \varepsilon)[0.645 + 3.14((T - 273.16)/1000) + 2.809((T - 273.16)/1000)^2 + 0.959((T - 273.16)/1000)^3] \tag{13-13}$$

where

ρc_p = volumetric heat capacitance (J/m^3-K),

T = temperature (K).

The above equation is applied for both the reflector pebbles and the fuel pebbles of the PB-HTGR. Two factors allow this application. First, the volume of the fuel particles relative to the volume of the graphite is small. Second, the volumetric heat capacity of the fuel particles is not greatly different from that of the graphite.

The volumetric heat capacitance term in Equation (13-1) for BT-HTGRs is calculated by volume weighting of the volumetric heat capacities of each type of material associated with each node in the reactor core. The volumetric heat capacity of the graphite in the blocks in a BT-HTGR is calculated using the tabular correlation shown in Table 13-4. The correlation applies to block material composed of H-451 graphite. The volumetric heat capacity of the reflector material in a BT-HTGR is also calculated using the tabular correlation shown in the table.

Table 13-4. Tabular correlation for volumetric heat capacity of graphite in fuel blocks in BT-HTGR.

Temperature (K)	Volumetric heat capacity (J/m^3-K)
255.38	1.073x106
394.30	1.698x106
533.16	2.229x106
627.0	2.589x106
810.94	2.835x106
949.83	3.011x106
1088.7	3.141x106
1227.6	3.239x106
1366.5	3.316x106
1505.4	3.377x106
1644.3	3.427x106
1783.2	3.468x106
1922.0	3.502x106
2199.8	3.534x106

The volumetric heat capacity of the fuel compacts in a BT-HTGR is calculated by the tabular correlation shown in Table 13-5.

Table 13-5. Tabular correlation for volumetric heat capacity of fuel compacts in BT-HTGR.

Temperature (K)	Volumetric heat capacity (J/m^3-K)
394.30	0.3612x106
533.16	1.386x106
672.0	1.743x106
810.94	1.905x106
949.83	1.992x106

Table 13-5. Tabular correlation for volumetric heat capacity of fuel compacts in BT-HTGR.

Temperature (K)	Volumetric heat capacity (J/m^3-K)
1088.7	2.046x106
1227.6	2.084x106
1366.5	2.113x106
1505.4	2.137x106
1644.3	2.157x106
1783.2	2.176x106
1922.0	2.1932x106
2069.0	2.209x106
2199.8	2.225x106

The volumetric heat capacity for the fuel blocks in a BT-HTGR [ρc_p term in Equation (13-1)] is calculated by the equation

$$\rho c_p = (1-f_c)(1-f_{cm})(\rho c_p)_B + (1-f_c)(f_{cm})(\rho c_p)_{cm} \tag{13-14}$$

where

ρc_p = volumetric heat capacity of fuel blocks (J/m^3-s),

f_c = fraction of area of coolant channel in horizontal plane with respect to entire area of fuel block in horizontal plane,

f_{cm} = fraction of area of fuel compacts in horizontal plane with respect to area exclusive of area of coolant channels of fuel block in horizontal plane,

$(\rho c_p)_B$ = volumetric heat capacity of graphite in fuel block (defined by tabular correlation in Table 13-4) (J/m^3-K),

$(\rho c_p)_{cm}$ = volumetric heat capacity of fuel compacts (defined by tabular correlation in Table 13-5) (J/m^3-K).

Carbon brick material is assumed to have the same heat capacity as reflector material.

The calculation of the volumetric heat source in the reactor core of a HTGR is calculated accounting for the fission and decay heat produced in the fuel, the heat produced by the oxidation of the graphite in the core and surrounding the reactor core, and the heat transferred to the coolant flowing through the reactor core. The transient and spatial distribution of fission and decay heat is calculated by the equation

$$q_{fd}(r, z) = G(t)F(r, z) \tag{13-15}$$

where

$q_{fd}(r,z)$ = volumetric heat generation due to fission and decay heat at radial coordinate r and axial coordinate z of the reactor core (W/m^3),

$G(t)$ = average volumetric heat generation in reactor core at time t due to fission and decay heat (user-defined) (W/m^3),

$F(r,z)$ = ratio of volumetric heat generation at position (r,z) in the reactor core to average core volumetric heat generation rate (user-defined).

The net volumetric heat generation is calculated by the equation

$$Q_v(r, z) = q_{fd}(r, z) + q_{ox}(r, z) - q_{cv}(r, z) \tag{13-16}$$

where

$Q_v(r,z)$ = net volumetric heat generation in reactor core at position (r,z) (W/m^3),

$q_{ox}(r,z)$ = volumetric heat generation due to oxidation of graphite at position (r,z) (W/m^3),

$q_{cv}(r,z)$ = volumetric rate of removal of heat at position (r,z) due to convective heat transfer to coolant flowing through the reactor core (W/m^3).

The volumetric rate of heat removal term in the above equation is calculated as described in Section 13.4 of this report. For an accident such as a conduction cooldown accident, the value of this term approaches zero. The volumetric rate of heat generation in the reactor core due to oxidation is calculated as described in Section 13.5.

The surface heat flux term in Equation (13-1) is a function of the convective and radiative heat transfer at the external surface of the reactor core. Models are used for convective heat transfer that account for forced flow and natural convection. These models are described elsewhere.[13-18] The model for radiative heat transfer is described in Section 13.7.

13.3 Flow Losses in HTGR Core

This section describes the models for calculating the flow losses in the reactor core region of a HTGR. The models for calculating flow losses in the PB-HTGR are described in Section 13.3.1 and the models for calculating flow losses in the BT-HTGR are summarized in Section 13.3.2.

13.3.1 Flow Losses in Core Region of PB-HTGR

Darcy's Law[13-33] is applied to calculate the flow losses in the reactor core pebble bed. The flow losses are calculated in terms of drag force (pressure loss gradient). The flow losses are calculated as a function of several variables; (1) porosity of pebble bed, (2) diameter of pebbles, (3) viscosity and density of gas in interstices of pebbles, and (4) velocity of gas in interstices of pebbles. The flow losses are calculated by the equation[13-34]

$$F_p = \varepsilon\left[\frac{\mu j}{k} + \frac{\rho j^2}{m}\right] \tag{13-17}$$

where

F_p = flow resistance (N/m^3),

ε = porosity of the debris,

μ = viscosity of the gas (kg/m-s),

ρ = density of the gas (kg/m^3),

j = superficial velocity of the gas (m/s),

k = Darcy permeability of the pebble bed (m^2),

m = passability of the debris bed (m).

The second term on the right hand side of the above equation represents the turbulent drag counterpart to the viscous drag represented by the first term.

The Darcy permeability is calculated by the equation[13-34]

$$k = \frac{\varepsilon^3 D_p^2}{150(1-\varepsilon)^2} \tag{13-18}$$

where

D_p = diameter of pebbles (m).

The passability of the pebble bed is calculated by the equation[13-34]

$$m = \frac{\varepsilon^3 D_p}{1.75(1-\varepsilon)} \tag{13-19}$$

The models for flow loss are implemented into the RELAP5-3D© code field equation for the momentum of gas in a porous medium such as the pebble bed core of a PB-HTGR. The flow losses are incorporated in the terms in the field equation for losses due to friction and form. A condensed version of the field equation for momentum is

$$\rho\frac{\partial v}{\partial t} + \frac{1}{2}\rho_g\frac{\partial v^2}{\partial x} = -\frac{\partial p}{\partial x} + \ldots \tag{13-20}$$

where

ρ = density of gas (kg/m^3),

v = velocity of gas (m/s),

t = time (s),

x = spatial coordinate (m),

p = pressure of gas (N/m^2).

In the above equation, the first term on the left side of the equation is the acceleration of the gas, the second term on the left hand side is the momentum flux, and the first term on the right hand side is the pressure gradient.

The numerical solution scheme in RELAP5-3D© is based on replacing the differential equation form of the field equations with finite difference equations partially implicit in time. The difference equations are based on the concept of control volumes and a staggered spatial mesh. The pressures and energies are defined at volumes, and the velocities are defined at junctions. When the momentum equation is finite differenced (using integration over the momentum control volume centered on a junction), an additional variable named occurs on the right hand side of Equation (13-20). This variable accounts for losses due to form loss, friction, and other losses prescribed by the code user. This additional term is calculated by the equation

$$H_{loss} = 0.5k_L v \tag{13-21}$$

where

k_L = loss coefficient corresponding with velocity v (unitless).

The loss coefficient k_L is related to the drag force calculated by Equation (13-17) as follows;

$$0.5k_L \rho v^2 = F_p \Delta x \tag{13-22}$$

where

Δx = length of RELAP5-3D© volume for which flow losses are being calculated (m).

Solving the above equation for k_L, the result is

$$k_L = \frac{2\Delta x F_p}{\varepsilon \rho v^2} \tag{13-23}$$

The value of k_L as calculated above is used for calculating the flow losses in a porous medium such as the pebble bed of a PB-HTGR. An assessment of the model described above showed that the model represents the flow losses of gas flowing through a porous medium.[13-19]

13.3.2 Flow Losses in Core Region of BT-HTGR

Extensions were not required to calculate the flow losses in the core region of the BT-HTGR. The models for flow losses due wall friction previously established in SCDAP/RELAP5-3D© are adequate for calculating the flow losses in the core region of a BT-HTGR.[13-17,13-18]

13.4 Convective Heat Transfer in HTGR

This section describes the models for calculating the convective heat transfer in the reactor core region of a HTGR. The models for calculating the heat removed from core material by convective heat transfer in the PB-HTGR are described in Section 13.4.1. The models for calculating convective heat transfer from core material in the BT-HTGR are described in Section 13.4.2. The calculation of the heat received by the gas flowing through the reactor core is described in Section 13.4.3.

13.4.1 Convective Heat transfer in Core Region of PB-HTGR

The movement of gases through the interstices of a pebble bed results in transfer of heat by convection from the pebbles to the gases. In general, the rate of heat transfer is calculated by empirical correlations as a function of fluid conditions and pebble characteristics. Correlations are available for two flow regimes; (1) forced flow, and (2) natural convection. The convective heat transfer is calculated in three steps. In the first step, the convective heat transfer at the surface of the pebbles is calculated applying the user-selected correlation for forced flow. In the second step, the convective heat transfer coefficient is calculated applying the correlation for natural convection. The larger of the two heat transfer coefficients is applied. In the third step, the surface area of the pebbles and temperature of the gas is applied to calculate the volumetric rate of heat removal from the pebbles by convection. The volumetric rate of heat removal is a term in Equation (13-1) for calculating the transient spatial distribution in temperature of the reactor core.

The Tung correlation is used to calculate the convective heat transfer for forced flow.[13-35,13-36] The correlation calculates the Nusselt number. The convective heat transfer coefficient is then calculated based on its relation to the Nusselt number. The Nusselt number is calculated by the equation

$$\mathrm{Nu_{conv}} = 0.29\mathrm{Re}^{0.8}\mathrm{Pr}^{0.5} \tag{13-24}$$

where

$\mathrm{Nu_{conv}}$ = Nusselt number for convection,

Re = Reynolds number,

Pr = Prandtl number.

The Nusselt number is related to the convective heat transfer coefficient by the equation

$$\mathrm{Nu} = hD_p/k \tag{13-25}$$

where

h = convective heat transfer coefficient (W/m^2-K),

D_p = diameter of pebbles (m),

k = thermal conductivity of gas (W/m-K).

The Reynolds number for the fluid in the interstices of the pebble bed is calculated by the equation

$$Re = \rho \varepsilon v D_p / \mu \tag{13-26}$$

where

ρ = density of gas (kg/m^3),

ε = porosity of debris bed,

v = velocity of gas (m/s) (εv = superficial velocity),

D_p = diameter of pebbles (m),

μ = viscosity of gas (kg/m-s).

The Prandtl number for the fluid in the interstices of the pebble bed is calculated by the equation

$$Pr = \mu c_p / k \tag{13-27}$$

where

μ = viscosity of gas (kg/m-s),

c_p = heat capacity of gas (J/kg-K),

k = thermal conductivity of gas (W/m-K).

Equation (13-24) is based on experiments in which the Prandtl number ranged from 0.7 to 5, the Reynolds number ranged from 8 to 2400, and the bed porosity ranged from 0.4 to 0.5. An alternative correlation to Equation (13-24) for calculating the Nusselt number for forced convection is the correlation presented by No.[13-26]

$$Nu_{conv} = 1.27 Pr^{0.333} Re^{0.36} / \varepsilon^{1.18} + 0.033 Pr^{0.5} Re^{0.86} / \varepsilon^{1.07} \tag{13-28}$$

The porosity in the above equation is calculated by Equation (13-4).

The Nusselt number for natural convection is also calculated and compared with that calculated for forced flow. If the Nusselt number for natural convection is greater than that for forced convection, then the natural convection Nusselt number is applied. The natural convection Nusselt number is calculated by the equation[13-37]

$$Nu_{nat} = KRa^{0.25} \tag{13-29}$$

where

Nu_{nat}	=	Nusselt number for natural convection,		
K	=	0.3	for	$0 \leq Ra < 50$
		0.4		$50 \leq Ra < 200$
		0.5		$200 \leq Ra < 10^6$
		0.6		$10^6 \leq Ra \leq 10^8$
Ra	=	Rayleigh number.		

The Rayleigh number in the above equation is calculated by the equation

$$Ra = GrPr = \frac{\rho_g^2 g D_p^3 \beta \Delta T}{\mu_g^2} Pr \tag{13-30}$$

where

g = acceleration of gravity (m/s^2),

ß = volume coefficient of expansion of gas (1/K),

ΔT = local temperature difference between pebbles and gas ($T - T_g$).

After the Nusselt number has been determined, the volumetric rate of heat removal in the pebble bed due to convective heat transfer can be calculated. This heat removal is used in Equation (13-14) to calculate the net volumetric heat generation rate at any location in the reactor core. The volumetric rate of heat removal is calculated by the equation

$$q_{cv}(r, z) = A_s \max(Nu_{conv}, Nu_{nat})(T - T_g) \tag{13-31}$$

where

$q_{cv}(r,z)$ = heat transferred to gas by convection (W/m^3),

A_s = surface area of pebbles per unit volume (m^2/m^3),

T = temperature of pebbles (K),

T_g = temperature of gas (K).

The surface area of pebbles per unit volume is calculated on the basis that the pebbles are spherical in shape and uniform in size. The resulting equation is

$$A_s = \frac{6(1-\varepsilon)}{D_p} \tag{13-32}$$

where

e = porosity of debris.

13.4.2 Convective Heat Transfer in Core Region of BT-HTGR and at Surfaces of Structures between Core and Containment

This section describes the model for calculating convective heat transfer in the core region of BT-HTGRs and at the surfaces of various structures between the reactor core and containment for PB-HTGRs and BT-HTGRs. The surfaces at which the convective heat transfer model may be applied include (1) outer surface of reactor core, (2) inner and outer surfaces of reactor vessel, (3) inner and outer surfaces of downcomer and upcomer used for cooling of reactor vessel by natural circulation of air from the atmosphere, and (4) inner surface of the containment. The convective heat transfer in the core region of the BT-HTGR and at these other various surfaces is calculated by the Dittus-Boelter correlation.[13-38] According to this correlation, the Nusselt number for convective heat transfer is calculated by the equation

$$\mathrm{Nu} = 0.023\mathrm{Re}^{0.8}\mathrm{Pr}^{0.4} \qquad (13\text{-}33)$$

where

Nu = Nusselt number,

Re = Reynolds number,

Pr = Prandtl number.

The Reynolds number is calculated by the equation

$$\mathrm{Re} = \rho_g|v|d_h/\mu \qquad (13\text{-}34)$$

where

ρ = density of the gas (kg/m3),

v = velocity of the gas (m/s),

d_h = hydraulic diameter of the coolant channel (m),

μ = viscosity of the gas (kg/m-s).

The fluid properties are calculated by the fluid properties package in SCDAP/RELAP5-3D©.[13-18,13-39] The hydraulic diameter is defined by the code user for each coolant channel in the BT-HTGR core in the fuel and reflector blocks and each gap between the fuel and reflector blocks. The code user also defines the hydraulic diameter for each RELAP5 volume interfacing the various surfaces between the reactor core and containment for PB-HTGRs and BT-HTGRs.

The Prandtl number is calculated by the equation

$$\mathrm{Pr} = \mu c_p/k \qquad (13\text{-}35)$$

where

c_p = heat capacity of gas (J/kg-K),

k = thermal conductivity of gas (W/m-K).

The convective heat transfer coefficient is calculated by the equation

$$h_c = kNu/d_h \tag{13-36}$$

where

h_c = convective heat transfer coefficient (W/m^2-K).

The volumetric rate of heat removal due to convective heat transfer to the gas flowing through the reactor core of a BT-HTGR is calculated by the equation

$$q_{cv} = A_s h_c (T - T_g) \tag{13-37}$$

where

q_{cv} = heat transferred from surface of core material to gas by convection and applied in Equation (13-14) (W/m^3),

A_s = surface area of graphite per unit volume (m^2/m^3),

T = temperature of surface of graphite (K),

T_g = bulk temperature of gas (K).

For the core of a BT-HTGR, the variable A_s is defined by the code user as a function of radial location in the reactor core.

13.4.3 Heat Transferred to Gas

The heat removed by convection from the surfaces at any location in the reactor core and at the surfaces of other structures between the core and containment is transferred to the gas in the RELAP5-3D© volume interfacing that surface. This amount of heat transfer is calculated at each time step for each RELAP5-3D© volume representing the gas at these locations.

For the gas in the core region of the reactor, the amount of heat transfer is calculated by the equation

$$Q_t = q_{cv} V_{mk} \tag{13-38}$$

where

Q_t = heat received by RELAP5-3D© volume with index i and which represents the gas at radial node m of axial node k in the numerical solution scheme calculating the transient temperature distribution in the reactor core (W),

q_{cv} = heat transferred from surface of core material to gas by convection and applied in Equation (13-14) (W/m^3),

V_{mk} = volume of radial node m of axial node k in the numerical solution scheme calculating the transient temperature distribution in the reactor core, and where the convective heat transfer per unit volume of the node is equal to (m^3).

In general, the gas flowing through each radial node of each axial node in the reactor core is represented by one RELAP5-3D© volume, and this volume does not represent gas in any other part of the reactor core.

13.5 Oxidation of Graphite in Contact with Air

The ingress of air into the reactor vessel of a HTGR may result in the oxidation of the graphite in the reactor vessel. The oxygen in air reacts with the graphite to produce CO, CO_2 and heat. The heat produced by oxidation may increase the temperature of the reactor core and accelerate the rate of reaction. Several different chemical reactions involving C, O_2, CO, and CO_2 may occur. These chemical reactions, the rate of these reactions and the heat produced or consumed by these chemical reactions vary with the temperature of the reactants.

For a temperature less than about 1420 K, the chemical reaction between graphite and air occurs in two steps in series. In the first step, the chemical reaction is

$$2C + O_2 \rightarrow 2CO + HF_1 \tag{13-39}$$

where

HF_1 = heat of formation (J/kg-mole of CO).

In the second step, the chemical reaction is

$$2CO + O_2 \rightarrow 2CO_2 + HF_2 \tag{13-40}$$

where

HF_2 = heat of formation (J/kg-mole of CO_2).

These two chemical reactions produce approximately 3.9×10^8 Joules of heat per kg-mole of produced CO_2, or 3.3x107 Joules per kg of oxidized graphite. The heat produced by these chemical reactions increases with the temperature at which the reaction occurred. A correlation between temperature and the heat produced by the two reactions is given by the equation[13-22]

$$HF_t = HF_1 + HF_2 = 3.486e2[9.369e4 + 0.7077T - 0.7e\text{-}4T^2 + 4.6e5/T] \tag{13-41}$$

where

HF_t = total heat of formation (J/kg of C oxidized),

T = temperature at which oxidation occurs (K).

The rate of oxidation and the configuration of oxidation is a function of temperature[13-22]. Experiments have shown that in general various types of graphite have similar rates of oxidation.[13-40] For temperatures less than 395 K, the oxidation occurs in a limited but relatively uniform manner throughout the graphite. For temperatures in the range of 395 K to 1248 K, the rate of oxidation is controlled by both chemical reactivity and in-pore diffusion. In this temperature range, the oxidation takes place near the surface of the graphite. For temperatures greater than 1248 K, the chemical reaction occurs rapidly and the oxidation occurs at the surface of the graphite. A schematic of these latter two oxidation processes is shown in Figure 13-4.

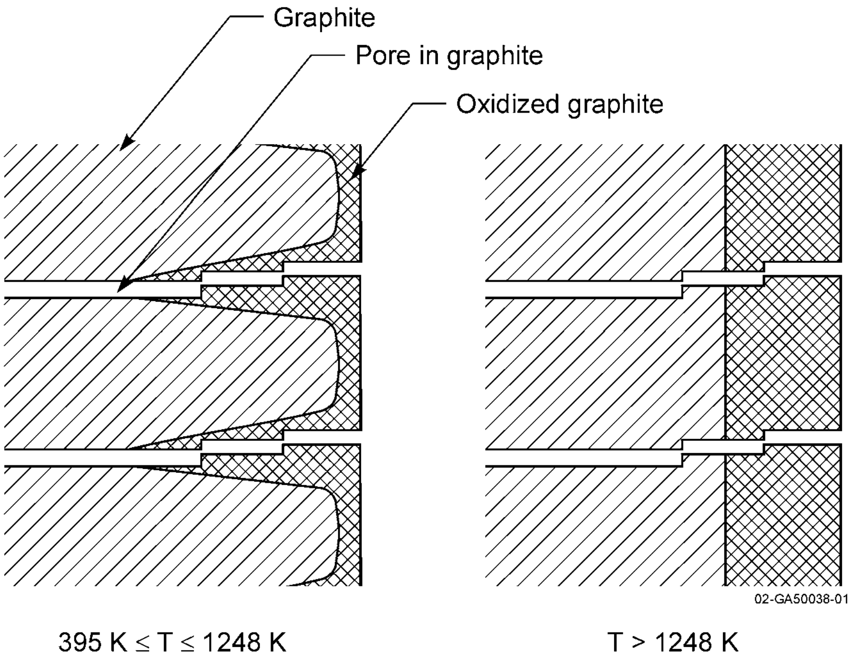

Figure 13-4. Schematic of oxidation in graphite for two ranges of temperature.

For graphite in the temperature range of 395 K to 1248 K, the rate of oxidation is calculated by the equation[13-22]

$$R_1 = 0.2475 \exp\left(\frac{-5710}{T}\right) \tag{13-42}$$

where

R_1 = rate of burnup of graphite for temperature in range of 395 K to 1248 K (kg of C oxidized/$m^2 \cdot s$).

For graphite at a temperature greater than 1248 K, the rate of oxidation is calculated by the correlation[13-22]

$$R_2 = 0.0156\exp\left(\frac{-2260}{T}\right) \tag{13-43}$$

where

R_2 = rate of burnup of graphite for temperature greater than 1248 K (kg of C oxidized/$m^2 \cdot s$).

The upper temperature limit for the validity of Equation (13-43) is 2073 K[13-22]. Since the maximum core temperature during an accident in a HTGR is not expected to exceed 2073 K, a correlation for the rate of oxidation for temperatures greater than 2073 K is not required.

If the temperature of the graphite is greater than 1420 K, then the Boudouard reaction[13-41] occurs. This reaction is described by the chemical equation

$$C + CO_2 \rightarrow 2CO \tag{13-44}$$

The rate of this chemical reaction is described by the equation[13-41]

$$R_{BD} = \frac{0.145\exp\left(\frac{-25000}{T}\right)P_{CO2}}{1 + 3.4e\text{-}5\exp\left(\frac{7000}{T}\right)P_{CO2}^{0.5}} \tag{13-45}$$

where

R_{BD} = rate of the Boudouard reaction (kg of C consumed/m^2-s),

P_{CO2} = partial pressure of CO_2.

The Boudouard reaction is endothermic and consumes about 1.4×10^7 Joules of heat per kg of consumed C.[13-40]

If the graphite is hot and thus oxidizes rapidly, the rate of oxidation may be limited by the rate of diffusion of air through the boundary layer at the surface of the graphite. In this case, the rate of oxidation is calculated by the equation

$$R_D = MW_c k_{mt} C_g y_b \tag{13-46}$$

where

R_D = limit on rate of oxidation imposed by diffusion of oxygen through boundary layer (kg of C oxidized/$m^2 \cdot s$),

k_{mt} = mass transfer coefficient at location at which rate of oxidation being calculated (m/s),

C_g = molar density of bulk gas (kg-mole/m^3),

y_b = mole-fraction of oxygen in bulk gas at location at which rate of oxidation being calculated,

MW_c = atomic weight of carbon (12.011).

The molar density of the bulk gas is calculated by the equation

$$C_g = \frac{P_{tot}}{RT} \tag{13-47}$$

where

P_{tot} = total pressure of bulk gas (Pa),

R = universal gas constant (8314. Pa-m^3/kg-mole-K),

T = temperature of bulk gas (K).

The mass transfer coefficient is calculated using the analogy between heat and mass transfer. According to this analogy[13-42]

$$k_{mt} = \frac{NuD_g}{d_h} \tag{13-48}$$

where

Nu = Nusselt number of the bulk gas (hd_h/k_g),

D_g = diffusivity of air in bulk gas (m^2/s),

d_h = characteristic length, (equal to diameter of pebbles for PB-HTGR and defined by code user for BT-HTGR) (m),

k_g = thermal conductivity of the bulk gas (W/m-K),

h = convective heat transfer coefficient (W/m^2-K).

The Nusselt number in the above equation is calculated by equations dependent on the mode of heat transfer. The equations for the Nusselt number for each mode of heat transfer have been defined previously in Section 13.4.

The heat and mass transfer analogy is valid provided the Prandtl number is approximately equal to the Schmidt number for the gas mixture.[13-42,13-43]

The Prandtl number is calculated by the equation

$$Pr = C_p\mu/k_g \tag{13-49}$$

where

Pr = Prandtl number,

μ = dynamic viscosity of bulk gas (kg/m-s),

C_p = heat capacity of bulk gas (J/kg-K).

The Schmidt number is calculated by the equation

$$Sc = \frac{\mu}{D_g\rho} \tag{13-50}$$

where

Sc = Schmidt number,

ρ = density of bulk gas (kg/m^3).

For a mixture of air and CO_2 at a temperature of 300 K and atmospheric pressure, the ratio of Schmidt number to Prandtl number is equal to 1.38. For cases in which the ratio of Schmidt to Prandtl number is not equal to 1.0, the calculation of the mass transfer coefficient may be improved by using the equation[13-22]

$$k_{mt} = \frac{NuD_g}{d_h}\left(\frac{Sc}{Pr}\right)^{0.333} \tag{13-51}$$

Several semi-empirical equations are available for calculating in an approximate manner the binary diffusivity of a mixture of two gases at low pressure. For a mixture of air and CO_2, one of these equations is[13-22]

$$D_g = \frac{1.45e\text{-}2T^{1.75}\left[\frac{1}{MW_{air}} + \frac{1}{MW_{CO2}}\right]^{0.5}}{P_{tot}[V_{air}^{0.333} + V_{CO2}^{0.333}]^2} \tag{13-52}$$

where

MW_{air} = molecular weight of air (28.9),

MW_{CO2} = molecular weight of CO_2 (44.01),

V_{air} = diffusion volume of air (19.7),

V_{CO2} = diffusion volume of CO_2 (26.9).

Another equation for calculating the binary diffusivity of a mixture of two gases is[13-32]

$$D_g = \frac{435.7e\text{-}4T^{1.5}\left[\frac{1}{MW_1} + \frac{1}{MW_2}\right]^{0.5}}{P_{tot}[V_1^{0.333} + V_2^{0.333}]^2} \tag{13-53}$$

where

MW_1 = molecular weight of first constituent (28.9 for air),

MW_2 = molecular weight of second constituent (44.01 for CO_2),

V_1 = molecular volume of first constituent (29.9 for air),

V_2 = molecular volume of second constituent (34.0 for CO_2),

P_{tot} = total pressure of gas mixture (Pa).

A third equation for calculating the binary diffusivity of a mixture of two gases is[13-33]

$$D_g = \frac{1.883e\text{-}2T^{1.75}\left[T^3\left(\frac{1}{MW_1} + \frac{1}{MW_2}\right)\right]^{0.5}}{P_{tot}[0.5(\sigma_1 + \sigma_2)]^2\Omega_{12}} \tag{13-54}$$

where

σ_1 = first Lennard-Jones collision parameter for first constituent (3.617 Angstroms for air),

σ_2 = first Lennard-Jones collision parameter for second constituent (3.996 Angstroms for CO_2),

Ω_{12} = dimensionless transport property defining intermolecular potential field for one molecule of first constituent and one molecule of second constituent.

The dimensionless parameter in the above equation is calculated by applying the second Lennard-Jones parameter and a table of gas properties[13-33]. The second Lennard-Jones parameter is calculated by the equation

$$K_{col} = \frac{T}{(\varepsilon_1\varepsilon_2)^{0.5}} \tag{13-55}$$

where

K_{col} = parameter for table lookup,

ε_1 = second Lennard-Jones parameter for first constituent (97.0 K for air),

ε_2 = second Lennard-Jones parameter for second constituent (190.0 K for CO_2).

The dimensionless parameter in Equation (13-54) is determined as a function of the temperature dependent table lookup parameter.[13-33]

The three equations for binary diffusivity calculate values for binary diffusivity that may vary by about a factor of two from each other. For a mixture of air and CO_2 at atmospheric pressure and a temperature of 298 K, the binary diffusivities as calculated by the Oh et al, Holman, and Bird et al equations are 2.25x10-5 m^2/s, 1.32x10-5 m^2/s, and 1.53x10-5 m^2/s, respectively. Equation (13-54) has been implemented into SCDAP/RELAP5-3D© as the equation for calculating binary diffusivity.

The parameters in Equation (13-54)[13-33] are also defined for a mixture of helium and air. For this mixture, the molecular weights of the two components are 4.0026 and 28.9, respectively. The first Lennard-Jones collision parameters for helium and air are 2.576 and 3.617 Angstroms, respectively. The second Lennard-Jones parameters for helium and air are 10.2 K and 97.0 K, respectively. For a mixture temperature of 1200 K, the dimensionless transport property in the denominator of Equation (13-54) is equal to 0.601. For a mixture temperature of 1200 K and a pressure of 1.0132x105 Pa (1 atm), Equation (13-54) calculates a value of 7.15x10^{-4} m^2/s for the binary diffusivity of the mixture.

The rate of mass transfer calculated using the diffusion coefficients calculated by Equations (13-52) through (13-54) underpredicts the rate of mass transfer for turbulent conditions. If substantial turbulent eddy motion is occurring, the rate of mass transfer may be much larger than that calculated on the basis of molecular diffusion.[13-32]

In addition to the rate of oxidation being limited by diffusion of oxygen through the boundary layer, the rate of oxidation may also be limited by the rate of bulk flow. This limit on the rate of oxidation is calculated by the equation

$$R_{Bn} = \frac{f_{OA} f_{AB} f_{CO} f_{FL} \rho_g \nu_g}{A_s \Delta z_n} \tag{13-56}$$

where

R_{Bn} = limit on oxidation imposed by bulk flow rate of oxygen at n-th axial node (kg of C oxidized /m^2·s),

f_{OA} = mass fraction of oxygen in air (0.2324),

f_{AB} = mass fraction of air in bulk flow (calculated by RELAP5-3D© variables quala and qualan)

f_{CO} = ratio of atomic weight of C to molecular weight of O_2 (0.37531),

f_{FL} = area of flow channels per unit area of cross section of reactor core (user-defined for BT-HTGR and equal to porosity of pebble bed for PB-HTGR),

ρ_g = density of gas (kg/m^3),

υ_g = bulk velocity of gas (m/s),

A_s = surface area in contact with bulk flow per unit volume of core (m^2/m^3),

Δz_n = height of axial node n (referenced from bottom of axial node n (m).

If the bulk velocity of gas is sufficiently small, then the bulk velocity instead of the rate of chemical reaction or rate of mass transfer through the boundary layer controls the rate of oxidation. This minimum bulk velocity is determined by equating Equation (13-56) to Equation (13-43) and solving for the velocity of the bulk gas. The result is

$$\nu_{gmb} = \left(\frac{0.0156 A_s \Delta z_n}{f_{OA} f_{AB} f_{CO} f_{FL} \rho_g}\right) \exp\left(\frac{-2260}{T}\right) \tag{13-57}$$

where

υ_{gmb} = minimum velocity of gas required for rate of oxidation to not be limited by bulk flow rate (m/s).

The above equation indicates that in general the bulk velocity limits the rate of oxidation of the graphite in a hot reactor core. For a PB-HTGR, calculations have indicated that the oxygen flowing into a pebble bed is consumed in about a 0.5 m high horizontal band of the reactor core.[13-20,13-44] For Δz_n= 0.5 m, $f_{OA} f_{OB}$ = 0.21, f_{CO} = 0.37531, f_{FL} = 0.39, A_s = 61 m^2/m^3, T = 1500 K, and ρ_g = 0.2355 kg/m^3, the above equation indicates that a bulk gas velocity of 14.6 m/s would be required to limit the rate of oxidation to the chemical reaction rate instead of the bulk flow rate. Experimental and calculation results indicate that a bulk velocity of order of 5 m/s or less occurs in a pebble bed due to natural circulation connected with a break in the primary system of a PB-HTGR.[13-44,13-45] Thus for pebbles at a temperature greater than 1500 K and an air pressure near atmospheric pressure, the rate oxidation is expected to be limited by the bulk gas velocity, and most of the oxidation is expected to be concentrated in a small region of the reactor core. The location of the region of oxidation and the rate of oxidation in this region are calculated by the equations described above.

The rate of oxidation may also be limited by the diffusion of O_2 and CO_2 across the boundary layer at the surfaces of the graphite in the reactor vessel. The minimum velocity of the air for the oxidation of hot graphite to not be limited by diffusion is determined by equating Equation (13-46) to Equation (13-45) and solving for the velocity of the bulk gas. For the case of a PB-HTGR, the result is

$$\nu_{gmd} = 570\left(\frac{\mu_g}{\rho_g \varepsilon D_p}\right)\left[\left(\frac{D_p T}{D_g P_{tot}}\right) Pr^{-0.5} \exp\left(\frac{-2260}{T}\right)\right]^{1.25} \tag{13-58}$$

In deriving the above equation, the Nusselt number in Equation (13-46) was calculated using Equation (13-24) in Section 13.4. For graphite and air at a temperature of 1500 K, and an air pressure of $1.0132x10^5$ Pa, the air properties in the above equation are; Pr = 0.705, D_g =$2.41x10^{-4}$ m^2/s, ρ_g =0.2355 kg/m^3, μg = $5.40x10^{-5}$ kg/m-s. For a PB-HTGR with pebbles having a diameter of $60x10^{-3}$ m, $f_{OA} f_{AB}$ = 0.2324, and for the defined gas conditions, the value of v_g is calculated to be 5.4 m/s. Thus for a flow velocity less than 5.4 m/s, the rate of oxidation may be limited by diffusion. Since the value of v_g from Equation (13-57) is significantly larger than that from Equation (13-58), the rate of oxidation for the defined conditions in general is limited by the bulk flow rate.

For a gas mixture consisting of three or more components, the diffusion coefficients can be approximated by calculation of the effective diffusion coefficients.[13-33,13-46] The effective diffusion coefficients are calculated by the equation

$$D_{i\text{-}m} = (1 - f_i) \Big/ \left(\sum_{j=1}^{n} \frac{f_j}{D_{i\text{-}j}}\right) \tag{13-59}$$

where

D_{i-m} = diffusion coefficient of i-th and m-th components of gas in gas mixture (m^2/s),

D_{i-j} = binary diffusion coefficient of i-th and j-th components in gas mixture (m^2/s),

f_i = mole fraction of i-th component of gas in gas mixture,

f_j = mole fraction of j-th component of gas in gas mixture,

n = number of components in gas mixture.

The volumetric heat generation due to oxidation is calculated by the equation

$$q_{ox}(r, z) = R_\chi A_s H_T \tag{13-60}$$

where

$q_{ox}(r,z)$ = volumetric heat generation due to oxidation of graphite at radial coordinate r and axial position z and applied in Equation (13-14) (W/m^3),

R_χ = rate of burnup of graphite (kg of C oxidized /m^2-s),

A_s = surface area of graphite per unit volume of reactor core (m^2/m^3),

H_T = heat of formation (J/kg of C oxidized).

In the above equation, the variable R_χ is calculated by the equation

$$R_\chi = \min(R_{12}, R_D, R_B) \tag{13-61}$$

where

R_{12} = for temperatures less than 1248 K and for temperatures greater than 1248 K (kg of C oxidized /m^2-s),

R_D = limit on rate of oxidation imposed by diffusion of oxygen through boundary layer (kg of C oxidized/m^2-s),

R_B = limit on rate of oxidation imposed by bulk flow rate of oxygen (kg of C oxidized/m^2-s).

For the case of temperature greater than 1420 K and the gas composed of CO2, the Boudouard reaction is modeled. For this reaction, the volumetric heat consumption is calculated by the equation

$$q_{ox}(r, z) = -R_{BD} A_s H_{BD} \tag{13-62}$$

where

R_{BD} = rate of burnup of graphite by Boudouard reaction (kg of C oxidized /m^2-s),

H_{BD} = heat required to drive the Boudouard reaction (1.4×10^7 Joules of heat per kg of consumed C).

The reaction of graphite with a gas containing air results in a change the composition of the gas. For the case of an accident involving the ingress of air, the gas is composed of some combination of air, CO_2, CO, N, A, and He. The RELAP5-3D© part of SCDAP/RELAP5-3D© calculates the composition of the gas in each volume representing the reactor system. For each volume at each time step, volumetric consumption or source rates are calculated for each component of the gas to account for the chemical reactions occurring on the surfaces of the volume. The reaction of CO with O_2 within the gas mixture is assumed to be negligible.

The volumetric consumption of air due to reaction with the graphite is calculated for each volume by the equation

$$\gamma_{ai} = -V_{mk}A_sR_\chi\left(\frac{MW_{air}}{MW_c}\right)\left(\frac{1}{f_{OA}}\right)\left(\frac{1}{V_{Ri}}\right) \tag{13-63}$$

where

γ_{ai} = volumetric consumption of air per unit volume in RELAP5-3D© volume with index i and which represents the gas at radial node m of axial node k in the numerical scheme calculating the transient temperature distribution in the reactor core (kg of air consumed/m^3-s),

V_{mk} = volume of radial node m of axial node k in numerical scheme used to calculate the transient temperature distribution in the reactor core, and where the RELAP5-3D© volume with index i represents the gas at that location (m^3),

A_s = surface area of reactor core per unit volume at radial node m of axial node k in numerical scheme used to calculate the transient temperature distribution in the reactor core (m^2/m^3),

R_χ = rate of reaction of oxygen in air with graphite at radial node m of axial node k in numerical scheme used to calculate the transient temperature distribution in the reactor core (kg of C oxidized /m^2-s),

MW_{air} = molecular weight of air (28.9),

MW_c = molecular weight of graphite (12.011),

f_{OA} = mole fraction of oxygen in air (0.2095),

V_{Ri} = volume of RELAP5-3D© volume with index i (m^3).

In general, the gas flowing through each radial node of each axial node in the numerical scheme for calculating the transient temperature distribution in the reactor core is represented by one RELAP5-3D© volume, and this volume does not represent in any other part of the reactor core.

The volumetric consumption of air results is nitrogen and argon being left as residual products. The production of these residual products is represented by the following volumetric production equations

$$\gamma_{ni} = (1 - f_{OA} - f_{AA}) V_{mk} A_s R_{\chi} \left(\frac{MW_n}{MW_c}\right)\left(\frac{1}{f_{OA}}\right)\left(\frac{1}{V_{Ri}}\right) \tag{13-64}$$

where

γ_{ni} = volumetric production rate of nitrogen (kg/m^3-s),

f_{AA} = mole fraction of argon in air (0.0096),

MW_n = atomic weight of nitrogen (28.016).

$$\gamma_{ai} = (1 - f_{OA} - f_{NA}) V_{mk} A_s R_{\chi} \left(\frac{MW_a}{MW_c}\right)\left(\frac{1}{f_{OA}}\right)\left(\frac{1}{V_{Ri}}\right) \tag{13-65}$$

where

γ_{ai} = volumetric production rate of argon (kg/m^3-s),

f_{NA} = mole fraction of nitrogen in air (0.7809),

MW_a = atomic weight of argon (39.944).

The volumetric production of CO_2 corresponding with the volumetric consumption of air is calculated by the equation

$$\gamma_{CO2i} = V_{mk} A_s R_{\chi} \left(\frac{MW_{CO2}}{MW_c}\right)\left(\frac{1}{V_{Ri}}\right) \tag{13-66}$$

where

γ_{CO2i} = volumetric rate of production of CO_2 in RELAP5-3D© volume with index i (kg/m^3-s),

MW_{CO2} = molecular weight of CO_2 (44.011).

At locations where the graphite is hotter than 1420 K and CO_2 is present in the gas, the Boudouard reaction occurs. The change in composition of the gas due to this reaction is calculated by the equations

$$\gamma_{COi} = 2 V_{mk} A_s R_{BD} \left(\frac{MW_{CO}}{MW_c}\right)\left(\frac{1}{V_{Ri}}\right) \tag{13-67}$$

where

γ_{COi} = volumetric rate of production of CO in RELAP5-3D© volume with index i (kg/m^3-s),

R_{BD} = rate of reaction of graphite with CO_2 (Boudouard reaction) at radial node m of axial node k in numerical scheme used to calculate the transient temperature distribution in the reactor core (kg/m^2-s),

MW_{CO} = molecular weight of CO (28.011).

$$\gamma_{CO2i} = -V_{mk}A_sR_{BD}\left(\frac{MW_{CO2}}{MW_c}\right)\left(\frac{1}{V_{Ri}}\right) \quad (13\text{-}68)$$

The internal energies of the various gases produced by chemical reactions are required by the RELAP5-3D© energy equation. The general form of the internal energy of the produced gases is

$$u_j = u_{0j} + c_{1j}T + 0.5c_{2j}(T - 250)^2 \quad (13\text{-}69)$$

where

u_j = internal energy of j-th component of gas added to a RELAP5-3D© volume (J/kg),

u_{0j}, c_{1j}, c_{2j} = coefficients in the calculation of internal energy for the j-th component of gas,

T = temperature of surface at which the component of gas was produced (K).

The coefficients in Equation (13-69) for each component of produced gas are defined elsewhere[13-17,13-18] or are being obtained from ongoing work.[13-47]

13.6 Oxidation of Graphite in Contact with Water Vapor

The ingress of water into a HTGR results in the oxidation of the graphite in the reactor core. For the HTGR direct Brayton cycle, water ingress may occur during a conduction cooldown accident due to a rupture in the precoolers and intercoolers. In an indirect cycle HTGR, water ingress may occur due to a rupture in a steam generator tube.[13-44] The oxidation of graphite causes a burn-off of the graphite. The rate of burn-off is not as intense as that for air ingress and the burn-off of the graphite has the beneficial effect of countering the increase in core reactivity caused by the ingress of water vapor.[13-44] The burn-off of the graphite increases the pressure in the reactor system and may cause coolant discharge due to excessive coolant pressure.[13-23] A 10% burn-off of graphite may reduce the strength of the graphite by 50%.[13-48]

When water vapor is in contact with graphite, the following chemical reaction occurs.

$$C + H_2O \rightarrow CO + H_2 \quad (13\text{-}70)$$

The above equation is a simplification of the actual chemical reactions. In reality, the oxidation of graphite consists of three distinct processes; (1) sorption of water molecules on active carbon sites, (2) chemical reaction of the sorbed water to form H_2 and CO, and (3) inhibition of water sorption by competitive sorption of H_2 molecules.[13-49] One of these processes produces heat and the other two processes absorb heat.[13-50] The activation energy varies with type of graphite. The activation energies for A3-3 graphite (matrix material), V482T2 graphite (structural graphite), and IG-110 graphite (structural material) are 1.85×10^5 J/mol, 2.46×10^5 J/mol, and 1.66×10^5 J/mol, respectively. [13-51,13-52]

Water vapor easily permeates the pores in graphite and thus the kinetics of the reaction are expressed in terms of fraction of total bulk of graphite reacted per unit time. The standard equation for the rate of reaction is the Langmuir-Hinshelwood equation.[13-49] This equation is

$$f_{ox} = \frac{F_b k_1 P_{H2O}}{1 + k_2 P_{H2}^n + k_3 P_{H2O}} \tag{13-71}$$

where

f_{ox} = fraction of graphite region oxidized (1/s),

F_b = correction factor for affect of burn-off,

P_{H2O} = partial pressure of water (Pa),

P_{H2} = partial pressure of hydrogen (Pa),

k_1, k_2, k_3, n= coefficients defined in Table 13-6.

The coefficients in the above equation are a function of temperature, partial pressure of water, and fraction of graphite burn-off. The coefficients k1, k2, k3, and n in the above equations are calculated by the correlations identified in Table 13-6. In this table, P_{H2O} is the partial pressure of water (Pa), T is the temperature of the graphite (K), and R is the universal gas constant (8314 Pa-m^3/kg-mole-K). While not expressed in the above equation, the rate of oxidation may also be affected by catalytic reactions with fission products in the graphite.

Table 13-6. Correlations for coefficients in kinetics equation for oxidation of graphite in contact with water.

		Correlation	
		Partial pressure of water (Pa)	
Coefficient	Units	$P_{H2O} \leq 300$	$300 < P_{H2O} < 3300$
k1	1/(s-Pa)	218 exp(-253500/RT)	0.11 exp(195400/RT)
k2	$Pa^{-0.75}$	1940 exp(-131900/RT)	8.2×10^{-8} exp(119700/RT)
k3	Pa^{-1}	1.02 exp(-47030/RT)	1.3×10^{-9} exp(131400/RT)
n		0.75	0.75

The factor F_b in the above equation accounts for the increase in oxidation with burn-off of the graphite. This factor is calculated by the equation

$$F_b = 0.447 + 0.8094b - 0.3221b^2 + 0.0681b^3 - 0.0613b^4 + 12.32e\text{-}6b^5 + 2.89e\text{-}5b^6 - 1.15e\text{-}6b^7 \tag{13-72}$$

where

b = burn-off of graphite in region (%).

The burn-off of graphite in any region of the reactor core is calculated by the equation

$$b = 100\int_0^t f_{ox} dt \tag{13-73}$$

where

b = burn-off of graphite in region (%).

The reaction of graphite with a gas containing water vapor results in a change in the composition of the gas. For the case of an accident involving the ingress of water vapor, the gas is composed of some combination of H_2O, CO, H_2, and He. The RELAP5-3D© part of SCDAP/RELAP5-3D© calculates the composition of the gas in each volume representing the reactor system. The composition is calculated accounting for the consumption and production of various components of the gas due to chemical reactions. For each volume at each time step, volumetric consumption or production rates are calculated to account for the chemical reactions occurring on the surfaces of the volume. The volumetric production of CO by reaction with H_2O is calculated by the equation

$$\gamma_{COi} = f_{ox}\rho_c V_{mk}\left(\frac{MW_{CO}}{MW_c}\right)\left(\frac{1}{V_{Ri}}\right) \tag{13-74}$$

where

γ_{COi} = volumetric generation rate of CO in RELAP5-3D© volume with index i (kg/ m^3-s),

ρ_c = density of graphite (kg/m^3),

V_{mk} = volume of radial node m of axial node k in numerical scheme used to calculate the transient temperature distribution in the reactor core, and where the RELAP5-3D© volume with index i represents the gas at that location (m^3),

MW_{CO} = molecular weight of CO (28.011),

MW_C = molecular weight of C (12.011),

V_{Ri} = volume of RELAP5-3D© volume with index i (m^3).

The volumetric production rate of hydrogen is calculated by the equation

$$\gamma_{H2i} = f_{ox}\rho_c V_{mk}\left(\frac{MW_{H2}}{MW_c}\right)\left(\frac{1}{V_{Ri}}\right) \tag{13-75}$$

where

γ_{H2i} = volumetric production rate of hydrogen in RELAP5-3D© volume with index i (kg/m^3-s),

MW_{H2} = molecular weight of H_2 (2.016).

The molecular consumption of water vapor is calculated by the equation

$$\gamma_{H2Oi} = -f_{ox}\rho_c V_{mk}\left(\frac{MW_{H2O}}{MW_c}\right)\left(\frac{1}{V_{Ri}}\right) \tag{13-76}$$

where

γ_{H2Oi} = volumetric consumption rate of water vapor in RELAP5-3D© volume with index i (kg/m^3-s),

MW_{H2O} = molecular weight of water vapor (18.016).

13.7 Transport of Decay Heat to Ultimate Heat Sink

HTGRs can be designed to transfer decay heat in a passive manner to heat sinks such as the atmosphere and the earth surrounding the reactor containment or building. This capability for passive cooling is in part due to the capability of a HTGR reactor core to endure temperatures as hot as 1900 K. Models are applied for calculating the transport of decay heat by conduction, radiation, and convection from the exterior surfaces of the reactor core to ultimate heat sinks such as the atmosphere and earth surrounding the reactor building. These models evaluate the capability of a reactor design to remove decay heat in a passive manner during accident such as the conduction cooldown accident. Structures in the path to the ultimate heat sink may include (1) reactor vessel, (2) upcomer, (3) downcomer, and (4) containment and surrounding earth. Decay heat is transported through these structures by conduction and between these structures by radiation and convection. RELAP5-3D© fluid transport models and radiation heat transfer models calculate the heat transfer at the surfaces of these structures. A two-dimensional (radial-axial) heat conduction model calculates the heat transfer through these structures. The MATPRO material property package[13-28] calculates the thermal conductivities and volumetric heat capacities of the various materials in the reactor vessel, upcomer, downcomer, containment, and any surrounding earth. Boundary conditions are applied to the heat conduction model that correspond with the heat transfer occurring by radiation and convection at the surfaces of the various structures in the reactor system. Thus the transfer of heat is modeled through the entire media from the center of the reactor core to the ultimate heat sink such as the atmosphere and the earth surrounding the reactor containment or building. A schematic of the modeling for the case of passive cooling only to containment and surrounding earth is shown in Figure 13-5. A schematic of the modeling for the case of passive cooling to the atmosphere, containment, and surrounding earth is shown in Figure 13-6. In this case, downcomer and upcomer structures define the path for the natural circulation of air from the atmosphere. The horizontal cross section of the upcomer may have two configurations. In the first configuration, the air flows upward through an annular flow path as shown in Figure 13-7. In the second configuration, the air flows upward through a series of individual structures arranged in a circle around the reactor vessel as shown in Figure 13-8. If the upcomer, downcomer, and containment have a square configuration instead of a circular configuration in a horizontal cross section, adjustments in the radii of these structures are made so the modeling approximates the overall heat transfer in the reactor system.

Models described in Section 13.4.2 calculate the convective heat transfer at the surfaces of the reactor core, reactor vessel, upcomer, downcomer, and containment. The models described below calculate the radiative heat transfer at the surfaces of these structures.

The heat flux due to radiation at the outer surface of the reactor core is calculated assuming the gas between the outer surface of the core and the inner surface of the vessel does not absorb any radiated heat. The heat flux is calculated by the equation

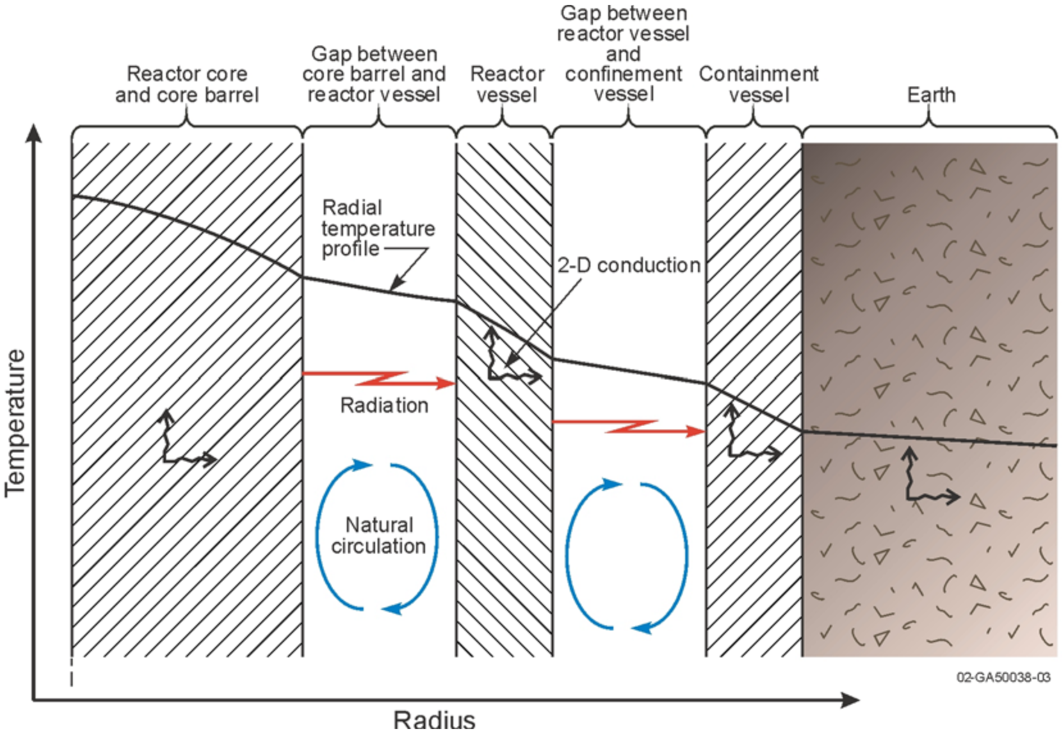
Reactor core and core barrel
Gap between core barrel and reactor vessel
Reactor vessel
Gap between reactor vessel and confinement vessel
Containment vessel
Earth
Radial temperature profile
2-D conduction
Radiation
Natural circulation
Temperature
Radius
02-GA50038-03

Figure 13-5. Schematic of heat transfer from reactor core to earth surrounding reactor.

$$q_{crad} = \sigma\left(\frac{1}{\frac{1}{e_c} + \left(\frac{R_c}{R_{vi}}\right)\left(\frac{1}{e_{vi}} - 1\right)}\right)(T_c^4 - T_{vi}^4) \tag{13-77}$$

where

q_{crad} = heat flux due to radiation at outer surface of reactor core (W/m^2),

σ = Stefan-Boltzmann constant (5.66840^{-8} W/m^2-K^4),

e_c = emissivity of outer surface of reactor core (unitless),

R_c = outer radius of reactor core (m),

R_{vi} = inner radius of reactor vessel (m),

e_{vi} = emissivity of inner surface of reactor vessel (unitless),

T_c = temperature of outer surface of reactor core (K),

T_{vi} = temperature of inner surface of reactor vessel (K).

The heat flux at the inner surface of the reactor vessel is calculated by the equation

$$q_{virad} = -\left(\frac{R_c}{R_{vi}}\right)q_{crad} \tag{13-78}$$

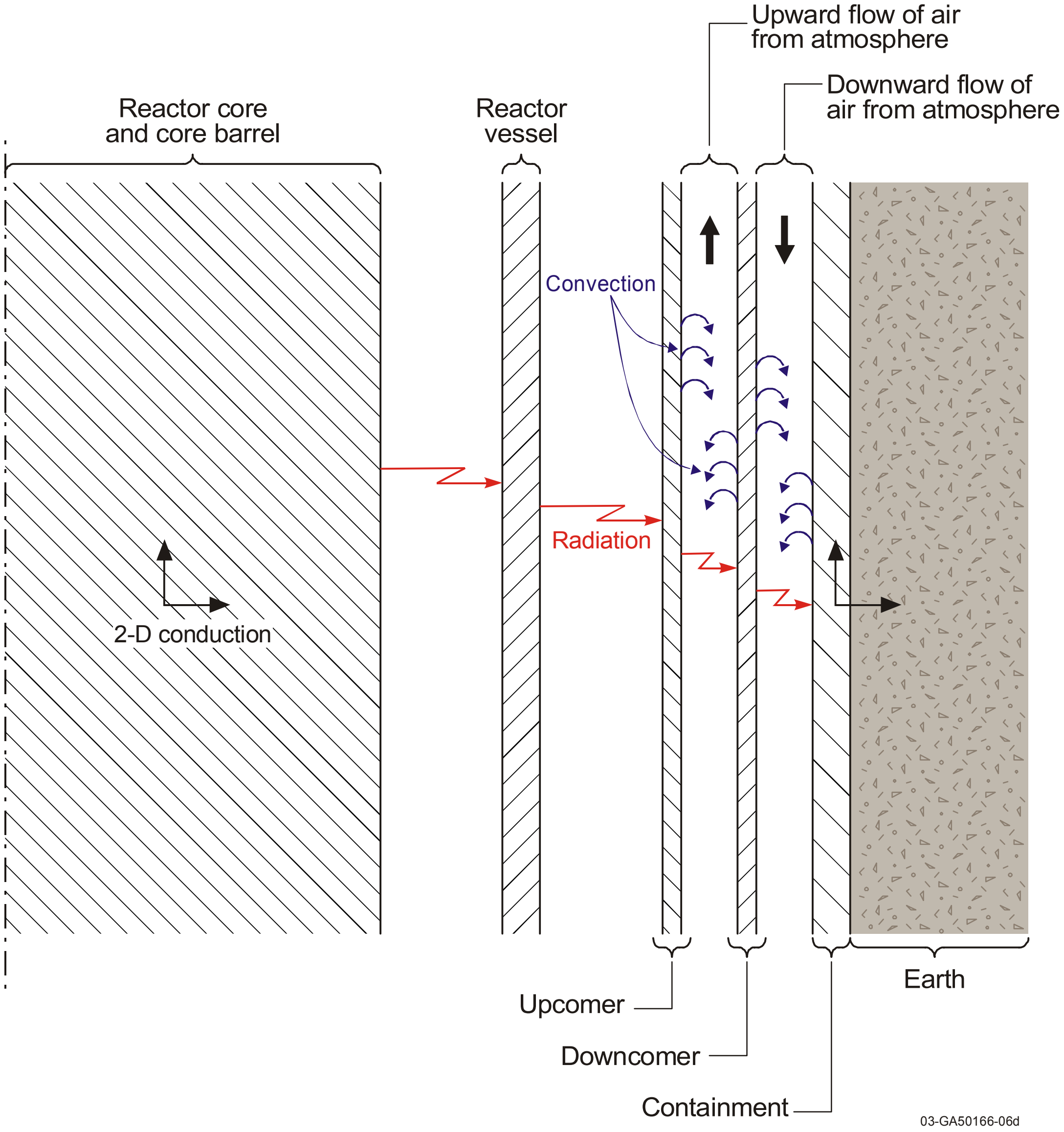
Upward flow of air from atmosphere
Downward flow of air from atmosphere
Reactor core and core barrel
Reactor vessel
Convection
Radiation
2-D conduction
Upcomer
Downcomer
Containment
Earth
03-GA50166-06d

Figure 13-6. Schematic of modeling for passive cooling to atmosphere, containment, and earth.

where

q_{virad} = heat flux due to radiation at the inner surface of the reactor vessel (W/m^2).

The radiative heat fluxes at other surfaces between the reactor vessel and containment are calculated using equations similar to Equations (13-77) and (13-78). For the case of a reactor system with no cooling of the reactor vessel by natural circulation of atmospheric air, radiative heat transfer is calculated between the outer surface of the reactor vessel and the inner surface of the containment. For the case of a reactor system with a downcomer and annular shaped upcomer for circulation of air from the atmosphere, radiative heat transfer is calculated between the outer surface of the reactor vessel and inner surface of the

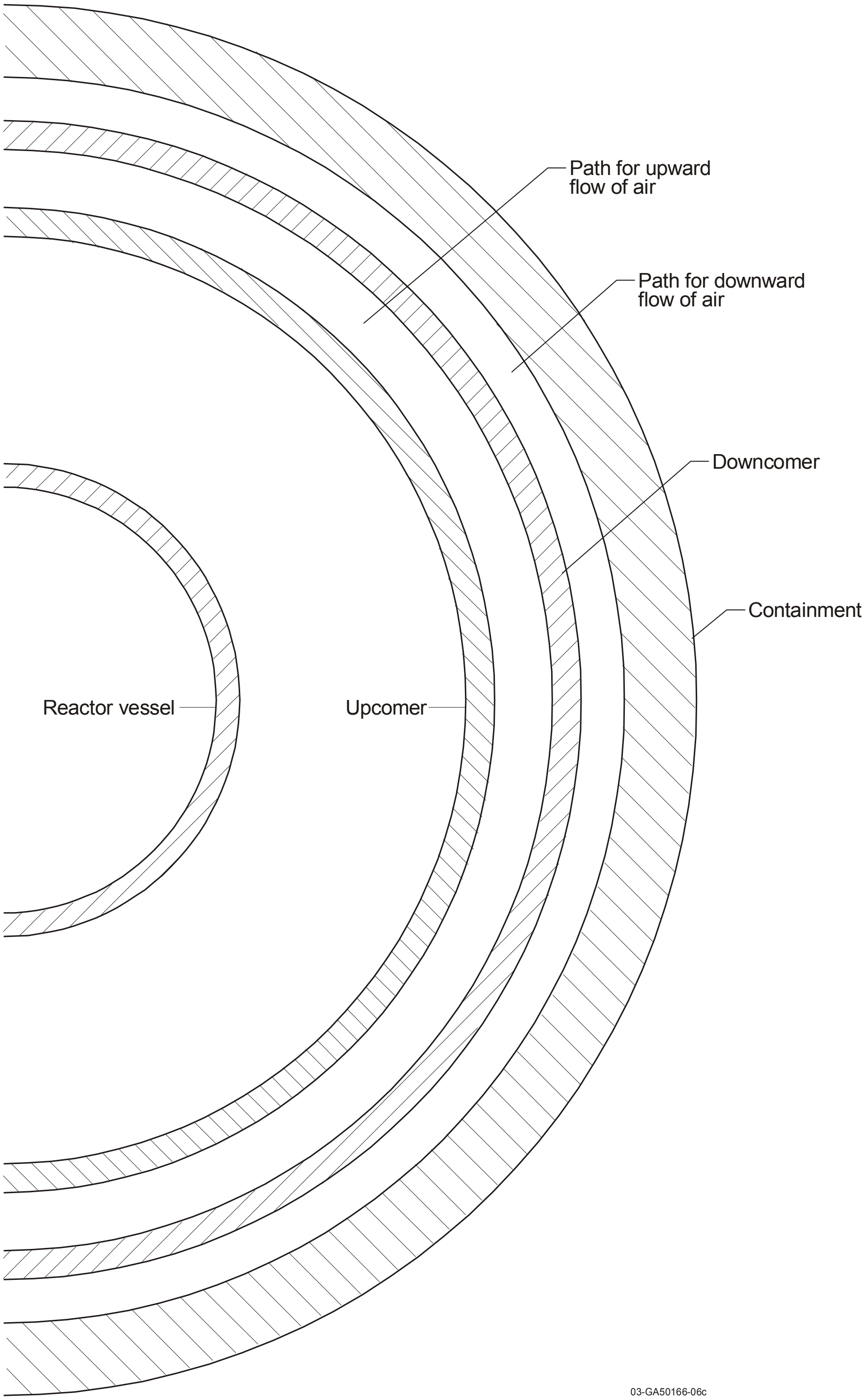
Path for upward flow of air
Path for downward flow of air
Downcomer
Containment
Reactor vessel
Upcomer
03-GA50166-06c

Figure 13-7. Horizontal cross section of upcomer and downcomer for annular shape of path for upward flow of air.

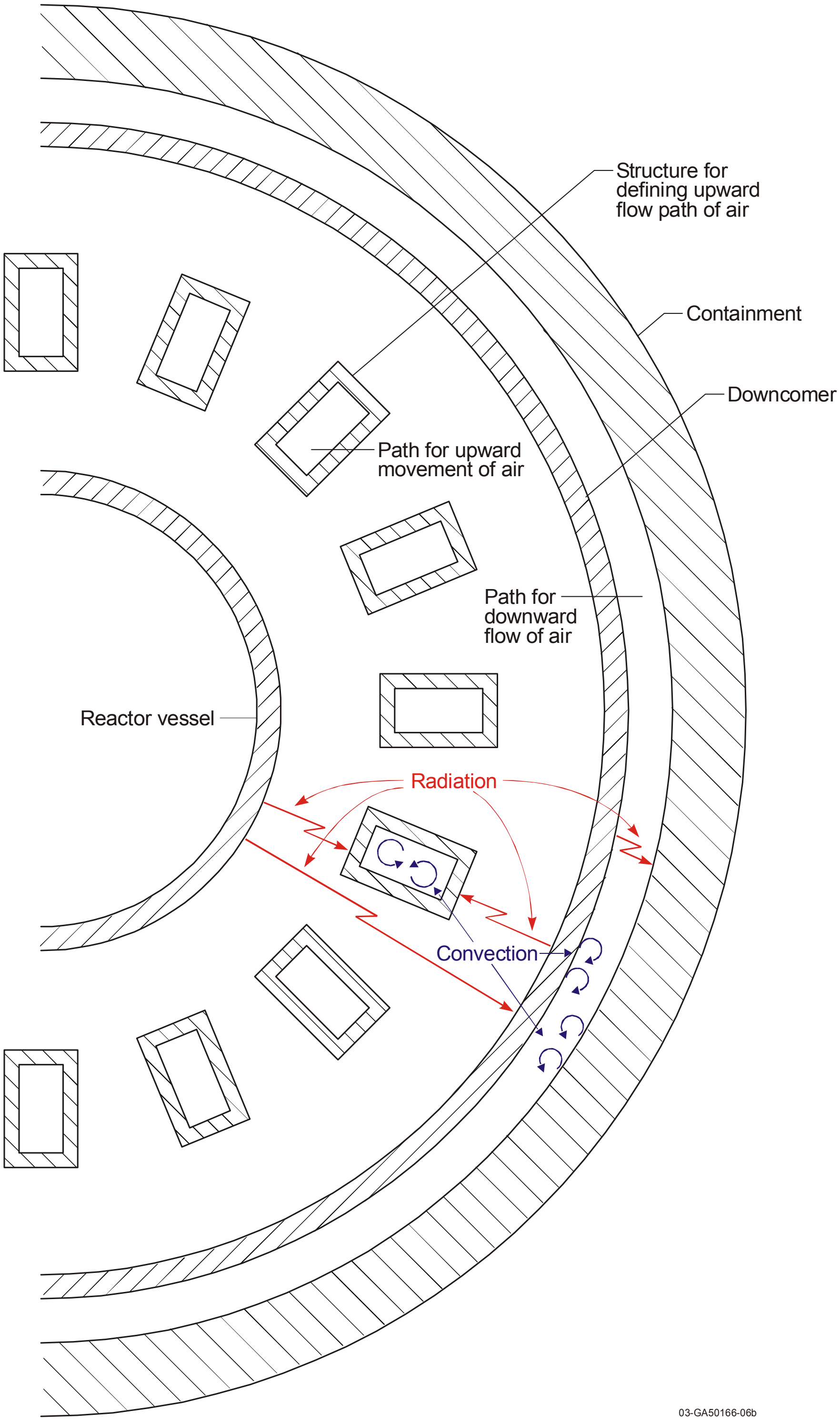
Structure for defining upward flow path of air
Containment
Downcomer
Path for upward movement of air
Path for downward flow of air
Reactor vessel
Radiation
Convection
03-GA50166-06b

Figure 13-8. Horizontal cross section of upcomer and downcomer for series of individual flow paths for upward flow of air.

upcomer, between the outer surface of the upcomer and inner surface of the downcomer, and between the outer surface of the downcomer and inner surface of the containment.

For the case of an upcomer composed of individual channels arranged in a series around the reactor vessel, radiative heat transfer is calculated between three pairs of surfaces as shown in Figure 13-9. The radiative heat flux at the outer surface of the reactor vessel is calculated by the equation

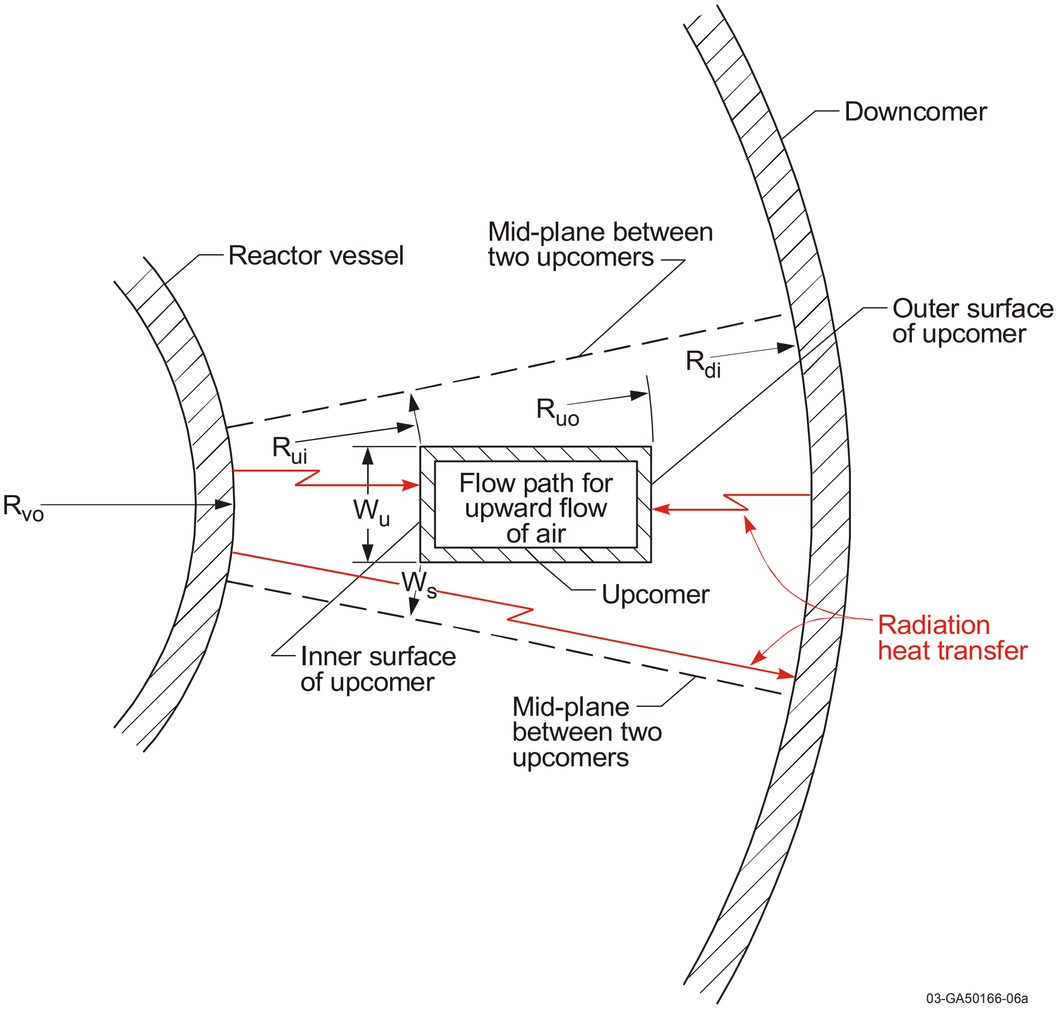
Downcomer
Reactor vessel
Mid-plane between two upcomers
Outer surface of upcomer
R_{di}
R_{uo}
R_{ui}
R_{vo}
W_u
Flow path for upward flow of air
W_s
Upcomer
Radiation heat transfer
Inner surface of upcomer
Mid-plane between two upcomers
03-GA50166-06a

Figure 13-9. Radiation heat transfer for case of individual upcomers arranged in series around reactor vessel.

$$q_{vo} = q_{vu1} + q_{vd1} \tag{13-79}$$

where

q_{vo} = average radiative heat flux at outer surface of reactor vessel (W/m^2),

q_{vu1} = radiative heat flux at outer surface of reactor vessel due to radiation between outer surface of reactor vessel and inner surface of upcomer (W/m^2),

q_{vd1} = radiative heat flux at outer surface of reactor vessel due to radiation between outer surface of reactor vessel and inner surface of downcomer (W/m^2).

The variable q_{vu1} in Equation (13-79) is calculated by the equation

$$q_{vu1} = \left(\frac{w_u}{w_s}\right)\sigma\left(\frac{1}{\frac{1}{e_{vo}} + \left(\frac{R_{vo}}{R_{ui}}\right)\left(\frac{1}{e_{ui}} - 1\right)}\right)(T_{vo}^4 - T_{ui}^4) \tag{13-80}$$

where

w_u = width of individual upcomer (defined in Figure 13-9) (m),

w_s = spacing between individual upcomers (defined in Figure 13-9) (m),

T_{vo} = temperature of outer surface of reactor vessel (K),

T_{ui} = temperature of inner surface of upcomer (K),

e_{vo} = emissivity of outer surface of reactor vessel,

e_{ui} = emissivity of inner surface of upcomer.

R_{vo} = radius of outer surface of reactor vessel (m),

R_{ui} = radius of inner surface of upcomer (m).

The variable q_{vd1} is calculated by the equation

$$q_{vd1} = \left(\frac{w_s - w_u}{w_s}\right)\sigma\left(\frac{1}{\frac{1}{e_{vo}} + \left(\frac{R_{vo}}{R_{di}}\right)\left(\frac{1}{e_{di}} - 1\right)}\right)(T_{vo}^4 - T_{di}^4) \tag{13-81}$$

where

T_{di} = temperature of inner surface of downcomer (K),

R_{di} = radius of inner surface of downcomer (m),

e_{di} = emissivity of inner surface of downcomer.

The radiative heat flux at the inner surface of the upcomer is calculated by the equation

$$q_{ui} = \left(\frac{R_{vo}}{R_{ui}}\right)q_{vu1} \tag{13-82}$$

where

q_{ui} = radiative heat flux at inner surface of upcomer (W/m^2).

The radiation heat flux at the inner surface of the downcomer is calculated by the equation

$$q_{di} = q_{vd1} + q_{ud1} \tag{13-83}$$

where

q_{di} = average radiation heat flux on inside surface of downcomer (W/m^2),

q_{ud1} = heat flux on inner surface of downcomer due to radiation between outer surface of upcomer and inner surface of downcomer (W/m^2).

The radiative heat flux on the outer surface of the upcomer is calculated by the equation

$$q_{uo} = \left(\frac{w_u}{w_s}\right)\sigma\left(\frac{1}{\frac{1}{e_{uo}} + \left(\frac{R_{uo}}{R_{di}}\right)\left(\frac{1}{e_{di}} - 1\right)}\right)(T_{uo}^4 - T_{di}^4) \tag{13-84}$$

The variable q_{ud1} is calculated by the equation

$$q_{ud1} = \left(\frac{R_{uo}}{R_{di}}\right)q_{uo} \tag{13-85}$$

13.8 Ingress of Air after Break in Coolant System

For a HTGR with gas turbomachinery in a different vessel than the reactor vessel, a break in one of the pipes connecting the two vessels may be regarded as a credible event. In the event of a break in a reactor without a containment filled with inert gas, air may enter the reactor core and provide oxygen for the oxidation of graphite in the core. For a conduction cooldown accident, the ingress of air begins with the diffusion of air into the reactor system from the location of a break. After the air has diffused to the top of the reactor vessel, the distribution of fluid densities in the reactor vessel allows a natural circulation path to develop and the ingress of air is greatly accelerated. A preliminary analysis of a PB HTGR indicated that the rate of flow of air into the reactor core is very small until the air has diffused from the location of the break to the top of the reactor vessel, and then a natural circulation loop may be initiated due to the elimination of the "bubble" of low density helium at the top of the vessel.[13-53] The natural circulation loop transports air into the reactor vessel relatively rapidly and may begin within nine hours after the pipe break.[13-13] This section describes the modeling used to calculate the diffusion of air into the region of the reactor core.

In the absence of chemical interaction or mixing, diffusion of a substance from one region to another within a single phase may be due to thermal diffusion, pressure diffusion, or molecular diffusion. Assuming that thermal and pressure diffusion are second order affects at best, the molecular diffusion can be expressed adequately by Fick's first law of diffusion. This law is expressed as:

$$\frac{\left(\frac{dm}{dt}\right)}{A} = -D_g\frac{\partial C_a}{\partial x} \tag{13-86}$$

where

dm/dt = mass flux (kg/s)

A = area of flow (m^2)

D_g = diffusion coefficient (m^2/s)

C_a = mass concentration (kg/m^3)

The diffusion coefficient, or diffusivity, is the proportionality constant between the flux density of the diffusing species, and the gradient of the concentration.

The general approach for the inclusion of the diffusion of a minority species, such as air or water vapor, through a working fluid, such as helium, will involve two steps. The first step will be modifications to model the transport, by diffusion only, of the minority species, and the second step will be modifications to model the transport of the working fluid in the reverse direction.

The situation being modeled is shown in Figure 13-10, and is represented by a series of hydrodynamic volumes with helium as the working fluid at one end and air as a minority specie at the other end. A relatively small amount of mass is transferred by diffusion during a hydrodynamic time step.

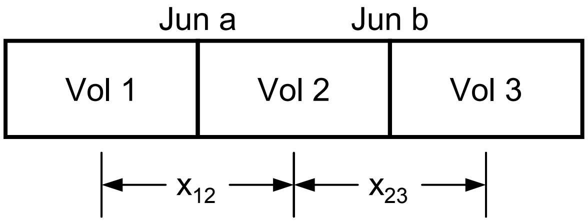

Figure 13-10. Definition of diffusion labels.

For the purposes of illustration, assume that Volume 1 above is filled with a working fluid such as pure He, and Volume 3 is filled with pure non-condensable, such as air. Based upon conservation of mass, the change in concentration of air in Volume 2 can be represented by the mass in-flux due to diffusion across junction b minus the mass out-flux due to diffusion across junction a, as in

$$\frac{m_2^{n+1} - m_2^n}{V_2} = \left(\frac{-D_a^n \left(\frac{m_2^n}{V_2} - \frac{m_1^n}{V_1} \right) A_a \Delta t}{V_2 \Delta x_{12}} \right) - \left(\frac{-D_b^n \left(\frac{m_3^n}{V_3} - \frac{m_2^n}{V_2} \right) A_b \Delta t}{V_2 \Delta x_{23}} \right) \tag{13-87}$$

where

m_2^{n+1} = mass of non-condensable in Volume 2 at time-step n+1,

m_1^n, m_2^n, m_3^n = mass of non-condensable in Volumes 1, 2, and 3, respectively, at time step n,

A_a, A_b = area of Junctions a and b, respectively,

V_1,V_2,V_3 = volume of hydrodynamic Volumes 1, 2, and 3,

$\Delta x_{12},\Delta x_{23}$ = distance from center of Volume 1 to center of Volume 2, and center of Volume 2 to center of Volume 3,

D_a,D_b = diffusion coefficient for properties at Junction a and b at time step n, respectively,

t = time (s).

It is recommended that the above explicit formulation be inserted into subroutine eqfinl, looping over all junctions in the loop. In order to avoid impacting the performance of this subroutine, it is recommended that the loop be protected by logical 'if' tests which verify that:

1. Junction mass flow by diffusion is below a (very small) hard-wired threshold, and

2. Non-condensable gas component is present in at least one of either the donor or donored volumes.

Considering diffusion only when mass-flow is near zero is appropriate because diffusion is a second order effect that would be overwhelmed by mass flows typically calculated by RELAP5-3D©. The very long time constants for transport by diffusion will allow the previous equation to be used explicitly in 'eqfinl'. Once the diffusion transport rate of the minor specie has been calculated, the masses can be moved into the RELAP5-3D© database through the RELAP5-3D© variables 'gaman' (noncondensable generation rate per unit volume), and 'enthn' (internal energy of the noncondensable source).

Semi-empirical equations are available for calculating the binary diffusivity of a mixture of two gases at low pressure. These equations have been described previously in Section 5 [Equations (13-52) through (13-55)].

13.8.1 Potential Limitations of Minority Specie Diffusion Modeling

There are two potential concerns in the implementation of modifications to model diffusion of a minority specie non-condensable through RELAP5-3D© volumes. These concerns are not possible to address at the theoretical level, but can be examined after testing. The first concern lies in the assumption of the validity of an explicit correlation for diffusion transport. This assumption is only valid while the concentration of the minority specie varies slightly during a time step. This assumption can be evaluated during developmental testing and modified as indicated by the test results.

The second potential concern lies in the numerics of RELAP5-3D©, and actually applies to the opposite end of the spectrum from the previous concern, in that it applies to the transport of very minor masses of non-condensable. If both the hydrodynamic time step and the non-condensable concentration in the donor volume is sufficiently small, then the initial mass transported into a volume will lie below the threshold quality for acceptance as non-condensable existing in the donored volume. One of the acceptance tests performed on the model should be to either lower the threshold quality before a non-condensable is accepted in a new volume, or to 'seed' the intermediate volumes with a small amount of non-condensable.

13.8.2 Diffusion of Working Fluid

In order to track the diffusion of a working fluid, which is helium in a HTGR, a term for transport by diffusion needs to be added to the field equations. Just as in the case of the diffusion of the minority specie, this task can be simplified by the fact that diffusion is significant only when the reactor system is stagnant and when the time scale of the diffusion is large compared with the size of the hydrodynamic time step. In this case, transfer of momentum is insignificant and the only parameter of interest is the mass transfer of each constituent into and from the volume of interest.

The calculation of the mass of working fluid transferred by diffusion is performed in a manner identical to the previous section. The insertion of this source term into the RELAP5-3D© database can be done in a manner identical to that of the non-condensable source term, 'gaman'. This requires that the variable 'sourcp' be modified in subroutine 'preseq', and that source term variables 'sourca', 'sourcm', and 'sourcg' be modified in subroutine 'vexplt'.

13.8.3 Limitation on Time Step Due To Diffusion

Depending on the mesh size, it may be necessary to limit the hydrodynamic time step due to the explicitness of the correlations. The time step must be limited to[13-54]

$$\Delta t \le \frac{1}{2}\frac{(\Delta x)^2}{D_g} \tag{13-88}$$

where

Δt = time step (s),

Δx = mesh interval (m), and

D_g = diffusion coefficient (m^2/s).

This limitation should be applied in subroutine 'courn1'.

13.9 References

13-6. Gittus, J. H., “The ESKOM Pebble Bed Modular Reactor,” *Nuclear Energy*, **38**, No. 4, pages 215-221, August 1999.

13-7. Siefken, L. J., E. W. Coryell, C. B. Davis, and E. A. Harvego, *Transient Analysis Needs for Generation IV Reactor Concepts*, INEEL/INT-2001-01228, September 2001.

13-8. Bennett, R. G., *Nuclear News*, pages 33-34, August, 2002.

13-9. US DOE, *Evaluation of the Gas Turbine Modular Helium Reactor*, DOE/GT/MHR-100002, Gas-Cooled Reactor Associates, San Diego, CA, February 1994.

13-10. Kunitomi, K., et al., “Conceptual Design of a 50-MW Severe-Accident-Free HTR and the Related Test Program of the HTTR,” *Nuclear Technology*, **123**, September 1998.

13-11. Borton, K., *Nuclear News*, pages 35-36, August 2002.

13-12. Rodriguez, C., and A. Baxter, “The Value of Helium-Cooled Reactor Technologies for Transmutation of Nuclear Waste,” *9th International Conference on Nuclear Engineering*, Nice, France, April, 2001.

13-13. Nicholls, D., “The Pebble Bed Modular Reactor,” *Nuclear News*, pages 25-40, September 2001.

13-14. Corradini, M. L., et al., *SCDAP/RELAP5 Independent Peer Review*, LA-12481, January 1993.

13-15. Carlson, K. E., R. A. Riemke, S. Z. Rouhani, R. W. Shumway, and W. L. Weaver, *RELAP5/MOD3 Code Manual, Volume III: Developmental Assessment Problems (DRAFT)*, NURUG/CR-5535, EGG-2596, June 1990.

13-16. Shieh, A. S., V. H. Ransom, and R. Krishnamuthy, *RELAP5/MOD3 Code Manual: Validation of Numerical Techniques in RELAP5/MOD3*, NUREG/CR-5535, EGG-2596, Vol. 6, October 1994.

13-17. The RELAP5 Development Team, *RELAP5/MOD3 Code Manual, Vol. IV: Models and Correlations*, NUREG/CR-5535, INEL-95/0174, August 1995.

13-18. The RELAP5-3D$^{©}$ Development Team, *RELAP5-3D$^{©}$ Code Manual*, INEEL-EXT-98-00834, Revision 2.0, July 2002.

13-19. Siefken, L. J., E. W. Coryell, E. A. Harvego, and J. J. Hohorst, *SCDAP/RELAP5/MOD3.3 Code Manual: Assessment of Modeling of Reactor Core Behavior During Severe Accidents*, NUREG/CR-6150, Vol. 5, Rev. 2, INEL-96/0422, January 2001.

13-20. Moormann, R., “Graphite Oxidation Phenomena during Massive Air Ingress Accidents in Nuclear High Temperature Gas Cooled Reactors with Pebble Bed Core,” *Ber. Bunsenges. Phys. Chem.*, 87, pages 1086-1090, 1983.

13-21. Kadak, A. C., “The MIT Modular Pebble Bed Reactor Project,” *Seminar on HTGR Applications and Development*, Institute of Nuclear Engineering Technology, Tsinghua University, Beijing, China, March 19-21, 2001.

13-22. Oh, C. H., B. J. Merrill, R. L. Moore, and D. A. Petti, “Air Ingress Analysis on a High Temperature Gas-Cooled Reactor,” *2001 ASME International Mechanical Engineering Congress and Exposition*, New York, New York, November 11-16, 2001.

13-23. Zuying, G., and Shi Lei, “Thermo-Hydraulic Transient Analysis of HTR?10,” Institute of Nuclear Energy Technology, Tsinghua University, Beijing, China, *Seminar on HTGR Application and Development*, Beijing, China, March 19-21, 2001.

13-24. Fletcher, C. D., *Computational Techniques for Fluid Dynamics, Volume 1*, Springer-Verlag, pages 107-121, 1988.

13-25. Siefken, L. J., E. W. Coryell, E. A. Harvego, and J. J. Hohorst, *SCDAP/RELAP5/MOD3.3 Code Manual: Modeling of Reactor Core and Vessel During Severe Accidents*, NUREG/CR-6150, Vol. 2, Rev. 2, INEL-96/0422, January 2001.

13-26. No, H. C., “Description of PBR System Simulation Code,” MIT, 2001.

13-27. Tanaka, M., and F. Chisaka, “Effective Thermal Conductivities of Discontinuous and Continuous Solid Systems,” *Kagaku Kogaku Ronbunshu*, **16**, pages 168-173, 1990, translated to English in Scripta Technica, Inc., 1991.

13-28. Siefken, L. J., E. W. Coryell, E. A. Harvego, and J. J. Hohorst, *SCDAP/RELAP5/MOD3.3 Code Manual: MATPRO - A Library of Materials Properties for Light-Water-Reactor Accident Analysis*, NUREG/CR-6150, Vol. 4, Rev. 2, INEL-96/0422, January 2001.

13-29. Niessen, H., and S. Ball, *Heat Transport and Afterheat Removal for Gas Cooled Reactors Under Accident Conditions*, IAEA-TECDOC-1163, International Atomic Energy Agency, 2000.

13-30. General Atomics, *Graphite Design Manual*, GA Document 906374, Issue A, 1982.

13-31. Davis, C. B., Personal communication, INEEL, December 2001.

13-32. Holman, J. P., *Heat Transfer*, McGraw-Hill Book Company, New York, New York 1981.

13-33. Bird, R. B., W. E. Stewart, and E. N. Lightfoot, *Transport Phenomena*, John Wiley & Sons, New York, New York 1960.

13-34. Chung, M., and I. Catton, “Post-Dryout Heat Transfer in a Multi-Dimensional Porous Bed,” *Nuclear Engineering and Design*, **128**, pages 289-304, 1991.

13-35. Tung, V. X., “Hydrodynamic and Thermal Aspects of Two-Phase Flow Through Porous Media,” Ph. D. Thesis, University of California, Los Angeles, 1988.

13-36. Tung, V. X., *Journal of Heat Transfer*, 1993.

13-37. Edwards, D. K., V. E. Denny and A. Mills, Jr., *Transfer Processes*, McGraw-Hill Book Co., New York, New York, 1979.

13-38. Dittus, F. W., and L. M. K. Boelter, "Heat Transfer in Automobile Radiators of the Tubular Type," *Publications in Engineering*, **2**, University of California, Berkeley, pages 443-461, 1930.

13-39. The SCDAP/RELAP5-3D© Code Development Team, *SCDAP/RELAP5-3D© Code Manual*, INEEL/EXT-02-00589, May 2002.

13-40. Katscher, W., and R. Moormann, “Graphite Corrosion Under Severe HTR Accident Conditions,” *IAEA Specialists Meeting on Graphite Component Structural Design*, JAERI, Tokai-mura, Japan, September 8-11, 1986.

13-41. Moormann, R. “Effect of Delays in Afterheat Removal on Consequences of Massive Air Ingress Accidents in High-temperature Gas Cooled Reactors,” *Journal of Nuclear Science and Technology*, **21** (11), pages 824-835, November, 1984.

13-42. Olander, D. R., “Materials Chemistry and Transport Modeling for Severe Accident Analyses in Light-Water Reactors, I: External Cladding Oxidation,” *Nuclear Engineering and Design,* **148**, pages 253-271, 1994.

13-43. Viskanta, R., R. R. Hobbins, and H. Esmaili, *Peer Review of the Modeling of Hydrogen Uptake in Fuel Rod Cladding during Severe Accidents*, ERI/NRC 98-204, USNRC Contract No. 04-92-045, October 1998.

13-44. Scherer, W., and H. Gerwin, *Scenarios of Hypothetical Water and Air Ingress in Small Modular HTGRs*, IAEA-TECDOC-784, 1994.

13-45. Schaaf, T., W. Froehling, H. Hohn, and S. Struth, “The NACOK Experimental Facility for Investigating an Air Ingress into the Core of a High Temperature Reactor,” *Kerntechnik,* **63**, 1998.

13-46. Takeda, T., et al., “Analysis of Air Ingress Process During the Primary-Pipe Rupture Accident of the HTGR,” JAERI-Conf-96-010, *Proceedings of the 3rd JAERI Symposium on HTGR Technologies*, Oarai, Japan, February 15-16, 1996.

13-47. Davis, C. B., Personal communication, INEEL, March 2003.

13-48. Russell, A., *Production Test IP-725 Increased Graphite Temperature Limit: F Reactor*, RL-EA-14, General Electric Co., Hanford Atomic Products Operation, December 1964.

13-49. Engle, G. B., *Assessment of Grade H-451 Graphite for Replaceable Fuel and Reflector Elements in HTGR*, GA-A14690, UC-77, General Atomics Company, December, 1977.

13-50. Malinauskas, A. P., "Kinetics of the Steam-Graphite Reaction," *Chemical Engineering Progress,* **104**, Vol. 66, 1970.

13-51. Hinssen, H. K., W. Katcher, and K.-J Loenissen, *Experimental Investigation of Corrosion of IG-110 Graphite by Steam*, Juel-Spez-578, FORSCHUNSZENTRUM Juelich, Germany, July, 1990.

13-52. Hinssen, H. K., et al., *Korrosion von graphitischen Hochtemperatureacktor-Werkstoffen mit Wasserdampf/Helium Mischungen im Druchbereich von 2-55 bar bei Temperaturen von 900-1150°C (1173-1423 K)*, Juel-2747, FORSCHUNSZENTRUM Juelich, Germany, 1989.

13-53. Moore, R. L., Personal communication, INEEL, December 2001.

13-54. Roache, P. J., *Computational Fluid Dynamics*, Hermosa Publishers, 1976